Geological Survey of Canada Open File 5643

REMOTE PREDICTIVE MAPPING:
An Aid for Northern Mapping

Edited by J.R. Harris

2008

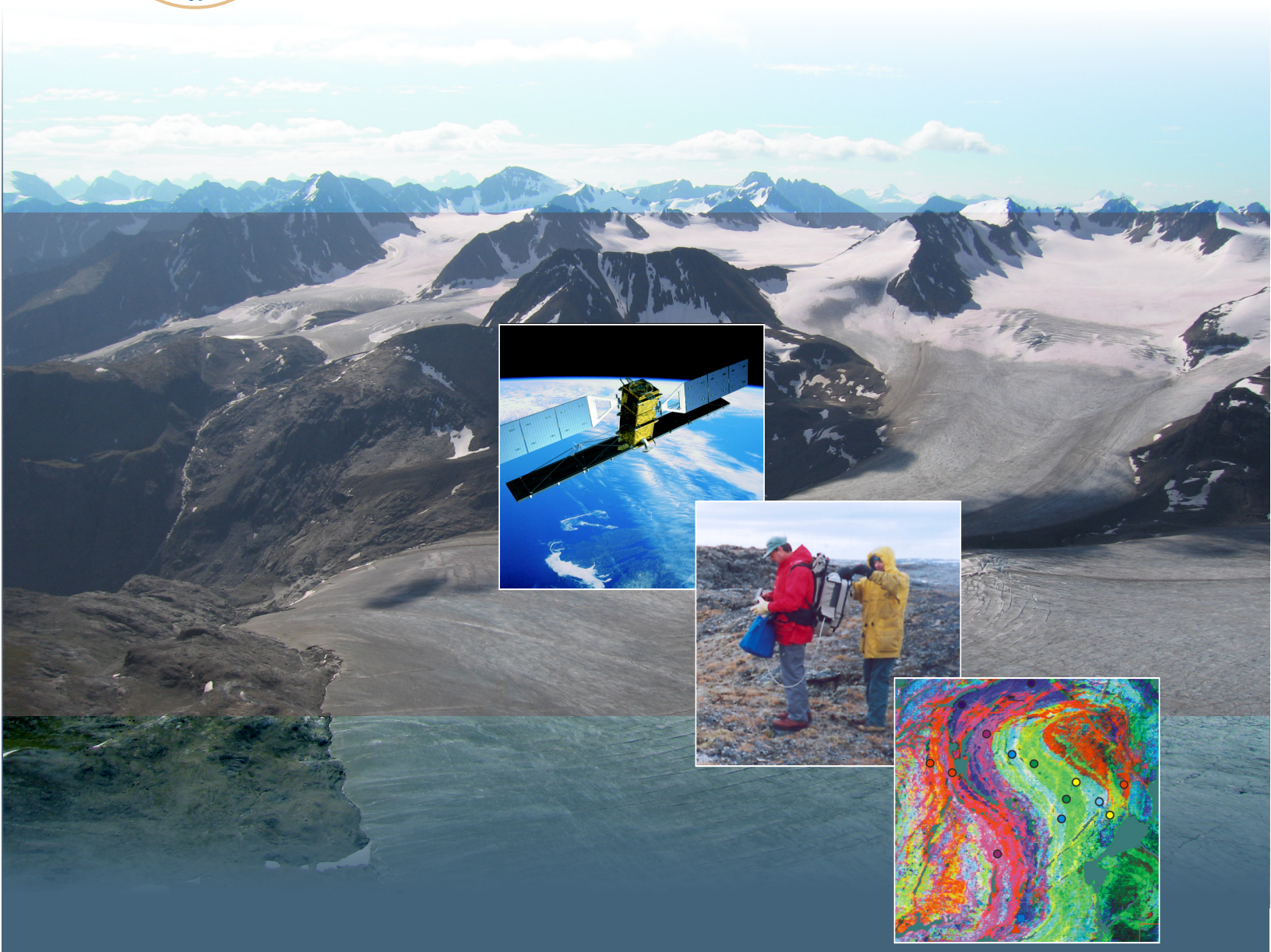

Natural Resources Canada
Ressources naturelles Canada

Canada

Geological Survey of Canada
Open File 5643

REMOTE PREDICTIVE MAPPING:
AN AID FOR NORTHERN MAPPING

J. R. Harris (Editor)

Geological Survey of Canada, Earth Sciences Sector, 601 Booth Street, Ottawa, Ontario K1A 0E8

J. R. Harris (editor)
2008: Remote Predictive Mapping: An Aid for Northern Mapping; Geological Survey of Canada, Open File 5643, 1 CD-ROM.

Open files are products that have not gone through the Geological Survey of Canada's formal publication process.

©Her Majesty the Queen in Right of Canada 2008
Available from:
Geological Survey of Canada
601 Booth Street
Ottawa, Ontario K1A 0E8

TABLE OF CONTENTS

CHAPTER 1. Introduction

J.R. Harris

What is RPM 1
Why RPM Is Needed 1
Basics 2
Platforms and Resolution 2
Manual Format 4
Acknowledgements 4

CHAPTER 2. Philosophy of Remote Predictive Mapping

J.R. Harris, E.M. Schetselaar, T. Lynds and E.A. de Kemp

Introduction 5
A Seven Step Method for Remote Predictive Mapping 6
Field Logistics and Planning 22
Organizational Aspects of Remote Predictive Mapping 25
Concluding Remarks 25
Acknowledgements 26
References 26

CHAPTER 3. Geophysics

M. Pilkington, P.B. Keating, and M.D. Thomas

Theoretical Principles 29
Mapping Applications of Gravity and Magnetic Data 29
Data Sources 29
Examples of Potential Field Maps and Their Utility 31
Summary 40
References 41
General Background Reading 42
Appendix 3-1. Rock Properties 43
Appendix 3-2. General Features of Potential Field Maps 47
Appendix 3-3. Shapes of Gravity and Magnetic Anomalies 51

CHAPTER 4. Gamma-Ray Spectrometry

K. Ford, J.R. Harris, R. Shives, J. Carson, and J. Buckle

Introduction 53
Data Sources 56
Interpretation 57
Data Visualization and Processing 62
Conclusions 96
References 96

CHAPTER 5. Optical Remote Sensing

J.R. Harris and L. Wickert

Theoretical Principles 99
Data 106
Data Interpretation for Geological Applications 111
Processing 122
References 134
Digital References 134

CHAPTER 6. Radar Remote Sensing

J.R. Harris, E. Grunsky, and V. Singhroy

Theoretical Principles 135
Data 138
Data Products and Processing 147

References 155
Appendix 6-1. Application of High-Resolution Radar Image Fusion for Mineral Exploration and Mapping 157

CASE STUDIES

Case Study 1. Snowbird Lake, Northwest Territories

J.R. Harris, E. Martel, M. Currie, K. Pierce, M. Pilkington, and P. Keating

Introduction 161
Objectives 161
Data 162
Integration 163
Field Logistics and Planning 169
Evaluation of the Remote Predictive Mapping Process 171
References 171

Case Study 2. LANDSAT, Magnetic, and Topographic Data for Regional Lithological Mapping, southeast Baffin Island

J.R. Harris, E.M. Schetselaar, E. de Kemp, and M.R. St-Onge

Introduction 173
Objectives 173
Data 175
General Conclusions and Recommendations for Remote Predictive Mapping 179
References 182

Case Study 3. The Advantages of High-Resolution Spectral and Spatial Hyperspectral Data for Lithological Mapping: An Example from southeast Baffin Island

J.R. Harris and M. St-Onge

Introduction 183
Objectives 183
Data 184
Summary 188
References 189

Case Study 4. Application of Remotely Sensed Data for Structural Mapping, southwest Baffin Island, Nunavut

J.R. Harris, M. Sanborn-Barrie, and M. St-Onge

Introduction 191
Data 191
Data Processing 193
Results 193
Summary and Discussion 200
References 201

Case Study 5. Application of Gamma-Ray Spectrometer Data for Lithological Mapping in a Cordilleran Environment, Sekwi Region, Northwest Territories

J.R. Harris, K. Ford, B. Charbonneau, and J. Buckle

Introduction 203
Objectives 203
Data 203
Data Processing and Integration 206
Results 207
Discussion and Implications for Remote Predictive Mapping 222
References 223

Case Study 6. Surficial Mapping of northern Baffin Island using LANDSAT and Topographic Data

O. Brown, J.R. Harris, and D. Utting

Introduction 225

Objectives 225
Data 225
Discussion and Implications for Remote Predictive Mapping 230
References 231

Case Study 7. Classification of Remotely Sensed Imagery for Surficial Geological Mapping in Canada's North

J.R. Harris, E. Grunsky, and I. McMartin

Introduction 233
Observations 233
Data 236
Discussion and Implications for Remote Predictive Mapping 243
References 244

Case Study 8. Geological Mapping Derived from Topography

W.A. Morris, H. Ugalde, H. Slavinski, and K. Markham

Abstract 245
Introduction 245
New Data Acquisition 246
Tools for Interpolating Digital Elevation Models 248
Examples of Topography-Derived Geological Mapping 250
Summary 256
References 257
Websites for Topographic Data 259

Case Study 9. Remote Predictive Mapping Case Study of the Boothia Mainland Area, Nunavut, Canada

E.M. Schetselaar and J.J. Ryan

Abstract 261
Introduction 261
The Boothia Integrated Geoscience Project 261
General Geology 261
Remote Predictive Mapping Methodology 262
Geological Image Interpretation Results before the 2005 Fieldwork (1st RPM Iteration) 269
Geological Fieldwork and Mapping Results after the 2005 Fieldwork (2nd RPM Iteration) 273
Remote Predictive Mapping Accuracy Assessment 276
Conclusions 278
Acknowledgements 279
References 280

Case Study 10. Lithological Mapping using ASTER, Belcher Islands, Nunavut

L.M. Wickert, P. Budketwitsch, and W.A. Morris

Introduction 283
Study Objectives 283
Geology 284
Data 285
Conclusions and Recommendations 294
Acknowledgements 295
References 295

POWERPOINT PRESENTATIONS

Chapter 2

Remote Sensing for Geology - An Introduction
[PowerPoint_Presentations\Chapter2\Remote_Sensing_for_Geology.ppt]
J.R. Harris

Chapter 3

Application of Magnetic Data to Geological Mapping and Mineral Exploration
[PowerPoint_Presentations\Chapter3\Application_of_Magnetic_Data.ppt]
P. Pilkington, P.B. Keating, and M.D. Thomas

An Exercise in Interpreting Magnetic Maps
[PowerPoint_Presentations\Chapter3\Interpreting_Magnetic_Maps.ppt]
M.D. Thomas

Chapter 4

Application of Gamma-Ray Spectrometer Data to Lithological Mapping
[PowerPoint_Presentations\Chapter4\Application_of_Gamma-Ray_Data.ppt]
J.R. Harris, K. Ford, P. Ponomarev, G. Bernius, and L. Dredge

Application of Gamma-Ray Spectrometry and Magnetic Data to Mineral Exploration, NATGAM (Gamma-Ray/Mag) Surveys

Part 1. Theory
[PowerPoint_Presentations\Chapter4\NATGAM_Part1_Theory.ppt]

Part 2. Applications
[PowerPoint_Presentations\Chapter4\NATGAM_Part2_Application.ppt]
R.B.K. Shives

Chapter 5

Optical Remote Sensing
[PowerPoint_Presentations\Chapter5\Optical_Remote_Sensing.ppt]
J.R. Harris

Hyperspectral Remote Sensing: A New Tool for Geological Mapping in Canada's North
[PowerPoint_Presentations\Chapter5\Hyperspectral_Remote_Sensing.ppt]
J.R. Harris, P. Ponomarev, M. Peshko, M. St-Onge, and P. Budkewitsch

Geological Mapping in Arctic Canada: A Review of Hyperspectral Remote Sensing Applications
[PowerPoint_Presentations\Chapter3\Hyperspectral_Remote_Sensing_in_Arctic_Canada.ppt]
L. Wickert, P. Budkewitsch, J.R. Harris, and B. Morris

Remote Predictive Mapping using ASTER: A Users' Guide
[PowerPoint_Presentations\Chapter5\RPM_ASTER_Users_Guide.ppt]
L. Wickert

Chapter 6

Radar Remote Sensing
[PowerPoint_Presentations\Chapter6\Radar_Remote_Sensing.ppt]
J.R. Harris

The Use of Multibeam RADARSAT-1 for Terrain Mapping in Alberta
[PowerPoint_Presentations\Chapter6\Multibeam_RADARSAT-1.ppt]
E. Grunsky

CHAPTER 1. Introduction

J.R. Harris
Geological Survey of Canada, 615 Booth Street, Ottawa, Ontario K1A 0E9
Corresponding author's email: Jeff.Harris@NRCan.gc.ca

WHAT IS RPM?

The remote predictive mapping method (RPM) simply involves deriving geological information from any available geoscience data. In many cases, the data can have been acquired remotely. These data may include sensing devices that measure a variety of properties of the Earth's surface and subsurface. The properties may include magnetic total field (from which magnetic susceptibility can be derived) measured by a magnetometer, radioelement emission measured by a gamma-ray spectrometer, density variations measured by a gravimeter, visible and infrared spectral reflectance measured by various optical and infrared sensors, emitted heat measured by a thermal radiometer, microwave backscatter by a radar, and terrain height measured by an altimeter or extracted from airphotos. These parameters can be useful alone or in combination for producing a remote predictive geologic map or a series of predictive maps. Field data, if available, can be incorporated into the RPM process to aid, verify, and geologically calibrate the interpretations made from the geoscience data.

The method of information extraction may involve photogeological interpretation of enhanced and/or fused images derived from the various data types or computer-assisted techniques that are useful for the identification of spectral and spatial patterns in the data. The output is most commonly a map showing predicted lithological units, structures, and suggested field traverses or a series of maps that show predicted units (bedrock, surficial, tectonic, etc.), various geological structures (faults, lineaments, contacts, fold axes glacial flow indicators, etc.), bedrock outcrop, and areas in which to focus field mapping. These maps can comprise a series of layers within a Geographical Information System (GIS) and be integrated with field mapping to assist in constructing a traditional geological map. In some cases, depending on the method(s) used to generate the map, a measure of uncertainty (or confidence) in the interpretation is also included. The predictive map or series of maps are by no means 'end products' but are intended to help assist, guide, and plan field-mapping campaigns, as well as assist in the production of the 'final' geological map. In cases where no existing geological information (or very minimal) exits, RPM maps serve as a first-order source for basic geological information and provide basic regional geological information with which to base future mapping or exploration programs. In areas where basic geological information exits, these maps may show areas where the predicted geology agrees and/or disagrees with the existing information. Both of these scenarios are important, as areas of agreement confirm what has been mapped traditionally and areas of disagreement point to areas that may require further field mapping and study. These maps can also be used in conjunction with field observations to build a geological map interactively (i.e. 'on the fly') while in the field. These predictive maps can also be useful for planning a field campaign by providing information on areas where more detailed mapping is required, areas of bedrock outcrop and/or wetlands, and areas where detailed traverses could be undertaken.

The RPM method differs from current methods for mapping the North, which traditionally relied on a homogeneous grid of traverses spaced 1 to 5 km apart over the area of interest regardless of the complexity of geology and supplemented with the interpretation of air photos. The advantage of RPM maps is that they can show areas that are geologically homogeneous as well as those that are heterogeneous, allowing more field emphasis to be placed on the complex terrain. In addition, the signatures that have been extracted from various geoscience data sets, over an area that has been verified (mapped), can be used to help predict areas with similar geology where mapping is not possible.

The RPM philosophy is nothing new! It follows the 'light-table' approach that has always been used by geologists. The RPM process involves compiling all available data from existing sources, studying the relationships between the data, and selecting the target areas for mapping and/or exploration from the integrated data. The difference is that more high-resolution digital (spectral and spatial) data and processing tools (GIS, image analysis, etc.) are now available to facilitate the compilation, integration, and analysis process.

WHY RPM IS NEEDED?

Mapping in the North is obviously an expensive proposition due to the remoteness, lack of infrastructure, logistical problems, and the generally short mapping season. Remote predictive mapping affords the opportunity to analyze and interpret all the existing geoscience data and make a 'best guess' at the geological conditions before embarking on fieldwork. These predictive maps can focus field activities and provide a

Harris, J.R., 2008, Introduction, Chapter 1 *in* Remote Predictive Mapping: An Aid for Northern Mapping, (ed.) J. R. Harris; Geological Survey of Canada, Open File 5643, p. 1-4.

base of information with which to build upon in accompanying mapping campaigns. Furthermore a predictive map can be re-evaluated and fine-tuned based on results from subsequent field mapping.

BASICS

Remote predictive mapping involves the use of a sensor that measures some property of the Earth's surface while not in direct contact with the surface. Magnetic data measures the magnetic susceptibility of the Earth's crust and can provide information on lithology, geological structure, depth to basement rocks, and alteration and/or mineralization. Gravity data records density variations, which can provide information on the type and distribution of various lithologies and major structures. Gamma-ray spectrometry provides information on the distribution of uranium, thorium, and potassium, which are elements common in many major rock-forming minerals as well as accessory minerals. Thus gamma-ray data can provide information on both surficial and bedrock lithologies as well as certain alteration styles (i.e. potassic). Magnetic and gravity data provide both surface and subsurface information, whereas gamma-ray spectrometry measures only what is emitted from the first few centimetres of the Earth's surface. Gamma-ray emission is prone to absorption by water and any surface feature containing water (wetlands, glacial sediments, etc.). However, experience has shown that given the right surficial and geological conditions, gamma-ray spctrometry is very useful for bedrock mapping.

Spectral information on specific rocks and minerals, as wells as geological structures, can be acquired by optical remote sensing, which involves the visible and reflected infrared portions of the electromagnetic (EM) spectrum. The basis of optical remote sensing is gathering information on the Earth's surface using reflected solar energy partitioned into a number of wavelengths ranging from the visible (0.4 μm), through the visible near infrared (~0.8–1.5 μm; VNIR), to the shortwave infrared (~1.5–2.5 μm; SWIR). Optical remote sensing, like gamma-ray spectrometery, is a surface sensing technique. Thus when used for bedrock mapping, vegetation and glacial cover can obscure the underlying lithology. Nevertheless, it is a very useful source of information for surficial mapping studies. In many cases, bedrock information is extracted from a combination of topographic, vegetation, and surficial patterns as they relate to the underlying bedrock. Many factors will determine the quantity and quality of the geological information that can be extracted from optical sensors. These include, among others, spectral and spatial resolution of the specific sensor, atmospheric conditions, geographic location, and season, as well as geological, surficial, and biophysical conditions. From a practical point-of-view, optical remote sensing is more useful for bedrock mapping in arid environments with little vegetation. Canada's North is a better environment for optical remote sensing than boreal regions of Canada due to the general lack of vegetation cover (with the exception of lichens). Recent emphasis on optical sensors with higher spectral and spatial resolution (hyperspectral) hold much promise for geological mapping tools.

Thermal remote sensing involves detecting radiant emission (heat) from the Earth and since rocks are characterized by different thermal properties (absolute temperature, emissivity, etc.), thermal remote sensing provides another source of geological information. Thermal sensors detect much longer wavelengths, typically from 8 to 14 μm, and can operate both day and night. However, the same restrictions for optical remote sensing noted above generally apply to thermal remote sensing.

Radar remote sensing uses much longer wavelength energy (1 mm – 60 cm) to gather information about the Earth's surface. Because of radar's image acquisition geometry (side viewing and directional) and longer wavelengths, information on surface morphology, topography, roughness, and texture can be extracted. Since this information often reflects the underlying bedrock and/or surface materials, radar is a useful tool for mapping geological structures, lithology, and surficial units. Again, radar is a surface remote sensing technique with very little penetration of the microwave energy into the ground, except in very special circumstances. Thus, as with other surface remote sensing techniques, vegetation and glacial cover hinder bedrock mapping. It should be noted that information content can vary appreciably on radar sensors depending on the various radar viewing parameters. The frequency and polarization of the microwave energy used for sensing as well as viewing geometry parameters, such as look direction and incidence angle, can have a strong effect on the surface information shown on radar imagery

PLATFORMS AND RESOLUTION

Potential field sensors (magnetic susceptibly and density) and gamma-ray spectrometers are commonly mounted on airborne platforms, whereas sensors that measure spectral reflectance and backscatter are mounted on both airborne and spaceborne platforms. Spaceborne platforms are generally more stable as they are not influenced by atmospheric effects (turbulence) that can lead to image distortions. However, airborne platforms are often required by geophysical and radiometric sensors to achieve higher spatial resolution. This is particularly the case for radiometric sensors as the

emission of radioelements decreases exponentially with height above the ground.

Spatial resolution is a key parameter for any remote sensor as this dictates how much ground detail can be imaged. For magnetic and radiometric data, the spatial resolution is defined by the line spacing and sample spacing along the line. Typically, the sample spacing is much greater along the line than the actual line spacing. Much of Canada is covered by magnetic data using 800 m line spacing, whereas the line spacing is typically 5 km for airborne gamma-ray spectrometer data. Obviously tighter line spacing will result in greater surface detail, which can be critical for detailed mapping and exploration. Geophysical data is often presented as profile data, but more typically it is interpolated (gridded) to a raster format comprising a specific number of lines and columns and based on a grid cell (pixel) of a specific dimension. For example, Geological Survey of Canada magnetic data are often gridded to a 200 m pixel, whereas gamma-ray data are gridded to a 250 m pixel. The gridding (interpolation) process results in oversampling of the data across line and undersampling of the data along the line. Generally, the data will be averaged (smoothed) as the result of gridding. This should be taken into account when statistically interpreting these data. Gridded data may be more appropriate for regional mapping whereas profile data may be more informative for detailed mapping and exploration.

Gravity data commonly is collected from ground stations, although recently more emphasis has been placed on airborne gravity acquisition. Data from ground acquisition are either displayed as point data, or as a raster map or image interpolated from the point data. Obviously the spatial detail (resolution) is dependent on the density of sample points. The same parameters discussed above for geophysical data apply to airborne gravity data.

Optical, thermal, and radar data are collected digitally using an airborne or satellite platform. Spatial resolution for optical remote sensors depends on the instantaneous field of view, which is determined by the sensor design as well as the flying height (altitude). Traditional sensors, such as LANDSAT and SPOT, have moderate spatial resolution (20–30 m pixel), whereas the newer sensors, such as ASTER, IKONOS, and airborne hyperspectral sensors, have spatial resolutions of less than 10 m. Spatial resolution of radar sensors (SAR) is independent of altitude, so that fine resolution (3-25 m) can be achieved from spaceborne platforms such as RADARSAT. Increased spatial resolution provides more detail for geological mapping, but also greater volumes of data to be manipulated and analyzed. Additionally, algorithms designed for manipulating the lower to moderate-resolution data sets tend to break down when applied to the high-resolution data sets.

Spectral resolution is defined by the number and bandwidth of each channel used to collect EM energy and is more of a concern with optical sensors. Since minerals and rocks can have unique spectral signatures when not obscured by vegetation and/or surficial cover, an increased number of channels of narrow bandwidth help to discriminate and identify the subtleties of spectral signatures that characterize a given mineral or rock. Traditional sensors, like LANDSAT, are characterized by low spectral resolution having only six broad channels spanning the VNIR and SWIR portions of the EM spectrum. Sensors like these may be able to discriminate certain rock units but cannot uniquely identify specific minerals or rocks (carbonates are an exception). Thus much emphasis in the last decade has been directed towards hyperspectral remote sensing, which employs optical sensors that have many narrow channels in the VNIR and SWIR portions of the EM spectrum. This provides the geologist with the potential for uniquely identifying minerals and rocks. However, the same limitations discussed above for optical sensors also apply to this new generation of airborne hyperspectral sensors. In fact, hyperspectral data requires more preprocessing (i.e. atmospheric correction and calibration) than lower resolution sensors like LANDSAT.

Processing

The various data (geophysical, optical, and radar) can be enhanced and manipulated to highlight various data attributes (spectral and spatial), which will in turn emphasize different geological characteristics of the data. The data also can be combined (or fused) with other data, emphasizing the complimentary nature of the specific data sets. These fused images are often useful for visual photogeological interpretation. This can be accomplished by using various image analysis systems (GeoSoft, PCI, ENVI, etc.) or GIS systems (ArcInfo, MapInfo, etc.). The various data can also be modelled (integrated), producing synergistic maps using a GIS.

Two streams of data processing can be utilized to produce a remote predictive geological map from the various types of remotely sensed data. The first method involves computer manipulation and fusion of the data, followed by visual interpretation of the enhanced data for each data set. These interpretations can then be integrated manually or digitally within a GIS, to create a final predictive map. The second method involves use of the computer to generate a predictive map automatically, using a computer algorithm (i.e. unsupervised classification) or semi-automatically using the geologist's input (knowledge) to a computer algorithm (i.e. supervised classification) to produce a predictive map. Both of these methods will be demonstrated in this manual.

MANUAL FORMAT

Chapter 2 presents a discussion of the RPM mapping philosophy, including data that can and should be collected, data sources, the types of geological products (maps and images) that can be produced from the data and data integration, and analysis methods. The accompanying chapters provide a succinct theoretical description of the various data types useful for producing a predictive map as well as examples of various derived products and enhancements useful for mapping. A number of the theory chapters include associated PowerPoint (Microsoft) files that summarize theoretical, technical, and processing issues for each of the data types discussed. The last part of the manual includes a number of case studies illustrating how various geoscience data were used to create bedrock and surficial predictive maps.

ACKNOWLEDGEMENTS

Many people have contributed to the making of this volume and without these people this endeavour would not have been possible. Firstly, I would like to thank all the authors for their valuable contributions. Your papers are much appreciated! Secondly, I would like to thank all the reviewers (too numerous to list individually) of each chapter and case study. Your comments and suggestions resulted in much better papers!

I also thank many people from the Geological Survey of Canada who supported this work over the past four years; especially Don Desnoyers, Don James, Simon Hamner, Dave Scott, and John Percival. I also thank Paul Budkewitsch, RPM Project Leader for the last two years, for his support and encouragement.

Sue Davis provided wonderful work in drafting design and figure production. This volume would not be possible without the expert and extremely professional layout work, editing, and advice provided by Elizabeth Ambrose. Thank you Elizabeth!

This work was conducted under the Remote Predictive Mapping (RPM) Project, which is part of the Northern Minerals Development (NMD) program at the Geological Survey of Canada.

CHAPTER 2. Remote Predictive Mapping: A Strategy for Geological Mapping of Canada's North

J.R. Harris, E.M. Schetselaar, T. Lynds, and E.A. de Kemp
Geological Survey of Canada, 615 Booth Street, Ottawa, Ontario K1A 0E9
Corresponding author's email:Jeff.Harris@NRCan.gc.ca

INTRODUCTION

Due to its vast territory and world-class mineral and energy potential, efficient methods are required for upgrading the geoscience knowledge base of Canada's North. An important part of this endeavour involves updating geological map coverage. In the past, the coverage and publication of traditional geological maps covering only a limited region demanded multiple years of fieldwork; more time-efficient approaches for mapping larger regions within shorter time spans are now required. As a result, an approach termed Remote Predictive Mapping (RPM) has been implemented since 2004 in pilot projects by the Geological Survey of Canada. Remote predictive mapping is an integrated geological mapping approach in which existing geological map data are recompiled on the basis of the interpretation of aerial photographs, satellite imagery, and airborne geophysical data before and during progressing fieldwork. Remote predictive mapping facilitates time-efficient production of consistent up-to-date digital geological map databases over large regions.

Remote predictive mapping is not an entirely new philosophy for geological mapping. Geologists have long assembled diverse layers (primarily aerial photographs and aeromagnetic contour maps) of geoscience data to study the relationships between the spatial patterns for resource exploration and mapping endeavours. In the past this has been accomplished using an 'analog' approach, forcing maps printed on Mylar to be portrayed on a uniform map scale on a light table. However, with the increasing availability of digital data sets and the routine use of geographic information systems (GIS), the task of studying relationships between data and producing innovative maps to assist field mapping has become easier and more versatile. Contrary to the 'light table' approach, GIS allow maps and image data to be combined, overlaid, and manipulated at any scale with any combination of layers and subjected to any integrated enhancement. Remote predictive mapping comprises the compilation and interpretation (visual or computer-assisted) of a variety of geoscience data to produce predictive maps containing structural, lithological, geophysical, and surficial information for the geologist before he or she actually begins field work. Predictive geological maps may be iteratively revised and upgraded to publishable geological maps on the basis of evolving insight by repeatedly integrating newly acquired field and laboratory data in the interpretation process. The predictive map(s) can also serve as a first-order geological map in areas where field mapping is not feasible. The fundamental difference between RPM and traditional ground-based mapping is that in the latter, the compilation of units away from field control (current and legacy field observations) is largely based on geological inference while in RPM this geological inference is repeatedly tested and calibrated against remote sensing imagery[1].

A predictive map does not represent *geological truth* but rather a *best estimate* of what that area may represent on the ground based on the signatures derived from the interpreted data (geophysical, geochemical, remotely sensed). For that matter, even a traditionally produced geological map may not represent the geological truth, as all maps, no matter how they are produced, may contain spatial and classification errors. Thus, geological features of a predictive map do not necessarily correspond to how these features would be classified on the ground by a field geologist. At the categorization level, the geological term attached to a unit or structural feature may even prove to be wrong; yet at the detection level, the identified feature may correspond to a hitherto unrecognized mappable unit or structure that can be targeted for follow-up fieldwork.

The amount, variety, and quality of data used are obviously key factors in how closely the predictive map comes to the geological patterns obtained by field mapping. Another factor is the nature of the geological terrane being mapped as different data sets and associated processing and enhancement techniques will vary depending on the bedrock, surficial, and topographic environment.

A remote predictive map can assist the geologist in a number of ways:

- by predicting areas that appear to be characterized on remotely sensed images by more complex and spatially heterogeneous geological patterns, thus focusing and prioritizing field work in these areas; likewise, areas with more homogenous signatures and simpler patterns can also be identified as possibly requiring less field work to geologically calibrate.
- by predicting map units that would tentatively be assigned to rock types and/or geological forma-

Harris, J.R., Schetselaar, E.M., Lynds, T., and de Kemp, E.A., 2008, Remote predictive mapping: A strategy for geological mapping of Canada's North, Chapter *2 in* Remote Predictive Mapping: An Aid for Northern Mapping, (ed.) J. R. Harris; Geological Survey of Canada, Open File 5643, p. 5-27.

tions (bedrock and surficial). This is based on establishing critical relationships between imaged physical properties (magnetic intensity, gravity, gamma-ray spectrometry, spectral reflectance, radar backscatter) and patterns obtained from available geological maps and field data.

- by predicting a variety of structures (foliation traces, faults, dykes, lineaments, glacial flow directions, etc.). The structural information can be used in advance of field work, to supplement field observations or as stand-alone geological information.
- by predicting the distribution of bedrock outcrop and other physiographic features such as wetlands, areas of forest fire burns, vegetation cover, and infrastructure. Thus predictive maps can present the geologist with a different paradigm for planning field traverses. Instead of regularly spaced traverse lines, more detailed traverses can be set up that are focused on more complex areas and on areas where bedrock outcrop has been identified. This is especially advantageous in Northern mapping campaigns where the territory is vast and mapping expenses are high.

The mechanics of producing interpretations from various geoscience data sets can be greatly facilitated by GIS technology. For example, image interpretation can be accomplished directly on a computer screen as opposed to interpreting on Mylar overlays. The advantage of this screen digitization process is that various enhanced images can be displayed quickly to facilitate interpretation by virtually real-time comparison between different data types at any scale. Much iteration can be undertaken and each digital interpretation can be stored as a different GIS layer. This by-passes the cumbersome procedure of scanning and digitizing hard-copy interpretations followed by georeferencing, which can introduce spatial errors. Similar to field mapping, the successful recognition and extraction of geological information is a learning process based on experience in interpreting image data in a variety of physiographic and geological settings.

A SEVEN-STEP METHOD FOR REMOTE PREDICTIVE MAPPING

Remote predictive mapping proceeds by the acquisition, processing, and geological interpretation of available remotely sensed data sets and results in predictive maps that outline interpreted units and structures in the survey area. RPM can be either completed in isolation from field-based mapping or can be intimately integrated with it in order to ground truth the interpretation as field mapping proceeds. Figure 2-1 shows a summary of the RPM process integrated into the work flow of a geological mapping project. The shaded portion represents the activities common to the 'traditional' geological mapping process, whereas the portion that is not shaded represents the additional activities of the RPM approach. Regardless of whether the interpretation of remotely sensed data is fully integrated into a geological mapping project or not, the following provides a systematic outline of RPM work flow. The various case studies in this volume demonstrate different aspects of this work flow.

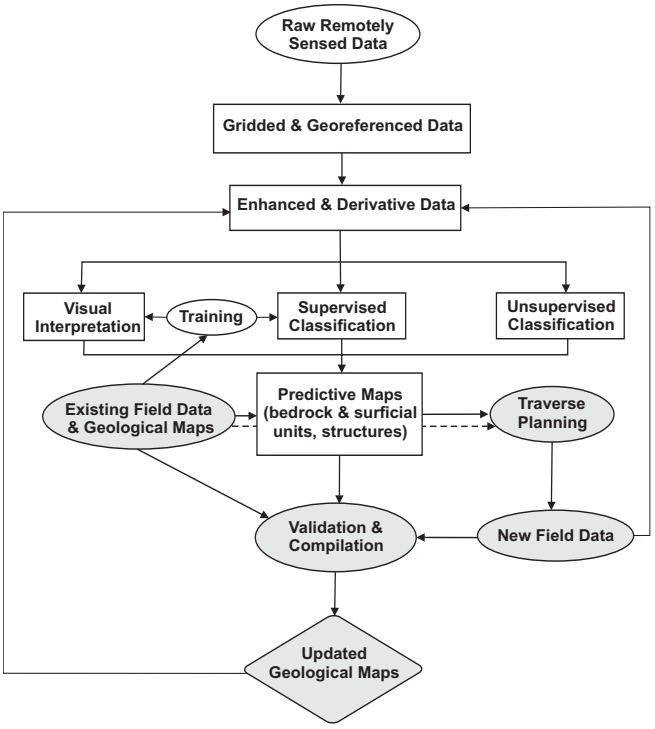

Figure 2-1. Flow chart showing how remote predictive mapping methodology can be integrated into a geological mapping project. Predictive maps can be produced by enhancing and fusing various remotely sensed data and visually extracting geological information from these products. Alternatively, a computer can be employed to automatically produce a predictive map (unsupervised approach) or by utilizing the geologist's expertise in concert with computer analysis (supervised approach). The geological interpretations are constrained or 'trained' by existing geological field data and existing geological maps.

Define Mapping Focus and Environment

The first step in a RPM mapping project is to define the mapping context, which includes the following:

i) mapping focus (bedrock, surficial),

ii) nature of the geological terrane – (sedimentary versus igneous and/or metamorphic),

iii) surficial conditions and degree of exposure, physiography,

1. Remote sensing in this paper refers to remote sensing sensu lato including image data generated from airborne geophysical surveys.

Table 2-1. Data sets used for remote predictive mapping.

Data	Where to Obtain	Cost
LANDSAT TM	Geogratis website (http://geogratis.cgdi.gc.ca/) MDA Geospatial Services	Free to download from Geogratis Cdn$720 per scene from MDA
RADARSAT	Geogratis website (100 m pixel mosaic of Canada) MDA Geospatial Services (http://www.rsi.ca/) – for individual scenes from the archive or acquire new data – commercial users Canadian Space Agency (CSA) – as above – for government users	mosaic –free to download MDA - Cdn$3,000-$4,000 /scene CSA - Cdn$300/ scene
Magnetic data	Geophysical Data Centre (GSC) (http:// gdcinfo.agg.nrcan.gc.ca)	Free to download
Gamma-ray spectrometry data	Geophysical Data Centre (http:// gdcinfo.agg.nrcan.gc.ca)	Free to download
DEM – CDED	Geobase (http://www.geobase.ca/)	Free to download
ASTER	USGS (http://edcdaac.usgs.gov/main.asp) Information can be found at: http://asterweb.jpl.nasa.gov/ http://asterweb.jpl.nasa.gov/gallery.asp	$40.0 US per scene
SPOT	IUNCTUS Geomatics Corp. http://www.terraengine.com/	$1200.0 per scene for SPOT 4 $1.00-$6.00 per sq km for SPOT 5
IKONOS	MDA Geospatial Services (http://www.rsi.ca/) Information can be found at: http://www.infoterraglobal.com/ikonos.htm http://www.satimagingcorp.com/gallery_ikonos.html	$15.0-$30.0 per sq km
QIUCKBIRD	MDA Geospatial Services (http://www.rsi.ca/) Information can be found at: http://www.satimagingcorp.com/gallery_quickbird.html http://www.ballaerospace.com/quickbird.html	See MDA website
ENVISAT	MDA Geospatial Services (http://www.rsi.ca/)	See MDA website
RESOURCESAT	MDA Geospatial Services (http://www.rsi.ca/)	$2750.0 per scene
IRS	MDA Geospatial Services (http://www.rsi.ca/)	$900.0-$2,500.0
ERS-1 Radar	MDA Geospatial Services (http://www.rsi.ca/)	$660.0 per scene
Airborne hyperspectral data	selected coverage of PROBE data – Baffin Island, Sudbury - Canada Centre for Remote Sensing (CCRS) and Geological Survey of Canada (GSC) – Geophysical Data Centre	Selected scenes free to download

iv) data availability, quantity, and quality.

The specific project will determine the data that will be most useful for mapping. Bedrock mapping projects that are planned in well exposed terrane and have thin residual till cover will benefit from the integration of magnetic, gamma-ray spectrometry, optical, and radar image data. In areas where sparse outcrops alternate with thick overburden, bedrock mapping will primarily profit from the interpretation of magnetic data.

In surficial mapping, optical and radar remote sensing techniques, together with gamma-ray spectrometry and digital terrain data, will contribute to distinguishing various types of surficial materials, identifying and mapping geomorphic features, and mapping streamlined glacial landforms that provide information on glacial movement.

Geological setting and physiography of the terrane in combination with the spatial and spectral resolution, penetration depth, season of image acquisition, and aerial coverage of the remote sensing system (including airborne geophysics) are all important factors when choosing data sets for geological interpretation.

Data Acquisition

Governments and private-sector contractors and/or vendors now provide much of the geoscience data in digital format that increasingly can be accessed through the internet. The core data types that can be acquired and interpreted for a RPM project are listed in Table 2-1 along with references to a sample list of websites to obtain them. Most of these data sets cover the complete Canadian landmass with the exception of gamma-ray spectrometry data (Fig. 2-2). Nonproprietary, medium-

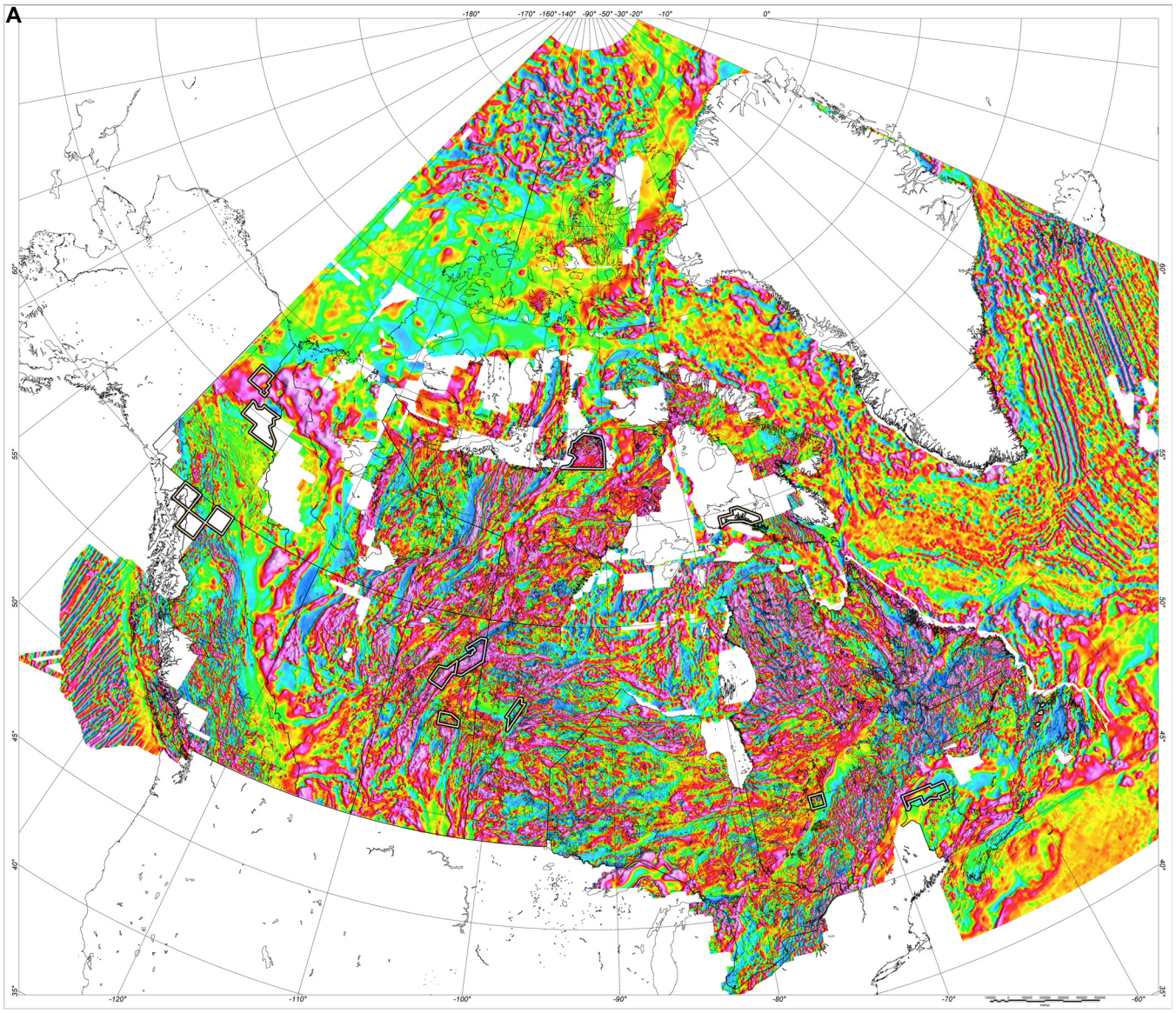

Figure 2-2. Map showing the portions of Canada for which geophysical data are available from the Geological Survey of Canada. **(A)** Map showing the parts of Canada for which regional magnetic data are available. Higher resolution magnetic data may be obtained from provincial geological surveys or through exploration companies.

to low-resolution geophysical data, including magnetic and gamma-ray data, can be obtained from the Geological Survey of Canada's Geophysical Data Centre. LANDSAT 7 enhanced thematic mapper scenes of 180 x 180 km optical remotely sensed data with one 60 metre resolution thermal band, six 30 metre multispectral bands in the visible to mid-infrared range, and one 15 metre panchromatic band in the visible range may be obtained, free of charge, from the Geogratis website (http://geogratis.gc.ca/). Radarsat data can be obtained from the Canadian Space Agency (CSA) for governmental users and MDA Geospatial Services (formerly Radarsat International) for nongovernmental users. Digital elevation data (DEM) (CDED at 1:50,000 and/or 1:250,000 scale) can be downloaded from the Canadian Council on Geomatics (CCOG) website (http://www.geobase.ca). The internet providers of optical remotely sensed data often include a quick-look download service that allows for the inspection of cloud cover of the scenes before download.

There are also a number of other specialized remote sensing systems included in Table 2-1 that do not yet provide complete coverage of the Canadian landmass. Optical sensors, including ASTER, SPOT, IKONOS, QUICKBIRD and airborne hyperspectral, can provide a wealth of geological information but these data are not available for all of Canada. However, when available their use should be considered, since they offer imagery with either higher spectral resolution (ASTER, 14 spectral bands) or higher spatial resolution (SPOT 5, IKONOS, QUICKBIRD). The higher

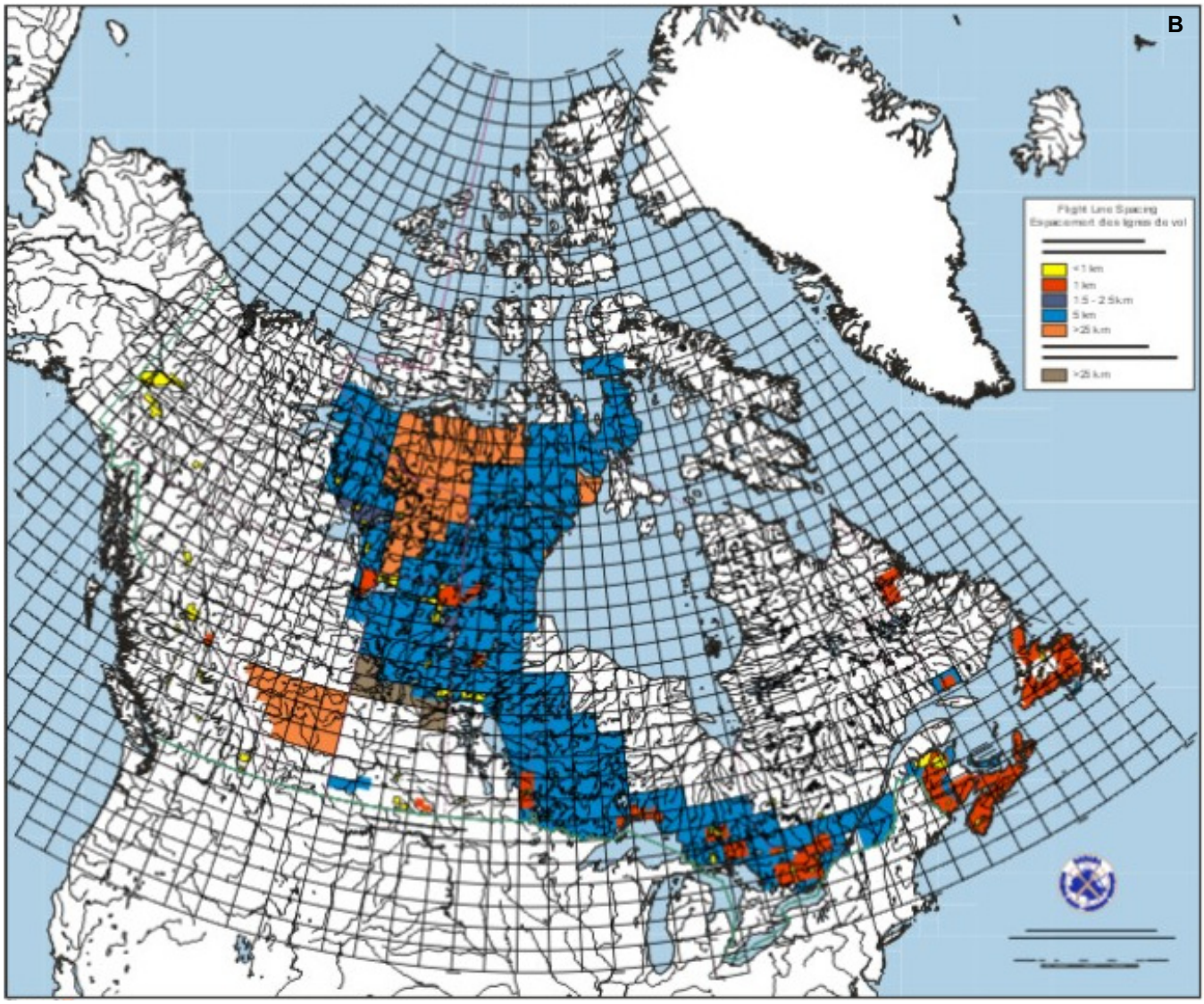

Figure 2-2 continued. (B) Map showing the regional gamma-ray spectrometer data coverage of Canada.

spatial resolution of the latter sensor systems with 4.0 to 2.4 metre multispectral and 1.0 to 0.40 metre panchromatic data acquisition is not only useful for mapping and logistical planning but also as a navigational guide in hand-held field computers.

Existing field and laboratory data and published geological maps can be integrated into the RPM process to guide, calibrate, and test interpretations (see Case Studies 5 and 9 of this volume). This can be accomplished by overlaying the field observations (lithological unit, strike and dip measurements) on the predictive map(s) in a GIS environment to assist in geologically calibrating interpreted units or structures. Field data can also be used in training computer classification algorithms. The statistical relationships between the numerical values of image data (representing spectral reflectance, magnetic field intensity, radar backscatter, etc) and lithological units can be computed at field stations and then used to predict other areas with similar signatures.

Geological mapping is increasingly being supported by digital field-data capture technology using hand-held computers and global positioning systems (GPS). This is a revolutionary development in RPM as it allows the validation of remote predictive maps on the outcrop. Simultaneous display of remote predictive maps and GPS position in real time may lead the mapping geologist to make small deviations from planned traverses to inspect subtle anomalous patterns that appear to be geologically significant when analyzed in the context of the immediate surroundings of an outcrop. This may apply, for example, to confirming the presence of a dyke, when short-wavelength linear magnetic anomalies from near surface magnetic bodies appear to be in close proximity to the field site.

Table 2-2. Remote predictive mapping data types and products (maps).

Data Source (including various enhancements)	Remote Predictive Mapping Product
Magnetics	Map of magnetic units (domains)
	Map of structures (faults (ductile, brittle), dykes, lineaments, foliation/bedding traces, folds, potential lithological contacts)
Gamma ray	Map of radioelement units (domains) that can provide insight into lithologies, different granitic phases, and regional metamorphic conditions
Digital elevation data (DEM)	Map of terrain units (based on relief)
	Glacial landforms
	Map of structures (based on topographic expression) – bedrock or glacial (ice-flow features)
	Map of drainage basins (watersheds)
LANDSAT	Map of structures (faults (ductile, brittle), dykes, lineaments, foliation/bedding traces, folds, potential lithological contacts)
	Map of spectral units (spectral absorption features due to white mica, clay minerals (potentially associated to hydrothermal alteration) and carbonates), especially carbonates – may represent a combination of bedrock lithology and surficial units
	Fe-oxide map (3/1 – ratio)
	Clay-alteration map, carbonate, white mica, and other OH-group minerals (5/7 – ratio)
	Map of vegetation (4/3 ratio)
	Outcrop map (1+7/4 or 7/4 ratio)
	Map of wetlands (band 4)
	Map showing forest fire burns
	Map of snow and ice
	Drainage map (can provide more detail than topographic maps, depending on the scale)
Radarsat data	Map of terrain units that may represent surficial or lithological units
	Map of structures (faults (ductile, brittle), dykes, lineaments, foliation/bedding traces, folds, potential lithological contacts)
Hyperspectral	Map of spectral units (can be calibrated to actual lithological units or specific minerals in certain enviornments)
	Map of structures (as above)
	Alteration map (if good exposure)

When integrating satellite image data (i.e. LANDSAT, ASTER, SPOT, RADARSAT), sufficient time (commonly 6 to 12 months) should be set aside for acquisition of new data before field mapping begins in order to allow time for processing and interpreting the data. Also any new airborne geophysical surveys should be planned far in advance so that the data may be flown, processed, and interpreted prior to field mapping. For optical and radar remotely sensed data, only a narrow window exists, typically from mid-June to mid-September, for acquiring new data in the North. The window for magnetic and radar data is much broader than that for optical data; however, a narrow window also exists for the collection of gamma-ray spectrometry data as any snow cover will absorb gamma-ray emissions. Provided that the weather and terrain conditions are favourable, it is recommended that gamma-ray spectrometry data be collected in parallel with magnetic data as this will provide a geometrically consistent airborne survey consisting of magnetic, total count, potassium, uranium, thorium, and topographic elevation channels, providing complementary geological information at reduced survey costs.

Dependent on the type of data sets acquired, various preprocessing steps may be required that have not been carried out by the data provider. When comparing field spectral measurements with optical remotely sensed data, for example, atmospheric correction algorithms are required (this is especially important when dealing with hyperspectral data – see Case Study 3 of this volume). This kind of preprocessing is not a trivial task and requires careful calibration routines to ensure the quality and integrity of the data is preserved. If this is not done properly then the analytical results obtained in a RPM project will be prone to error.

Georegistration

The data acquired for RPM may come in different map datum and projections, although most spatial data warehouses in Canada now adhere to the NAD83 datum and UTM projection for the scales of mapping typically employed in RPM (1:50 000 to 1:500 000 scales). Nevertheless, if legacy data in NAD27, province, or at larger scales or GPS data with standard WGS84 datum settings are used, datum and projection transformations must be employed in order to assure appropriate georegistration of the RPM data sets. After

the necessary datum and map projection transformations have been applied, it is good practice to make an assessment of errors between data sets by comparing the discrepancies between the landmarks (in Canada these are usually characteristic shapes along lake shores or river intersections) on various map and image layers due to nonsystematic digitizing and/or registration errors.

Data Processing and Enhancement

A wide range of processing and enhancement methods can be used to facilitate extraction of geological information from RPM data sets (Table 2-2). Examples of enhanced image data (mainly from Canada's North) are shown in Figures 2-3 to 2-7. Generally the methods employed depend on the data type to be enhanced. Derivatives of potential field data include vertical derivatives, upward continuation, analytic signal, magnetic susceptibility, and pseudogravity, among others (see Chapter 3 of this volume). Grids of measured magnetic and gravity data, as well as their derivatives, are improved by applying contrast-enhancement and relief-shading algorithms or both in combination (Milligan and Gunn, 1997). Spatial convolution-filters and colour-enhancement techniques, such as decorrelation stretch (Gillespie et al., 1986) and saturation enhancement (Kruse and Raines, 1994) may be applied to enhance optical remotely sensed (Chapter 5 of this volume), multibeam radar (Chapter 6 of this volume) and gamma-ray spectrometry (Chapter 4 of this volume) data, while band ratios or pairwise principal component analysis (Jensen, 1995; Jolliffe, 2004; Richards and Jia, 2006) are useful to enhance geological information on multispectral or multibeam radar imagery. Most of these enhancements can be generated semi-automatically using computer algorithms available with GIS and/or image analysis systems. User input, however, is always important to fine-tune the enhancement, since this is guided by insight on how the dynamic range and spatial frequency distribution of the imaged physical properties are associated to geology.

In addition to the enhancement of individual data types, image fusion (Harris et al., 1999) combines image data into single images to highlight features of interest and assist in the analysis of complementary geological information. Figure 2-3A shows an image fusion example in which gamma-ray spectrometry data have been combined with shaded-relief magnetic and topographic data. Rendering data as a 3-D surface is also instructive for studying the spatial relationships between different data types. For example, in Figure 2-3B, total field magnetic data is overlaid on a 3-D surface of the potassium (% K) gamma-ray spectrometry channel, resulting in a surface that resembles topographic relief. This facilitates studying the spatial relationships between each data set. Areas of anomalous response for both data sets can be seen at sites a and b (Fig. 2-3B), whereas areas of low response in the gamma-ray and high magnetic response can be seen at site c. Figure 2-3C shows another 3-D surface visualization where the colour rendering is modulated by the uranium (eU ppm) gamma-ray spectrometry channel and the 'relief' is modulated by ground-based measurements of uranium. Areas of high uranium emission, based on both the ground and airborne data, are found at locations a and b.

Data Analysis and Interpretation

Once derivatives and enhanced data are available for geological feature extraction, two basic approaches can be employed for producing remote predictive maps (see Fig. 2-2). These include visual interpretation of enhanced and fused imagery and computer-assisted interpretation methods. The subsequent sections discuss these methods and demonstrate how they can be employed in remote predictive mapping. Furthermore, Case Studies 2, 5, 6, and 7 of this volume deal with the application of classification techniques using a variety of geoscience data for geological mapping.

Visual Image Interpretation

Visual interpretation of the enhanced remotely sensed data can be based either on making hard-copy images or by digitizing on a computer screen. The latter method is more flexible as it allows for instantaneous display of different data sets, thus facilitating the extraction of complementary information while weighing the geological significance of image patterns in each of the data layers. It can provide interpretations of units, unit contacts, or faults that are automatically georeferenced to the database, can be virtually overlain on other data for comparison, and serve as a basis for geological map compilation once new field data are acquired. Case Study 4 of this volume utilized this approach for producing structural maps of southwest Baffin Island.

Regardless of the data type being rendered, visual interpretation is based on recognizing geological features using seven diagnostic elements. These include tone and/or colour, texture, patterns, shape, size, shadow, and association (Lillesand and Kieffer, 2000; Drury, 2001). Examples of how each of the elements may contribute to recognizing geological features are shown in Figure 2-4.

Tone and/or colour refers to the relative brightness or colour of objects in an image. It is the most fundamental element of image interpretation, as its variation also allows appreciating other elements, such as texture, pattern, and shape. Figure 2-4A shows how erosional remnants of a sedimentary cover consisting of

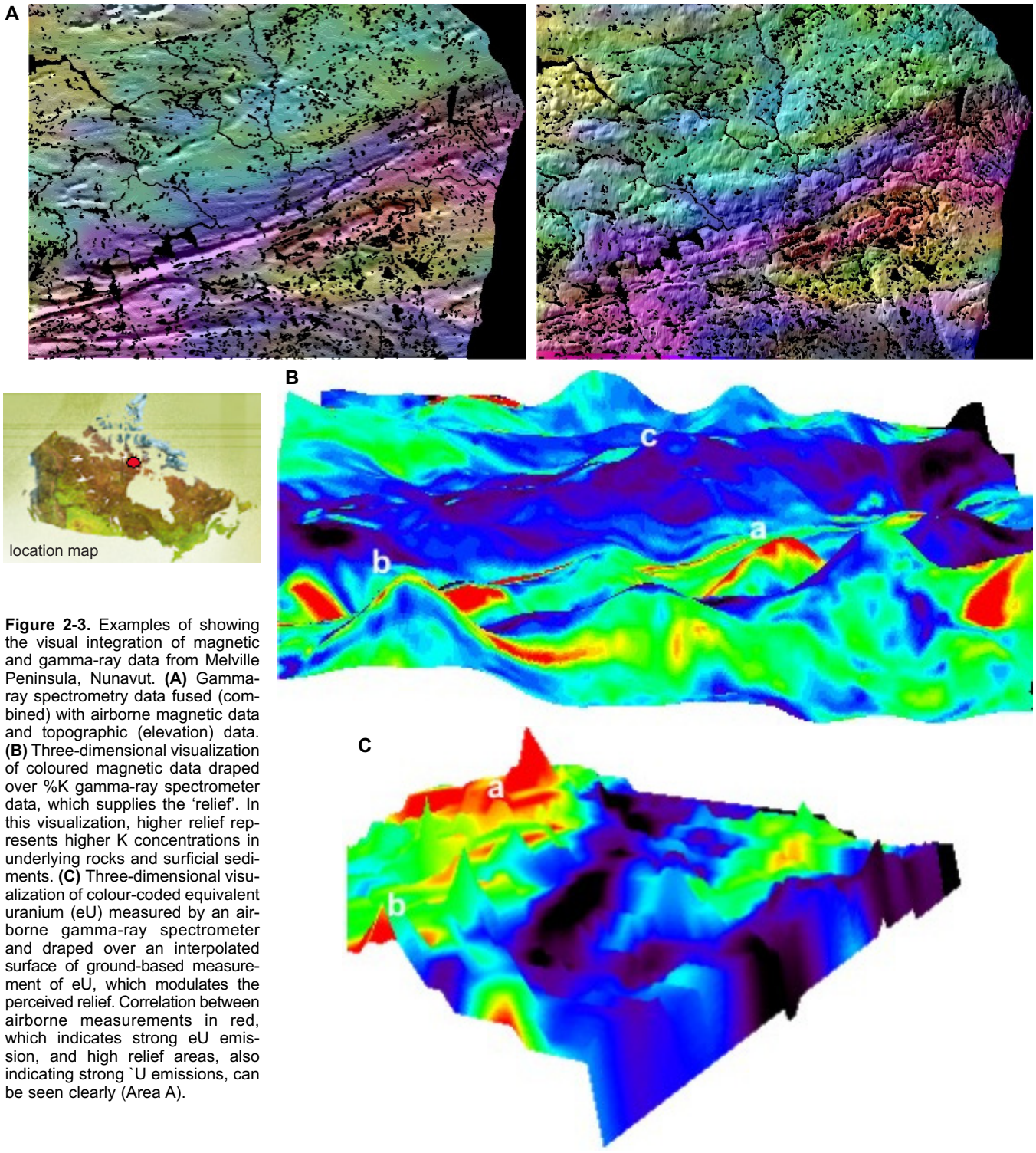

Figure 2-3. Examples of showing the visual integration of magnetic and gamma-ray data from Melville Peninsula, Nunavut. **(A)** Gamma-ray spectrometry data fused (combined) with airborne magnetic data and topographic (elevation) data. **(B)** Three-dimensional visualization of coloured magnetic data draped over %K gamma-ray spectrometer data, which supplies the 'relief'. In this visualization, higher relief represents higher K concentrations in underlying rocks and surficial sediments. **(C)** Three-dimensional visualization of colour-coded equivalent uranium (eU) measured by an airborne gamma-ray spectrometer and draped over an interpolated surface of ground-based measurement of eU, which modulates the perceived relief. Correlation between airborne measurements in red, which indicates strong eU emission, and high relief areas, also indicating strong `U emissions, can be seen clearly (Area A).

Ordovician limestone can be differentiated from underlying Archean granitoid basement by its relatively bright tone on a LANDSAT TM colour image of southwestern Baffin Island, Nunavut.

Texture refers to the magnitude and spatial frequency of tonal variations and can be qualified as smooth, moderately coarse, or coarse. Figure 2-4B shows an airborne C-band radar image acquired over the north shore of Lake Superior, near Marathon, Ontario. Various image textures can be seen clearly, ranging from smooth (representing lakes), fine (representing boreal-forest areas), to coarse and blocky (representing hilly terrain).

Shape refers to the general outline and form of individual objects in an image. This is one of the most diagnostic elements in visual interpretation. Figure 2-

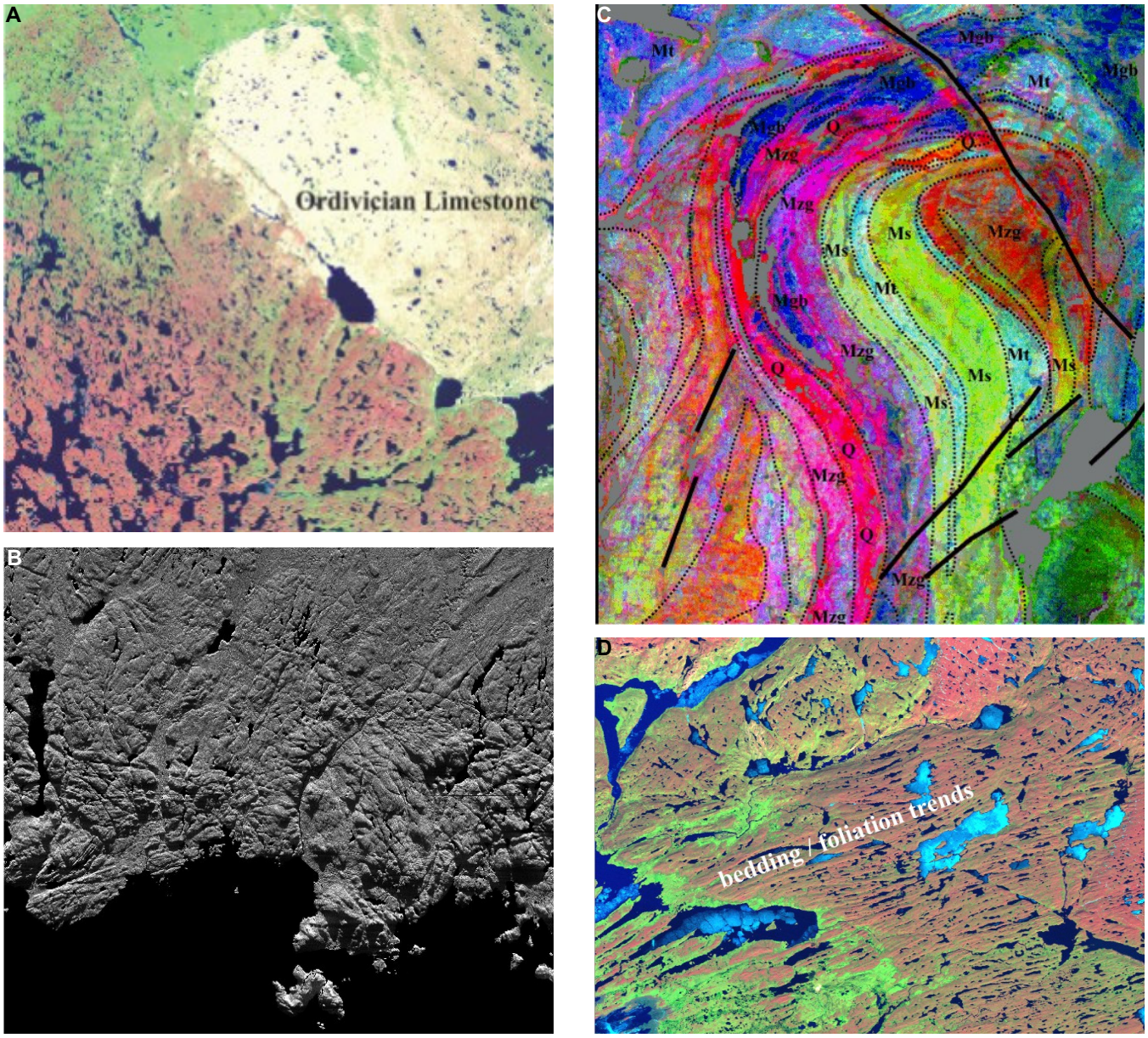

Figure 2-4. Images demonstrating the use of various photogeological interpretation elements. **(A)** Tone/colour: LANDSAT colour composite image (bands 7,4,2 corresponding to red, green, and blue) of a portion of southwestern Baffin Island in which the younger cover rocks (Ordovician limestone) are white compared to the reds and greens of the underlying Archean basement rocks. **(B)** Texture: Airborne C-band radar image of northern Lake Superior centred on the Coldwell Alkaline Intrusive Complex. Different textures reflect different surface cover and rock types. **(C)** Shape: Enhanced hyperspectral image of a small portion of southeastern Baffin Island. The elliptical shape defines a large fold. Annotation represents individual rock units (Mgb = metagabbro, Ms = metasediment, Mt = metatonalite, Mzg = monzogranite, Q = quartzite; black lines are interpreted faults). **(D)** Pattern: LANDSAT colour composite image (bands 7, 4, 2 correspond to red, green, and blue) of a small portion of central Baffin Island. The northeast-southwest-striking linear pattern represents foliation and bedding trends in the Piling Group sedimentary rocks.

4C is a hyperspectral image of a small portion (approximately 5 by 5 km) of southeast Baffin Island showing a mushroom-shaped, superposed fold pattern.

Pattern refers to the repetitive arrangement of discernable features in an image. Figure 2-4D shows a regular repetition of northeast-trending linear features (structural form lines-bedding traces in the Piling Group of metasedimentary rocks) on a LANDSAT image of central Baffin Island.

Size refers to the dimensions of an object relative to other objects in an image, as well as its absolute size. A circular anomaly with a radius of 100 metres or less could potentially be associated with a kimberlite pipe, whereas a circular magnetic anomaly with a radius of several kilometres is more likely a plutonic feature. An example demonstrating size (and shape) is shown in Figure 2-4E, which is a colour LANDSAT image of the Grenville Province north of Kingston, Ontario. Two variably sized intrusive bodies can be clearly seen

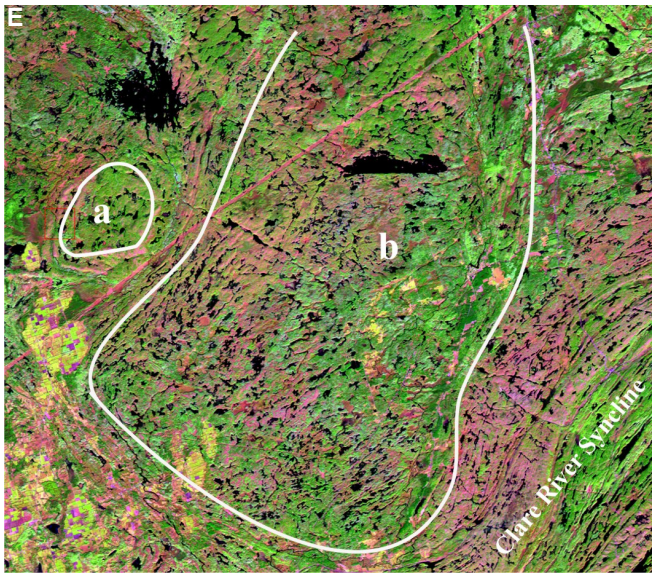

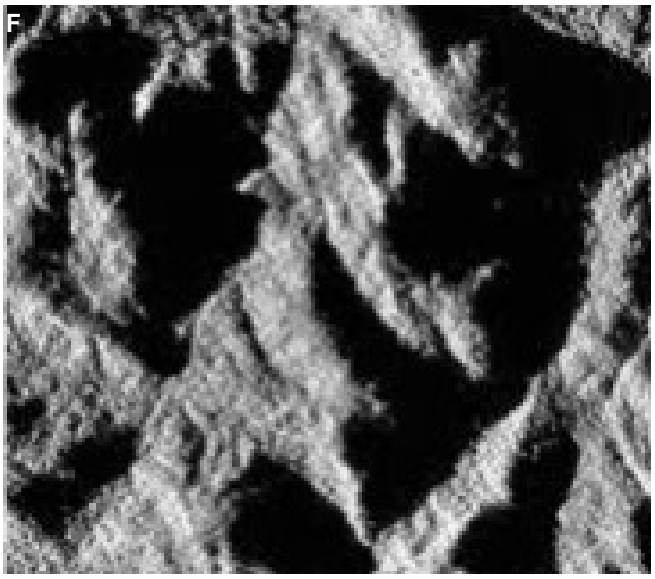

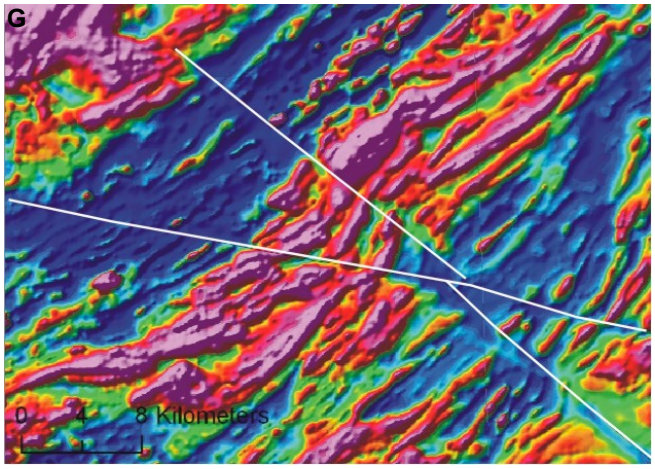

Figure 2-4 continued. **(E)** Size: LANDSAT colour composite image (bands 7, 4, 2 corresponding to red, green, and blue) of a small portion of the Grenville Tectonic Province north of Kingston, Ontario in which a small and a larger pluton body can be clearly seen. **(F)** Shadow: An airborne radar image of Precambrian terrane in northern Ontario in which radar shadows help to enhance the rugged relief. **(G)** Example from the Archean Churchill Province showing the association between magnetic lineaments in the Boothia mainland.

(labeled A and B in Fig. 2-4E) around which are folded metasediments that define parts of the Clare River Syncline.

Shadow refers to the part of an object that is obstructed from incoming radiation from a natural, active, or artificial energy source. Shadow provides a perception of the profile or relative height of a target. It, however, may also hamper the identification of an object since it lowers or completely obstructs the reflectance from that object. An example of the application of shadow is shown in an airborne radar image of the Precambrian Shield in Ontario (Fig. 2-4F). Imaged at an incidence angle of 45º, the areas of shadow (black) on the slopes facing away from the radar look-direction help to highlight the rugged topographic relief of this locale.

Association refers to the relationship of an object with other recognizable objects in the vicinity. The identification of features that one would expect to associate with other features may provide information to facilitate identification. Typical geological examples include radial drainage patterns around circular objects, such as those associated with impact structures, and intrusive and tectonic domes and volcanoes. Figure 2-4G shows an example from the Archean Churchill Province of an association between magnetic lineaments in the Boothia mainland. Two magnetic lineaments offset linear magnetic anomaly patterns associated with the foliation trends in the Archean metagranitoids. The approximate 60 degree angle between the magnetic lineaments associated with the apparent dextral and sinistral offsets of the magnetic anomaly patterns, aids the inference that this pair of magnetic lineaments reflects a conjugate set of brittle shears.

Visual interpretation starts with selecting data that best reflects geology. This selection is guided by interactively overlaying digitized geological maps on various enhanced image data sets. Figure 2-5 shows an example of a visual interpretation effort for bedrock mapping from an enhanced and integrated remotely sensed data set acquired over the Taltson magmatic zone, which is exposed in northeast Alberta (Schetselaar, 2000). The interpretation of the gridded magnetic data shown in Figure 2-5C was based on a

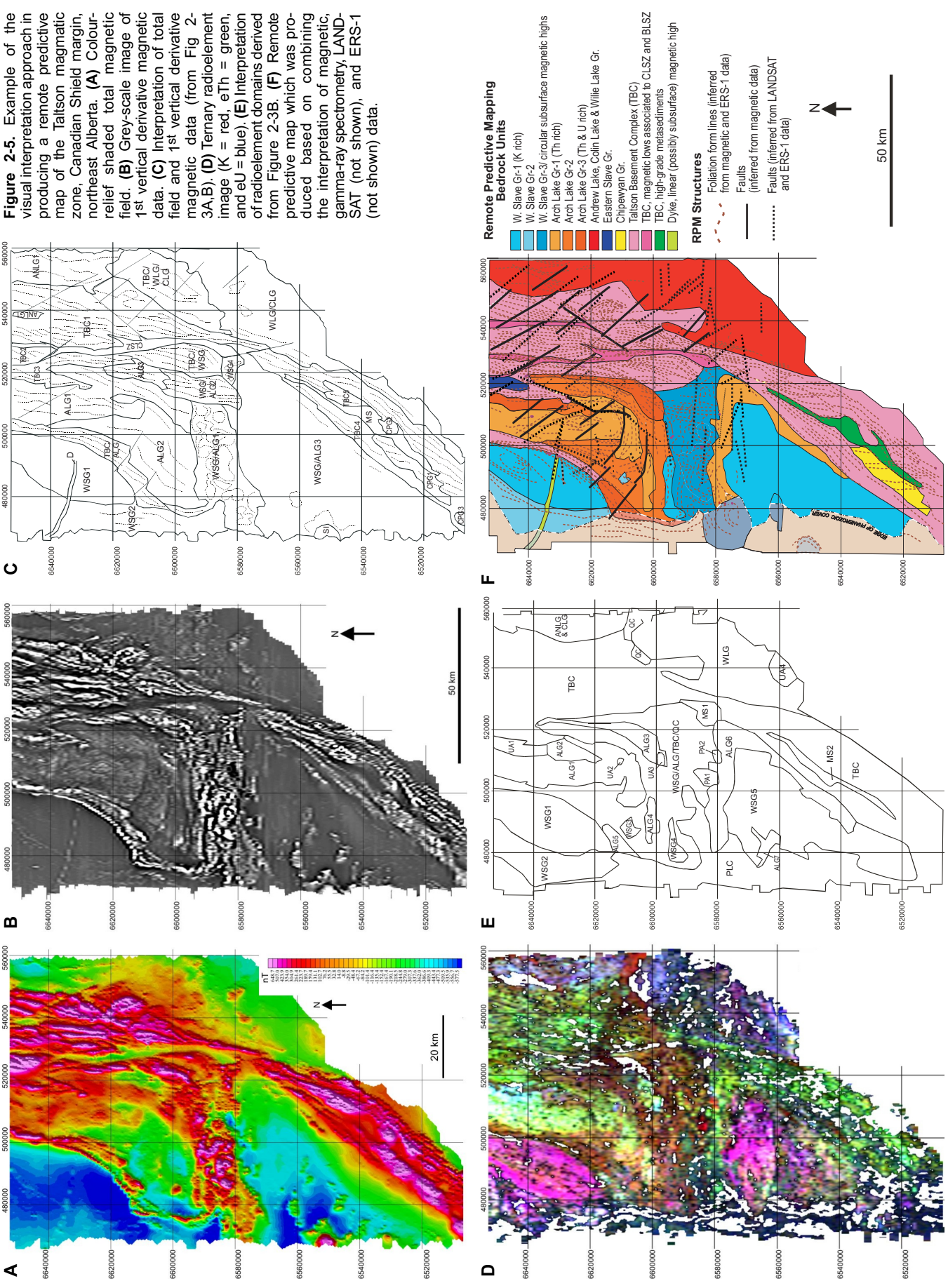

Figure 2-5. Example of the visual interpretation approach in producing a remote predictive map of the Taltson magmatic zone, Canadian Shield margin, northeast Alberta. **(A)** Colour-relief shaded total magnetic field. **(B)** Grey-scale image of 1st vertical derivative magnetic data. **(C)** Interpretation of total field and 1st vertical derivative magnetic data (from Fig 2-3A,B). **(D)** Ternary radioelement image (K = red, eTh = green, and eU = blue). **(E)** Interpretation of radioelement domains derived from Figure 2-3B. **(F)** Remote predictive map which was produced based on combining the interpretation of magnetic, gamma-ray spectrometry, LANDSAT (not shown), and ERS-1 (not shown) data.

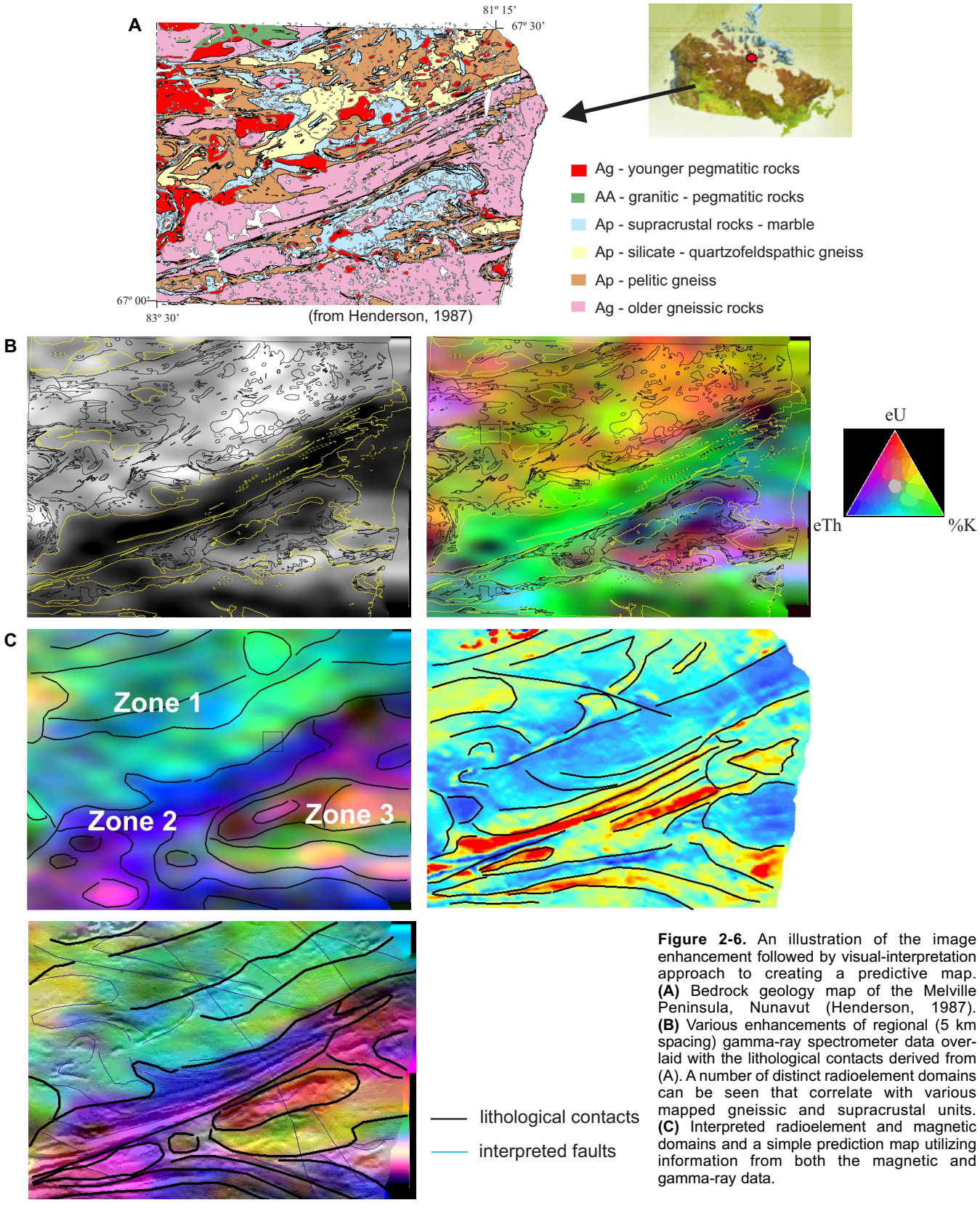

Figure 2-6. An illustration of the image enhancement followed by visual-interpretation approach to creating a predictive map. **(A)** Bedrock geology map of the Melville Peninsula, Nunavut (Henderson, 1987). **(B)** Various enhancements of regional (5 km spacing) gamma-ray spectrometer data overlaid with the lithological contacts derived from (A). A number of distinct radioelement domains can be seen that correlate with various mapped gneissic and supracrustal units. **(C)** Interpreted radioelement and magnetic domains and a simple prediction map utilizing information from both the magnetic and gamma-ray data.

colour-shaded relief image of the total magnetic field (Fig. 2-5A) and a grey-scale image of its 1st vertical derivative (Fig. 2-5B). A separate interpretation of radioelement domains (Fig. 2-5E) was based on a ternary radioelement image displaying K, eTh, and eU in red, green, and blue primaries, respectively (Fig. 2-5D). A remote predictive map showing the outlines of geological units and structures (Fig. 2-5F) was gener-

ated by reconciling conflicts between the interpretations of magnetic, gamma-ray spectrometry LANDSAT, and ERS-1 data and integrating the information from the data layers with available geological maps. The gamma-ray spectrometry data were particularly useful for distinguishing various granitoid plutons and internal zoning within them, whereas the magnetic data permitted differentiation of the plutons from gneissic basement and enclaves of supracrustal rocks within the gneissic basement. The magnetic data, in addition to LANDSAT and ERS-1 data (not shown), also allowed the outlining of dykes and other geological structures (e.g. regional foliation, folds, shear zones, and faults).

Another example of the visual interpretation approach is illustrated in Figure 2-6, which shows a portion of the Melville Peninsula in northern Canada. Various enhancements of the gamma-ray spectrometry data were produced (Fig. 2-6B) (see Chapter 4 of this volume) and these images were visually interpreted producing unit maps (a combination of radioelement and magnetic units or domains) (Fig. 2-6C). The gamma-ray data show three major geological divisions: (1) the northwest portion of the area has variable radiometric signatures and magnetic response, reflecting older pelitic and silicate gneiss interspersed with younger pegmatitic rocks, some of which have a distinct radiometric signature (see Zone 1 on Fig. 2-6C); (2) a central zone, trending northeast, represents supracrustal and basement gneissic rocks (Penrhyn Group) of the Foxe fold belt; and (3) a southern zone reflecting supracrustal marble that is variably high in equivalent uranium (eU) and equivalent thorium (eTh). The linear magnetic anomaly patterns reflect tight upright folds that comprise the fold belt. The magnetic data define a sharp contact on the north side of the belt; however the gamma-ray data define a much more diffuse contact, reflecting older gneissic rocks that have a low radioelement response. The interpreted units derived from the gamma-ray and magnetic data (Fig. 2-6C) show many similarities to the existing geological map (Fig. 2-6A) but also discrepancies, which provide follow-up targets for field evaluation.

If field data (observations from outcrops or rock samples) or existing geology maps are available they can be used to geologically calibrate image interpretations. Digitized geological themes (i.e. lithology, tectonic domains, structure, geochronology, mineralogy, and alteration) may be overlaid on various enhanced images to establish the relationships between mapped geological features and image 'signatures'. Corresponding patterns between both guide the geological interpretation in areas beyond the coverage of geological field data. Discrepancies between the geological map and image signatures within the coverage of existing data, on the other hand, can provide rationale for reinterpreting map units and structures. The interpretations can be overlaid on the existing geology map and adjustments can be made to reconcile differences between the two (Fig. 2-7C). Modified map(s) with some measure of geological calibration (i.e. units are given a potential lithological type) can then be produced (Fig. 2-7B). Figure 2-7C–E shows different ways to assist in the calibration process. Here a geology map is used as a base over which the various visualizations of field data are overlaid so that areas of agreement and disagreement can be identified for follow-up field mapping.

Numerical Interpretation Methods

In addition, or as a compliment to visual interpretation, numerical interpretation methods can be used to produce remote predictive maps (Fig. 2-1). Automated numerical methods can include supervised and unsupervised classification and image segmentation algorithms (Lillesand and Kieffer, 2000; Richards and Jia, 2006). These methods provide alternatives for extracting geological information in a systematic and unbiased manner, although visual interpretation is commonly judged to outperform methods of automated pattern recognition. However, numerical methods are superior to visual methods at simultaneously manipulating and interpreting multiple data sets having a large number of image variables.

Supervised classification methods allow geologists to have input into the map-making process by using geological field data during the training stage of the classification (see Case Studies 2, 5, 6, and 7 of this volume). In supervised classification, decision rules for class allocation are derived from multivariate statistics computed from the relationships between classes and image variables at the sample sites (i.e. field sites considered representative for bedrock or surficial units). The decision rules are used in the classification stage to allocate all pixels or grid cells to particular classes. The available classification algorithms differ in the way probability density functions for each class are modelled and estimated from the training data. The classification algorithms can be broadly categorized into (1) parametric classifiers that model the class probability density functions with the estimated parameters of a multivariate normal distribution or (2) nonparametric classifiers that directly estimate the class probability density functions from the data. A recommended practice is to experiment with a number of algorithms in an area where the geology is well known so that the performance of the different algorithms can be evaluated.

Figure 2-8 shows an example of supervised classification applied to gamma-ray spectrometry data over the Melville Peninsula, Nunavut. Training sites (Fig. 2-8B) for three major bedrock units (granite, gneiss, and

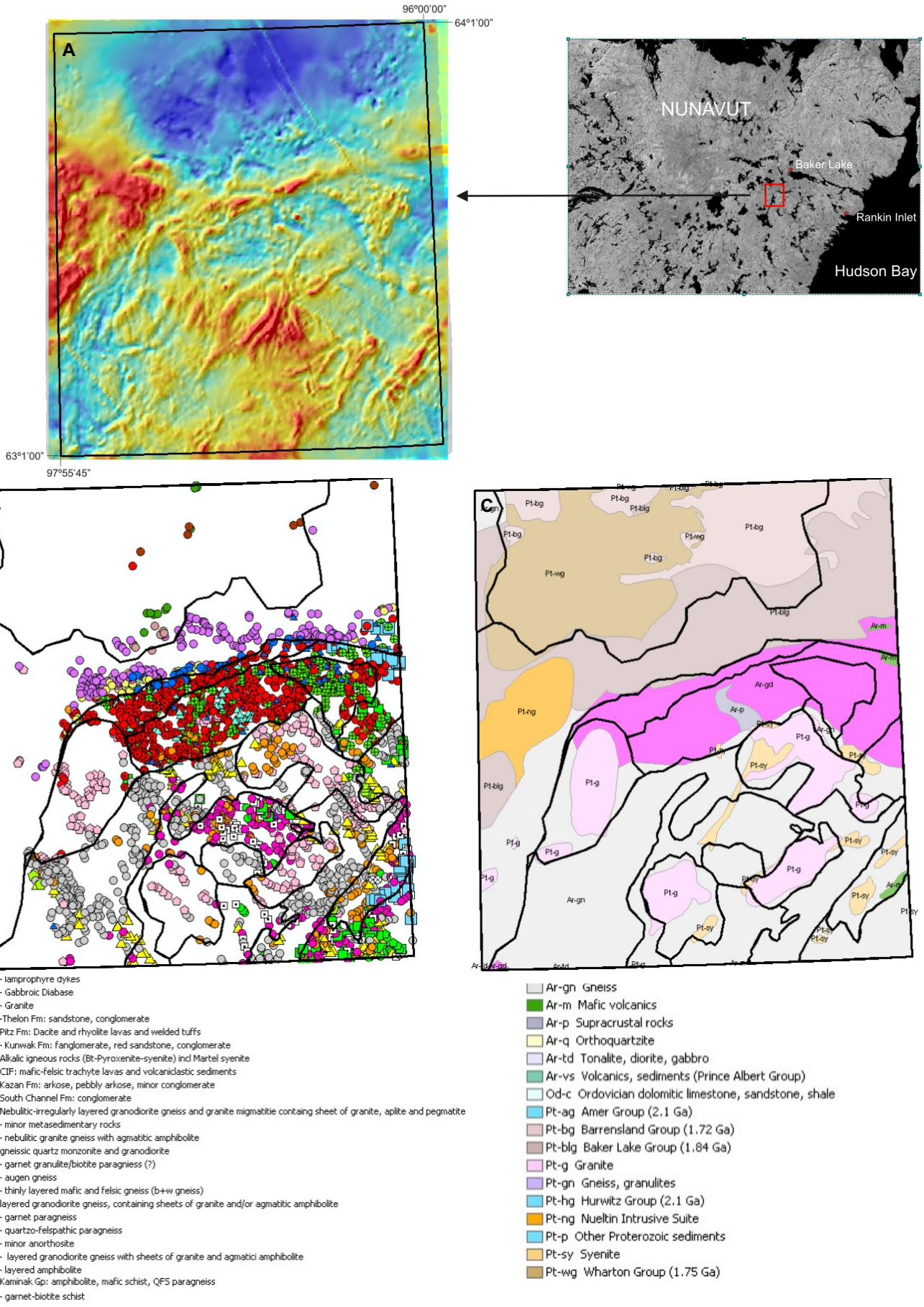
A
96°00'00"
64°1'00"
63°1'00"
97°55'45"
NUNAVUT
Baker Lake
Rankin Inlet
Hudson Bay
B
C
14 - lamprophyre dykes
12 - Gabbroic Diabase
11 - Granite
10 -Thelon Fm: sandstone, conglomerate
9 - Pitz Fm: Dacite and rhyolite lavas and welded tuffs
91 - Kunwak Fm: fanglomerate, red sandstone, conglomerate
8 - Alkalic igneous rocks (Bt-Pyroxenite-syenite) incl Martel syenite
7 - CIF: mafic-felsic trachyte lavas and volcaniclastic sediments
6 - Kazan Fm: arkose, pebbly arkose, minor conglomerate
5 - South Channel Fm: conglomerate
4 - Nebulitic-irregularly layered granodiorite gneiss and granite migmatitie containg sheet of granite, aplite and pegmatite
42 - minor metasedimentary rocks
43 - nebulitic granite gneiss with agmatitic amphibolite
3 - gneissic quartz monzonite and granodiorite
31 - garnet granulite/biotite paragniess (?)
32 - augen gneiss
33 - thinly layered mafic and felsic gneiss (b+w gneiss)
2 - layered granodiorite gneiss, containing sheets of granite and/or agmatitic amphibolite
21 - garnet paragneiss
22 - quartzo-felspathic paragneiss
23 - minor anorthosite
24 - layered granodiorite gneiss with sheets of granite and agmatici amphibolite
13 - layered amphibolite
1 - Kaminak Gp: amphibolite, mafic schist, QFS paragneiss
15 - garnet-biotite schist
Ar-gn Gneiss
Ar-m Mafic volcanics
Ar-p Supracrustal rocks
Ar-q Orthoquartzite
Ar-td Tonalite, diorite, gabbro
Ar-vs Volcanics, sediments (Prince Albert Group)
Od-c Ordovician dolomitic limestone, sandstone, shale
Pt-ag Amer Group (2.1 Ga)
Pt-bg Barrensland Group (1.72 Ga)
Pt-blg Baker Lake Group (1.84 Ga)
Pt-g Granite
Pt-gn Gneiss, granulites
Pt-hg Hurwitz Group (2.1 Ga)
Pt-ng Nueltin Intrusive Suite
Pt-p Other Proterozoic sediments
Pt-sy Syenite
Pt-wg Wharton Group (1.75 Ga)

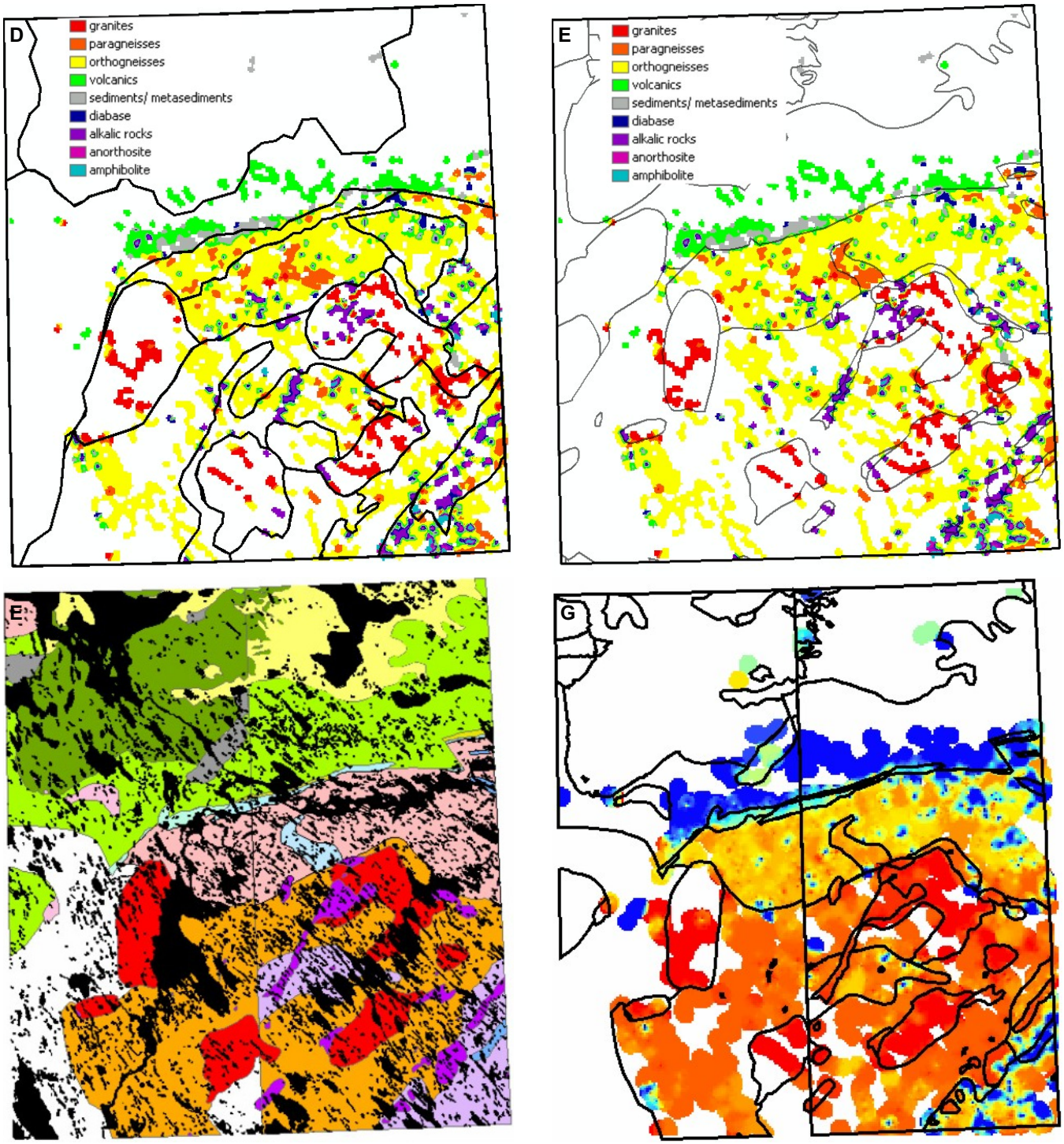

Figure 2-7. An example of combining field data with a magnetic domain map from the Thirty Mile Lake area (NTS 065P), Nunavut. **(A)** Shaded and coloured magnetic data. **(B)** Existing field stations, which have been colour coded to rock type and recorded in a GIS database. **(C)** Interpreted magnetic domains overlaid on an existing geology map. **(D)** Field stations colour-coded to generalized rock units and overlaid on an interpreted magnetic domain map. **(E)** Same as previous example (D) except colour-coded field stations are overlaid on the existing geology map. **(F)** Mapped (generalized) geology. **(G)** Interpolation of rock-type data that was recorded in the field overlaid over geology polygons. Rock units were generalized into major rock categories and each major rock unit was assigned a 1 byte number (0 -255) so that more felsic units (i.e. granite) had a higher number (i.e. 255) followed by intermediate and more mafic units, which were assigned a lower number in the GIS database. These values were then interpolated using an IDW (inverse-distance-weighted) interpolation algorithm with a 3 km fixed radius. The resulting map was coloured coded so that more felsic units are shown in warmer colours (red-orange), intermediate rocks in yellows, and sedimentary rocks in blue. Note the correlation between the colours and the mapped units. The areas within the mapped units that display a variety of colours (perhaps reflecting different lithologies than have been mapped) deserve follow-up in the field. The rock units were generalized by using GIS selection and query routines within the GIS environment.

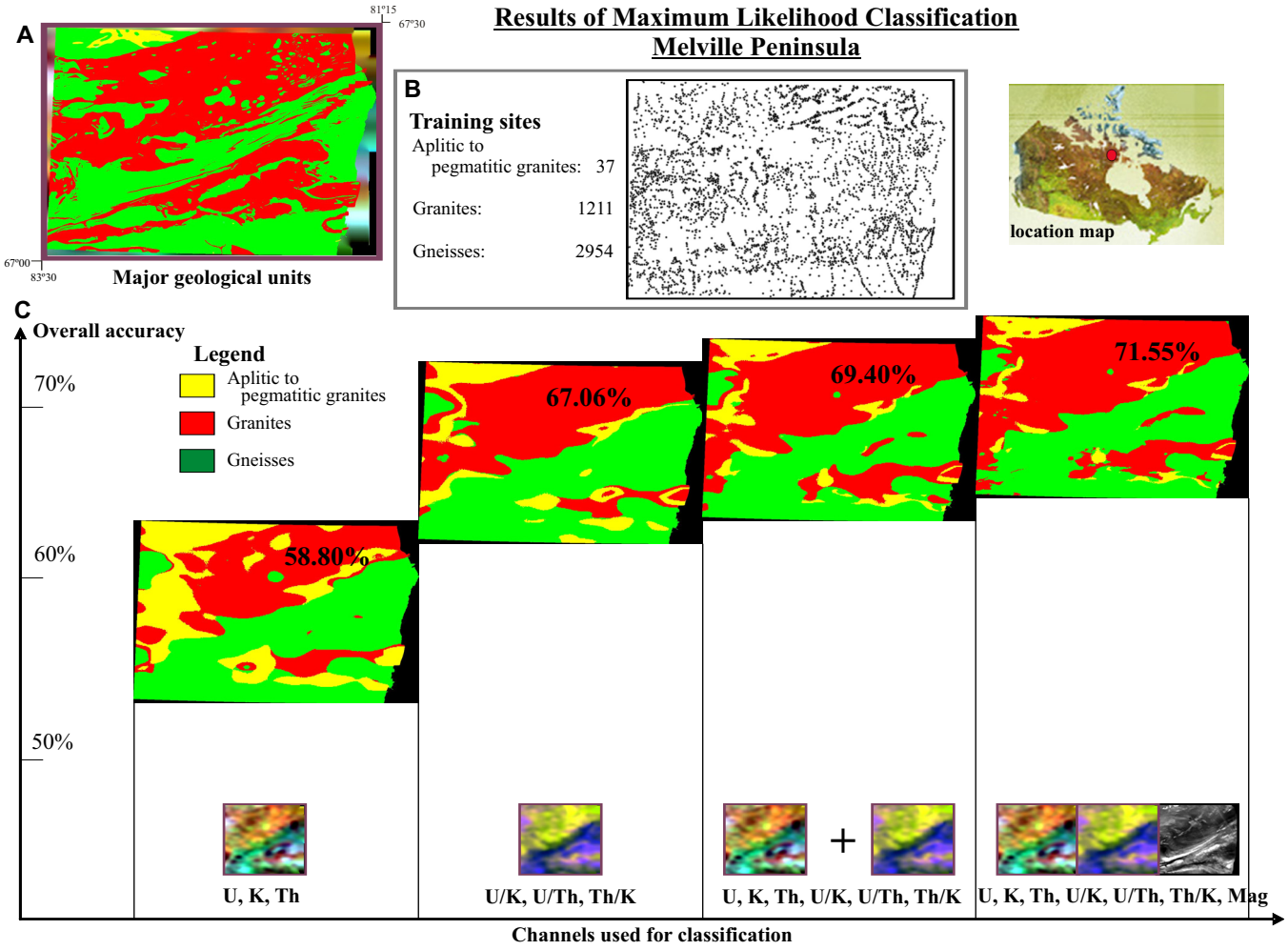

Figure 2-8. An example of a supervised computer approach whereby predictive maps of major geological and/or tectonic units are produced from training areas. **(A)** Major units derived from generalization of mapped geology from the Melville Peninsula, Nunavut. **(B)** Training areas, which were derived from field stations and used for generating statistics from the input magnetic and gamma-ray spectrometer data. **(C)** Prediction maps of the major units derived from supervised classification using signatures from the geophysical data over the grouped training sites (see (B)). Each predictive map shown in (C) was derived from the data shown below each map. These include just the gamma-ray data (raw and ratios), the combined gamma data, as well as the gamma and magnetic data together. The vertical axes (labeled overall accuracy) shows the accuracy of the predictive map when compared to what has been mapped (geological map shown in (A)). Note that the highest accuracy was achieved using all the gamma-ray data as well as the magnetic data. Both the similarities and differences between the predictions and the existing map are important for field mapping purposes.

pegmatitic granite) have been selected from the geological map (Fig. 2-8A) and statistics from various combinations of the gamma-ray and magnetic data have been computed and used to classify the data into the three major units using a maximum likelihood classification algorithm. Note the obvious similarity between the classified maps and the mapped geology. Classification accuracy (as measured against the 'traditional' geology map) increases when both gamma-ray and magnetic data are used. Classification accuracies range from 59% using eU, eTh, and %K to 71% when the entire gamma (raw and ratios) and total field magnetic data are used to produce the predictive map.

Another example of supervised classification applied to bedrock mapping is shown in Figure 2-9. Parametric methods (maximum likelihood and a predictive classifier) and a nonparametric method (artificial neural network classifier) were used to predict the ten lithological units in a training area in northeastern Alberta (Schetselaar et al., 2000). The training area is included in the area shown in the visual interpretation example of Figure 2-5. The resulting classification patterns yielded a correlation of 65 to 70% with the mapped geological units in the training area. The discrepancies between the classified patterns and the compiled geological map were used to identify targets for refinement of the geological map or as potential exploration targets. Some of the targets included internal zonations in granitoid plutons, uranium anomalies, and magnetic intrusive units in the near subsurface. Similar to visual image interpretation, this study suggests that supervised classification is a useful method to assist geologists in fieldwork planning and in identifying targets for map refinement and exploration.

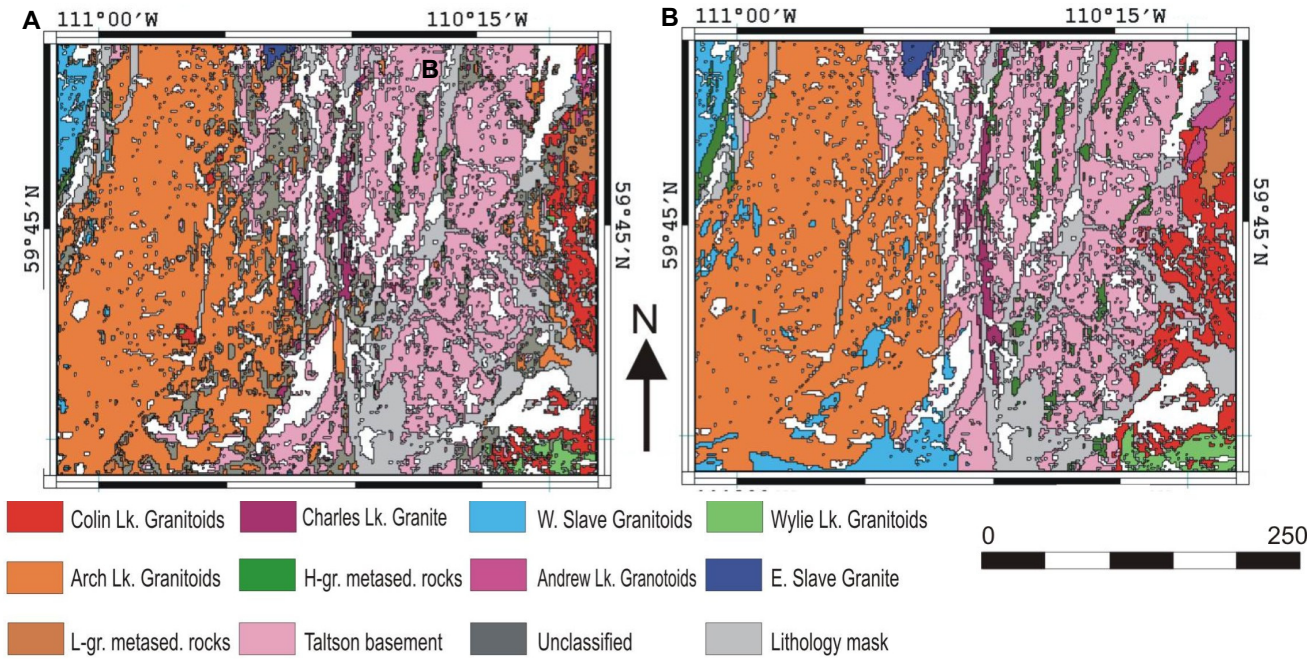

Figure 2-9. Supervised classification results from the Taltson magmatic zone, northeast Alberta (the classification results are located within the area of the visual interpretation example shown in Fig. 2-5). **(A)** Classification results obtained with a maximum likelihood algorithm. **(B)** Geological map compilation of the same area (after McDonough et al., 1995). Discrepancies between the geological map compilation and the classification results serve as follow-up mapping and exploration targets.

Contrary to supervised classification, unsupervised classification employs cluster algorithms to automatically produce a predictive map of image patterns with no direct input by the geologist (Harris, 1989). This form of classification is most often used when no field observations or reliable geological map are available (see Case Study 5 of this volume). The unsupervised approach may also be useful to extract unique anomalous patterns (interpretable as geological units or structures) from the image data that are not yet included in the existing geological knowledge base of the area. An example of unsupervised classification over the Melville Peninsula, in which a radioelement domain map is generated from the K, eTh, and eU gamma-ray spectrometry channels and their ratios, is shown in Figure 2-10. As previously discussed for the image fusion example shown in Figure 2-3A, the major division between the gneissic and younger granitic rocks in the north and northwest portion of the map (Zone 1) and the supracrustal and gneissic rocks of the Foxe fold belt in the south and southeast part of the map (Zone 2 and 3) are clearly demarcated. Generally the radioelement responses are lower in the southeast (Zone 2), except over the supracrustal rocks that are dominated by marble (Zone 3).

Graphic Information System Compilation of Remote Prediction Mapping Interpretation Results

The RPM process, as discussed in the preceding section, can result in one predictive map or a series of digital layers that can be mixed and matched within a GIS to create a number of predictive maps. Digitized geological themes (lithological, tectonic domains, structure, geochronology, mineralogy, and alteration – see Table 2-2) are overlaid on various enhanced images to establish the relationships between mapped geological features and image 'signatures'. Furthermore, when digital interpretations are stored as GIS files, they automatically become part of the georeferenced database. This bypasses the need for manual digitization and georeferencing of hard-copy interpretations.

Typically, structural interpretations (bedrock and surficial features) are first undertaken, creating a series of 'structural layers' (i.e. separate GIS files) that can also contribute to the final compiled map (e.g. form lines, folds, faults, contacts, domains, glacial flow forms) or be saved as separate maps that form part of a portfolio for the study area. This is followed by interpretation of geological divisions (e.g. rock units, tectonic domains, surficial materials), either by visual interpretation and/or by computer-assisted (i.e. classification) interpretation. For the spectral differentiation of units, it is often advantageous to restrict unit interpretations to areas of bedrock and residual weathered bedrock by masking vegetation, snow, ice, and water. The masking is accomplished by defining thresholds in the pixel values of the ground-cover classes using image-slicing techniques.

The full GIS database, including the interpretative layers, can be taken into the field and maintained by a GIS specialist at the field camp. It is advantageous to have a GIS specialist in the field to maintain and

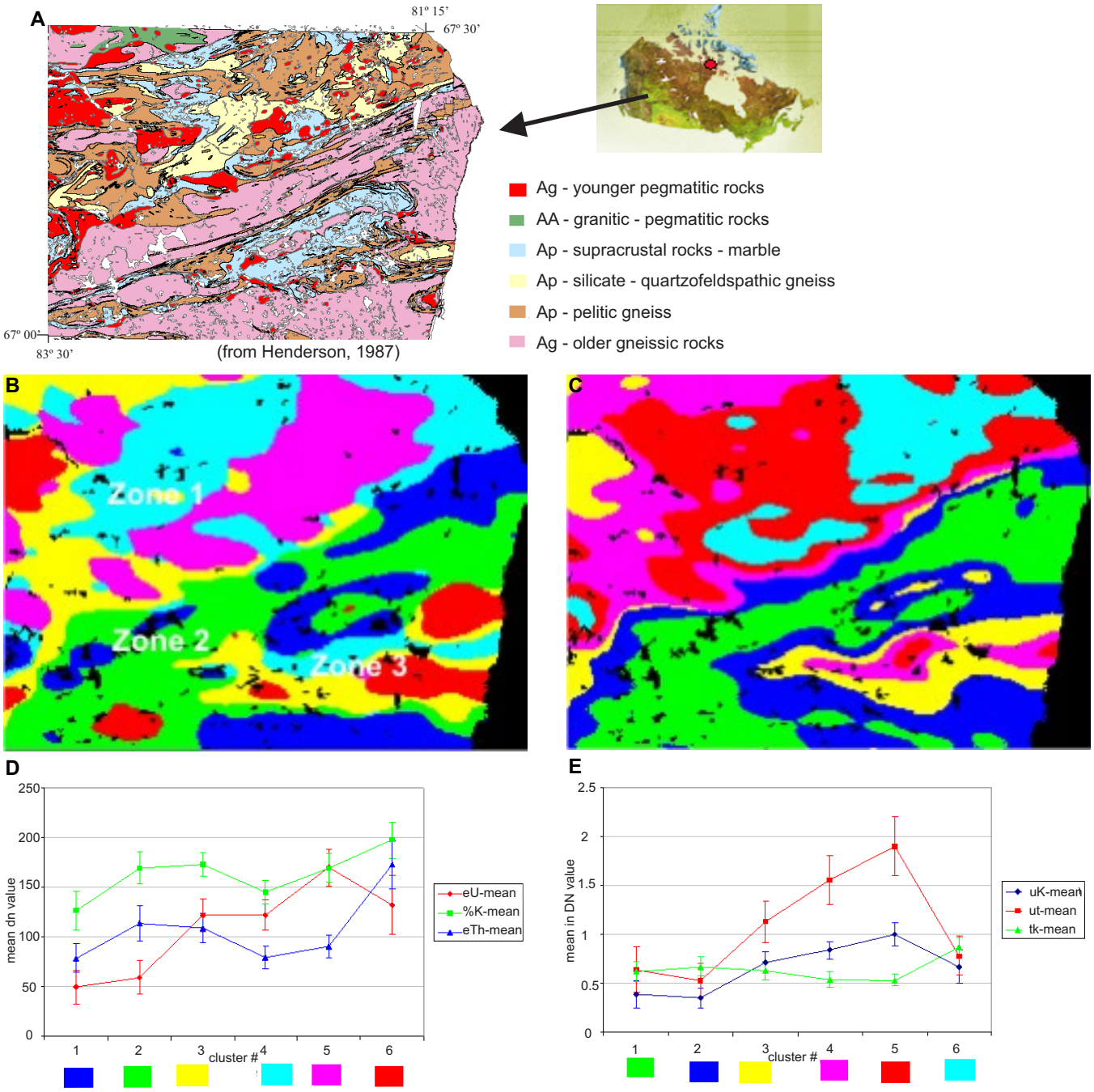

Figure 2-10. An example of an unsupervised computer approach in which a predictive map of radioelement domains is produced automatically. **(A)** Geology map of Melville Peninsula, Nunavut. **(B)** Radioelement (cluster) domain map derived from raw eU, eTh, and %K data. **(C)** Radioelement (cluster) domain map derived from ratio gamma data U/Th, U/K, and Th/K. In both maps, it can be seen in places that distinct radioelement domains correlate with mapped units but there are also areas that differ appreciably from the map. **(D)** and **(E)** Statistical plots showing mean radioelement values and associated standard deviation for each radioelement domain (cluster). Cluster colours are correlated to the maps shown in (C) and (D). Three different radioelement zones (zones 1-3) reflecting different lithological/tectonic regimes can be clearly seen on the unsupervised maps.

update the RPM database on a daily basis and manage incoming field data collected on hand-held computers. In addition, the GIS specialist can maintain the hand-held computers, provide cartographic and plotting capabilities, assist in the analysis and quality control of newly collected field data, help adapt the mapping strategy based on the comparison of new data to the RPM predictions, and begin digital compilation (with the mapping geologists) of the new geological map(s) while in the field.

FIELD LOGISTICS AND PLANNING

Remote predictive maps offer field geologists an excellent opportunity to better plan ground-based traverses, saving time, money, and resources (e.g. fuel) in the

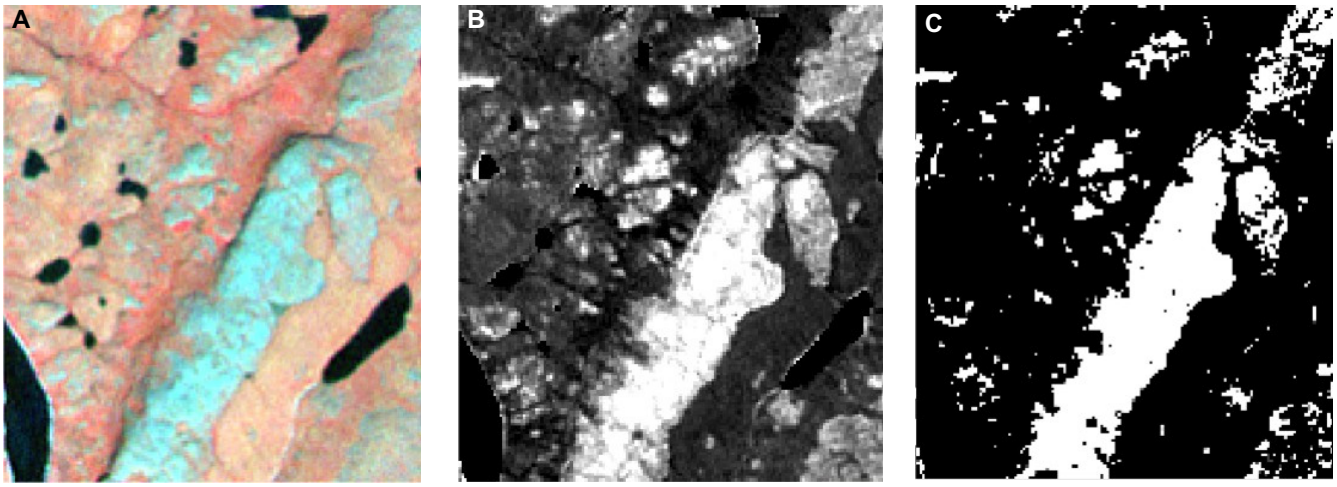

Figure 2-11. Example of an outcrop map derived from LANDSAT data. **(A)** LANDSAT colour composite image (bands 4, 3, and 2 corresponding to red, green, and blue). Red is vegetation and cyan is outcrop. **(B)** Ratio image of bands 7 and 4 that enhances the outcrop (based on the difference in spectral reflectance), which are the white areas. **(C)** Outcrop map.

field. In addition, better integration of remotely sensed data into field programs, especially optical and radar imagery, can provide a map of terrain units, including outcrop and wetland areas (Fig 2-11). The combined geological and terrain information provided by RPM allows focusing field mapping on areas where surficial conditions (higher density of outcrop, non-wetlands, terrain accessibility, etc.) are more amenable for fieldwork or areas where the geology, as determined from the predictive map, is more complex. Given this scenario, field traverses would be located heterogeneously throughout one large mapping area over multiple years of fieldwork instead of preparing a layout of regularly distributed traverses per field season (see field traverses on the predictive map shown in Fig. 2-12 and Case Study 9 of this volume). This strategic approach may prove to be more efficient and less costly than the traditional approach because it allows more effort to be expended on accessible areas with more variable or complex geology.

Validation of Remote Predictive Maps

Like all predictions, remote predictive maps have an inherent degree of uncertainty. In fact all geological maps, no matter how they are produced have an inherent degree of uncertainty. To assess the value and accuracy of a remote predictive map, it is important to understand map uncertainty and to have methods for assessing it (see Case Studies 2, 5, 6, and 7 of this volume for validation methods). Firstly, a qualitative assessment could be made by comparing the patterns of the remote predictive map with the patterns of the geological map compilation based on newly acquired field data. This should give some first-order overall insight to the performance of the prediction. It should be noted, however, that discrepancies between mapped geology and the predictive maps are not necessarily

Table 2-3. Confusion matrix comparing the coincidence percentages between unit-generalized remote predictive and published 1:250 000 scale geological maps of NTS sheets 57a and 57b of the Boothia mainland area. The elements on the diagonal of the confusion matrix represent the number of grid cells the RPM and geological map are in agreement, the off-diagonal elements show the number of grid cells where the maps are in conflict. The summed rows of the matrix represent the user accuracy, i.e., the total percentage of grid cells of the RPM that is in agreement with the geological map for a particular unit. The summed columns of the matrix represent the producer accuracy, i.e., the total percentage of grid cells of the geological map that is in agreement with the RPM for a particular class. The average user and producer accuracies, together with the overall accuracy (the summed grid cells of the diagonal elements, divided by the total number of grid cells of the area), are listed below the matrix.

		Generalized units geological map, Ryan et al. (2008a,b)				
		Metagabbro	Metagranitoid	Granulite	Supracrustal	Accuracy
Generalized Units Remote Predictive Map 2005	Metagabbro	0	59317	0	88574	0
	Metagranitoid	0	25049011	619862	2255361	0.9
	Granulite	0	139197	1915960	10424	0.93
	Supracrustal	0	708235	34447	621956	0.46
	Reliability	0	0.97	0.75	0.21	
Average accuracy	57.00%					
Average reliability	64.00%					
Overall accuracy	**87.60%**					

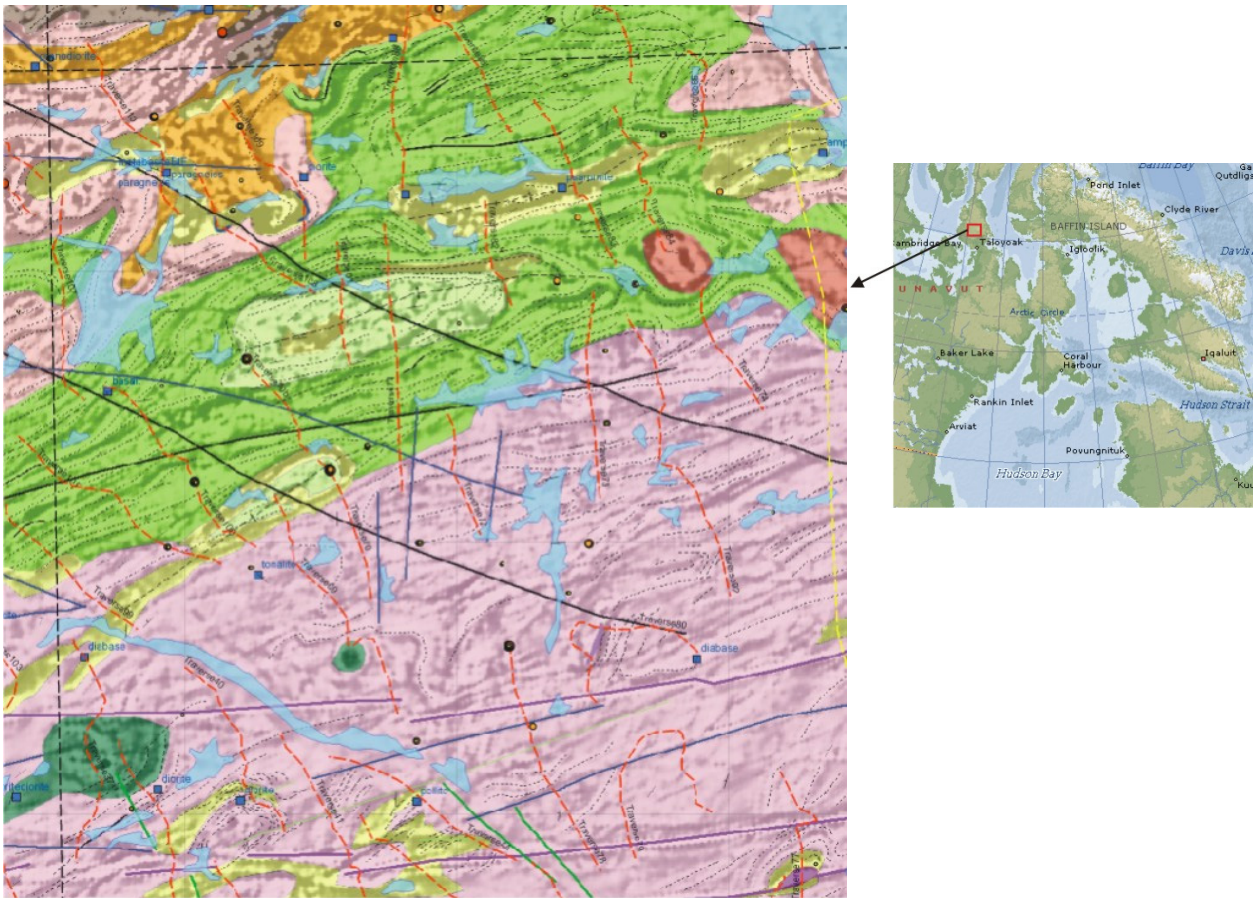

Interpreted Units

Interpreted from total magnetic field, 1sd VD derivative aeromagnetic, Landsat ETM image data, rock sample descriptions Tunneys Pasture (augmented by local areial photograph interpretation.

Hydrography

Palaeozoic Cover

Hydrography

Diabase Dykes

Diabase outcrops (east-west-trending dyke swarm)

Diabase outcrops (northwest-southeast-trending McKenzie dyke swarm)

Mafic to Felsic Intrusions / Intrusive Complexes

Linear discordant magnetic highs (late synkinematic granitoids)

Magnetic foliation wrapped circular anomalies (pre- to synkinematic plutons)

Small circular magnetic highs (post-kinematic (mafic?) intrusions, gridding artefact?)

Small circular magnetic lows (post-kinematic (felsic?) intrusions, gridding artefact?)

Undifferentiated Orthogneiss and Granitoids

Curvilinearly patterned magnetic lows (undifferentiated strongly foliated to layered gneissic granitoids and tonalite)

Linearly patterned to smooth intermediate magnetic background (undifferentiated foliated granitoids, tonalite, and orthogneiss)

Granulite-Grade Belt

Elongated magnetic highs in linear magnetic lows (mafic gneiss/granulite or amphibolite)

Linearly patterned magnetic lows (granulite-grade paragneiss, granite gneiss, and charnokite)

Linearly patterned magnetic highs (intermediate to mafic granulite and gneiss)

Supracrustals (Archean-Paleoproterozoic)

Landsat curvilinears (supracrustals of Chantrey Group)

Bright tone elongated layered units on airphotos (marble or quartzite)

Curvilinear patterned magnetic highs (intermediate to mafic schist, gneiss, and amphibolite)

Small prominent linear anomalies (banded iron formation, psammite, or mafic to ultramafic rocks)

Curvilinear magnetic high enclaves (high magnetic susceptable supracrustals intermediate to mafic schist, gneiss, and amphibolite)

Curvilinear branched magnetic lows with low magnetic relief (low magnetic susceptable supracrustals, mainly psammite, Ga-bearing paragneiss and pelite)

Integrated Structures

Magnetic dyke east-west trending

Magnetic dyke northwest-southeast trending

Magnetic synform

Magnetic antiform

Magnetic contact

Magnetic contact unconformable

Magnetic fault

Magnetic foliation

Landsat contact

Landsat fault

Landsat foliation

Landsat lineament

Landsat shear zone

Foot

Helicopter

Figure 2-12. Example of a portion of an integrated predictive map produced for the Geological Survey of Canada Boothia mapping project. This map was interpreted largely from enhanced magnetic and LANDSAT data, as well as the analysis of field samples, which are stored at Tunney's Pasture in Ottawa (a GSC storage site). The predicted map comprises interpreted lithological units, structures, and lineaments. The predicted lithological units were tentatively assigned to rock type based on the analysis of hand samples that were georeferenced to a locational database within a GIS. Field traverses (foot and helicopter), which were planned based on predicted units and outcrop density, are shown as red and yellow lines.

interpretation errors, but could point to real geological features that are not represented or are wrongly represented on the geological map. Such discrepancies could occur because units are generalized or poorly represented due to sparsely distributed field data or because there is no field control at all. One can also apply more systematic approaches by tallying the agreements and non-agreements between the units of the RPM and geological map at the visited field locations at various levels of map generalization. The results of this validation method can be represented in a confusion matrix (Table 2-3) in which the diagonal elements represent the number of field stations where RPM and geological maps are in agreement. In contrast, off-diagonal elements represent the number of field stations where RPM and geological maps are in conflict. The sum of the diagonal elements divided by the total number of field stations provides a measure of the overall accuracy of the prediction. In addition, the sums of the rows and the columns of the confusion matrix provide the class accuracies and class reliabilities, respectively. This method of assessment assumes that the RPM and geological maps have the same unit legend. To generate a consistent legend, the RPM legend may have to be revised to a legend developed from data gathered in the field. Alternatively, the class names in both the RPM and geological maps could be strictly adhered to (and only field stations at which the RPM and geological maps have the exact same unit names will be considered correctly classified). This is likely to result in very low prediction accuracies that do not reflect the spatial agreement between the units of the RPM and geological maps. The discrepancies between the legends obtained from RPM and geological maps, as a result of the incongruence between field and image diagnostics, is an urgent issue on the RPM research agenda. Recent work in geography suggests that quantitative measures of semantic class similarity are feasible (e.g. Ahlqvist and Gahegan, 2005). Such measures may be used to improve on the accuracy assessment methodology for RPM as well.

OPTIMIZING ORGANIZATIONS TO SUPPORT REMOTE PREDICTIVE MAPPING

Full integration of RPM into a mapping project can present organizations with operational opportunities and challenges. It is critical that RPM human resource requirements and fundamental changes in work patterns are addressed (Franklin, 2001; Schilling, 2007). Remote predictive mapping presents us with a heuristic change in how the mapping problem is approached and can have impact on the organizational aspects of how mapping is conducted. Remote predictive mapping may be implemented by a single individual with straightforward short-term goals in mind that will have limited organizational impact. Alternatively, RPM activities may mandate large multidisciplinary teams with a long-term objective of mapping vast terranes. To increase the benefits in the latter case, it is helpful to think through the administrative, technical, and training support structures that are required. Staff may need to take time to acquire specific skills in predictive mapping, remote sensing, GIS, or integration techniques.

For example, geologists may need to know how to do on-screen GIS interpretations, or a remote-sensing expert may need to upgrade basic knowledge of geological principals. This could require a commitment of time and money for an organization. Consideration could also be given to the development of in-house training case studies, specifically tailored to the type of terranes an organization must deal with. For the mapping process to be successful, organizations and projects need to use scientists and technicians having broad backgrounds.

CONCLUDING REMARKS

Adoption of the RPM strategy necessitates a shift in a mapping paradigm that results in adjustments for traditional field geologists, remote sensing, and GIS specialists and to a survey organization as a whole. However, in principal, it is not such a great leap for those that routinely interpret airphotos (which still form an extremely valuable data source for RPM) in support of their mapping endeavours to interpret imagery acquired by Earth orbiting satellites or airborne systems to produce a remote predictive map. Remote predictive mapping can be applied at various levels of sophistication of digital processing and numerical interpretation methods. The visual interpretation of one or a few images and map layers can be as effective as computer-assisted pattern recognition from many image variables.

Success of an RPM strategy requires the adoption of a multidisciplinary team approach including geophysicists, remote-sensing specialists, GIS experts, and field mappers. This approach fosters team work both in the office and in the field. Furthermore, the RPM strategy allows for the production of not only one final predictive map but a number of intermediary map products (see Table 2-2) that may be useful for further mapping and exploration activities in the same area in future generations. Instead of publishing a hard-copy map exclusively, a series of images, interpretations, field observations and notes, meta-data records, and predictive maps can be published on a CD or DVD or through the internet in a GIS-friendly format providing a permanent archive of all the geoscience data for use by geologists and explorationists. This would ultimately allow for alternative interpretations to be made by others.

The RPM methodology is not static but constantly evolving with new sensor systems, methods to process and integrate data, and innovations in geospatial data infrastructures to implement RPM. In the future, high-resolution remotely sensed data (i.e. SPOT 5) may replace airphotos. Data from high-resolution sensors cover wider areas, are easier to georeference (i.e. geo-referenced data can be ordered directly from the vendor), and thus more easily incorporated into a digital GIS database than airphotos, and provide a base for interpretation, plotting, and in-field navigation using hand-held computers. In many cases in the North, their geographic accuracy is better than the existing topographic maps. Furthermore high-resolution imagery can be collected for stereo viewing (i.e. overlapping acquisition swaths) facilitating geological interpretation.

The following suggestions for future RPM programs are based on our experience with mapping campaigns that have utilized RPM methods:

- Satellite and geophysical imagery (both magnetic and gamma-ray spectrometer) should be acquired early in the mapping project. This allows ample time for analysis and interpretation before field-work begins. For example, if mapping is planned in a northern location in the summer of 2008, the satellite and geophysical data should have been collected in the summer of 2007 to allow for data-base building and RPM interpretation.
- High-resolution satellite imagery (SPOT5, IKONOS, QUICKBIRD, etc.) are extremely useful for basic interpretation, as a navigational layer in field-data capture systems, and as a base for plotting compilation work. The current issue is cost and image size; however both of these will likely become less significant in the future as technology improves and costs are reduced.
- If legacy data are available, a point data set of field sites and associated observations should be compiled in a GIS layer to support integrated geological image interpretation. This guides the digital compilation of units and structures, and substantiates their allocation to field-established classifications.
- Ground truthing during fieldwork is facilitated by uploading RPM interpretations on hand-held computers. This enables geologists to verify the existence of predicted geological features while traversing in the field.
- Screen digitizing of georeferenced geophysical and remotely sensed imagery is recommended to exploit the complementary information of multivariate image data during image interpretation and to avoid the time consuming and error-prone process of capturing interpretations made on hard-copy maps and Mylar overlays.
- RPM products can be used to assist in producing a topographic base for navigation and in predicting areas of bedrock exposure for planning traverses.
- RPM interpretations should ideally be performed by mapping geologists (with the help of GIS or remote-sensing specialists). This allows geologists to play an integral role in the RPM process, gain insight into the relationships between field and image data, and help understand how the various imagery and enhancement techniques, in concert with field data and maps, contribute to the extraction of geological information.
- Remote predictive mapping should lead to faster and less costly mapping cycles and the production of a database of primary and interpreted data sets that can be easily reused in mapping and exploration. The success of RPM will largely depend on the GIS and remote-sensing literacy of the future Earth scientists and on a deepened understanding of the relationships between remotely sensed physical properties and field and/or laboratory observations. The onus is on those for whom bridging the gap between the outcrop and multivariate birds-eye image perspective has become second nature. Only then can the complementary value of the exhaustive geological information, derived from sparsely distributed field sites and the indefinite but spatially extensive geological information obtained by remote sensing, be synergistically exploited for geological exploration of the vast Canadian landmass.

ACKNOWLEDGEMENTS

The authors would like to thank Eric Grunsky from the Geological Survey, Don James from the Canada-Nunavut Geoscience Office, and an anonymous reviewer for thoughtful comments and suggestions that have lead to a much clearer and better presentation of this chapter. This work was carried out and funded under the Remote Predictive Mapping Project, part of NRCan's Earth Sciences Sector's (ESS) Northern Minerals Development Program.

REFERENCES

Ahlqvist, O and Gahegan, M.
2005: Probing the relationship between classification error and class similarity; Photogrammetric Engineering and Remote Sensing, v. 71, p. 1365-1373.

Drury, S.A.
2001: Image Interpretation in Geology, 3rd edition Cheltenham, UK: Nelson Thornes; Malden, MA : Blackwell Science, 304 p.

Franklin, U.
2001: The Real World of Technology; Anansi Press, Canada, 209 p.

Gillespie, A.R., Kahle, A.B., and Walker, R.E.
1986: Colour enhancement of highly correlated images. I. Decorrelation and HSI contrast stretches; Remote Sensing of the Environment, v. 20, p. 209-235.

Harris, J.R.
1989: Clustering of gamma ray spectrometer data using a computer image analysis system, *in* Statistical Applications in the Earth Sciences, (ed.) F.P. Agterberg and G.F. Bonham-Carter; Geological Survey of Canada, Paper 89-9, p. 19-32.

Harris, J.R., Viljoen, D., and Rencz, A.
1999: Integration and visualization of geoscience data, Chapter 6 *in* Manual of Remote Sensing, Volume 3: Remote Sensing for the Earth Sciences, 3rd edition, (ed.) A. Rencz; John Wiley and Sons Inc., New York, v. 3, p. 307-354.

Henderson, J.A.
1987: Geology of southeastern Melville Peninsula, District of Franklin, Northwest Territories; Geological Survey of Canada, Map 1655A, scale 1:100,000.

Jensen J.R.
1995: Introductory Digital Image Processing: A Remote Sensing Perspective, 2rd edition; Prentice Hall, 316 p.

Jolliffe, I.T.
2004: Principal Component Analysis, 2nd edition; Springer-Verlag, New York, Springer Series in Statistics, 486 p.

Kruse, F. and Raines, G.
1994: A technique for enhancing digital color images by contrast stretching in Munsell color space, *in* Proceedings of the ERIM Third Thematic Conference, Environmental Research Institute of Michigan, Ann Arbor, MI, p. 755-760.

Lillesand, T.M. and Kieffer, R.W.
2000: Remote Sensing and Image Interpretation, 4th edition; John Wiley and Sons Inc., New York, 724 p.

McDonough, M.R., McNicoll, V. J., and Schetselaar E.M.
1995: Age and kinematics of crustal shortening and escape in a two sided oblique-slip collisional and magmatic orogen, Paleoproterozoic Talston Magmatic Zone, northeastern Alberta, *in* LITHOPROBE Alberta Basement Transects Workshop, (ed.) G.M. Ross; Lithoprobe Report No. 47, Lithoprobe Secretariat, University of British Columbia, p. 265-309.

Milligan, P.R. and Gunn, P.J.
1997: Enhancement and presentation of airborne geophysical data; AGSO Journal of Australian Geology and Geophysics, v. 17, p. 63-75.

Richards, J.A. and Jia, X.
2006: Remote Sensing Digital Image Analysis: An Introduction; Springer-Verlag, New York, 4th edition, 439 p.

Ryan, J.J., Nadeau, L., Hinchey, A.M., James, D.T., Young, M.D., Williams, S.P., and Schetselaar, E.M.
2008a: Geology, southern Boothia mainland area, Pelly Bay-Rae Strait-Harrison Island map area, Nunavut; Geological Survey of Canada, Open File, scale 1:250 000, in prep.

Ryan, J.J., Nadeau, L., Hinchey, A.M., James, D.T., Sandeman, H.A., and Schetselaar, E.M.
2008b: Bedrock geology of the southern Boothia mainland area (Pelly Bay-Rae Strait-Spence Bay map areas), Kitikmeot region, Nunavut, *in* Current Research 2008; Geological Survey of Canada, in prep.

Schetselaar, E.M.
2000: Integrated analyses of granite - gneiss terrain from field and multisource remotely sensed data: A case study from the Canadian Shield; Ph.D. thesis, Institute for Aerospace Survey and Earth Sciences (ITC) Netherlands, ITC dissertation 73, 269 p.

Schetselaar, E.M., Chung, C.F., and Kim, K.
2000: Classification of bedrock units in vegetated granite-gneiss terrain by the integration of airborne geophysical images and primary field data; Remote Sensing of Environment, v. 71, p. 89-105.

Schilling, M.
2007: Strategic Management of Technological Innovation: McGraw-Hill Education, Singapore, 312 p.

CHAPTER 3. Geophysics

M. Pilkington, P. B. Keating, and M. D. Thomas
Geological Survey of Canada, 615 Booth Street, Ottawa, Ontario K1A 0E9
Corresponding author's email:mpilking@NRCan.gc.ca

THEORETICAL PRINCIPLES

The Earth's gravity and magnetic fields are described as potential fields. Generally, the relatively short wavelength (<1,000 km) variations of both gravity and magnetic fields are controlled by changes in rock properties residing in the Earth's crust. Density is the critical physical property influencing the gravity field, and magnetic susceptibility and natural remanent magnetization (NRM) control the magnetic field (see Appendix 3-1). Gravity and magnetic data contribute to geoscientific studies in two principal ways. They provide a means of mapping geology and they can be modelled quantitatively to yield information on the shape, size, and depth of geological bodies. For remote predictive mapping (RPM) applications, the former approach is considered, which does not involve any quantitative modelling, but attempts to present the potential field or processed versions of it in such a way as to assist in the mapping of lithological and structural features.

MAPPING APPLICATIONS OF GRAVITY AND MAGNETIC DATA

The fundamental tenet of geological mapping with potential fields is *trends of gravity and magnetic features mimic those of the outcropping geology.* Hence, structural features and changes in lithology are reflected in the potential field maps. However, a one-to-one connection between some geological feature, e.g., a pluton, and the resulting potential field is not always guaranteed. There must be a contrast in the physical property (i.e. density or magnetization) between the pluton and its surroundings which is large enough to produce an anomaly that can be detected by either a gravity or magnetic survey. If not, then no anomaly is produced and the pluton cannot be mapped from the potential field data alone. Similarly, faulting that juxtaposes two different lithologies with the same density (or magnetization) will not produce a gravity (or magnetic) anomaly. The identification of lithology from potential field maps can be ambiguous as magnetic and density properties of different rock types can be very similar. Nevertheless, individual anomalies may signify the presence of a specific lithology or formation. Patterns of anomalies and the shapes of groups of anomalies also may reflect certain lithologies, formations, or geological domains. They can also indicate different styles of deformation, i.e., brittle versus ductile. Since there is some ambiguity present in what lithology, or more precisely, what contrast in the physical properties of the lithologies is producing a given anomaly, it is desirable to have some knowledge of the densities and magnetizations of the rock types likely encountered in a given area. This knowledge can come from known (published) compilations of physical rock properties, or preferably, from measurements on samples taken from the area of interest or from the adjacent areas.

Table 3-1 Magnetic and gravity products available from the Geoscience Data Repository. The 200 metre grid of magnetic data is usually sufficient for regional-scale mapping. Bracketed values denote the grid interval.

Magnetics	
Total field	[200 m]
Vertical gradient	[200 m]
Total field	[1000 m]
Gravity	
Bouguer	[2000 m]
Vertical gradient	[2000 m]
Horizontal gradient	[2000 m]
Isostatic residual	[2000 m]
Observed	[2000 m]
Point data	[not gridded]

DATA SOURCES

Gravity and magnetic data for Canada are easily accessible through the internet using the Geoscience Data Repository (GDR) from the website (http://gdr.nrcan.gc.ca). The GDR is a collection of Earth Sciences Sector geoscience databases that is managed and accessed by a series of information services. This site allows you to discover, view, and download, free of charge, magnetic and gravity data. The magnetic data, maintained by the Geological Survey of Canada, are derived from the holdings of the Canadian Aeromagnetic Database and have been collected as part of an ongoing program to map the intensity of the Earth's magnetic field over the Canadian landmass and adjacent offshore areas. The gravity data, maintained by the Geodetic Survey Division, Geomatics Canada, are compiled from the holdings of the Canadian Geodetic Information System. As of September 2005, a number of gravity and magnetic products became available (Table 3-1). Gravity and magnetic data are available in gridded format for most of Canada. Gravity data also are available as point data, that is, values at the original gravity station locations.

In addition to the products listed in Table 3-1, grids from some high-resolution surveys flown at a line

Pilkington, M., Keating, P.B., and Thomas, M.D., 2008, Geophysics, Chapter *3 in* Remote Predictive Mapping: An Aid for Northern Mapping, (ed.) J. R. Harris; Geological Survey of Canada, Open File 5643, p. 29-52.

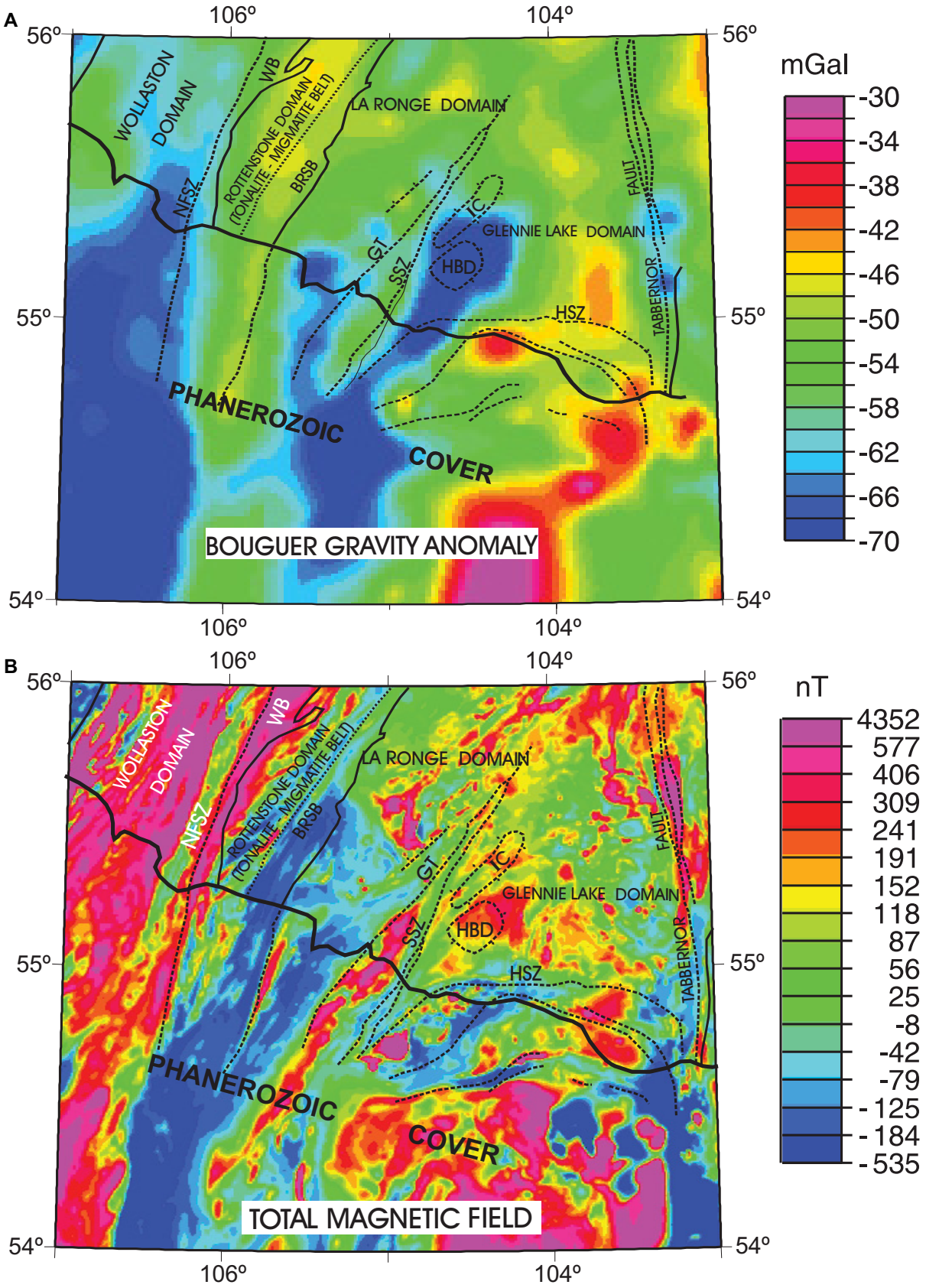

Figure 3-1. Comparison of **(A)** Bouguer gravity anomaly and **(B)** total magnetic field maps covering an area of the southern margin of the Trans-Hudson Orogen and the adjacent Phanerozoic cover. Selected geological features are superposed. BRSB = Birch Rapids Straight Belt (part of the Rottenstone Domain); GT = Guncoat Thrust; HBD = Hunter Bay Dome; HSZ = Hartley Shear Zone; IC = Istwatikan Complex; NFSZ = Needle Falls Shear Zone; SSZ = Stanley Shear Zone; WB = Wathaman Batholith. Heavy line marks the southern margin of the Canadian Shield. Dashed lines represent the shear zones and faults.

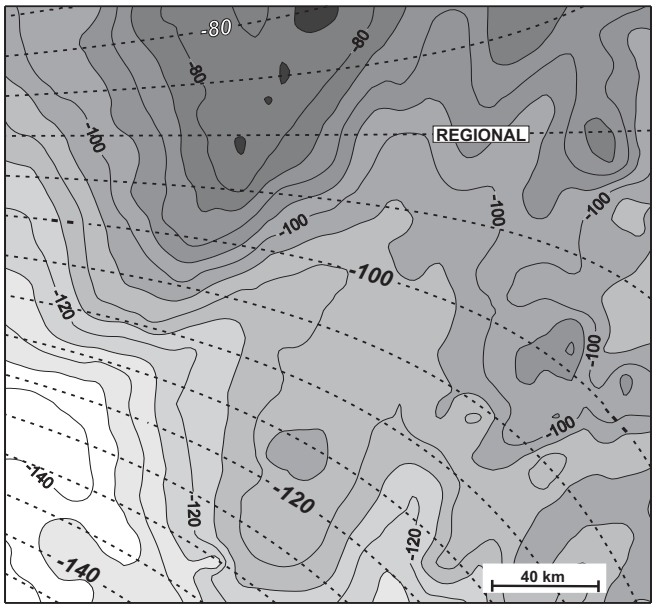

Figure 3-2. Bouguer gravity map of area in southwestern Alberta (solid line contour interval is 5 mGal). Dashed contours represent the regional component of the Bouguer gravity field (contour interval 5 mGal) determined by polynomial regression.

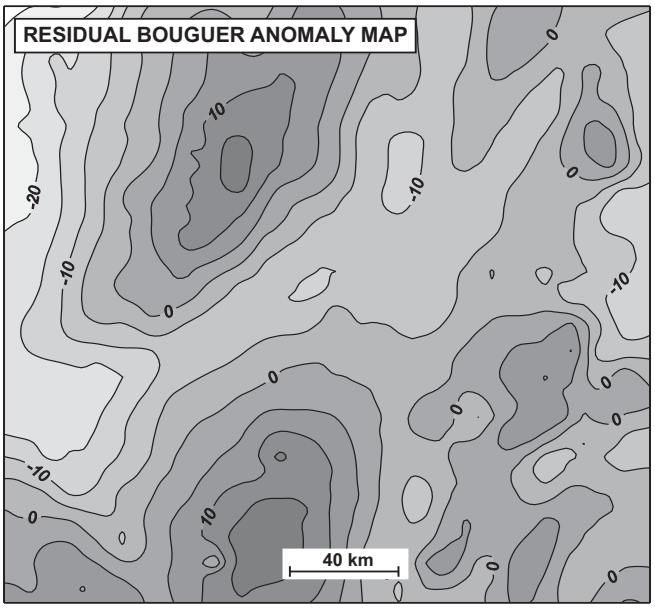

Figure 3-3. Residual Bouguer gravity anomaly map of area in southwestern Alberta once the regional component of the Bouguer gravity field has been removed (contour interval 5 mGal).

spacing of 200 or 400 m are also available. In the case of recent surveys, the point data (also called line data) are also available. A typical example is the Boothia Peninsula survey.

More information on the collection, distribution, and access to data can be found on the Geophysical Data Centre website (http://gdcinfo.agg.nrcan.gc.ca).

EXAMPLES OF POTENTIAL FIELD MAPS AND THEIR UTILITY

Gravity Maps

Bouguer Anomaly Maps

The Bouguer gravity anomaly map is the most common form of gravity map. The utility of the Bouguer map may be appreciated from Figure 3-1, which illustrates the mapping capabilities of such maps. Structures and lithological trends can be seen to extend from the exposed geology of the Trans-Hudson Orogen in the north under adjacent Phanerozoic sedimentary cover further south. Here, granitic rocks typically produce negative anomalies, whereas mafic and ultramafic rocks are associated with positive anomalies. Consequently, in many cases, distinct anomalies can be linked to such rock types, particularly in crystalline terrains where these rocks generally represent end members in the density spectrum. Naturally, many other rock types, having intermediate density characteristics, may produce anomalies that are not as distinct or prominent and may be more difficult to tie to a particular lithology without first 'calibrating' the anomalies in an area of good exposure.

Residual Gravity Anomaly Maps

Gravity anomalies with wavelengths much larger than those anomalies caused by near-surface density changes (the ones of interest) are classed as regional. Phenomena such as variations in depth to the Moho or intra-crustal discontinuities, and changes in sedimentary facies and metamorphic grade can produce regional anomalies. These can be removed by a variety of mathematical or graphical methods, in a process known as filtering or regional-residual separation. Once the regional signal is removed, the remaining gravity field is termed the residual gravity field. Various corrections are applied to gravity measurements: the free air correction takes into account the reduction of gravitational attraction with increasing measurement height and the latitude correction the variation of attraction as a function of latitude (the shape of Earth is an ellipsoid, i.e., a flattened sphere). The Bouguer correction accounts for the attraction of material between the location of the measurement point and the reference datum, generally the ellipsoid surface itself. In rugged terrain, it is recommenced that a terrain or topographic correction be done. In which case, detailed knowledge of the topography is needed.

Superimposed on the Bouguer gravity map of Figure 3-2 is the regional gravity field that has been modelled as a low-order polynomial. The regional field is essentially a broad increase from the southwest to the north, which in turn causes the Bouguer gravity values to have a similar increase northward. Representations of the data, such as this grey-scale map shown in Figure 3-2, will tend to be dominated by the regional gravity character and the smaller scale features are suppressed,

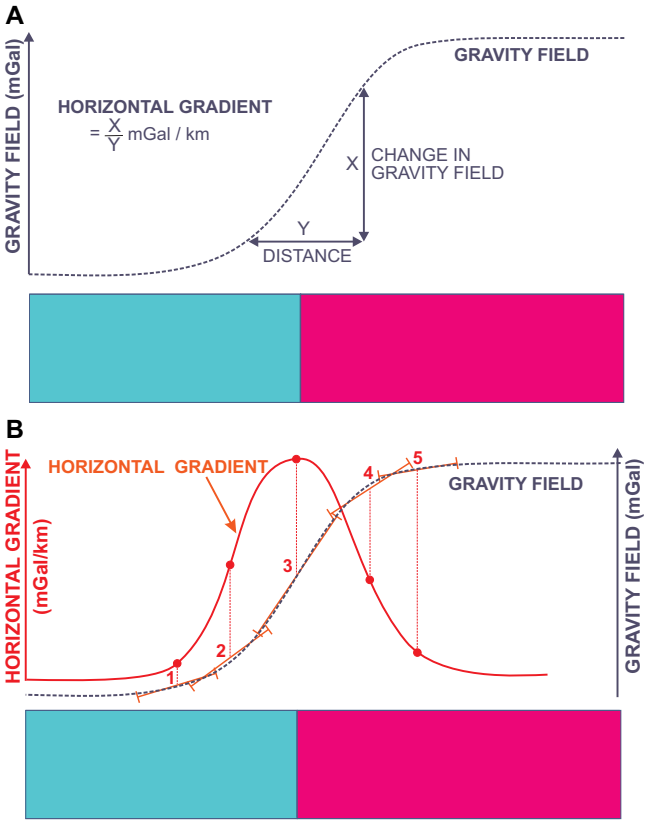

Figure 3-4. (A) Bouguer gravity profile across a vertical geological boundary. The horizontal gradient of a section of the profile is defined as change in gravity (X) divided by the distance (Y) over which the change takes place. **(B)** Plot of the horizontal gradient corresponding to the Bouguer profile, which is based on gradient values computed for five sections of the profile.

hence removing the regional gravity field is desirable to emphasize these small-scale details. When the regional gravity field is subtracted from the Bouguer map, the residual anomaly map (Fig. 3-3) is obtained. This displays a series of distinct anomalies having northeast trends, and the average level of the field is now similar over the whole area.

Horizontal Gravity Gradient Maps

Another way of enhancing the effects of near-surface density changes and suppressing any regional, longer wavelength gravity anomalies present is to display gravity anomalies in the form of horizontal gravity gradient maps. The magnitude of the local horizontal gradient may be computed for Bouguer anomaly maps at points on a grid and contoured. The concept of horizontal gradient may be easily appreciated by looking at it from a one-dimensional perspective (Fig. 3-4). The horizontal gravity gradient is simply the change in gravity over a given distance (Fig. 3-4A). In Figure 3-4B a series of five straight lines is fitted to a Bouguer gravity profile across a vertical geological contact. The magnitude of the horizontal gradient of each of these line segments is plotted as large dots, and these define a bell-shaped curve. The peak of the horizontal gradient curve is located over the contact. In map format, such peaks are manifested as ridge-like features, which fall along or close to geological contacts associated with lateral changes in density. Horizontal gradient maps enhance short-wavelength features, while suppressing long-wavelength signals. It should be recognized that horizontal gradient maps do not contain features similar in character to Bouguer gravity maps. Rather, they contain a series of linear or curvilinear ridge-like features. Importantly, the axes of the ridges trace steep geological contacts across which there are significant changes in density. As a result, horizontal gradient maps are very useful for mapping structural trends and major lithological boundaries. A horizontal gradient map derived from the Bouguer gravity map of

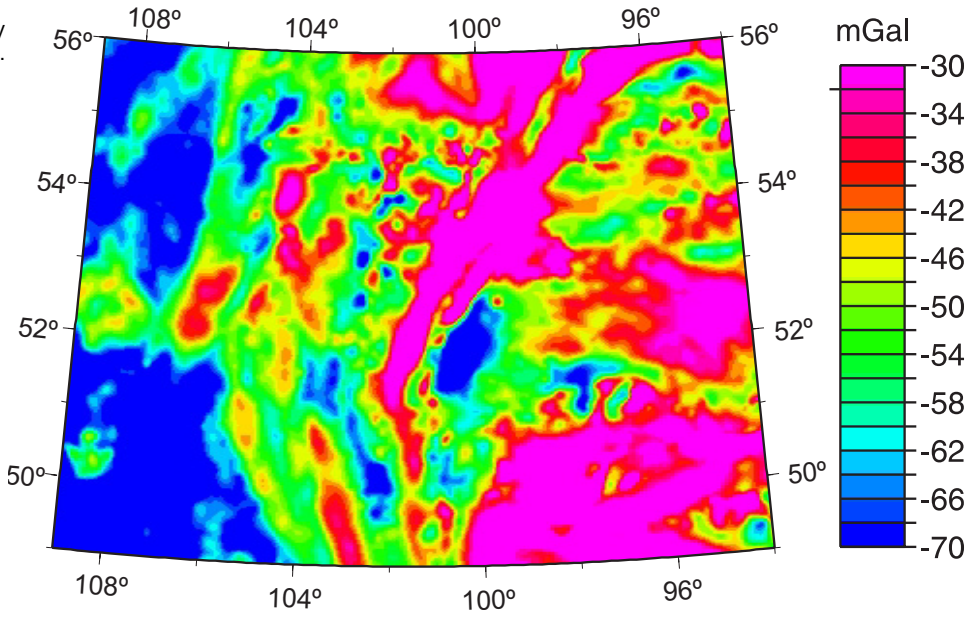

Figure 3-5. Bouguer gravity anomaly map of part of the Trans-Hudson Orogen.

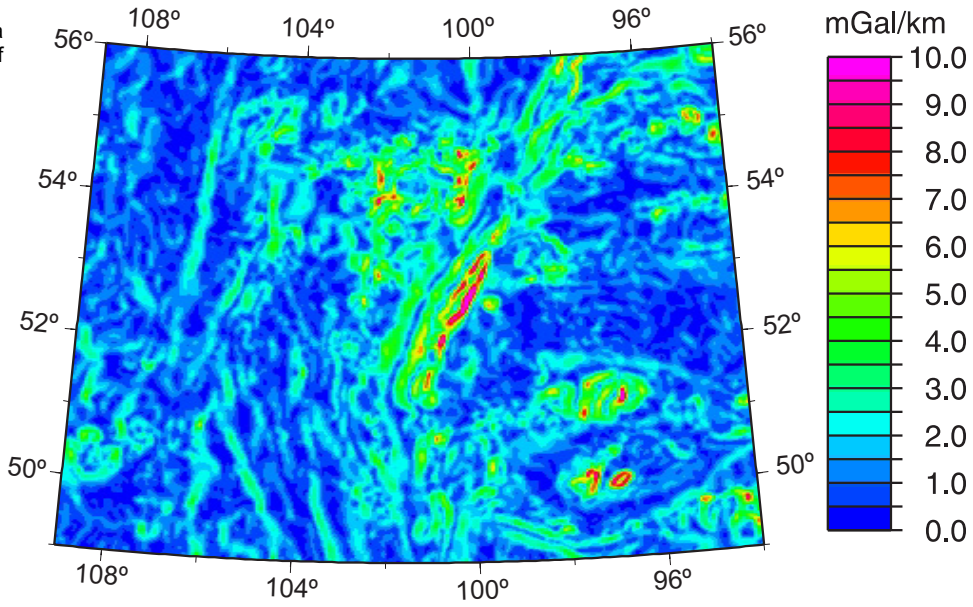

Figure. 3-6. Horizontal gradient of a Bouguer gravity anomaly map of part of the Trans-Hudson Orogen.

Figure 3-5 over a section of the Trans-Hudson Orogen is shown in Figure 3-6.

Vertical Gravity Gradient Maps

Another product of Bouguer gravity maps is the vertical gradient (or first vertical derivative) map, a type of map that is, perhaps, more commonly associated with aeromagnetic surveys. The vertical gradient of the gravity field is usually obtained using a theoretical approach, rather than the direct measurement approach used in some aeromagnetic surveys. An explanation of how the vertical gradient relates to the measured field is shown in Figure 3-7, which shows two gravity profiles across a body having a positive density contrast. One profile represents the gravity field computed at ground level and the other is the field computed at a height of 2.5 km (the large separation is utilized in order that a difference between the two curves is clearly discernible). The vertical gradient, in this case, is derived by subtracting the ground profile from that calculated at 2.5 km elevation, dividing the difference by 2.5, and reversing the sign. The reversal of sign follows a convention adopted in the calculation of magnetic vertical gradients, designed to produce positive gradient values directly above magnetic bodies. The vertical gradient signature associated with the body consists of a dominant, central positive component and flanking, subordinate negative components. A characteristic and useful feature of gradient anomalies is that they are narrower than their counterparts in the measured field. Thus, vertical gradient maps provide greater resolution than do maps of the measured field, with vertical gradient anomalies related to near-surface geological features tending to be emphasized at the expense of those related to deeper ones. Another useful feature of gradient maps is that the zero contour coincides with vertical contacts between geological bodies. In Figure 3-7, the zero value of the vertical gradient falls near, but not exactly at the contacts. This results from the large difference in the heights at which the two profiles were computed. As the difference becomes smaller, the zero value moves closer towards the con-

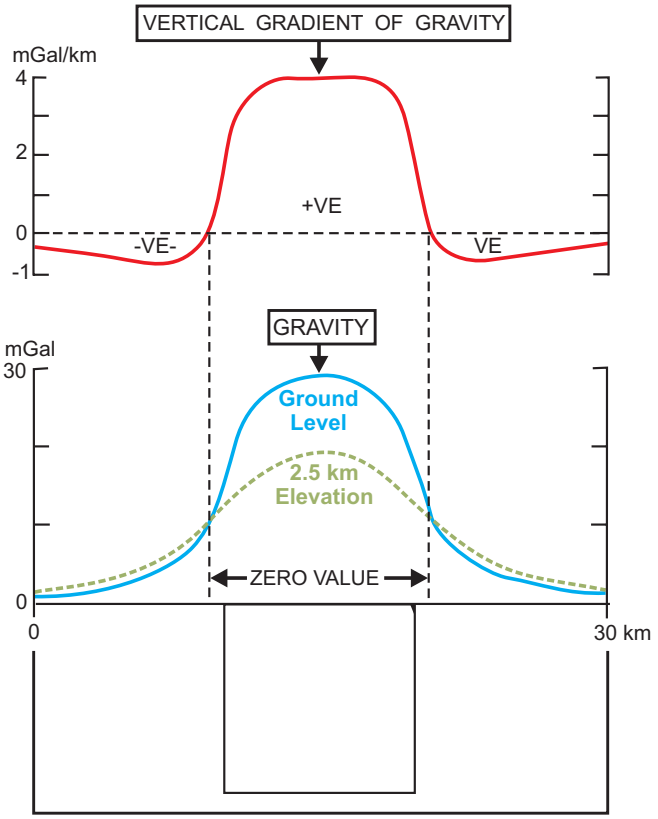

Figure 3-7. Bottom: Gravity field over a body with positive density contrast measured at ground elevation and at 2.5 km above ground. Top: Vertical gravity gradient over the same body. The gradient is equal to the difference between the two gravity profiles divided by the difference in height at which the profiles were measured.

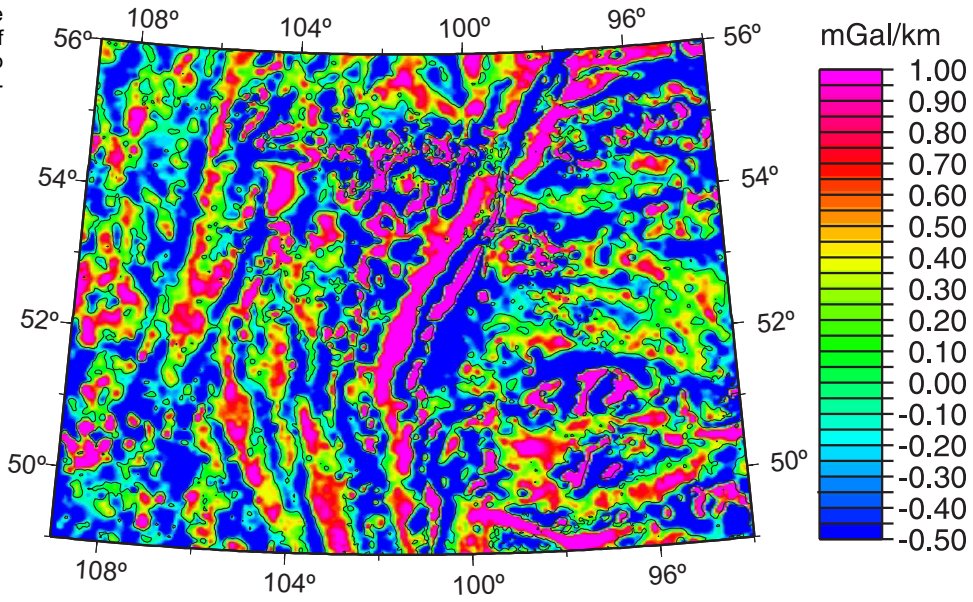

Figure 3-8. Vertical gradient of the Bouguer gravity anomaly map for part of the Trans-Hudson Orogen. The zero value contour, which theoretically coincides with steep boundaries, is added.

tact. In practice, the vertical gradient is not computed in the simplistic manner used for the demonstration provided by Figure 3-7, but rather is computed with more sophisticated mathematical operators. A vertical gravity gradient map for part of the Trans-Hudson Orogen is shown in Figure 3-8.

Magnetic Maps

Total Field Magnetic Maps

An example of a total field magnetic map, covering a region of the Trans-Hudson Orogen, is presented in Figure 3-9. The patterns of colours depicted on the map show the strength of the measured magnetic field and hence reflect how magnetic the rocks are. Trends in the anomalies, therefore, represent trends caused by the distribution of magnetic minerals (Appendix 3-1), which reflect the geological make-up of the area. The general appearance of such maps is influenced by the way data were collected: flight height and line spacing of the measurements and how they are displayed (see Appendix 3-2). The character of individual anomalies is dependent on the shape of the magnetized region or source, its depth, and its magnetization. In Figure 3-9, it is straightforward to see the predominant geological trends at this scale. East of 96º, the dominant strike of the anomalies is east-west. West of 104º, the trends are in a north-northeast direction north of 51º, whereas south of 51º, no dominant trend is apparent. More discussion on the interpretation of total field maps and other related products is given below in the 'Interpreting Maps' section.

Shaded Relief Magnetic Maps

Sometimes the intensity and spatial distribution of magnetic variations within a region are such that a total field image may appear somewhat muted, containing little information. Such images can be enhanced using a technique known as shading or shaded relief. The process simulates the effects of light directed on the three-dimensional surface defined by the grid of magnetic anomaly values. The intensity of light reflected back from a slope on the surface will vary according to the steepness of the slope. The proportion of illuminating light reflected back is known as the reflectance, and attains a maximum for slopes that are perpendicular to the direction of the light. The overall effect is one of areas of varying brightness and areas of shadow, an effect very similar to that created by the sun shining over a range of hills. The light direction and its inclination from the horizontal can be varied, thereby providing different images of the same data set. Depending on the direction and inclination, certain features may be enhanced or suppressed. Generally, magnetic features are enhanced when the light direction is oriented at right angles to them. The value of shaded relief maps is demonstrated in Figure 3-10, which shows an area within the Slave Province. Linear short wavelength anomalies related to the MacKenzie dykes are emphasized by light directed at right angles to their trend (Fig. 3-10A), but are suppressed when the light direction is parallel to the trend (Fig. 3-10B).

Magnetic Vertical Gradient Maps

The vertical gradient (or first vertical derivative) of potential fields has been discussed previously in the section dealing with gravity maps. The vertical gradient is sometimes measured in aeromagnetic surveys, but it may also be calculated from measurements made using a single magnetometer. The advantages of magnetic vertical gradient maps over magnetic total field maps are as follows.

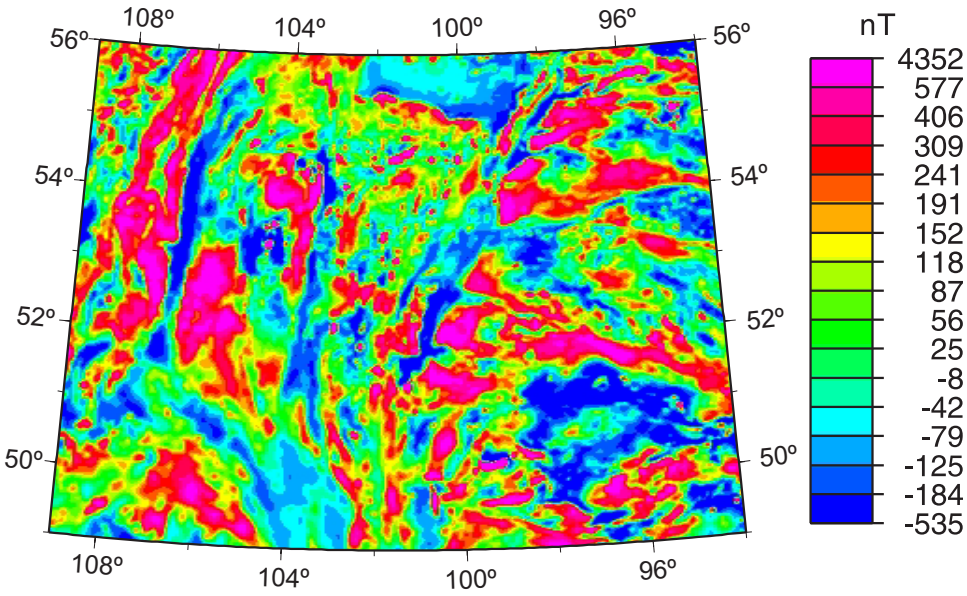

Figure 3-9. Total magnetic field anomaly map of part of the Trans-Hudson Orogen.

- Closely spaced geological units are better resolved (because vertical gradient anomalies are narrower).
- Vertical gradient anomalies produced by near-surface geological features are emphasized relative to those associated with deeper features (regional-scale anomalies tend to be suppressed).
- Vertical contacts are delineated directly by the zero contour at high magnetic latitudes.

Vertical (or steep) contacts are delineated by the zero contour at high magnetic latitudes, because the inclination of the Earth's field is also steep at high latitudes (the zero contour of the vertical gradient of gravity falls at or close to vertical or steep contacts at all latitudes, because the gravity field is everywhere directed vertically). An example of a magnetic vertical gradient map, covering a portion of the Trans-Hudson Orogen, is shown in Figure 3-11.

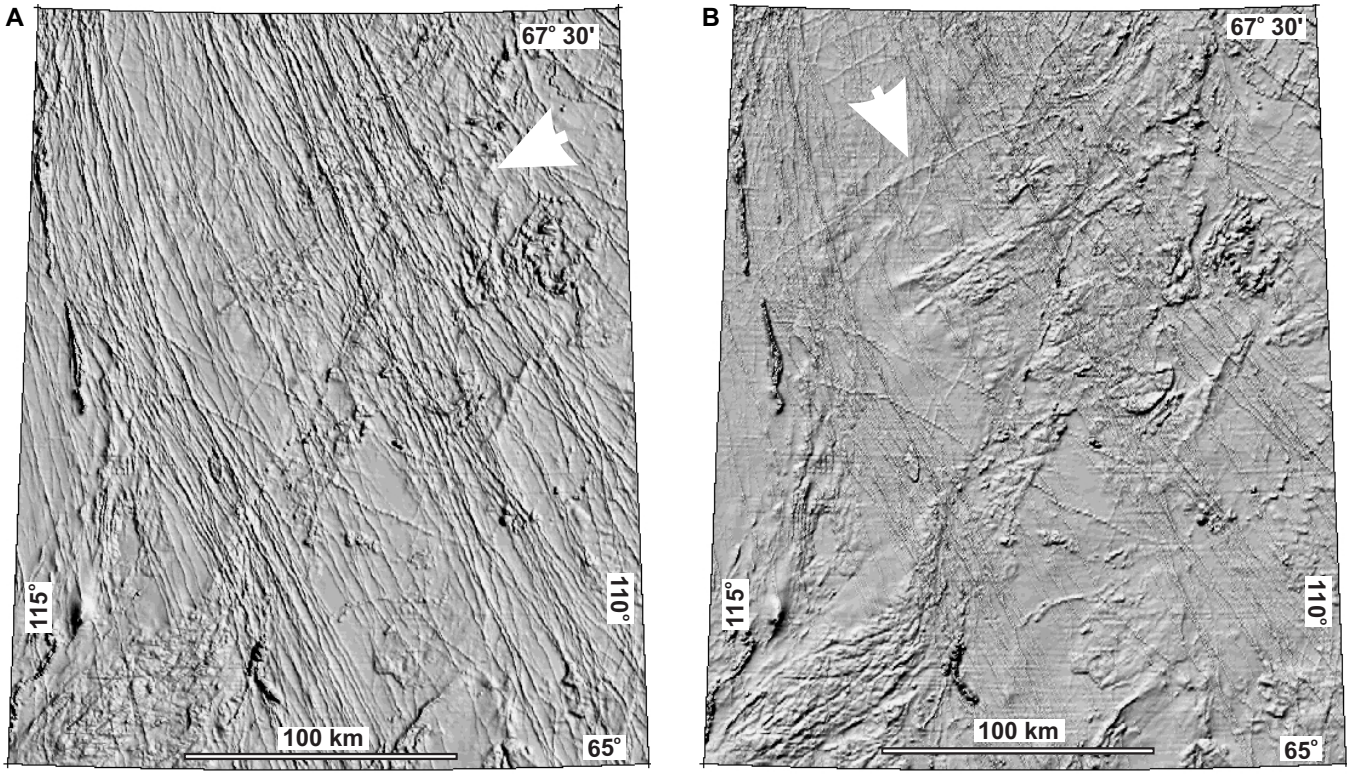

Figure 3-10. (A) Shaded relief aeromagnetic map of part of the Slave Province produced by illumination directed along 245º. **(B)** Shaded relief aeromagnetic map of part of the Slave Province produced by illumination directed along 155º.

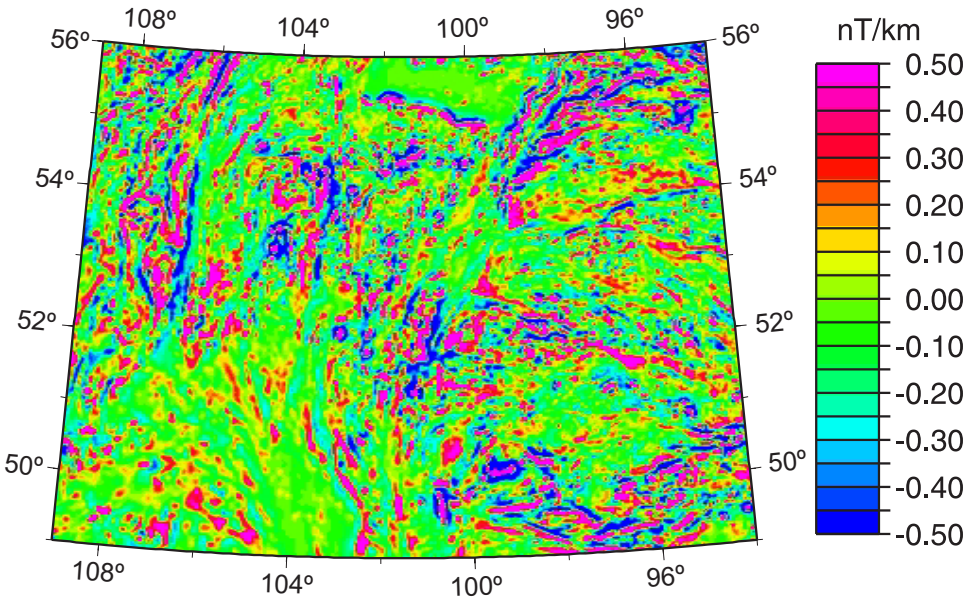

Figure 3-11. Vertical gradient of the total magnetic field map for part of the Trans-Hudson Orogen.

Tilt Maps

The tilt (which is related to the instantaneous phase) is defined as the arctangent of the ratio of the vertical gradient to the magnitude of horizontal gradient of the magnetic field. The horizontal gradient achieves a maximum near or over source edges and tends to zero elsewhere. The vertical gradient is positive over the source, zero over or near source edges, and negative elsewhere. As a result, the instantaneous phase of the magnetic field tends to be positive over sources bodies, zero over source edges, and negative elsewhere. One advantage of the use of the tilt is that, being a ratio, anomalies due to both weak and strongly magnetized sources are given equal weight. Hence, subtle (and often short-wavelength) anomalies are enhanced. Linear and quasi-linear geological features, such as faults, appear as lows whereas dykes often appear as maxima in the tilt map. The disadvantage is that, since the tilt is based on a ratio, all the original amplitude information in the magnetic field is lost, so strongly magnetized sources may produce the same tilt response as weakly magnetized sources. The tilt for a portion of the Trans-Hudson Orogen is shown in Figure 3-12.

Analytic Signal Maps

The analytic signal is defined as the absolute value of the square root of the sum of the two horizontal and the vertical derivatives of the total magnetic field. The main property of the analytic signal is that it reaches a maximum value directly over lateral magnetization contrasts (contacts) and that this maximum's location is independent of the orientation of the Earth's magnetic field and of the magnetization direction of the bodies. The benefit of these properties is that no assumptions

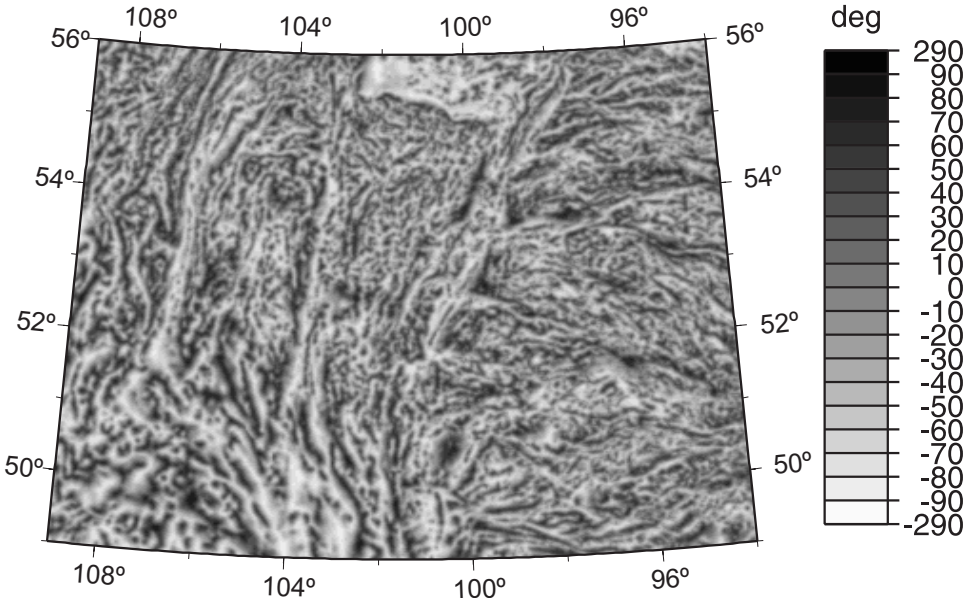

Figure 3-12. Tilt (or instantaneous phase) for part of the Trans-Hudson Orogen.

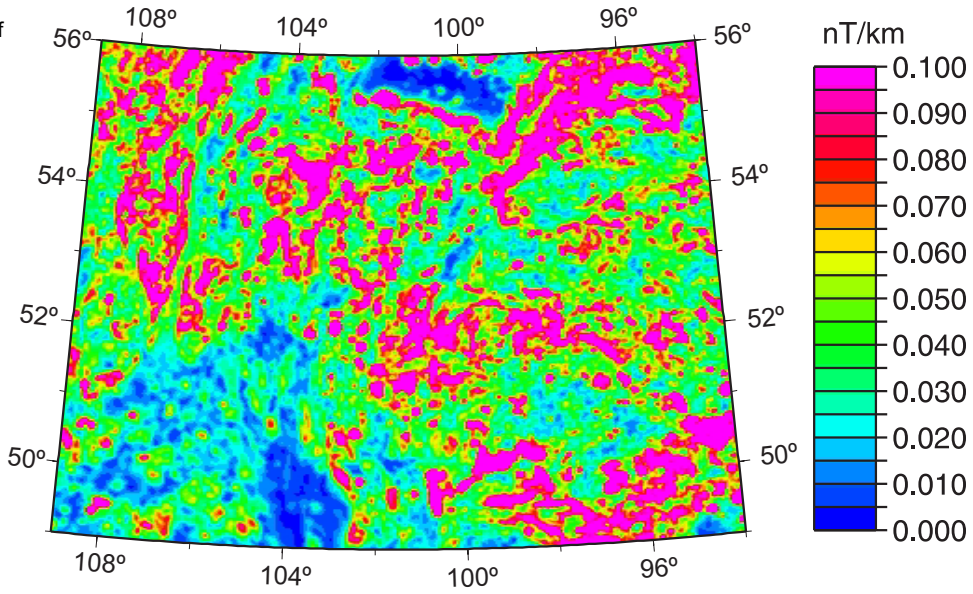

Figure 3-13. Analytic signal for part of the Trans-Hudson Orogen.

about the nature of the magnetization of the sources are required. However, this is only true for two-dimensional structures. For three-dimensional structures (e.g. intrusives), the shape of the analytic signal is almost independent of the Earth's field and magnetization directions. The analytic signal gives maxima directly over contacts, sheets (thin dykes), and cylinders. For a thick dyke, two series of maxima, slightly offset outward from their true location, are observed. As a result, dykes can appear a bit thicker than they really are. The use of derivatives to define the analytic signal accentuates near-surface effects and noise in the data. As a result, the analytic signal maxima often form discontinuous trends, even along seemingly continuous total field anomalies. Nevertheless, the location of analytic signal maxima can be taken to indicate the position of contrasts between differently magnetized bodies, and as such, can be used to locate geological contacts. Figure 3-13 shows the analytic signal for part of the Trans-Hudson Orogen.

Contact Maps

Introduction

Mapping the locations of lateral magnetization contrasts, i.e., the edges of magnetic sources, is one of the most basic and useful applications of magnetic survey data in geological mapping. Delineating the extent of units with similar magnetic properties follows the geological mapping approach of dividing the surface into rocks having similar properties. Whether or not the magnetization changes exactly mimic lithological ones, mapping such contrasts provides invaluable information on structural regimes, and deformation styles and trends.

There is more than one method of contact mapping, each with its own pros and cons. The five methods under consideration here all aim to define contact locations based on maximizing a given function over the source body edge. The locations of these maxima can then be plotted over the magnetic field, vertical derivative, etc., to enhance the interpretation. Details on how the different methods are implemented are given in Pilkington and Keating (2004).

Two study areas are used to underline the response of each method to differing geological environments and data quality. One is a Precambrian crystalline terrane from the Canadian Shield and the other is a sedimentary basin area containing magnetized sources within the sedimentary section.

Source Effects

Figure 3-14 illustrates the concept of contact mapping. From bottom to top, it shows a number of magnetic source bodies (with idealized, simple shapes), the magnetic field they produce, and then five different functions that are calculated from the magnetic field. All these functions aim to produce a maximum or peak in their behaviour over a source body edge. Considering the profile plotted for the total field horizontal gradient magnitude (TF-hgm), the curve shows peaks over the edges of bodies A to E. Not all of the peaks are the same shape, some are wider, some higher, and some have smaller, 'secondary' peaks close to the more pronounced peaks (e.g. body C). Some peak locations are also not exactly over the body edge (body A, Figure 3-14). Each of the five different contact mapping functions in Figure 3-14, total field horizontal gradient magnitude (TF-hgm), pseudogravity horizontal gradient magnitude (PSG-hgm), tilt horizontal gradient magnitude (TI-hgm), analytic signal (AS) and local wavenumber (LW) have their own limitations and char-

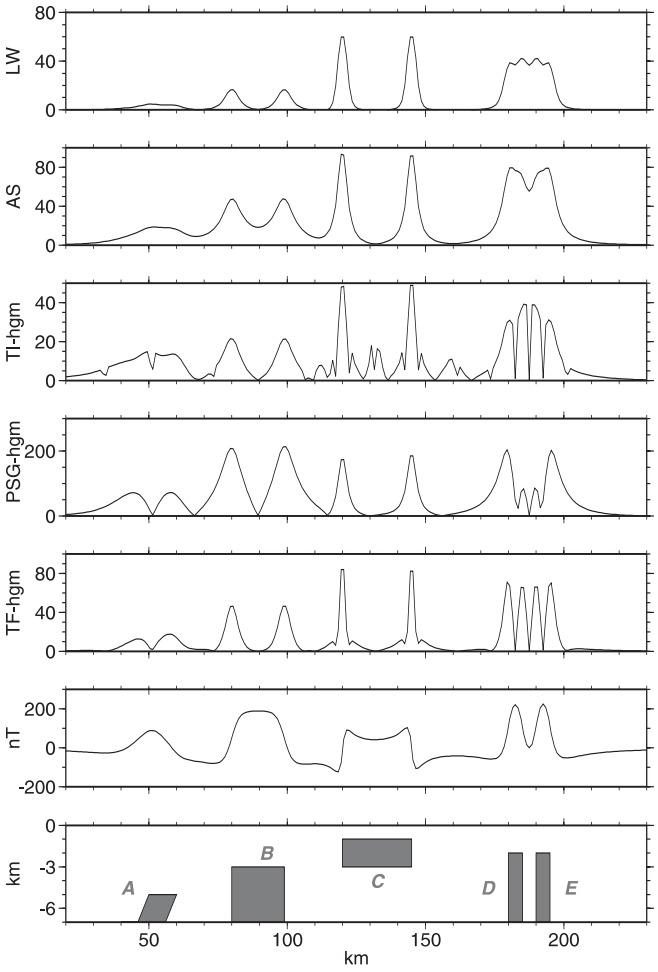

Figure 3-14. Responses of the five contact mapping methods to some simple bodies. Note the fall-off in resolving power (particularly analytic signal (**AS**) and local wavenumber (**LW**)) with increasing source depth, shifting of maxima due to dip (total field horizontal gradient magnitude (**TF-hgm**) and pseudogravity horizontal gradient magnitude (**PSG-hgm**)), and the appearance of false maxima in the tilt horizontal gradient magnitude (**TI-hgm**) due to interference and dipolar effects. All bodies have the same susceptibility and are magnetized in a vertical field.

acteristics which are discussed in more detail below. For a summary of the comparison, see Table 3-2.

For methods TF-hgm and TI-hgm, secondary or false maxima (not located above the source edge) are caused by dipolar sources and interference effects, respectively (see body C, Fig. 3-14). For linear source edges, this leads to tracks of secondary maxima mimicking the trends of the primary maxima located over the body edge. Interference between the effects of closely spaced sources is usually present in most data sets. For most of the methods considered, interference causes a merging of the peaks associated with edges, resulting in a single maximum (peak) replacing the theoretical two (cf., body D, Fig. 13-4). For TI-hgm, however, interference causes additional maxima between source edges, occurring over both wide bodies and between separated bodies.

Table 3-2. Summary of characteristics for different contact mapping methods.

Contact Method	Magnetization and Dip Effects	Secondary Maxima	Noise Sensitivity
TF-hgm	Yes	Yes	Low
TI-hgm	No	Yes	Low
PSG-hgm	Yes	No	Low
AS	No	No	Medium
LW	No	No	Medium

Source depth has a significant effect on all five methods when considering thick bodies, i.e., those that cannot be considered as isolated contacts. Increasing the depth of isolated edges only leads to decreased maxima magnitudes; the maxima remain over the contacts. For thick bodies, the interference between the body edges affects the contact mapping methods in different ways. For TF-hgm and PSG-hgm, maxima migrate away from body edges as the source depth increases beyond a half body-width. For TI-hgm, AS, and LW, maxima migrate inward, resulting in a single maximum at the centre of the body. For example, the two edges of body A (Fig. 3-14) are barely resolved by these three methods. The AS and LW responses of body D are also close to merging into a single maximum. AS has the poorest resolving power for a given depth, but along with TI-hgm, AS and LW produce edge maxima for bodies with depths less than half the body width (bodies B and C, Fig. 3-14). Dip affects maxima locations for the TF-hgm and PSG-hgm methods, causing an offset (down-dip) in the maxima position relative to the body edge. TF-hgm offsets are smaller than for PSG-hgm, with the maximum offset occurring over a contact with infinite depth extent. For thin sources, as their thickness increases, the maximum migrates down-dip. For a source with constant thickness, as depth increases, the maximum migrates up-dip. As in the case of dip, only the TF-hgm and PSG-hgm methods are affected by non-vertical magnetization effects. Both these methods require prior reduction to the pole (see Appendix 3-3). If not removed, magnetization components remain, and maxima will tend to be shifted away from the direction of this magnetization. Similar to dip, TF-hgm maxima are offset less than PSG-hgm for the same magnetization.

Tehery Lake

Magnetic data in this region were collected in 1975 at an 800 m flight line spacing and 300 m mean terrain clearance with a proton magnetometer. Data locations are based on visual flight path recovery and data values were digitized at contour-flight line intercepts. The Tehery Lake area in the Western Churchill Province is presently a region of active mineral exploration but has

not been mapped systematically since helicopter reconnaissance projects of the 1960s and 70s.

The results of contact mapping using all of the five methods on this data set (25 x 28 km) are given in Figure 3-15. The total magnetic field highlights the dominant northeast-southwest lithological and structural trends that form part of an Archean high-grade granite-gneiss domain. The magnetic highs are on the order of a few hundred nanotesla and are ascribed to mafic metavolcanic units contrasting with adjacent weakly magnetic quartzofeldspathic and quartz-arenite metasedimentary units. Clearly, AS and LW perform poorly with maxima trends even from strong anomalies being discontinuous. For feature A (see Fig. 3-15 for location) the poor resolving power of AS and LW leads to only a single maximum over this unit compared to the other three methods that show two parallel maxima trends resolving both edges. Along this feature, the AS and LW maxima appear to line up with the east-west flight line direction. Weaker anomalies fail to produce well defined maxima alignments and interference between anomalies disrupts the continuity of individual features and can result in merging of unrelated trends. Methods AS and LW are not as stable as the other methods in the presence of noise or poorer quality data.

The continuity of maxima of the TI-hgm, TF-hgm, and PSG-hgm methods (Fig. 3-15) is less affected by the data quality issues discussed above. PSG-hgm has the smallest number of maxima since the derivative of the integrated magnetic field is used. Additionally, we expect all maxima to be caused by contacts, although due to the integration, some maxima will undoubtedly be lost due to the lower resolving power that this operation imposes. TF-hgm gives a greater number of maxima due to a higher level of derivative used in its calculation, and also because of the possibility of secondary maxima. Generally, TF-hgm and PSG-hgm maxima are coincident, with similar levels of continuity along contact trends. Locations where TF-hgm maxima occur, but with no accompanying PSG-hgm maxima, are mostly on the edges of magnetic highs, implying that they correspond to real contacts and are not false maxima. TI-hgm produces the most maxima. There is general agreement between locations of TF- and TI-hgm maxima for isolated bodies. For more complex anomalies, the coincidence of maxima is poorer, most likely because of interference effects. TF- and TI-hgm trends are comparable but differences arise along some anomaly edges with TI-hgm maxima being less continuous than the TF-hgm maxima. This is likely due to the slightly greater resolution of the TI-hgm technique, resulting in greater variability of solutions along a given trend due to detection of off-trend features. In low gradient areas where TI-hgm maxima occur but with no accompanying TF-hgm solutions, this usually suggests false solutions based on our expectations from modelling experiments.

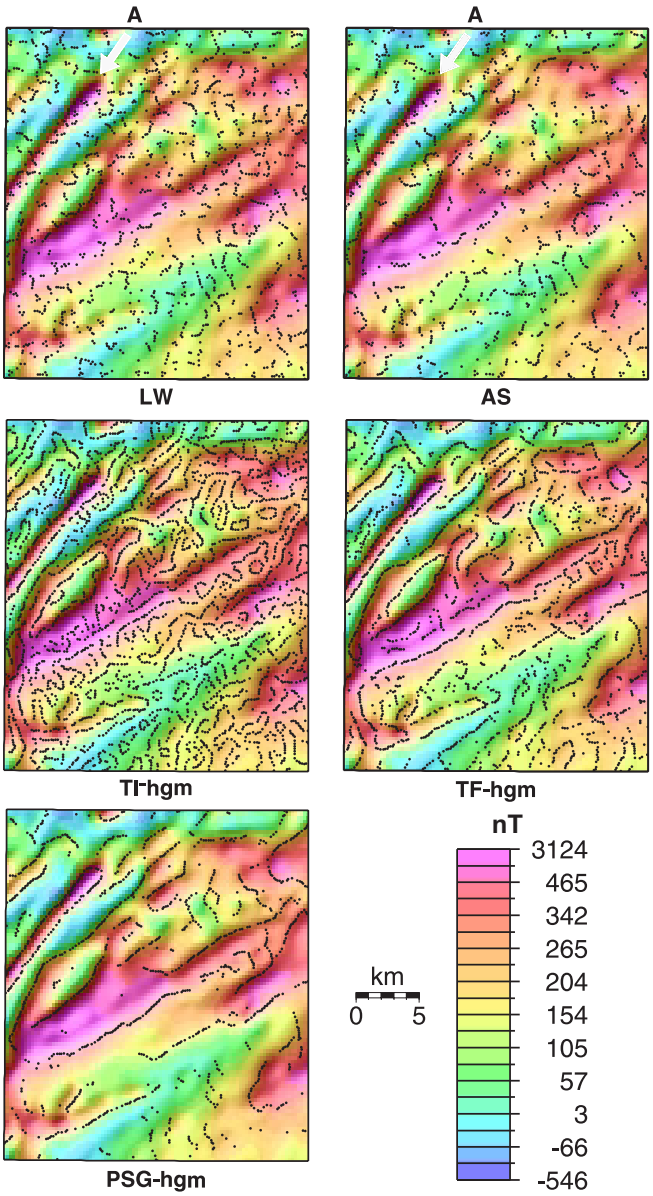

Figure 3-15. Contact maxima (as black dots) overlying the total magnetic field for a portion of the Tehery Lake region. Note the poor resolution of feature A in the local wavenumber (LW) and analytic signal (AS) maxima. PSG-hgm = pseudogravity horizontal gradient magnitude; TF-hgm = total field horizontal gradient magnitude; TI-hgm = tilt horizontal gradient magnitude.

Colville Hills

Data were acquired from 1999 to 2001 at an 800 m flight line spacing and 200 m mean terrain clearance with a caesium-vapour magnetometer. Navigation was GPS-based with digital data acquisition. The Colville Hills are being actively explored for hydrocarbons and this data forms part of a multi-year high-resolution aeromagnetic survey project focusing on the Mackenzie Valley corridor. Reflection seismic surveys indicate crystalline basement at depths of approxi-

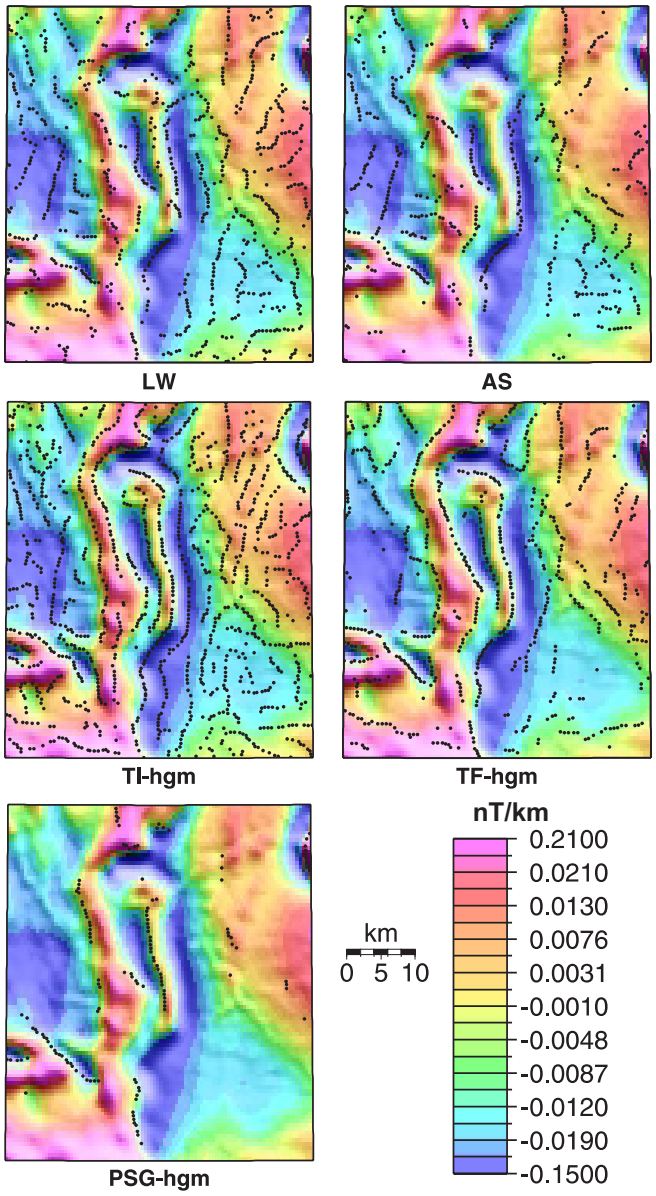

Figure 3-16. Contact maxima (as black dots) overlying the vertical gradient of the magnetic field for a portion of the Colville Lakes region. AS = analytic signal; LW = local wavenumber; PSG-hgm = pseudogravity horizontal gradient magnitude; TF-hgm = total field horizontal gradient magnitude; TI-hgm = tilt horizontal gradient magnitude.

mately 10 km in the area. Sills of the Tweed Lake basalts occur within the sedimentary section at depths of 1 to 2 km. Basement and intrasedimentary sources are easily distinguished magnetically through their characteristic anomaly wavelengths. The deeper basement sources cause longer wavelength anomalies compared to the shallower sills. Contact maps for the area (Fig. 3-16) are dominated by edges and internal structure or compositional changes of the sills. PSG-hgm, again, has a low number of solutions, picking up only the larger gradient features (note that the vertical gradient is plotted in Fig. 3-16). Since the data is of better quality in this study area, LW and AS perform much better. Both methods produce coherent trends with no indication of flight line-related effects. TF-hgm and TI-hgm show a similar distribution of solutions with the latter having greater detail in the low-amplitude region to the southeast (where LW and AS highlight similar trends). TI-hgm does however appear to exhibit some interference (false) maxima to the east of the central north-south-trending sill. These interference maxima mimic the sill trends, occur in a low-gradient area, and are not delineated in any other maxima map.

SUMMARY

No one method has all of the desirable properties for producing reliable contact maps (Table 3-2). Techniques not affected by magnetization or dip suffer from noise amplification (AS, LW) while the most stable method (PGS-hgm) may not detect as many body edges due to integration of the magnetic field. Theoretical arguments also limit the successful application of other techniques (TI-hgm, TF-hgm) to bodies with large thickness to depth ratios. The two field data examples highlight the relative advantages of each approach. For the Tehery Lake example, where the predominant dip is near vertical and remanent magnetizations are expected to be small, TF-hgm and PSG-hgm can be successfully used. This is fortuitous since both the AS and LW methods are incapable of producing usable solutions due to the poor data quality. TI-hgm solutions are also stable and reliable in this environment. For the Colville Hills, where sources (sills) are near horizontal, plate-like, and may have appreciable remanent magnetizations, TF-hgm, TI-hgm, and PSG-hgm methods are all prone to either maxima offsets or secondary maxima. In this area, AS and LW methods provide good information since they are not influenced by dip and magnetization effects, and the survey data quality is sufficient to reliably calculate these two quantities.

Using at least two of the five methods in concert is probably the best approach. Co-located solutions from different methods provides increased confidence in the reliability of a given contact location and lessens the adverse effects of source magnetization, dip, interference, and depth extent.

Methods TF-hgm and PSG-hgm provide the best stability in the presence of noisy, low-quality data sets and should be the first choice for contact mapping. They also provide coherent, continuous trends, which are advantageous when drawing contacts. AS, TI-hgm, and LW methods are only applicable to recently acquired, high-quality data sets and even then, should be used with caution. PSG-hgm and TF-hgm plots should be used in conjunction to check that contacts from AS, TI-hgm, and LW are reliable, i.e., they are not false or secondary trends that merely parallel the real contacts.

Table 3-3. Gravity and magnetic data products.

Quantity	Use	Mapping	Noisy?
Bouguer Gravity	General	Lithology + structure	No
Horizontal Gravity Gradient	Highlight contacts + remove regional effects	Contacts + structure	No
Vertical Gravity Gradient	Emphasize fine details + remove regional effects	Lithology + structure	No
Total Magnetic Field	General	Lithology + structure	No
Shaded Relief	Emphasize specific directional trends + fine details	Mainly structure	Possibly
Vertical Magnetic Gradient	Emphasize fine details	Lithology + structure	Possibly
Tilt	Emphasize low-amplitude areas	Mainly structure	No
Analytic Signal	Highlight contacts	Mainly contacts	Often
Contact	Map contacts	Structure + contacts	Depends

Interpreting Maps

Geological mapping from magnetic and gravity data is essentially an exercise in pattern recognition. The basic approach is to divide the region into areas that have similar character, based on the amplitude, shapes and textures seen on the magnetic maps. For mapping applications in general, gravity data can only be used sparingly, since gravity measurements are only available at such wide spacing (usually >10km for most government data). Hence, gravity data does not provide detailed information at small scales, but becomes useful if larger areas (>100km) are being studied. Consequently, most mapping relies heavily upon the magnetic data, which are focused on below. Areas can be initially divided up based on the amplitude of the anomalies, i.e., separating the area into magnetic regions where amplitudes of the magnetic field are comparable. The division can be made into magnetic regions where amplitudes are high and nonmagnetic regions where amplitudes are low. Negative anomalies on maps do not necessarily imply negative or reversely magnetized rocks; they generally just show areas of weakly magnetized lithologies. Once amplitude information is taken into account, then the patterns/textures of trends/features within these areas can be evaluated. Different 'units' can be distinguished based on the strike of anomaly trends by grouping together regions having similar strike (assuming a constant direction is apparent). Similarly, regions can be defined on the basis of similar texture or pattern of anomalies. The resulting areas do not have a geological interpretation; they are merely areas defined by similarities in amplitude, trends, and patterns of anomalies. Broad geological inferences can, however, be made. Outlines of the subdivisions may indicate lithology or structure, e.g., ovoid magnetic regions suggest intrusions, particularly if they interrupt the surrounding dominant strike direction(s). Sinuous trends suggest ductile deformation, while truncation of trends or region outlines would suggest brittle deformation and faulting. Inferring rock type in a region defined by the magnetic data requires additional independent geological knowledge, usually from geological mapping within or adjacent to the area of interest. In this process, magnetic anomaly characteristics can be compared with the known geology and correlations between the two can be established. Importantly, this comparison may dictate which lithologies can be distinguished and which cannot. It is more likely that more than one lithology will produce similar strength anomalies, since magnetic properties may not vary significantly between different rock types (see Appendix 3-1), so this ambiguity will remain in the interpreted map.

No one type of gravity or magnetic map will provide all the information to make a complete interpretation. Table 3-3 lists the most useful map products and what their main applications are. Clearly, there is overlap between the different products, but since they all provide somewhat independent representations of the original data, it is recommended that all that are available be used in an interpretation.

REFERENCES

Baranov, V.
1957: A new method for interpretation of aeromagnetic maps: Pseudo-gravimetric anomalies; Geophysics, v. 22, p. 359-382.

Clark, D.A.
1983: Comments on magnetic properties; Bulletin of the Australian Society of Exploration Geophysicists, v. 14, p. 49-62.

Clark, D.A. and Emerson, D.W.
1991: Notes on rock magnetization characteristics in applied geophysical studies; Exploration Geophysics, v. 22, p. 547-555.

Dods, S.D., Teskey, D.J., and Hood, P.J.
1985: The new series of one to one million scale magnetic anomaly maps of the Geological Survey of Canada: Compilation techniques and interpretation, *in* Utility of Regional Gravity and Magnetic Anomaly Maps, (ed.) W.J. Hinze; Society of Exploration Geophysicists, p. 69-87.

Pilkington, M. and Keating, P.B.
2004: Contact mapping from gridded magnetic data - a comparison of techniques; Exploration Geophysics, v. 35, p. 306-311.

Piper, J.D.A.
1987: Palaeomagnetism and the Continental Crust; Open University Press, Milton Keynes and Halsted Press, John Wiley and Sons, New York, 434 p.

Reynolds, R.L., Rosenbaum, J.G., Hudson, M.R., and Fishman, N.S.
1990: Rock magnetism, the distribution of magnetic minerals in the Earth's crust, and aeromagnetic anomalies, *in* Geologic Applications of Modern Aeromagnetic Surveys, (ed.) W.F. Hanna; U.S. Geological Survey, Bulletin 1924, p. 24-45.

GENERAL BACKGROUND READING

Blakely, R.J.
1995: Potential theory in gravity and magnetic applications; Cambridge University Press, 441 p.

Breiner, S.
1981: Applications for portable magnetometers, Chapter 5 *in* Practical Geophysics for the Exploration Geologist, (comp) R. Van Blaricom; Northwest Mining Association, Spokane, Washington, p. 205-237.

Goodacre, A. and Keating, P. (Editors)
1996: Notes based on Canadian Geophysical Union Short Course: Interpretation of Gravity and Magnetic Anomalies for Non-Specialists; Canadian Geophysical Union, 442 p.

Grant, F.S.
1985a: Aeromagnetics, geology and ore environments, I. Magnetite in igneous, sedimentary and metamorphic rocks: An overview; Geoexploration, v. 23, p. 303-333.
1985b: Aeromagnetics, geology and ore environments, II. Magnetite and ore environments; Geoexploration, v. 23, p. 335-362.

Telford, W.M., Geldart, L.P., Sheriff, R.E., and Keys, D.A.
1982: Applied Geophysics; Cambridge University Press, 860 p.

APPENDIX 3-1. Rock Properties

Mineralogical Controls

The fundamental factor influencing potential field anomalies is the mineralogy of the rocks, which controls density and magnetic susceptibility. The gravity field reflects the bulk or whole-rock mineralogy, i.e. the principal rock-forming minerals that constitute and define a particular rock type: e.g., quartz, feldspar, and biotite. Within a given rock type, the defining mineralogy is not likely to vary substantially, hence the density characteristics tend to remain fairly uniform. On the other hand, the magnetic field is controlled by the accessory minerals in a rock, principally magnetite, which only constitutes about 1.5% of crustal minerals (Clark and Emerson, 1991). Accessory minerals are generally ignored in petrological classifications (based on silicate mineralogy), and so specific lithologies may exhibit a wide range of magnetic susceptibility. The distribution of accessory magnetic minerals may not be uniform for various reasons, e.g., concentration in distinct layers, uneven hydrothermal alteration, and variable conditions of differentiation in plutonic rocks. The densities of common rock types range generally from about 2.00 to 3.2 g/cm^3, and so relative differences are usually not more than a few tens of percent. On the other hand, the magnetic susceptibilities of common rocks range from practically zero to about 300 x 10^{-3} SI. The relative variation of susceptibility is therefore orders of magnitude greater than the relative variation of rock density, a difference that is reflected in the range of values of the respective potential field. Such differences between gravity and magnetic maps may be enhanced by the fact that the density of a specific rock type is likely to be fairly uniform, whereas its susceptibility may vary significantly. Therefore, even if gravity and magnetic data are collected at the same points, the magnetic field would be more variable than the gravity field.

Density

Rock density is essentially a function of the major rock-forming minerals. In igneous and metamorphic rocks, quartz and feldspar are important constituents. Mafic minerals such as biotite, hornblende, and pyroxene may also be present in significant amounts. Since mafic minerals are invariably denser than felsic minerals or quartz, an increase in these results in an increase in density. The influence of these heavier minerals on rock densities is illustrated by the gradual increase in density of igneous rocks in progressing from felsic-rich granite to mafic-rich ultramafics (Table 3A1-1). Among sedimentary rocks there is a wide range of density for sandstone and shale. In such rocks, age and depth of burial are a major control on density. In the case of sandstones, porosity can also be a significant factor. Sedimentary rocks are generally less dense than igneous and metamorphic rocks but there are always exceptions. Table 3A1-1 provides a general guide to rock densities, but since there can be regional differences in rock types, density may vary from area to area. For this reason, measurements of density should be conducted wherever possible to establish local values.

Table 3A1-1. Rock densities.

Rock Type	Density (g/cm^3)
Plutonic Rocks	
Granite	2.60 - 2.67
Granodiorite	2.7
Diorite	2.77
Gabbro	2.90 - 3.00
Ultramafic	3.00 - 3.30
Anorthosite	2.72
Volcanic Rocks	
Rhyolite	2.60 - 2.65
Andesite	2.85
Basalt	2.90 - 3.00
Metamorphic Rocks	
Quartzofeldspathic	
Gneiss	2.70 - 2.75
Argillite/Slate	2.70 - 2.75
Sedimentary Rocks	
Sandstone	2.00 - 2.65
Shale	2.00 - 2.70
Greywacke	2.65 - 2.75
Limestone	2.7

Magnetization – Remanent versus Induced

Magnetic anomalies produced by the Earth's crust are controlled by two principal sources: magnetization induced by the Earth's present magnetic field and natural remanent magnetization (NRM), which is a fossil (permanent) magnetization acquired under the influence of Earth's field some time in the past. A rock's induced magnetization is quantified by a parameter known as the magnetic susceptibility (k). Magnetite is probably the most common host of induced magnetization. The two types of magnetizations can reside together in the same rock because they can occupy different magnetic grains or elements of a grain known as magnetic domains. For example, magnetite with grain sizes 0.01 to 20 μm is in the pseudo-single domain (PSD) range and can carry a stable and, possibly intense natural remanent magnetization. It mimics the behaviour of truly single-domain (SD) magnetite (grain size < 0.01 μm) and is characterized by low susceptibilities. Grains larger than 20 μm have a multi-domain (MD) state, in which susceptibilities are higher and nat-

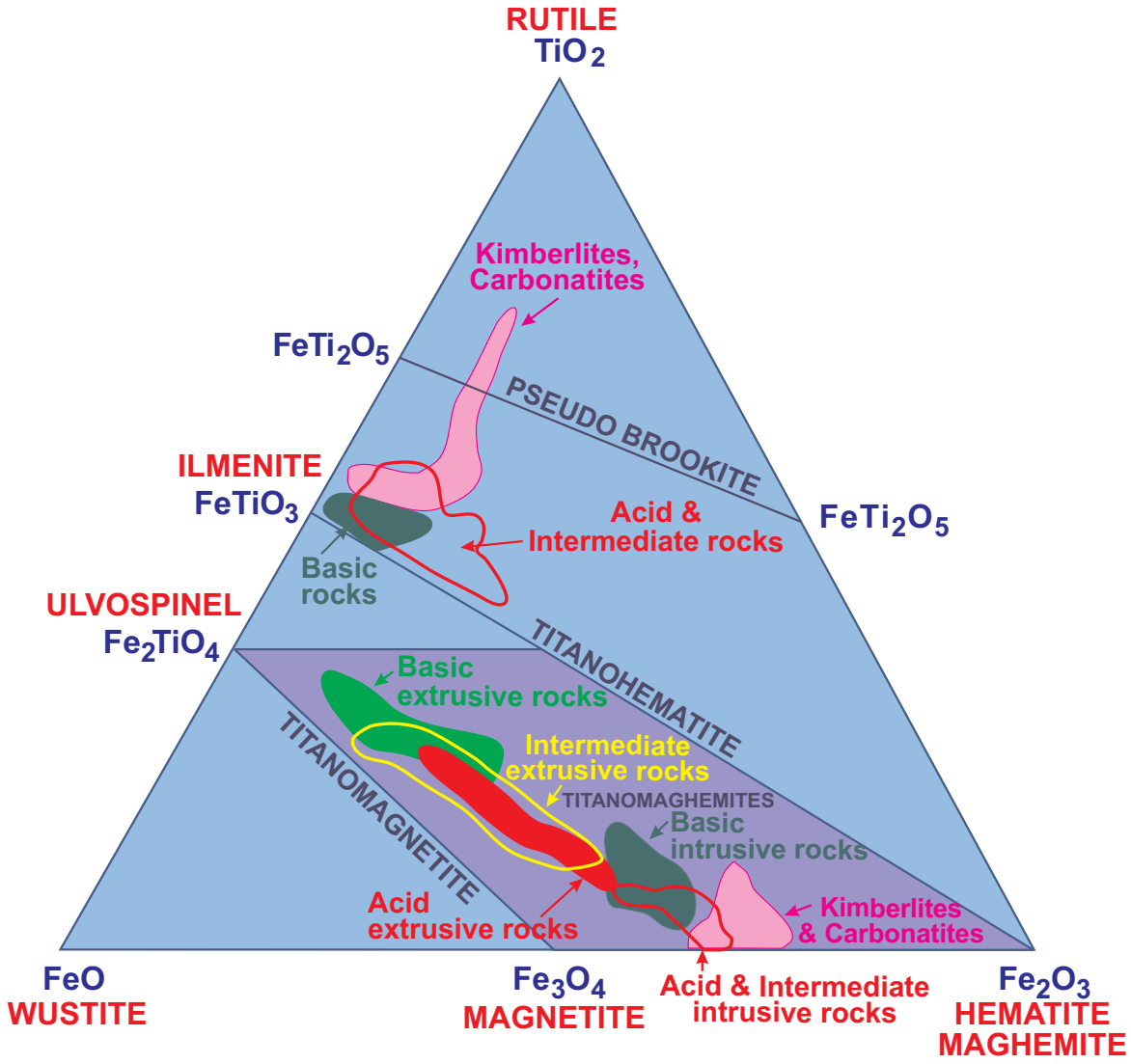

Figure 3A1-1. Ternary phase diagram of iron and titanium oxides illustrating the compositions of natural titanomagnetites and ilmenites in igneous rocks (after Piper, 1987, Fig. 2.2).

ural remanent magnetization lower. Therefore, the relative volumes of single-, pseudo-single-, and multi-domain magnetite control whether remanent or induced magnetization (susceptibility) is predominant in producing a magnetic anomaly.

Magnetic anomalies are predominantly caused by induced magnetization (as measured by the susceptibility content) within rocks. This is fortunate since any natural remanent magnetization present could be in a direction different from the present field and the resulting anomaly would be much different in shape (and often more complex) than with just a predominance of induced magnetization. In cases where a natural remanent magnetization is much larger than the induced magnetization and has a direction opposite to the Earth's field, then this will cause a negative rather than positive anomaly. The ratio of remanent magnetization to induced magnetization is referred to as the Koenigsberger ratio (Q). See Clark (1983) and Clark and Emerson (1991) for further information on rock magnetizations.

Magnetic Minerals

Some of the most important magnetic minerals are iron oxides and solid-solution series of these oxides with titanium oxides. They plot within the ternary system FeO-TiO_2-Fe_2O_3 (Fig. 3A1-1). The most important group of magnetic minerals that produce magnetic anomalies are those of the magnetite-ulvospinel solid-solution series (Reynolds et al., 1990), known as titanomagnetites. The susceptibility of titanomagnetites is effectively zero for ulvospinel contents greater than about 70% (Reynolds et al., 1990), but it is significant and fairly uniform for the rest of the series. Second in importance to the titanomagnetites are the titanohematites (Clark and Emerson, 1991), which represent the ilmenite-hematite solid-solution series. Titanohematites, composed of between 50 mole% and

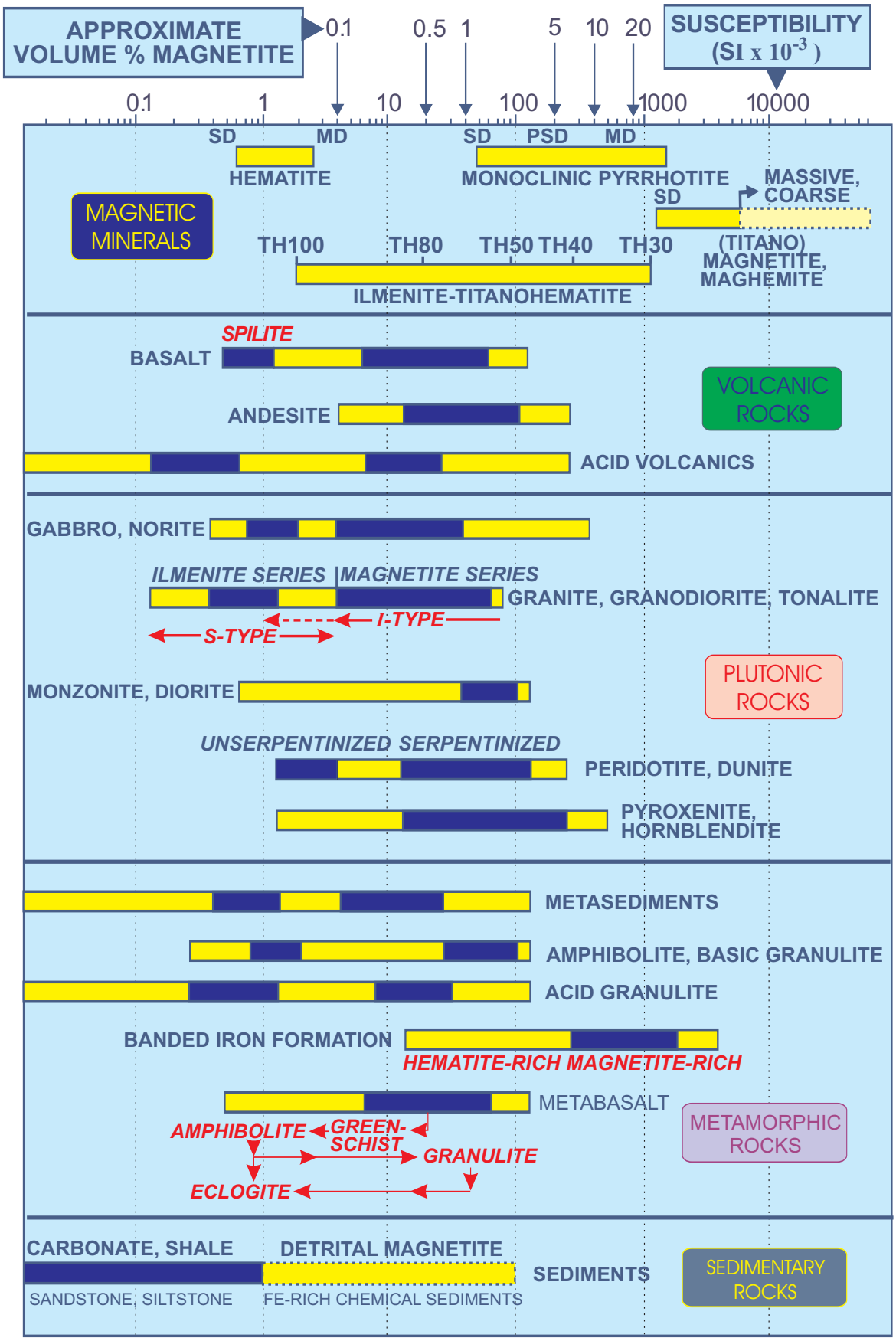

Figure 3A1-2. Ranges of magnetic susceptibilities for various minerals and rock types (modified from Clark and Emerson, 1991, Fig. 3). Distributions of susceptibilities are commonly bimodal; modal ranges are indicated by dark sections.

Table 3A1-2. Magnetic susceptibilities of paramagnetic minerals.

Minerals	(x 10^{-3} SI)
Amphibole	0.2 - 0.9
Biotite	0.7 - 2.9
Garnet	0.4 - 2.7
Olivine	1.3 - 1.6
Pyroxene	0.9 - 3.6
Pyrite	0.03 - 5.3
Chalcopyrite	0.02 - 0.4

Table 3A1-3. Magnetic susceptibilities of ferrimagnetic minerals.

Minerals	(x 10^{-3} SI)
Ilmenite	2 - 3800
Hematite	0.5 - 40
Maghemite	2000 - 2500
Magnetite	1000 - 5700
Titano-magnetite	130 - 620
Titano-maghemite	2800
Pyrrhotite (Fe_7S_8)	3200

80 mole% ilmenite, are strongly magnetic and effective carriers of natural remanent magnetization. More ilmenite-rich varieties are paramagnetic at room temperature, and hematite-rich ones are relatively weakly magnetic. Natural titanomagnetites tend to be oxidized towards the titanohematite trend (Fig. 3A1-1), and are more correctly termed titanomaghemites.

Magnetite (Fe_3O_4) is a common magnetic mineral found in igneous, metamorphic, and sedimentary rocks. Hematite (αFe_2O_3) is common in oxidized igneous rocks and sediments formed in oxidizing conditions. Maghematite (γFe_2O_3), with the same composition as hematite, is formed by low-temperature oxidation of magnetite in subaerial and submarine environments. It is found in oceanic basalts and laterites. The second most important group of magnetic minerals is one comprising iron sulphides, the most magnetic of which is pyrrhotite. A common type of pyrrhotite occurring in nature is monoclinic pyrrhotite having the composition Fe_7S_8. Pyrrhotite is found in basic igneous rocks, low- to medium-grade metamorphic rocks, and sedimentary rocks.

Susceptibilities of Minerals and Rocks

Magnetic susceptibilities of some minerals are given in Tables 3A1-2 and 3A1-3, respectively. It is noticeable that the ferrimagnetic minerals have susceptibilities that are generally two or three orders of magnitude larger than paramagnetic susceptibilities. Note that to obtain susceptibilities in cgs units divide values in tables by 4π (which equals 12.566). The range of susceptibilities in common rock types is featured in Figure 3A1-2, (after Clark and Emerson, 1991). Below are some of the key points relating to the information in this diagram.

- Every rock type of sedimentary, igneous, or metamorphic origin has a wide range of magnetic susceptibility; the ranges overlap significantly, thus susceptibility alone generally is not diagnostic of lithology.
- Many rock types have a bimodal distribution of susceptibility values; generally these represent distinct populations within each rock type for which ferrimagnetic minerals are absent or present. In the weakly magnetic subpopulation, Fe is incorporated into paramagnetic silicates mainly as Fe^{2+}.
- Within each magnetic subpopulation, susceptibility tends to increase with basicity.
- The bimodal pattern in granite reflects two distinct categories:
  magnetite series - relatively oxidized = I-Type,
  ilmenite series - more reduced = S-Type.
- In the metamorphic group, different grades of metamorphism have a considerable impact on the susceptibility of basic igneous rocks, such as basalt and/or diabase. Regional metamorphism to greenschist or amphibolite grade tends to lower susceptibility, but further increase up to granulite grade may produce secondary magnetite. Eclogite grade destroys all magnetite and partitions iron into weakly magnetic silicates.
- Sedimentary rocks typically have very low susceptibilities, although some immature clastics may contain significant amounts of magnetite.
- The Fe content of sediments and the Fe^{3+}/Fe^{2+} ratio, which reflects redox conditions during sedimentation, are critical factors controlling development of secondary magnetite during metamorphism. Thus, magnetic patterns over metasediments tend to reflect variations in sedimentary facies as well as metamorphic conditions. Pyrrhotite is the principal magnetic mineral in many metasedimentary rocks, especially in mineralized areas.
- Ultramafic rocks, such as pyroxenite, hornblendite, and serpentinized dunite in zoned Alaskan-type complexes, are generally highly magnetic.
- Serpentinization creates abundant magnetite. Dunite, peridotite, and pyroxenite yield Fe atoms from weakly magnetic olivine and pyroxene, which are oxidized to produce magnetite.

APPENDIX 3-2. General Features of Potential Field Maps

Typically, when a gravity and magnetic map of the same region are viewed side by side, the magnetic map appears to contain significantly more detail (Fig. 3-1). True comparison is difficult, because the two different fields being measured have different characters and different responses to changes in the physical properties of rocks. The main factor controlling the general appearance of each map (assuming the geology is the same) is the data spacing (distance between measurement points) and for mainly magnetic data, the flight elevation (or flight height). Another difference that can change the appearance of a given map is the choice of colour scheme used to display the data.

Data Spacing

Spacing of the data measurement locations is an important control on the amount of detail portrayed in a potential field map. This point is well illustrated by gravity and magnetic maps for the margin of the Canadian Shield in the Trans-Hudson Orogen (Fig. 3-1), displaying data collected under Canada's national gravity and magnetic mapping programs. The distribution of data in the two maps is significantly different. Gravity data are spaced about 10 to 15 km apart, arranged in an irregular grid pattern. On the other hand, aeromagnetic data were collected along flight lines spaced 805 m apart. Modern magnetometers sample the magnetic field every tenth of a second along each flight line, providing a point magnetic value roughly every 3 to 10 m, depending on the aircraft's speed. The magnetic surveys covering the region of Figure 3-1 were done mainly in the 1960s, when the magnetic field was plotted on analog charts, which were used to produce contour maps. These maps were later digitized at the intersection of the contours and the flight lines (Dods et al., 1985). Data spacing is therefore a function of the distance between the contour lines and can be as much as a few hundred metres. The much closer spacing of aeromagnetic data clearly results in much greater resolution and detail in the magnetic map compared to the gravity map.

Flight Elevation

Another factor influencing detail in the case of aeromagnetic maps is flight elevation (flight height). In measuring a magnetic field, the distance between the magnetometer and the source of the field will influence the amplitude of the measured anomaly. The fall-off rate (how quickly the amplitude decreases as this distance increases) is dependent on the shape of the magnetic source: those with a point-like or sphere-like shape will have the most rapid fall-off while sources that are more laterally (and vertically) extensive, e.g., the contact between two formations, will have a low fall-off rate. As the height above the source increases, the anomaly decreases in amplitude and also broadens. The increased resolution of anomalies with decreasing distance from the source to the sensor is illustrated through comparison of two aeromagnetic surveys carried out over the same area, one survey flown at a 305 m elevation and the other at about 3 km (Fig. 3A2-1). This figure also illustrates, equivalently, the suppression of a signal as a body becomes more deeply buried.

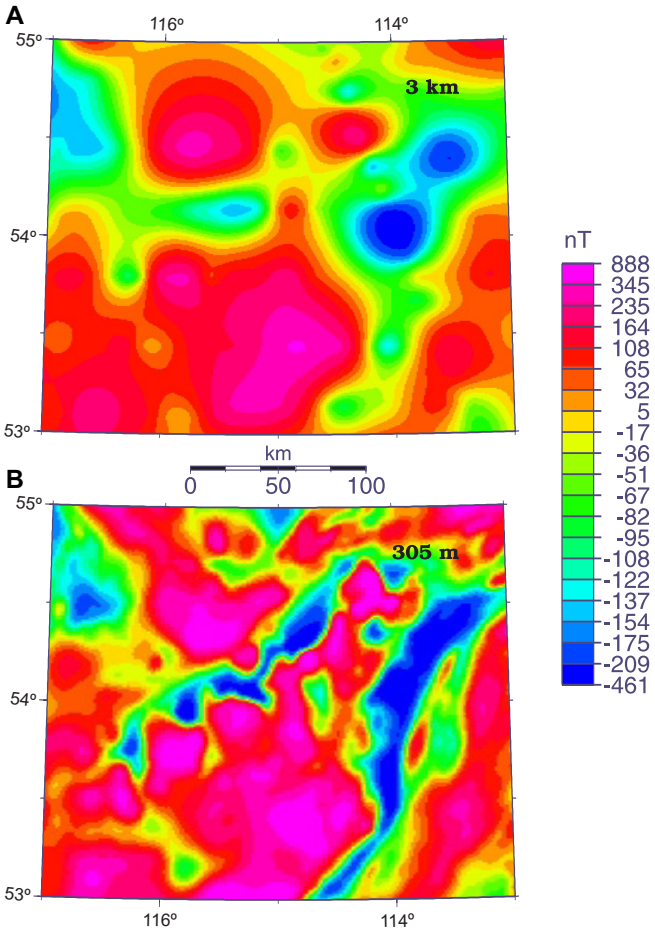

Figure 3A2-1. Comparison of two aeromagnetic surveys carried out over the same area in Alberta, one survey flown at 3 km elevation **(A)** and the other at about 305 m **(B)**.

Flight Line Spacing

Aeromagnetic surveys are usually flown in a direction perpendicular to the general geological strike of the study area at a line spacing that is about four times the flight height. For example, most of the regional surveys conducted by the Geological Survey of Canada (GSC) were flown at a height of 300 m and at a line spacing of 800 m. Some modern high-resolution surveys have been flown at a height of 120 m and a line spacing of 400 m (e.g. Boothia Peninsula). Obviously, flying at a closer line spacing and lower height results in maps

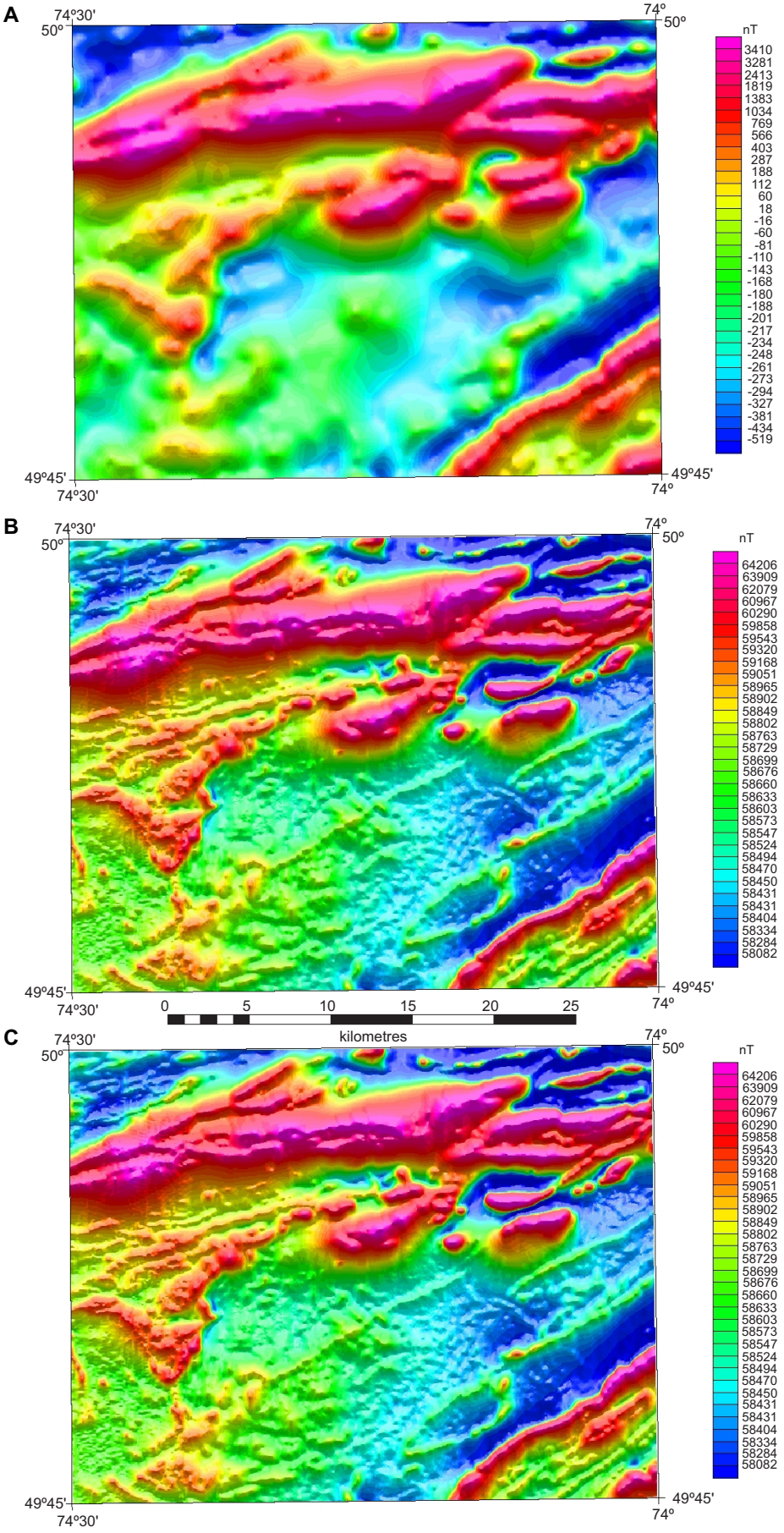

Figure 3A2-2. Magnetic field measured by three surveys in the Chibougamau area (Quebec). **(A)** 1947 survey (line spacing of 800 m; flight height of 150 m). **(B)** 1972-8 survey (line spacing of 200 m; flight height of 120 m). **(C)** 1989 and 1991 survey (line spacing of 100 m; flight height of 45 m).

that have a much higher resolution and show greater detail. The following examples are from the Chibougamau area (Quebec). The area (NTS 32G 16) was first flown by a GSC regional survey at a line spacing of 800 m and a flight height of 150 m in 1947 (Fig. 3A2-2A). The area was later flown in 1972 and 1978 by two combined magnetic/time-domain electromagnetic (EM) airborne surveys at a line spacing of 200 m and a height of 120 m (Fig. 3A2-2B). In 1989 and 1991, the same area was flown again by two combined magnetic/helicopter EM surveys. In that case, the line spacing was 100 m and the magnetic sensor was about 45 m above ground (Fig. 3A2-2C). The older surveys were flown using visual navigation while the recent ones (1989 and 1991) were flown using electronic navigation (transponders).

Pixels and Point Data

Remote sensing data are digital 'photographs'. The smallest element is called a pixel and represents the average reflectance of the ground at a particular (or range of) wavelength(s). For example, a satellite image that has a pixel size of 10 m represents the average of what the sensor sees over an area of 10 x 10 m. On the other hand, geophysical data are point data that have to be interpolated to produce a grid. Interpolation is possible because potential field data (magnetic and gravity) obey Laplace's equation. It follows that the field varies smoothly between measurement points. The minimum curvature algorithm is often used for interpolation.

Map Colours

Magnetic data are commonly portrayed as coloured total field maps. These are produced by gridding the data and assigning a particular colour to each grid cell, based on the magnetic value of the cell. Such maps allow a ready appreciation of patterns and of relatively strongly and weakly magnetized areas, magnetic expressions of which are commonly referred to as highs and lows, respectively. Division of the total range of anomaly values (known also as the dynamic range) into a number of intervals can be done in different ways, which can significantly affect the appearance of the resulting map. The simplest approach is to dividing the range into equal intervals. This is called linear equalization, and it can result in an effective image, particularly when the populations of grid cells within intervals are similar. However, if the populations for some intervals are very large (i.e. the interval covers a large area of the map), detail within those intervals may be lacking. The problem can be circumvented by dividing the dynamic range using a process known as histogram equalization. The range is divided into a number of intervals within which the populations of grid cells are identical. A result of this process is that the ranges of individual intervals are not necessarily the same. Noticeably, intervals at the uppermost and lowermost ends of the dynamic range are relatively expanded.

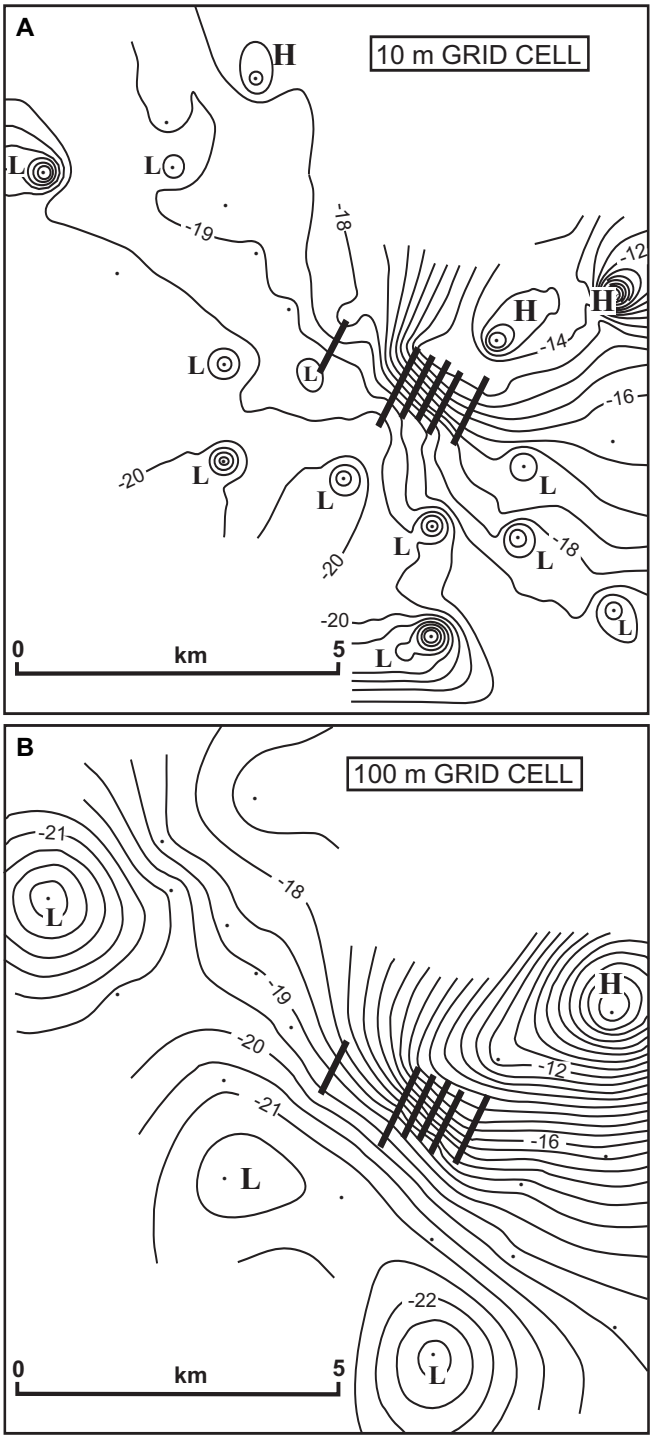

Figure 3A2-3. Comparison of contoured gravity data in the area of Canoe Landing Lake sulphide deposit, Bathurst mining camp. Maps were contoured automatically using grid cells measuring 10 m **(A)** and 100 m **(B)**. A search radius of 1250 m was used in each case.

Artefacts ('Bull's Eyes')

Distinct circular anomalies may be an artefact of data distribution and gridding, and should be treated with

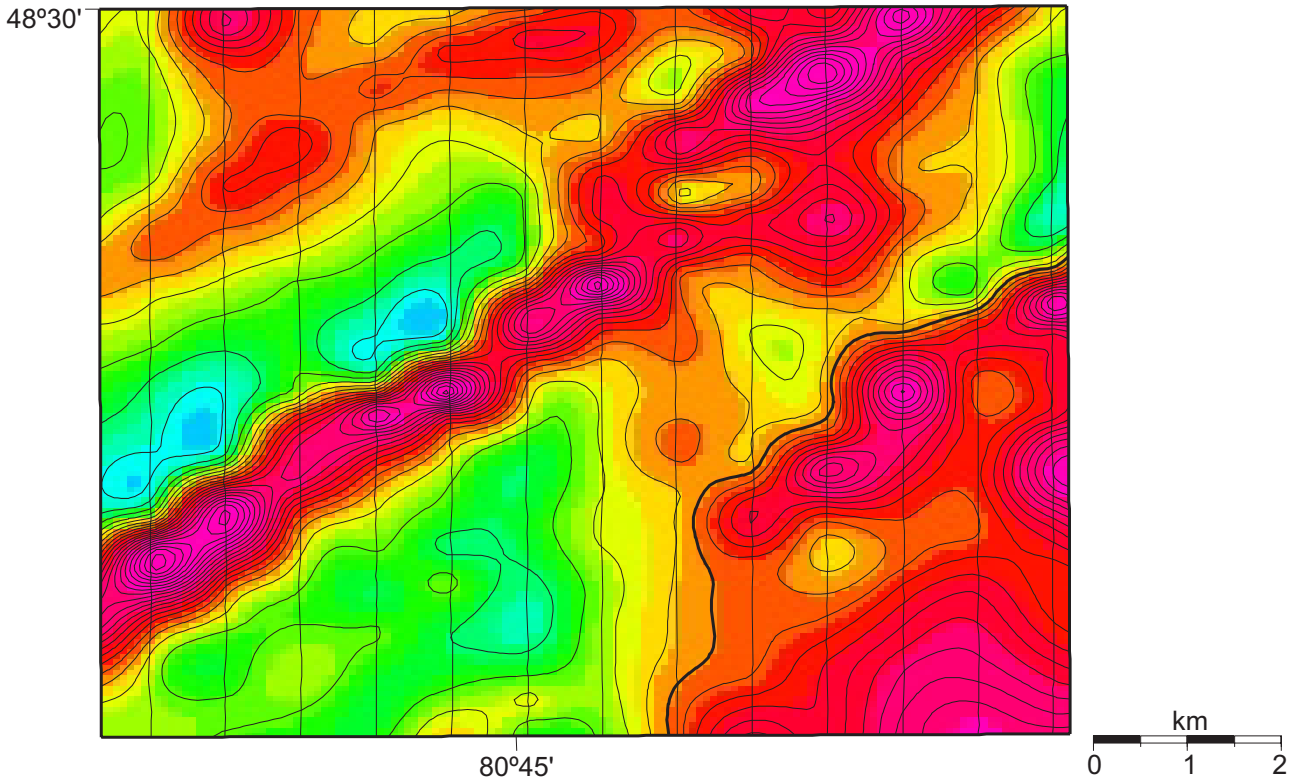

Figure 3A2-4. Magnetic field over a dyke with the north-south flight lines plotted as thick black lines. Bull's eyes are centred where flight lines intersect the dyke.

caution. These kinds of artefacts occur on both gravity and magnetic maps, but with different characteristics. For gravity data, these circular anomalies or 'bull's eyes' may be defined on the basis of a single point. In such cases, the validity of the point itself may be called into question, or how the gridding of the data was carried out may be the fundamental reason. If the size of the grid cell specified by the user is much smaller than the average distance between data points, circular anomalies may be generated around observation points. These may be erroneously interpreted to signify the presence of discrete geological bodies. This is illustrated using a gravity data set in the region of the Canoe Landing Lake massive sulphide deposit in the Bathurst mining camp (Fig. 3A2-3). Here, detailed gravity observations at 25 m intervals were made along six lines crossing the deposit. Additional observations spaced roughly 0.5 to 3 km apart were made around the deposit to define the background gravity field. Contouring of the data using a grid size of 10 m produced a map with several bull's-eye anomalies (Fig 3A2-3A), which have no geological significance. When the grid size is increased to 100 m, the bull's eyes disappear (Fig. 3A2-3B), and the gravity field is much smoother and probably more representative of reality. In this case, the measurements producing the bull's eyes are reliable. It is the gridding interval that has produced the unwanted effects. For aeromagnetic data, the same kind of effect is often seen, but is mostly found along linear anomalies, most commonly those produced by dykes. Figure 3A2-4 shows the magnetic field over a dyke and the flight lines (plotted in black) along which the survey measurements were taken. As can be seen, the bull's eyes are centred at points where a flight line intersects the dyke. When the data are gridded, new interpolated values are calculated between the measured points but the function used in the interpolation is too smooth to accurately recover the true value. This results in the interpolated value being smaller than the surrounding true values, and leads to high values only around the measurement points along the flight line. Bull's eyes can be avoided by judicious processing of the survey data; however, if reprocessing is not possible, it is sufficient to be aware of the appearance and occurrence of these features.

APPENDIX 3-3. Shapes of Gravity and Magnetic Anomalies

The gravity anomaly for a specific body with a given shape and depth depends on the density contrast between the body and its surroundings. It will be positive or negative depending on the sign of the contrast. The magnetic anomaly for the same body, however, is not just a function of the magnetization contrast but also the Earth's magnetic field, since the magnetic anomaly is an expression of two entities, positive and negative poles, whose effects are combined to produce the anomaly. For this reason, when a magnetic anomaly is observed in profile, part of the profile may have negative values, and part will have positive values. If the magnetization is entirely induced and the Earth's field is steeply dipping, as it is throughout Canada, the positive component of the body's magnetization will dominate.

If the Earth's magnetic field in an area were vertical, the magnetic anomaly would also be symmetrical, because the negative pole in a body would lie vertically above the positive pole. However, the Earth's magnetic field is vertical only at the magnetic poles themselves. Everywhere else it is inclined, and thus positive and negative poles will also adopt an inclined attitude relative to one another, as illustrated in Figure 3A3-1. The Earth's field produces the distribution of poles as shown, which generates a secondary field depicted by the indicated pattern of lines of force. The upper, negative pole is closer to the surface and produces a relatively large positive component, whereas the deeper, positive pole produces a smaller negative effect. The positive pole is offset horizontally with respect to the negative, and thus the peaks of the respective anomalies will likewise be offset. If the secondary field is small and the total field is measured in the direction of the Earth's field, no anomalous component of the field will be detected near A and C on Figure 3A3-1 (where the secondary lines of force are roughly perpendicular to the primary field), and the anomaly will peak near B where the directions of the secondary and primary fields are the same. This results in a slight offset of the peak of the resultant anomaly towards the south.

In Canada, the Earth's field is inclined at angles ranging from about 70 to 90º from the horizontal, so it is not unusual to observe a small negative anomaly on the north side of positive anomalies. It is important to recognize that these are not necessarily related to bodies with low or no magnetization or even to reversed remanent magnetizations. Such negative anomalies may simply originate from the same body producing the more prominent high. The problem of negative 'artefacts' is worse in southern latitudes where the inclination of the Earth's field is lower. Baranov (1957)

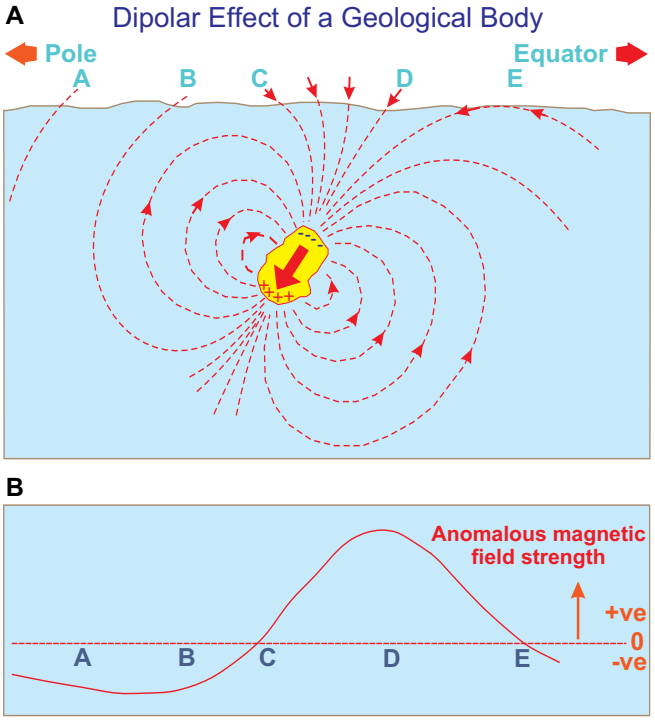

Figure 3A3-1. (A) Pattern of lines of force around a body magnetized by the Earth's field, showing the distribution of positive and negative magnetizations. **(B)** The resulting magnetic profile.

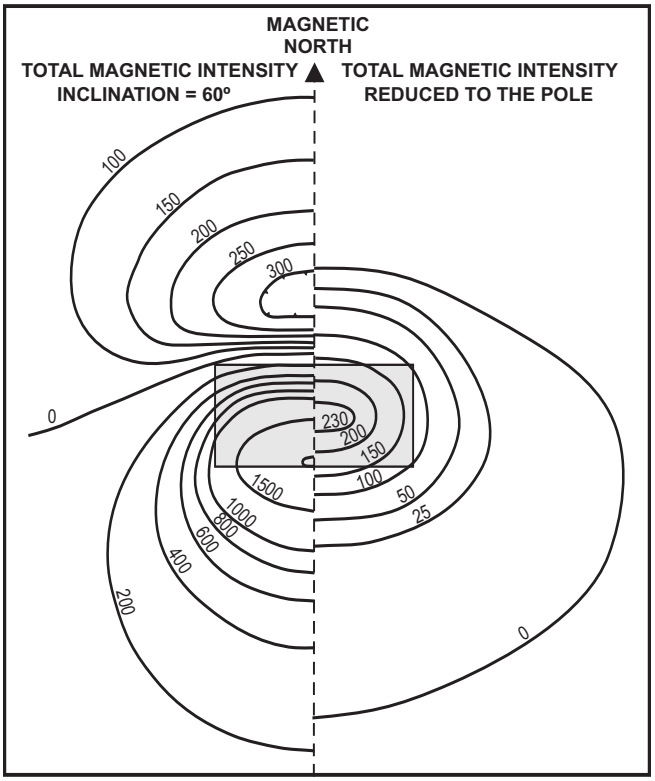

Figure 3A3-2. Example of a total field magnetic anomaly over a vertical prism of infinite depth extent, before (left) and after (right) being reduced to the pole (after Baranov, 1957).

presented a method for eliminating such artefacts by a process that has come to be known as reduction to the pole. Total field magnetic anomalies measured at a certain inclination can be transformed into the anomaly that would be measured if the location was moved to the north magnetic pole (where the field is vertical). This process therefore simplifies the appearance of anomalies by removing the asymmetry caused by the Earth's field inclination. Reduction to the pole assumes that there is no remanent magnetization. The resulting anomalies are simpler to interpret than total field anomalies, since they are located vertically with respect to the magnetized bodies (i.e. their peaks are not displaced laterally from the body). An example of a total field magnetic anomaly reduced to the pole is shown in Figure 3A3-2.

CHAPTER 4. Gamma-Ray Spectrometry

K Ford, J.R. Harris, R. Shives, J. Carson, and J. Buckle
Geological Survey of Canada, 615 Booth Street, Ottawa, Ontario K1A 0E9
Corresponding author's email: Jeff.Harris@NRCan.gc.ca

INTRODUCTION

All rocks and soils are naturally radioactive, containing various proportions of a variety of radioactive elements. The natural decay of these elements produces a variety of types of radiation (alpha, beta, and gamma) at specific energy levels. Only gamma-ray radiation has sufficient range to be useful for airborne geophysical surveying for geological mapping and mineral exploration. Gamma-ray spectrometry (GRS) provides a method of measuring concentrations of individual radioactive elements (in particular potassium, uranium, and thorium) in support of bedrock and surficial geological mapping, exploration for a variety of mineral commodities, and for environmental radiation monitoring.

Gamma rays are released through the spontaneous decay of radioactive elements. The three most common, naturally occurring radioactive elements are potassium, uranium, and thorium, which are found at some concentration in most rock-forming minerals. Potassium, for example, occurs mainly in the mineral feldspar, which is an abundant and widespread mineral in the Earth's crust, and is a prominent component of most rocks. It also occurs in other common rock-forming minerals, such as biotite and muscovite. Uranium and thorium are generally present in low concentrations (measured in parts per million (ppm)) in a wide range of minerals. The range of radioactive element concentrations in most common rock types is shown in Table 4-1 (Killeen, 1979).

Directly or indirectly, these three radioactive elements can provide an indication of economic concentrations of many other metals. High concentrations of uranium, for example, may directly represent a target of economic interest. They also may be used as indirect indicators of mineralization if they occur as trace elements associated with mineralization, or if they are enriched or depleted due to alteration. An example of mapping alteration would be potassic alteration associated with some styles of mineralization. Maps that show the distribution of radioactive elements provide information about fundamental mineralogical and geochemical properties of bedrock and surficial deposits, and have proven highly useful for geological mapping, mineral exploration, and environmental studies, often indicating geological features not seen by other techniques.

Gamma-ray spectrometry (GRS) is a surface technique only, providing a direct measurement of the surface of the Earth, with no significant depth of penetration. The source of most gamma radiation is limited to the top 30 centimetres of the Earth's surface. This surface-only characteristic allows us to reliably relate the measured radioactive element contrasts to mapped bedrock and surficial geology, and alteration associated with mineral deposits. All rocks, and the materials

Table 4-1. Radioelement concentrations in different classes of rocks (Killeen, 1979).

Rock Type	Potassium (%)		Uranium (ppm)		Thorium (ppm)	
	Mean	Range	Mean	Range	Mean	Range
Acid Extrusives	3.1	1.0 – 6.2	4.1	0.8 – 16.4	11.9	1.1 – 41.0
Acid Intrusives	3.4	0.1 – 7.6	4.5	0.1 – 30.0	25.7	0.1 – 253.1
Intermediate Extrusives	1.1	1.1 – 2.5	1.1	0.2 – 2.6	2.4	0.4 – 6.4
Intermediate Intrusives	2.1	0.1 – 6.2	3.2	0.1 – 23.4	12.2	0.4 – 106.0
Basic Extrusives	0.7	0.06 – 2.4	0.8	0.03 – 3.3	2.2	0.05 – 8.8
Basic Intrusives	0.8	0.01 – 2.6	0.8	0.01 – 5.7	2.3	0.03 – 15.0
Ultrabasic	0.3	0 – 0.8	0.3	0 – 1.6	1.4	0 – 7.5
Alkali Feldspathoidal Intermediate	6.5	2.0 – 9.0	29.7	1.9 – 62.0	133.9	9.5 – 265.0
Alkali Feldspathoidal Intermediate	4.2	1.0 – 9.9	55.8	0.3 – 720.0	132.6	0.4 – 880.0
Alkali Feldspathoidal Basic Extrusives	1.9	0.2 – 6.9	2.4	0.5 – 12.0	8.2	2.1 – 60.0
Alkali Feldspathoidal Basic Intrusives	1.8	0.3 – 4.8	2.3	0.4 – 5.4	8.4	2.8 – 19.6
Chemical Sedimentary Rocks	0.6	0.02 – 8.4	3.6	0.03 – 26.7	14.9	0.03 – 132.0
Carbonates	0.3	0.01 – 3.5	2	0.03 – 18.0	1.3	0.03 – 10.8
Detrital Sedimentary Rocks	1.5	0.01 – 9.7	4.8	0.01 – 80.0	12.4	0.2 – 362.0
Metamorphosed Igneous Rocks	2.5	0.1 – 6.1	4	0.1 – 148.5	14.8	0.1 – 104.2
Metamorphosed Sedimentary Rocks	2.1	0.01 – 5.3	3	0.1 – 53.4	12	0.1 – 91.4

Pilkington, M., Keating, P.B., and Thomas, M.D., 2008, Gamma-ray spectrometry, Chapter 4 *in* Remote Predictive Mapping: An Aid for Northern Mapping, (ed.) J. R. Harris; Geological Survey of Canada, Open File 5643, p. 53-97.

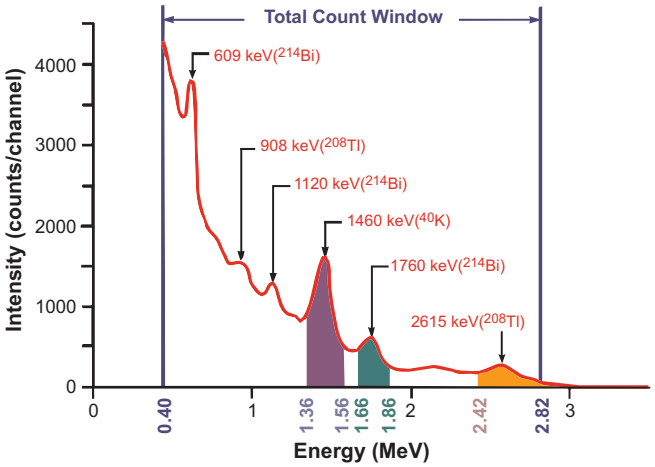

Figure 4-1. Typical gamma-ray spectrometry energy windows.

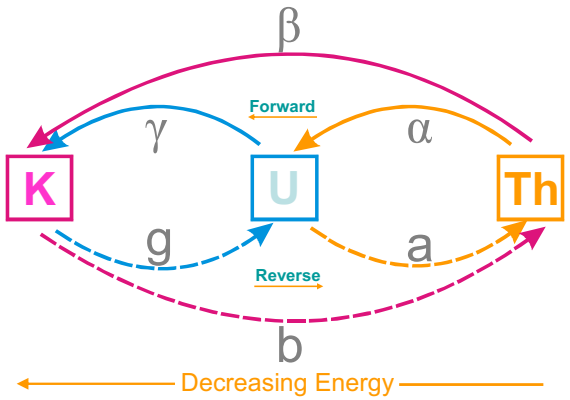

Figure 4-2. Schematic representation of the interaction between the K, U, and Th energy windows indicates the stripping factors that are used to remove the interference denoted by the arrows. The 'upward' or reverse-stripping factors, a, b, and g, are generally small.

derived from them, are radioactive, containing detectable amounts of a variety of radioactive elements. A gamma-ray spectrometer is designed to detect the gamma rays associated with these radioactive elements and to accurately sort the detected gamma rays by their respective energies. It is this sorting ability that distinguishes the spectrometer from instruments that measure only total radioactivity.

Airborne gamma-ray spectrometry (AGRS) surveys provide valuable, systematic coverage of large areas. Ground gamma-ray spectrometry (GGRS) greatly improves the resolution of individual radioactive element sources. The resulting geochemical information provides important information, significantly improving bedrock and surficial geological mapping and mineral exploration.

The Gamma-Ray Energy Spectrum

The primary acquisition data set is a multi-channel gamma-ray energy spectrum. A typical natural radiation energy spectrum (Fig. 4-1) depicts the relative count rates at each energy level from 0 to 3 MeV. The area from 0 to 0.4 MeV is not used as it is dominated by Compton scattering of higher energy radiation (Grasty, 1979).

For geological mapping, the K^{40} (potassium), Bi^{214} (uranium), and Tl^{208} (thorium) peaks are of interest. During an airborne survey, the full spectrum of counts is recorded once per second, using a 256-channel histogram. During post-flight data processing, the counts for the radioelements of interest (K^{40}, Bi^{214}, Tl^{208}) are accumulated. The summation includes the counts for a range of energies (a 'window' or 'region of interest') centred on each peak. The standard energy windows used are shown in Table 4-2.

Table 4-2. Typical gamma-ray spectrometry energy windows.

Name	Element	Peak (keV)	Window Range (keV)
K	K^{40}	1460	1360 - 1560
U	Bi^{214}	1760	1660 - 1860
Th	Tl^{208}	2615	2410 - 2810
Total Count			410 - 2810

The accumulated count rates are then converted to equivalent ground concentrations of potassium, uranium, and thorium using a set of calibration constants that are characteristic of the spectrometer system.

The term 'equivalent' or the abbreviation 'e' is used for reporting concentrations of uranium and thorium determined by gamma-ray spectrometry. These concentrations are determined indirectly from their daughter products (Bi^{214} and Tl^{208}, respectively), which are assumed to be in equilibrium with their parent isotope. Potassium concentration is determined directly from K^{40}.

Calibration of Gamma-Ray Spectrometers

The gamma-ray spectrum is subject to a certain amount of interference caused by Compton scattering of higher energy gamma radiation into the potassium and uranium regions of interest and by the inclusion of a very low-intensity uranium peak in the thorium region of interest. The effect of these interferences can be removed if the spectrometer has been properly calibrated, by determining a set of six constants, called 'stripping ratios'. The relationship between the stripping ratios and the measured count rates is illustrated in Figure 4-2.

Ground and aircraft gamma-ray spectrometer systems can be calibrated by recording a series of measurements of count rates on concrete calibration pads containing small, known concentrations of radioactive elements (Grasty et al., 1991).

Both airborne and ground instruments are calibrated, using international standards developed by the Geological Survey of Canada (GSC), to ensure consis-

tent, accurate estimates of K, eU, and eTh. Four calibration pads are required for proper spectrometer calibration, including three containing known concentrations of potassium (K^{40}), uranium (Bi^{214}), and thorium (Tl^{208}). A fourth pad, made from the same concrete used for the others but with no additional material, acts as a blank or 'control'. The same pads are used for calibrating both handheld portable spectrometers and larger systems installed in fixed-wing aircraft or helicopters.

This calibration procedure yields the six stripping ratios for a spectrometer system and for ground spectrometers the sensitivity of the spectrometer (count-rate per unit of concentration of potassium, uranium, and thorium) measured in cps/ppm or cps/%. These values are only applicable for a small source at ground level and can be used to convert counts measured at ground level to equivalent ground concentrations of potassium, uranium, and thorium.

Additional calibration is needed for airborne spectrometer systems where it is necessary to know the variation of the calibration constants at different terrain clearances. Variations in the stripping ratios and count rates with height and the sensitivity of the spectrometer system at the planned flying height are determined by relating the count rates measured in a series of flights (at different heights) over a test strip to the equivalent ground concentrations of potassium, uranium, and thorium, which are determined from measurements taken at ground level with a properly calibrated hand-held spectrometer. The computed sensitivities are only applicable at a specific 'planned' flying height for the survey, typically 120 m. (Charbonneau and Darnley, 1970).

Airborne Gamma-Ray Spectrometry Surveys

All types of airborne geophysical surveys are normally flown in a direction perpendicular to the main geological strike of the survey area. For airborne gamma-ray spectrometry surveying, the line spacing depends on the objectives of the survey: in reconnaissance surveys it may vary between 2000 and 5000 m, in regional surveys it may vary between 500 and 2000 m, and in detailed surveys flown for mineral exploration flight line spacing can be as little as 100 or 200 m. The flight elevation in fixed-wing surveys that include gamma-ray spectrometry is normally 120 m, although it may vary between 100 and 150 m. For helicopter-borne surveys with gamma-ray spectrometry the detectors are mounted in the helicopter, and the nominal terrain clearance varies between 60 and 120 m, depending on local terrain conditions and the configuration of other survey equipment.

A typical gamma-ray system includes a 256-channel spectrometer recording data at 1-second intervals. Surveys flown with a fixed-wing aircraft usually consist of 50 litres of NaI(Tl) crystals in the main detector array, with between 8 and 12 litres of NaI(Tl) crystals in the upward-looking detector array. Surveys flown using a helicopter will usually consist of 33 litres of NaI(Tl) crystals in the main detector array with between 4 and 8 litres in the upward-looking array. After energy calibration of the spectra, counts from the main detector are recorded in the five windows listed in Table 4-2. Cosmic radiation (3000-6000 keV) is also recorded. Radiation in the upward-looking detector is recorded in a radon window (1660-1860 keV). Comprehensive descriptions of airborne and ground gamma-ray spectrometry surveys including fundamentals, instrumentation, calibration, data processing, and interpretation are covered by Grasty et al. (1991), Grasty and Minty (1995), Shives et al. (1995), Dickson and Scott (1997), Horsfall (1997), Minty (1997), Minty et al. (1997), Wilford et al. (1997), and the International Atomic Energy Agency (2003), and references therein.

During the course of the survey, verification tests must be carried out periodically to ensure that the spectrometry system is functioning correctly. These include

- daily energy resolution checks using Cs^{137} unless online energy calibration monitoring is available, in which case weekly checks using Cs^{137} will be sufficient;
- daily thorium source tests to confirm the stability of the stripping ratios;
- a test line, near the survey location, must be flown at the start and, if possible, at the end of each sortie in order to ensure that the overall sensitivity of the gamma-ray spectrometry system is maintained constant;
- also to facilitate monitoring of background radon changes, daily tests should include flights at survey altitude at the beginning and end of each day over a large body of water;
- at least once during a survey, the radar altimeter, which measures terrain clearance, must be calibrated.

Survey Data Corrections

The following is a simplified outline of the processing that is applied to raw gamma-ray spectrometry measurements to obtain equivalent ground concentrations of potassium, uranium, and thorium. For further details, refer to Grasty et al. (1991), and Grasty and Minty (1995).

- The windowed counts used in gamma-ray spectrometry can be obtained directly from the raw spectra recorded in real time or from spectra recon-

structed using spectral-enhancement methods, such as Noise Adjusted Singular Value Decomposition (NASVD) or by Minimum Noise Fraction (MNF), both of which improve the signal-to-noise ratio compared to recorded spectra (International Atomic Energy Agency, 2003). These spectral-enhancement techniques impose rigorous constraints on the means of measuring raw spectra (see Grasty and Minty, 1995). The use of these techniques will not change the average responses for an area but will reduce the noise in individual readings. It has been estimated (Grasty, 1979) that NASVD yield an improvement similar to doubling the volume of detector used for a survey.

- Window extraction – the count rates in the various windows must first be determined to reduce the volume of data to be transferred from the field records to the processing database.

After the accumulated counts for the three regions of interest (K^{40}, Bi^{214}, and Tl^{208}) have been accumulated from the spectrum, they are processed as follows:

- Dead-time correction – this is the first step in the reduction sequence for radiometric data. It is carried out using electronically measured dead-time data. Dead-time correction should be applied to each window in the downward-looking detector (including the cosmic and total count windows), but not to the upward-looking data, as these are processed by different circuits.
- Filtering to prepare for background corrections – digital filtering of the radar altimeter data, the cosmic channel, and the radon background data from the upward-looking detector.
- Subtract cosmic, aircraft, and radon background counts – the background counts can be determined using upward-looking detectors and/or by flying over bodies of water. These background counts are then subtracted from the accumulated counts.
- Calculation of the effective height used to adjust stripping ratios for altitude and to carry out attenuation corrections – the stripping ratios computed by the pad calibration procedure are applicable only at ground level. The equivalent stripping ratios at the observed terrain clearance are derived from the ground-level stripping ratios, using the factors derived from the test strip.
- Apply stripping ratio corrections – the effects of Compton scattering are removed by applying the stripping ratio corrections computed at the measured height.
- Adjust count rate for attenuation with height using the count-rate attenuation factors (determined from the test strip), the count rate at the observed terrain clearance is converted to an equivalent count rate at the planned flying height.
- Apply sensitivities to compute equivalent ground concentration – the final background-corrected, stripped, height-adjusted count rates are converted to equivalent ground concentration of potassium (K, %), equivalent uranium (eU, ppm), and equivalent thorium (eTh, ppm) by dividing by the sensitivities (measured in cps/ppm or cps/%).
- Calculation of radioactive element ratios and exposure – the diagnostic ratios (eU/eTh, eU/K, and eTh/K) and exposure rate are computed from the K, eU, and eTh concentrations. Due to statistical uncertainties in the individual radioelement measurements, some care should be taken in the calculation of these ratios. Ratios should be determined using radioactive element concentrations and not corrected counts. An acceptable method of determining ratios includes neglecting any data points where the potassium concentration is less than a predetermined threshold, usually 0.25%, as these measurements are likely to be over water; progressively sum the element concentrations of pairs of adjacent points on either side of the data point until the total accumulated concentration exceeds a threshold value. This threshold is normally set to be equivalent to at least 100 counts for both the numerator and denominator; calculate the ratios using the accumulated sums of concentration values. With this method, the errors associated with the calculated ratios will be similar for all data points.

Note that stripping ratios, attenuation coefficients, and sensitivities must be carefully determined for each acquisition system. Proper application of these constants during processing usually results in seamless data sets across individual survey boundaries, regardless of the acquisition system used. Over-water values should not be deleted from a data set or set to zero as such values contain useful data quality information. Due to the statistical nature of the gamma-ray spectrometry technique 'negative' concentrations are acceptable in low average count-rate areas. If background corrections are properly determined and applied correctly, then radioactive element concentrations should yield a mean concentration of zero over large bodies of water.

DATA SOURCES

Most of the airborne gamma-ray spectrometry data for Canada was collected through a variety of Federal and Federal/Provincial cooperative programs to support ongoing and future geological mapping activities and

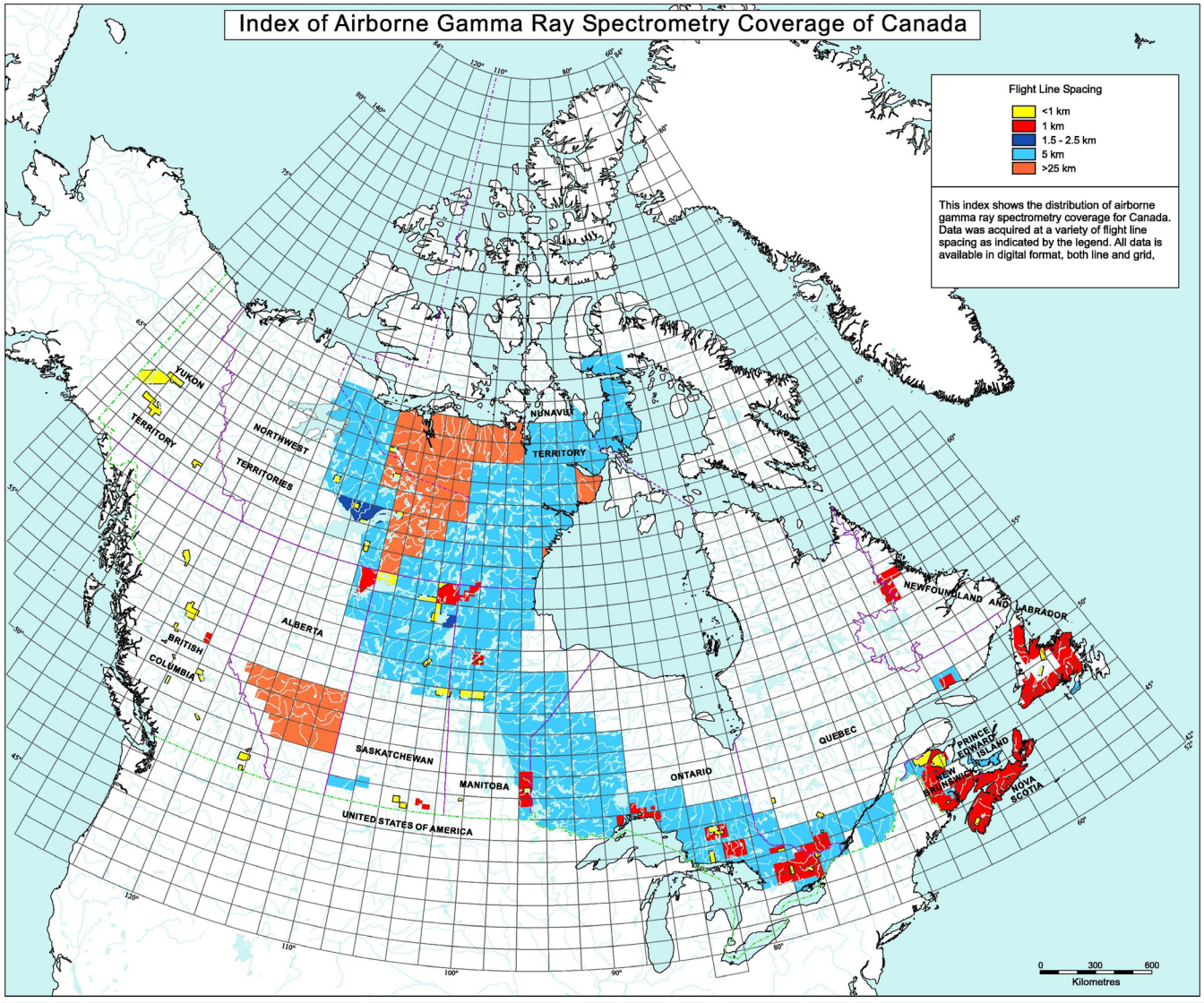

Figure 4-3. Airborne gamma-ray spectrometry coverage of Canada (November 2005).

mineral resource exploration. For these reasons survey areas were initially chosen because of their high mineral potential.

Systematic AGRS data have been acquired from about 1970 to the present, using a variety of aircraft and instrument packages. The aircraft flew along a pattern of parallel flight lines, typically at 120 m terrain clearance (height above the ground). Typical flight line spacing includes 200 to 500 m, 1000 m, 5000 m, and some at 25000 m; typically, aircraft fly at a speed of approximately 120 knots (190 km/h). Most data were acquired by sampling at 1-second intervals (some of the older data were sampled every 2.5 seconds), which is equivalent to about 60 m on the ground. Figure 4-3 shows an index map of AGRS coverage for Canada. Figure 4-4 shows the Ternary Radioactivity Map of Canada compiled from the digital archives of the Geological Survey of Canada.

Radioactivity data for Canada are easily accessible through the internet using the Geoscience Data Repository (GDR) at http://gdr.nrcan.gc.ca. These radioactivity data are derived from the digital archives of the Radiation Geophysics Section. The original flight line and gridded data for over 300 surveys are currently available from the GDR website. Grids of Canada, gridded with 250 m cell size using all digitally archived survey data are also available from the GDR website.

More information regarding the collection, distribution, and applications of gamma-ray spectrometry data can be found by visiting the Radiation Geophysics website at http://gsc.nrcan.gc.ca/gamma.

INTERPRETATION

Unlike conventional magnetic, electromagnetic, gravity, and seismic techniques that measure physical rock properties, often in response to induced effects, and

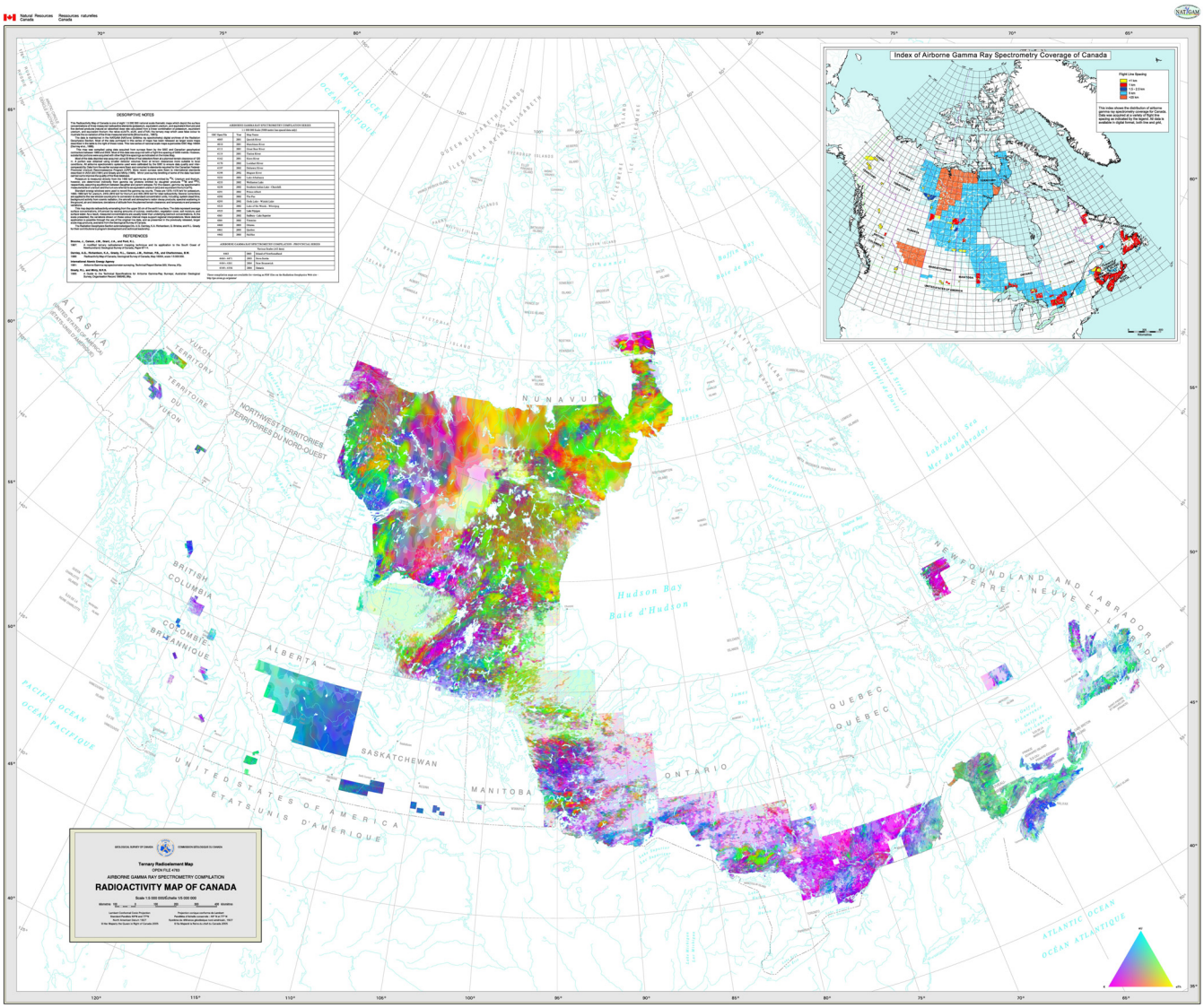

Figure 4-4. Ternary radioactivity map of Canada (Carson et al., 2005).

that may detect variations at considerable depths to source, from tens to thousands of metres, AGRS and GGRS measure variations in radioactivity emanating from the top 30 cm of the Earth's surface. The three most abundant natural radioactive elements, potassium, uranium and thorium, occur as major, mobile and immobile elements, respectively, in varying proportions, in all rocks and soils.

As the concentration of each radioactive element varies between different rock types, a gamma-ray spectrometer can be used to measure these variations and effectively map the different rock types. Where the normal radioactive signature is altered by a mineralizing process, the resulting alteration-related signature provides exploration guidance. Interpretation becomes complicated when these bedrock-related signatures become obscured by overlying transported surficial material or by extreme weathering effects. In Canada, extensive glaciation has mechanically reworked and transported bedrock derived material. However, the resulting overburden usually reflects local bedrock chemistry. Only when the surficial material is composed predominantly of reworked material, such as glaciofluvial- or glaciolacustrine-type deposits, does the resulting radioactivity signature not reflect the underlying bedrock. Effective interpretation, therefore, requires some knowledge not only of the radioactive element contents of rock types expected to be found in the survey area, but also knowledge of the glacial history of that area.

Interpretation of AGRS data requires understanding of some basic concepts of gamma-ray spectrometry and the importance of proper controls on system calibration, data acquisition, data processing, and presentation methods. Some basic concepts are listed here:

- AGRS is a remote sensing, geophysical technique that provides information about the distribution of

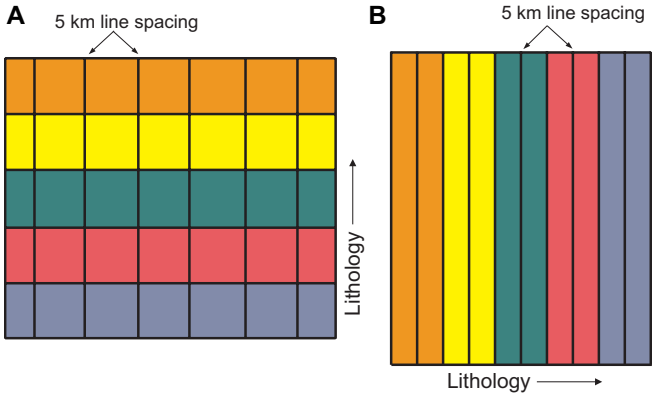

Figure 4-5. Diagram showing the orientation of flight lines with respect to lithology. **(A)** Perpendicular to strike of the lithology (which is the normal flight pattern). **(B)** Parallel to strike of lithology.

K, U, and Th, which is directly interpretable in terms of surface geology.

- AGRS is a surface technique only – interpretation requires an understanding of the nature of the surficial materials and their relationship to bedrock geology.
- Although AGRS measures a physical phenomenon, it is for geological and exploration purposes best considered in geochemical terms 'Airborne Geochemistry'.
- Unlike a camera lens, a gamma-ray spectrometer does not have a 'fixed field of view' – a highly radioactive point source may be detected even when it lies outside some nominal field of view.
- For large geological targets, the gamma-ray flux decreases exponentially with distance from the source.
- A single AGRS measurement provides an estimate of the average surface concentration for an area of several thousand square metres, composed of variable proportions of bedrock, overburden, soil moisture, water, and vegetation.
- Typically, bedrock concentrations are higher than AGRS values – concentrations in glacial drift are only slightly higher than AGRS values. AGRS ratio values (eU/eTh, eU/K, and eTh/K) tend to closely approximate ratio values at ground level.
- Ratio patterns can enhance subtle variations in elemental concentrations due to lithological changes or alteration processes associated with mineralization.
- Not all ratio anomalies are created equal – caution should be used when interpreting ratio patterns, as questionable high-ratio anomalies can be generated by low count rates in the denominator.
- The usefulness of AGRS in geological mapping and mineral exploration depends on two factors: (1) the extent to which radioelement distribution relates to bedrock differences and the extent to which these are recognizably modified by mineralizing processes, and (2) the extent to which bedrock radioelement content is reflected in surficial materials that can be spatially related to bedrock sources.

Effective application of AGRS to geological mapping and mineral exploration must take into account knowledge of how the radioactive element distributions relate to normal lithologic signatures; how these normal lithologic signatures are recognizably modified by mineralizing processes (alteration signatures); how these lithological and alteration signatures are incorporated into surficial materials; and how these surficial materials can be spatially related to bedrock sources. Remote predictive mapping (RPM) applications and methodology should be directed towards improving knowledge in these four basic tenets of effective AGRS interpretation.

Interpretation Issues

Resolution and Line Spacing

AGRS data is collected along lines that are spaced anywhere from 5000 to less than 500 m apart. The data are densely sampled along the line, however sparsely across line depending on the line spacing. This could potentially lead to problems of gridding (interpolating) the data, thereby creating a continuous image as opposed to a profile presentation. As the data are sampled along line (<100 m), correlation along line is not a problem. However, the problem can be summarized succinctly as follows: if there is little spatial correlation across each flight line, then interpolation of the data should not be undertaken. An additional concern related to line spacing is the orientation of the flight line with respect to the prevailing strike of rock units, as summarized in Figure 4-5. A variogram (Fig. 4-6) can be used to test whether spatial correlation exists both along and across line. Figure 4-7 shows variograms of AGRS data acquired over the Melville Peninsula, Nunavut with 5 km flight line spacing. Clearly, as might be expected, spatial correlation exists along the flight line with a range parameter from 500 to 1000 m (Fig. 4-7). However, correlation also exists, albeit at much greater distances (30 000-40 000 m), across the line as well, indicating that, in general, gamma-ray data, even at 5000 m spacing, can be gridded[1].

Like any other remote sensor, spatial resolution plays a significant role in determining how much geo-

1. The correlation will increase depending on the orientation of the flight line with respect to the strike of the lithology (see Figs. 4-5, 4-6). Correlation will increase if the flight lines are parallel to the strike of lithology.

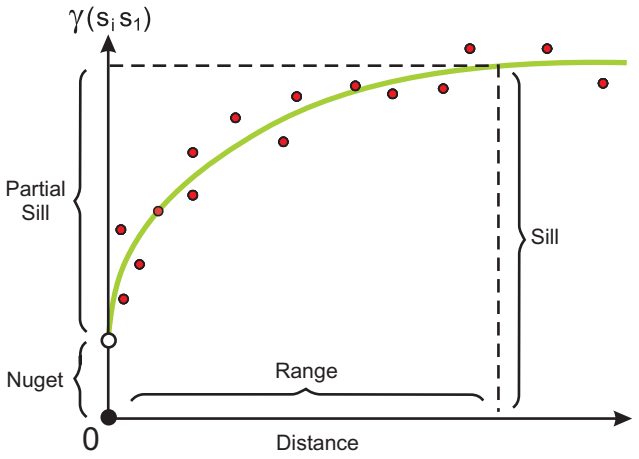

Figure 4-6. Ideal variogram showing the range, sill, and nugget. Range represents the distance at which sample points are no longer spatially associated. Sill represents the portion of the variogram where the model flattens, indicating where samples are no longer associated. Nugget represents small-scale variations at distances of less than the lag distance.

logical detail can be extracted from the imagery, either in a visual sense or through the use of computer-processing techniques. With respect to gamma-ray data, this is clearly illustrated in Figure 4-8, which shows gridded, ternary images of an area in southwestern Nova Scotia at three different line spacing. It is interesting to note in this example of the various phases of the South Mountain Batholith, that the same basic geological information (i.e. the major geological features) is available at larger line spacing (lower resolution) as compared to the higher resolution surveys. In fact, the overall correlation between the images acquired at different line spacing is statistically similar (Fig. 4-9). The difference is a simple matter of detail. In fact, details of rapidly varying surface cover conditions, such as soil moisture and surface water, are often suppressed on lower resolution data in which much of the response is from regional bedrock patterns.

Grid versus Profile Data Presentations

Gridded data are useful for regional mapping; however, due to the smoothing effect of the interpolation process, the detail offered along line in profile data is much greater (Fig. 4-10). Many of the small-scale variations that may be useful for mineral exploration applications (e.g. identification of small anomalies) are averaged out in the interpolation process. This supports the use of both gridded and profile data from regional to more detailed mapping studies.

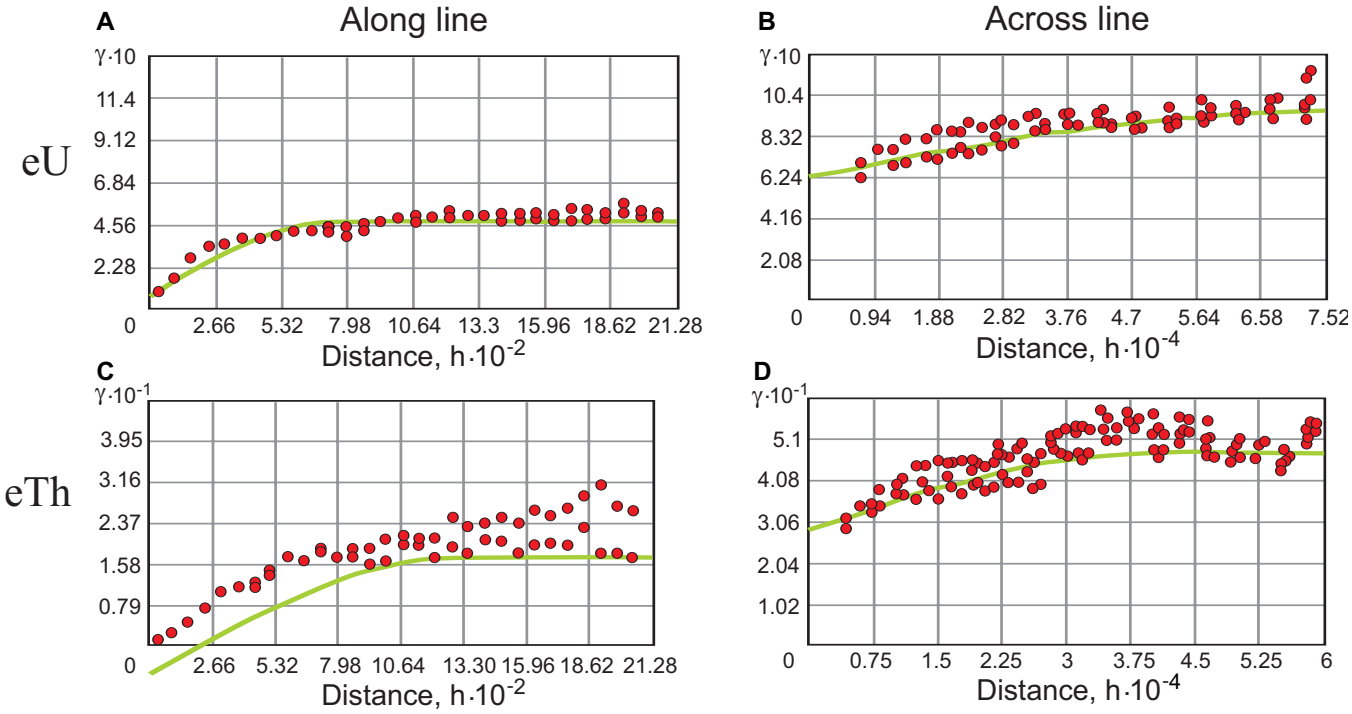

- good structure along line with ranges from 500 m (eU) to 1 km (%K, eTh)
- variograms are well behaved with small sills and very little nugget along line
- surprisingly a reasonable variogram can be achieved across lines, although the ranges are much higher (30-40 km), and sills are much higher, as is the nugget

Figure 4-7. Variograms calculated from gamma-ray sample points acquired over the Melville Peninsula, Nunavut. **(A)** eU along line (see Fig. 4-16 for reference). **(B)** eU across line. **(C)** eTh along line. **(D)** eTh across line. Note the differences in variogram structure (variation of sill, range, and nugget).

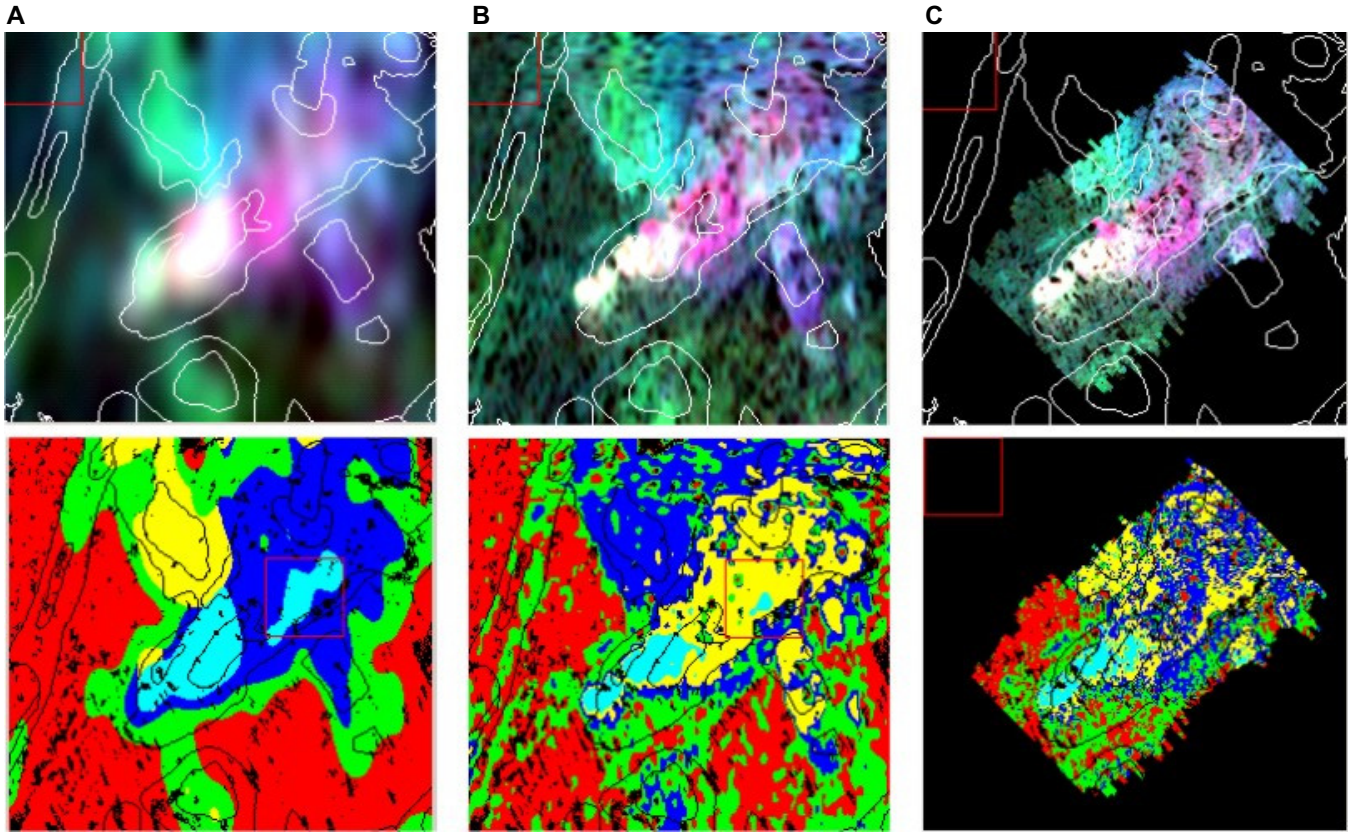

Figure 4-8. Interpolated ternary gamma-ray data of different line spacing (top map) and classified maps (bottom maps; unsupervised K-means algorithm) over the South Mountain Batholith in southwestern Nova Scotia. **(A)** 5 km data in which eU (ppm), eTh (ppm), and K (%) have been displayed through red, green, and blue colours, respectively. Shown below is a classified map indicating the five distinct radioelement classes that define the South Mountain Batholith and surrounding area. **(B)** 1 km data in which eU, eTh (ppm), and K (%) have been displayed through red, green, and blue colours, respectively. Shown on the bottom is a classified map indicating the five distinct radioelement classes that define the South Mountain Batholith and surrounding area. **(C)** 250 m data in which eU (ppm), eTh (ppm), and K (%) have been displayed through red, green, and blue colours, respectively. The bottom mapshows the five distinct radioelement classes that define the South Mountain Batholith and surrounding area. Note the difference in the detail of the radiolement domains provided by the higher resolution data. However, the overall general patterns of radioelement zones are similar, regardless of spatial resolution.

Bedrock Response versus Surficial Response

Gamma-ray data are erroneously thought to be a tool only for mapping surficial cover, and not bedrock. Even though gamma rays originate from the top 30 centimetres of the ground, given the right surface conditions of thin, residual till cover or, as may often be the case, a significant percentage of locally derived bedrock material is incorporated into the overburden, the surface response can often reflect underlying bedrock patterns (Fig. 4-11). As with any other surface remote-sensing technique, the geological environment must be assessed beforehand in order to determine what data types will be appropriate for predictive mapping.

How much of the gamma-ray response can be attributed to bedrock and how much to surficial cover? This of course again will depend on the geological environment, but as a general indication, a study over the Melville Peninsula has resulted in the following observations. A plot of gamma-ray response by mapped surficial unit is shown in Figure 4-12. Clearly, a variation in the gamma-ray signal by surficial units can be seen, especially for eU. However, Figure 4-11 clearly indicates a similar gamma-ray response pattern to the mapped geology as well as a unique statistical response. If one was to measure the variability of the

Figure 4-9. Correlation between gamma-ray data derived from different line spacing for eU (ppm), eTh (ppm), and K (%). The correlations between the data are moderate to strong with the lowest correlations between data with the largest difference in line spacing (i.e. 5 km vs. 250 m). Sample data set is from southwestern Nova Scotia, the same as that used in Figure 4-8.

	eU-5 km	**eU-1 km**	**eU-0.25 km**
eU - 5 km		0.84	0.76
eU - 1 km			0.87
eU - 0.25 km			
	eTh-5 km	**eTh-1 km**	**eTh-0.25 km**
eTh - 5 km		0.75	0.63
eTh - 1 km			0.85
eTh - 0.25 km			
	%K-5 km	**%K-1 km**	**%K-0.25 km**
%K - 5 km		0.82	0.67
%K - 1 km			0.86
%K - 0.25 km			

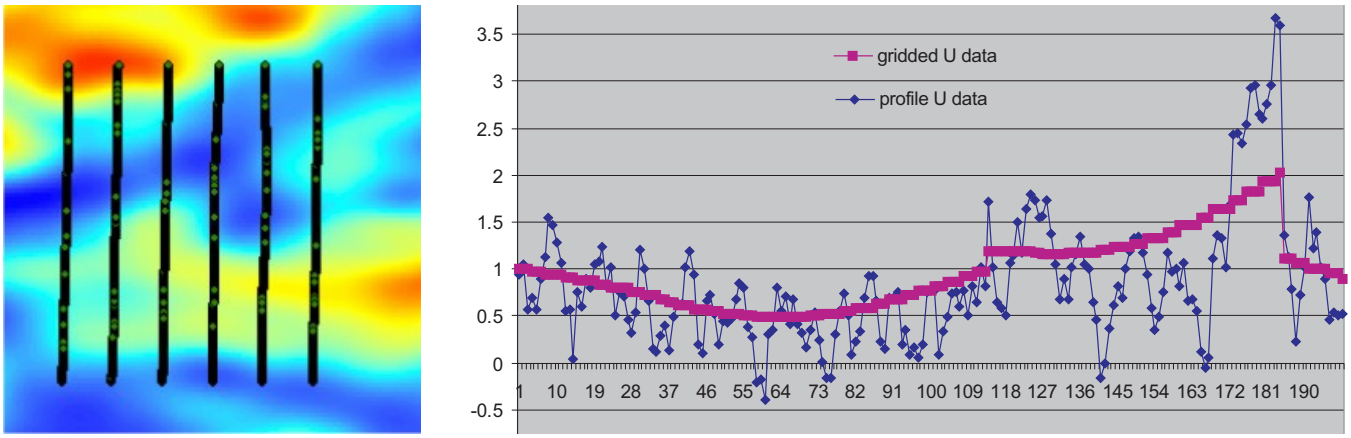

Figure 4-10. A portion of a gridded eU image with the location of the profiles and associated profiles (along line) compared to eU data derived from the interpolated grid. Note the smoothing effect due to the interpolation process (profile data are in blue and gridded data are in magenta).

surficial response over a geological unit (Fig. 4-12C), a small portion of the response can be attributed to surface cover. The range of response, in this area, is greater for the bedrock than for the surface cover (Fig. 4-13). In fact, the gamma-ray data can show significant variations within a given rock unit (Fig. 4-14). This is useful for mapping purposes, as it points to discrepancies or inconsistencies in the geological field data that can be indicated on a predictive map and followed up in the field.

Variations in vegetation and soil moisture can have an effect on the gamma-ray signal originating from the ground. Increased vegetation cover, for example, can suppress the gamma-ray response, as is illustrated in Figure 4-15. In this example, only the potassium channel displays any significant affect from the vegetation, as the difference in response between clear-cut and forested areas is on the order of 20%, with greater emission from the clear-cut areas. The differences in mean values for the 4 classes are significant at the 95% level. Equivalent thorium appears to be the direct opposite of %K, with the highest response from the thickest vegetation cover (forest). The results from this study are preliminary. Additional ground follow-up studies are required to evaluate the influence of other factors, including variations in soil moisture and overburden chemistry.

DATA VISUALIZATION AND PROCESSING

Variables and Standard Survey Products

AGRS data are usually represented by four measured variables, potassium (K, %), equivalent uranium (eU, ppm), equivalent thorium (eTh, ppm), and total air absorbed dose rate (nGy/h). Five derived products are also required to fully present the AGRS data. These include the three radioactive element ratios (eU/eTh, eU/K (ppm/%), and eTh/K (ppm/%)), the ternary radioactive element map (Broome et al., 1987), and the natural air absorbed dose rate (nGy/h). The complete display of all these data requires a minimum of seven contour maps, excluding the ternary map, or eight colour interval maps or images, including the ternary map. Examples of standard colour interval maps and ternary radioactive element maps are shown in Figures 4-16 and 4-17. Most map products require the data to be interpolated onto a regular grid. Many of the standard gridding algorithms are unsuited to AGRS data because of the inherent statistical variations. A suitable gridding algorithm is one that takes the average of all data points lying within a circular or elliptical area, inversely weighted for distance from the grid point.

The ternary or three-component radioactive element map (Figs. 4-16H, 4-17H) is an effective method of displaying variations in total radioactivity and the relative abundances of the three radioactive elements. Areas of the image with the same colour will have similar ratios of K, eU, eTh, and the intensity of that colour is a measure of the total radioactivity. This allows the map to represent the radioactive element distribution better than any of the other single variable or ratio maps. The ternary map is often easier to work with to get an overview of the distribution of radioactivity; however, it does not replace the more detailed, quantitative information available on the other seven maps (total or natural air absorbed dose rate, K, eU, eTh, eU/eTh, eU/K, and eTh/K).

Often, depending on the complexity of the geology, subtle variations in K, U, and/or Th may not be readily apparent. For these reasons, the proper interpretation of GRS data requires the examination of all of the measured variables and associated derived products (Figs. 4-16, 4-17). Ratio maps can enhance or reinforce subtle variations in the measured variables, which can be particularly important, especially when dealing with varying intensities of alteration associated with a mineralizing process. For example, potassium alteration (enrichment) associated with certain types of mineral deposits may occur in host rocks with normally low to

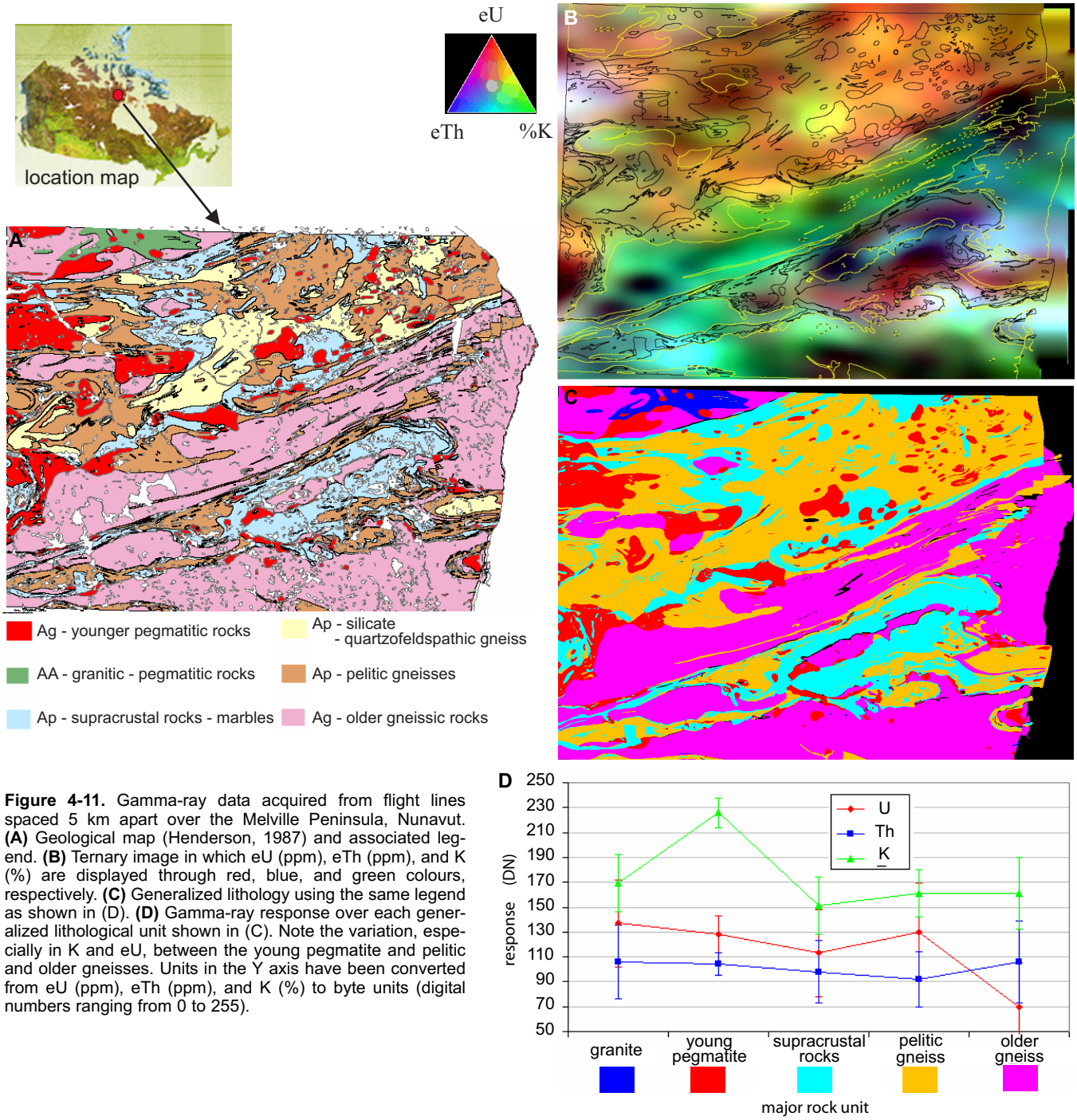

Figure 4-11. Gamma-ray data acquired from flight lines spaced 5 km apart over the Melville Peninsula, Nunavut. **(A)** Geological map (Henderson, 1987) and associated legend. **(B)** Ternary image in which eU (ppm), eTh (ppm), and K (%) are displayed through red, blue, and green colours, respectively. **(C)** Generalized lithology using the same legend as shown in (D). **(D)** Gamma-ray response over each generalized lithological unit shown in (C). Note the variation, especially in K and eU, between the young pegmatite and pelitic and older gneisses. Units in the Y axis have been converted from eU (ppm), eTh (ppm), and K (%) to byte units (digital numbers ranging from 0 to 255).

moderate levels of K, resulting in a high total K signature. This would be easily recognized if this alteration occurred in isolation. However, there may be normal, high K rock types in close proximity to the altered rocks. In this situation, the K associated with the alteration may not be distinguishable from other high K rock types. The ratio maps, in particular the eTh/K ratio, can be a sensitive indicator of K alteration associated with mineralization and can be used as a direct indicator of mineralization. The addition of K associated with alteration will normally result in a low eTh/K ratio because thorium is relatively immobile so its concentration remains constant. Shives et al. (1995, 1997) present a number of case histories that demonstrate the use of AGRS and GGRS to map potassium alteration associated with different styles of mineralization, including volcanogenic massive sulphides, polymetallic, magmatic-hydrothermal (Au-Co-Cu-Bi-W-As (Olympic Dam-type)), and porphyry Cu-Au-(Mo) deposits. On a regional scale, subtle variations in the measured variables, which are clearly reinforced on the ratio maps, are shown by the eU, eTh, and eU/eTh maps for southern Nova Scotia (Ford and O'Reilly, 1985; Ford et al., 1989) (Fig. 4-17). Within the peralu-

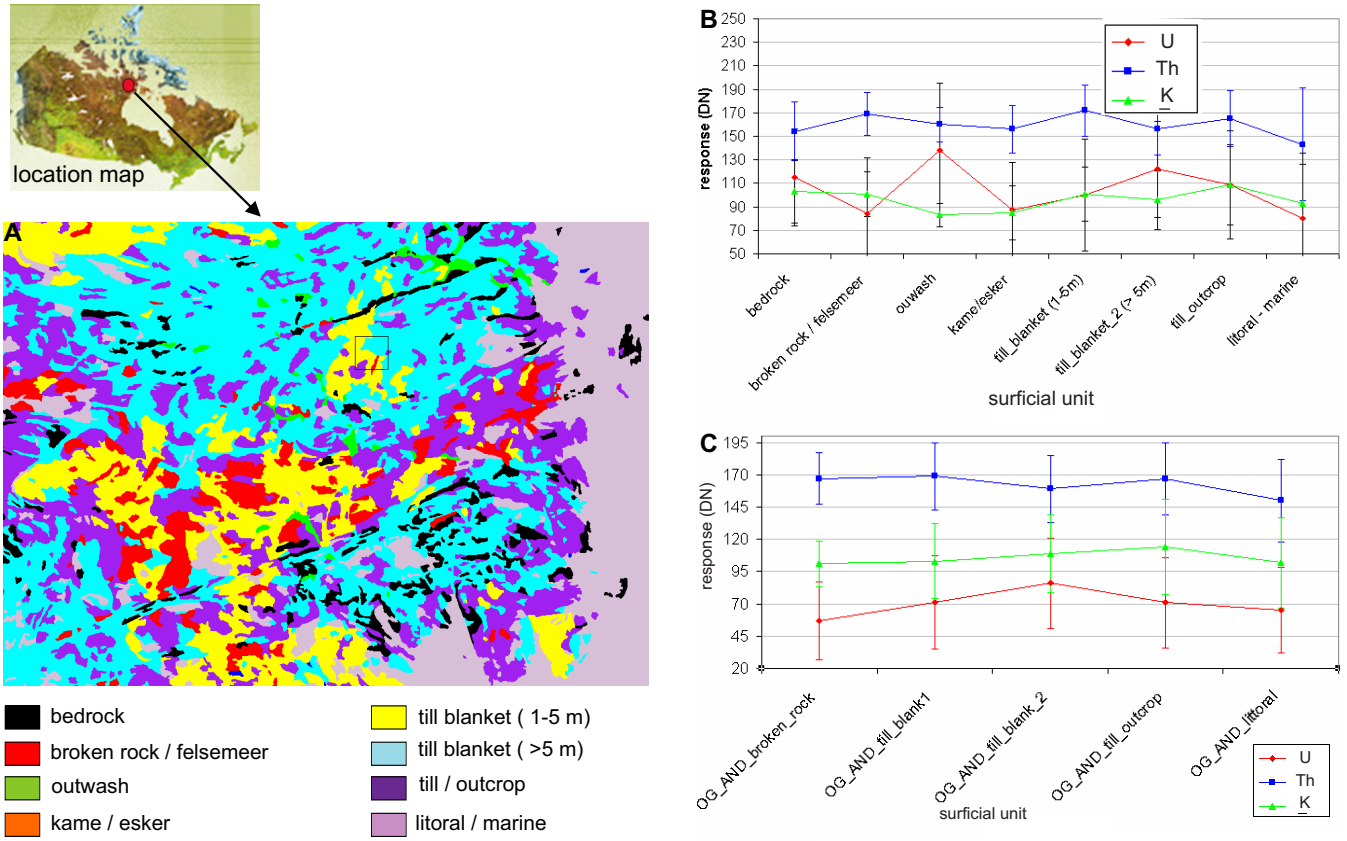

Figure 4-12. (A) Surficial geological map (Dredge, 1994) of the Melville Peninsula, Nunavut. **(B)** Plot of the gamma-ray response by the surficial unit. **(C)** Plot of older gneisses (see Fig. 4-11) by the surficial unit. Note the variation in gamma-ray response within the older gneissic lithology (C).

minous granitic rocks of southern Nova Scotia, uranium concentrations generally increase and thorium concentrations decrease with increasing magmatic differentiation, resulting in abnormally high eU/eTh ratios associated with the most evolved parts of these granitic intrusions.

While gridding GRS data to produce colour interval maps or images it is important to visually represent the geographic variations of a single variable; a multivari-

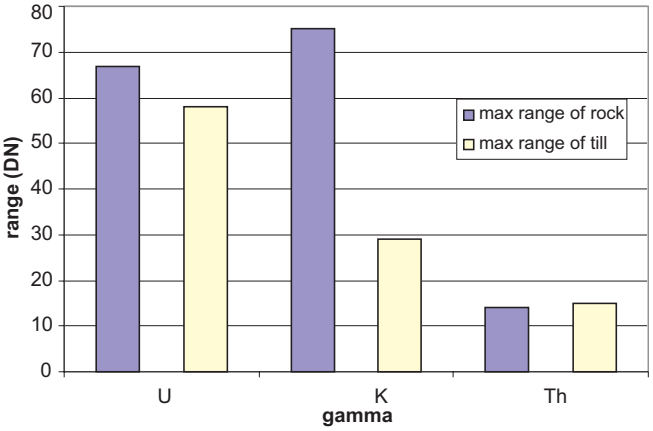

Figure 4-13. Bar chart showing the variation (range) in gamma-ray response for eU, eTh, and %K over bedrock and till, Melville Peninsula, Nunavut. Variation for eU and %K is greater for bedrock than till, indicating that compositional variations in the bedrock contribute more to the range of radioelement variations.

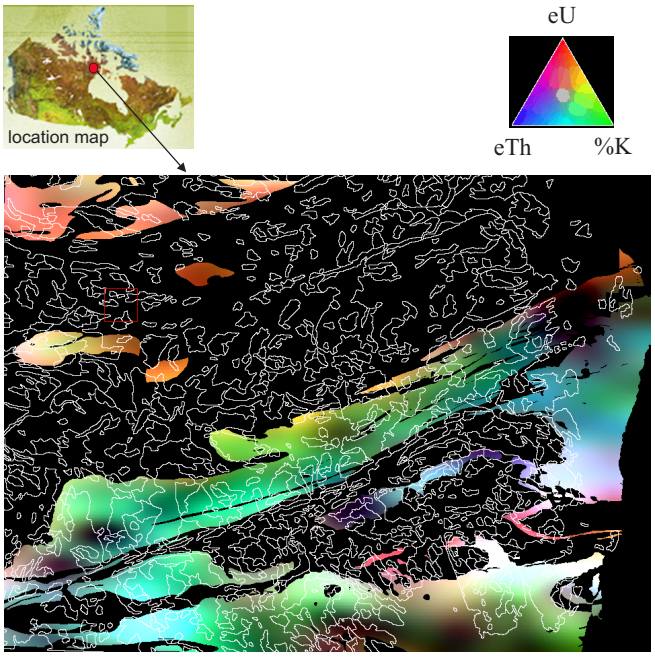

Figure 4-14. Ternary image (eU, %K, eTh – red, green, blue) of just the older gneissic units from Melville Peninsula, Nunavut. Note the variation in gamma-ray response within the gneisses, especially prevalent is the dichotomy in response between the north (with high eU and moderate %K) and south (mostly higher %K and lower eTh and eU).

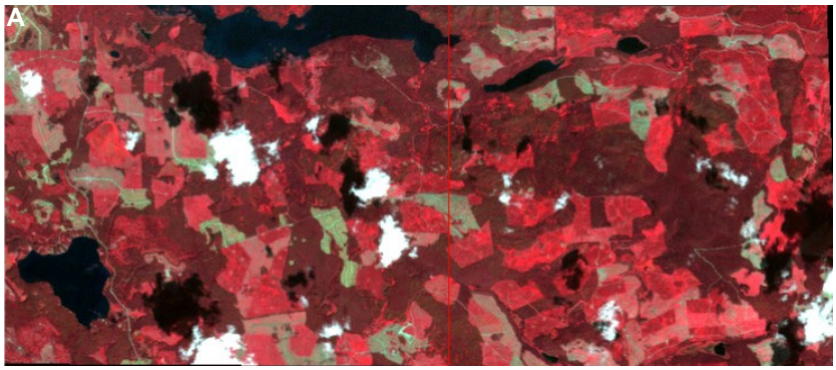

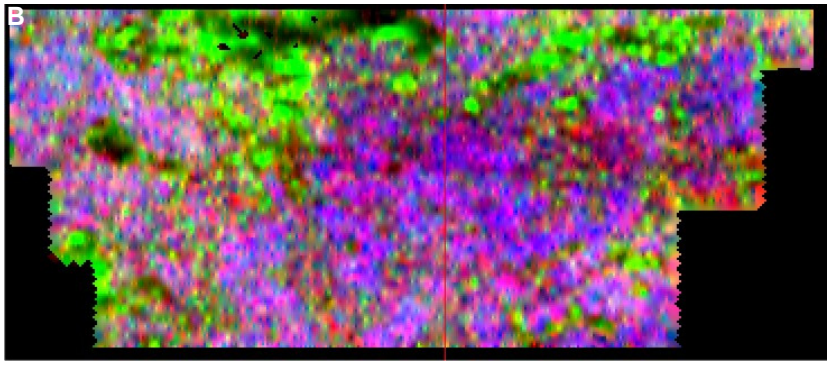

location map

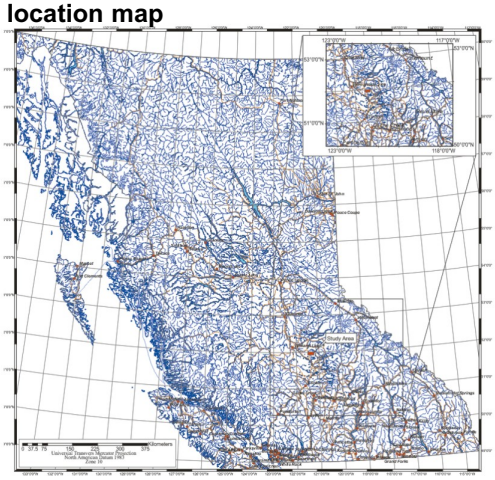

eTh

Code	Count	Average	Median
stats_bare.txt	185	27.4541	29.0
stats_forest.txt	394	51.1066	50.0
stats_med.txt	312	58.7917	59.0
stats_old.txt	202	58.0792	44.0
Total	1093	50.5855	50.0

C

%K

Code	Count	Average	Median
stats_bare.txt	185	141.119	181.0
stats_forest.txt	394	117.457	115.0
stats_med.txt	312	155.66	167.0
stats_old.txt	202	130.861	138.0
Total	1093	134.844	143.0

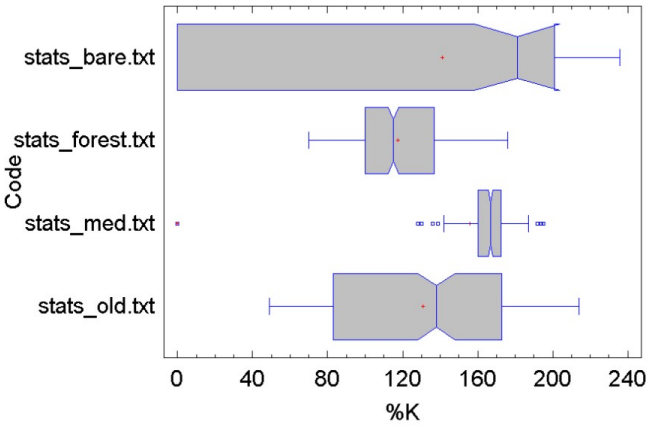

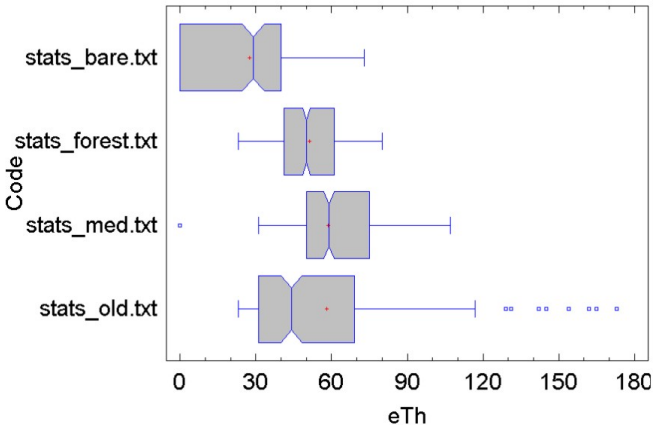

eU

Code	Count	Average	Median
stats_bare.txt	185	141.119	181.0
stats_forest.txt	394	117.457	115.0
stats_med.txt	312	155.66	167.0
stats_old.txt	202	130.861	138.0
Total	1093	134.844	143.0

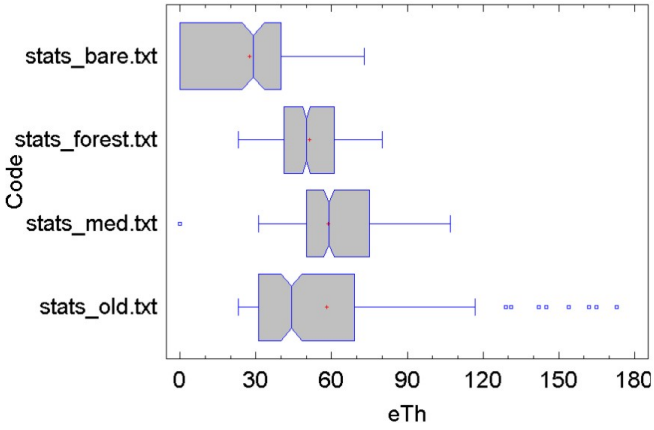

Figure 4-15. A series of images and plots showing the effect of vegetation and moisture content on gamma-ray response. **(A)** LANDSAT colour composite image (bands 4, 3, 2 displayed through red, green, and blue). **(B)** Gamma-ray ternary image. **(C)** Box and whisker plots showing the gamma-ray response for eU, eTh, and %K for bare ground (stats_bare), forested areas (stats_forest), younger regrowth (stats_med), and old regrowth (stats_old) areas. Variations in the response as a function of forest cover and different stages of regrowth can be clearly seen.

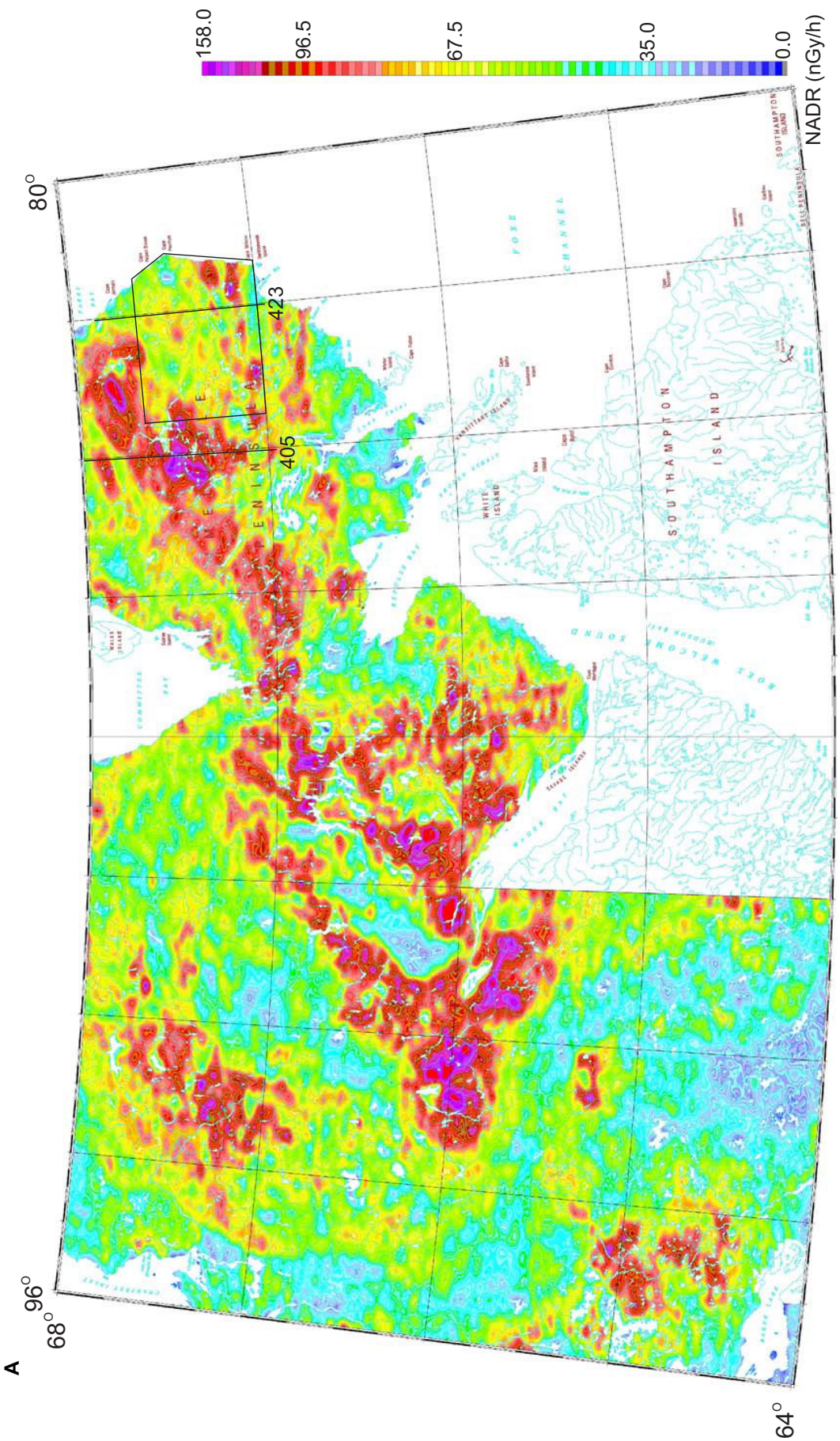

Figure 4-16. Complete set of standard gamma-ray images offered by the Geological Survey of Canada for the Quoich River area, Nunavut. The maps are compiled from 5000 metre line spaced airborne gamma-ray spectrometry data (Holman et al., 2001). The Melville Peninsula study area is outlined in black. **(A)** Radioactivity map of Natural Air Absorbed Dose Rate (NADR), which is a linear combination of the K, eU, and eTh concentrations and represents the total radioactivity from natural sources.

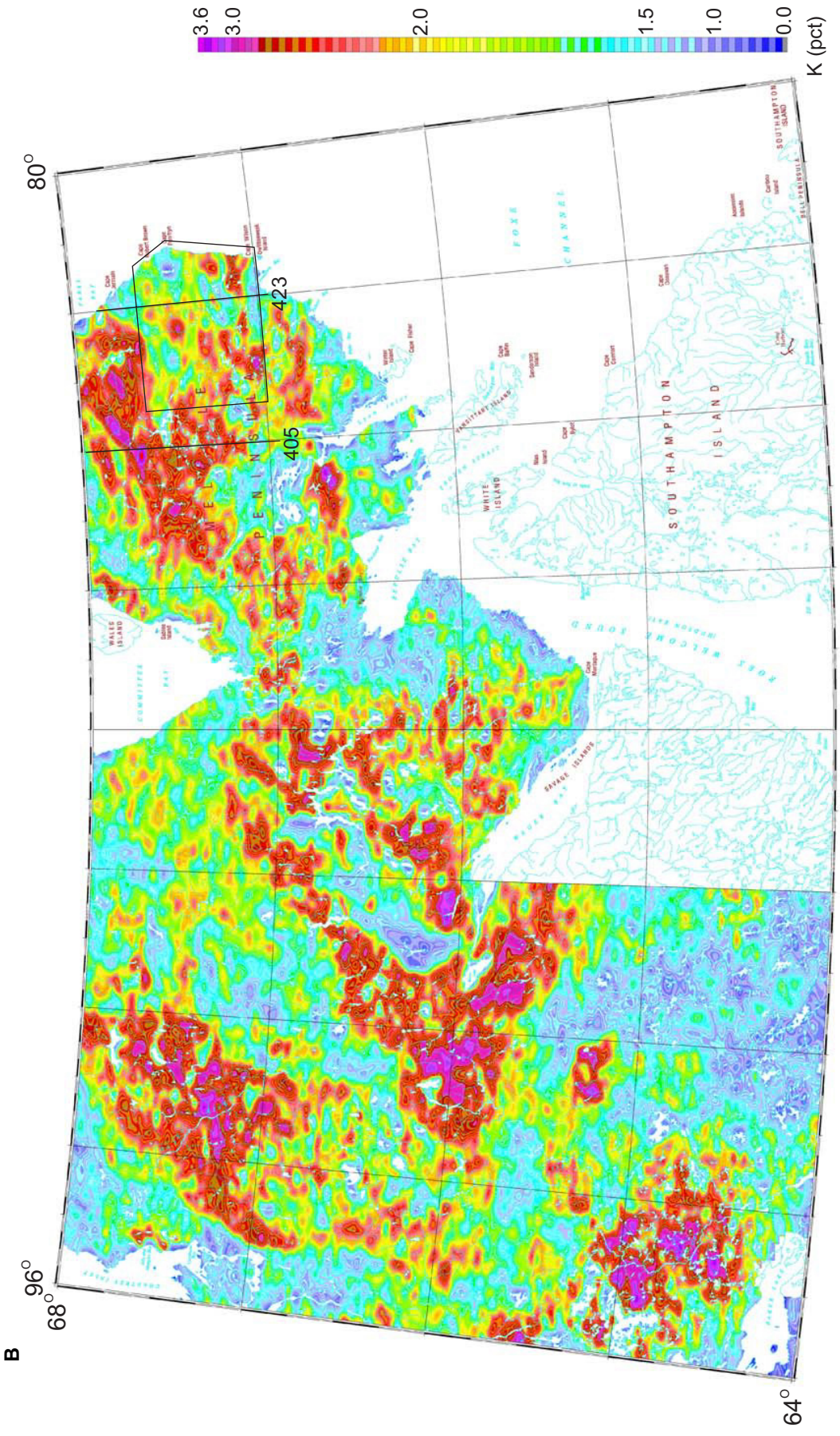

Figure 4-16 continued. (B) Radioactivity map of potassium (pct = percent) distribution for the Quoich River area. The Melville Peninsula study area outlined in black.

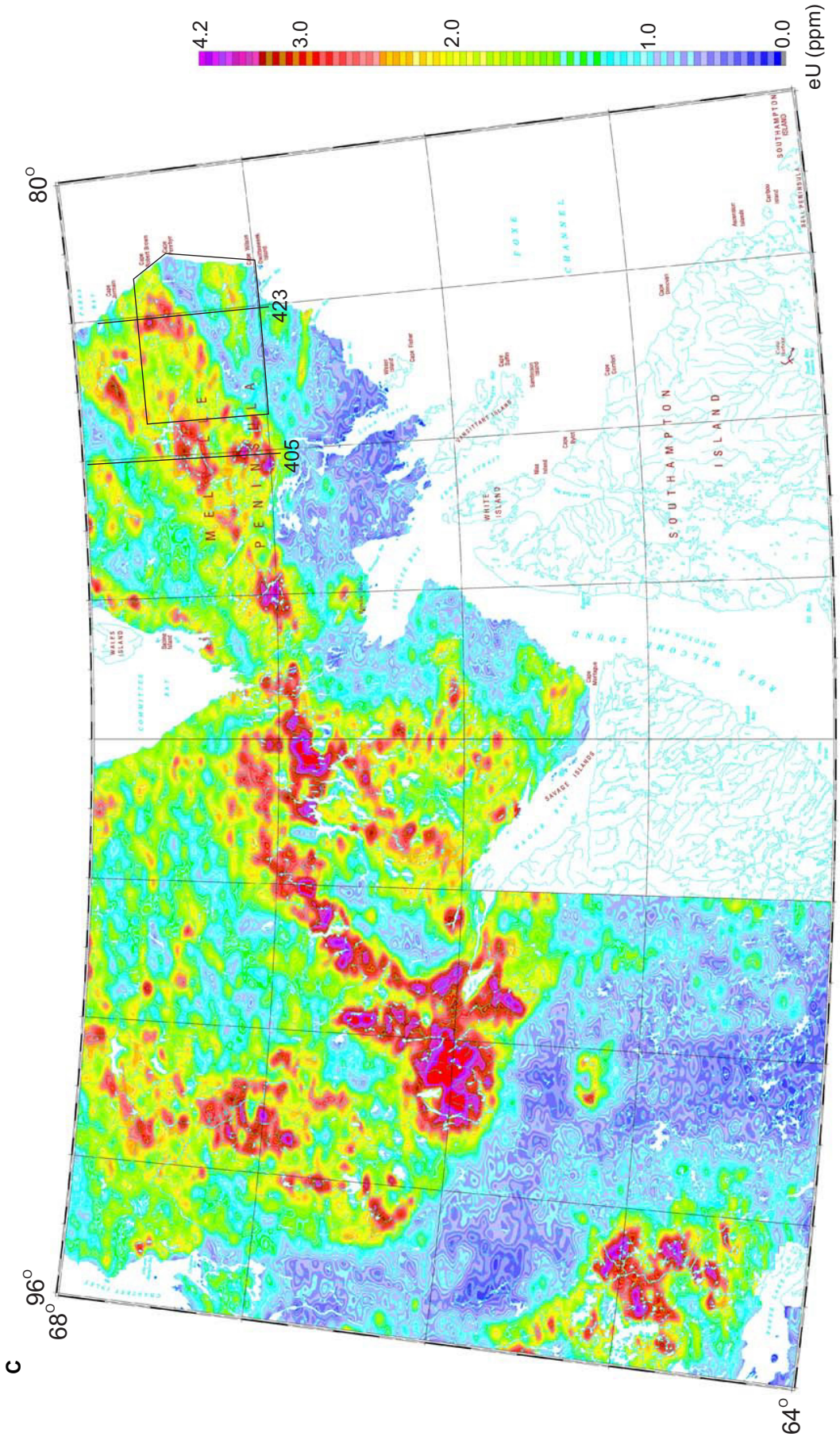

Figure 4-16 continued. (C) Radioactivity map of equivalent uranium (ppm) distribution for the Quoich River area. The Melville Peninsula study area is outlined in black.

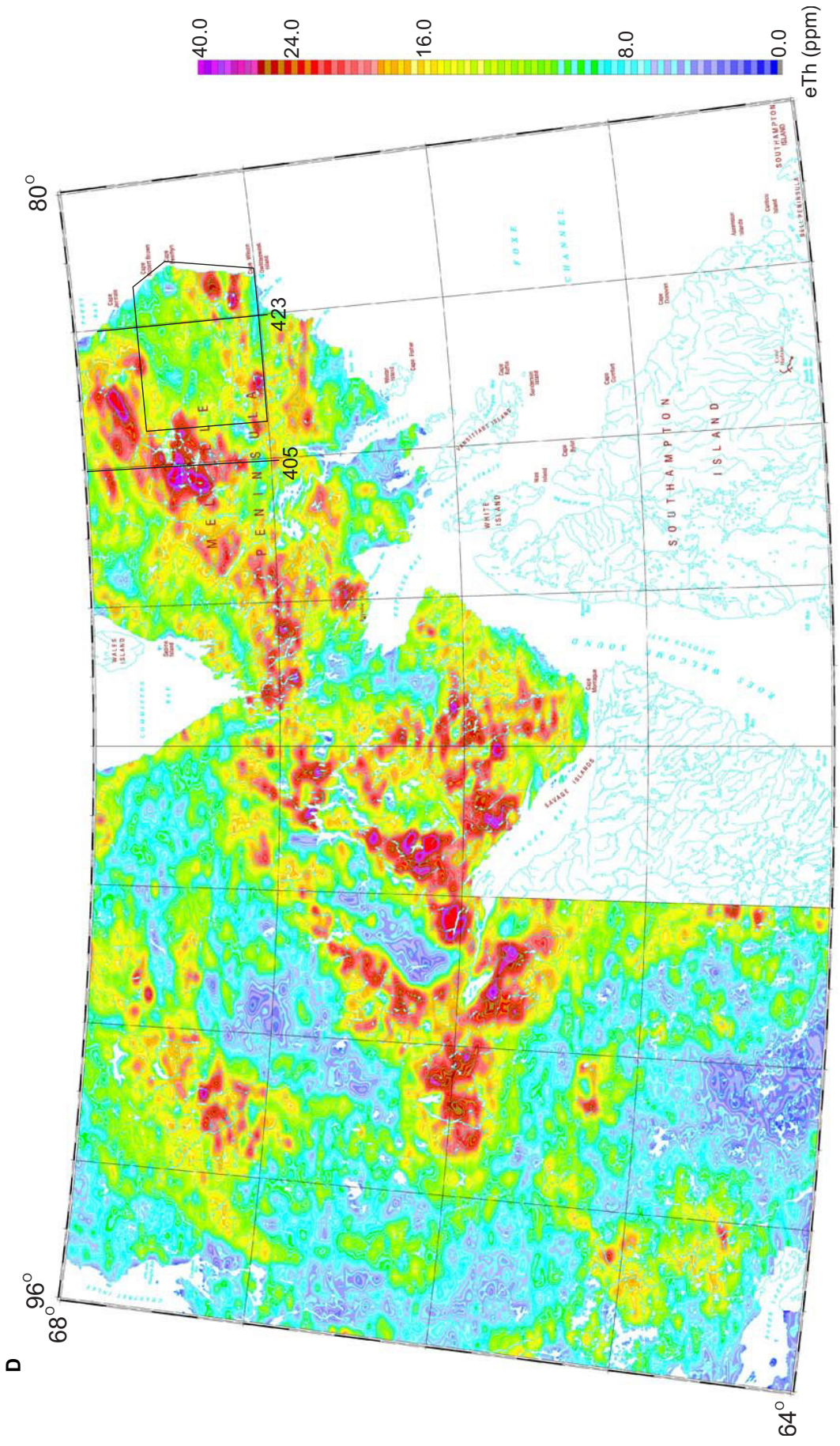

Figure 4-16 continued. (D) Radioactivity map of equivalent thorium (ppm) distribution for the Quoich River area. The Melville Peninsula study area is outlined in black.

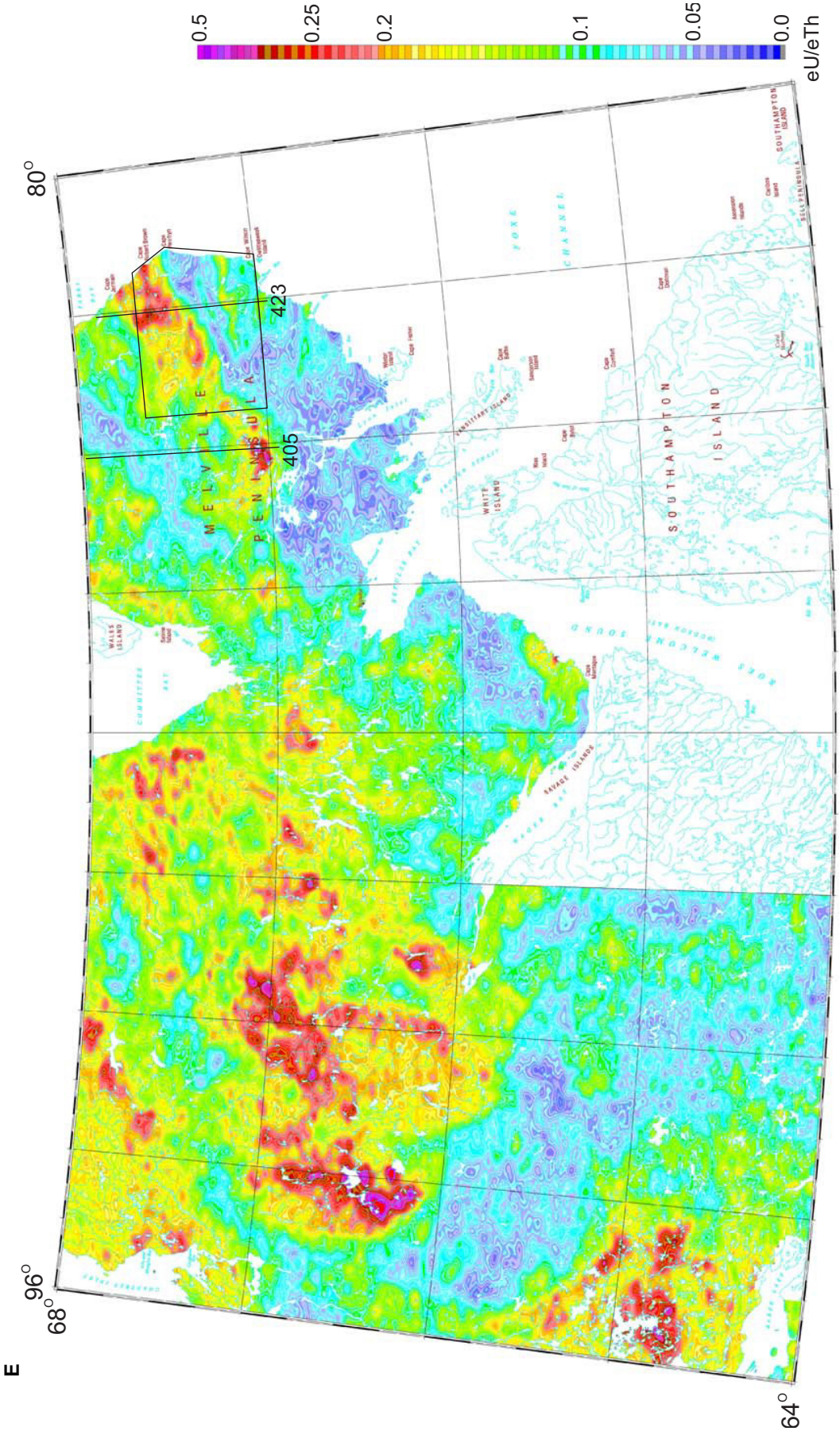

Figure 4-16 continued. (E) Radioactivity map of the equivalent uranium/equivalent thorium ratio (eU/eTh) distribution for the Quoich River area. The Melville Peninsula study area is outlined in black.

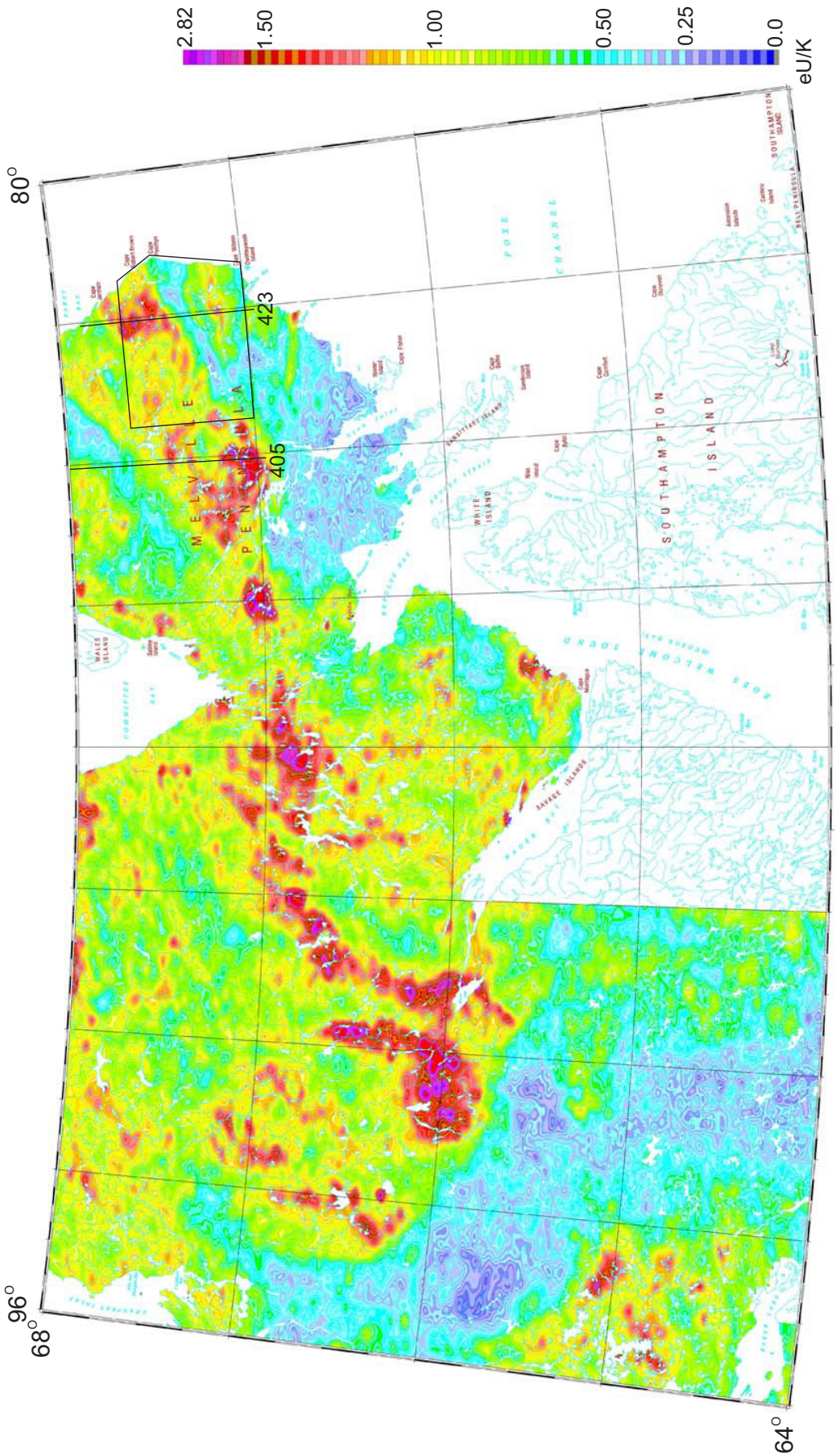

Figure 4-16 continued. (F) Radioactivity map of the equivalent uranium/potassium ratio (eU/K; ppm/%x10^{-4}) tfor the Quoich River area. Melville Peninsula study area is outlined in black.

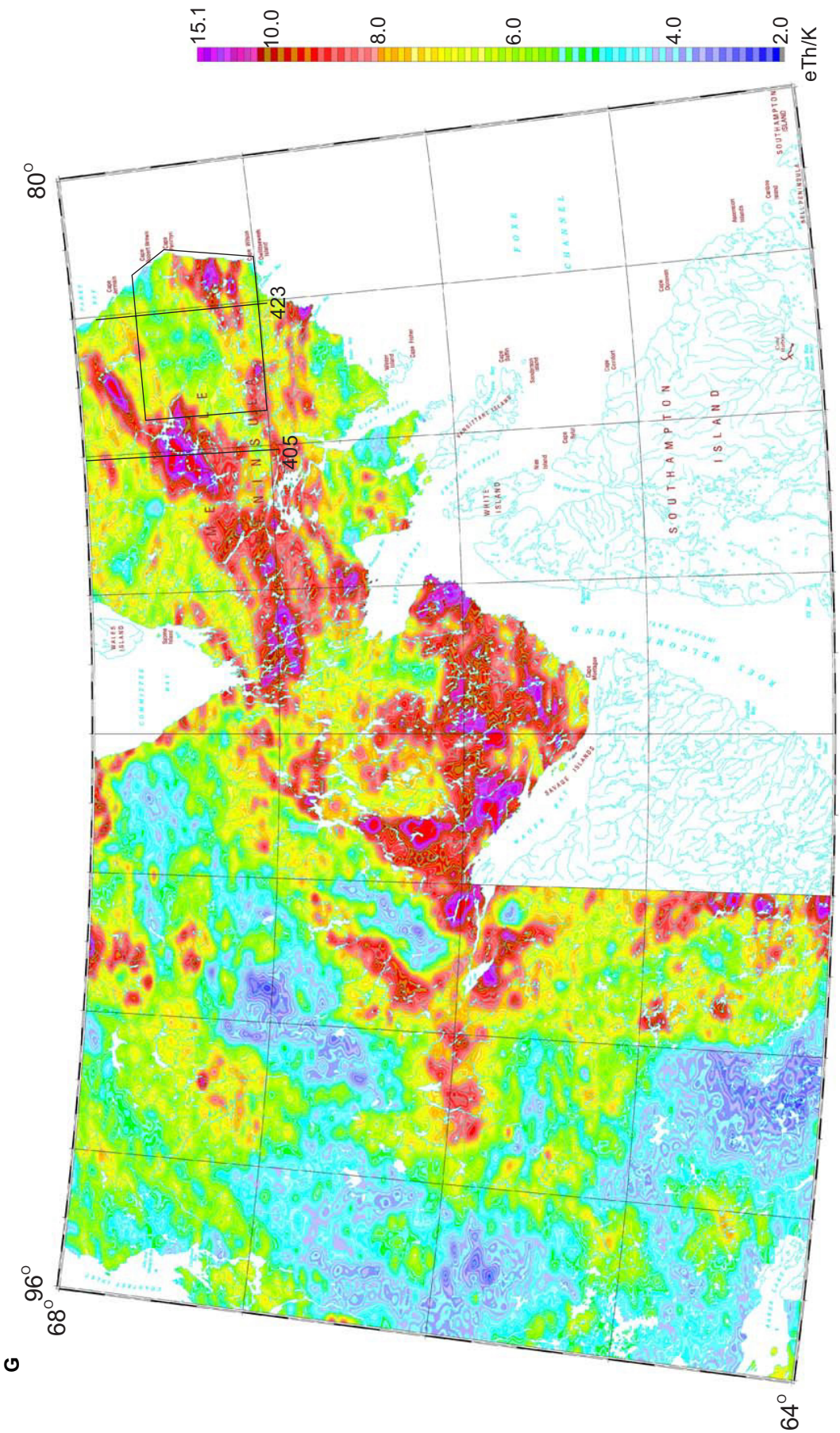

Figure 4-16 continued. (G) Radioactivity map of equivalent thorium/potassium ratio (eTh/K; ppm/% x 10^{-4}) for the Quoich River area. The Melville Peninsula study area is outlined in black.

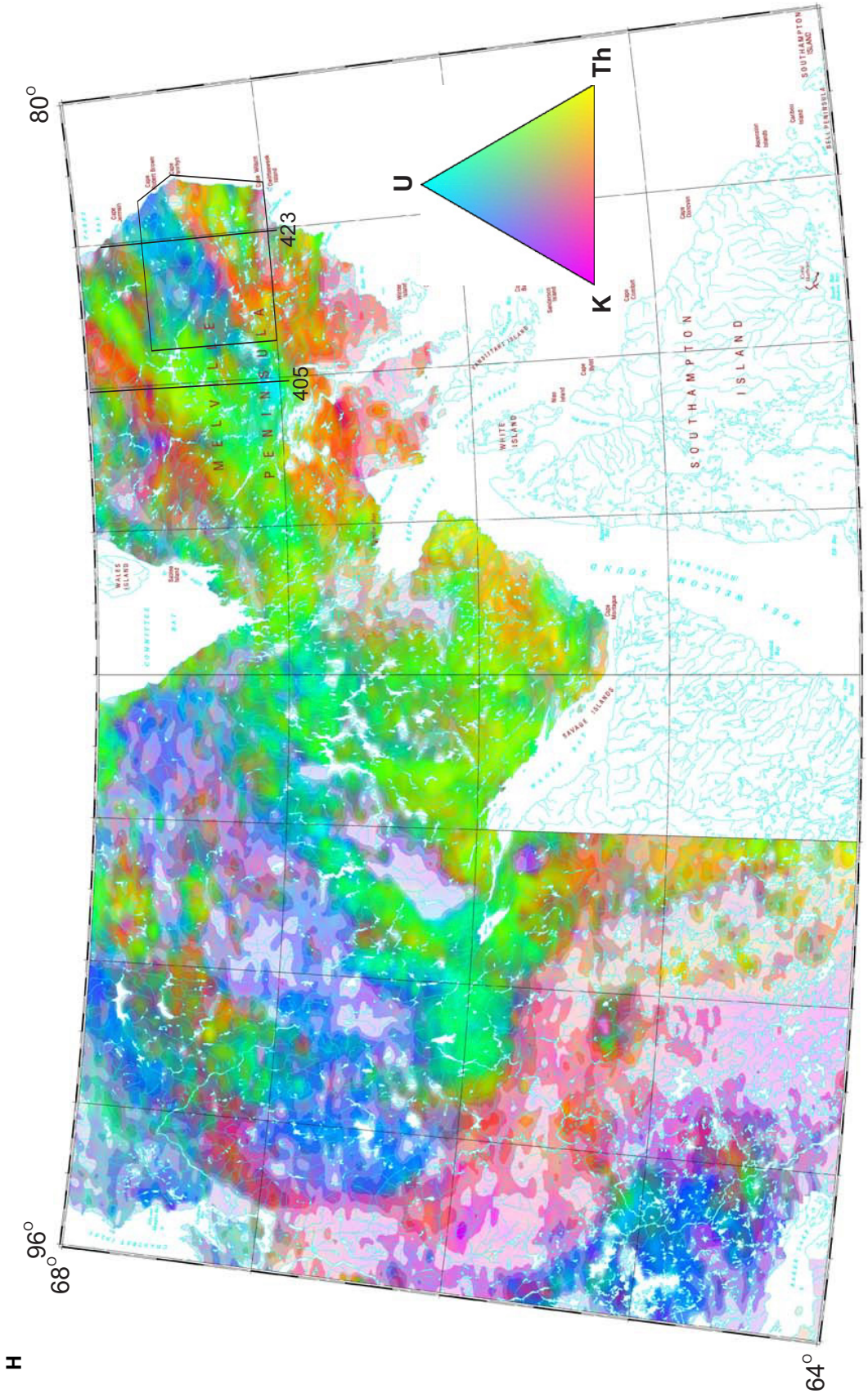

Figure 4-16 continued. (H) Ternary radioelement map for the Quoich River area. The Melville Peninsula study area is outlined in black.

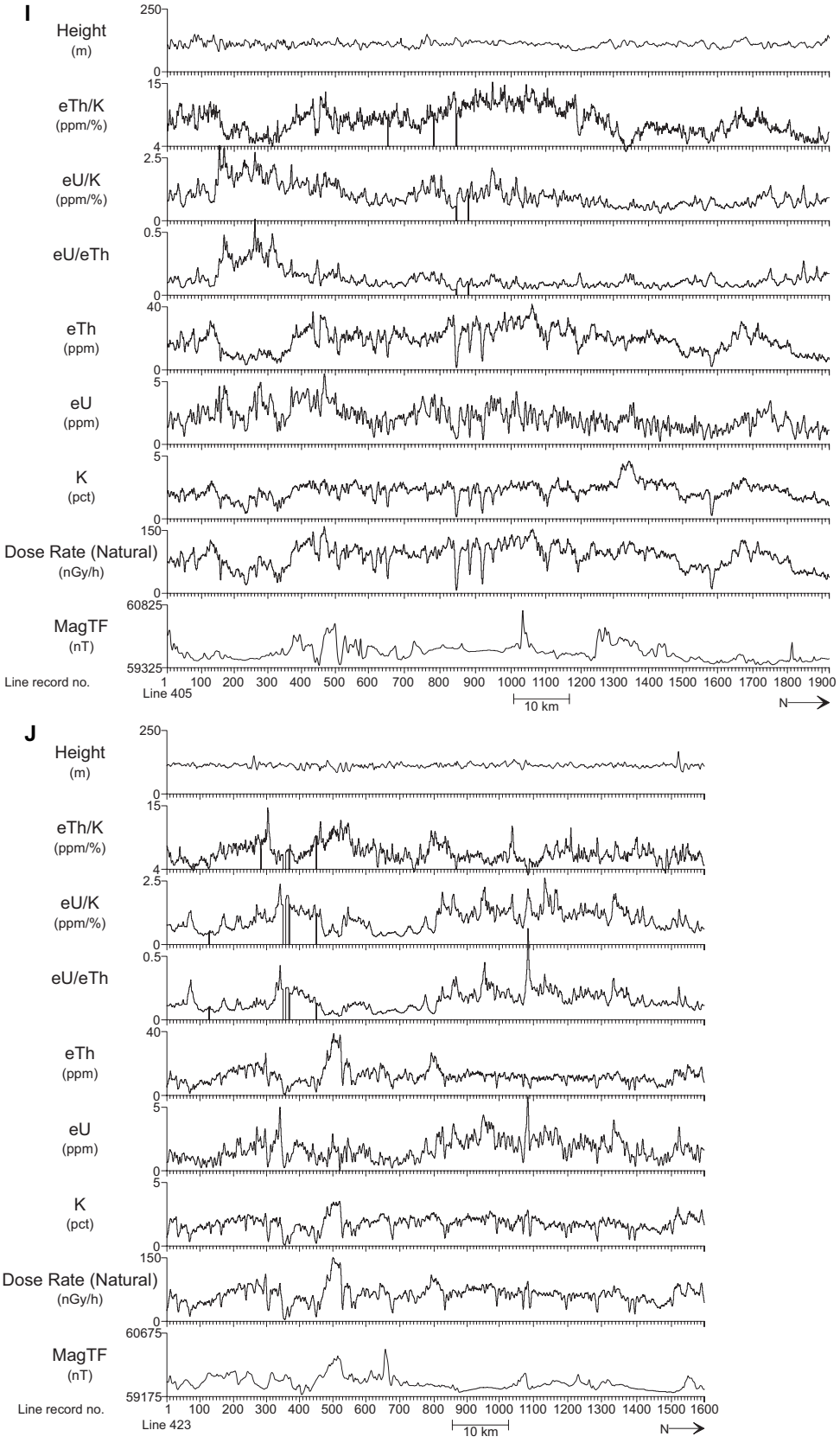

Figure 4-16 continued. Airborne gamma-ray spectrometric multivariable stacked profiles from flight lines 405 **(I)** and 423 **(J)** in the southern Melville Peninsula area, Nunavut. Note the broad elevated eU/eTh ratio area between records 160 and 350 on line 405 (Fig. 4-16I), which is coincident with a broad low eTh area. Within this area, narrower high eU/eTh ratio anomalies are coincident with high eU anomalies. These signatures are typical of the late pegmatitic intrusive rocks that are commonly anomalous for uranium. Figure 4-16J shows two significant eU and eU/eTh ratio anomalies that can be lost if only the total radioactivity data is visualized. The locations of the flight lines are shown on Figure 4-16A-G.

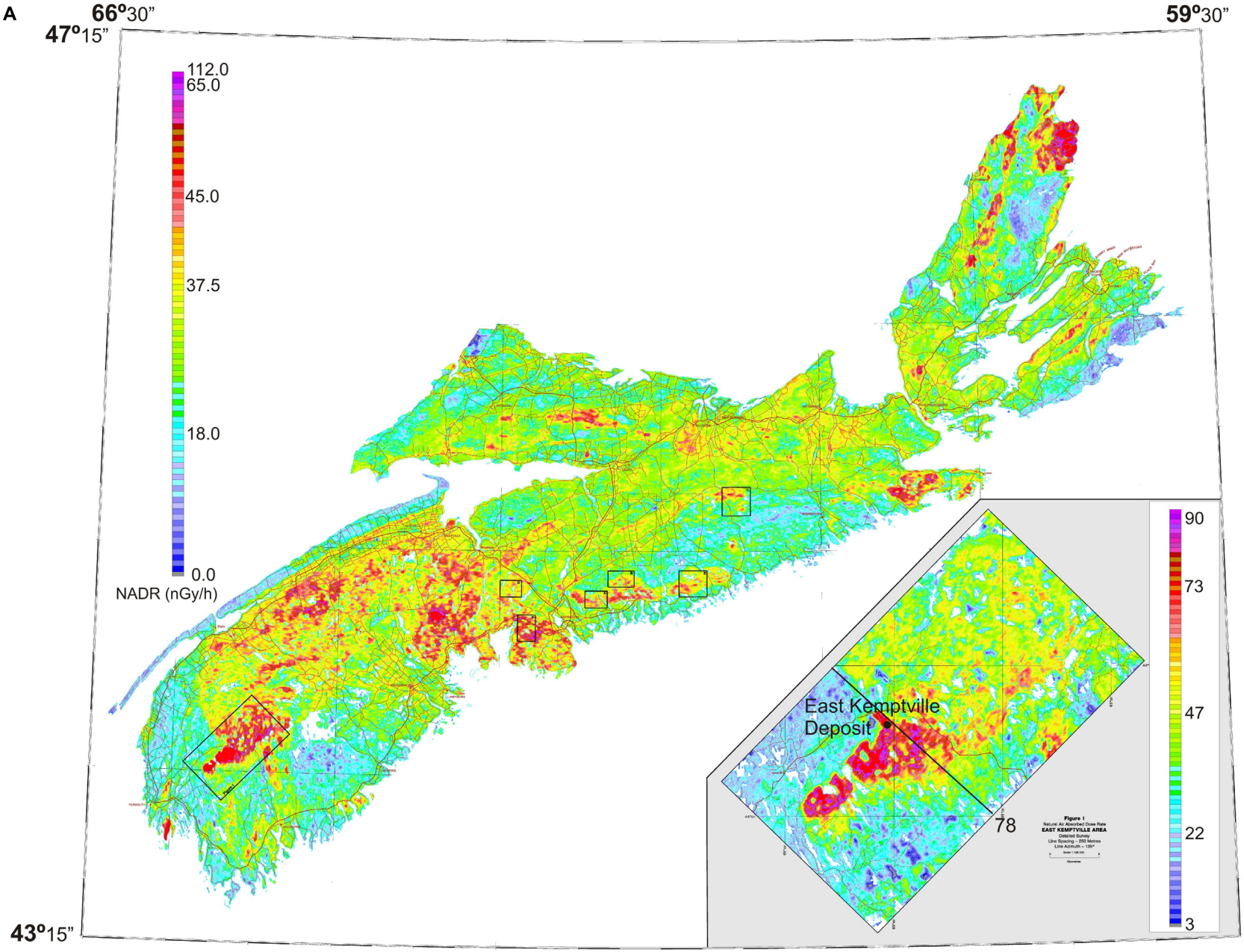

Figure 4-17. Complete set of standard gamma-ray images offered by the Geological Survey of Canada for the province of Nova Scotia compiled from 1000 metre line spaced airborne gamma-ray spectrometry data (Carson et al., 2003). Inset maps compiled from 250 metre line spaced airborne gamma-ray spectrometry data for the East Kemptville area outlined by the black rectangle in the bottom left corner of larger maps. **(A)** Radioactivity maps of the Natural Air Absorbed Dose Rate (nGy/h).

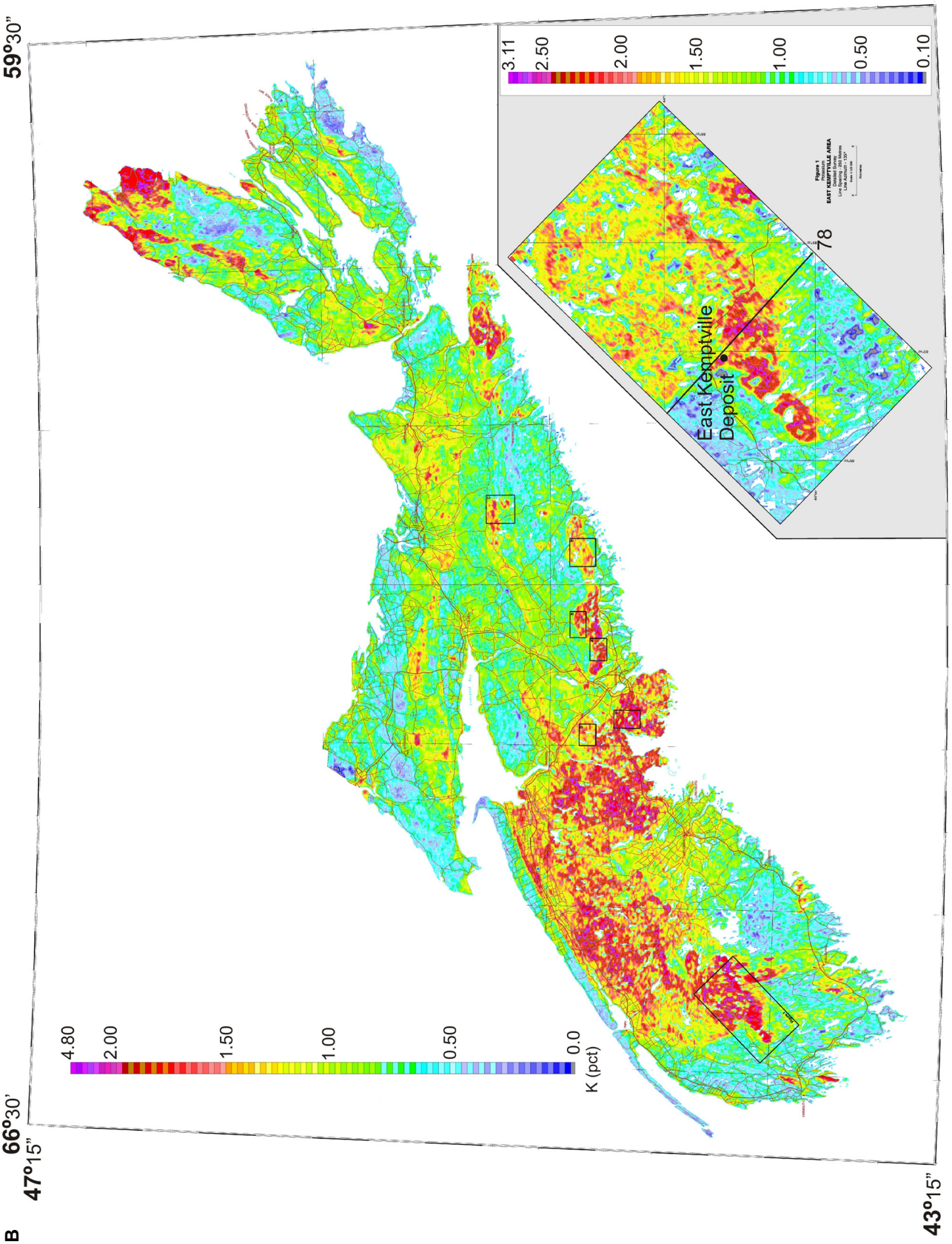

Figure 4-17. (B) Radioactivity maps of potassium (pct = percent) for the Province of Nova Scotia (large map) and the East Kemptville area (inset).

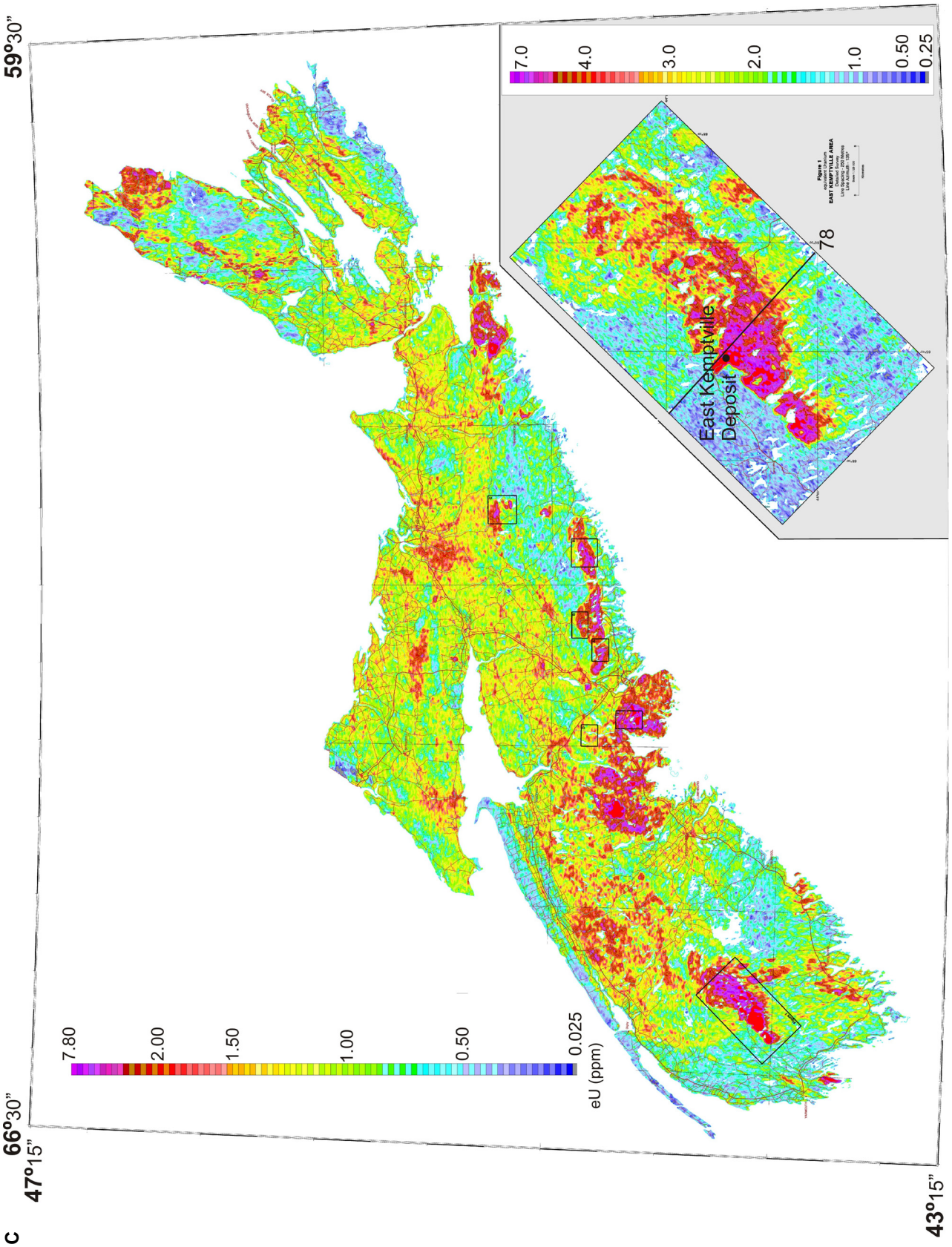

Figure 4-17 continued. (C) Radioactivity map of equivalent uranium (ppm) for the Province of Nova Scotia (large map) and the East Kemptville area (inset).

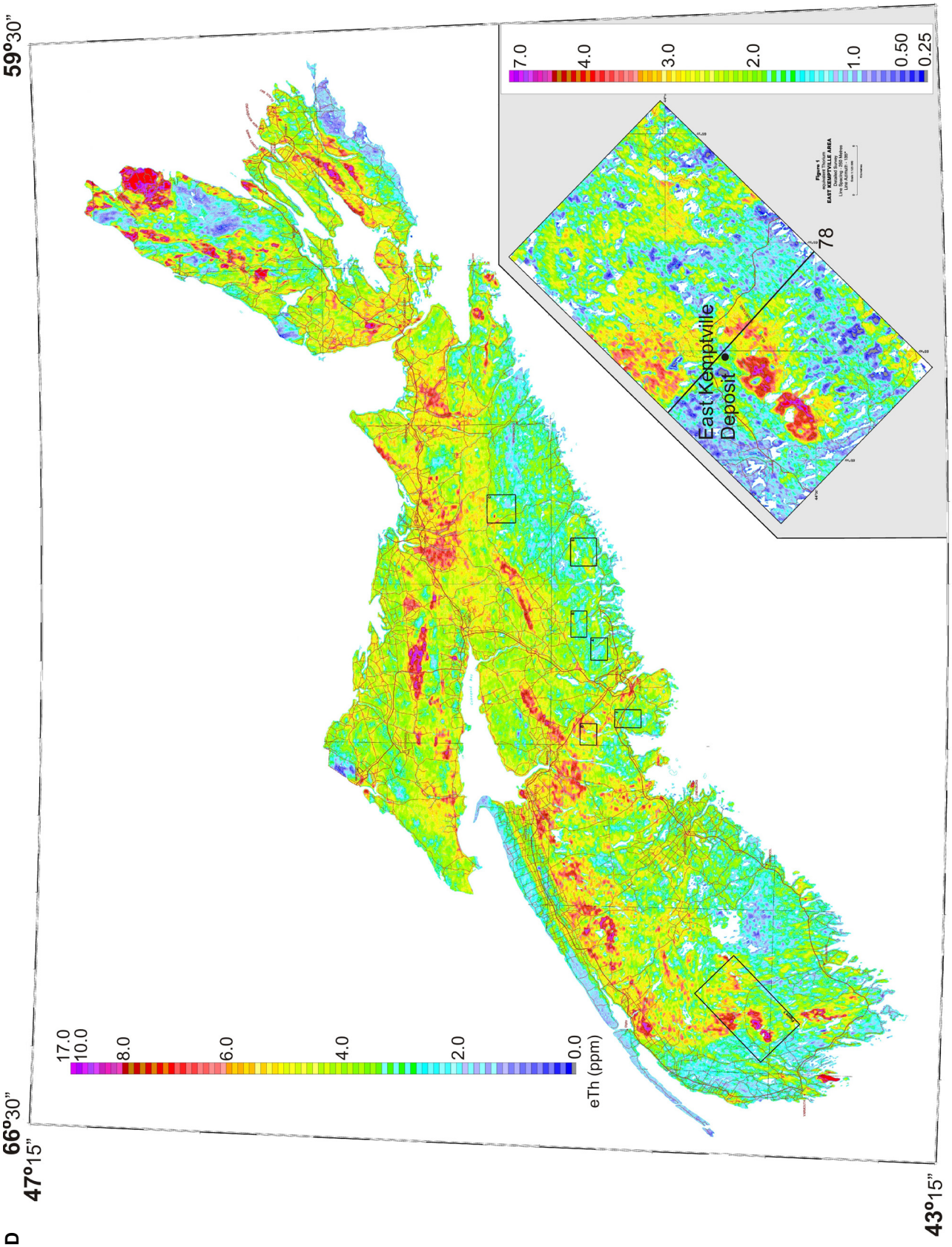

Figure 4-17 continued. (D) Radioactivity map of equivalent thorium (ppm) for the Province of Nova Scotia (large map) and the East Kemptville area (inset).

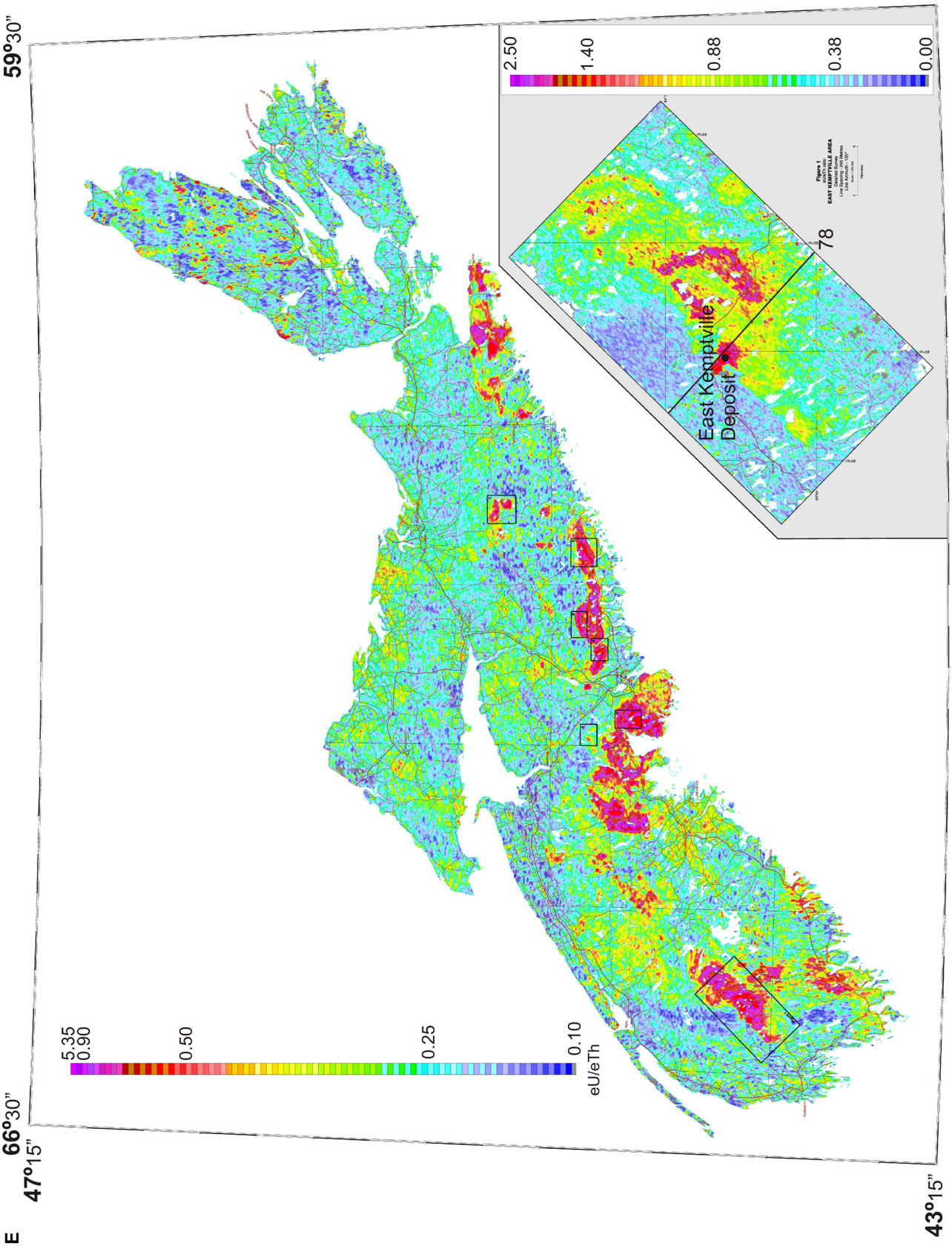

Figure 4-17 continued. (E) Radioactivity map of the equivalent uranium/equivalent thorium ratio for the Province of Nova Scotia (large map) and the East Kemptville area (inset).

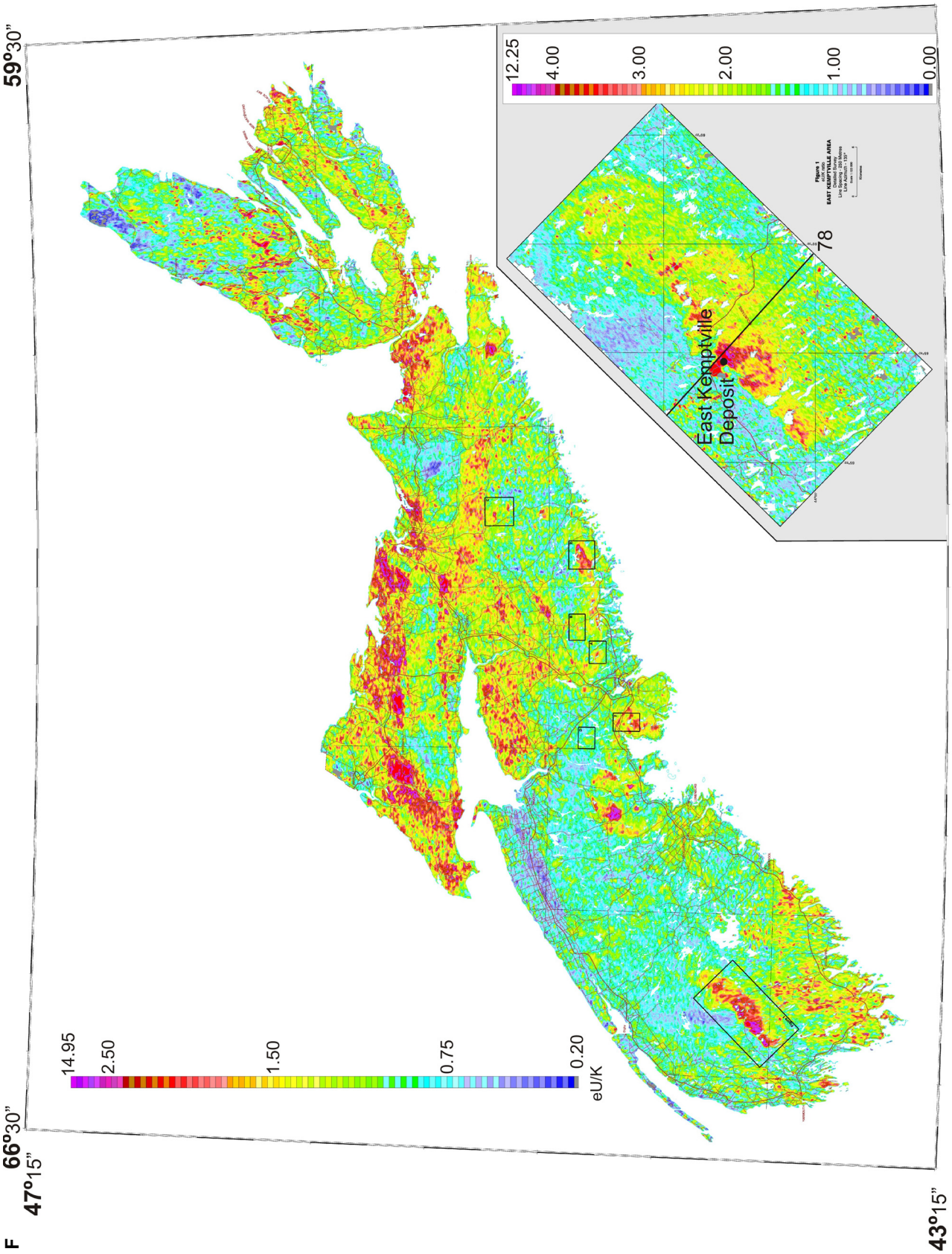

Figure 4-17 continued. (F) Radioactivity map of equivalent uranium/potassium ratio for the Province of Nova Scotia (large map) and for the East Kemptville area (inset).

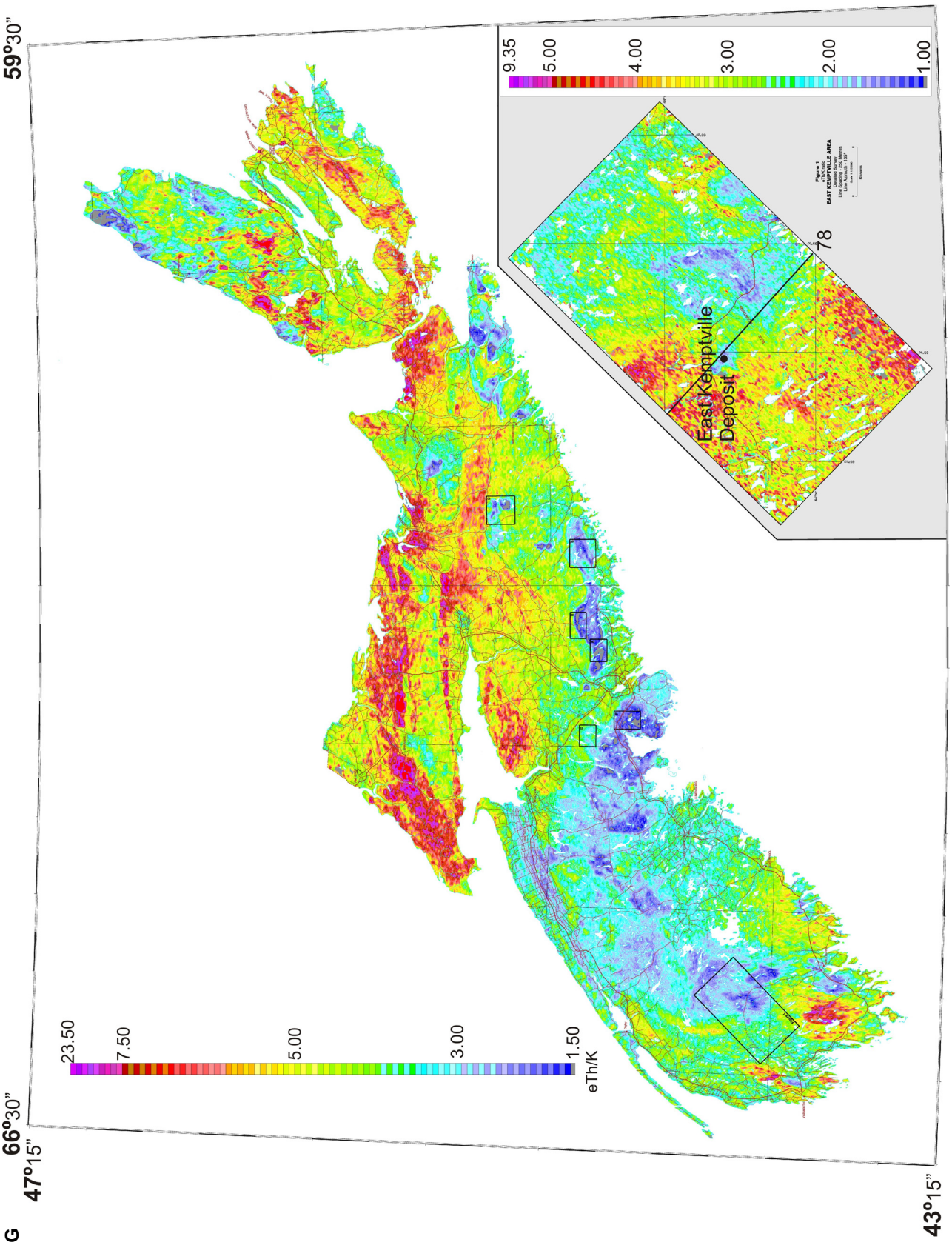

Figure 4-17 continued. (G) Radioactivity map of the equivalent thorium/potassium ratio (eTh/K) for the Province of Nova Scotia (large map) and for the East Kemptville area (inset).

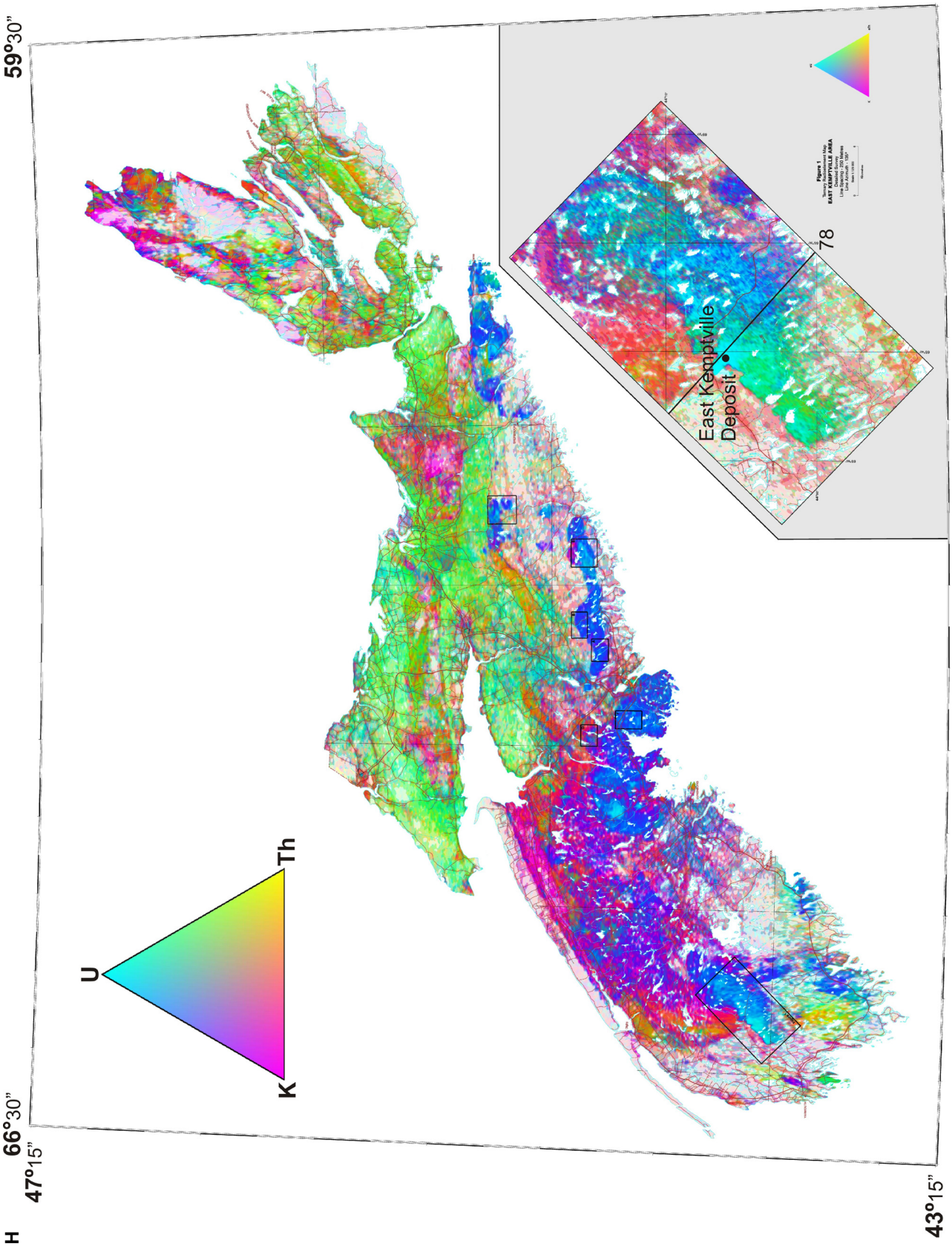

Figure 4-17 continued. (H) Ternary radioelement map for the Province of Nova Scotia (large map) and for the East Kemptville area (inset).

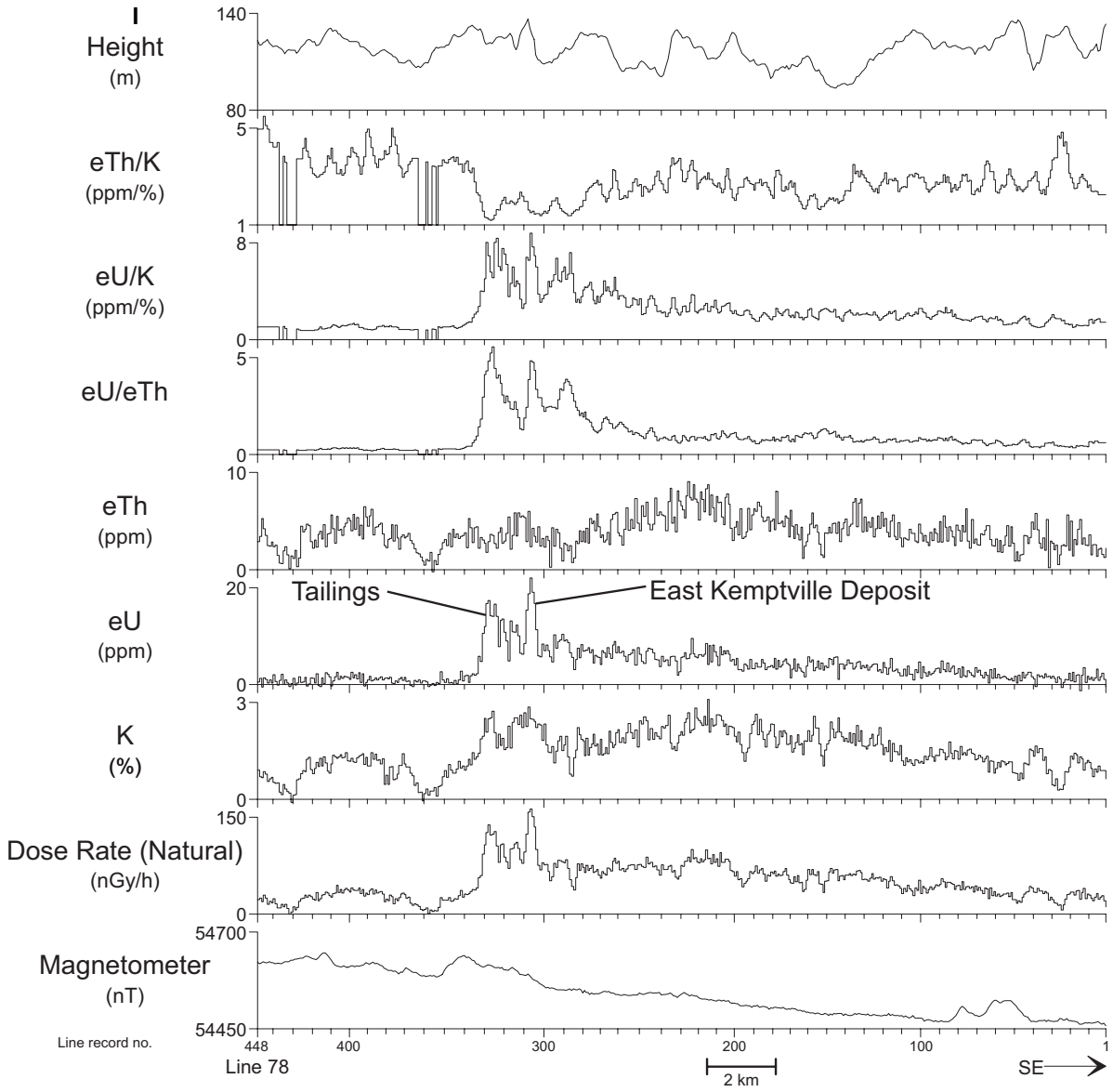

Figure 4-17 continued. (I) Multivariable stacked profile from a detailed, 250 m line spaced, airborne gamma-ray spectrometry survey over the East Kemptville tin deposit, southwestern Nova Scotia. Note the high eU and eU/eTh ratio signature associated with the tin deposit and the Davis Lake pluton. Also note the progressive decrease of eU levels and increase of eTh levels in the down-ice dispersal direction (left to right) away from the deposit anomaly. The location of flight line 78 is shown on the inset maps of Figure 4-17A-G.

able stacked-profile display is an essential tool for the visual analysis of all variables at each sample point. A stacked-profile presentation format permits the viewing of point-to-point data for all variables (measured and derived). Gridding airborne gamma- ray spectrometry data, particularly if the data was collected with a coarse flight line spacing, requires a significant amount of interpolation, which will result in the loss of some detailed point-to-point information. Viewing of the point-to-point or line data in a stacked-profile format requires only a minimum amount of along-line filtering, thereby preserving more of the detailed point-to-point information. Examples of multivariable stacked profiles are shown in Figure 4-16I and 4-17I.

Examples of Standard Airborne Gamma-Ray Spectrometry Products

Quoich River – Melville Peninsula, Nunavut

Figure 4-16A to 4-16H shows a set of standard AGRS maps and image products for the Quoich River area, Nunavut: Figure 4-16A – Natural Air Absorbed Dose Rate (NADR); Figure 4-16B – potassium (K); Figure 4-16C – equivalent uranium (eU); Figure 4-16D – equivalent thorium (eTh); Figure 4-16E – equivalent uranium/equivalent thorium ratio (eU/eTh); Figure 4-16F – equivalent uranium/potassium ratio (eU/K); Figure 4-16G – equivalent thorium/potassium ratio (eTh/K); and Figure 4-16H – ternary radioelement map. These maps were compiled from 5000 m line

spaced AGRS data (Holman et al., 2001). The location of the Melville Peninsula study area is outlined and the location of two flight lines (405 and 423), whose data are presented as multivariable stacked profiles (Fig. 4-16I,J) to illustrate the higher level of point-to-point detail, are also presented. These maps represent a standard package of maps required for the complete display of all measured and derived products.

The bedrock geology of the southern Melville Peninsula is dominated by a variety of Archean gneisses and schists. The younger, Paleoproterozoic Penrhyn Group forms northeast-trending synclines and anticlines and consists of metasedimentary rocks, including quartzite and marble. Numerous aplitic to pegmatitic sills and plutons intrude the Penrhyn Group rocks. Many of these younger intrusive rocks are anomalously radioactive (Delpierre, 1982) and can be clearly identified by elevated levels in eU (Fig. 4-16C) and eU/eTh (Fig. 4-16E), and by blue shades on the ternary radioelement map (Fig. 4-16H), which represent a relative increase of U with respect to K and Th. These signatures are clearly illustrated on the two multivariable stacked profiles (Figs. 4-16I,J).

Towards the southwest corner of the Quoich River area, north and east of Baker Lake, the regional AGRS patterns show a prominent, generally northwest-southeast-trending feature that crosscuts or truncates the main northeast-southwest regional structural and lithological trends. This feature is characterized by generally lower radioactive element and ratio signatures and is particularly prominent on the eU, eU/eTh, and eU/K maps. A regional till sampling and geochemical study (Dredge et al., 2005) straddled the northeast edge of this low-radioactivity feature west of Wager Bay. This study documented a distinct break in the ICP and INAA elemental distribution patterns that coincided with the northeast edge of this feature. Dredge et al. (2005) also noted that the low AGRS signatures were coincident with an area dominated by meltwater erosion and deposition features.

Nova Scotia

Figure 4-17A to 4-17H shows a set of standard AGRS maps and images for the Province of Nova Scotia: Figure 4-17A – Natural Air Absorbed Dose Rate (NADR); Figure 4-17B – potassium (K); Figure 4-17C – equivalent uranium (eU); Figure 4-17D – equivalent thorium (eTh); Figure 4-17E – equivalent uranium/equivalent thorium ratio (eU/eTh); Figure 4-17F – equivalent uranium/potassium ratio (eU/K); Figure 4-17G – equivalent thorium/potassium ratio (eTh/K); and Figure 4-17H – ternary radioelement map. These maps were compiled from 1000 m line spaced AGRS data (Carson et al., 2003). The inset maps show AGRS data collected with flight lines spaced 250 m apart for the

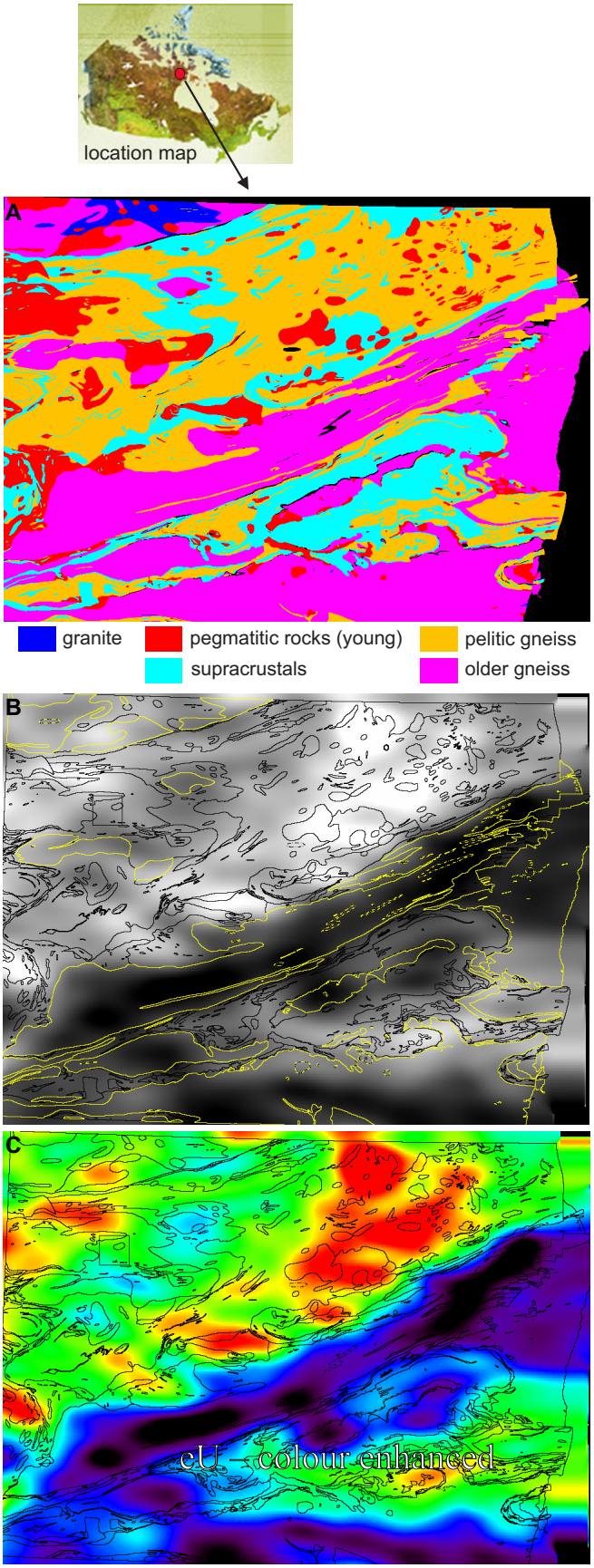

Figure 4-18. Visualizations of gamma-ray spectrometer data over the Melville Peninsula, Nunavut. **(A)** Mapped geology (Henderson, 1987). **(B)** Black and white map of eU (ppm). **(C)** Colour map of eU (ppm).

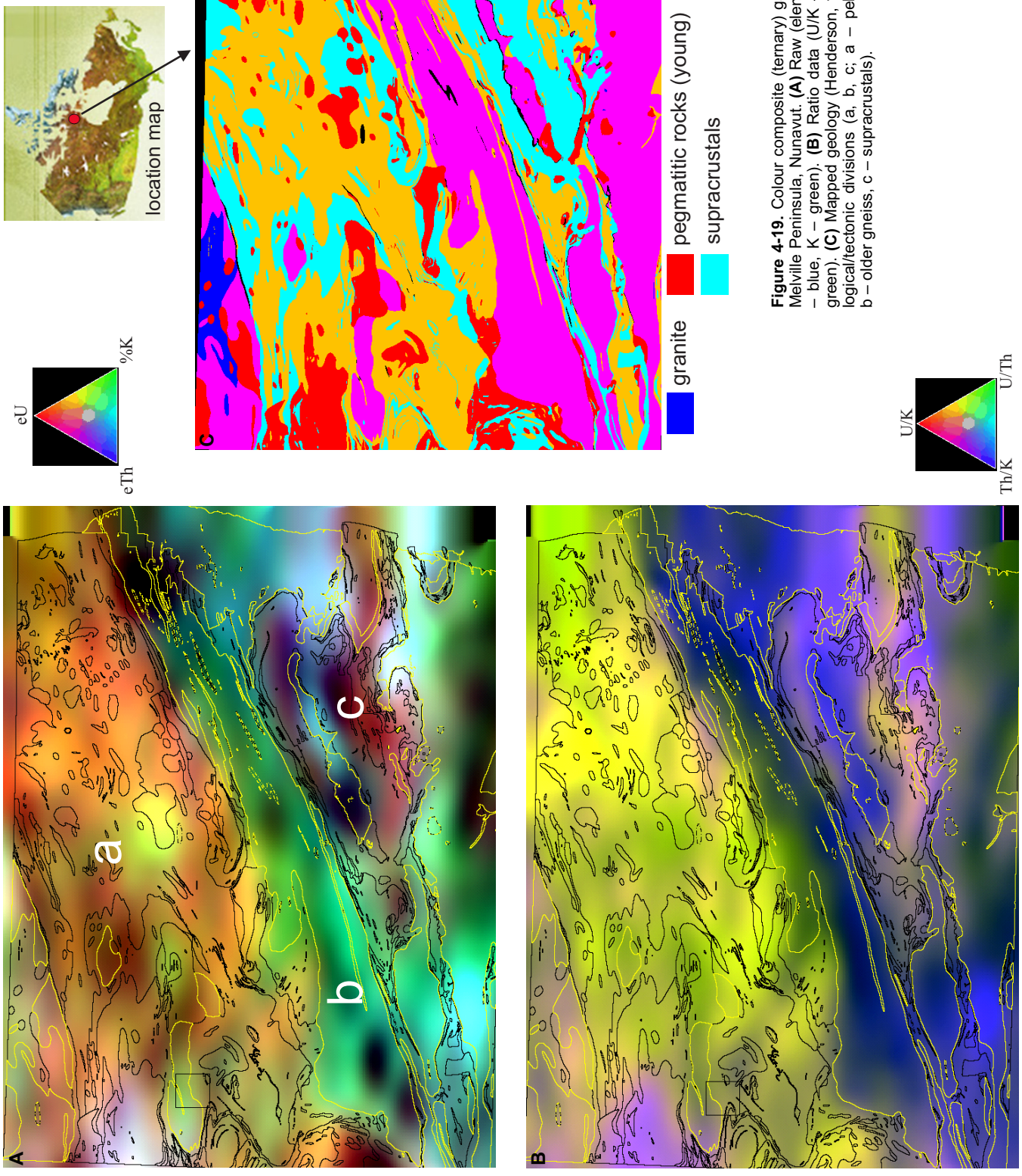

Figure 4-19. Colour composite (ternary) gamma-ray images over the Melville Peninsula, Nunavut. **(A)** Raw (elemental) data (eU – red, eTh – blue, K – green). **(B)** Ratio data (U/K – red, Th/K– blue, U/Th – green). **(C)** Mapped geology (Henderson, 1987). Note the major geological/tectonic divisions (a, b, c; a – pelitic gneiss and pegmatite, b – older gneiss, c – supracrustals).

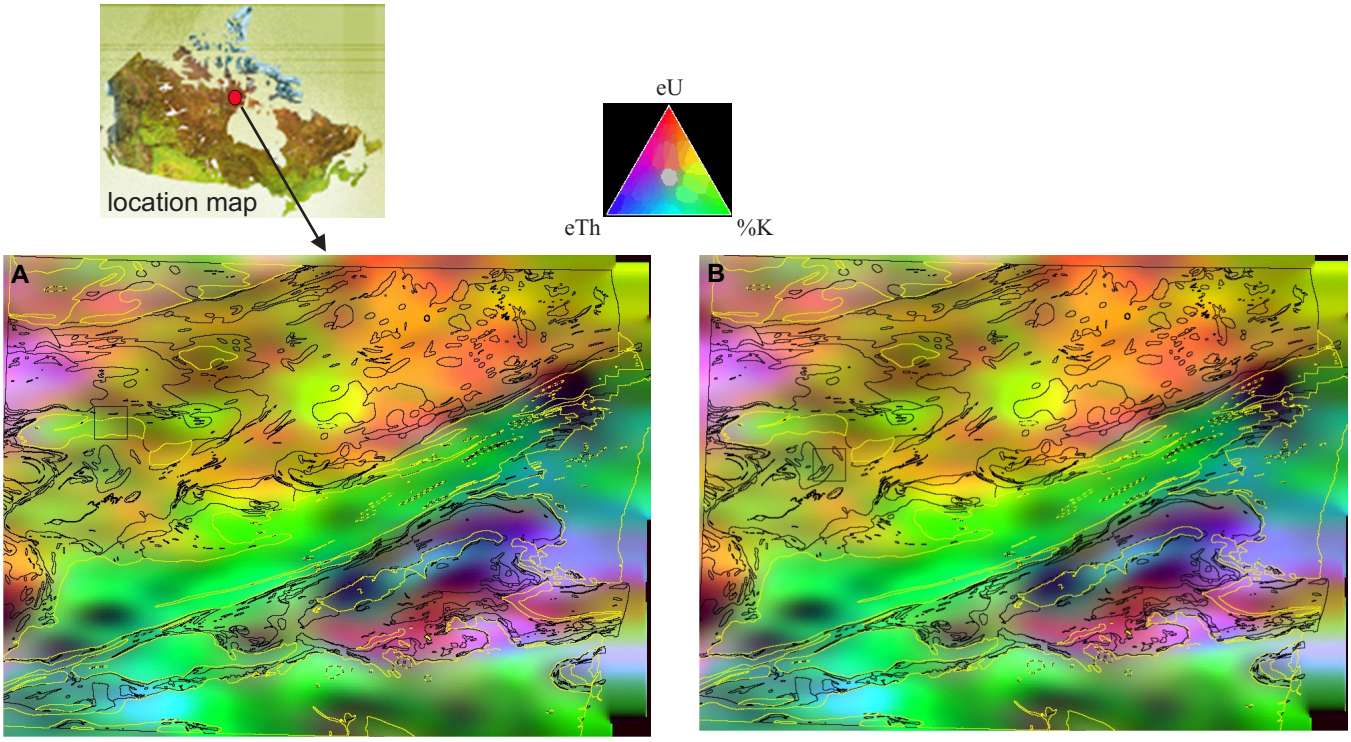

Figure 4-20. Colour composite (ternary) gamma-ray images over the Melville Peninsula, Nunavut (eU – red, eTh – blue, K – green). **(A)** Decorrelation stretch and **(B)** saturation stretch. The decorrelation stretch takes the raw or elemental data, transforms the data using the principal component analysis (PCA) transform, stretches the histogram of each component image, and then applies an inverse PCA transform recreating stretched versions of the data, which are then displayed through colours red-green-blue. The saturation stretch takes the raw or elemental data and transforms them to intensity-hue-saturation colour coordinates, stretches the saturation image, and then transforms the data back to red-green-blue coordinates.

area around the East Kemptville tin deposit. The location of the flight line (Fig. 4-17I) over the East Kemptville tin deposit is also presented.

A strong eU/eTh ratio anomaly is coincident with the Davis Lake Pluton, which hosts the East Kemptville tin deposit. Follow-up investigations (Ford and O'Reilly, 1985; Ford, 1993) in the East Kemptville area and elsewhere in Nova Scotia confirm direct correlations between the high eU/eTh values, as measured by the airborne surveys, and the most evolved phases of these composite granitic intrusions. These more evolved phases, characterized by unusually high eU/eTh ratios, also exhibit elemental variations that suggest varying degrees of late- and/or post-magmatic metasomatism and hydrothermal alteration. High eU/eTh ratio signatures elsewhere suggest that these more evolved phases are more extensive than previously recognized.

The common association of granophile-element mineralization with areas of pervasive alteration and anomalous radioactive element signatures has important applications for mineral exploration.

In addition to mineral exploration applications, the East Kemptville detailed survey illustrates important surficial mapping applications. Sharp increases in eU and eTh along the northwest contact of the Davis Lake Pluton with metasediments of the Meguma Group, southwest of the East Kemptville tin deposit, are coincident with an abrupt change between Meguma-derived tills to the northwest and granite-derived tills to the southeast. Along the southeast contact, however, radioactive element patterns are more diffuse, reflecting dispersion of granite-derived till southeastward over the Meguma Group bedrock for up to 5 km. In this case, the diminishing down-ice radioactive element values southeast from the contact relate to diminishing down-ice concentrations of granite-derived clasts and matrix material.

Data Visualization

Single Band

Gamma-ray data can be presented as profiles (Figs. 4-16I,J, 4-17I), as gridded black and white images or as coloured images (Fig. 4-18). Gamma-ray data usually vary over a narrow range of values compared with other geophysical data, such as total magnetic field data. The data can be displayed as an image in concentration units or contrast stretched to a byte format. The advantage of colour images is that the human eye can distinguish a much larger range of colours compared to black and white tones.

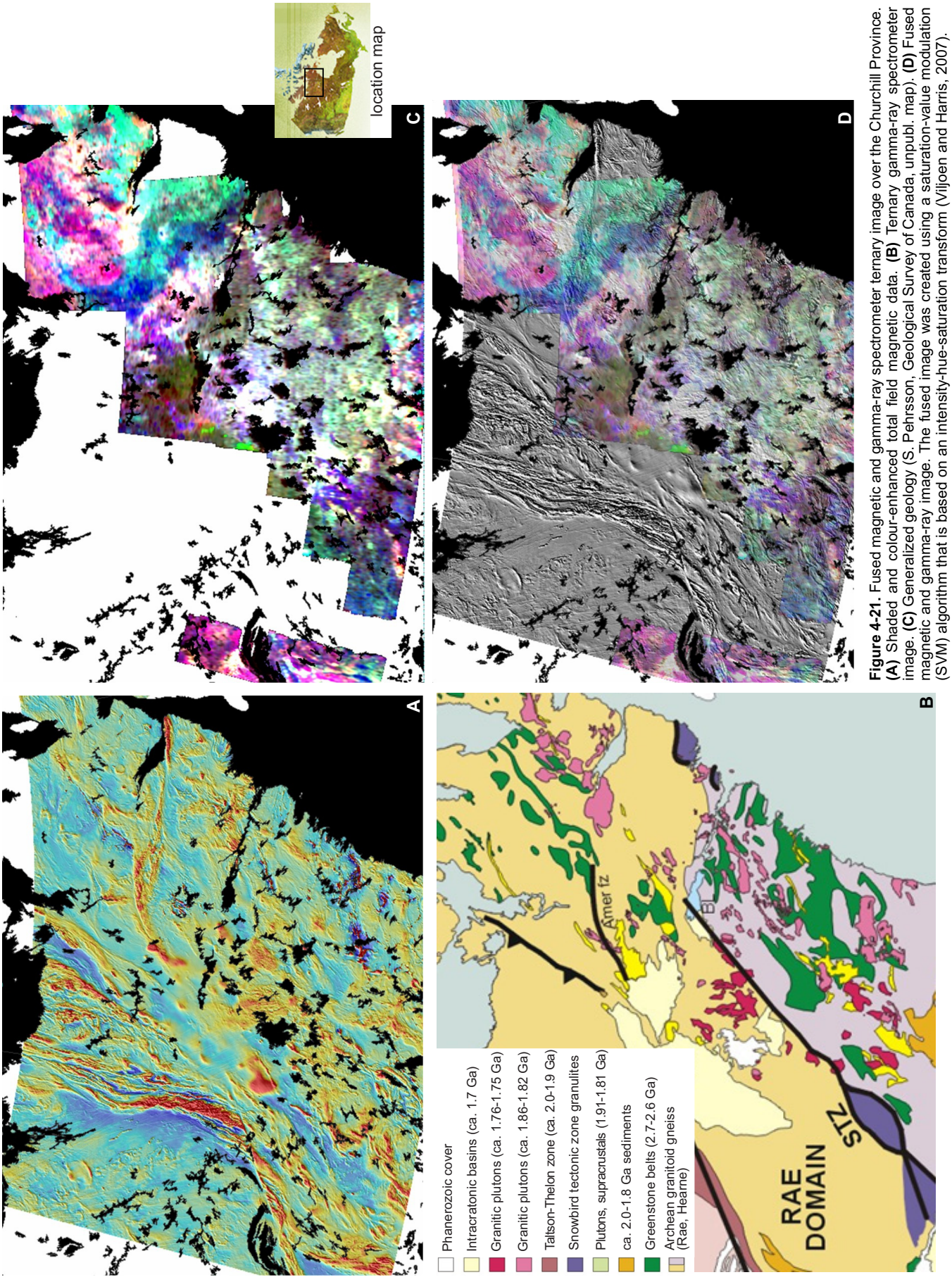

Figure 4-21. Fused magnetic and gamma-ray spectrometer ternary image over the Churchill Province. **(A)** Shaded and colour-enhanced total field magnetic data. **(B)** Ternary gamma-ray spectrometer image. **(C)** Generalized geology (S. Pehrsson, Geological Survey of Canada, unpubl. map). **(D)** Fused magnetic and gamma-ray image. The fused image was created using a saturation-value modulation (SVM) algorithm that is based on an intensity-hue-saturation transform (Viljoen and Harris, 2007).

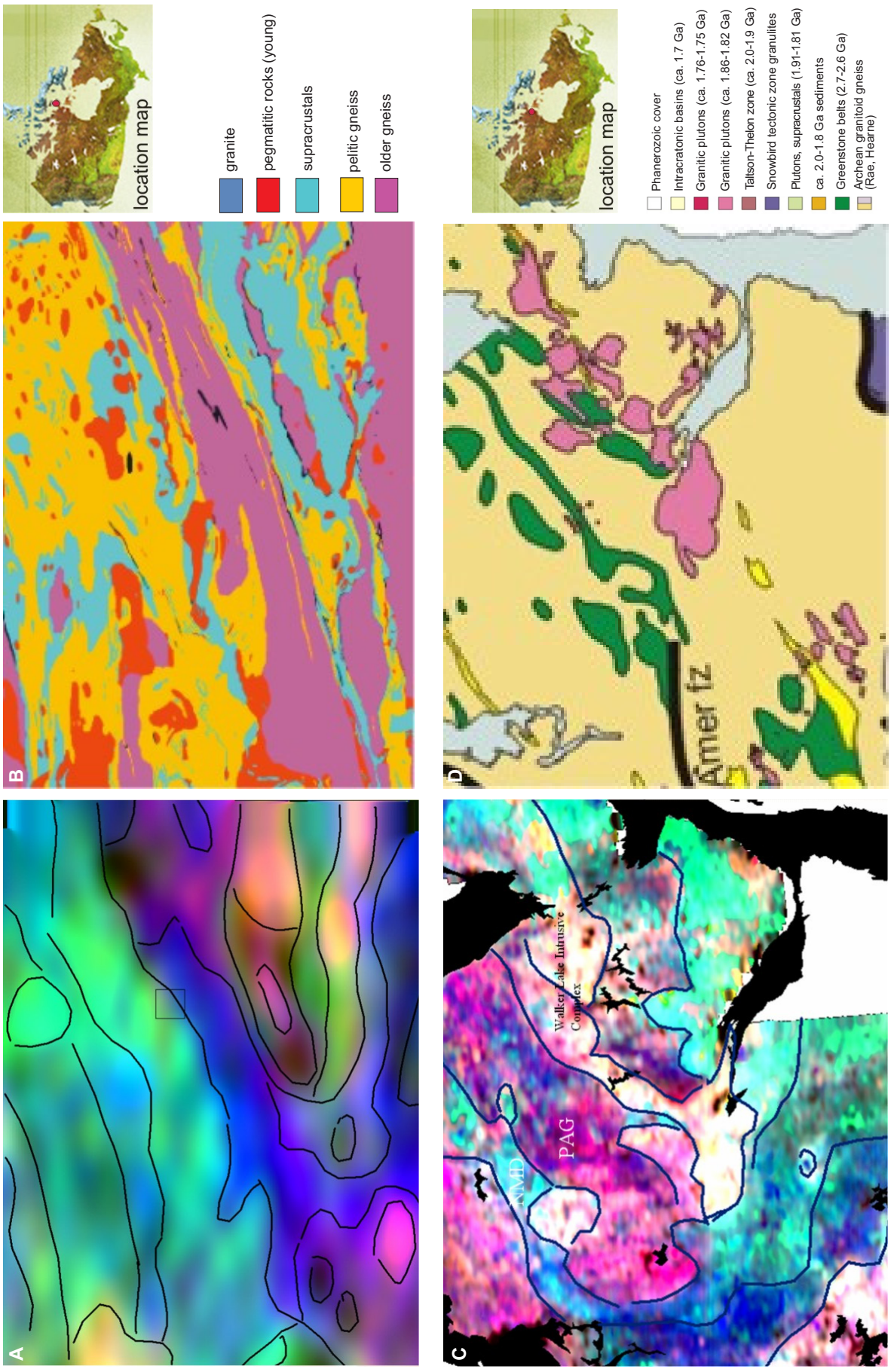

Figure 4-22. Geological interpretations of gamma-ray spectrometer data. **(A)** Ternary image over the Melville Peninsula, Nunavut and interpretations of radioelement domains that are similar to the mapped lithology. **(B)** Mapped geology (Henderson, 1987). **(C)** Ternary gamma-ray image of a portion of the Churchill Province and associated interpretation of radioelement domains that reflect small-scale compositional and metamorphic domains (Rob Berman, oral comm., 2007). **(D)** Geological map of the same area as shown in (B) (S. Pehrsson, Geological Survey of Canada, unpubl. map).

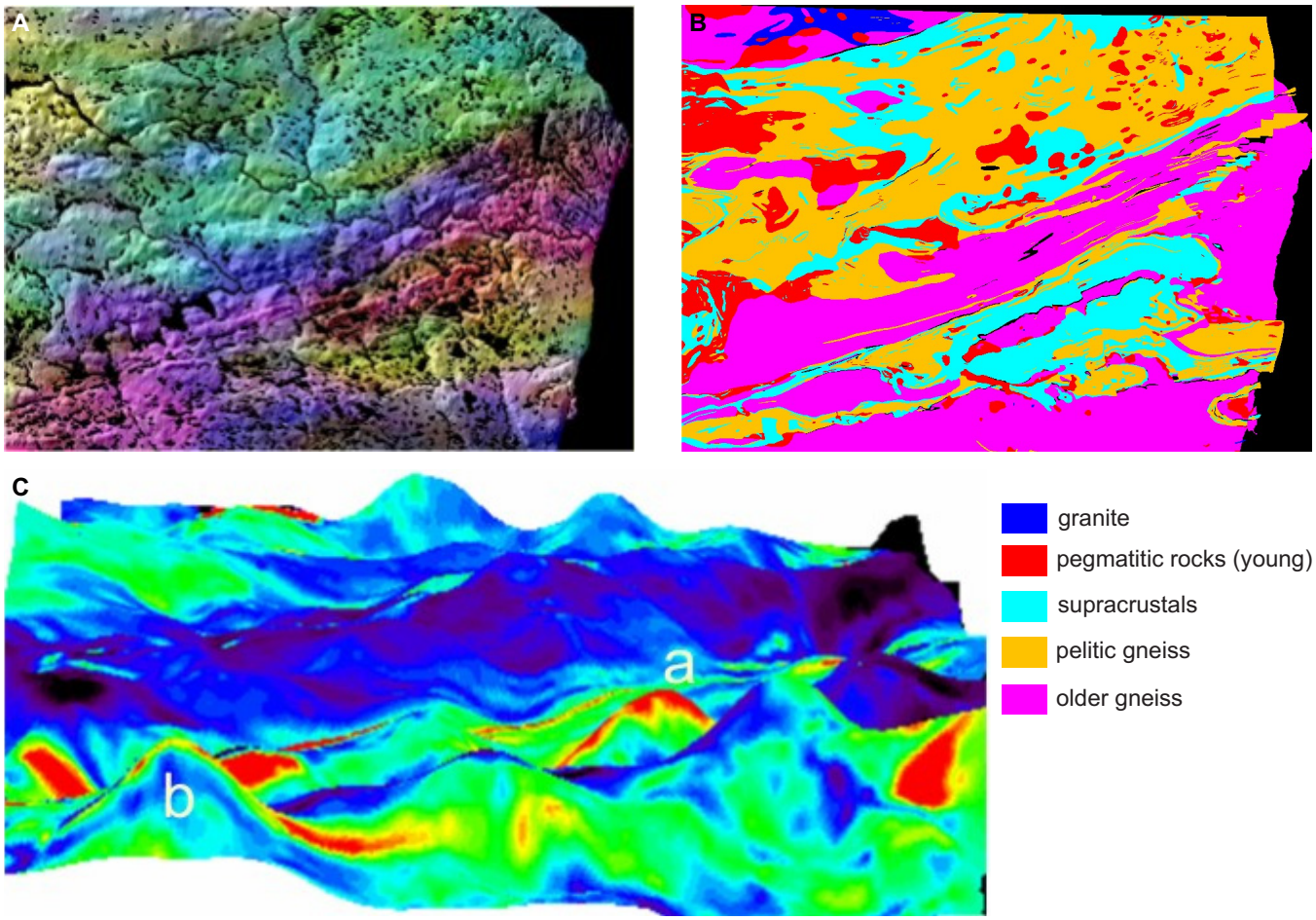

Figure 4-23. An example of fused gamma-ray imagery over the Melville Peninsula, Nunavut (see Fig. 4-22 for location). **(A)** Digital Elevation Model (DEM) fused with gamma-ray ternary image showing topographic patterns that can be directly related to the radioelement response. **(B)** Mapped geology (Henderson, 1987). **(C)** 2.5-D visualization of magnetic data provides 'topographic relief' with eU gamma-ray spectrometer data providing the colour. Areas labelled a and b indicate areas of correlation between magnetic and eU data.

Multiband

Like optical LANDSAT and/or multibeam radar data, gamma-ray channels (bands) can be displayed as ternary colour composite images (Figs. 4-16H, 4-17G, 4-19), allowing for the interpretation of three channels of data (raw (elemental) or ratio) using an additive mix of the primary colours (red-green-blue) of the computer display system.

Enhancement

Similar to any raster-based data set, the data can be contrast stretched to improve the dynamic range of the data. A decorrelation and/or saturation stretch (Gillespie et al., 1986), often applied to improve the colour range of LANDSAT data, can also be applied to gamma-ray data using most image analysis systems (Fig. 4-20). These stretches are more than simple arithmetic transforms that utilize simple mathematical functions (linear, square root, etc.) to transform the data. They involve either a multivariate statistical transform of the data (decorrelation stretch) or a colour-space transform (saturation stretch). In both cases the goal is the same, to provide an enhanced image in which potential geological features are enhanced though a wide range of hues.

Fusion

Like optical and microwave data, gamma-ray data may be fused with other data creating images that offer complimentary information from the combined data sets in one image. A fusion of gamma-ray and magnetic data (Fig. 4-21) often provides an image in which many geological features can be identified including geological and/or tectonic domains (Fig. 4-22A), faults, lineaments, plutons (Figs. 4-8, 4-17), various rock units, and, in some cases, metamorphic domains (Fig. 4-22C).

Gamma-ray data can also be fused with topographic data creating an image in which potential gamma-ray anomalies can be directly compared to topographic patterns (Fig. 4-23A). This can be applied to help determine the source of gamma-ray anomalies. Gamma-ray image data can also be fused with other geophysical variables, such as total magnetic field data (Fig. 4-23C)

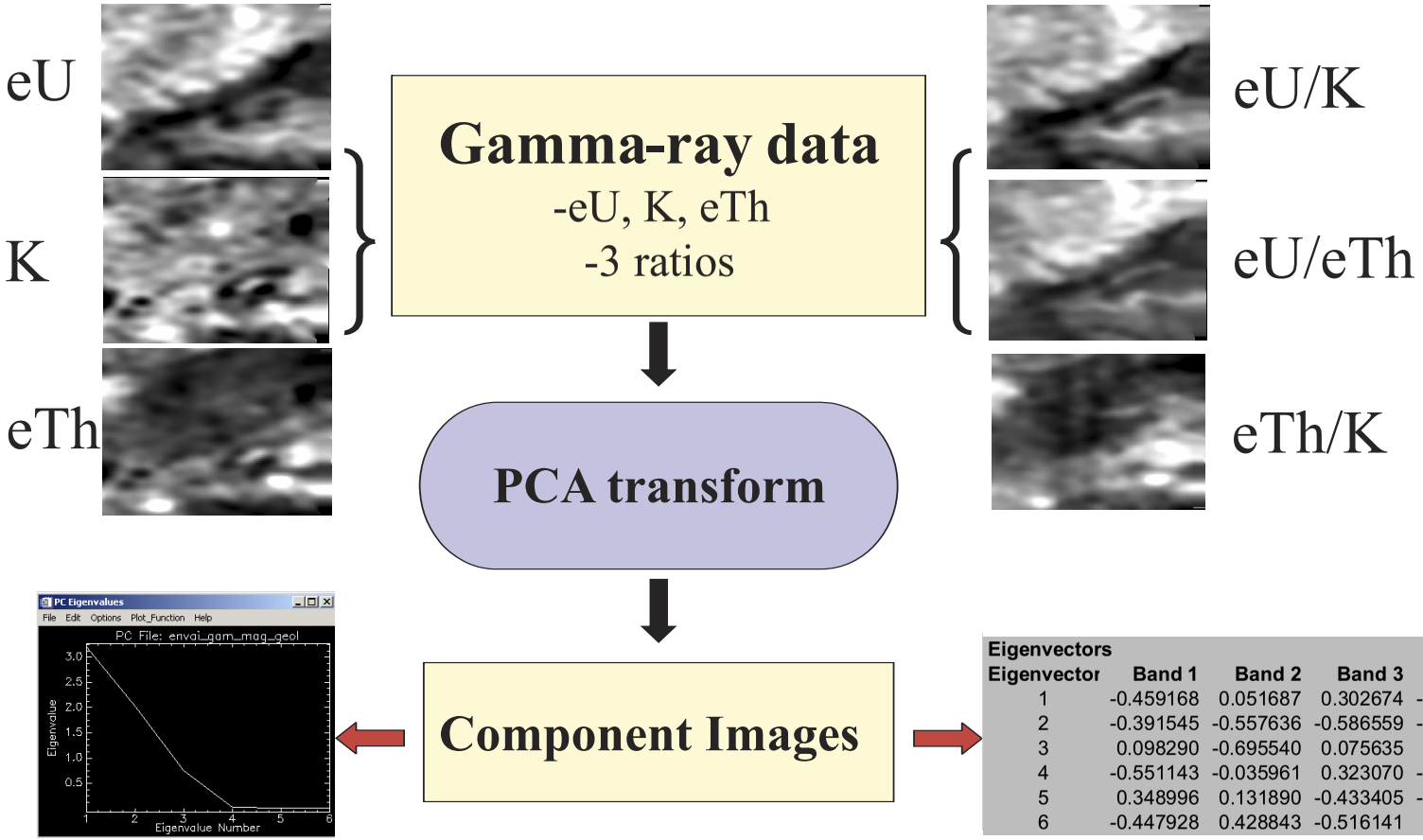

Eigenvectors

Eigenvector	Band 1	Band 2	Band 3	Band 4	Band 5	Band 6
1	-0.459168	0.051687	0.302674	-0.502126	-0.552439	0.370894
2	-0.391545	-0.557636	-0.586559	-0.235042	-0.077008	-0.361259
3	0.098290	-0.695540	0.075635	0.324585	0.021609	0.628506
4	-0.551143	-0.035961	0.323070	-0.111571	0.759344	0.039028
5	0.348996	0.131890	-0.433405	-0.604325	0.332324	0.444206
6	-0.447928	0.428843	-0.516141	0.457835	-0.037034	0.371575

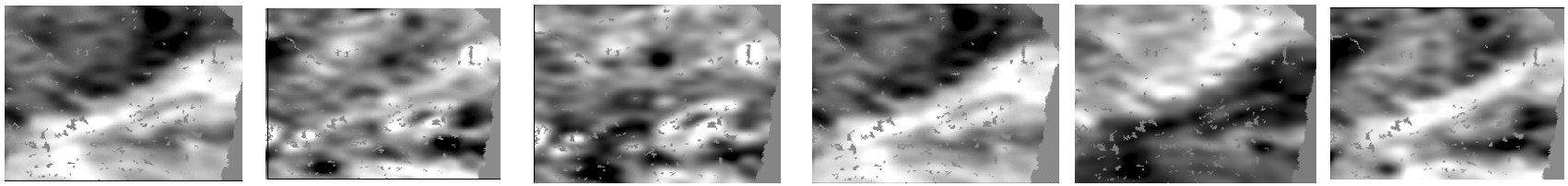

PCA 1 +ve K, Th | PCA2 +ve U | PCA3 +ve Th, -ve K | PCA4 -ve UK | PCA5 +ve UK, +ve TK | PCA6 +ve TK, -ve UK

Figure 4-24. A description of the Principal Component Transform (PCA). This example shows PCA applied to gamma-ray data over the Melville Peninsula, Nunavut (see Fig. 4-22 for location). Raw (elemental) data (eU, eTh, K) and ratio data are transformed using PCA creating component images (PCA1 to 6), which are linear combinations of the input data. The first few component images contain most of the information (variance) of the data set (see the table of eigenvalues). The individual contribution of each input band (i.e. eU, eTh, K, and ratios) can be obtained from a table of eigenvectors (component loadings).

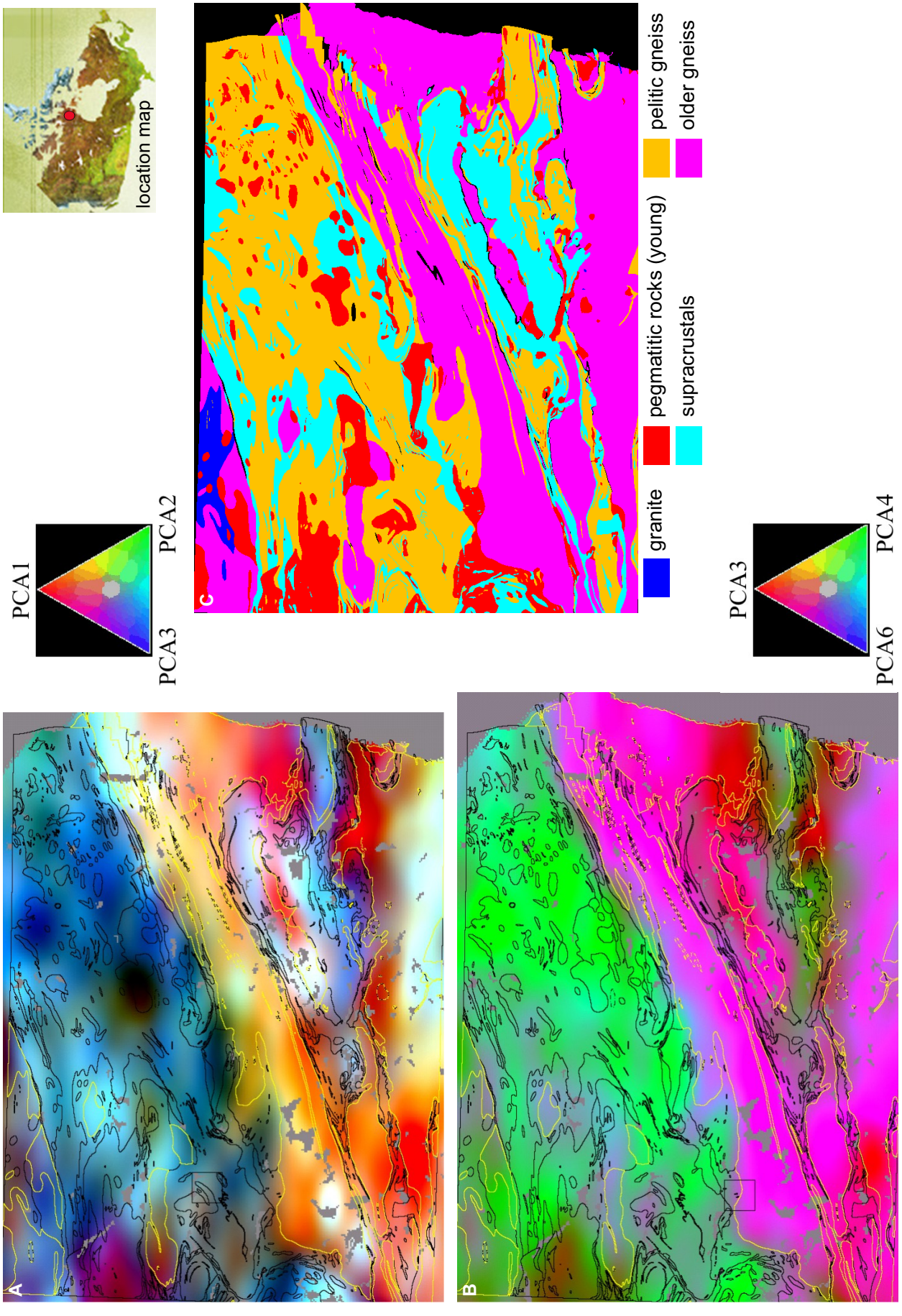

Figure 4-25. Ternary gamma-ray images of PCA component images from the Melville Peninsula, Nunavut. **(A)** PCA 1, 2, 3 (red, green, blue), **(B)** PCA 3, 4, 6 (red, green, blue), **(C)** Generalized geology (Henderson, 1987). The ternary images comprising the PCA component images provide good enhancement of major geological/tectonic units (compare with the geological map shown in C).

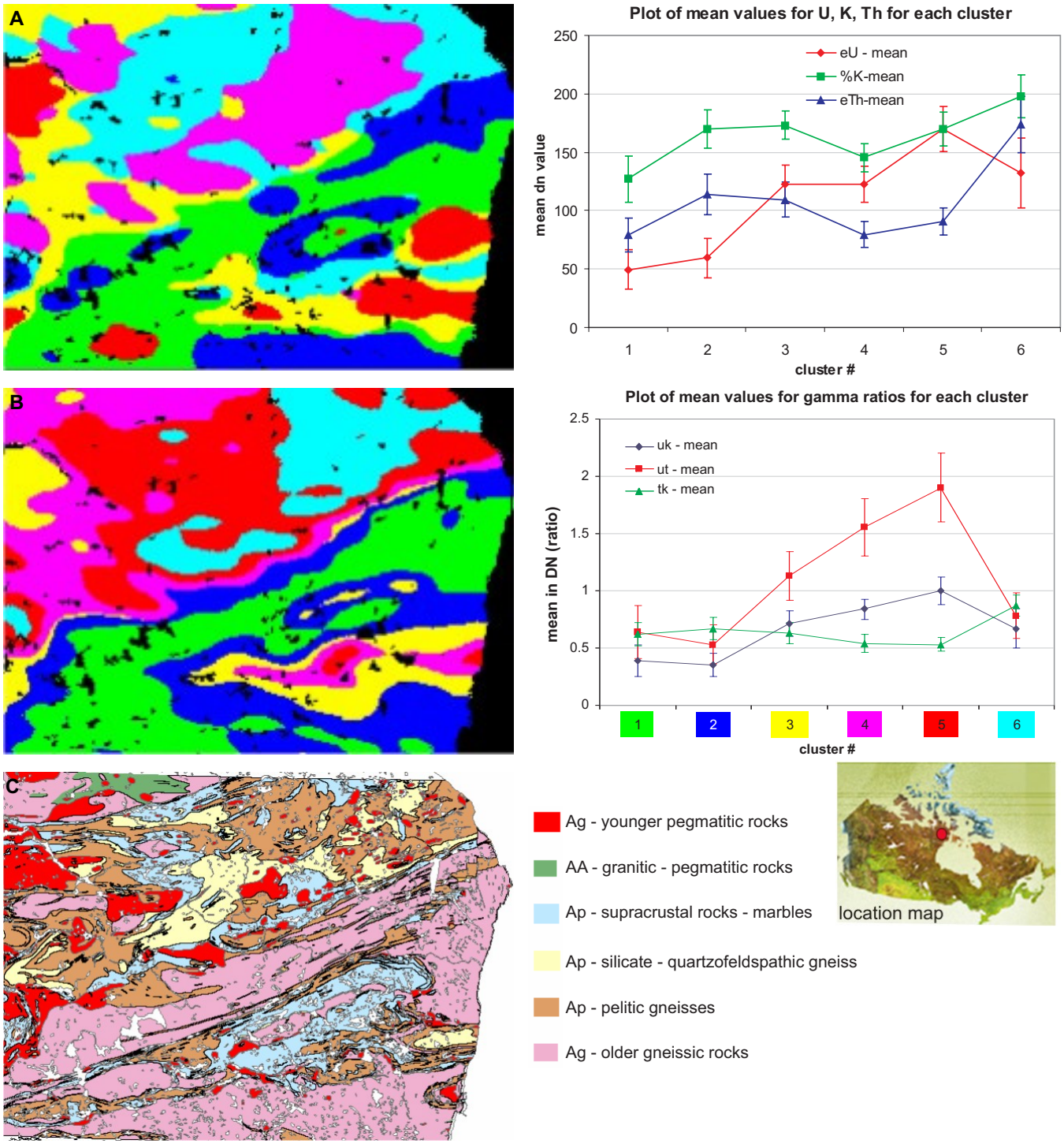

Figure 4-26. Unsupervised classification of gamma-ray data over the Melville Peninsula, Nunavut showing automatically generated radioelement domains. **(A)** Classification (prediction) map of radioelement domains derived from eU, eTh, and K. **(B)** Classification (prediction) map of radioelement domains derived from ratio data (eU/eTh, eU/K, eTh/K). **(C)** Mapped geology (Henderson, 1987). The classification maps, which show radioelement domains (i.e. areas that display similar gamma-ray response – see associated plots of gamma-ray response for each cluster (radioelement domain)), show a good correspondence to the mapped geology but also show areas that, based on radioelement response, differ from the mapped geology. These areas warrant checking in the field.

.

or other gamma-ray images; for example, eTh/K on K may potentially illustrate the location of potassium alteration zones.

2.5 Dimensional Visualizations

Different perspective views (2.5-D) can be employed to not only fuse different data types but also to effectively visualize the relationships (both spatial and signature response) between them. Figure 4-23C shows a

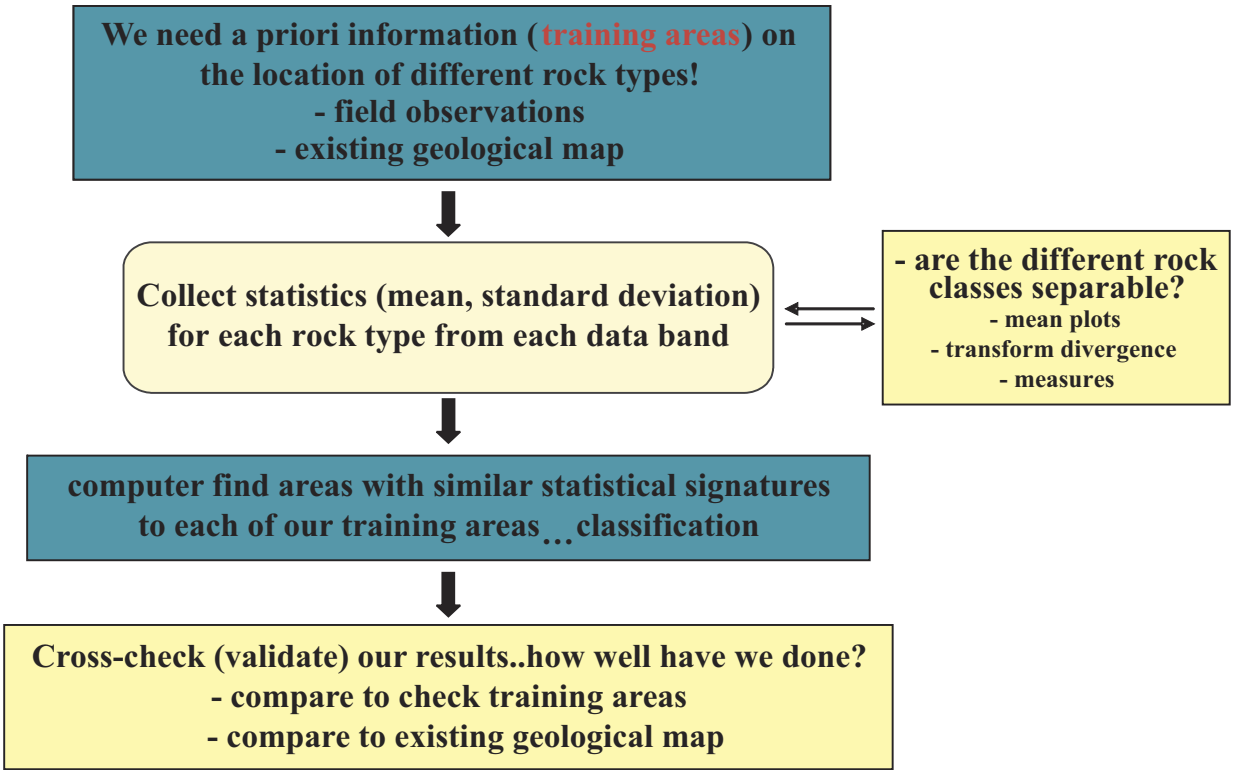

Figure 4-27. A supervised classification process involves collecting representative statistics for each image to be classified (eU, eTh, K, etc.) for each rock type. These are referred to as "training areas". Statistical measures (i.e. transformed divergence) are then calculated to determine whether the training areas are statistically separable. If they are, then a classification algorithm (maximum likelihood, neural networks, etc.) is selected to classify the entire image from all or a selected set of input bands using the statistics derived from the training areas. This produces a classification (or prediction) map that can be validated using cross-correlation measures (i.e. the classification is compared to a check training site or the geological map itself).

2.5-D perspective image in which the relief reflects the magnetic total field and the colour reflects eU response over the Melville Peninsula, Nunavut. Correlations between the two data types can be seen over the supracrustal rocks (labelled a and b on Fig. 4-23C).

Computer-Assisted Analysis

Gamma-ray data often comprises 7 channels of data, as mentioned above, thus multivariate processing techniques can be applied to the data both for enhancement and classification purposes.

Principle Component Analysis

The principal component analysis (PCA) transform can be applied to make a reduced data set comprising a series of component images that are a linear combination of all the gamma data. Individually these component images often reveal geological information (Fig. 4-24) but when combined in colour ternary images (Fig. 4-25) geological features are often enhanced by variations in colour.

Classification

The computer can be used to enhance gamma-ray data to create images for visual interpretation, as discussed above. However, the same classification techniques applied to LANDSAT and radar data can also be applied to gamma-ray data to create predictive maps automatically or semi-automatically.

Unsupervised

Various combinations of the gamma-ray data channels can be classified using an unsupervised classification algorithm to produce a thematic map of radioelement domains (classes) that show a distinct statistical separation (Fig. 4-26). The advantage of this approach is that it requires little input by the geologist other than specifying the number of classes. In many cases, this type of predictive map reveals patterns that can be directly related to lithological variations (Fig. 4-26).

Supervised

Supervised classification (Fig. 4-27) involves the use of training area data (from the GRS data) that is representative of each rock type to be classified. These signatures are then used to classify the image into classes that have similar statistics to the training areas (Fig. 4-27). The results of a supervised classification (maximum likelihood) of major tectonic divisions over the Melville Peninsula, Nunavut using a number of combinations of gamma-ray channels, as well as total field magnetic data, is presented in Figure 4-28. Using all GRS chan-

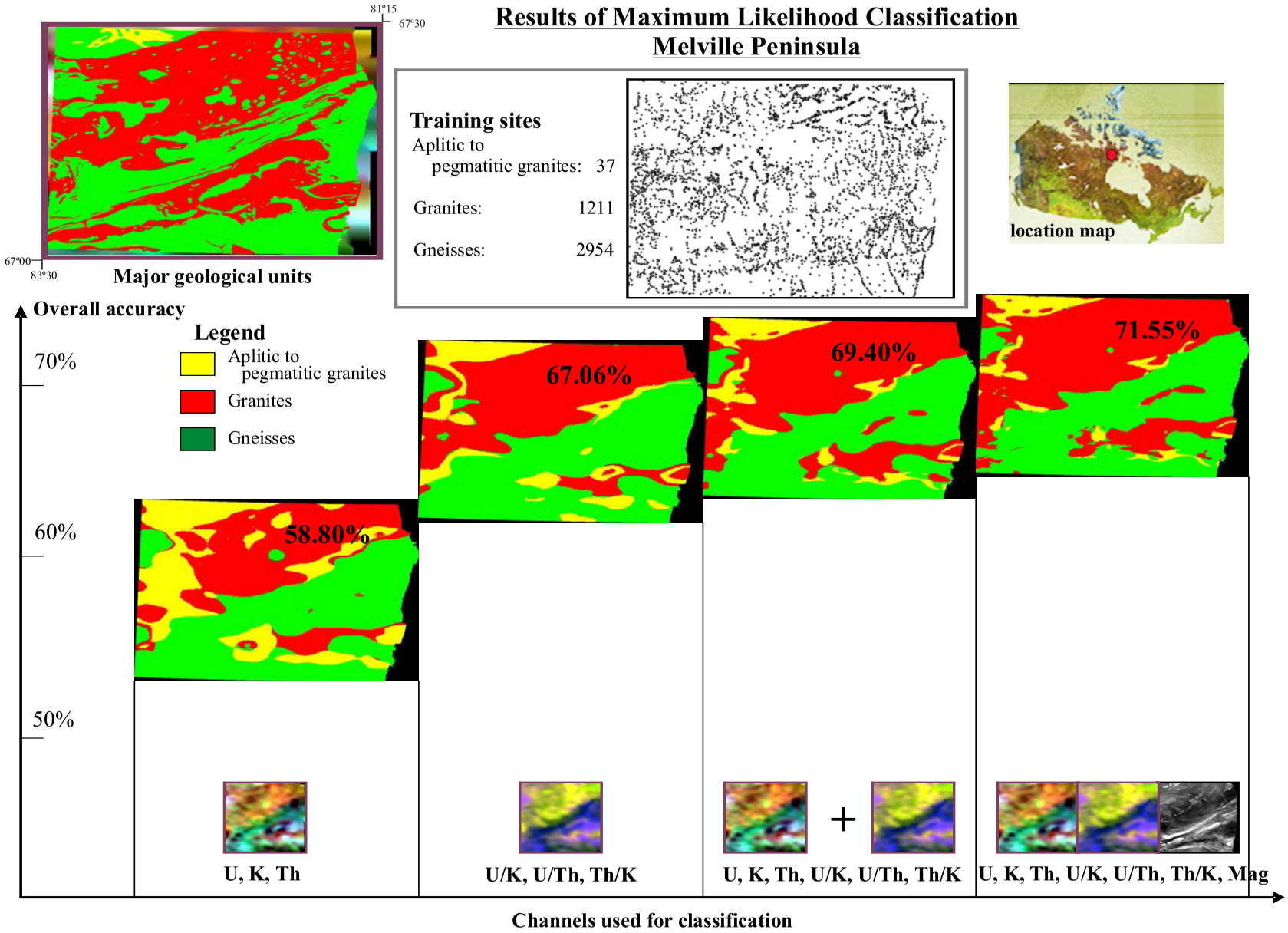

Figure 4-28. Supervised classification (prediction) of major geological units using a maximum likelihood algorithm applied to gamma-ray and magnetic data over the Melville Peninsula, Nunavut. The goal of this exercise was to determine whether the major geological units could be successfully predicted using gamma-ray data in concert with magnetic data. Training samples for each of the major units were gathered from legacy field data (point locations). Some of these were used for classification whereas others were used for validation (cross-correlation) (see description for Fig. 4-27). The accuracy, when compared to the check training sites, varied from close to 60% accuracy, when just using eTh, eU, and K for classification, to 72% when using all the gamma-ray data (raw (elemental) + ratios) and the magnetic data.

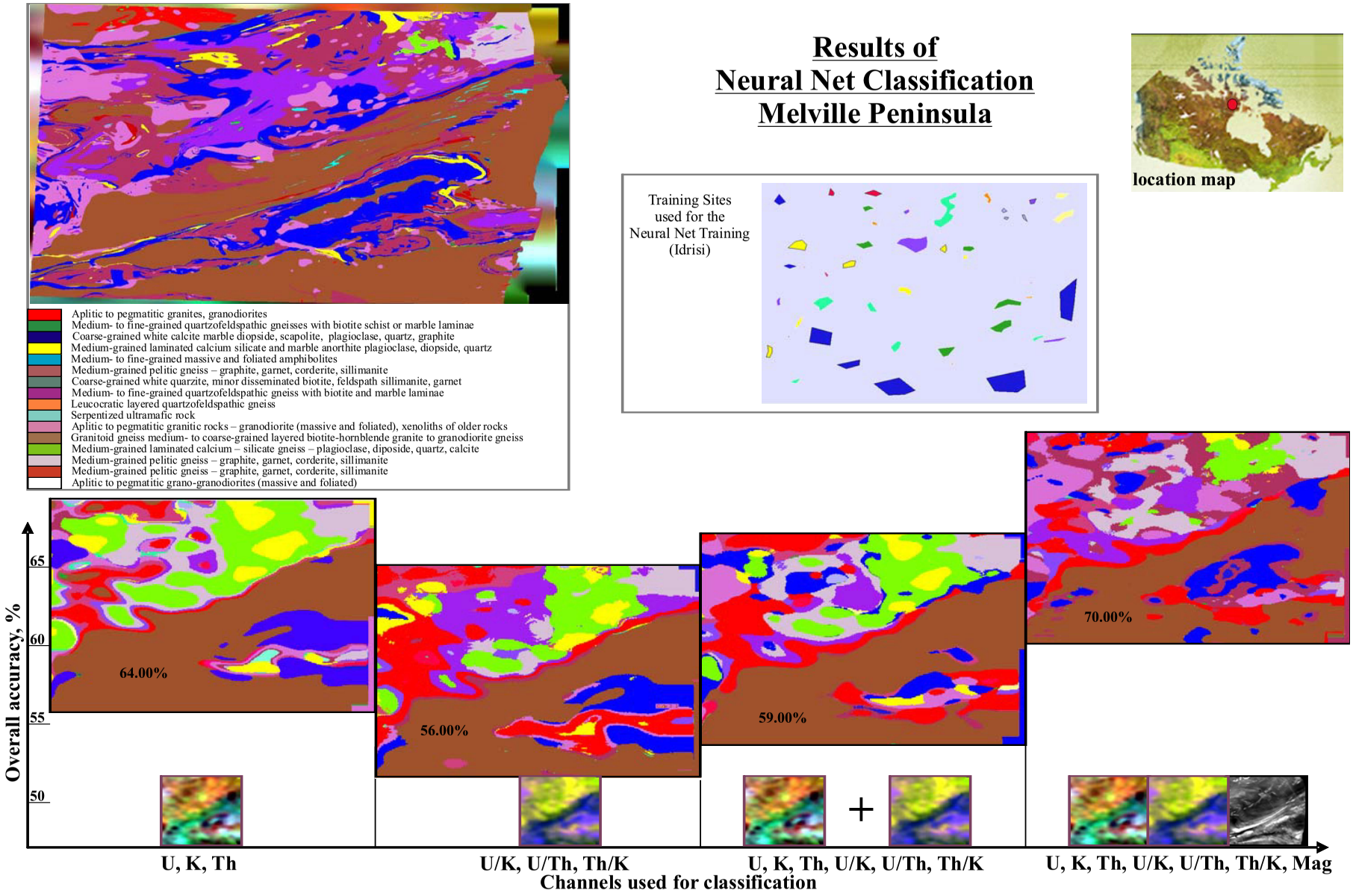

Figure 4-29. Supervised classification (prediction) of geological units using a neural network algorithm applied to gamma-ray and magnetic data over the Melville Peninsula, Nunavut. The goal of this exercise was to determine whether the geological units could be successfully predicted using gamma-ray data in concert with magnetic data. Training samples for each of the major units were gathered from the geological map areas. Some of these were used for classification , whereas others were used for validation (cross-correlation) (see description for Fig. 4-27). The accuracy, when compared to the check training sites, varied from close to 60% accuracy, when just using eTh, eU, and K for classification, to 72%, when using all the gamma-ray data (raw (elemental) + ratios) and the magnetic data. Accuracies varied from 56% using the gamma-ratio data to 70% using all the gamma-ray data (raw (elemental) + ratios) and the magnetic data.

nels, a classification accuracy of the major tectonic units of close to 70% can be achieved. The misclassified areas (30%) comprise variations in gamma response due to both surficial and bedrock variations.

Different supervised classification algorithms are available and at present much emphasis is being placed on neural network classifiers that are quite robust and often lead to very positive results. Figure 4-29 presents a neural network classification of lithological units (as opposed to major tectonic units as presented in Fig. 4-28) over the Melville Peninsula. In this example, a 64% classification accuracy of the lithological units was achieved when using just eU, eTh, and K. This increased to 70% when the magnetic data was included.

CONCLUSIONS

The ability of gamma-ray spectrometry to map the distribution of potassium, uranium, and thorium at the surface of the Earth provides powerful assistance for regional and local bedrock and surficial geological mapping. Important direct and indirect exploration guidance in a wide variety of geological settings is also provided, as is important information for environmental radiation monitoring and land-use planning.

Data enhancement and presentation methods can provide valuable interpretation assistance of gamma-ray spectrometry data. Ratio maps, including ternary K-U-Th colour presentations, are useful but, in the absence of corresponding radioelement concentration maps, are ambiguous. Flight line data, presented as stacked profiles, provide more detail than the inherently smoothed contour maps.

Proper interpretation of gamma-ray spectrometric data requires a clear understanding of petrology, surficial and bedrock geology, and geochemistry as well as the gamma-ray spectrometric method itself.

Despite the availability of large quantities of airborne gamma-ray spectrometry data collected since the 1970s and the development and publication of numerous case histories that clearly demonstrate the application to mapping and mineral exploration, the technique remains under-utilized and poorly understood by many potential end-users. The challenge remains to further develop techniques and case histories that continue to illustrate the broad range of applications, and to effectively disseminate this knowledge.

REFERENCES

Broome, J., Carson, J.M., Grant, J.A., and Ford, K.L.
1987: A Modified Ternary Radioelement Mapping Technique and Its Application to the South Coast of Newfoundland; Geological Survey of Canada, Paper 87-14, scale 1: 500 000.

Carson, J.M., Holman, P.B., Ford, K.L., Grant, J.A., and Shives, R.B.K.
2003: Airborne Gamma Ray Spectrometry Compilation, Nova Scotia; Geological Survey of Canada, Open Files 4464-4471, scale 1:500 000.

Carson, J.M., Holman, P.B., Ford, K.L., Grant, J.A., and Shives, R.B.K.
2005: Airborne Gamma Ray Spectrometry Compilation, Ternary Radioelement Map, Radioactivity Map of Canada; Geological Survey of Canada, Open File 4763, scale 1: 5 000 000.

Charbonneau, B.W. and Darnley, A.G.
1970: A Test Strip for Calibration of Airborne Gamma-Ray Spectrometers, *in* Report of Activities, Part B, (ed.) R.G. Blackadar; Geological Survey of Canada, Paper 70-1B, p. 27-32.

Delpierre, M.E.
1982: Anomaly '60': A uriniferous granite pluton on Melville Peninsula, N.W.T., *in* Uranium in Granites, (ed.) Y.T. Maurice; Geological Survey of Canada, Paper 81-23, p. 115-118.

Dickson, B.L. and Scott, K.M.
1997: Interpretation of aerial gamma-ray surveys – adding the geochemical factors; AGSO Journal of Australian Geology and Geophysics, v. 17, p. 187-200.

Dredge, L.A.
1994: Surficial Geology, Barrow River, District of Franklin, Northwest Territories; Geological Survey of Canada, Map 1849A, scale 1:200 000

Dredge, L.A, McMartin, I., and Ford, K.
2005: Till Geochemistry, Gamma Ray Spectrometry and Gold Grain Counts, Wager Bay, Mainland Nunavut (NTS 56G); Geological Survey of Canada, Open File 5014, 184 p.

Ford, K.L.
1993: Radioelement mapping of parts of the Musquodoboit Batholith and Liscomb complex, Meguma zone Nova Scotia, *in* Mineral Deposit Studies in Nova Scotia Volume 2, (ed.) A.L. Sangster; Geological Survey of Canada, Paper 91-9, p. 71-111.

Ford, K.L. and O'Reilly, G.A.
1985: Airborne gamma-ray spectrometric surveys as an indicator of granophile element specialization and associated mineral deposits in the granitic rocks of the Meguma Zone of Nova Scotia, Canada, *in* High Heat Production (HHP) Granites, Hydrothermal Circulation and Ore Genesis; The Institution of Mining and Metallurgy, London, England, p. 113-133.

Ford, K.L., MacDonald, M.A., Finck, P.W., Boner, F.J., Ham, L.J., Horne, R.J. Corey, M.C., and Graves, R.M.
1989: Airborne gamma ray spectrometry, and bedrock and surficial geology of the Davis Lake Pluton, *in* Mines and Minerals Report of Activities 1989, Part A; Nova Scotia Department of Mines and Energy, Report 89-3.

Gillespie, A. R., Kahle, A.B., and Walker, R.E.
1986: Color enhancement of highly correlated images. I. Decorrelation and HIS contrast stretches; Remote Sensing of Environment, v. 20, p. 209-235.

Grasty, R.L.
1979: Gamma-ray spectrometric methods in uranium exploration - theory and operation procedures, *in* Geophysics and Geochemistry in the Search for Metallic Ores, (ed.) P.J. Hood; Geological Survey of Canada, Economic Geology Report 31, p. 147-162.

Grasty, R.L. and Minty, B.R.S.
1995: A Guide to the Technical Specifications for Airborne Gamma-Ray Surveys; Australian Geological Survey Organisation, Record 1995/60, 89 p.

Grasty, R.L., Holman, P.B., and Blanchard, Y.B.
1991: Transportable Calibration Pads for Ground and Airborne Gamma-Ray Spectrometers; Geological Survey of Canada, Paper 90-23, 25 p.

Grasty, R.L., Mellander, H., and Parker M.
1991: Airborne Gamma-Ray Spectrometer Surveying; International Atomic Energy Agency, Technical Report Series 323, Vienna, 97 p.

Henderson, J.R.
1987: Geology, southeastern Melville Peninsula, District of Franklin, Northwest Territories; Geological Survey of Canada, Map 1655A, scale 1:100 000

Holman, P.B., Carson, J.M., Ford, K.L., Grant, J.A., and Shives, R.B.K.
2001: Airborne Gamma Ray Spectrometry Compilation Series, Quoich River, Nunavut; Geological Survey of Canada, Open File 4005, scale 1:1 000 000.

Horsfall, K.R.
1997: Airborne magnetic and gamma-ray data acquisition; AGSO Journal of Australian Geology and Geophysics, v. 17, p. 23-30.

International Atomic Energy Agency
2003: Guidelines for Radioelement Mapping Using Gamma Ray Spectrometry Data; IAEA-TECDOC-1363, 173 p.

Killeen, P.G.
1979: Gamma-ray spectrometric methods in uranium exploration - application and interpretation, in Geophysics and Geochemistry in Search for Metallic Ores,(ed.) P.J. Hood; Geological Survey of Canada, Economic Geology Report 31, p. 163-230.

Minty, B.R.S.
1997: Fundamentals of airborne gamma-ray spectrometry; AGSO Journal of Australian Geology and Geophysics, v. 17, p. 39-50.

Minty, B.R.S., Luyendyk, A.P.J., and Brodie, R.C.
1997: Calibration and data processing for airborne gamma-ray spectrometry; AGSO Journal of Australian Geology and Geophysics, v. 17, p. 51-62.

Shives, R.B.K., Ford, K.L., and Charbonneau, B.W.
1995: Applications of Gamma-Ray Spectrometric/Magnetic/VLF-EM Surveys – Workshop Manual; Geological Survey of Canada, Open File 3061, 82 p.

Shives, R.B.K., Charbonneau, B.W., and Ford, K.L.
1997: The detection of potassic alteration by gamma-ray spectrometry - recognition of alteration related to mineralization, *in* Proceedings of Exploration 97: Fourth Decennial International Conference on Mineral Exploration: Geophysics and Geochemistry at the Millennium, (ed.) A.G. Gubins; p. 741-752.

Viljoen, D. and Harris, J.R.
2007: Saturation and value modulation (SVM): A new method for integrating color and grayscale imagery, *in* D.R. Soller, ed., Digital Mapping Techniques '06 -- Workshop Proceedings: United S.tates Geological Survey, Open-file Report 2007-1285.

CHAPTER 5. Optical Remote Sensing

J.R. Harris and L. Wickert
Geological Survey of Canada, 615 Booth Street, Ottawa, Ontario K1A 0E9
Corresponding author's email: Jeff.Harris@NRCan.gc.ca

THEORETICAL PRINCIPLES

Optical remote sensing is based on creating an image using reflected solar energy from the visible (V), near-infrared (NIR), and short-wave infrared (SWIR) portion of the electromagnetic spectrum (EM) ranging in wavelengths from 0.4 to 3.0 micrometres (μm) (or 400 to 3000 nanometres (nm)) (Fig. 5-1). The sun is the source of energy for optical remote sensing; hence optical sensors (i.e. LANDSAT) are *passive*, as no energy is generated by the remote sensing platform in the data acquisition process. Data generated are readily available in digital format, in the form of a raster or grid in which individual image elements, called *pixels*, contain a *digital number* (DN) that is proportional to the amount of solar energy reflected at a given wavelength. Optical sensors are further characterized by a series of bands (or channels) (Fig. 5-1), each providing a separate image that can be viewed and interpreted

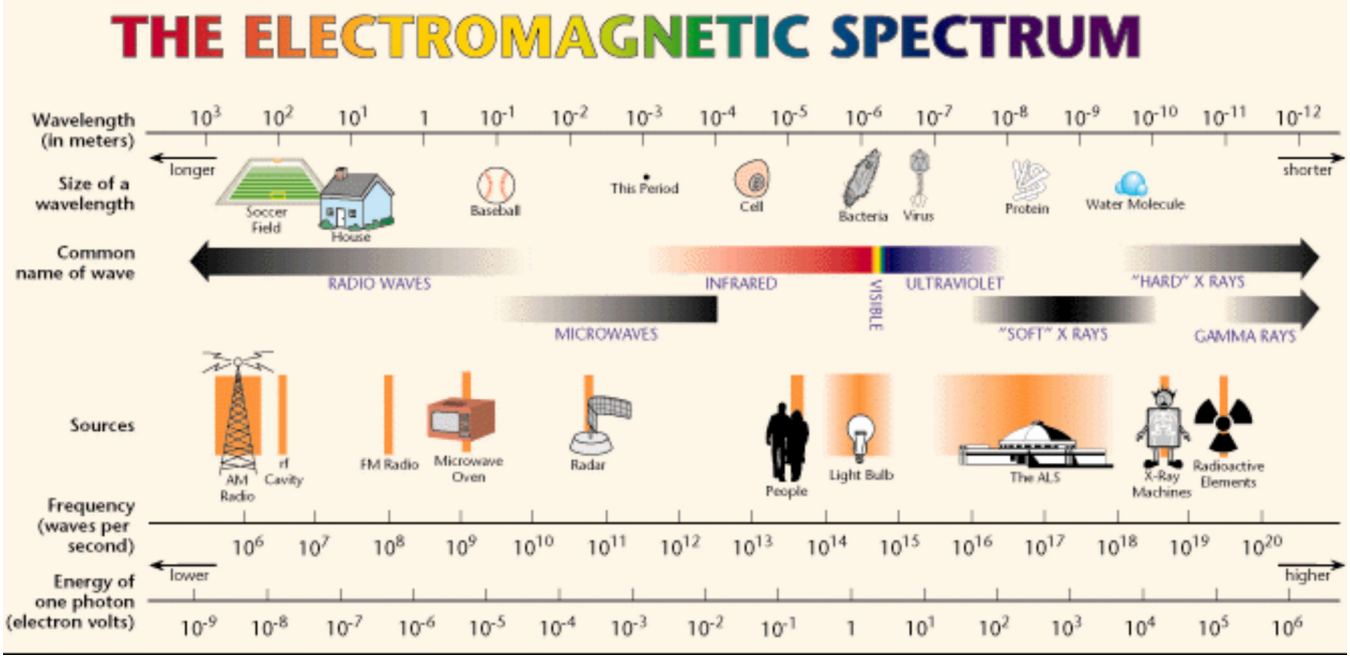

Band (Channel)	Wavelength (*u* m)	Nominal spectral location	Principal applications
1	0.45-0.52	Blue	Water body penetration – useful for coastal water mapping, soil (outcrop)/ vegetation discrimination, forest type mapping, and cultural feature
2	0.52-0.60	Green	Measure green reflectance peak for vegetation discrimination and vigour – cultural feature identification
3	0.63-0.69	Red	Chlorophyll absorption
4	0.76-0.90	Near-infrared (NIR)	High reflectance by vegetation – useful for vegetation type, vigour biomass content, delineating water bodies, and soil moisture discrimination
5	1.55-1.75	Shortwave infrared (SWIR)	Vegetation moisture content, soli moisture
6	10.4-12.5	Thermal infrared (TIR)	Soil moisture, thermal (heat) mapping
7	2.08-2.35	Shortwave infrared (SWIR)	Discrimination of mineral and rock types

Figure 5-1. Diagram of the electromagnetic spectrum (EM).

Harris, J.R. and Wickert, L., 2008, Optical Remote Sensing, Chapter 5 *in* Remote Predictive Mapping: An Aid for Northern Mapping, (ed.) J. R. Harris; Geological Survey of Canada, Open File 5643, p. 99-134.

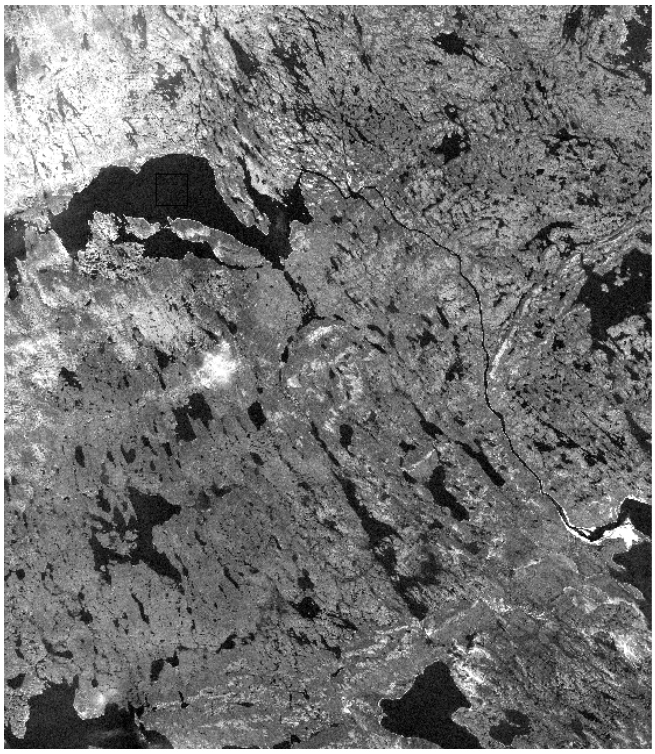

LANDSAT TM band 1(0.45-0.52 micrometres) - blue wavelength

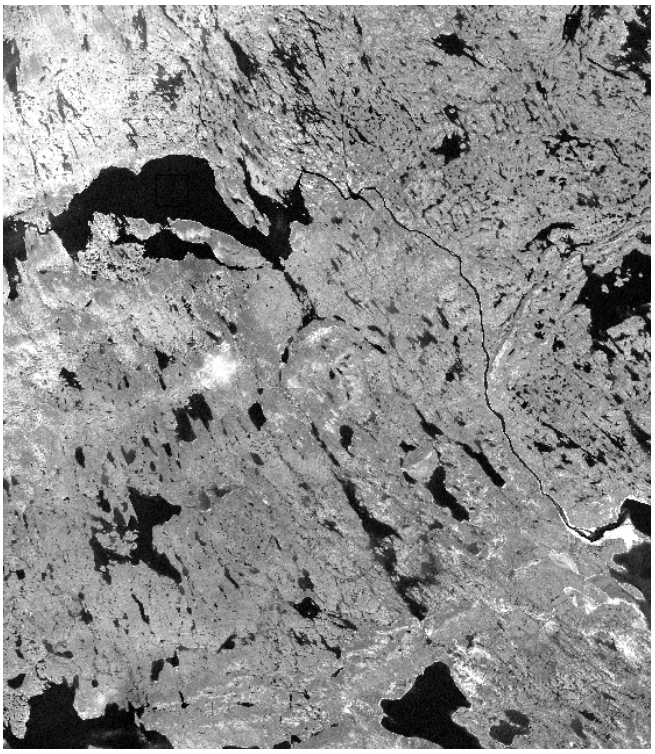

LANDSAT TM band 2 (0.52-0.60 micrometres) - green wavelength

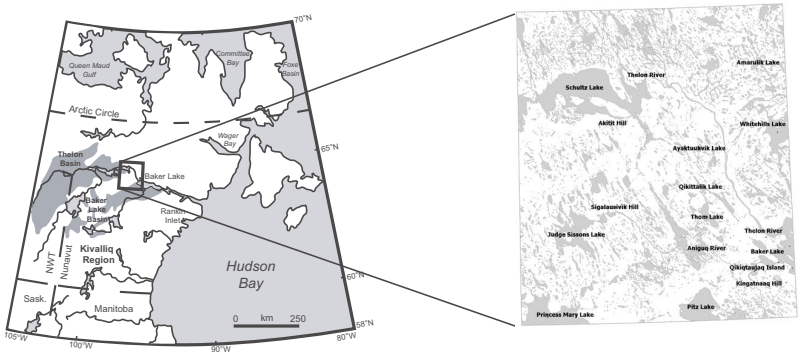

Figure 5-2. LANDSAT imagery over the Shultz Lake area (NTS 66a map sheet, 64-65º latitude and 95-96º longitude), Nunavut. **(A)** Images of six individual bands (channels) (see Fig. 5-1 for wavelengths).

separately (Fig. 5-2A) or combined as red-green-blue (RGB) ternary images (Fig. 5-2B) in which the colour variations are created by the combination of three channels. A different looking image in which different terrain and surficial features are enhanced will result for each band as the incoming solar energy will interact differently with the atmosphere and the Earth's surface (see Fig. 5-3), depending on the wavelength.

The number of channels and their location within the EM defines the *spectral coverage* of the sensor. Additional channels, or increased spectral coverage, increase the application of the optical sensor, as different parts of the electromagnetic spectrum are more suited for discriminating features of different material types (i.e. different minerals). For example, the visible near-infrared (VNIR) portion is particularly good at discriminating various iron-bearing minerals whereas clays and carbonates are better discriminated in the short-wave infrared (SWIR) portion (Fig. 5-4). Decreasing the bandwidth of the sensor channels (i.e. width of the channels in microns) dictates the spectral resolution of the sensor. This is often accompanied by an increase in the number of channels available. Higher spectral resolution and an increased number of channels increases the probability of unequivocally identifying various earth materials (such as specific minerals or groups of minerals defining a particular lithology) as opposed to simply discriminating materials or mineral groups. Figure 5-5 shows spectra for two clay minerals (alunite and kaolinite) based on different spectral-resolution sensors and ground-based spectrometers. Recently much emphasis has been placed on hyperspectral remote sensing, which simply means an optical sensor with many bands. LANDSAT, for example has 6 channels in the VNIR and SWIR, whereas a hyperspectral optical sensor, such as the airborne

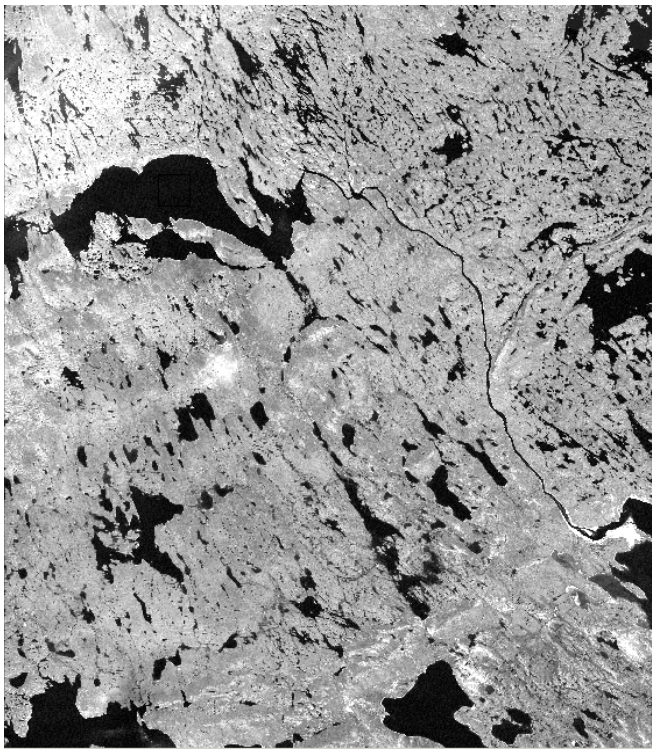

LANDSAT TM band 3 (0.60-0.69 micrometres)
- red wavelength

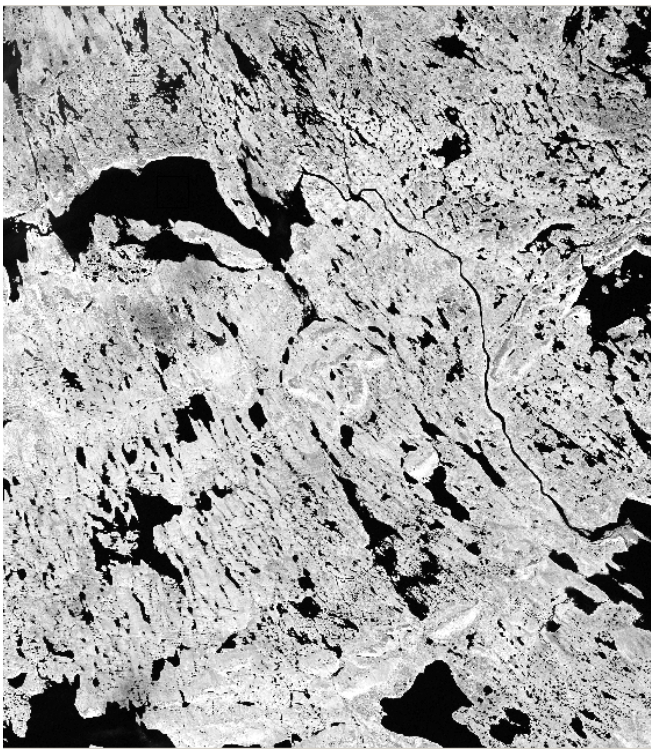

LANDSAT TM band 4 (0.76-0.90 micrometres)
- infrared wavelength

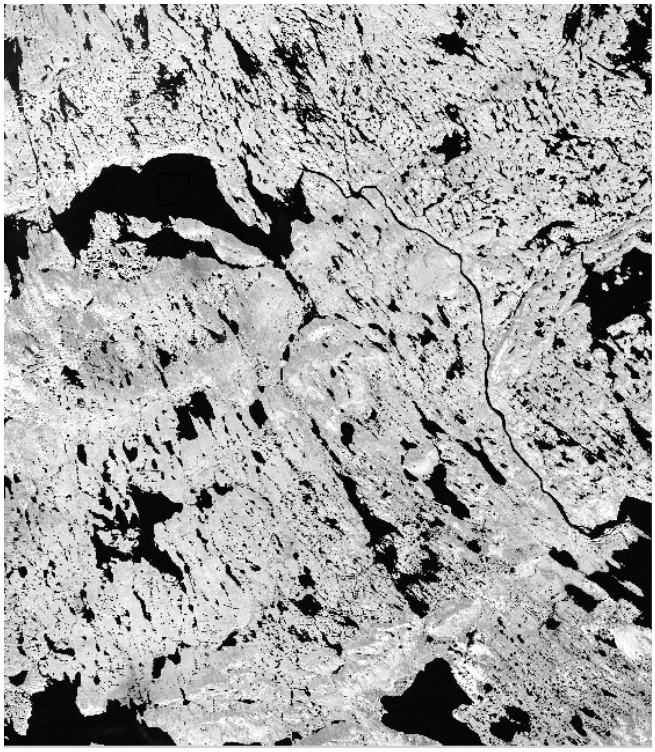

LANDSAT TM band 5 (1.55-1.75 micrometres)
- infrared wavelength

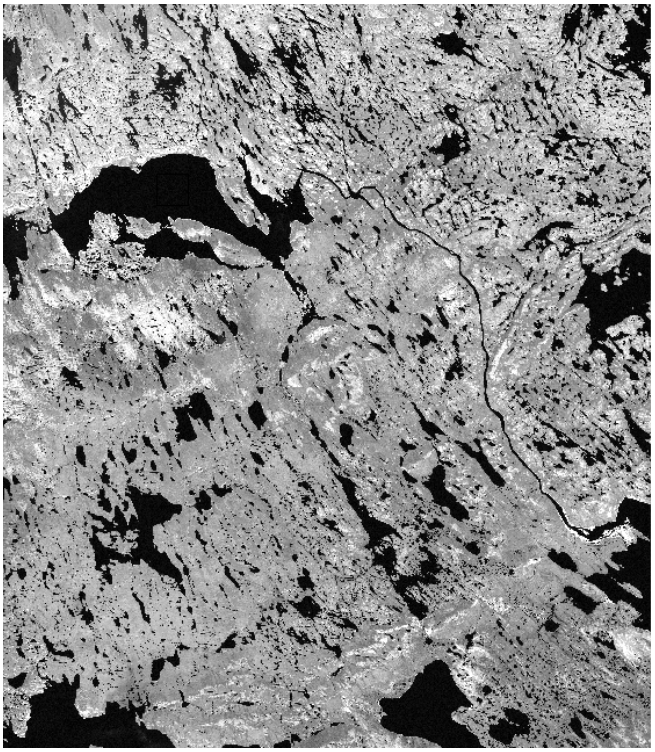

LANDSAT TM band 7 (2.08-2.35 micrometres)
- infrared wavelength

Figure 5-2A continued

.

PROBE system, has 128 channels in the same portion of the EM spectrum (see Table 5-1 for a summary of selected sensors). Optical sensors exploit the variable reflectance characteristics of the surface chemistry and



LANDSAT TM bands 3,2,1
- RGB - Natural Colour Composite
- vegetated areas are green

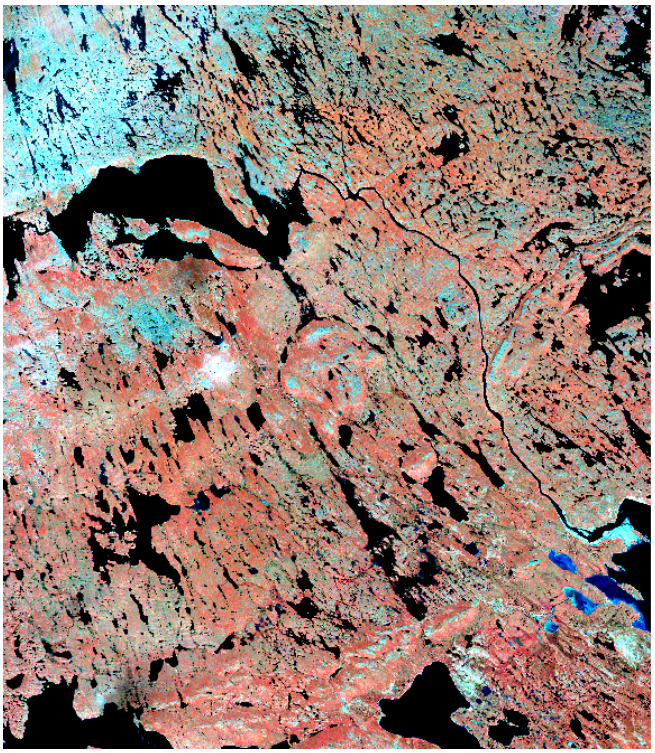

LANDSAT TM bands 4,3,2
- RGB - False Colour Composite
- vegetated areas are red and bedrock outcrop is cyan

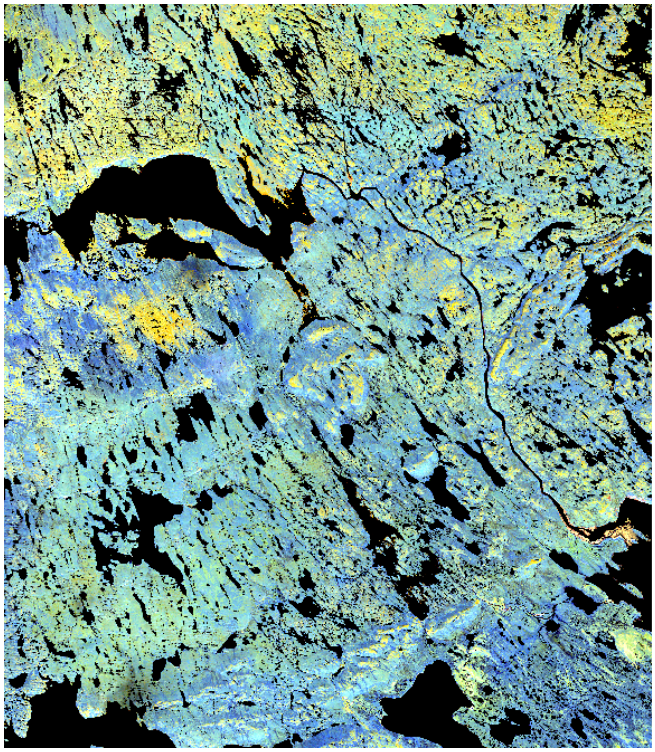

LANDSAT TM bands 7,5,4
- RGB - False Colour Composite - Infrared bands
- vegetated areas are bluish and
bedrock outcrop is yellow

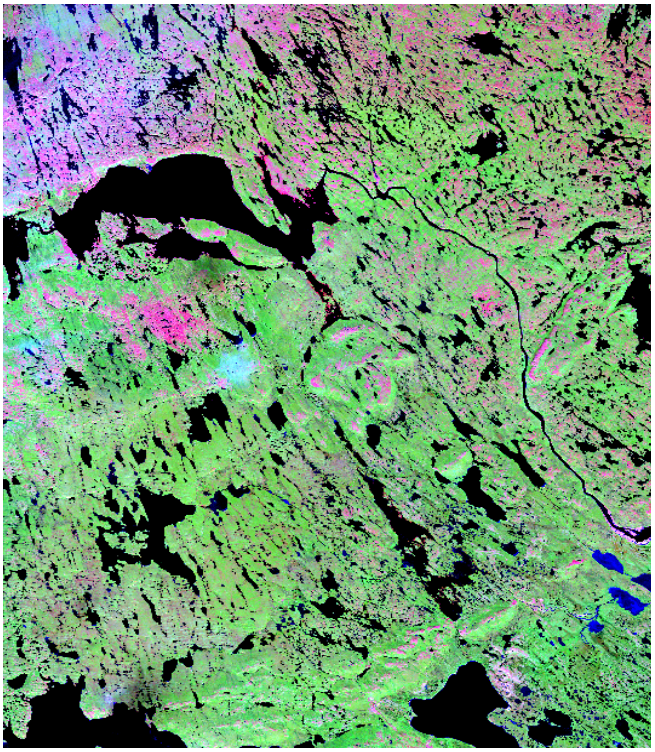

LANDSAT TM bands 7,5,4
- RGB - False Colour Composite
- Infrared bands and visible bands
- vegetated areas are green and bedrock outcrop is pink

Figure 5-2 continued. (B) Different colour composite ternary images. Viewing LANDSAT multi-spectral data using an image analysis system or GIS involves a colour display utilizing three primary colours; red , green and blue. Therefore, three channels of data can be displayed through these colours creating what is called a colour composite or ternary image.

Table 5-1. Summary of the characteristics of selected optical sensors.

Sensor Name	Type	Number of Channels	Spectral Range	Spectral Resolution	Spatial Resolution	Scale
LANDSAT 7 ETM+	Optical – Multispectral satellite-based	8 (3-V, 1-NIR, 2-MIR, 1-TIR, 1-pan)	0.4 - 2.35 µm, and 10.4 - 12.5 µm	65 - 260 nm and 380 nm (pan)	30 m pixels (60 m - TIR and 15 m - pan)	Regional
IKONOS	Optical – Multispectral satellite-based	4 (3-V, 1-NIR)	0.445 - 0.853 µm	66 - 96 nm	4 m pixels	Local
ASTER	Optical – Multispectral satellite-based	14 (3-V, 6-SWIR, 5-TIR)	0.52 - 0.86 µm, 1.60 - 2.43 µm, 8.125 - 11.65 µm	60 - 100 nm, 40 - 70 nm, 350 - 700 nm	15, 30, and 90 m pixels	Regional
HYPERION	Optical – Hyperspectral airborne	220	0.35 - 2.5 µm	~15 nm	30 m pixels	Regional
CASI	Optical – Hyperspectral airborne	100	0.4 - 1.1 µm	~20 nm	up to 1.23 m pixels cross-track	Local
SFSI	Optical – Hyperspectral airborne	234	1.2 - 2.4 µm	~10 nm	depends on altitude flown	Local
HyMap	Optical – Hyperspectral airborne	228	0.4 - 2.5 µm	~20 nm	typically 3 to 10 m pixels, depending on altitude flown	Local
PROBE-1	Optical – Hyperspectral airborne	226	0.4 - 2.5 µm	~20 nm	typically 3 to 10 m pixels, depends on altitude flown	Local

Note: MIR = mid-infrared; NIR = near infrared; SWIR = short-wave infrared; TIR = thermal infrared; V = visible.

architecture in these spectral regions. Interaction of the incoming energy with the surface is controlled by processes at the molecular level (vibrations, oscillations of molecules), which determines whether the energy is absorbed, reflected, or transmitted and in turn results in a unique spectral signature for the particular target. This is particularly important in geological remote sensing, as certain groups of minerals have specific spectral characteristics or signatures (Fig. 5-4) that can be uniquely identified depending on the *spectral resolution* of the sensor.

Another important consideration is spatial resolution, which for optical sensors is defined by the flying height and instantaneous field of view. The amount of information about the viewed surface that can be extracted from an image is strongly dependent on the spatial resolution of the sensor (Fig. 5-6). Moderate-resolution sensors such as LANDSAT (30 m resolution for multi-spectral bands and 15 m resolution for the panchromatic band) are useful for regional mapping campaigns (at a scale of more than 1:50,000) and can offer information on lithology, structure, and infrastructure for field-planning purposes. Paralleling the recent

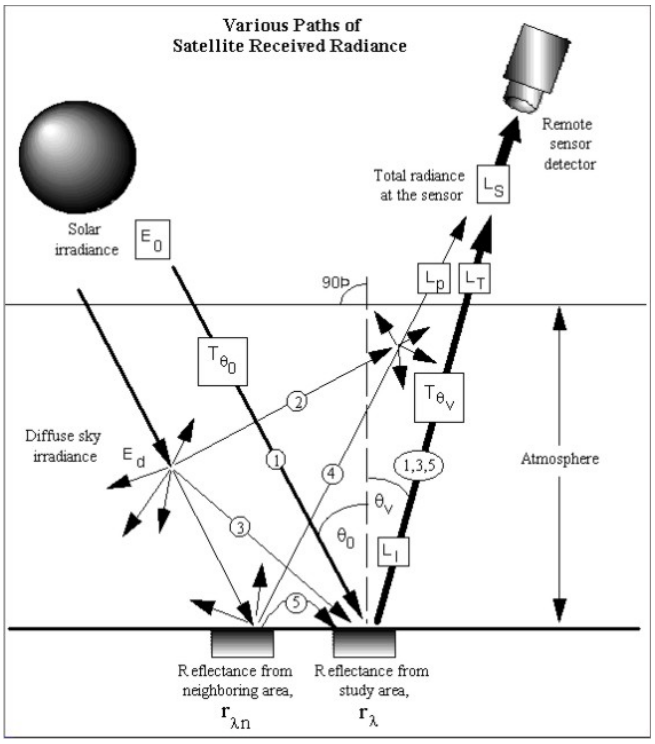

Figure 5-3. Path of solar radiation from the sun to the ground and the reflection back to the sensor. The influence of the intervening atmosphere is many and varied and includes absorption, scattering, transmittance, and reflection. Atmospheric windows comprise portions of the electromagnetic spectrum where the incoming solar radiation is not completely absorbed by atmospheric gases, such as water, ozone, and carbon dioxide. The interaction with the ground and subsequent reflection from the ground and back through the atmosphere to the sensor is equally as complex. Path 1 – direct; Path 2 – scattered; Path 3 – indirect; Path 4 – scattering from nearby areas; Path 5 – reflection from nearby areas (from Jensen, 1996).

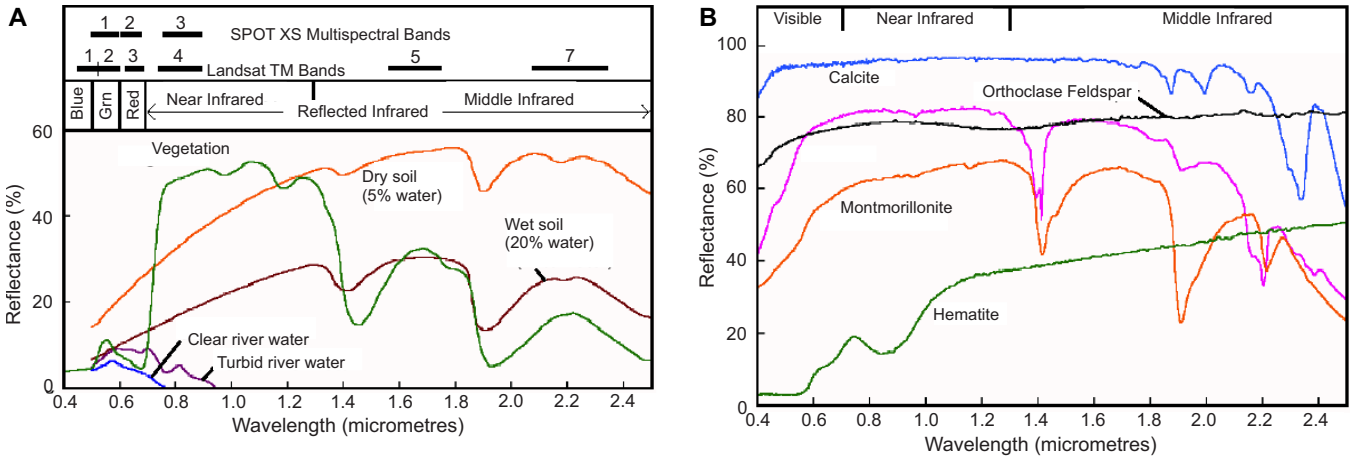

Figure 5-4. Spectral curves of various features. **(A)** Typical spectral curves for vegetation, soil, and water from the visible to short-wave infrared portion of the EM spectrum. These curves show the amount of energy reflected (% reflectance in wavelengths ranging from 0.4 to 2.4 micrometres). Also shown are the wavelength (bands) positions of two commonly used optical satellite systems (LANDSAT and SPOT). **(B)** Typical spectra for various minerals from the visible to short-wave infrared portion of the EM spectrum (measured in the lab using a reflectance spectrometer). The various reflectance peaks and troughs (absorption bands) uniquely define the various minerals.

development of optical sensors offering high-spectral resolution (i.e. hyperspectral), are sensors that offer metre to sub-metre spatial resolution from space (e.g. IKONOS, QUICKBIRD). This imagery, although expensive to purchase, rivals aerial photography in terms of spatial resolution and the amount of terrain detail that can be *seen*. This type of high-spatial resolution imagery is very useful for not only detailed mapping but also for logistical planning activities. A new generation of optical sensors is now offering increased spatial and spectral resolution (i.e. ASTER, IRS, SPOT 5); however, the trade-off is a smaller footprint (i.e. less coverage on the ground).

Another feature of a sensor is its *dynamic range*, or signal to noise ratio, which is the amplitude of the signal relative to the amplitude of the noise of the sensor. The higher the signal-to-noise (S/N) ratio, the better a signal can be resolved and identified.

Overall, the resolving capability of a sensor is a combination of spectral coverage, spectral resolution, spatial resolution, and signal to noise. These characteristics of a sensor (airborne- and satellite-based) are fixed and cannot be altered post-sensor construction. Optical sensors are typically classified as multispectral or hyperspectral. Multispectral sensors have a limited number of bands (generally less than 30) of wider bandwidth (i.e. 100 nm or more). Hyperspectral sensors, in contrast, are characterized by many bands (i.e. 30 to in the hundreds) with very narrow bandwidth (i.e. 3 to 20 nm).

Since optical sensors utilize reflected solar energy, there is a need to deal with complicating factors such as the atmosphere (Fig. 5-3), which can seriously degrade image quality. Obviously, imaging is not possible in cloudy conditions but even in apparent cloud-free conditions the effects of the atmosphere (e.g. scattering, absorption) must be taken into account in the imaging process. Often atmospheric corrections must be applied in order to quantitatively interpret the data. This is

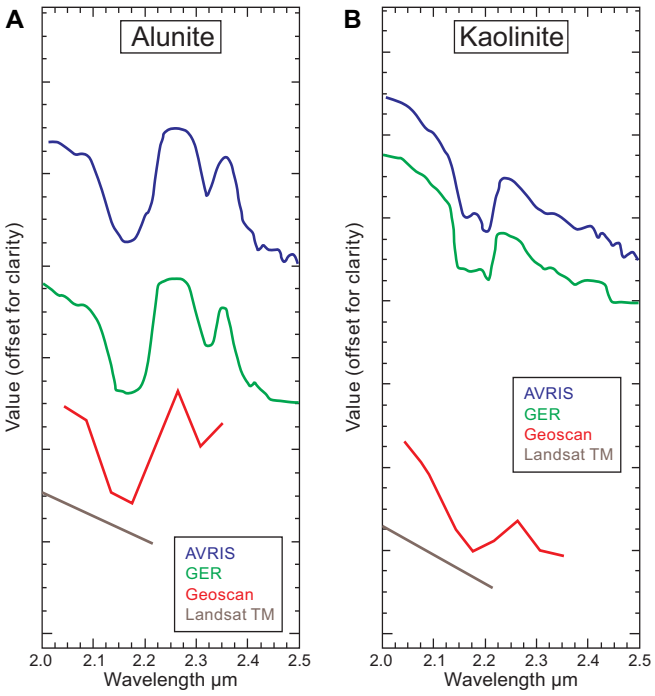

Figure 5-5. Plots show the different appearance of spectral curves over the SWIR portion of the EM spectrum for the clay minerals, alunite and kaolinite, as a function of different spectral resolutions. **(A)** Spectra for alunite derived from the airborne AVIRIS system (256 channels), ground-based GER (244 channels at a nominally 10 nm bandwidth), Geoscan (7 channels), and LANDSAT TM (2 channels). **(B)** The same spectral curves as in (A), except spectra is for kaolinite. The importance of spectral resolution can be clearly seen on the above spectral plots. Alunite and kaolinite can be uniquely identified based on their spectral characteristics (absorption troughs between 2.1 and 2.2 µm) using AVIRIS (airborne sensor) and GER (ground-based spectrometer), which have sufficient spectral resolution to resolve the spectral characteristics. However, because LANDSAT is characterized by very low spectral resolution (only 2 bands in the SWIR), these minerals cannot be uniquely identified or separated.

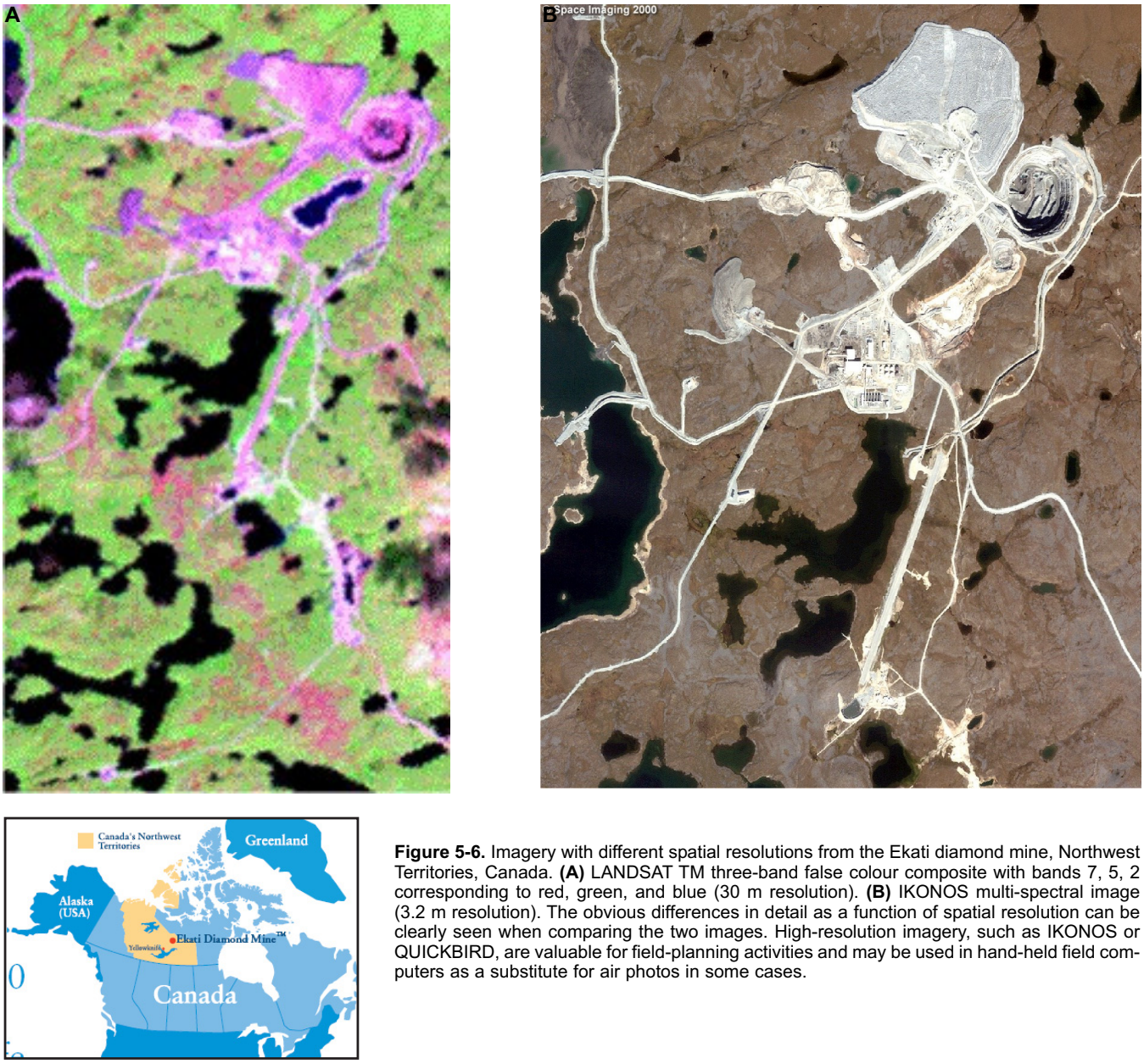

Figure 5-6. Imagery with different spatial resolutions from the Ekati diamond mine, Northwest Territories, Canada. **(A)** LANDSAT TM three-band false colour composite with bands 7, 5, 2 corresponding to red, green, and blue (30 m resolution). **(B)** IKONOS multi-spectral image (3.2 m resolution). The obvious differences in detail as a function of spatial resolution can be clearly seen when comparing the two images. High-resolution imagery, such as IKONOS or QUICKBIRD, are valuable for field-planning activities and may be used in hand-held field computers as a substitute for air photos in some cases.

especially true for optical remote sensing in the North where the effects of the atmosphere is compounded by low sun (illumination) angles, which can have a serious effect on the quality (low signal-to-noise ratio) of the resulting data. The path that solar energy takes from source (sun) to destination (sensor) is complex (Fig. 5-3) and many variables can have a profound effect on the resulting imagery. These effects must be accounted for (corrected) in the final image product. This is especially true for hyperspectral sensors.

It must be stressed that optical remote sensing only collects information on the surface of the earth, unlike magnetic remote sensing. As mentioned above, cloud cover will completely reflect and/ or absorb incoming solar radiation so this is a limiting factor for optical remote sensing. However, when complete coverage of a study area is obtained, this will normally suffice for future mapping programs as the objects of interest (i.e. geology, terrain) do not change appreciably over time. However, the season in which the data are required will make a significant difference in the way a given area will appear (i.e. snow vs. no snow, fall senescence etc.) as well as acquisition geometries (sun angle). Imagery acquired in winter look appreciably different than imagery collected of the same area in the summer (Fig. 5-7). As a result of lower sun angles[1], winter imagery

1. The bidirectional reflectance factor (BRF) relates the reflectance from a target to the reflectance observed from a Lambertian surface (equal scattering in all directions) and is dependent on viewing angle and sun angle.

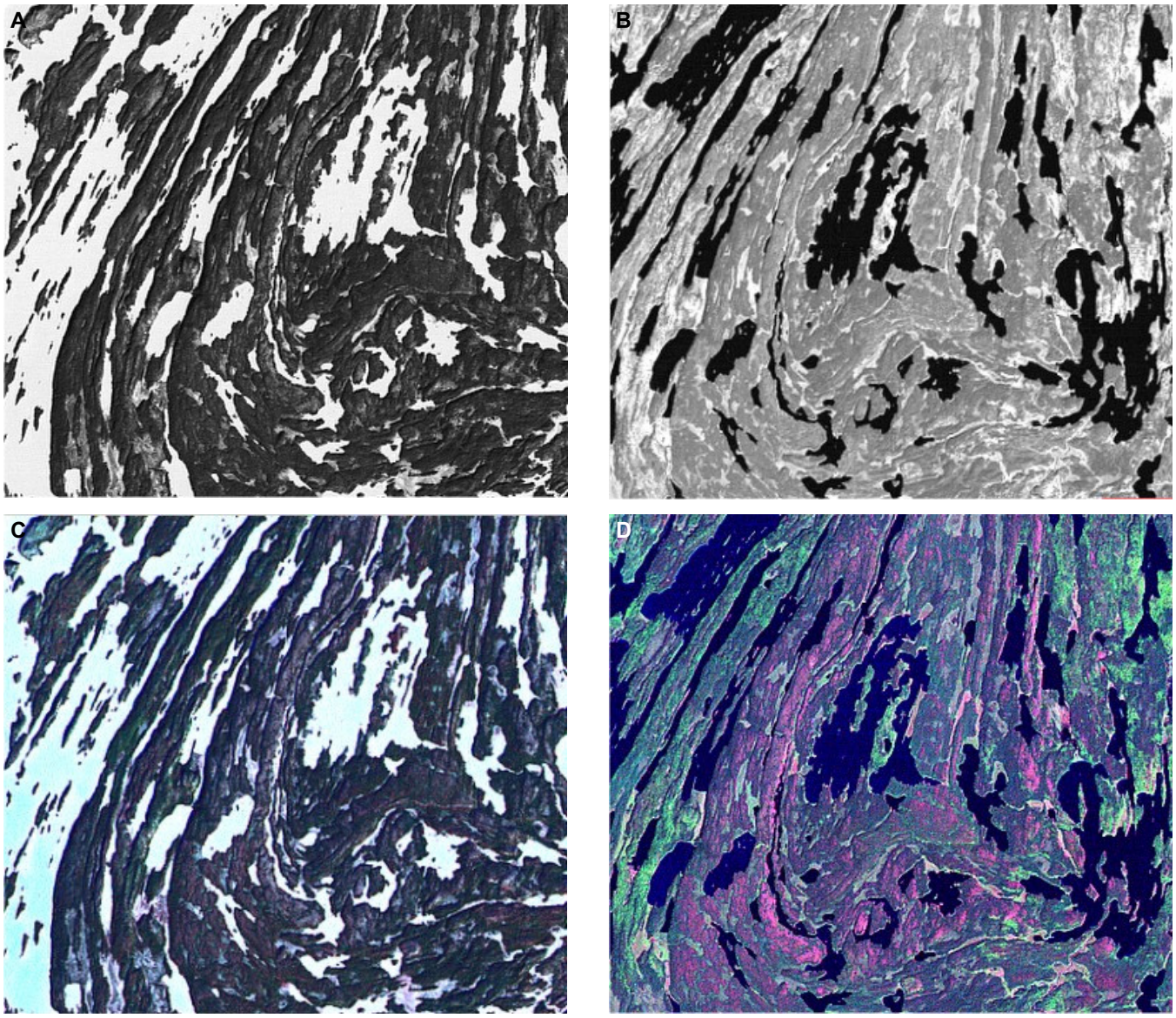

Figure 5-7. Summer and winter LANDSAT imagery over a portion of Manitoba (Flin-Flon area), Canada. **(A)** LANDSAT band 4 winter image: white is snow. Note the pseudo 2.5-D shadowing effect due to the low sun angle. **(B)** LANDSAT band 4 summer image. **(C)** LANDSAT colour composite (ternary) winter image – bands 7, 4, 1 – RGB. **(D)** LANDSAT colour composite (ternary) summer image – bands 7, 4, 1 – RGB. (source: David Viljoen, Geological Survey of Canada).

often provides a good source for structural mapping due to the pseudo 2.5-dimension[2] shadowing effect (Fig. 5-7A,C). Therefore, the season of acquisition is as important as spectral and spatial resolution for geological mapping applications.

DATA

A variety of optical sensors are available for geological mapping and a summary of the characteristics of selected instruments are provided in Table 5-1. Sensors are often broadly divided by their host platform, that is, whether they are satellite -based or airborne-based. Satellite-based sensors have the advantage of providing synoptic coverage from a stable platform (i.e. no atmosphere). They are expensive to build and deploy in lower earth orbits, but once in orbit have a life span of many years and the costs of data acquisition per scene are generally low. However, satellite-based sensors are limited in other ways. Given that the orbit is fixed and the pointing direction isn't generally adjustable, optical sensors are very dependent on good weather for successful data acquisition. In some areas of the world (i.e. tropics and northern regions), this is a considerable problem due to perpetual cloud cover. Furthermore, in recent years newer optical sensors are being mounted on smaller satellites because of cost considerations,

2. 3-D is often mistakenly confused with 2.5-D. True 3-D data have three location coordinates (X, Y, Z), whereas 2.5-D data have two location coordinates (X and Y) and an attribute (Z, i.e. elevation)

and hence have payload limitations that may limit sensor storage, leading to limitations on data scene size and spatial resolution. HYPERION, one of the few satellite-based hyperspectral sensors presently in orbit, has limited spatial resolution (30 m) and swath width (7.5 km), and has serious problems with signal to noise. Generally, for satellite-based sensors there is a trade off between high-spatial resolution and bandwidth. For example, in the case of the IKONOS satellites, the spatial resolution is 4 m for four bands of data, which contrasts with the 14 bands available from the ASTER satellite-based sensor that provides a lower spatial resolution of 15 to 60 m.

Airborne sensors are typically mounted on small aircraft and engaged for project or site specific acquisitions. Hence, the cost per scene is much higher, and this will vary across the globe due to varying mobilization/demobilization considerations. Aircraft generally fly close to the surface of the earth (less than 10 km), hence airborne data is characterized by much better spatial resolution (i.e. 3 to 10 m pixels or less). Acquisition of data from hyperspectral sensors with high broad spectral coverage (i.e. VNIR + SWIR) and high spatial and spectral resolution is therefore possible with airborne platforms. The biggest challenge with airborne hyperspectral data is correcting and processing the large volume of data generated.

Error Correction and Registration

Raw optical remote-sensing data (Level 0) once collected is typically corrected to Level 1 data, which accounts for known radiometric and geometric errors. This data is generally delivered as a 'path' image, which is an image that is orthogonal to the path over which it was collected, but has not been adjusted to represent its true position over the surface of the Earth (georectification). A number of Level 1 subtypes exist, which vary depending on the sensor. For example, ASTER L1A data has the Level 0 to Level 1 corrections calculated, but they are only appended, not applied, whereas for ASTER L1B data these have been applied. For LANDSAT imagery, various data products are available, including L1G, in which the data have been orthorectified (using simple Geotopo global digital elevation data). Generally, such labelling is typically employed more for satellite-based imagery, and variations in terminology may also be observed.

Post-processing of the data past Level 1 is often required, depending on the sensor and the application of the data. Most sensors, even commercial ones (i.e. IKONOS, QUICKBIRD), deliver a product formatted with digital numbers. For non-quantitative applications, the data could be used directly, but in most cases it is preferable to take digital numbers using the following corrections:

- gains and offsets or unit conversion coefficients applied to convert the data from digital number (DN) to radiance ($W/m^2/sr/\mu m$)
- atmospheric correction to convert the data from radiance to relative reflectance or at surface reflectance.

For some sensors, particularly those which are categorized as 'research sensors' (i.e. ASTER, HYPERION), many other corrections are necessary to address known errors with the instruments. For most applications only major sources of instrument error will require correction, whereas for others more precise correction will be required. Most hyperspectral datasets will require accurate atmospheric correction as the data is often used to generate precise spectral signatures of various Earth features.

A number of different commercial products are available for precise and detailed atmospheric correction, including ACORN and FLAASH. These are more widely applied to hyperspectral data, but may also be used for multispectral data (i.e. ASTER). Other correction techniques that are simpler than those employed by the above packages include Internal Average Relative Reflectance (IARR), Flat Field Calibration (FFC), and Empirical Line Correction (ELC). These simpler techniques, which result in relative as opposed to absolute reflectances, are often appropriate for broadband and multispectral sensors. A comprehensive summary of atmospheric correction methods is provided by the United States Geological Survey. (United States Geological Survey, 2003).

Selected Optical Sensors Useful for Remote Predictive Mapping

There is a wide range of optical sensors available for use, and for the inexperienced user, it can be a daunting task choosing the sensor that is most appropriate for a given geological application. Hence, an effort has been made here to both provide a summary of the sensors best suited to remote predictive mapping applications. A summary of the characteristics of each of these sensors is provided in Table 5-1 along with a *Remote Sensing Reference Chart*, which visually summarizes the bands and bandwidths for the optical sensors most useful for geological interpretation (Fig. 5-8).

Satellite-Based Sensors

The web-links in the Digital References section provide more information on the sensors discussed below.

IKONOS and QUICKBIRD

IKONOS is a commercial satellite deployed in a sun-synchronous orbit (651 km altitude) by Space Imaging in 1999 (now owned by GeoEye). It is has extremely

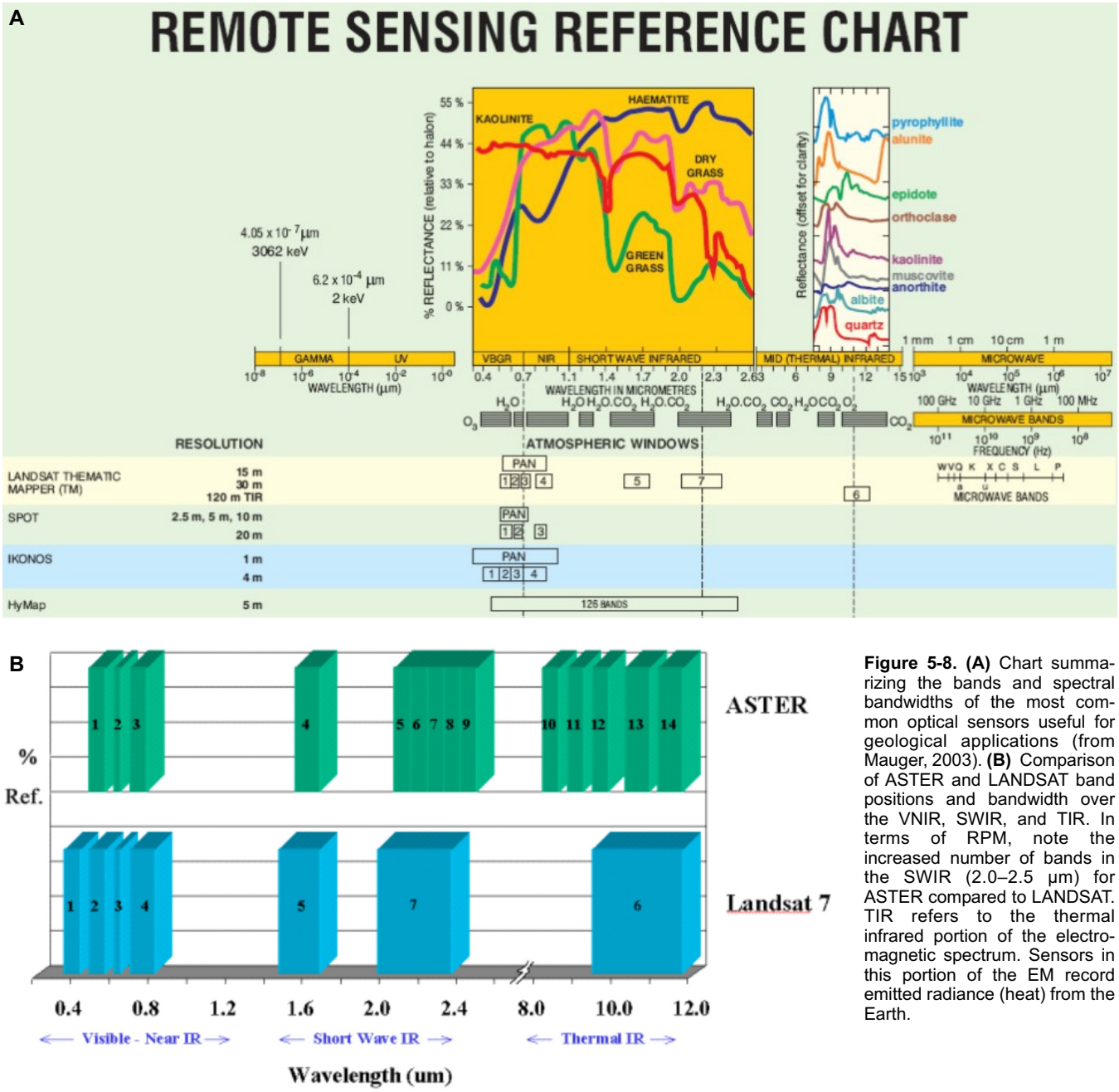

Figure 5-8. (A) Chart summarizing the bands and spectral bandwidths of the most common optical sensors useful for geological applications (from Mauger, 2003). **(B)** Comparison of ASTER and LANDSAT band positions and bandwidth over the VNIR, SWIR, and TIR. In terms of RPM, note the increased number of bands in the SWIR (2.0–2.5 µm) for ASTER compared to LANDSAT. TIR refers to the thermal infrared portion of the electromagnetic spectrum. Sensors in this portion of the EM record emitted radiance (heat) from the Earth.

high spatial resolution with two sensors, one with a 403 nm panchromatic band at 1 m resolution, and a second multispectral sensor with 4 bands (MS-1 to MS-4 at blue, green, red, and near infrared) at 4 m resolution (at 26º off -nadir, slightly better resolution at nadir)[3] (Fig. 5-9A,B). Images can be ordered from either telescope or both, and combinations of products are also available, including orthorectified products.

QUICKBIRD is also commercially operated, and was launched by Digital Globe in 2001. It is in a synchronous orbit, slightly lower in altitude than IKONOS (450 km), with a 3 to 7 day revisit cycle. It has two sensors, similar to IKONOS but has slightly higher spatial resolution. The single-band 550 nm panchromatic band sensor provides imagery with a spatial resolution of 0.61 m, and the 4 band multispectral sensor (blue, green, red, and near infrared), provides 2.44 m resolution, both at nadir. As with IKONOS, a variety of different image products are available.

The strength of IKONOS and QUICKBIRD lies in their ability to generate high-quality, high-resolution imagery over an area of interest, which can to some degree replace the use of airphotos. IKONOS has an image swath of 11.3 km (nadir), and 13.8 km (26° off-

3. Nadir refers to sensors that point directly downward, whereas off-nadir sensors are slightly side-looking.

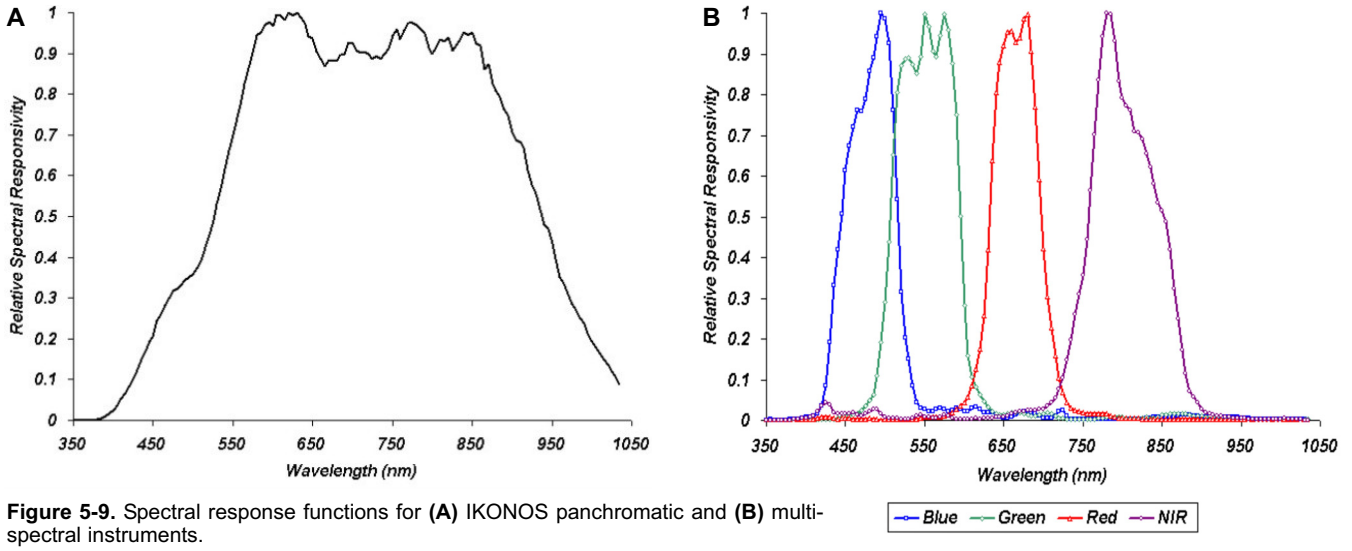

Figure 5-9. Spectral response functions for **(A)** IKONOS panchromatic and **(B)** multispectral instruments.

nadir), and QUICKBIRD has a slightly larger image swath of 16.5 km (nadir). IKONOS and QUICKBIRD images are particularly useful for initial site surveys and fieldwork planning and mapping. Although the imagery from both satellites is of very high quality, the price of the imagery is quite expensive. Acquisition of a new scene may be greater than $3,000. A more cost-effective solution is to order imagery from the data already imaged and contained within the data archive for each instrument, which costs approximately $1,000 or less.

SPOT

The SPOT series of satellites have been operational since 1986 and comprise four satellites culminating in SPOT 5, which was launched in May 2002. The sensors' oblique viewing capability (i.e. steerable beam) offers frequent imaging of a given geographic area as well as stereoscopic viewing. SPOT 5 comprises two panchromatic channels characterized by 5m spatial resolution and three bands in the VNIR with 10 m pixels and one SWIR band with a 20 m pixel and a swath width of 60 km (Table 5-1). The two panchromatic bands can be combined to generate a 2.5µm product that is ideal for mapping and logistical applications.

LANDSAT

LANDSAT 7 ETM+ is the latest in a series of LANDSAT satellites (LANDSAT 1 to 5 and 7) deployed by the United States Government, in conjunction with NASA, USGS, and JPB (Jet Propulsion Laboratory). LANDSAT 5, which is still operational, was followed by LANDSAT 7, which was deployed in April 1999 in a sun-synchronous orbit at an altitude of 705 km. It has a repeat cycle of 16 days and a nominal equatorial crossing of 10 am local time. In 2003, LANDSAT 7 experienced significant problems with its scan-line corrector (SLC), which caused a major disruption in operations. However, a solution was found and the satellite is still operational.

The LANDSAT 7 satellite has an advanced version of the Thematic Mapper (TM) sensor that was deployed on LANDSAT 5, called Enhanced Thematic Mapper Plus (ETM+). The ETM+ sensor comprises three different telescopes, covering a wide range of the EM spectrum. There are four bands in the VNIR (1 – blue-green, 2 – green, 3 – red, and 4 – near infrared), two bands in the SWIR (5 and 7), one band in the thermal infrared (TIR) (6, with data available at low and high gain) and one panchromatic band (8). Band 8 has a spatial resolution of 15 m, bands 1 to 5 and 7 have a spatial resolution of 30 m, and the thermal band (6) has a spatial resolution of 60 m.

The LANDSAT series of satellites provided the first global coverage of optical multispectral, broadband data suitable for geological applications, and have been instrumental in introducing remote sensing as an exploration and mapping tool to the geological community world-wide. The next generation of LANDSAT satellites, termed the LANDSAT Data Continuity Mission (LDCM), has a planned launch date of approximately 2012.

ASTER

The ASTER sensor is one of five different sensors aboard the Terra Satellite, which was produced and launched by a joint venture (TERRA) involving the United States Government (NASA), and the Japanese Government's Ministry of Economy Trade and Industry (METI). ASTER is the flagship sensor on TERRA (the others being CERES, MISR, MODIS, MOPPET), designed as the first stage of a series of new Earth Observation Satellites (EOS) by the United States and international partners. TERRA was launched into a sun-synchronous orbit at Vanenburg Airforce

Base on December 19, 1999 and first started acquiring data on February 24, 2000. TERRA has a 16 day repeat cycle, and an equatorial crossing at approximately 10:30 am (one minute behind LANDSAT and 30 minutes ahead of HYPERION). A PowerPoint presentation included with this Open File provides more information on ASTER and various data and preprocessing issues (Wickert, unpubl.).

The main objective of ASTER was to assist in improving the understanding of local- and regional-scale processes on or near the Earth's surface and lower atmosphere. ASTER is a multispectral sensor with a total of 14 channels acquired by four individual telescopes. There are three bands in the VNIR (1,2,3N), a second back-looking telescope with a single band in the VNIR (3B), six bands in the SWIR (4,5,6,7,8,9), and five bands in the TIR (10,11,12,13,14). Note that the VNIR does not have the blue band found in LANDSAT. The VNIR telescopes have a spatial resolution of 15 m, slightly better than LANDSAT's 30 m, and the SWIR and TIR have a spatial resolution of 30 and 90 m, respectively. The increased multispectral mapping capability provided by the additional SWIR and TIR bands makes it a very interesting tool for RPM applications. Although ASTER has limited spatial and spectral resolution when compared to a hyperspectral sensor, it clearly provides an opportunity to carry out spectral mapping on a regional scale (i.e. 1:250,000), and has been shown in some applications to provide results at scales of 1:50,000 or better (Cudahy, 2002; Oliver and van der Wielen, 2006).

ASTER has also been evaluated directly as a tool for RPM with successful results (Wickert et al., 2005; see also the PowerPoint presentation included with this volume). ASTER is a significant sensor for RPM as it offers an increased number of channels of narrower bandwidth in the SWIR and TIR compared to LANDSAT (Fig. 5-8). The narrower bandwidth makes it possible to resolve between different spectral responses in the SWIR that are grouped together into two broad bands in LANDSAT. Thus ASTER can resolve between different mineral groups (i.e. different groups of clays) that may be associated with specific lithologies or alteration zones associated with a variety of mineral deposit types. Although this is still much less than the ability to differentiate between different mineral species, which is part of the potential of hyperspectral sensors (Fig. 5-5), the global availability of ASTER as a satellite-based platform and it's low cost ($US 80/scene) makes ASTER an excellent exploration and mapping tool for geological applications. Many examples of how ASTER data can be utilized in RPM applications are illustrated in later in the volume (see the PowerPoint presentation included with this volume).

HYPERION

HYPERION, the first publicly available satellite-based hyperspectral sensor, was launched by the United States Geological Survey in 2000. It was built as a satellite version of the airborne TRWIS sensor. HYPERION is a 'pushbroom' hyperspectral sensor with a total of 220 channels ranging from 0.35 to 2.5 μm, with very narrow bandwidths (10 nm), and a spatial resolution of 30 m. HYPERION consists of two spectrometers, one over the VNIR (357-1055 nm), and the second over the SWIR (851-2576 nm). Of the 220 total bands, only 180 bands can be used due to spectral overlap and misalignment or missing data. Overall, the narrow bandwidth provides for excellent spectral resolution, providing the capability to discriminate between different minerals spectrally, even though the pixel size is the same as LANDSAT (30 m). With its increased channels and associated high spectral resolution, this sensor is a major technological step-up from multispectral sensors, as the sensor is capable of mapping mineral end-members.

Unfortunately, HYPERION data has a very low signal-to-noise ratio (S/N) relative to that of a typical airborne sensor such as HyMap. The S/N for HYPERION is on the order of 50:1, and is particularly low over the SWIR part of the electromagnetic spectrum. This contrasts to a reported S/N for HyMap of more than 500:1. This means that more subtle spectral-absorption features will be more difficult to differentiate in HYPERION data, and that good illumination conditions (little to no cloud, high sun angle) are of particular concern for the acquisition of this imagery.

Airborne Sensors

Several airborne hyperspectral sensors are available that have provided limited coverage of the Canadian landmass. Only selected areas have been covered by hyperspectral data, including parts of Baffin Island (available through the Geological Survey of Canada and the Canada Centre of Remote Sensing (CCRS) and the Sudbury Basin in Ontario (available through CCRS).

The SFSI sensor is a pushbroom imaging spectrometer. It has 234 bands, covering the range of 1219 to 2437 nm (1.219–2.437 μm), with an average spectral sampling interval of 5.2 nm, and a nominal bandwidth of 10 nm (Neville et al., 2003). The CASI sensor acquires data in up to 228 spectral channels between the wavelengths 400 to 1000 nm. The AVIRIS sensor is operated by the NASA Jet Propulsion Laboratory (JPL) and collects 224 bands between the wavelengths of 400 to 2500 nm. The PROBE sensor, developed by Earth Search Sciences Inc., collects 128 channels in the 400 to 2500 nm range. The PROBE can be flown over a range of altitudes providing imagery ranging from 1 to 10 m and swath widths from 1 to 6 km. A case study

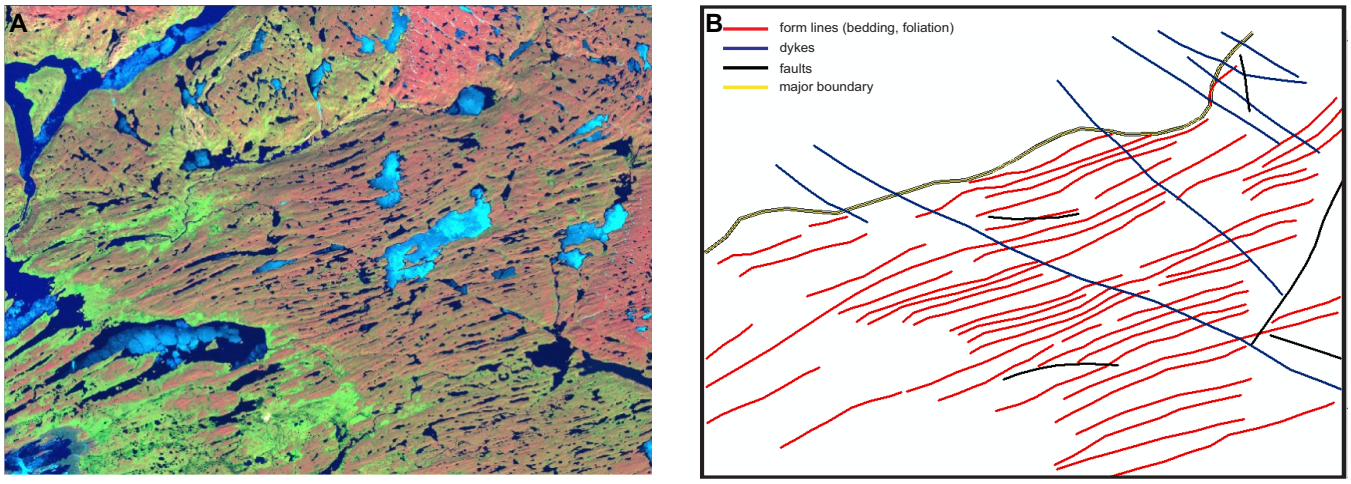

Figure 5-10. Structural interpretations derived from LANDSAT data over central Baffin Island, Nunavut, Canada. **(A)** This is a LANDSAT TM image of central Baffin Island centred over the Paleo-Proterozoic Piling Group. It is a colour composite ternary image in which TM bands 7, 5, and 2 have been displayed in red, green, and blue colours, respectively. Bands 7 and 5 are positioned in the short-wave infrared portion of the electromagnetic spectrum and record energy that our eyes cannot see, whereas band 2 records reflected green energy from the visible portion of the electromagnetic spectrum. When the 3 bands are displayed as a colour composite, it provides an image with a wealth of detail on the surficial and bedrock geology of the Earth's surface. In this image, the east-northwest to west-southwest ridges, which reflect turbidite bedding, can be clearly seen in the bottom two thirds of the image. Some tight folds can also be seen in these rocks. The east-northwest to west-southwest contact between the Piling Group and Archean granitoid rocks in the top portion of the image marks a dramatic change in pattern between the two rock units. The granitoid rocks are massive and specific intrusions are circular in shape. A large northwest-southeast-trending dyke, which is expressed as a belt of linear lakes, can be seen running from the lower right to the upper left of the image. Many fractures (lineaments) can also be seen in the image, the majority of which trend northwest-southeast. The red areas represent exposed and weathered bedrock, the green areas are vegetation, and the blue are lakes. At the time of image acquisition, ice occupied many of the lakes, which is evidenced by the cyan colours. The image dimensions are approximately 40 by 20 km. **(B)** A simple structural interpretation of LANDSAT image.

presented at the end of this manual presents a mapping example of airborne PROBE data in Baffin Island (see Case Study 3, this volume). Generally, hyperspectral data requires a significant amount of preprocessing before the data are usable (White et al., 2004, Hitchcock and White, 2007).

DATA INTERPRETATION FOR GEOLOGICAL APPLICATIONS

Structure

Bedrock

Optical imagery can be used to assist in mapping geological structures. Lineament mapping on remotely sensed data has long been undertaken by geoscientists. However, the art of lineament mapping can be taken further by employing simple principles of visual interpretation (especially pattern, shape, and context) in concert with field observations (if available) and the and greatly improved with the inspection of magnetic data to add some measure of geological calibration to the lineament interpretation (Fig. 5-10).

Factors that should be considered when using optical imagery such as LANDSAT for structural mapping include

- season of acquisition geological terrain,
- biophysical environment, including degree of surficial cover,
- degree of preprocessing (georeferencing, etc.).

Winter imagery offers pseudo 3-D enhancement of the terrain due to lower sun angles that can increase surface shadowing, which may be useful for structural interpretations (Fig. 5-7). Fall imagery is often a preferred choice in Boreal forest terrain due to the maximum differences in vegetation, as senescence can in turn enhance different geological structures. However, above the tree line, summer imagery may be preferred due to the absence of appreciable amounts of snow cover. If LANDSAT data is to be used, particularly if *free* data is preferred, then the geologist may not have a choice and will have to make due with what is available on the *Geogratis* website (http://geogratis.cgdi.gc.ca) or the TerraLOOK (United States Geological Survey – USGS) website (http://glovis.usgs.gov).

The nature of the geological terrain is obviously of particular importance as much more structural information can often be extracted from older complex terrains than younger flat-lying sedimentary terrains (Fig. 5-11). The amount of structural information that can be

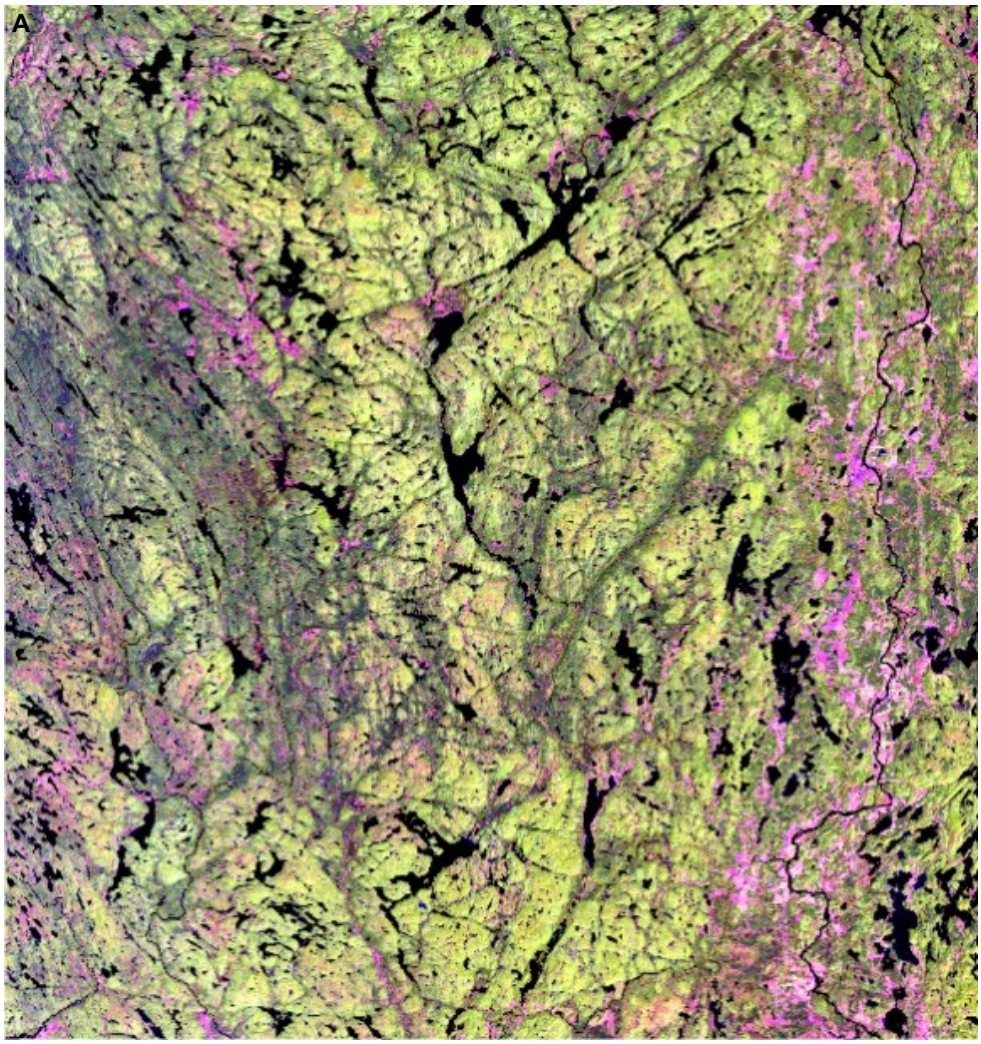

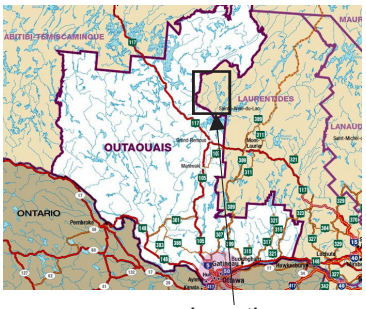

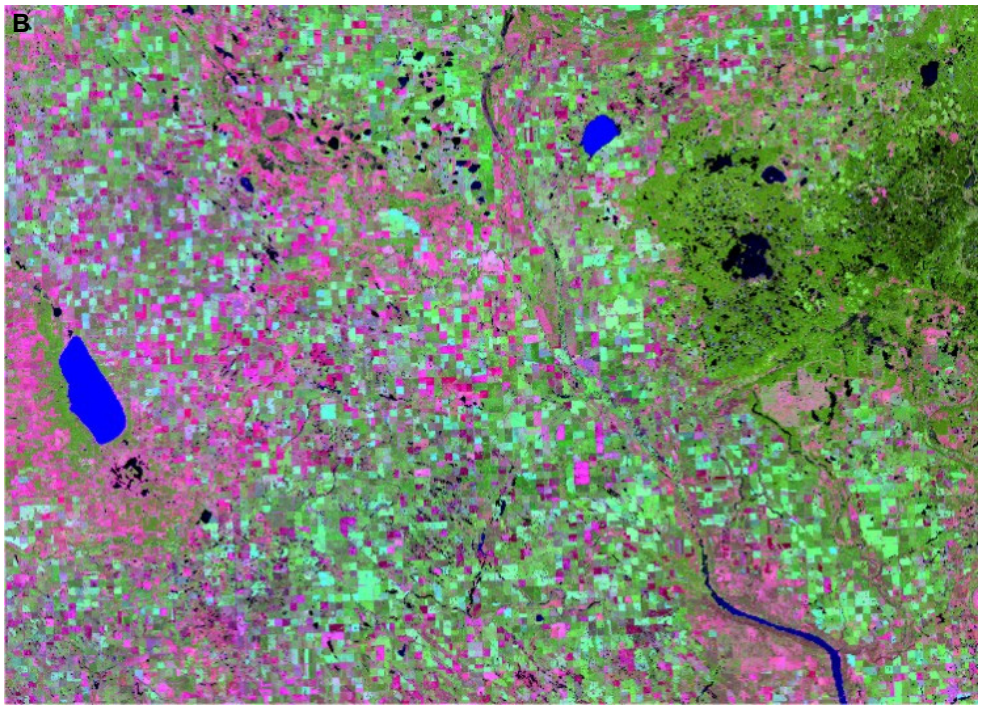

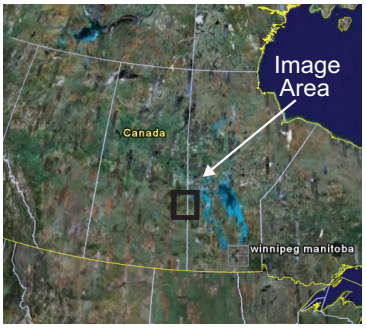

Figure 5-11. LANDSAT images of different geological environments. **(A)** Bands 542 red-green-blue colour composite of the Grenville tectonic province north of Ottawa. **(B)** Bands 542 red-green-blue colour composite of the western Canada sedimentary basin along the Saskatchewan - Manitoba border, northwest of Winnipeg. The image covers approximately 100 by 80 km. The Grenville image offers a wealth of structural information (folds, faults, lineaments, lithological contacts), as glaciers have scoured out and enhanced zones of weakness that reflect various geological structures, many of which are expressed as distinct topographic features. The basin scene, which is characterized by flat topography, horizontal lithologies, and agricultural land, offers less information on geological structures.

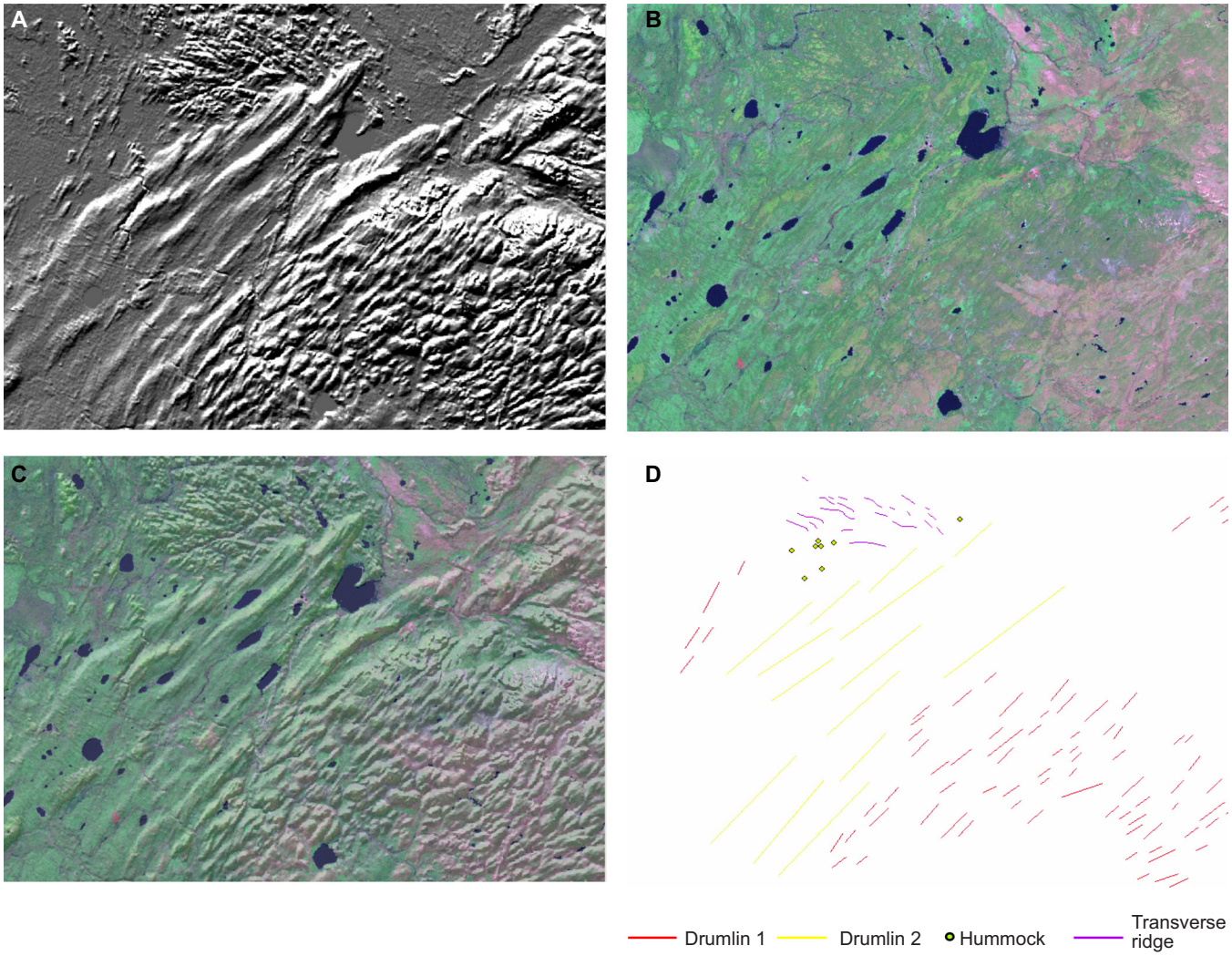

Figure 5-12. Imagery used for mapping glacial features, Alberta, Canada. **(A)** Shaded relief DEM – shaded from the northwest – SRTM 3 arc second Space Shuttle data. **(B)** LANDSAT 742 (RGB) of same area. **(C)** Fused (combined) DEM and LANDSAT images. **(D)** An interpretation of the glacial features and landforms. The shaded DEM derived from SRTM data (shuttle radar) offers a clear portrayal of glacial landforms (see (D)) and when combined with LANDSAT data offers a unique image in which both topographic and spectral characteristics of the landscape are evident, allowing for a detailed interpretation of glacial-flow features and stream-lined landforms.

interpreted from optical imagery is also affected by the type, thickness, and extent of surficial cover and vegetation.

Raw data requires preprocessing such as georeferencing to a map projection if it is to be used synergistically with other geoscience datasets within a GIS. However, if LANDSAT data is to be used then this can be downloaded for free in an orthorectified format in either a UTM or Lambert conformal projection from Geogratis.

Landforms and Glacial Structure

Optical imagery can provide useful information on terrain morphology, glacial landforms, and stream-lined landforms that reflect glacial dispersal directions (Fig. 5-12C). The degree of topographic and/or morphologic enhancement will depend on the season (see above) and latitude, as variations in both factors will result in different sun elevation and azimuth angles. Combining (fusing) this data with digital elevation data (DEM) often results in a superior image (Fig. 5-12B) in which glacial landforms are clearly seen.

Simple visual photogeological interpretation of enhanced imagery can be undertaken, as shown in Figures 5-10 and 5-12, or automatic and semi-automatic techniques can be employed to extract linear features (i.e. glacial lineaments), however this approach entails input from the geologists to screen out non-geological lineaments (Fig. 5-13).

Lithology

Mapping lithology based on optical imagery can be problematic due to surficial and vegetation cover, which can obscure the underlying rock. However, often the surficial and vegetation cover can be used as a proxy for mapping the underlying bedrock as certain

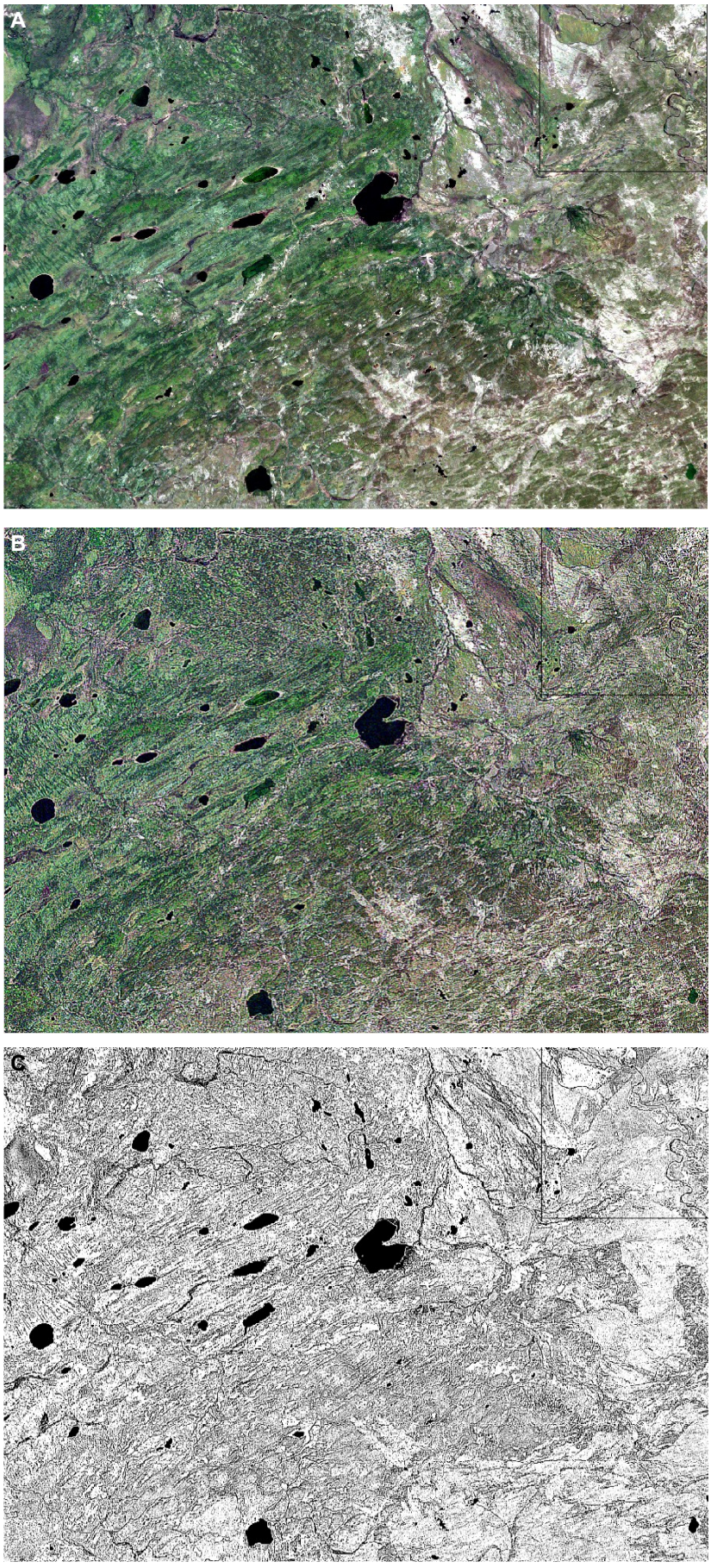

Figure 5-13. Spatial frequency enhancement of LANDSAT data from the same location as Figure 5-12. **(A)** LANDSAT 742 (RGB) image. **(B)** High- frequency enhancement (high-pass spatial filter) of LANDSAT image shown in (A). **(C)** Linear features derived from spatially enhanced LANDSAT image. The extraction of linear elements in the LANDSAT image (shown in C) must be screened by the geologist to delete features that may be cultural in origin, i.e. roads, field boundaries. This image may be vectorized and imported to GIS, forming a interpretative layer in a regional geological GIS database.

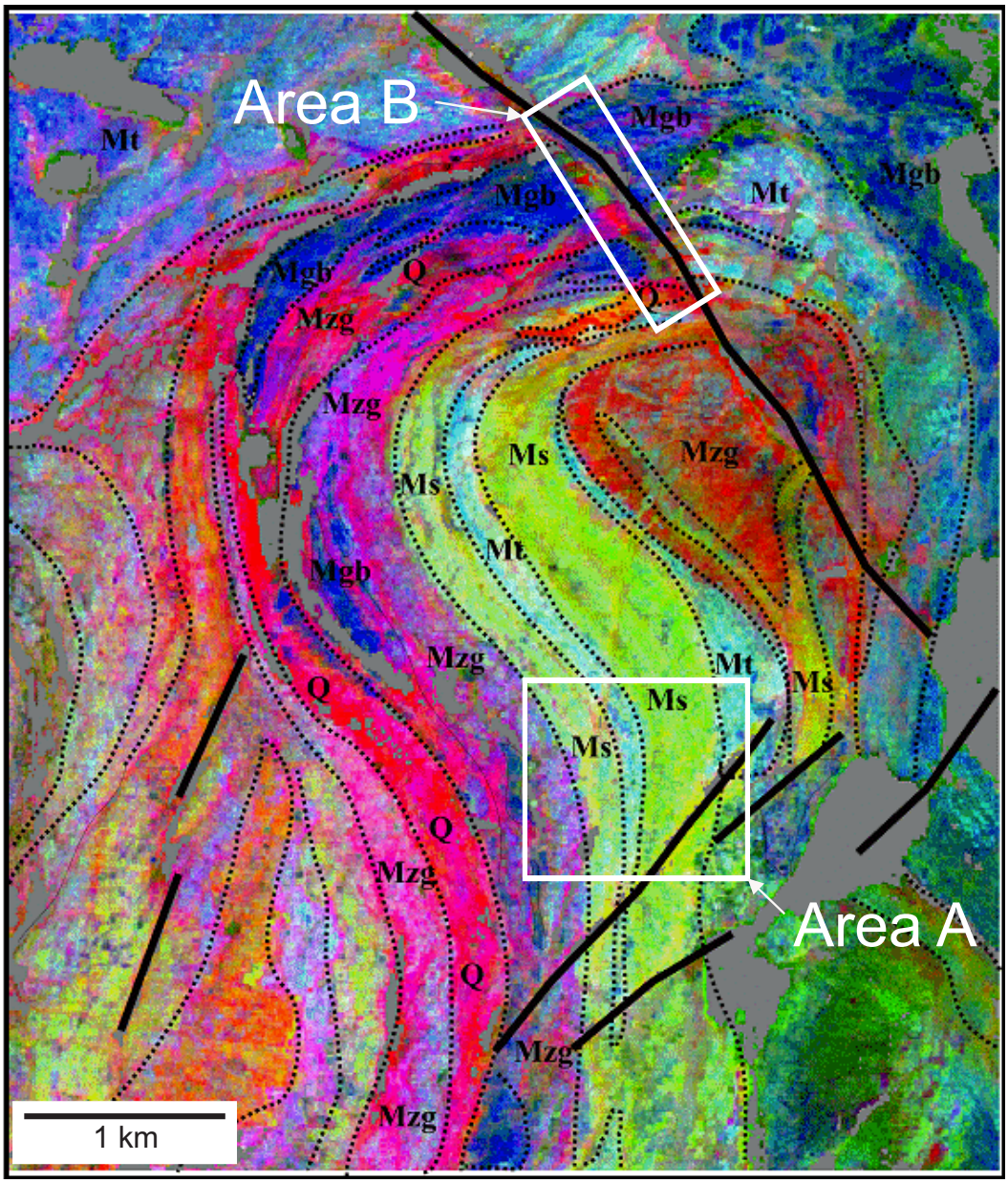

Figure 5-14. An enhanced hyperspectral image derived from airborne probe data acquired over southeast Baffin Island during August 2000. The image is approximately 6 km across and 8 km long. The various colours of the enhanced image correlate with different rock units. The dark blue areas represent vegetation, which grows preferentially over metagabbro rocks; therefore, the vegetation in this area can be used as a mapping proxy for these rocks. The hyperspectral imagery was enhanced using a Minimum Noise Fraction (MNF) transform. (Mgb – metagabbro, Ms – metasediments, Mt – metatonalite, Mzg – monzogranites, Q – quartzite, black lines represent interpreted faults).

vegetation species will grow preferentially over certain rock types or the weathered residue of the underlying rock, assuming this has not been transported by glaciers (i.e. residual) and reflects in part the bedrock composition (Fig. 5-14). Another approach is to mask out areas of surficial and vegetation cover using image analysis masking techniques concentrating analysis on the exposed bedrock or weathered residual material (Fig. 5-15).

The Canadian North has relatively good exposure, which makes the mapping of lithology possible, certainly more so than Boreal environments further south. However, lichen cover can be problematic as it tends to dampen spectral signatures of rocks and sometimes masks important features of individual spectra. Furthermore, optical sensors respond to surface characteristics only, as previously discussed; therefore spectral signatures often reflect the weathered residue from the underlying bedrock as opposed to the mineral constituents of the rocks themselves. In many cases this actually facilitates the discrimination of the rocks as the rocks are highlighted by differences in the associated iron and clay weathering products (Fig. 5-16). Thus spectral signatures often represent the residual by-product of a lithology as opposed to the actual minerals comprising the rocks. However, many rocks cannot be distinguished solely on their unweathered spectral profiles; hence this is a viable and valuable approach.

Regional differences in lithologies (i.e. basement versus supracrustals) can often be seen on moderate-resolution sensors such as LANDSAT (Figs. 5-17, 5-18)

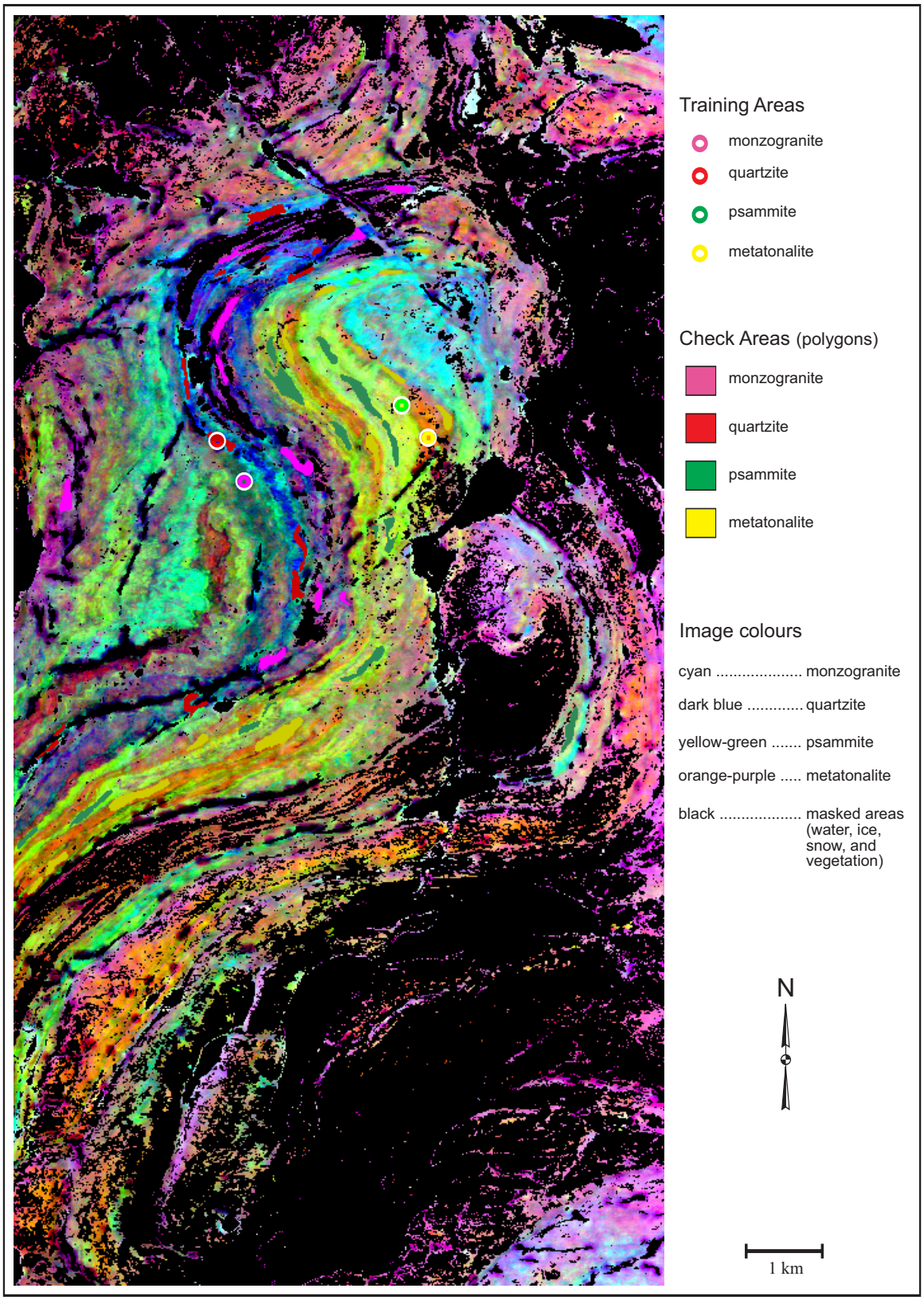

Figure 5-15. An example of an enhanced and masked hyperspectral image of southeastern Baffin Island, Canada. Same area as is shown in Figure 5-14 except with a larger regional extent (6 by 13 km). The black areas represent vegetation, snow, and ice that have been masked using spectral and image-processing techniques, which allows further analysis and processing to be concentrated on areas of exposed or weathered bedrock directly. Training areas are representative areas of different lithologies on the ground. These areas are used to extract statistics (spectral reflectance curves) of each rock unit from the hyperspectral data that can be used for classification. Check areas are areas on the ground that represent known rock units and are used to verify the classification maps derived from the spectral data obtained from the training areas.

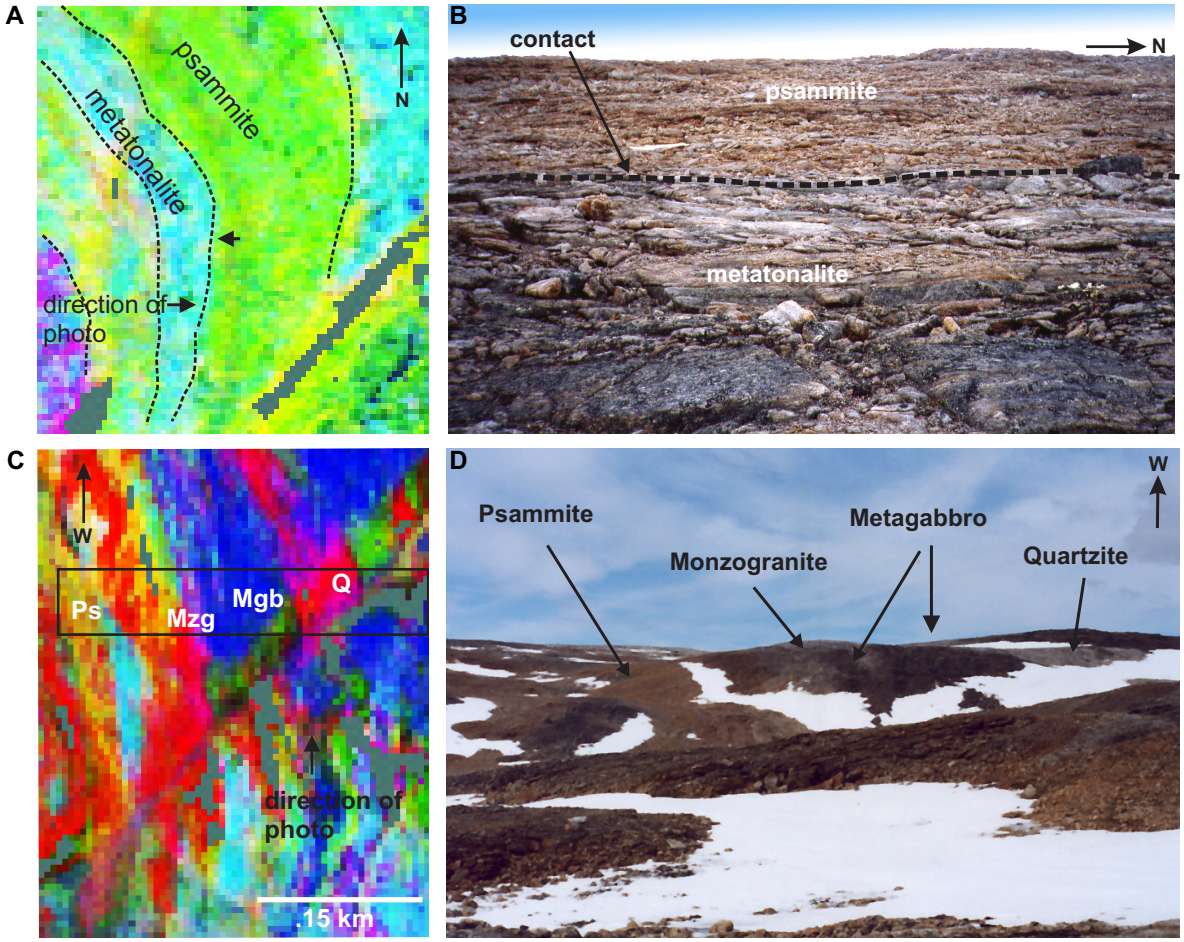

Figure 5-16. Portions (A and B) of the hyperspectral data shown in Figure 5-14 (see boxes on Fig. 5-14 for exact location showing various lithologies). **(A)** In Area A, the colours clearly correlate with psammite, metatonalite, and monzogranite. **(B)** A field photograph showing the contact between metatonalite and psammite (see (A) for location of photo). Note the difference in weathering colour as the psammites contain much more iron (weathered pyrite and Fe-garnet) and weather to a rusty orange colour. **(C)** In Area B, the colours clearly correlate with psammite, metatonalite, and monzogranite. **(D)** A field photograph showing the contacts between psammite, monzogranite, metagabbro, and quartzite. See (C) for location and direction of photograph. Note the difference in weathering colour, which the hyperspectral sensor can image clearly. See Harris et al. (2005, 2006a,b) for more details.

on the basis of various combinations of bands in ternary (colour composite) images. However, higher spatial and spectral resolution sensors (i.e. hyperspectral), can obviously offer more detailed information on lithology simply due to the increased resolution (Fig. 5-19, 5-20).

Surficial Units

Vegetation (Fig. 5-21) and wetlands can be easily identified on optical imagery as can bedrock outcrops (Fig. 5-22) in most cases, although the spectral signatures of outcrop can be confused with other features such as exposed eskers and other glacial features. Various image analysis methods for outcrop identification can be employed, ranging from empirical ratios to supervised classification (see below). In addition, areas of fire burns can be identified, which may reveal areas where the probability of outcrop is higher thus facilitating field traversing (Fig. 5-23).

Surficial materials can often be recognized on LANDSAT imagery through simple visual interpretation based on tones and/or colour, shape, form, and texture and also through classification techniques (see below). Maps of surficial units can be produced that compare favourably to mapped surficial units and, depending on the scale, can sometimes offer more information on surficial units than that shown on maps (Fig. 5-24).

Logistics

Optical imagery can also be used to help in field planning and logistics, although spatial resolution may be a limitation when compared to traditional airphotos. However, with the development of sensors with extremely high spatial resolution from space (i.e. IKONOS, QUICKBIRD), logistical planning from satellite-based data is now possible (Fig. 5-6). The major limitation with this type of imagery is the generally high cost when compared to the purchase of existing airphotos.

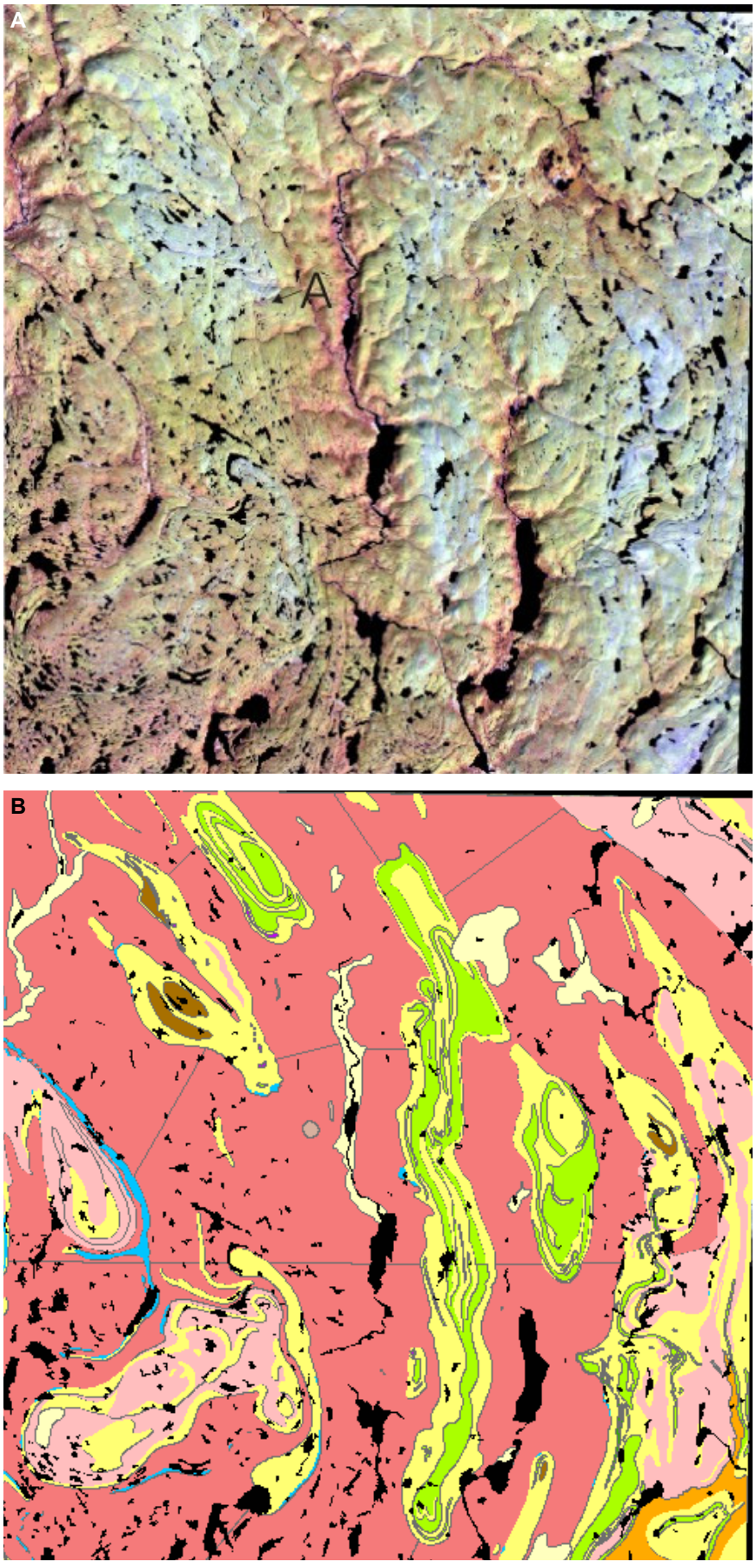



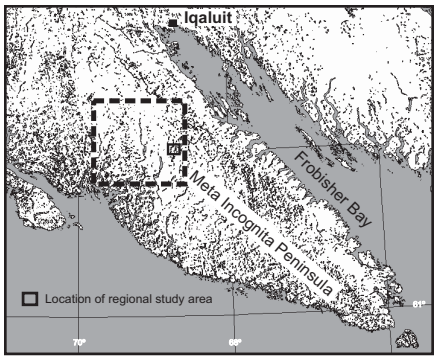

Figure 5-17. LANDSAT image of southeast Baffin Island, Canada and associated geological map. **(A)** LANDSAT 743 (RGB) colour composite image. **(B)** Geological map (St-Onge et al., 1998). Note that the supracrustal rocks, which define broad doubly plunging folds, are clearly displayed in shades of blue and cyan whereas the basement rocks are displayed in shades of green. Vegetation is red. Despite the low spectral resolution of LANDSAT data, these rock units appear very differently from a spectral point of view, thus allowing regional mapping of the major rock units as well as the pattern and nature of the folds. A small outcrop of carbonate rocks can also be clearly seen (Area A). LANDSAT data ares especially useful for mapping carbonate-bearing rocks due to their unique signature (even at low spectral resolutions) in the SWIR portion of the EM spectrum.

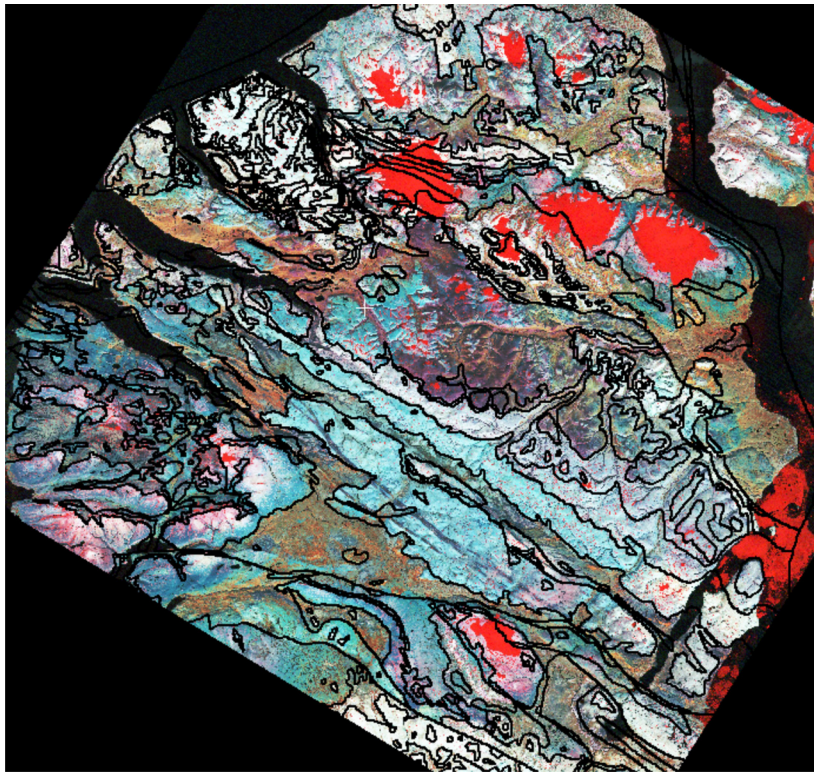

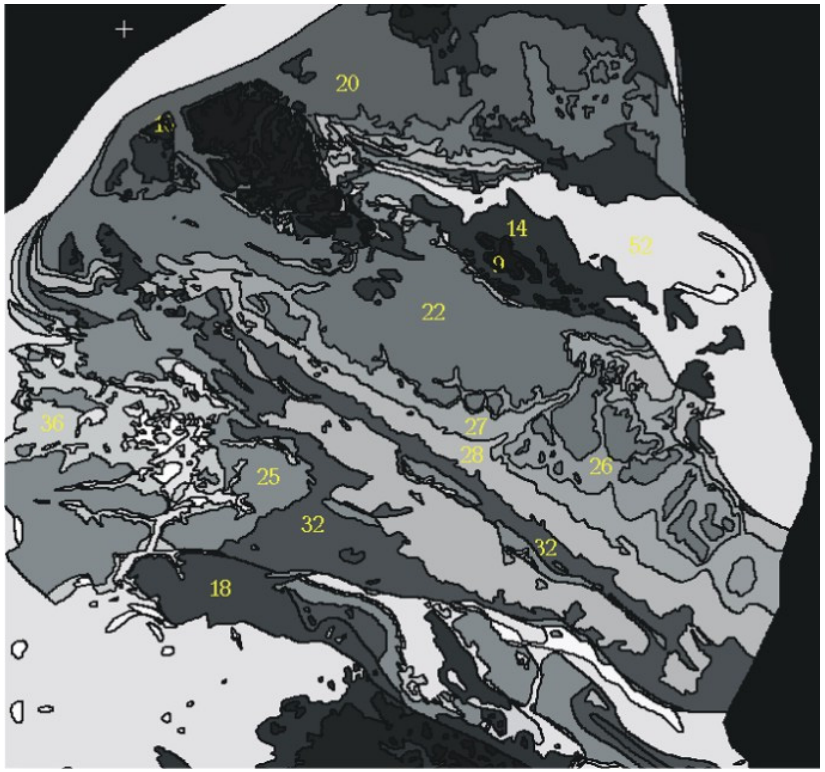



Figure 5-18. LANDSAT image of northern Baffin Island, 543 (RGB) colour composite image of an area approximately 125 by 125 km. Differences in spectral responses clearly reflect lithological differences (red is snow and ice). The accompanying table shows unit (lithological descriptions) for geology. The index number refers to a number on the geological map. For further details see Rencz et al. (2000).

Age	Group	Formation	Map Unit	Index	Lithology
Paleozoic	Admirality Group	Frobisher Bay	Ofb	9	limestone
		Ship Point	Osp	10	sandstone, dolomite
		Turner Cliffs	COtc	14	dolostone
Proterozoic	Bylot Supergroup				
	Nunatsiak Group	Elwin subgroup	mPBel	20	feldspathic sandstones, quartz arenite
				25	
		Strathcona Sound	mPBss	22	undivided, dolostone, shale, sandstone
		Athole Point	mPBap	26	limestone
	Uluksan Group	Victor Bay	mPBvb	27	undivided limestone and shale
		Society Cliffs	mPBsc	28	dolostone
	Eqalulik Group	Fabricious Fiord	mPBff	18	feldspathic sandstones, arkose (more feldspar)
		Arctic Bay	mPBab	32	shale
Archean		Nauyat	mPBna	36	basalt, siltstone
	Mary River Group	Mary River (undivided)	AMu	52	mainly basalts
		Plutonic rocks	Agr	68	granitic

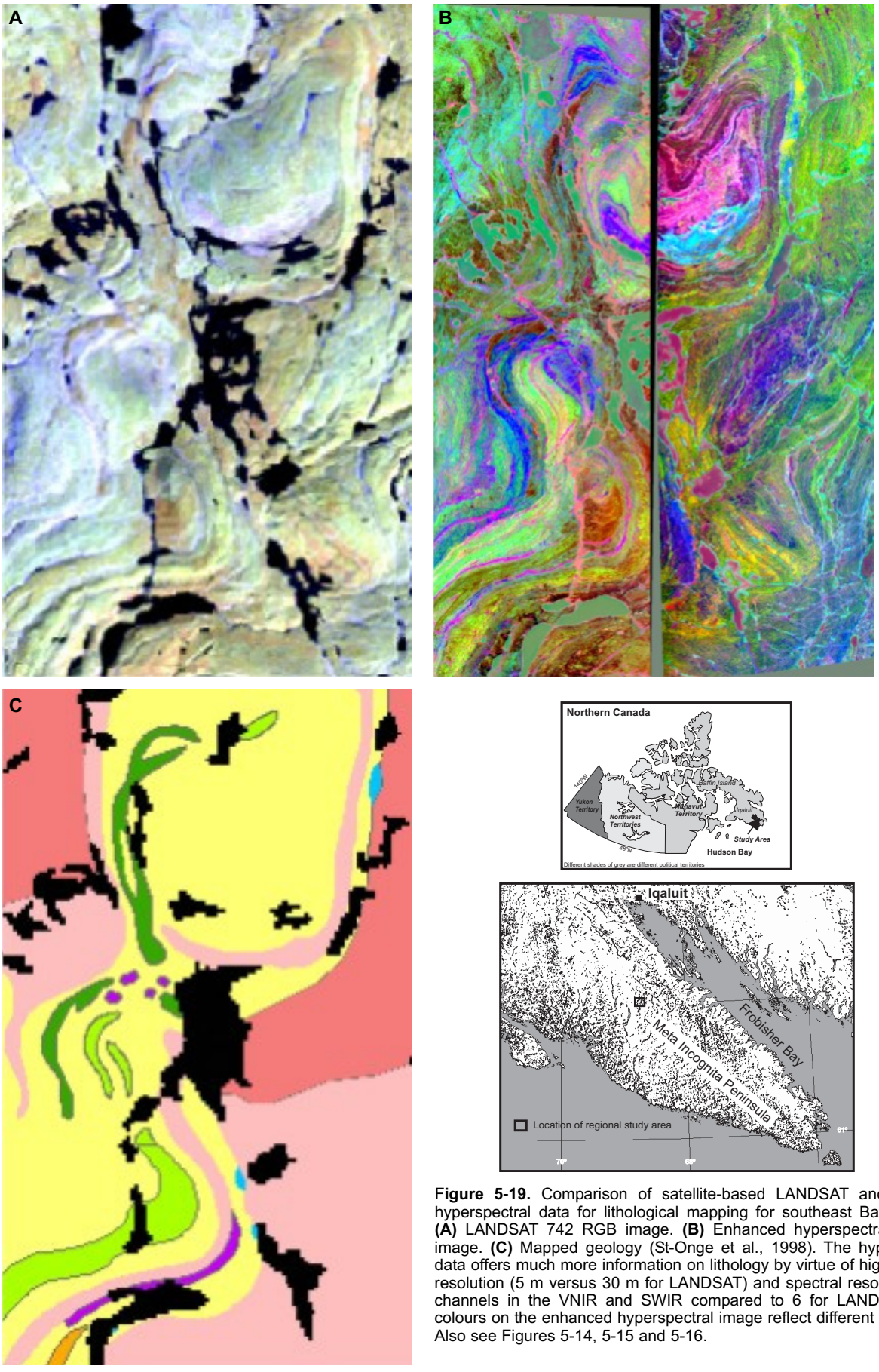

Figure 5-19. Comparison of satellite-based LANDSAT and airborne hyperspectral data for lithological mapping for southeast Baffin Island. **(A)** LANDSAT 742 RGB image. **(B)** Enhanced hyperspectral PROBE image. **(C)** Mapped geology (St-Onge et al., 1998). The hyperspectral data offers much more information on lithology by virtue of higher spatial resolution (5 m versus 30 m for LANDSAT) and spectral resolution (128 channels in the VNIR and SWIR compared to 6 for LANDSAT). The colours on the enhanced hyperspectral image reflect different lithologies. Also see Figures 5-14, 5-15 and 5-16.

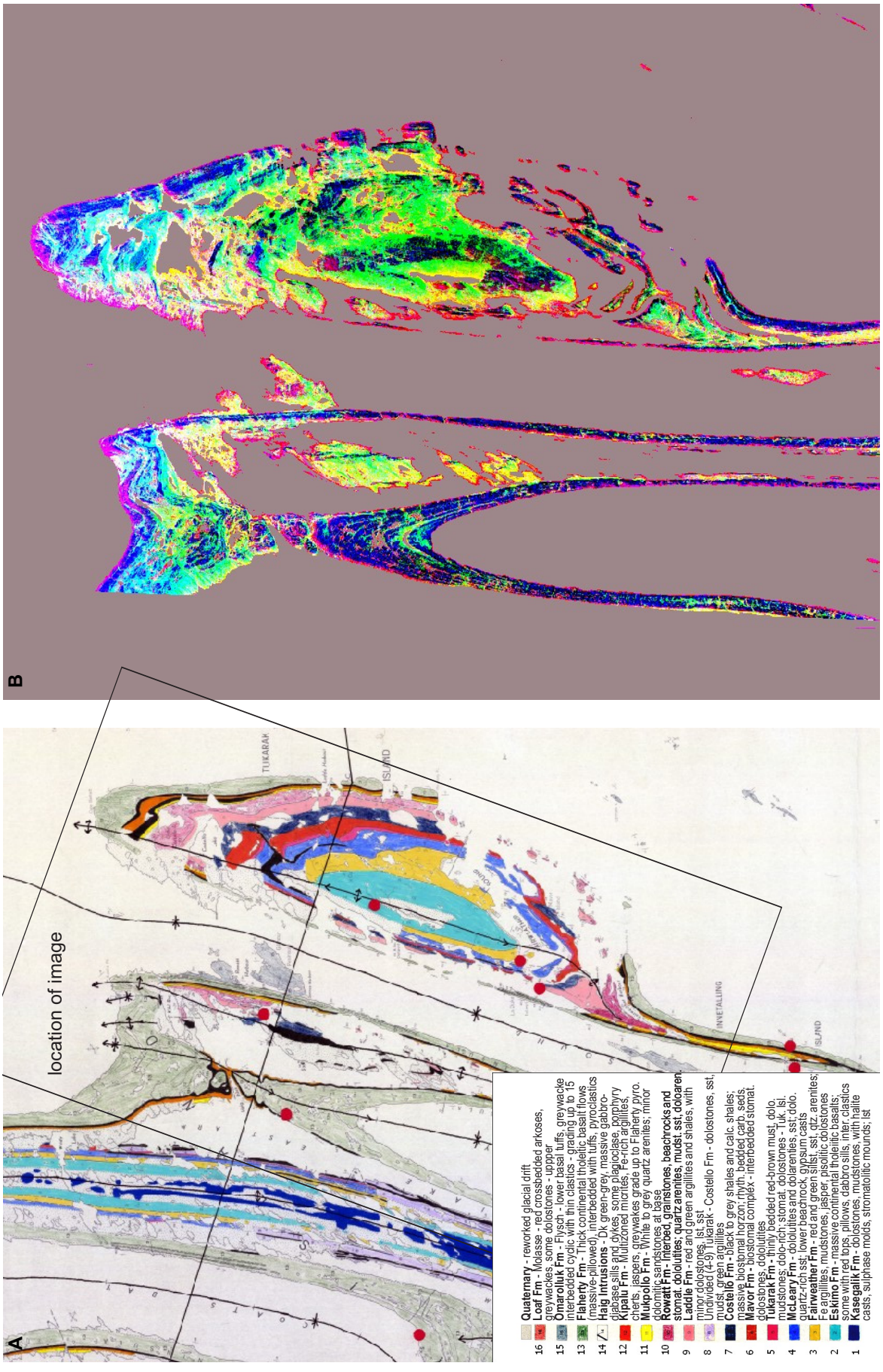

Figure 5-20. A comparison between mapped geology and an ASTER colour composite image of a portion of the Belcher Islands. **(A)** Mapped geology (Jackson, 1960), focused on Tukarak Island. **(B)** MNF transformation of the 6 ASTER SWIR bands 4 thru 9. The image highlights the bedrock geology of the Belcher Islands. In this image, the focus is Tukarak Island. In the geological map, produced by Jackson (1960), some of the surface is mapped by overburden and the bedrock geology is not interpreted. However, this is overcome by the use of the ASTER SWIR imagery. Although the contacts are a little less distinct where there is overburden, it is still possible to differentiate the bedrock lithology. This illustrates that ASTER imagery is useful as a relatively detailed regional mapping tool, despite its 30 m resolution. Generally it is said it is good for mapping at approximately 1:50 000 scale, but this illustrates that in some cases with little overburden, the detail of mapping may be much more. For this processing, the data were first cross-talk corrected and the water was masked, followed by the forward MNF transformation being applied.

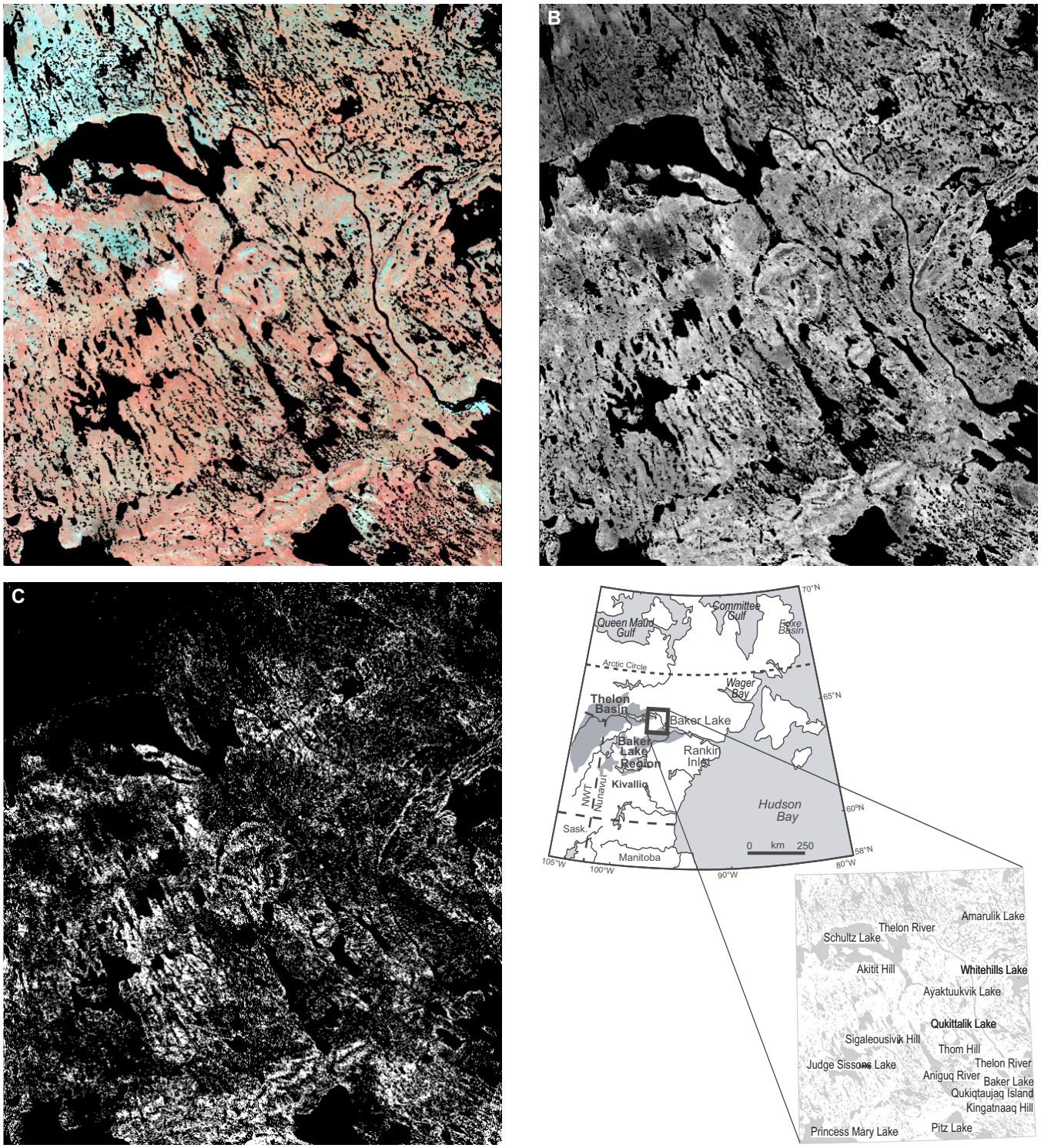

Figure 5-21. Vegetation identification on LANDSAT imagery over Shultz Lake, Northwest Territories, Canada (NTS 66a map sheet). **(A)** False colour composite image -432- (RGB) with vegetation in red, and outcrop and weathered rubble in blue. **(B)** 4/3 ratio image. This particular ratio enhances vegetation (white tones) by maximizing the difference between extreme infrared reflectance and red absorption by vegetation. **(C)** Threshold of 4/3 ratio image producing a binary map of vegetated areas.

PROCESSING

Visual Enhancement

Contrast enhancement involves stretching the distribution of the data (histogram) to utilize the full 8-bit display space (Figs. 5-25A,B, 26A,B) thus improving the contrast of the image, which in turn can help to distinguish various geological features. In addition, spatial-filtering (edge enhancement and high-frequency enhancement) techniques are useful for highlighting geological structures (Figs. 5-25C,D, 5-26D).

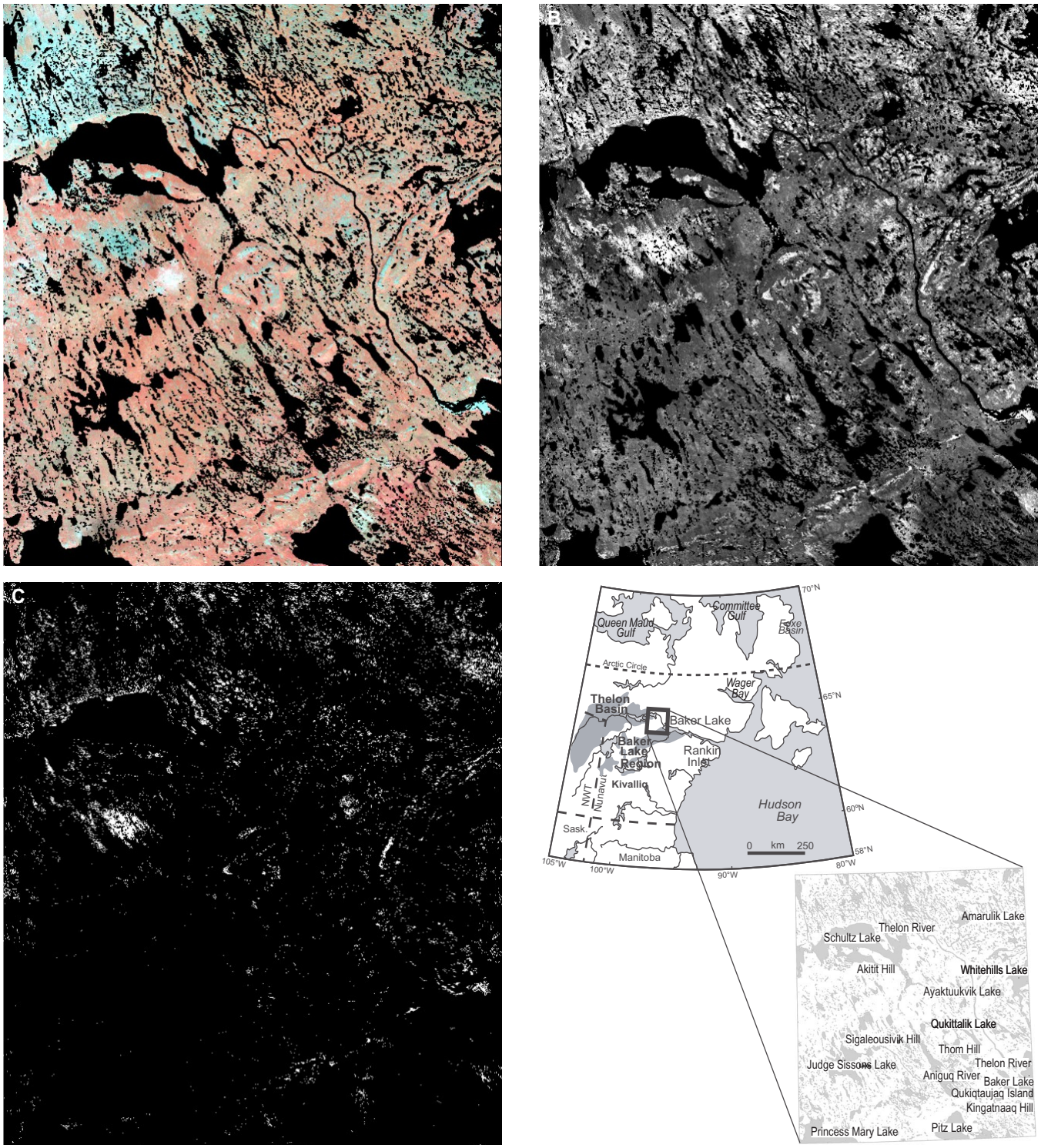

Figure 5-22. Example of outcrop identification on LANDSAT imagery over Shultz Lake, Nunavut, Canada (NTS66a map sheet) **(A)** False colour composite image - bands 4, 3, 2 (red, green, blue) with vegetation in red, and outcrop and weathered rubble in blue. **(B)** 7/4 ratio image. This particular ratio enhances outcrops (white tones) by maximizing the difference between infrared reflectance and infrared absorption of exposed ground. A 1/4 ratio could also be used except in hazy atmospheric conditions where band 1 (blue energy) will be preferentially scattered, thus increasing the overall albedo of the image and reducing the overall effectiveness of the ratio for discriminating outcrop. **(C**) Threshold of 7/4 ratio image producing a binary map of outcrop areas.

Ternary images offer significant advantages over single channel black and white displays for geological interpretation as they combine three channels of often complimentary information, which results in a better portrayal of geological features (Figs. 5-2, 5-25). Some of the common colour combinations of LANDSAT data used for geological interpretation in Northern environments are listed in Table 5-2.

Table 5-2. Ternary for best combinations for geology from LANDSAT imagery.

Feature	Best Ternary Red-Green-Blue Band Colour Combinations	Comments
Vegetation	Bands 4, 3, 2 – false colour composite (FCC)	Vegetation appears red
	Bands 3, 2, 1 – natural or true colour composite (TCC)	Vegetation appears green (natural to our eyes)
Outcrop	Bands 3, 2, 1	Outcrop appears white
	Bands 4, 3, 2	Outcrop appear blue to cyan
	Bands 7, 4, 2	Outcrop appears pink
Roads / Infrastructure	Bands 3, 2, 1	Roads appear white
	Bands 4, 3, 2	Roads appear cyan

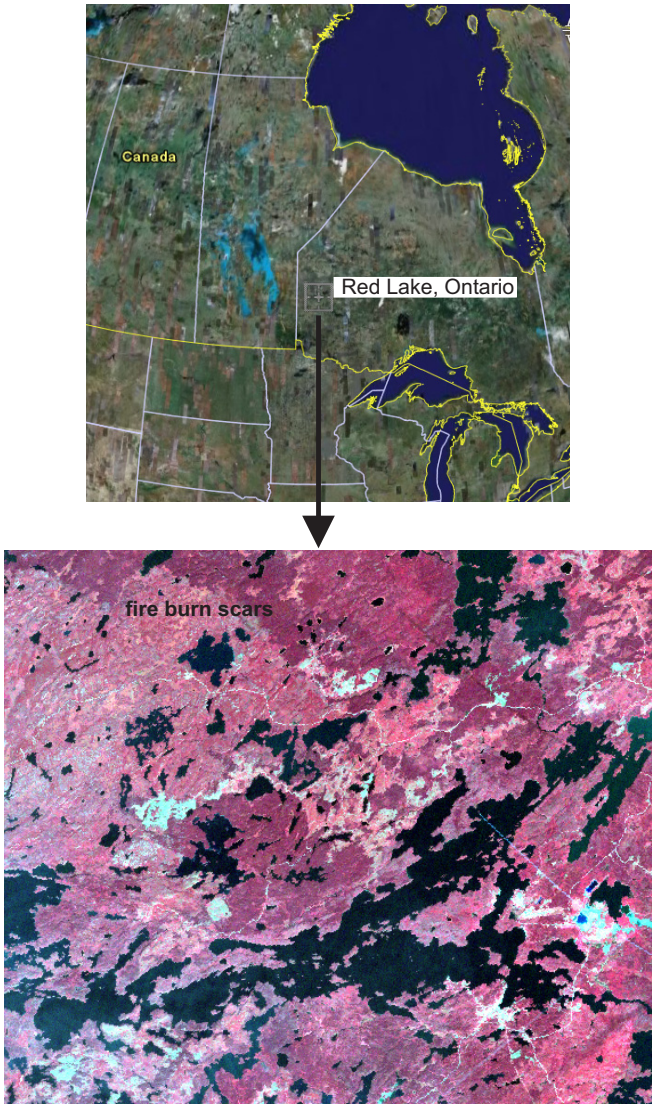

Figure 5-23. LANDSAT false colour composite – bands 4, 3, 2 (red, green, blue) – of Red Lake Ontario showing fire burns (scars) where the probability of finding outcrop may be higher. The burn scars are shown in various shades of red and reflect different stages of regrowth.

Band ratios are extremely useful for highlighting the spectral differences (i.e. reflection versus absorption) for various surface features including vegetation (Fig. 5-21B), iron- and clay-bearing rocks (Fig. 5-27), and bedrock outcrop (Fig. 5-22B). Band ratio images can be used to highlight or identify these features for further spectral and spatial analysis, or used as masks to exclude areas from further processing and analysis.

Multivariate Processing

Optical multispectral imagery, such as LANDSAT, is amenable to multivariate processing. Principle component analysis (PCA) is a common transformation that can be applied to optical data and serves as a valuable enhancement technique (see Chapter 2). PCA describes the distribution of multivariate data using a new set of transformed axes (components) that are linear combinations of all the input bands. Each component represents a mix of the input bands (the influence of each band is measured by an eigenvector), and can be displayed as an individual black and white image or three components can be displayed as a red-green-blue (RGB) ternary image (Fig. 5-28). The resulting component images can provide enhancement of individual features within the terrain (i.e. vegetation, moisture regimes, and rock and surficial units) (Fig. 5-28).

Data Fusion

Data fusion is now a standard visualization technique for combining various geoscience data sets. Fusion is accomplished by using a number of image-processing techniques (e.g. colour space transforms, arithmetic operators, wavelet transforms), the aim of which is to produce an enhanced image suitable for visual interpretation in which the fused data compliments one another. Fused imagery provides an image that is greater than the sum of its individual inputs. For example, LANDSAT can be fused with digital elevation data (DEM), offering an image that shows spectral patterns by variations in hue but with enhanced topography, which is useful for highlighting geomorphic patterns (Figs 5-12, 5-29B). The DEM data may also be used to construct a 2.5-D visualization of the terrain (Fig. 5-29C). LANDSAT data may be fused with thematic data (i.e. geological map data) (Fig. 5-29D) so that the mapped patterns can be directly compared to the spectral patterns seen on the LANDSAT data. Alternatively, LANDSAT data can be merged with geophysical data (Fig. 5-30), in order to compare magnetic patterns with topographic and spectral patterns.

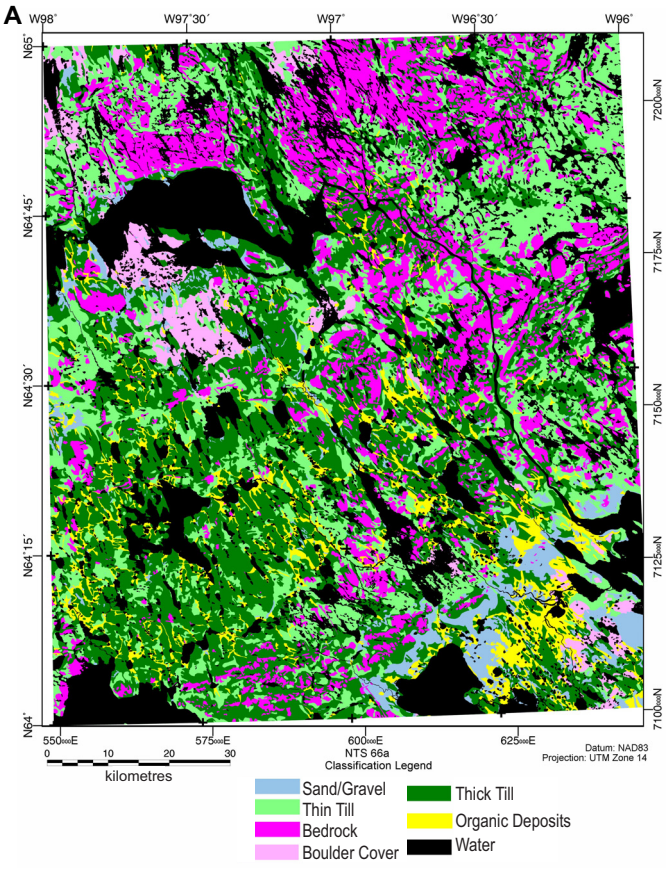

Figure 5-24. Classification of LANDSAT data into generalized surficial units for Shultz Lake, Nunavut (NTS 66a map sheet). **(A)** Supervised classification based on training areas. **(B)** Generalized surficial map. The map in (A) represents a surficial materials map based on differences in spectral signatures for each generalized surficial unit derived from LANDSAT data. Note the general similarity with the mapped surficial units. See Grunsky et al. (2006) for further details.

Computer-Assisted Processing

Supervised Classification

A spectral map[4] can be created from optical imagery by using *a priori* information on rock or surficial units. This *a priori* information can take the form of training areas over known rock or surficial units and can be derived by a number of methods:

- inspection of airphotos or high-resolution satellite imagery,
- field observations or locations chosen in the field,
- inspection of geological maps in concert with observations on optical imagery.

Once suitable training areas have been selected that the geologist feels are representative of the units to be

4. A spectral map is based on variations in spectral signatures extracted from optical imagery. Geological calibration of these spectral classes must be undertaken by fieldwork or comparison to other supporting geoscience data sets.

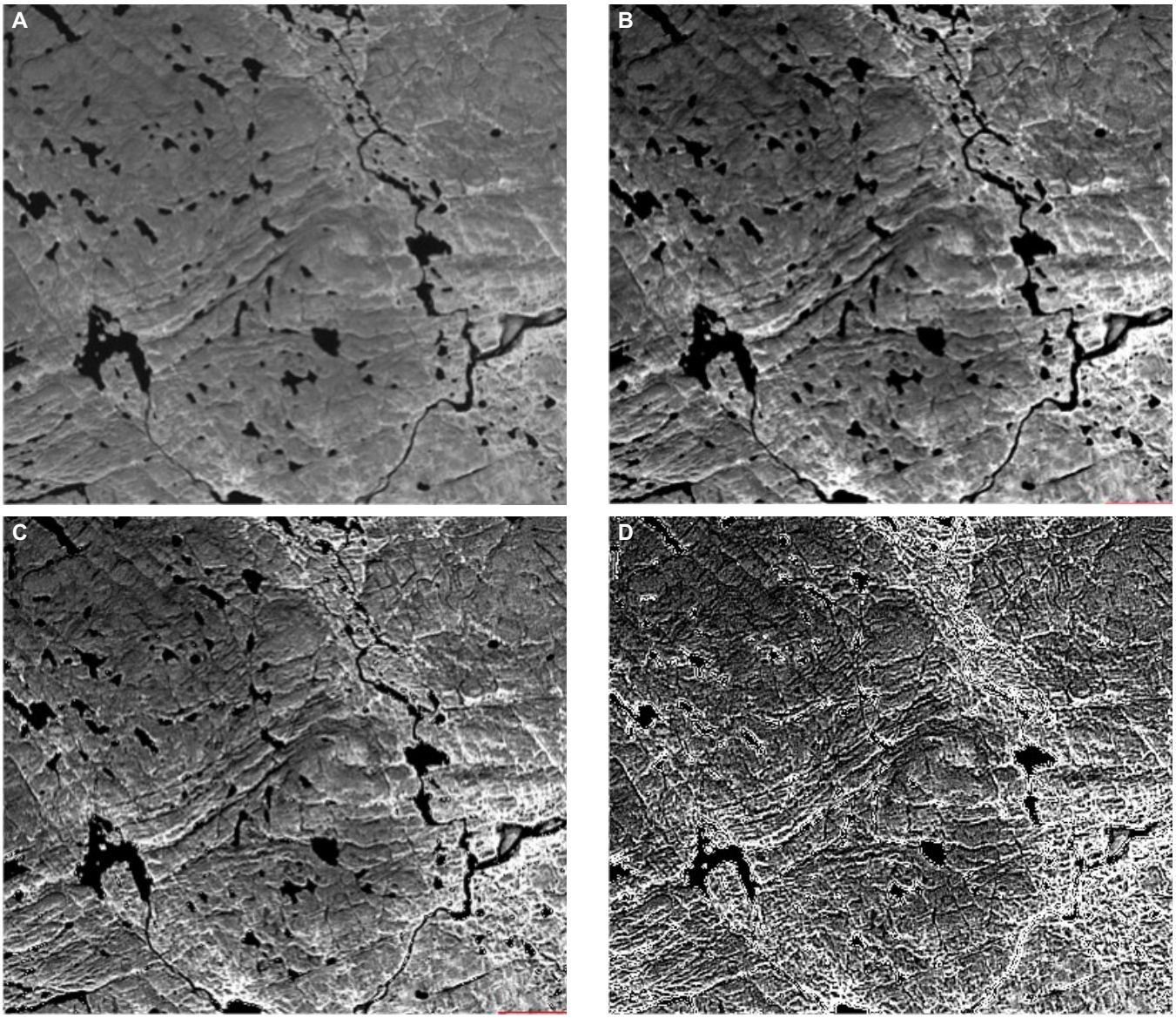



Figure 5-25. Enhancements of single-band LANDSAT imagery of the Thirty Mile Lake area, Nunavut (NTS 65P map sheet). **(A)** Raw band 4 image.. **(B)** Contrast-enhanced band 4 image. **(C**) Filtered band 4 image using an edge-enhancement spatial filter. **(D)** Filtered band 4 image using a 25 x 25 high-frequency spatial filter. Images (A) and (B) represent the difference between raw and contrast-stretched imagery. Contrast enhancement involves using a mathematical function (look-up-table or LUT) to stretch the raw data (expressed in bytes) to the full display range (0 -255 grey levels), thus improving the contrast and colour distribution of the image. Images (C) and (D) represent enhancements of selected spatial frequencies in the imagery to highlight linear elements often representing geological structures of various types. This is accomplished by utilizing spatial filters applied iteratively on a pixel-to-pixel basis to the raw image (same description applies as for Fig. 5-24).

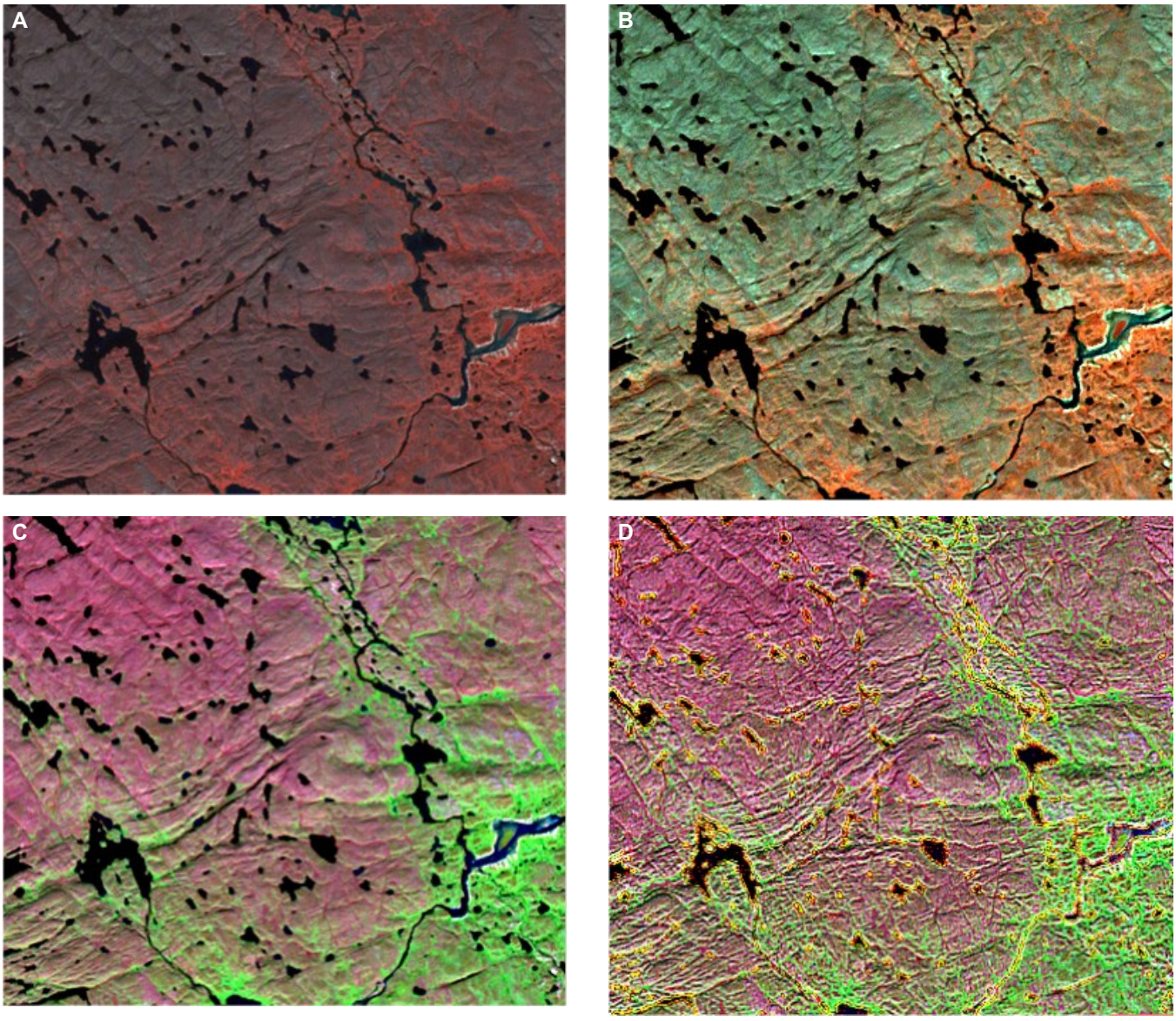



Figure 5-26. Enhancement of colour composite LANDSAT imagery of the Thirty Mile Lake area, Nunavut (NTS 65P map sheet). **(A)** Raw image of bands 4, 3, and 2 (red, green, and blue). **(B)** Contrast-enhanced image from bands 4, 3, and 2 (red, green, and blue, respectively). **(C)** Contrast-enhanced image from bands 7, 4, and 1 (red, green, and blue, respectively). **(D)** Spatially filtered image from bands 7, 4, and 1 (red, green, and blue, respectively) to enhance linear features and patterns.

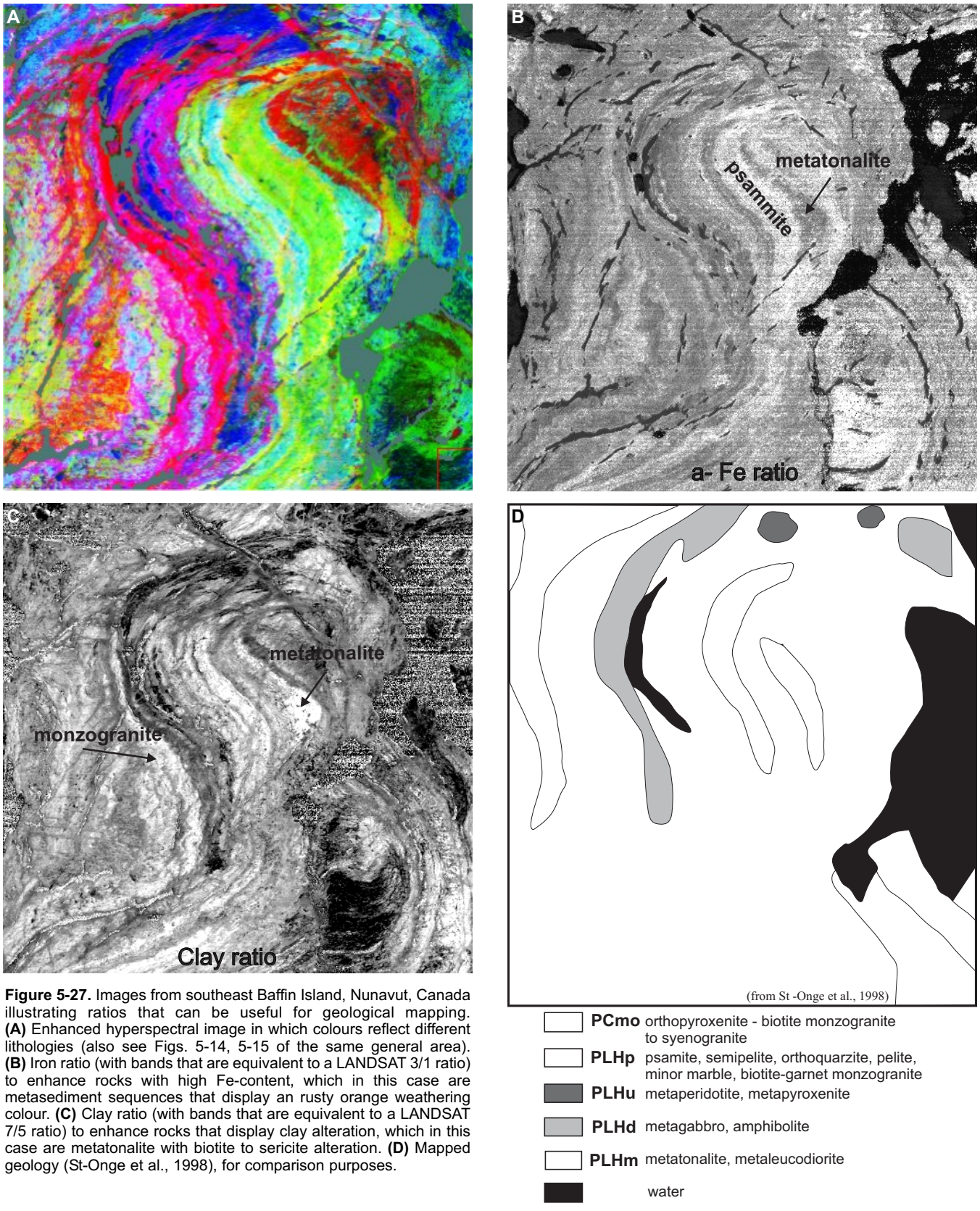

Figure 5-27. Images from southeast Baffin Island, Nunavut, Canada illustrating ratios that can be useful for geological mapping. **(A)** Enhanced hyperspectral image in which colours reflect different lithologies (also see Figs. 5-14, 5-15 of the same general area). **(B)** Iron ratio (with bands that are equivalent to a LANDSAT 3/1 ratio) to enhance rocks with high Fe-content, which in this case are metasediment sequences that display an rusty orange weathering colour. **(C)** Clay ratio (with bands that are equivalent to a LANDSAT 7/5 ratio) to enhance rocks that display clay alteration, which in this case are metatonalite with biotite to sericite alteration. **(D)** Mapped geology (St-Onge et al., 1998), for comparison purposes.

classified, spectral signatures (statistics) are extracted and compared to one another using a variety of statistical techniques (i.e. transformed divergence) to test whether the spectral signatures are statistically separable. If the signatures are unique, the data is then classified using the statistics from each training area by employing a classification algorithm (i.e. maximum

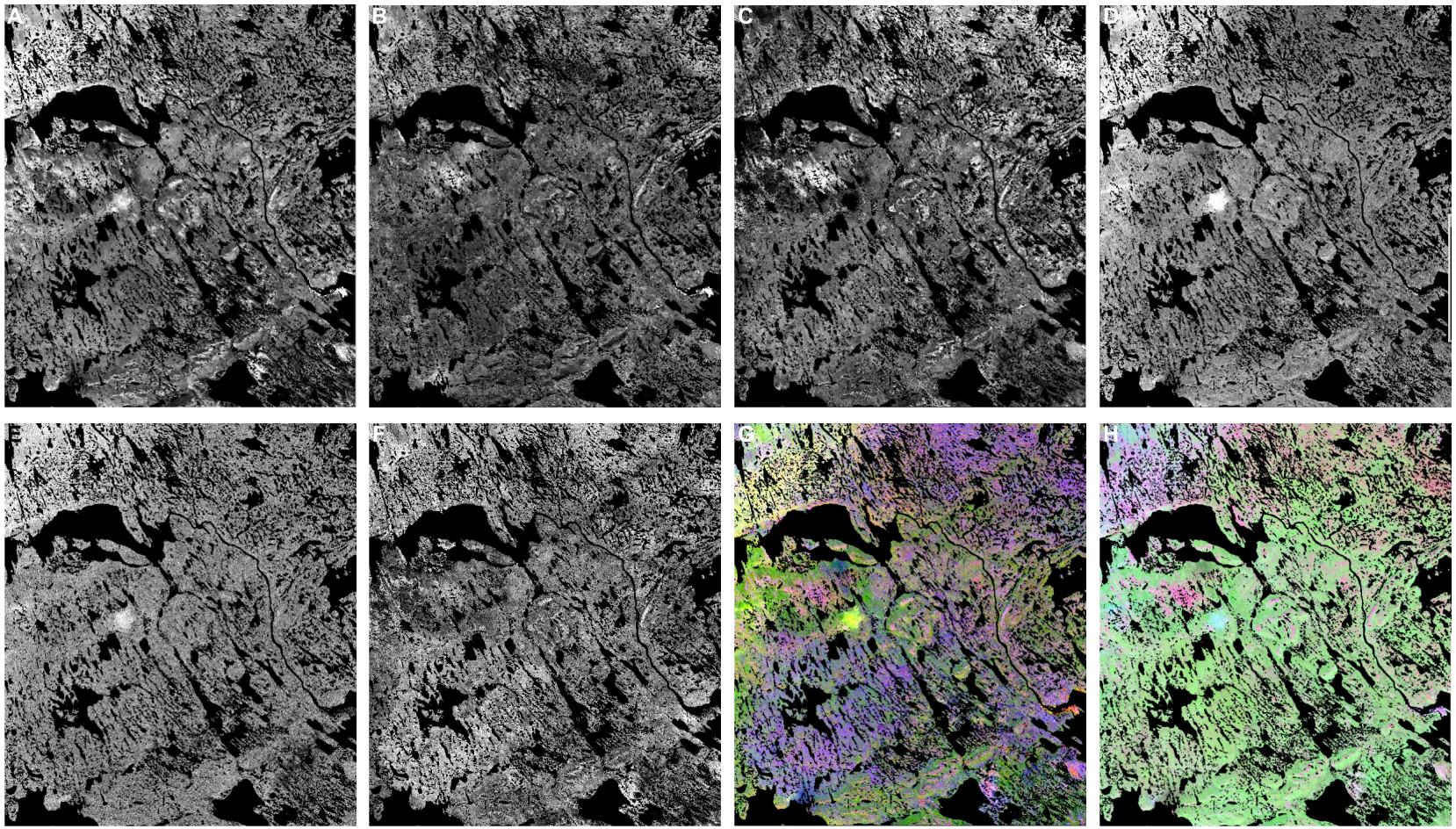

I

Eigenvector	Band 5	Band 6	Band 7	Band 8	Band 9	Band 10
Band 5	0.445671	0.461415	0.455001	0.106660	0.405428	0.453535
Band 6	0.307774	0.220697	0.109163	-0.815042	-0.432887	-0.037502
Band 7	-0.157972	-0.325305	-0.346575	-0.448650	0.436446	0.579346
Band 8	0.590447	0.203555	-0.755720	0.188894	-0.027840	-0.048667
Band 9	0.577083	-0.762266	0.260678	0.039601	0.057963	-0.114218
Band 10	0.006644	0.136052	-0.013382	-0.292907	0.673519	-0.664713

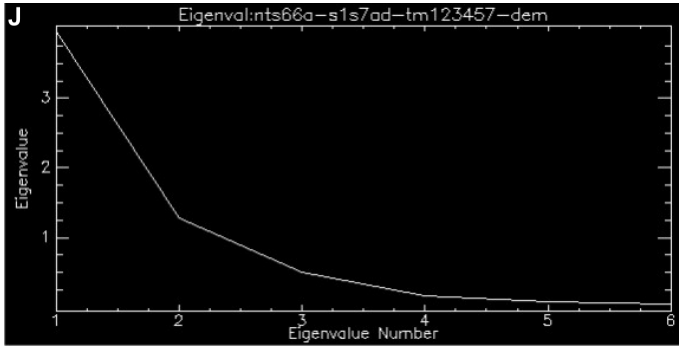

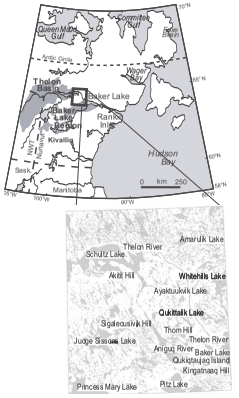

Figure 5-28. Principal component transform (PCA) applied to LANDSAT data over Shultz Lake (NTS 66a), Nunavut, Canada. **(A-F)** Individual component images derived from the transform. **(G)** Colour composite ternary image of PCA using bands 1, 4, and 6 (red, green, and blue, respectively). **(H)** Colour composite ternary image of LANDSAT bands 7, 4, and 2 (red, green, and blue, respectively). **(I)** Table of eigenvectors (component loadings). PCA 1 is a linear mix of all input channels; PCA 2 has a high weighting from band 5 (LANDSAT band 1) and a large negative weighting from band 9 (LANDSAT band 5). **(J)** Plot of eigenvalues. PCA 1, 2, and 3 contain most of the variance of the data set. See Figure 5-24 for a larger location map.

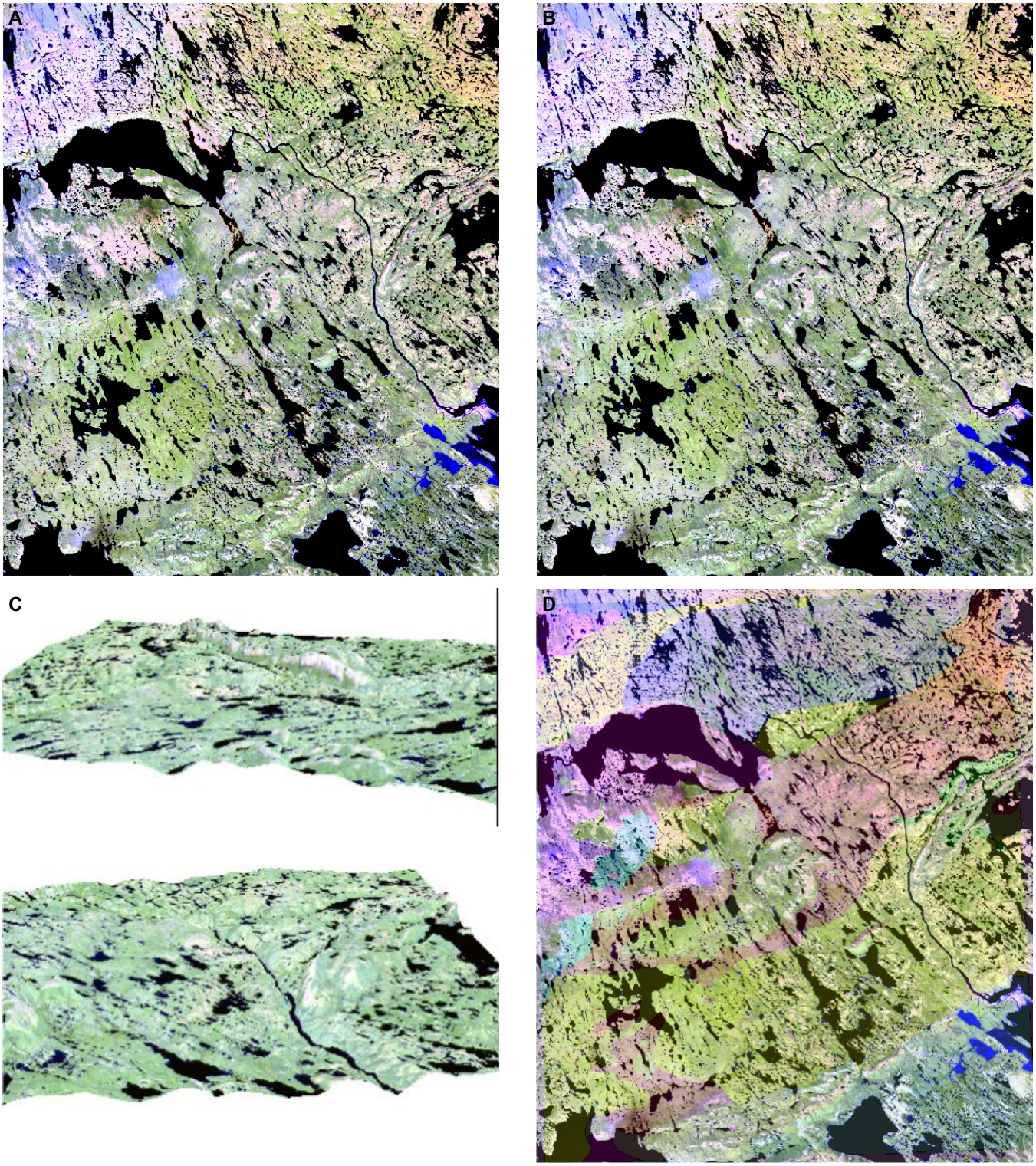

Figure 5-29. Fused images over Shultz Lake (NTS 66a), Nunavut. **(A)** LANDSAT bands 7, 4, and 2 (red, green, and blue, respectively) false colour composite image. **(B)** LANDSAT image fused with a digital elevation data (DEM). Note the enhancement of the topography while maintaining spectral (colour) variations. **(C)** LANDSAT data fused with a DEM and viewed in 2.5-D. **(D)** LANDSAT image fused with a geological map; the colours reflect different mapped units.

likelihood, neural networks etc.), resulting in a classified (predictive) map of geological units (Fig. 5-31).

Often it is prudent to divide the original training areas into two (or more) groups for cross-validation. Thus one group of training areas can be used for classification and the other group to validate the classification through what is called a confusion matrix. Another method for validating the accuracy of the classification

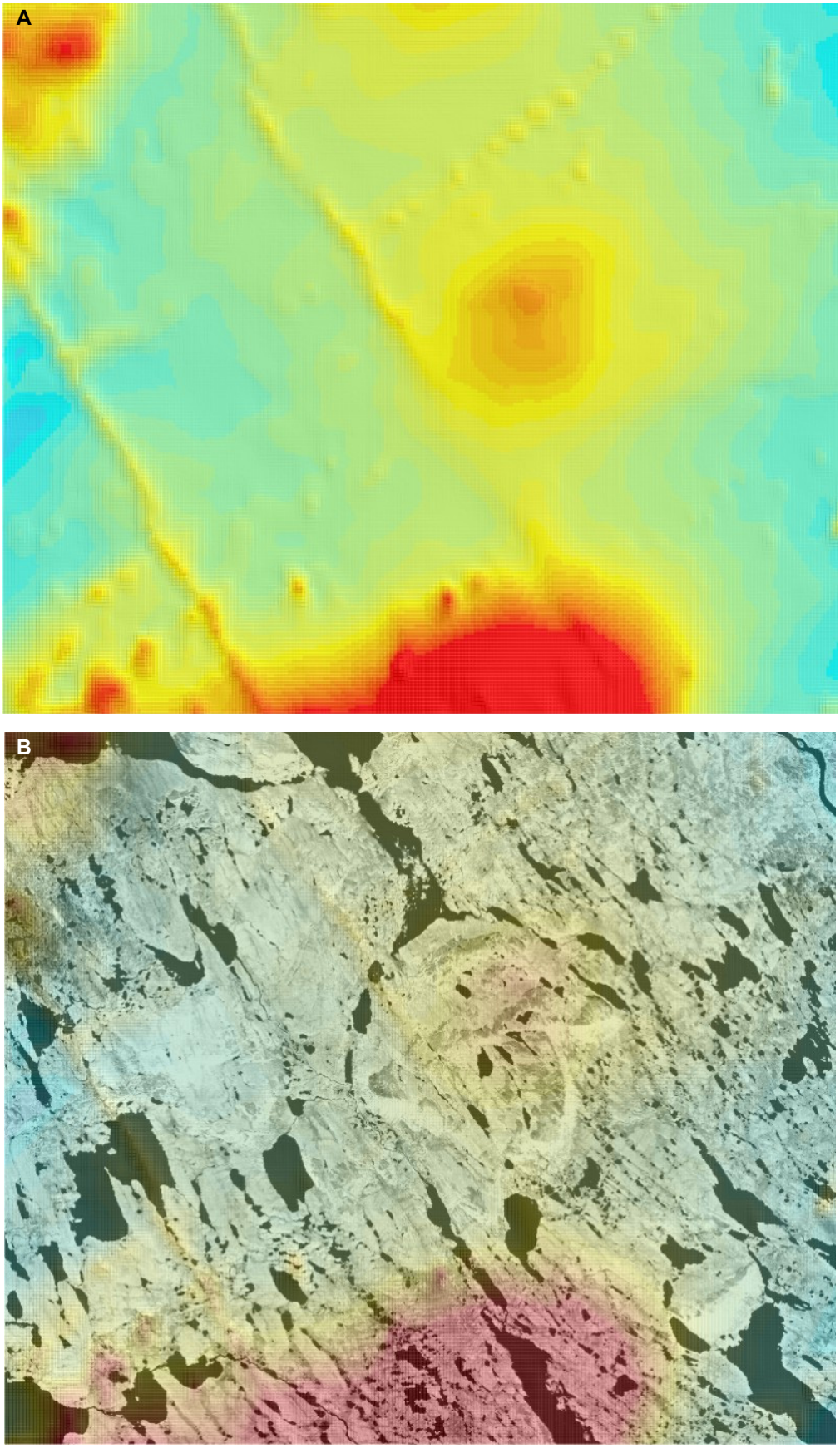

Figure 5-30. Magnetic data fused with LANDSAT data over a portion of Shultz Lake (NTS 66a). The coloured magnetic data representing the total field magnetic response has been fused with a band 4 LANDSAT image allowing for the comparison of patterns seen on each image.

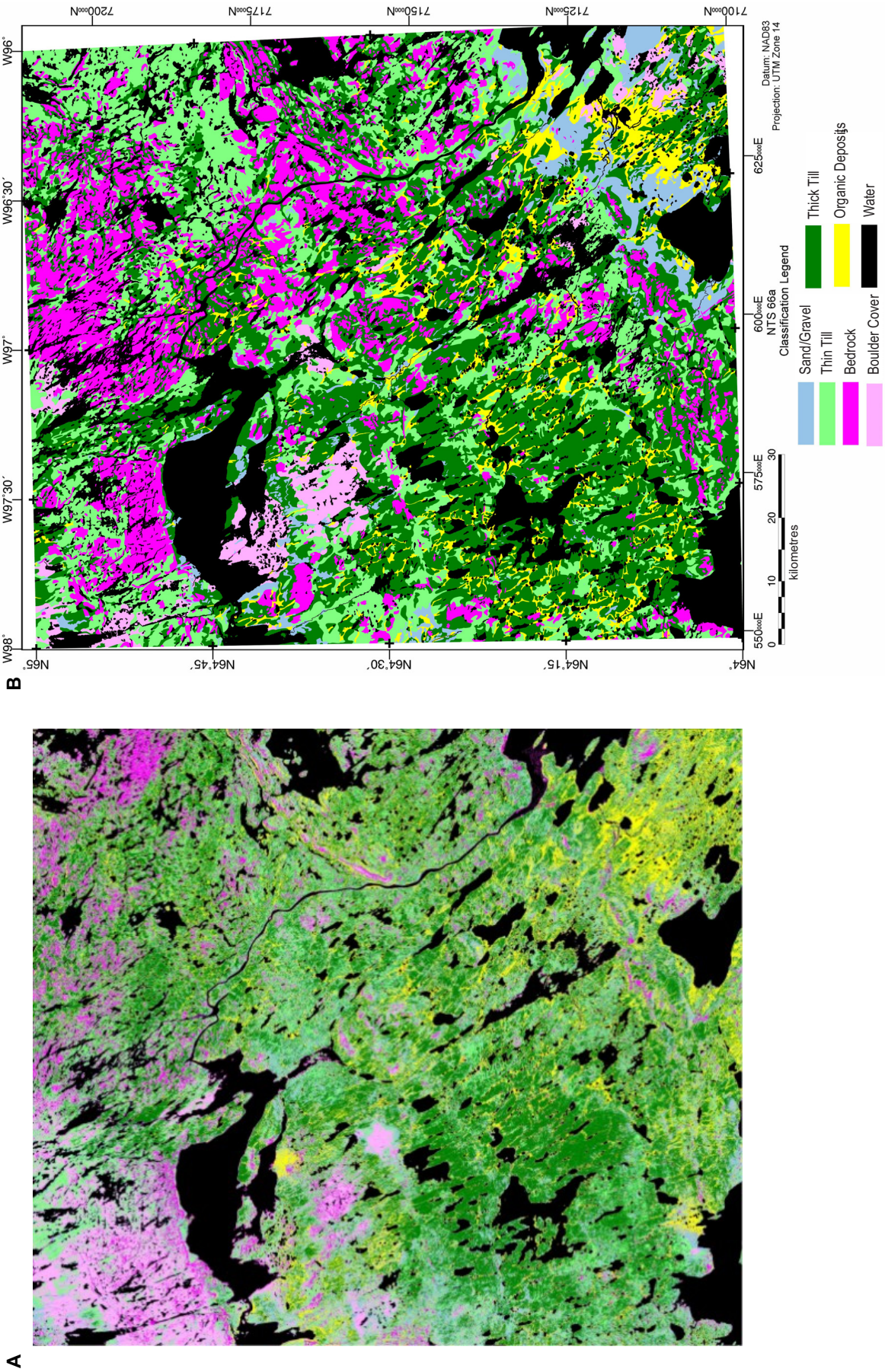

Figure 5-31. Predictive (classified) maps derived from LANDSAT data over Shultz Lake (NTS 66a), Nunavut. **(A)** Classified map derived from a supervised classification (maximum likelihood) of LANDSAT data using training areas identified from air photos and field observations. **(B)** Generalized surficial geology map (see Grunsky et al. (2006) for further details).

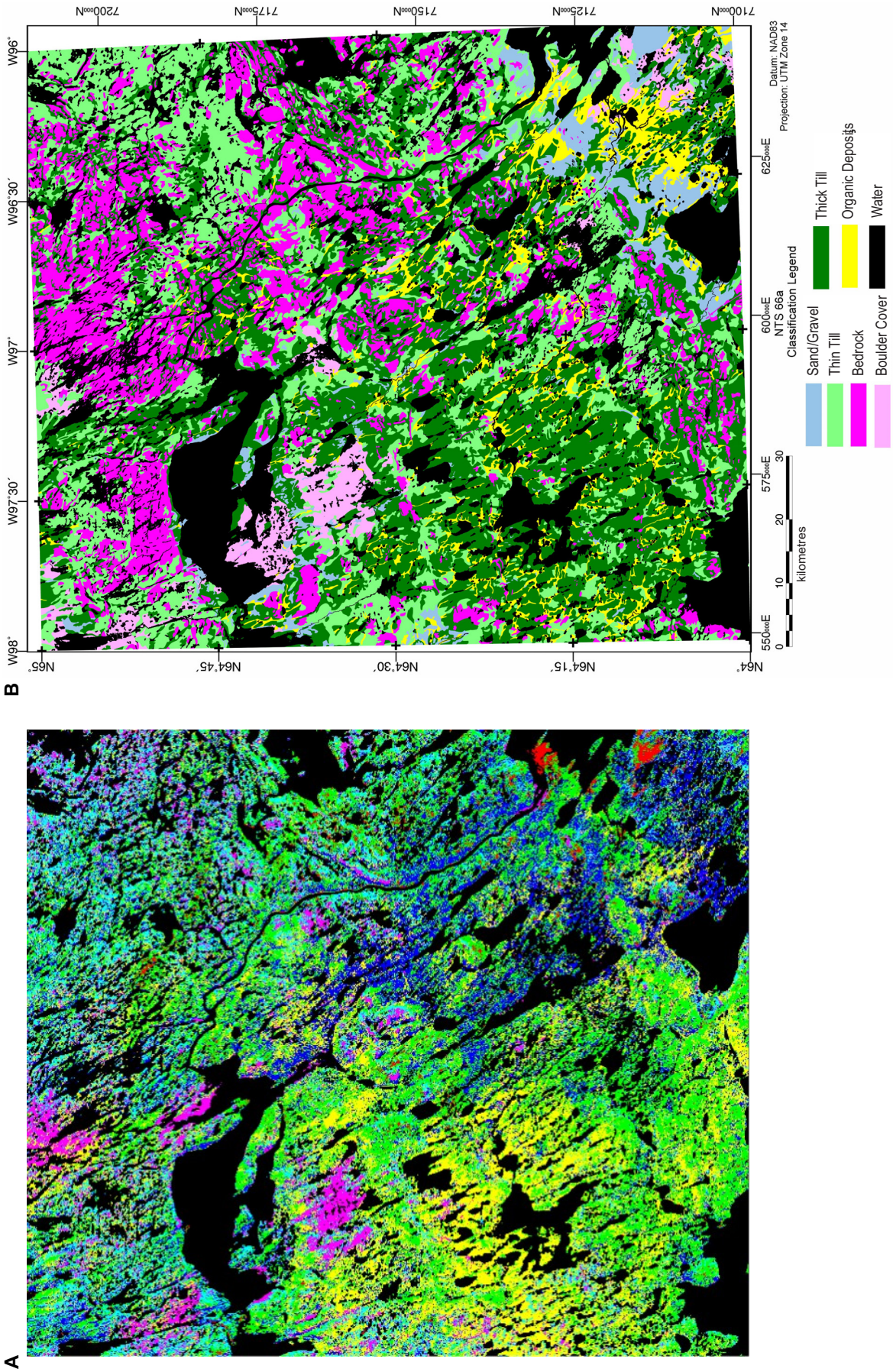

Figure 5-32. Predictive (classified) map derived from LANDSAT data over Shultz Lake (NTS 66a), Nunavut. **(A)** Classified map derived from an unsupervised (automatic) classification (K-means clustering) of LANDSAT data. **(B)** Generalized surficial geology map.

is to compare the classified map to sites visited in the field.

Classification of optical imagery is often only undertaken on the spectral information. However, optical imagery also has the potential to offer much textural information[5], which can be used in the classification process in concert with spectral (tonal) information.

Unsupervised Classification

A spectral map can also be produced automatically without input by the geologist using a process known as unsupervised classification or data clustering. Typically the geologist will provide the number of units (or clusters) to be found in the multiband optical data and select a clustering algorithm (i.e. K-means, N-dimensional histogram etc.), which will automatically find like statistical data clusters and produce a thematic map (Fig. 5-32) of these clusters. However, the geologist must make geological sense of this map to determine what the resulting units represent. This normally involves 'ground truthing' (i.e. field mapping) and/or examination of other supporting geoscience data sets to geologically calibrate the spectral classes.

REFERENCES

Cudahy, T.
2002: Mapping the Earth with ASTER; Australian Commonwealth Scientific and Industrial Research Organisation (CSIRO) ASTER Workshop, Geological Remote Sensing Group Annual Meeting, December 5-7, 2002.

Grunsky, E., Harris, J.R., and McMartin, I.
2006: Predictive Mapping of Surficial Materials, Shultz Lake Area (NTS 66A), Nunavut, Canada; Geological Survey of Canada, Open File 5153, 1 DVD.

Harris, J.R., Rogge, D., Hitchcock, Ijewliw, O., and Wright, D.
2005: Mapping lithology in Canada's Arctic: Application of hyperspectral data using the minimum noise fraction transformation and matched filtering; Canadian Journal of Earth Science, v. 42, p. 2173-2193.

Harris, J.R., Ponomarev, P., Shang, J., and Rogge, D.
2006a: Noise reduction and best band selection techniques for improving classification results using hyperspectral data: Application to lithological mapping in Canada's Arctic; Canadian Journal of Remote Sensing, v. 32, p. 341-354.

Harris, J.R., Ponomarev, P., Shang, J., Budkewitsch, P., and Rogge, D.
2006b: A comparison of automatic and supervised methods for extracting lithological end members from hyperspectral data: application to lithological mapping in southern Baffin Island, Nunavut, *in* Current Research 2006-C4; Geological Survey of Canada.

Hitchcock, R. and White, H.P.
2007: Processing EO-1 Hyperion Data using ISDAS; Geomatics Canada, Technical Note 2, 30 p.

Jackson, G.D.
1960: Belcher Islands, Northwest Territories 33M, 34D,E; Geological Survey of Canada, Paper 60-20, 13 p

Jensen, J.R.
1996: Introductory Digital Image Processing: A Remote Sensing Perspective; Prentice Hall, 316 p.

Mauger, A.J.
2003: Comparison of various remote sensing and spectral imaging sensors; Exploration, MESA Journal, v. 29, 3 p.

Neville, R.A., Sun, L., and Staenz, K.
2003: Detection of spectral line curvature in imaging spectrometer data, *in* Algorithms for Multispectral, Hyperspectral, and Ultraspectral Imagery IX; Proceedings of SPIE (Society of Photographic Instrumentation Engineers), Orlando, Florida, p. 144-154.

Oliver, S. and van der Wielen, S.
2006: Mineral mapping with ASTER; AUSGEO NEWS (Geoscience Australia), v. 28, June 2006, http://www.ga.gov.au/ausgeonews/ausgeonews200606/aster.jsp

Rencz, A., Harris, J.R., Sangster, D., and Budkewitsch, P.
2000: Spectral characteristics of bedrock map units using LANDSAT TM and topographic data: Application to bedrock mapping in Borden Peninsula, Nunavut, *in* Current Research 2000-C4; Geological Survey of Canada.

St-Onge, M.R., Scott, D.J., and Wodicka, N.
1998a: Geology, Hidden Bay, District of Franklin, Northwest Territories; Geological Survey of Canada, Open File 3536, scale 1:100 000.

1998b: Geology, McKellar Bay, District of Franklin, Northwest Territories; Geological Survey of Canada, Open File 3537, scale 1:100 000.

United States Geological Survey Spectroscopy Lab
2003: Surface Reflectance Calibration of Terrestrial Imaging Spectroscopy Data: A Tutorial Using AVIRIS; http://speclab.cr.usgs.gov/PAPERS.calibration.tutorial/

White, H.P., Khurshid, S.K., Hitchcock, R., Neville, R., Sun, L., Champagne, C.M., and Staenz, K.
2004: From at-sensor observation to at-surface reflectance - calibration steps for earth observation hyperspectral sensors, *in* Proceedings of Institute of Electrical and Electronics Engineers (IEEE) International Geoscience and Remote Sensing Symposium (IGARSS), Anchorage, Alaska, September 20-24, 2004, v. 5, p. 3241-3244.

Wickert, L.M., Budkewtisch, P., Harris. J.A., and Morris, M.A.
2005: Effective application of ASTER imagery for geological mapping and mineral resource evaluation; Geological Association of Canada-Mineralogical Association of Canada Annual Meeting, Halifax, May 15–18, 2005, oral presentation.

DIGITAL REFERENCES

ASTER JPL Website, NASA:
http://asterweb.jpl.nasa.gov/index.asp

HYPERION Sensor, EO-1 Website:
http://eo1.usgs.gov/sensors.php

IKONOS Imagery, GeoEye:
www.geoeye.com/products/imagery/ikonos/default.htm

LANDSAT JPL Website, NASA, the LANDSAT Program:
http://landsat.gsfc.nasa.gov/

LANDSAT, USGS Website: http://landsat.usgs.gov/index.php

QUICKBIRD Imagery, Digital Globe:
www.digitalglobe.com

General optical remote sensing:
http://ccrs.nrcan.gc.ca/glossary/index_e.php

5. Texture is defined as rapid changes in tonal response in an image and defines spatial patterns that are a mix of different spatial frequencies.

as well as for the planning of boat versus helicopter supported traverses (Fig. CS1-8).

EVALUATION OF THE REMOTE PREDICTIVE MAPPING PROCESS

The RPM process was largely successful, as major lithological domains, some lithological units, and major structural trends and generations were identified and mapped. Complex areas requiring more field follow-up were delineated. Also, areas of poor exposure were identified, which facilitated targeted field mapping.

In this particular area, outcrop could not be unequivocally identified in all cases and was sometimes confused with sandy deposits such as eskers. The process of outcrop identification is presently being fine-tuned to reduce confusion with other surface features. In this study, it was suggested that a forest fire distribution map would have been beneficial as burnt areas have a greater probability of bedrock exposure. For this area, the magnetic data in conjunction with the existing field observations were the most useful data for producing a predictive geological map.

REFERENCES

Hanmer, S. and Kopf, C.
1993: The Snowbird tectonic zone in District of Mackenzie, Northwest Territories, *in* Current Research, Part C; Geological Survey of Canada, Paper 93-1C, p. 41-52.

Harper, C.T., Kraus, J., Demmans, C.J., Huebert, C., Coulson, I.M., and Rainville, S.
2001: Phelps Lake Project: Geology and mineral potential of the Bonokoski Lake area (NTS 64M-11, -12, -13, and -14), *in* Summary of Investigations 2001, Volume 2; Saskatchewan Geological Survey Miscellaneous Report 2001-4.2, p. 3-18.

Martel, E.
2005: Geology of the Snowbird Lake area, western Churchill Province, NWT; Northwest Territories Open File 2005-05, 27 p.

Martel. E. and Pierce, K.
2006: An Arc View 3.x Digital Geological Atlas of the Snowbird Lake Area, NTS 65D; Northwest Territories Open File 2006-02, CD-ROM.

Martel, E., Harris, J.R., Currie, M., and Pierce, K.
2005: Snowbird Lake (NTS 65D) Remote Predictive Mapping and Geoscience Data Compilation; Northwest Territories Open File 2005-08, 1 CD-ROM.

Relf
2003:

Roscoe and Miller
1986:

Taylor, F.C.
1963: Snowbird Lake Map Area, District of Mackenzie; Geological Survey of Canada, Memoir 333, 23 p.

CHAPTER 6. Radar Remote Sensing

J.R. Harris[1], E. Grunsky[1], and V. Singhroy[2]
1. Geological Survey of Canada, 615 Booth Street, Ottawa, Ontario K1A 0E9
2. Canada Centre for Remote Sensing, 588 Booth Street, Ottawa, Ontario K1A 0Y7
Corresponding author's email: Jeff.Harris@NRCan.gc.ca

THEORETICAL PRINCIPALS

Radar imagery generated using microwave wavelengths create images that offer a much different perspective of the Earth's surface than those created using optical and/or infrared sensors (Fig. 6-1). Radar imagery is particularly useful for highlighting topography, morphology, surface roughness, and moisture content.

With radar imagery, data are acquired using side-viewing geometry, either from an airborne or satellite borne platform (Fig. 6-2). The acquisition geometry produces imagery in which topography is enhanced but also results in various image distortions that can be difficult to rectify. To remove these distortions requires the use of a digital elevation model (DEM) and specialized processing software.

The basic operating principal for imaging radar involves a sensor that generates microwave energy (i.e. active sensor) and beams it in discrete pulses towards an object (i.e. the ground) where it interacts with the object. Some of the energy is reflected back (or backscattered) to the sensor, which records some property of the signal (amplitude and/or frequency). This recorded backscatter is transformed into an image showing objects that reflect a great deal of microwave energy as bright compared to objects that do not, which appear dark.

Radar sensors generate their own energy using much longer wavelengths (typically 3-23 cm) than optical sensors. This longer wavelength, in combination with its active sensing capability, provides a number of advantages, one of which being that radar sensors can collect an image during the day or night. Another advantage of the longer wavelengths is that the sensors are not affected by clouds. Radar images offers a very different and unique perspective of the Earth, one in which topographic and surface roughness patterns are enhanced (Fig. 6-1).

Spatial resolution is defined by two parameters: range and azimuth (Fig. 6-2). The majority of all imaging radars are now synthetic aperture radars (SAR) because these offer better spatial resolution in the azimuth direction. Spatial resolution in the range direction depends on the radar pulse length, whereas azimuth resolution is theoretically equal to half the length of the synthetic antennae. SARs make use of the well known Doppler principal to achieve fine spatial resolution. However, the monochromatic nature of SAR results in image noise (termed speckle), which imparts a salt-and-pepper-like appearance to radar imagery. This effect can be reduced by spatial-filtering techniques or by a process referred to as multi-looking.

Interpretation and processing of radar imagery is generally more complex than optical imagery as both system (acquisition) and terrain parameters will contribute to the appearance of a radar image (Table 6-1). These parameters are not mutually exclusive and a change in a system parameter will change the backscatter response of a terrain parameter. For example, when using a 3 cm wavelength ('X- band'), a given surface (i.e. a grassy field) may be seen as rough, resulting in diffuse backscatter (bright on the image), whereas when using a 22 cm wavelength (i.e. L-band), the same surface will be seen as smooth, resulting in mineral reflection (dark on the image).

Wavelength will affect the strength of the radar return as a function of surface roughness. All spaceborne SARs presently imaging the Earth employ either 6 cm wavelengths (C-band) or 22 cm wavelengths (L-band). C-band radars result in a broader range of backscatter than does L-band radars, which tend to see the Earth as either smooth or rough. Varying the incidence angle will also affect how rough the radar 'sees' the surface and thus the backscatter response. Steeper incidence angles (15-25º) will result in a greater backscatter response from topography whereas shallower incidence angles (>30º) will respond more to surface roughness (Fig. 6-3). Thus, steeper incidence angles will result in better topographic enhancement in moderately rolling terranes than will shallower incidence angles. The choice of incidence angle will affect the resulting appearance (geometry) of a radar image. Imaging mountainous terrane using a steep incidence angle will result in image distortions known as layover and foreshortening and in some cases can render the imagery uninterpretable (Fig. 6-4). The radar energy used for sensing can either be like-or cross-polarized; the choice of polarization will affect the amount of backscatter from the surface. Typically, like polarization (H transmit and receive or V transmit and receive) results in more backscatter than cross-polarized signals. The majority of spaceborne imaging systems employ like polarization (HH) as this typically results in a wide range of backscatter from the Earth's surface. Radar is a directional sensor (Fig. 6-1); therefore the

Harris, J.R., Grunsky, E., and Singhroy, V., 2008, Radar remote sensing, Chapter *6 in* Remote Predictive Mapping: An Aid for Northern Mapping, (ed.) J. R. Harris; Geological Survey of Canada, Open File 5643, p. 135-160.

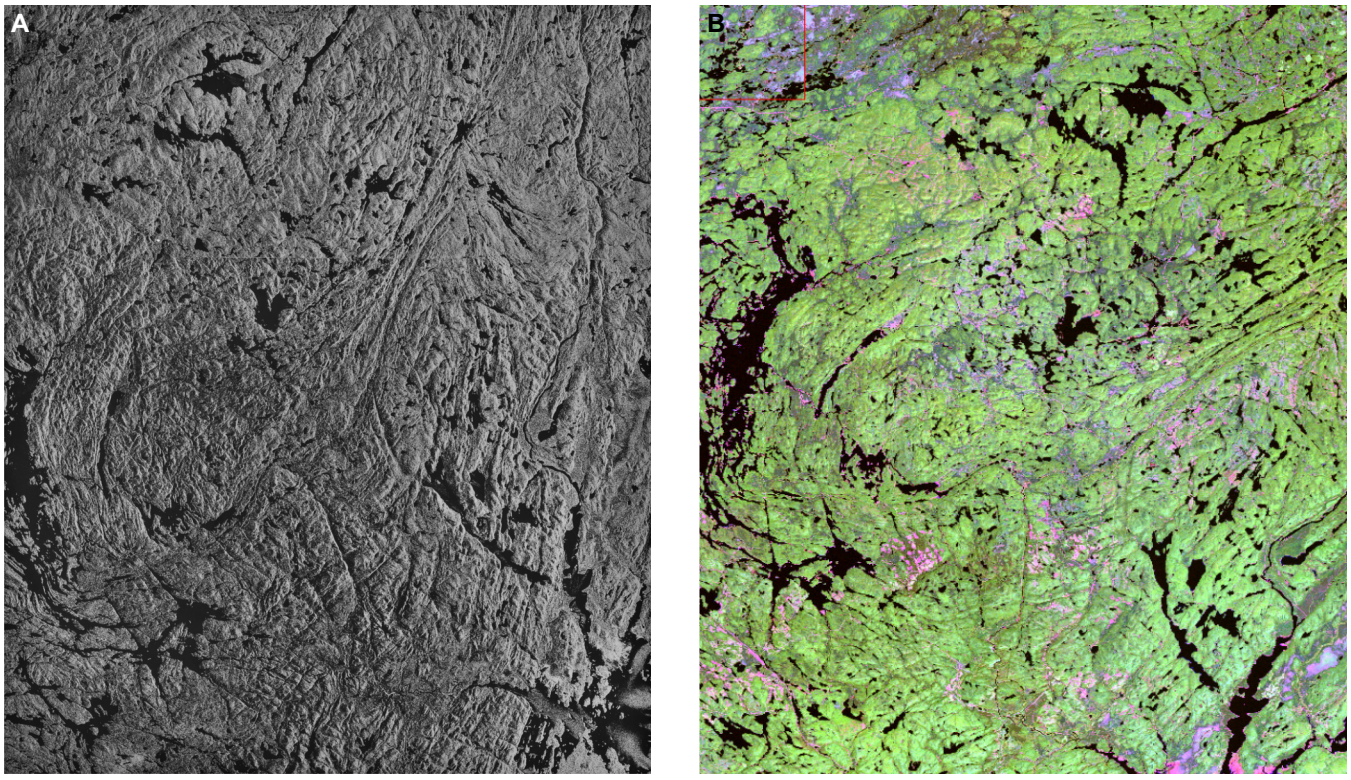

Figure 6-1. LANDSAT and Seasat radar images of part of the Grenville Province, north of Ottawa, in the vicinity of the Baskatong Reservoir in Quebec. **(A)** Seasat SAR image acquired in the summer of 1978. **(B)** LANDSAT colour composite image (bands 742 – red, green, blue) of the same area. Note the topographic enhancement provided by the radar as a function of its side-viewing geometry and steep incidence angle. The LANDSAT provides less topographic enhancement but more spectral contrast between land cover. See Harris et al. (1987) for more details about the use of these images for mapping lithotectonic domains in the Grenville tectonic province of Ontario and Quebec.

radar look direction will have an appreciable effect on the overall appearance of the image and in particular determine which features are enhanced. For example, topographic ridges trending parallel to the radar flight line and thus perpendicular to the radar look direction will be enhanced, whereas those that are orthogonal to the flight line (parallel to the look direction) will be suppressed (Fig. 6-5).

As well as radar system parameters, terrain parameters also affect radar backscatter; terrain parameters include surface morphology (i.e. topography), surface roughness, and dielectric properties (moisture) (Table 6-1). There are three basic scattering types (specular, diffuse, and dihedral) that affect backscatter (Fig. 6-6). Rough surfaces (relative to wavelength) will cause diffuse scattering, which results in moderate to bright tones on a radar image. Smooth surfaces will result in specular reflection, where most of the radar energy is scattered away from the sensor obeying Snells Law. This results in very little backscatter and dark tones on

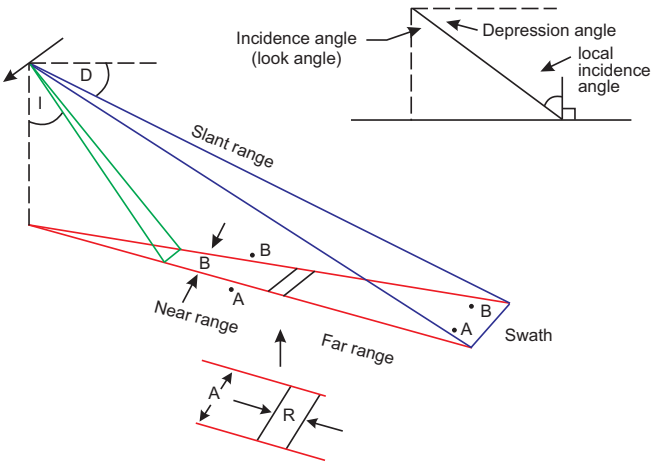

Figure 6-2. Radar acquisition geometry and associated terminology. A = azimuth, D = depression angle, I = Incidence angle, R = range.

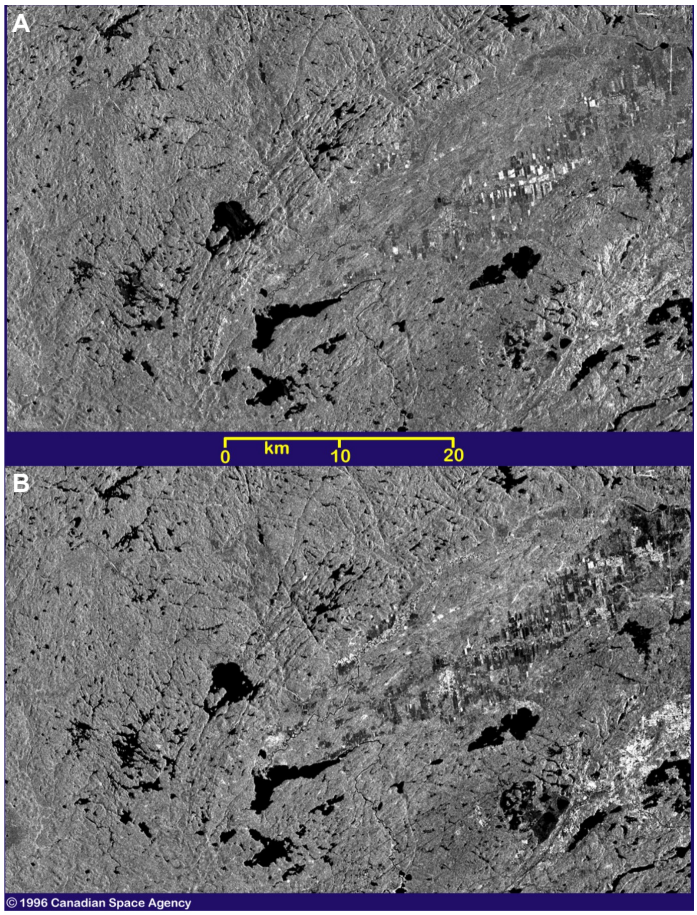

Figure 6-3. RADARSAT imagery of the Sudbury mining district (Ontario) showing the effect of different incidence angles on the appearance of the terrain. **(A)** S1 beam mode (20-27º incidence angle). **(B)** S7 beam mode (45-49º incidence angle). Note that the image acquired with a steeper incidence angle provides better enhancement of the topography (also see Fig. 6-1). Image provided by the Canada Centre for Remote Sensing (CCRS).

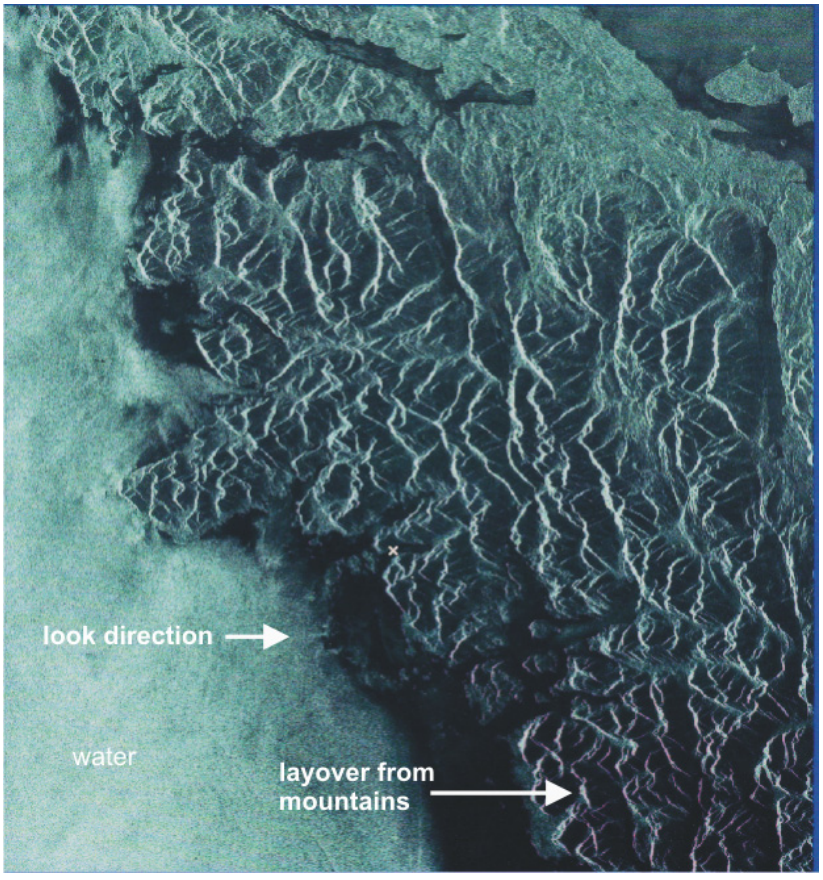

Figure 6-4. ERS-1 C-band SAR image of the mountainous terrain of the Brooks Peninsula, British Columbia. The steep incidence angle (approximately 22º) used to acquire this image has resulted in severe terrain distortion, which is referred to as layover and foreshortening.

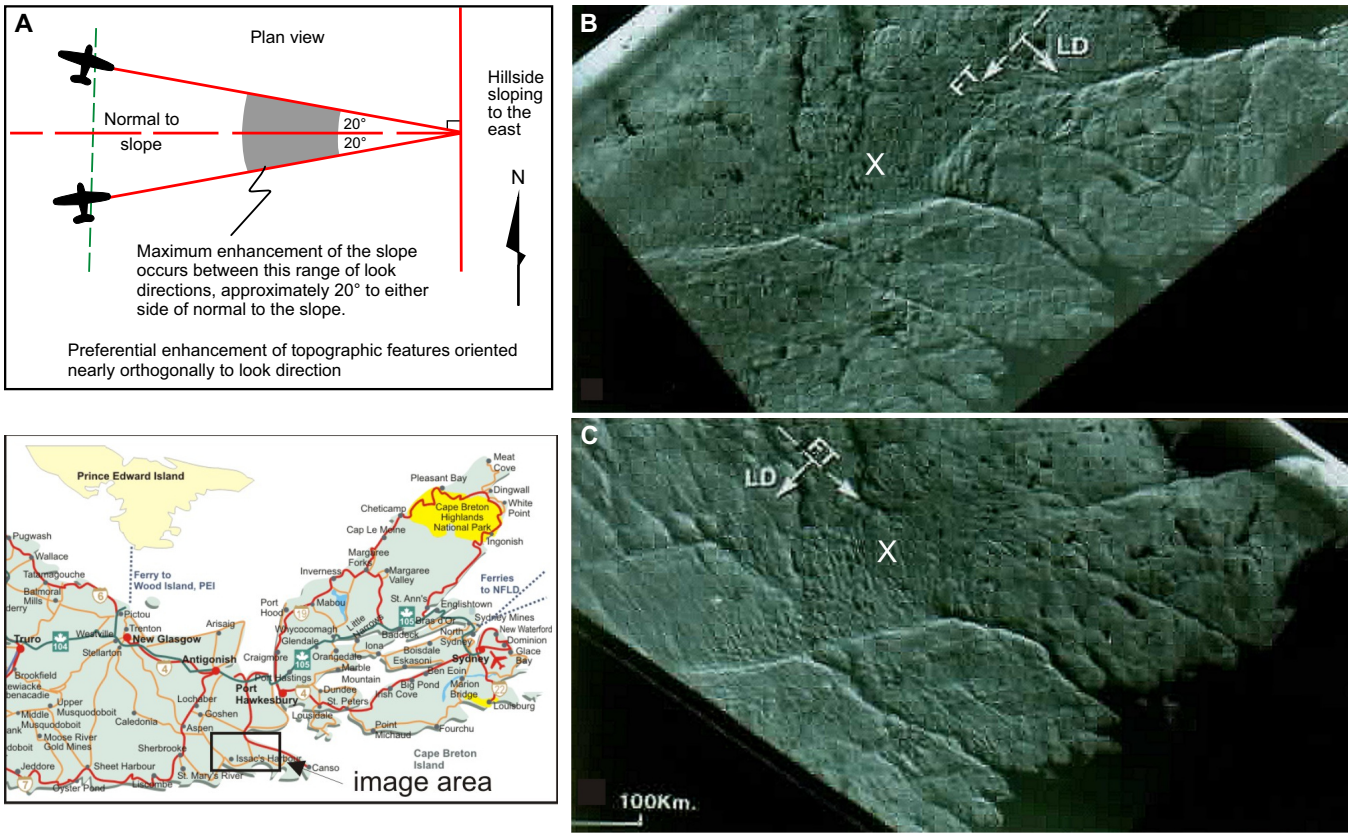

Figure 6-5. The effect of radar look-direction. **(A)** Conditions required for maximum terrain enhancement. **(B)** Airborne C-band image of eastern Nova Scotia with a look direction toward the southeast. **(C)** Airborne C-band image of eastern Nova Scotia with a look direction toward the southwest. Note the differences in appearance of the terrain between the two images, especially at the area labelled X (a drumlin field). The drumlins are almost transparent to the radar image in image B, as the look direction is parallel to the long axes of the drumlins. Whereas in image C, the look direction is almost perpendicular to the long axes of the drumlins, resulting in higher backscatter from the slopes facing the radar. FT - flight track, LD – look direction.

the radar image. Dihedral (corner) reflectors, often caused by man-made features, will result in a great deal of backscatter and thus bright tones on a radar image. Figure 6-7 shows the differences in backscatter as a function of surface roughness for two different lithologies. In this example, the siltstone weathers to a smooth surface and has less backscatter than the limestone, which weathers to a rough surface. The degree of topographic enhancement depends on incidence angle and the slope angle (Fig. 6-8) as well as look direction (Fig. 6-5). Dielectric properties, which control how much radar energy is conducted into the Earth's surface, are largely controlled by moisture. In general, the higher the moisture content of a given feature (soil, forest canopy, etc.) the higher the backscatter as compared to the same feature with a lower moisture content (Fig. 6-9).

DATA

Selected Radar Sensors Useful for Remote Predictive Mapping

Several satellite-borne radar systems are available for geological mapping. Table 6-2 provides a summary of the most commonly used for geological applications.

Examples of Radar Applications

Airborne and satellite-borne radar sensors only collect information from the Earth's surface with little penetra-

Table 6-1. Radar parameters.

Radar Parameters	Effect on Image
System Parameters	
Wavelength (frequency)	affects how rough the surface 'looks' to the radar
Incidence Angle	affects the degree of topographic enhancement
Polarization	affects the amount of backscatter
Look direction	topographic features striking parallel to the flight track and perpendicular to the look direction will be preferentially enhanced
Terrain Parameters	
Topography/terrain morphology	radar can provide enhancement of topographic patterns depending on the incidence angle and radar look direction
Surface roughness	rougher surfaces result in higher radar backscatter (depending on wavelength)
Dielectric	controlled by surface moisture – moist soil (higher dielectric constant) results in more radar backscatter

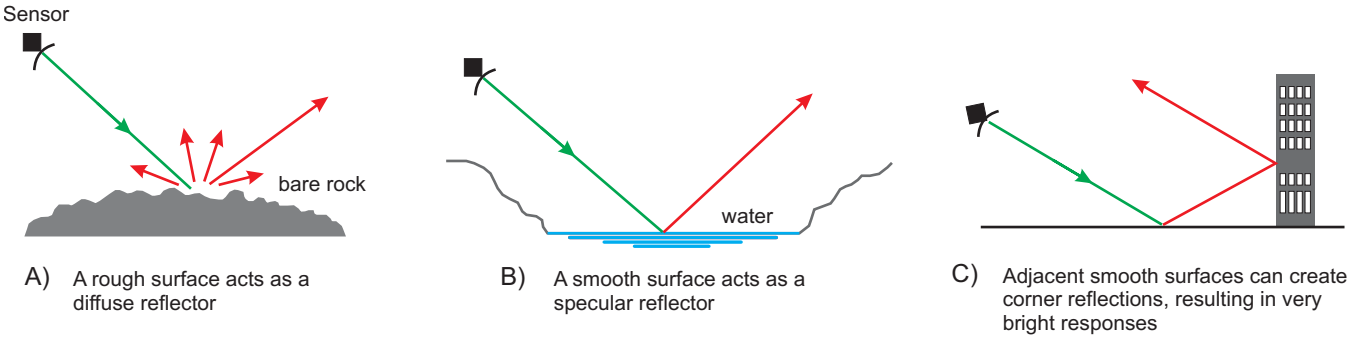

Figure 6-6. Three basic types of radar scattering mechanisms: **(A)** specular, **(B)** diffuse, and **(C)** dihedral (corner) reflectors. (A) and (C) result in moderate to intense backscatter, and thus bright tones on a radar image, whereas (B) results in little to no backscatter, and thus dark tones on a radar image. Diagram from Lillesand and Kiefer (1987).

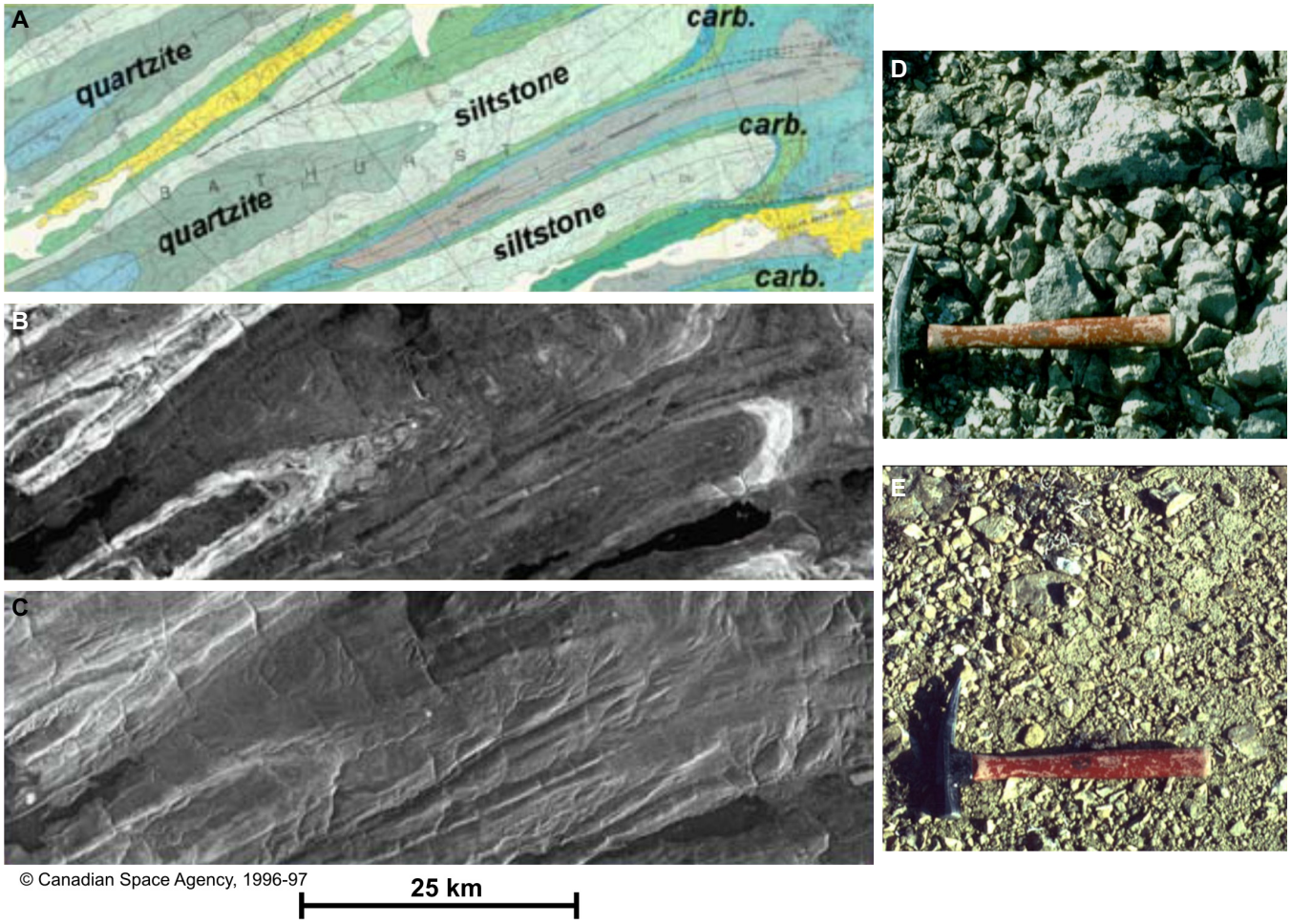

Figure 6 7. Example of the effect of surface roughness of different lithologies on radar backscatter. This is a RADARSAT S7 image of a portion of Bathurst Island, northern Canada. **(A)** Geological map from Harrison and de Freitas (1998). **(B, C)** Radar imagery of folds defined by limestone and siltstone. The limestone weathers to a rough surface **(D)** resulting in strong backscatter, and thus a bright tone on the image, whereas the siltstone weathers to a smooth surface **(E)**, which results in less backscatter and thus a darker tone. Imagery and photos from Budkewitsch and D'Iorio (1997).

tion into the ground, except in very special circumstances. In areas of the world that are very dry (characterized by very low dielectric properties), penetration of up to 6 metres has been achieved using long wavelengths (i.e. 22 cm). For example, the Shuttle Imaging Radar, which operated during the 1980s, was able to produce imagery of paleo-channels in the Sahara desert that were buried under, in some cases, 6 m of bone-dry sand! Much of Canada's North, although a cold desert, does have appreciable moisture content, thus precluding any significant penetration of the radar signal into the ground.

Structure

Radar imagery generally provides useful information on bedrock structures, although, as previously mentioned, this depends on the incidence angle (Fig. 6-3) and look

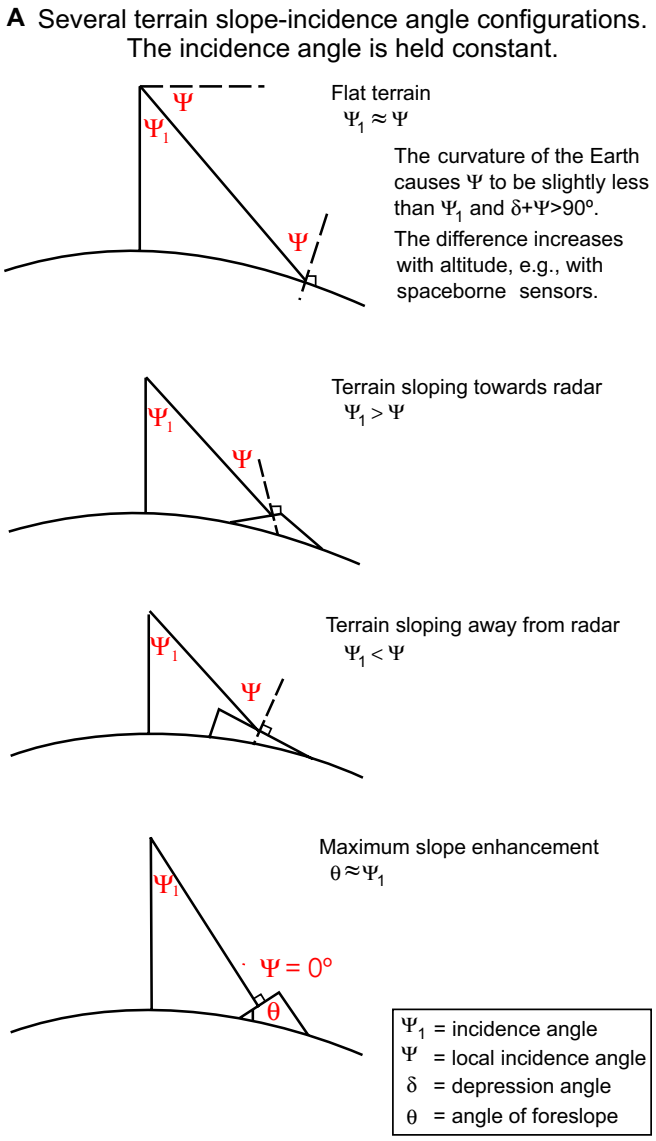

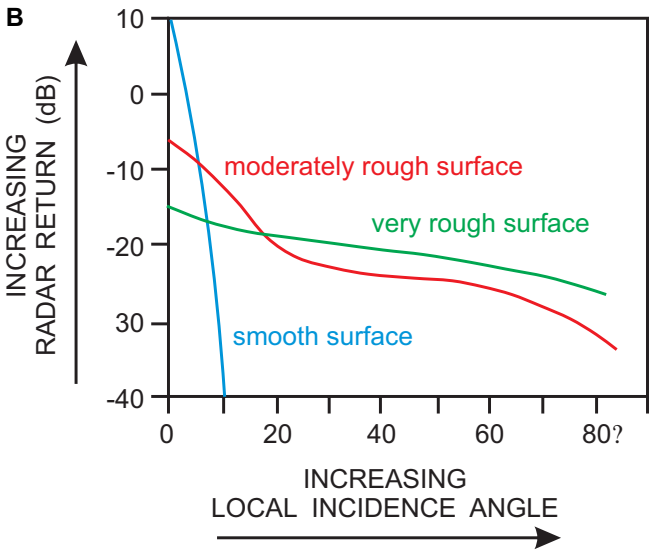

Figure 6-8. Diagrams showing the effect of varying incidence angles on topographic enhancement. **(A)** The degree of topographic enhancement depends on the incidence angle, slope angle, and the local incidence angle, which is defined by the angle between the incoming radar beam and the normal to the slope. A local incidence angle of 0º will result in the maximum backscatter. **(B)** Plot of local incidence angle versus backscatter. Incidence angles for moderately rough surfaces (such as the Earth's surface) between 0º and nominally 26º result in higher backscatter and better topographic enhancement (given the appropriate look direction) than local incidence angles between 30 and 60º. Thus in a high percentage of the terrane that characterizes much of Canada's North, steep incidence angles are required for topographic enhancement. However, to maximize differences in surface roughness, shallower incidence angles should be used (>30º to <60º).

direction (Fig. 6-5), as well as the geological terrane (Singhroy and Saint-Jean, R., 1999). If a steep incidence angle is used for imaging, the look direction is perpendicular to geological structures (Fig. 6-5), and the bedrock structure corresponds to topographic variations, then the resulting imagery can provide a detailed image of bedrock structure in which foliation and/or bedding trajectories (from lines), folds, faults, and lineaments

Table 6-2. Summary of the main characteristics of radar sensors available for remote predictive mapping, as well as where the data may be acquired.

Sensor	Characteristics	Availability	Where to Purchase
Seasat	L-band (22 cm), 22º incidence angle, HH polarization	Selected scenes	Canada Centre for Remote Sensing (CCRS)
RADARSAT I and II	C-band (6 cm), various incidence angle modes (20-47º), multi-polarization	Total coverage of Canada	Canada Space Agency (CSA) – MDA – Geospatial Services
JERS-1	L-band (22 cm) – 18 m spatial resolution – HH polarization – 35º incidence angle	Selected areas	Japanese Space Agency
ERS-1	C-band (6 cm) – 23º incidence angle, 10 to 30 m spatial resolution	Selected areas	European Space Agency (ESA) – MDA – Geospatial Services
ASAR	C-band (6 cm) – five polarizations (VV,HH,VV/HH,HV/HH,VH/VV) – 30 m spatial resolution	Selected areas	European Space Agency – MDA – Geospatial Services
Shuttle Radar (SIR)	C and L-band imagery	Selected areas of the world	Earth Resources Observation and Science (EROS) http://edc.usgs.gov/

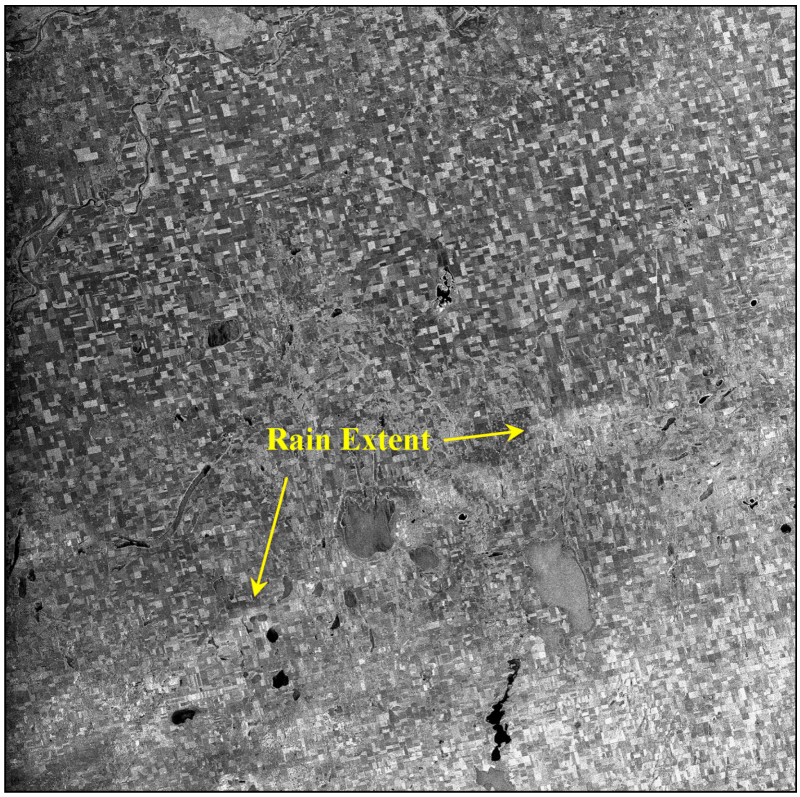

Figure 6-9. Example of a RADARSAT image of Melfort, Saskatchewan, A recent rain event can be clearly seen. The rain has increased the dielectric property of the soil, which has resulted in greater backscatter than the surrounding area. Image provided by Canadian Centre for Remote Sensing.

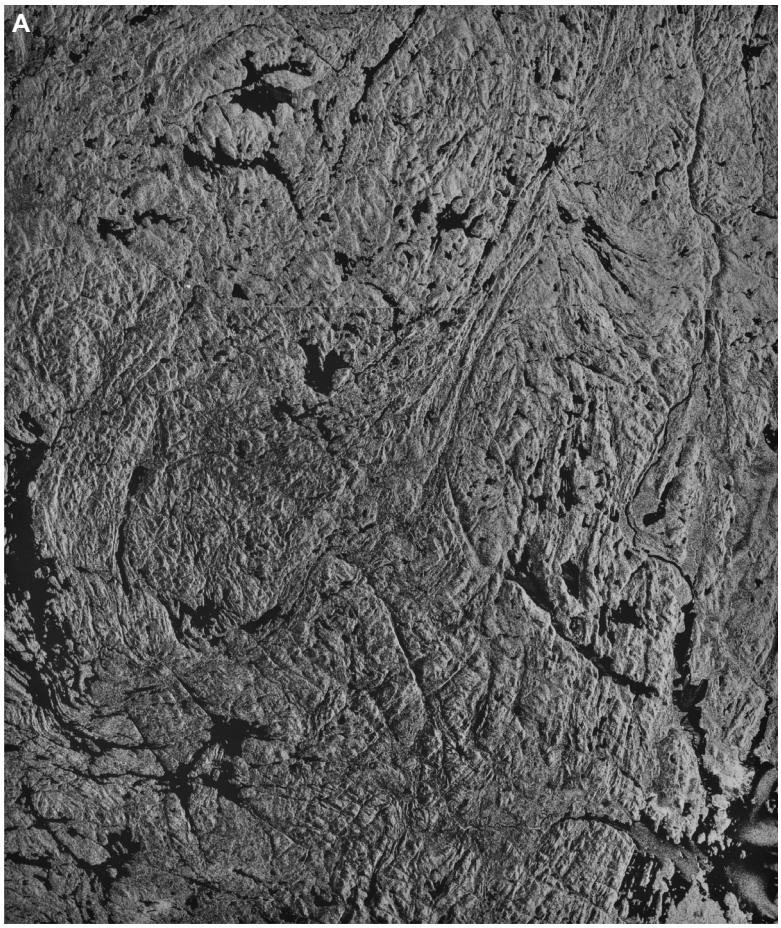

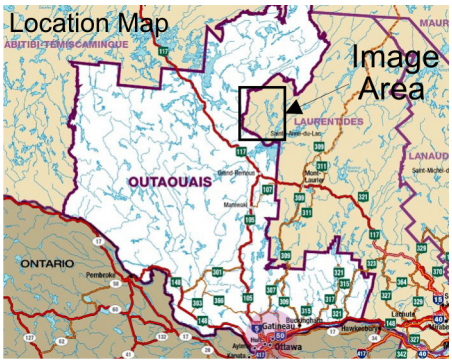

Figure 6-10. Example of a SEASAT SAR image of the Grenville Province acquired during July 1978 and the associated structural interpretations. **(A)** SEASAT l-band (23 cm) image – 22º incidence angle, west look-direction.

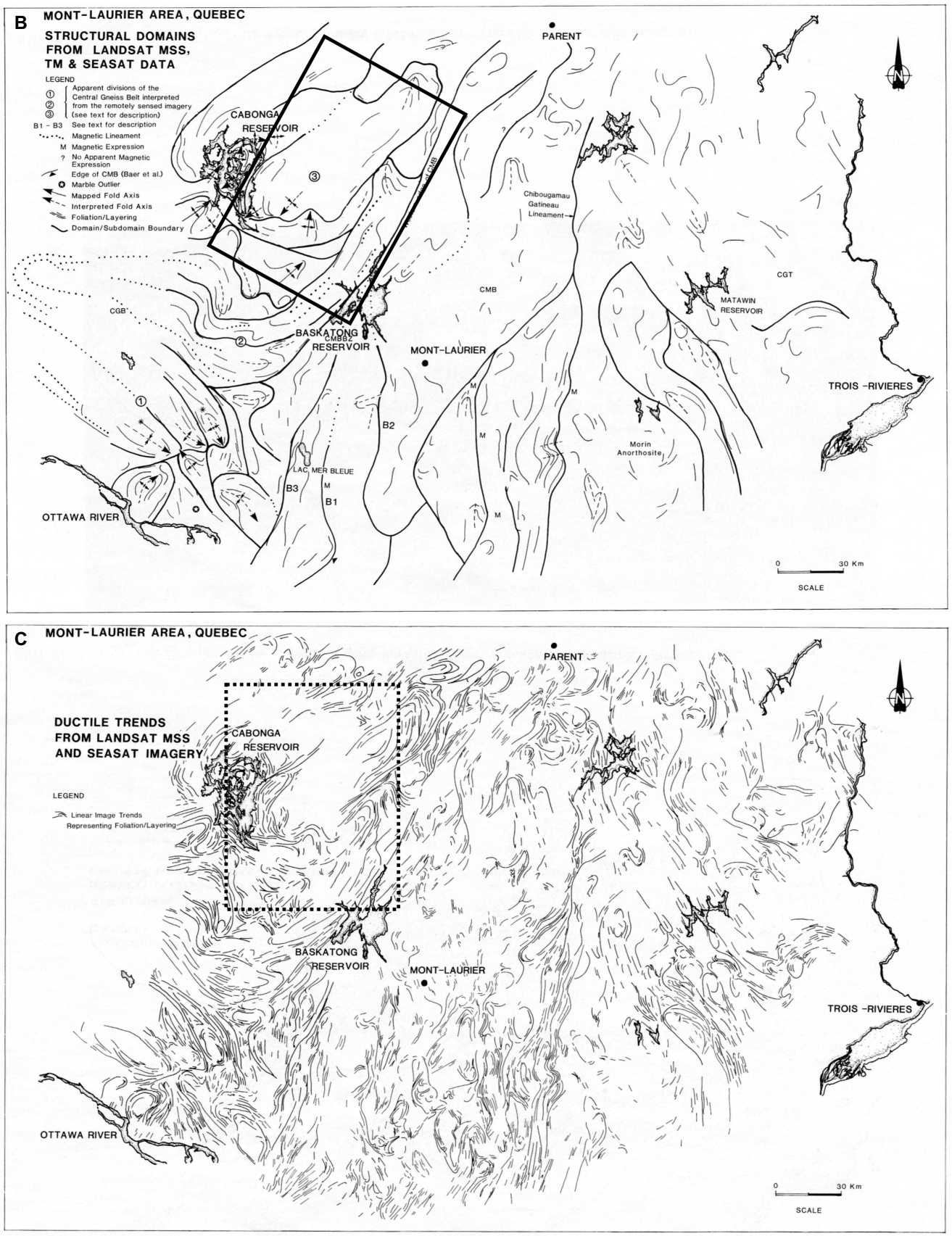

Figure 6-10 continued. (B) Interpreted tectonic domains. **(C)** Structural interpretation. The interpretations cover a much larger area than the image; only a portion of the SEASAT imagery is shown so that structural details on the imagery can be clearly seen. The steep incidence angle of SEASAT provides very good topographic enhancement, which in this area allows for detailed structural interpretations. See Harris et al. (1987) for more details on the geological interpretation of remotely sensed imagery in the Grenville Province.

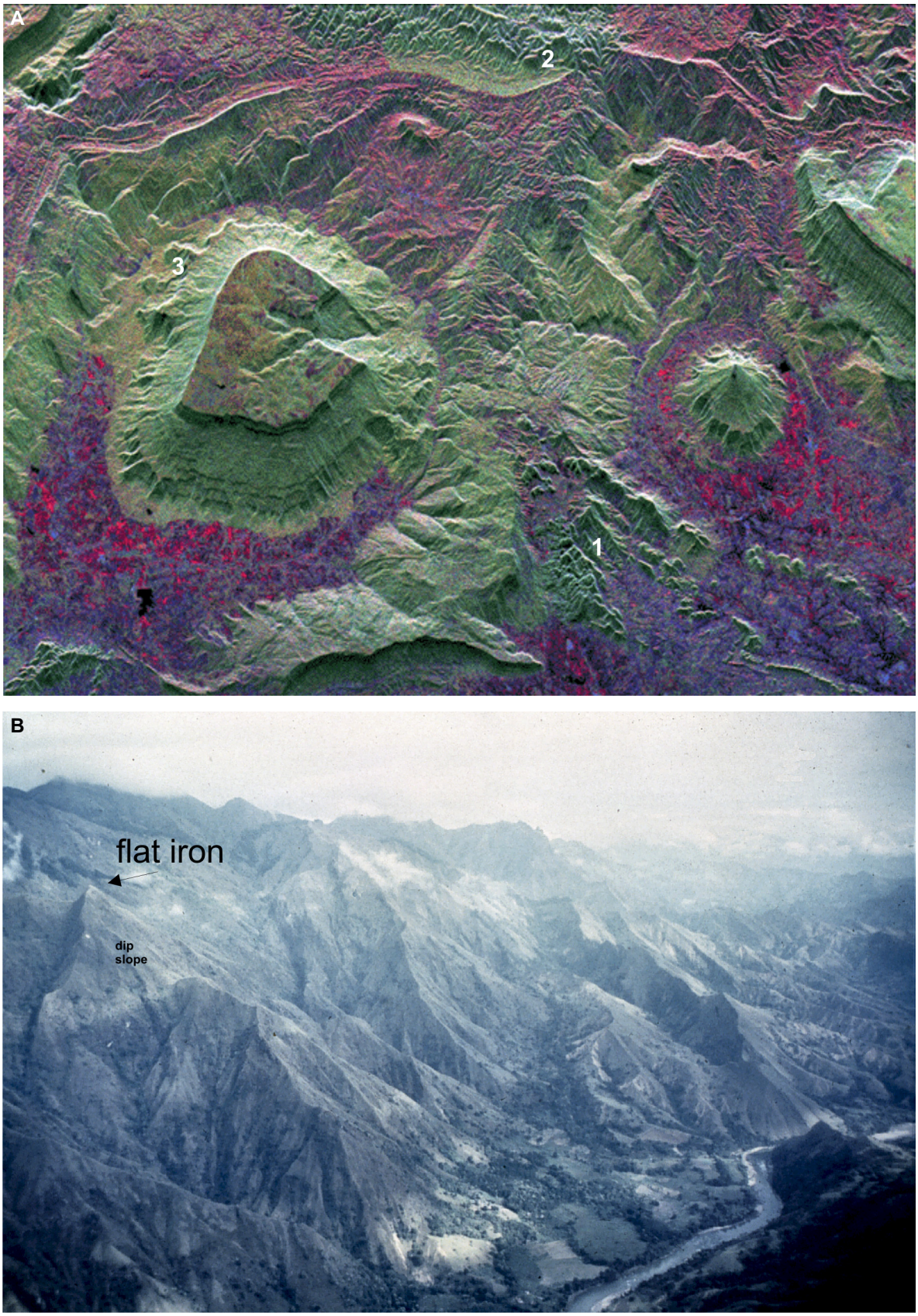

Figure 6-11. (A) An example of a SIR-C/X (Space Shuttle) C (6 cm) and X-band (3 cm) composite image of a mountainous area in north-central Thailand acquired on October 3, 1994. Colour composite radar image. Red has been assigned to an L-band HH image, green to an L-band HV image, and blue to a C-band HV image. Several examples of 'flat-iron' erosional features can be seen (areas 1, 2, 3), which give an indication of dip direction and angle. The vertex of the V points up-dip and narrower Vs indicate a steeper dip. **(B)** Ground photo showing 'flat-iron' dip slopes.

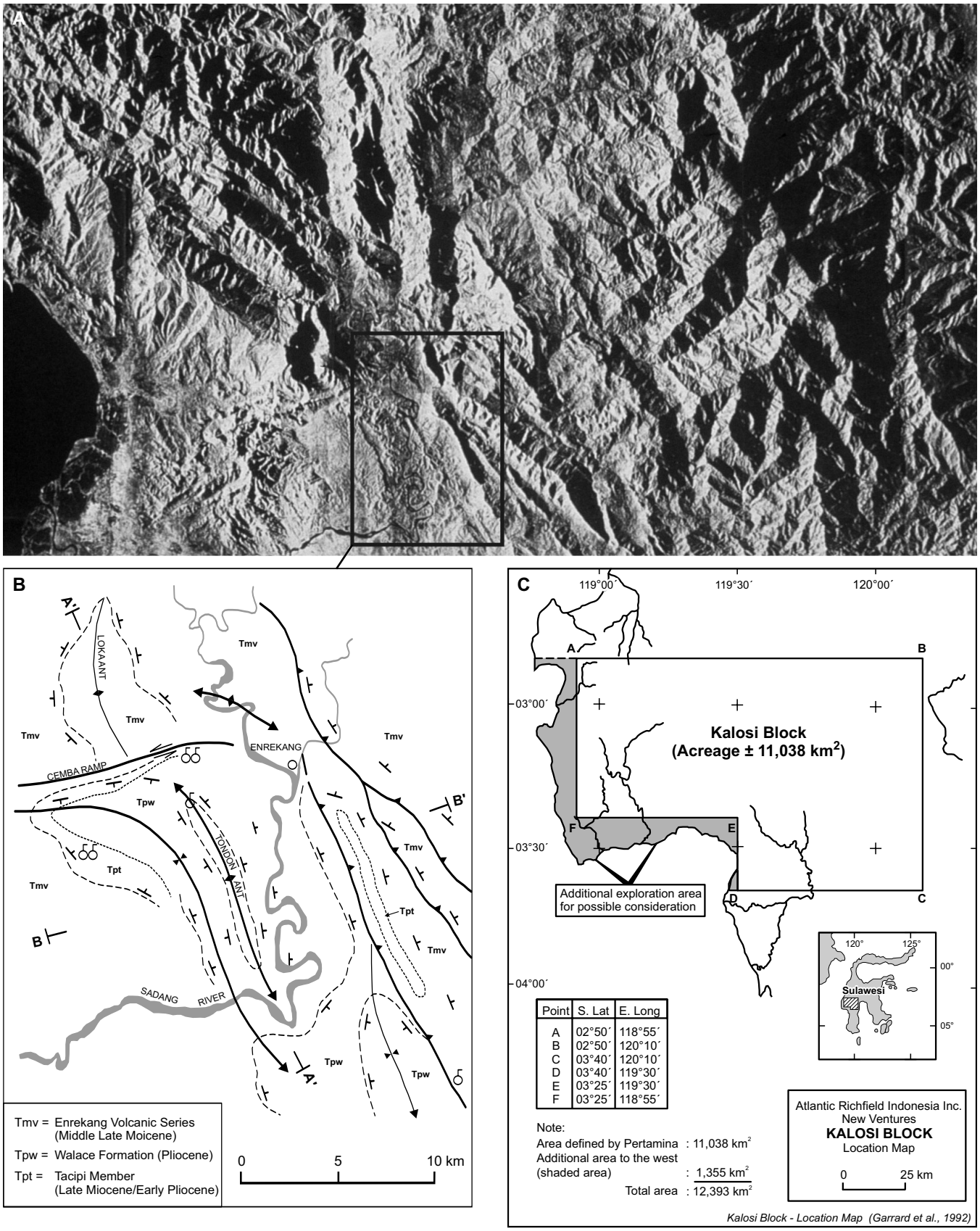

Figure 6-12. Example of the structural interpretation of an X-band airborne SAR image acquired over the Island of Sulawesi, Indonesia fold and thrust belt. **(A)** X-band SAR image. **(B)** Structural interpretation. **(C)** Location map (Fig. 1 from Garrard et al., 1992). The relatively young geological terrane allows for not only the mapping of the strike and the form of the regional structural features but also the estimation of dips based on 'flat-iron' patterns (see Fig. 6-11).

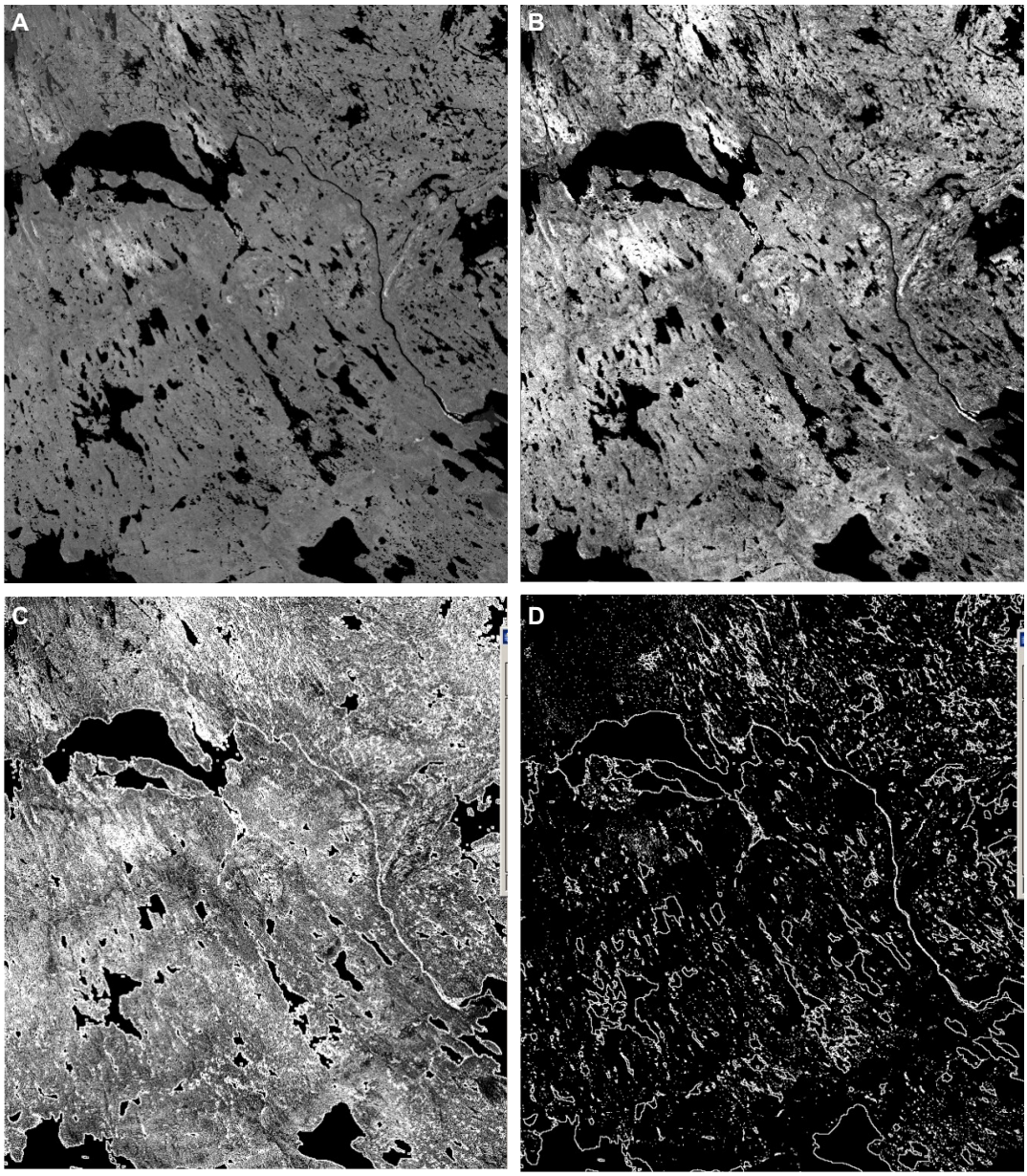

Figure 6-13. Examples of enhanced and filtered radar images of Shultz Lake, Nunavut (NTS map sheet 66a). **(A)** Raw RADARSAT S7 image. **(B)** Contrast enhancement. **(C)** Spatially filtered using a 3 by 3 median filter. **(D)** Threshold of filtered image (in C) highlighting linear elements in the image.

can be clearly identified (Fig. 6-10), although it is not always possible to derive information on dips (Fig. 6-11). In younger, less eroded terranes, a qualitative measure of both the strike and dip of bedding/foliation can often be obtained that enables not only the identification of fold structures but also whether they represent an anticline or syncline (Fig. 6-12).

Lithology

As noted previously, radar backscatter generally is a function of surface parameters, and the difference in weathering styles between lithological units may result in an image in which the various lithologies can be identified as a function of varying surface roughness (Fig. 6-7). However, the individual rock types often cannot be unequivocally identified without supporting data and field work. Furthermore, as surficial cover will modify the roughness and moisture characteristics of the in situ bedrock, often backscatter will reflect the characteristics of the surficial cover as opposed to the underlying bedrock, unless the surficial material is residual. This is the case for most remote sensors that derive their signature from the surface (i.e. optical, gamma-ray spectrometer). This makes radar a better choice for mapping various surficial materials (see below).

Surficial Structure

As previously discussed, radar utilizes a side-viewing acquisition geometry (Fig. 6-2), which in part results in the enhancement of geomorphic and topographic patterns, making it ideal for mapping oriented glacial features such as drumlins, flow-lines, and eskers (Fig. 6-5). However, tempering the ability of radar to map these features is the look direction bias (Fig. 6-5),

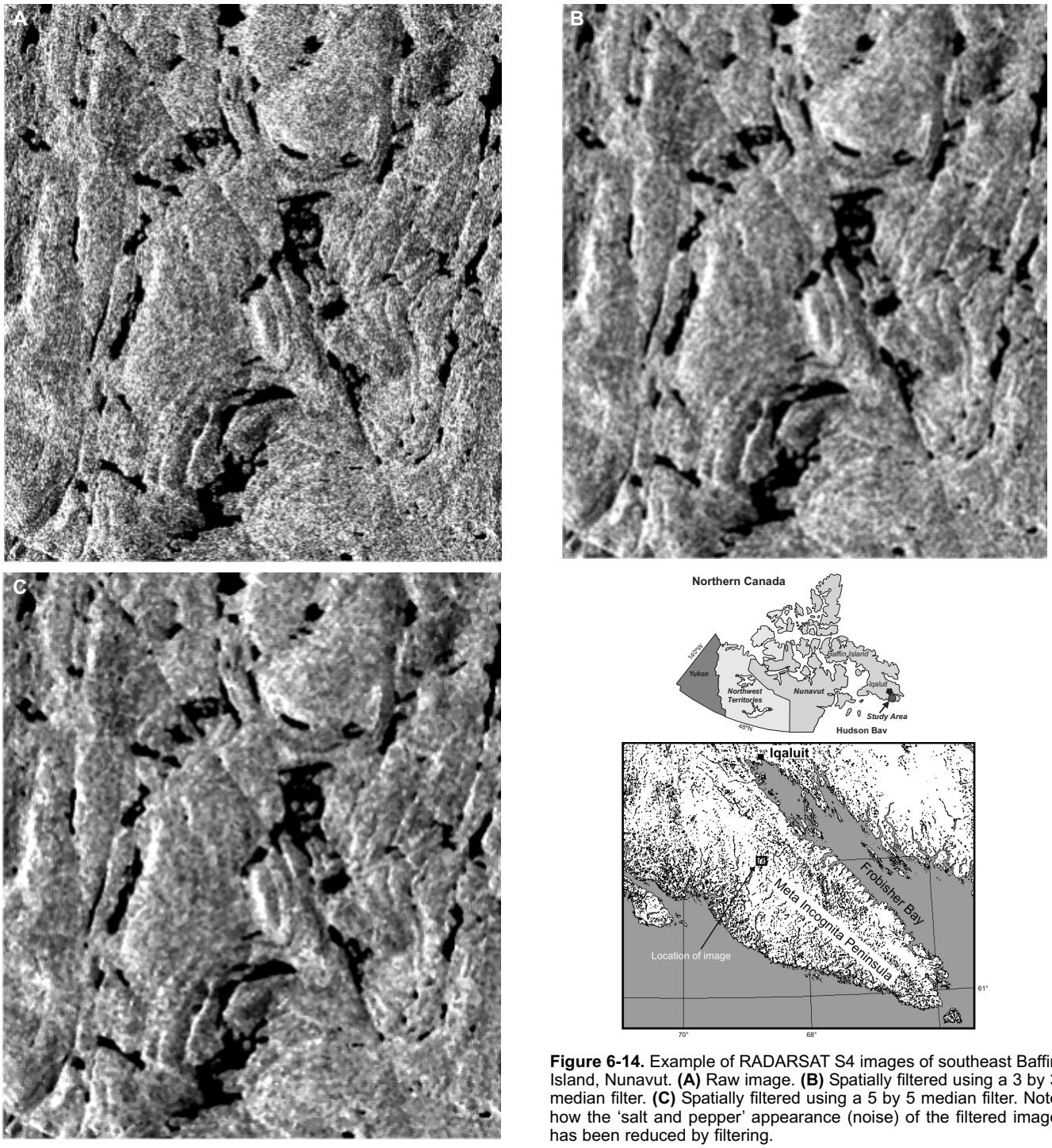

Figure 6-14. Example of RADARSAT S4 images of southeast Baffin Island, Nunavut. **(A)** Raw image. **(B)** Spatially filtered using a 3 by 3 median filter. **(C)** Spatially filtered using a 5 by 5 median filter. Note how the 'salt and pepper' appearance (noise) of the filtered image has been reduced by filtering.

which can suppress topographic features trending parallel to the radar look direction. To counteract this bias, both descending and ascending RADARSAT images are often acquired of the same area, which provides two different look directions. One should note that the difference in look direction, defined as the intersection angle between ascending and descending orbits, increases as one moves towards the poles. This obviously favours radar remote sensing of northern environments where the angle between ascending and descending orbits can be as great as 30º (see Grunsky et al., 2006 for a discussion of how ascending and descending orbits were used to advantage to map surficial features).

Surficial Units

Since radar backscatter is primarily a function of surface parameters (see above), radar can often provide useful information of about surface materials as a function of variations in surface roughness, moisture, and topography.

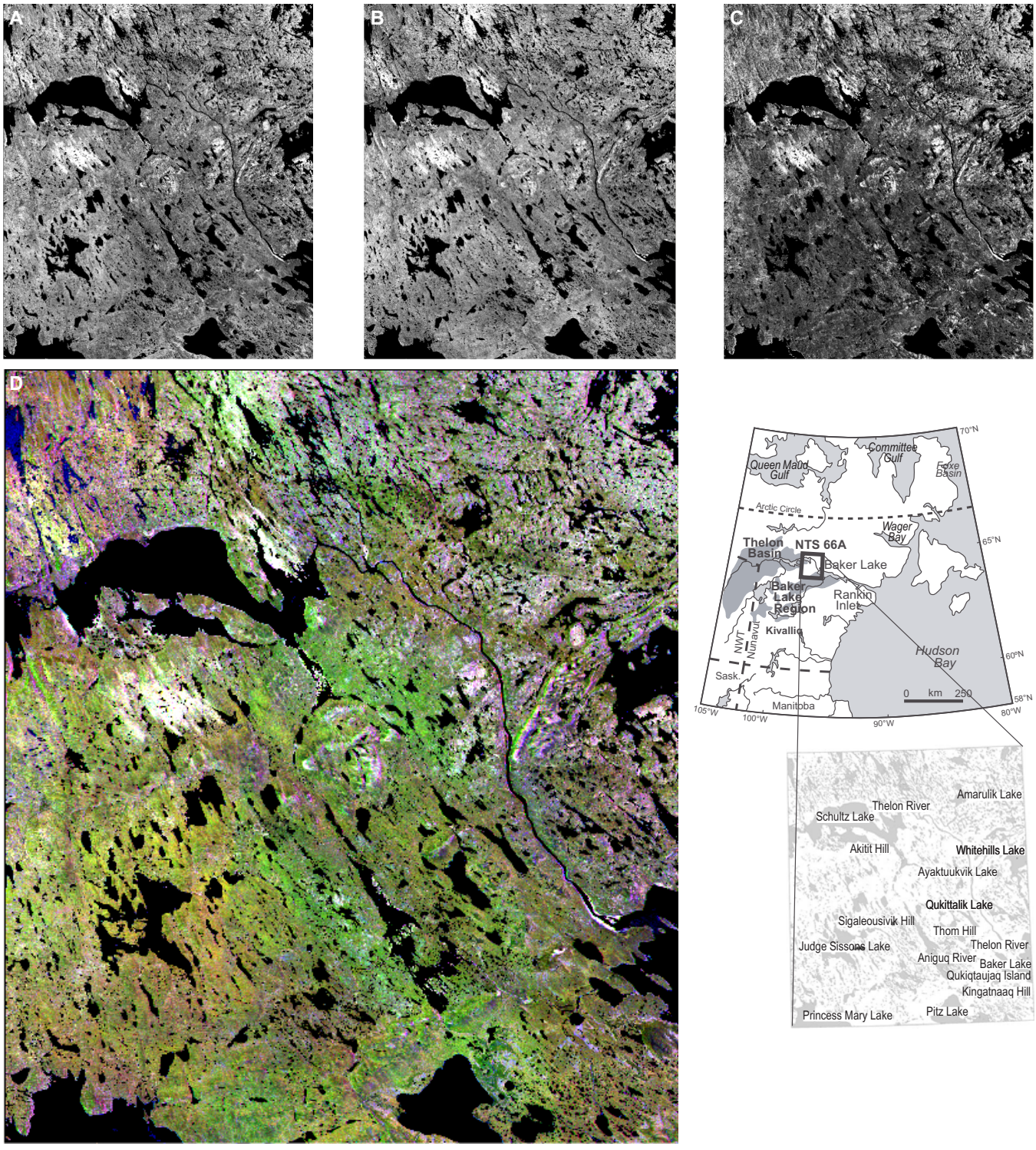

Figure 6-15. Examples of RADARSAT multi-beam colour composite images of Shultz Lake, Nunavut (NTS map sheet 66a). **(A)** S7 (standard beam mode 7) descending mode. **(B)** S7 ascending mode. **(C)** S1 descending mode. **(D)** Colour ternary radar composite (red = S7 descending, green = S7 ascending, S1 descending = blue).

DATA PRODUCTS AND PROCESSING

Visual

Single-Band Synthetic Aperture Radar Imagery

Radar data is collected as a single-band image at a given wavelength, incidence angle, and polarization. As with single-band optical imagery, radar imagery can be contrast enhanced (Fig. 6-13A,B) or spatially filtered (Fig. 6-13C,D) to enhance structural patterns. One peculiar aspect of SAR imagery is the phenomena know as speckle, which imparts a salt-and-pepper appearance (noise) to SAR imagery (Fig. 6-14A). This

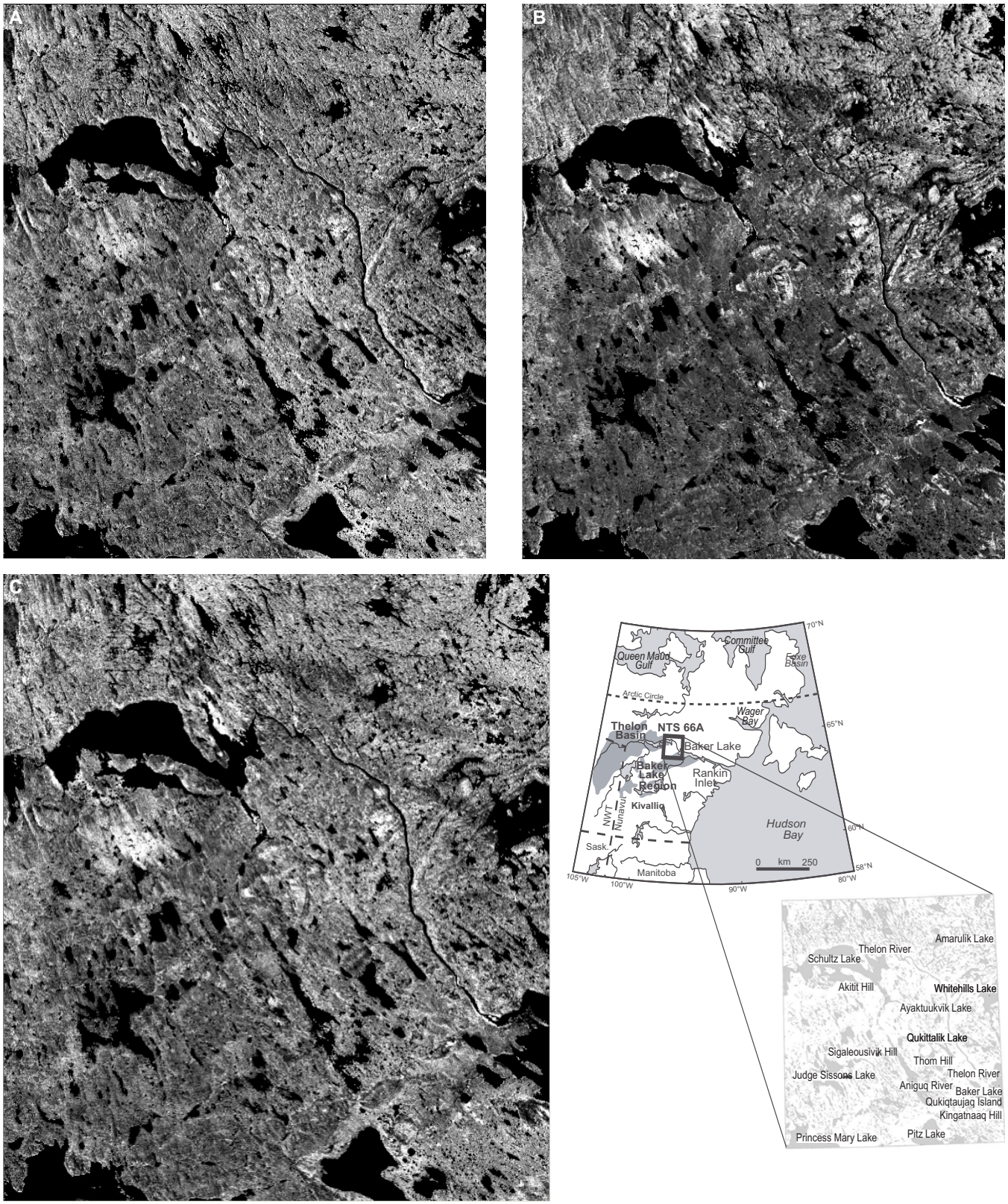

Figure 6-16. Example of how RADARSAT standard beam 1 (S1) ascending and descending modes can be arithmetically combined to create an image that maximizes enhancement of topography using images of Shultz Lake, Nunavut (NTS map sheet 66a). **(A)** Image from S1 ascending mode (S1a). **(B)** Image from S1 descending mode (S1d). **(C)** Arithmetic combination of the images shown in (A) and (B) using the equation (S1a + S1d) / 2.

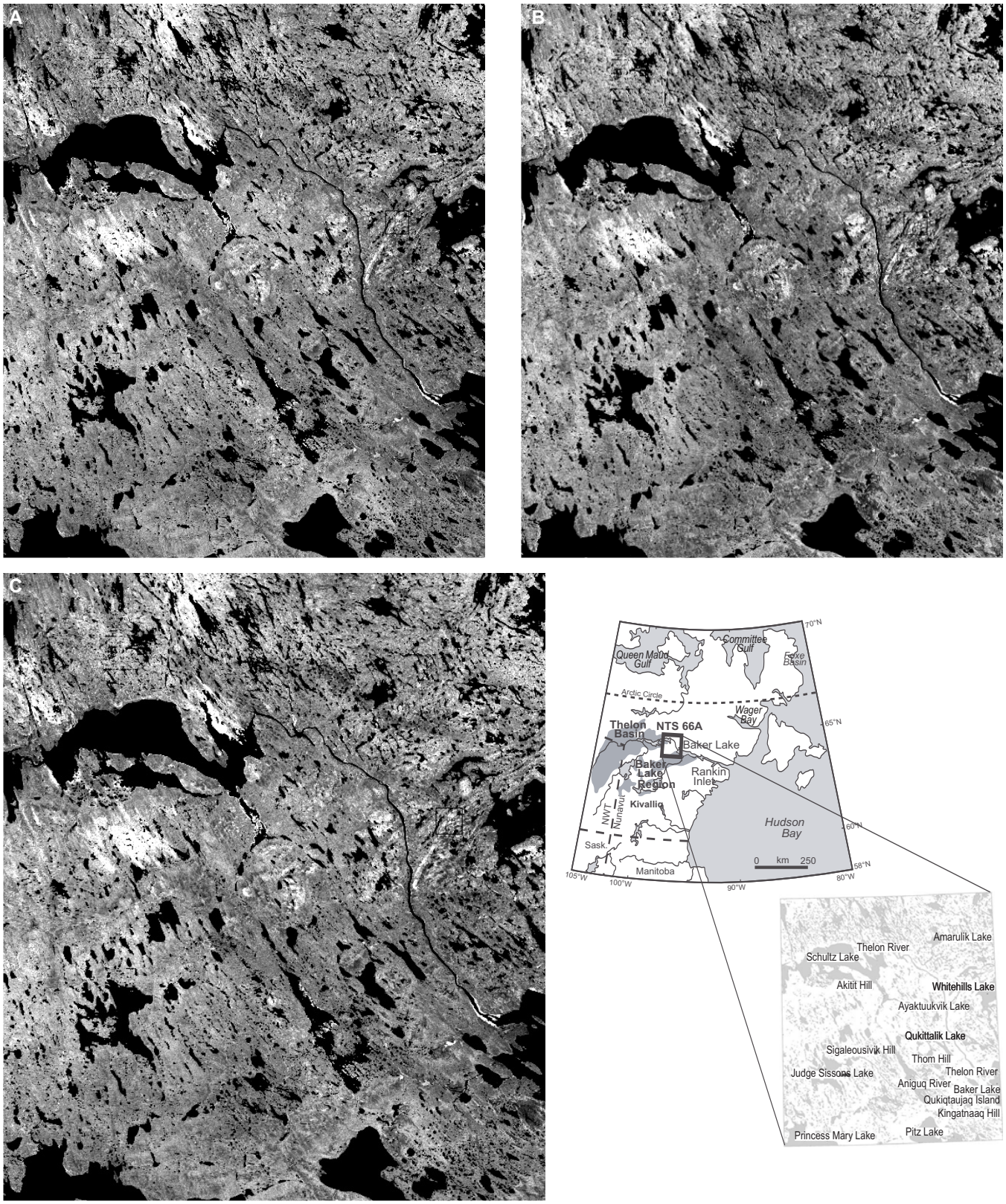

Figure 6-17. Example of how RADARSAT standard beam 7 (S7) ascending and descending modes can be arithmetically combined to create an image that maximizes the enhancement of topography using images of Shultz Lake, Nunavut (NTS map sheet 66a). **(A)** Image produced from S7 ascending mode (S7a). **(B)** Image produced from S7 descending mode (S7d). **(C)** Arithmetic combination of the images shown in (A) and (B) using the equation (S7a + S7d) / 2.

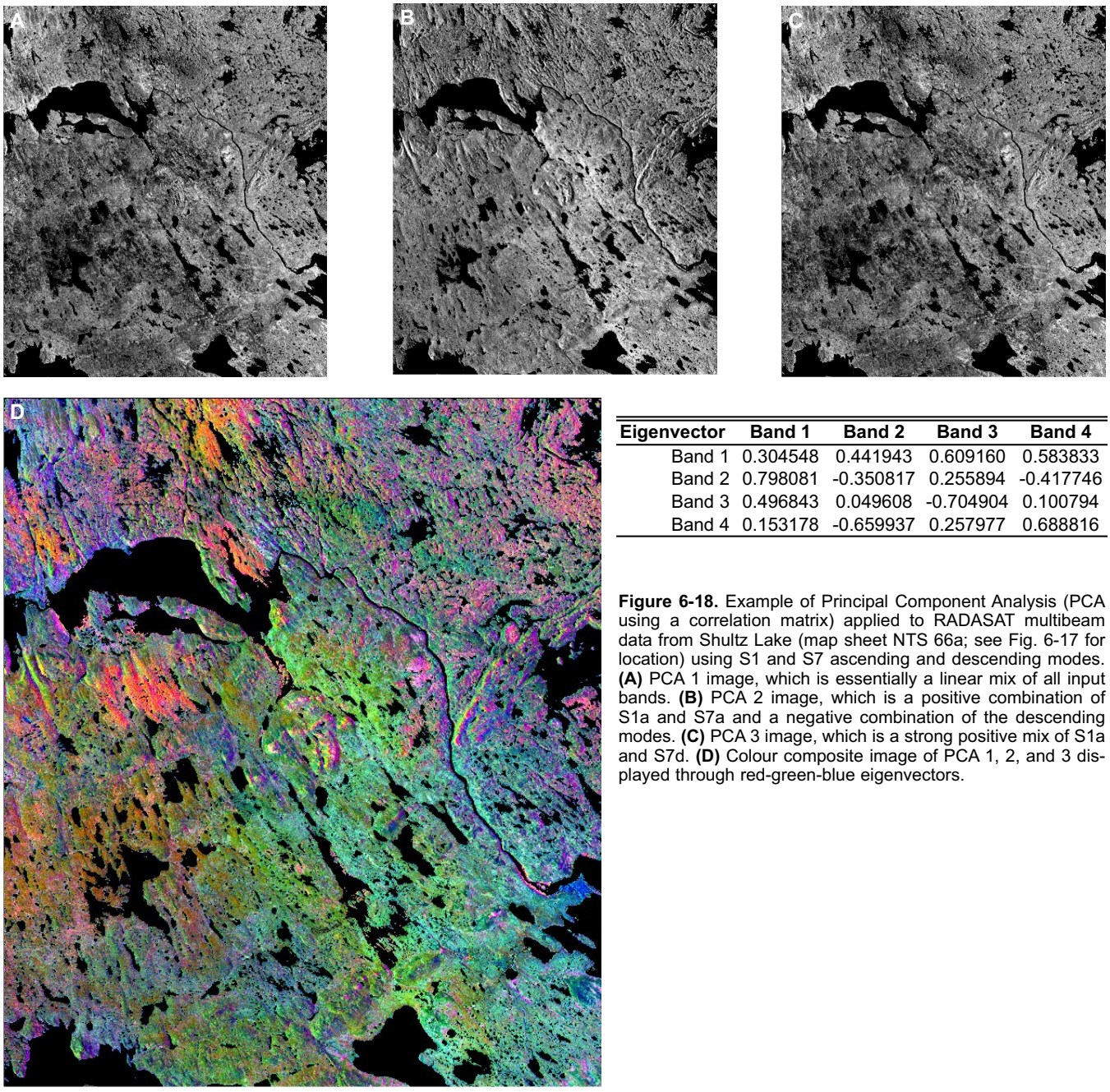

Eigenvector	Band 1	Band 2	Band 3	Band 4
Band 1	0.304548	0.441943	0.609160	0.583833
Band 2	0.798081	-0.350817	0.255894	-0.417746
Band 3	0.496843	0.049608	-0.704904	0.100794
Band 4	0.153178	-0.659937	0.257977	0.688816

Figure 6-18. Example of Principal Component Analysis (PCA using a correlation matrix) applied to RADASAT multibeam data from Shultz Lake (map sheet NTS 66a; see Fig. 6-17 for location) using S1 and S7 ascending and descending modes. **(A)** PCA 1 image, which is essentially a linear mix of all input bands. **(B)** PCA 2 image, which is a positive combination of S1a and S7a and a negative combination of the descending modes. **(C)** PCA 3 image, which is a strong positive mix of S1a and S7d. **(D)** Colour composite image of PCA 1, 2, and 3 displayed through red-green-blue eigenvectors.

is due to the monochromatic character of SAR data and its use of frequency phase information to produce an image. This noise can be reduced or suppressed by spatial-filtering techniques using a wide range of spatial filters (e.g. median, mean) or specifically designed filters (frost, sobel, etc.) to reduce speckle, thus creating imagery that is more amenable for both visual and quantitative interpretation (Fig. 6-14B,C).

Multiple-Band Synthetic Aperture Radar Imagery

RADARSAT has several acquisition modes that comprise different incidence angles as well as different look directions (ascending versus descending mode). Imagery acquired using different acquisition modes can be processed using the same multivariate techniques that are applied to optical data. Red-green-blue (RGB) ternary images can be produced from different radar acquisition modes (Fig. 6-15), which results in imagery that enhance varying aspects of the terrain. Specific characteristics of the surface can be enhanced by using different acquisition modes (incidence angle, look direction, wavelength), thus the additive colours seen on ternary radar images (Fig. 6-15) can be used for mapping surface patterns as a function of variation in topography, surface roughness, and moisture.

Arithmetic processing of different RADARSAT acquisition modes can be undertaken to create useful images

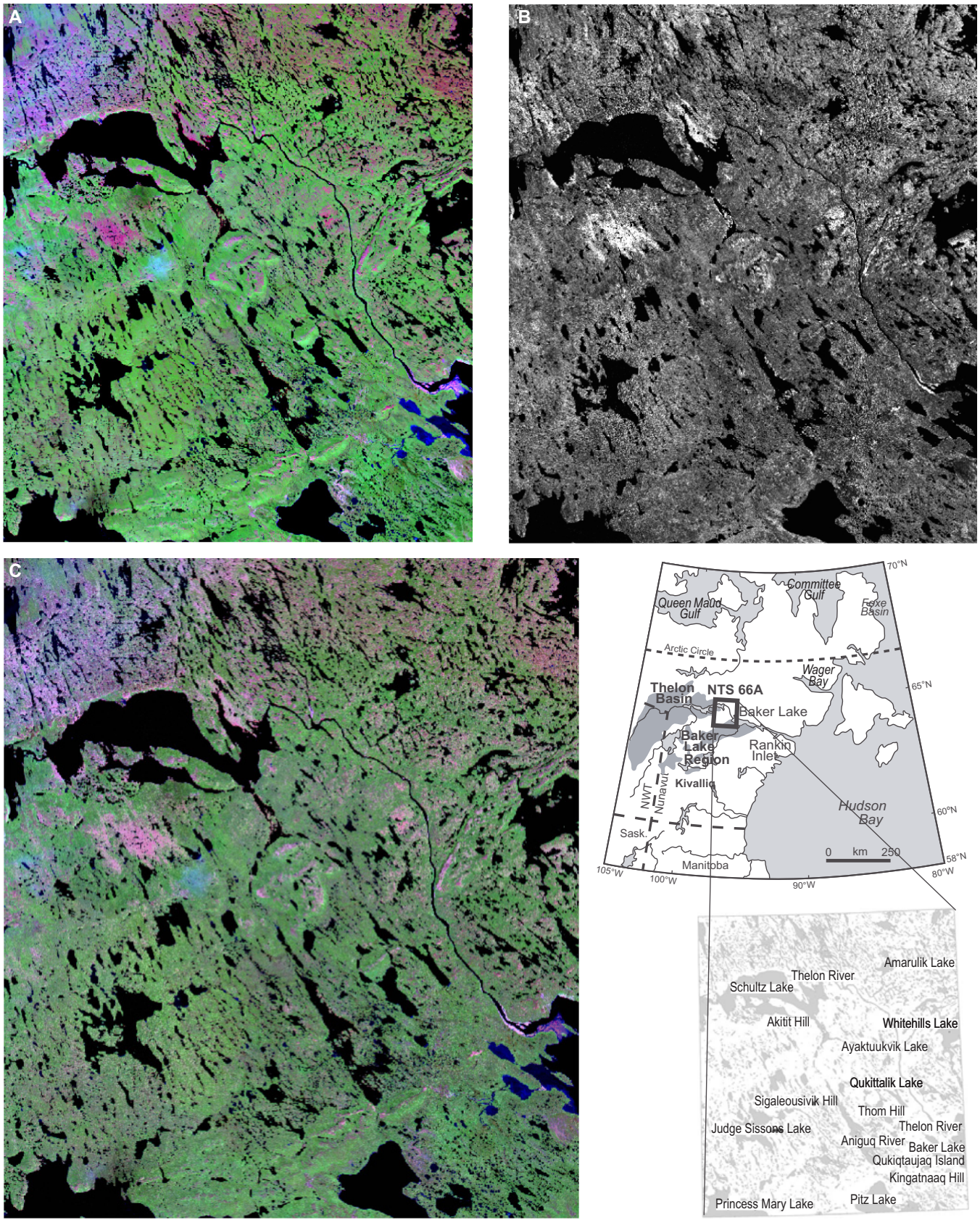

Figure 6-19. Example of data fusion of imagery over Shultz Lake, Nunavut (map sheet NTS 66a). **(A)** LANDSAT TM colour composite image (bands 7, 4, and 2 correspond to red, green, and blue). **(B)** Image created from RADARSAT S7d (descending mode). **(C)** Red-green-blue combination of radar and LANDSAT data (red = LANDSAT band 7, green = LANDSAT band 4, blue = Radar (S7d).

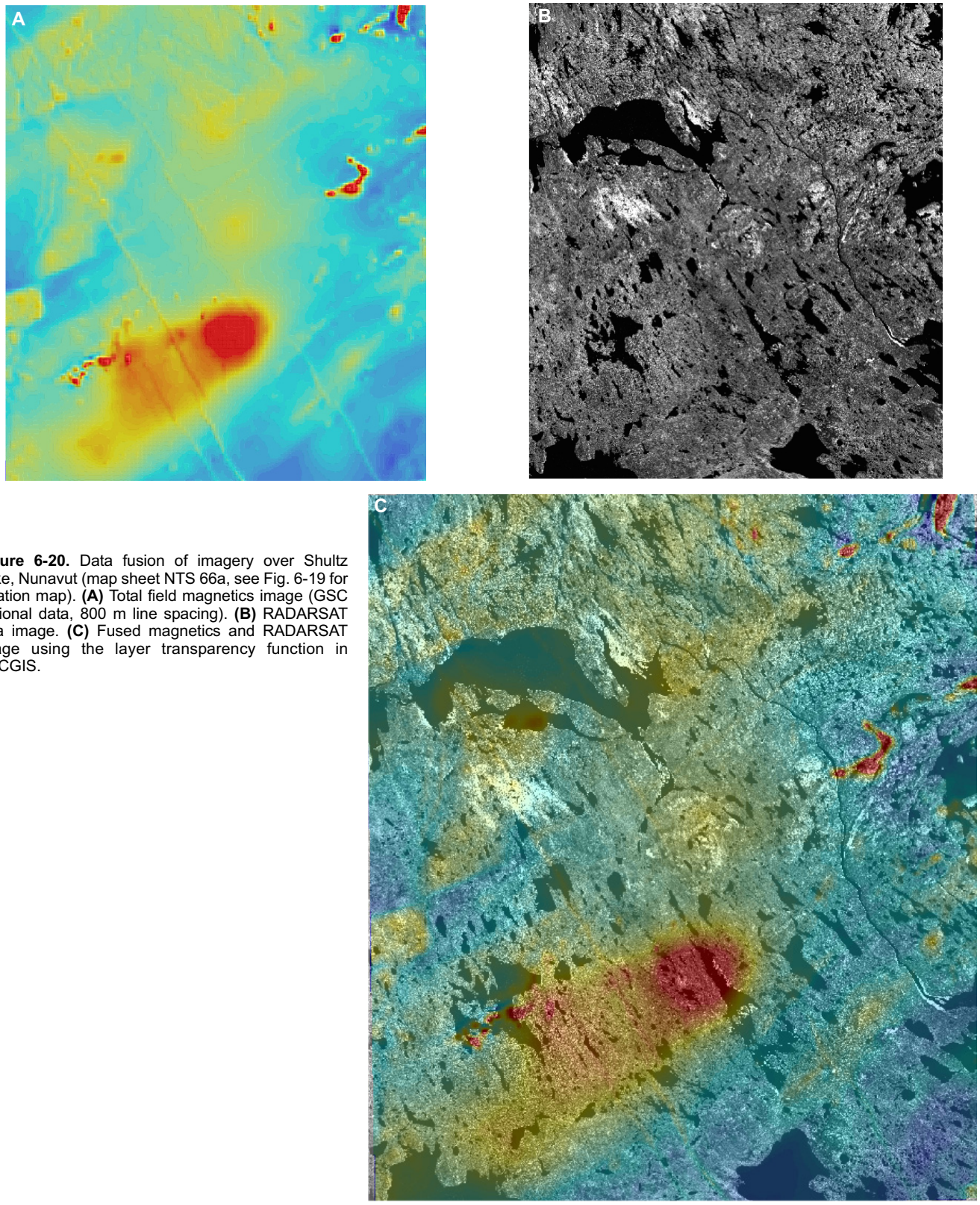

Figure 6-20. Data fusion of imagery over Shultz Lake, Nunavut (map sheet NTS 66a, see Fig. 6-19 for location map). **(A)** Total field magnetics image (GSC regional data, 800 m line spacing). **(B)** RADARSAT S7a image. **(C)** Fused magnetics and RADARSAT image using the layer transparency function in ARCGIS.

for geological interpretation. For example, an arithmetic combination of imagery acquired using steep incidence angles (S1) and different orbits (e.g. ascending and descending) can result in an image that offers good enhancement of topographic patterns (Fig. 6-16). Conversely, ascending and descending orbits of RADARSAT imagery acquired at shallower incidence angles (S3-S7) can offer an image ideal for the interpretation of surficial patterns related to variations in surface roughness (Fig. 6-17).

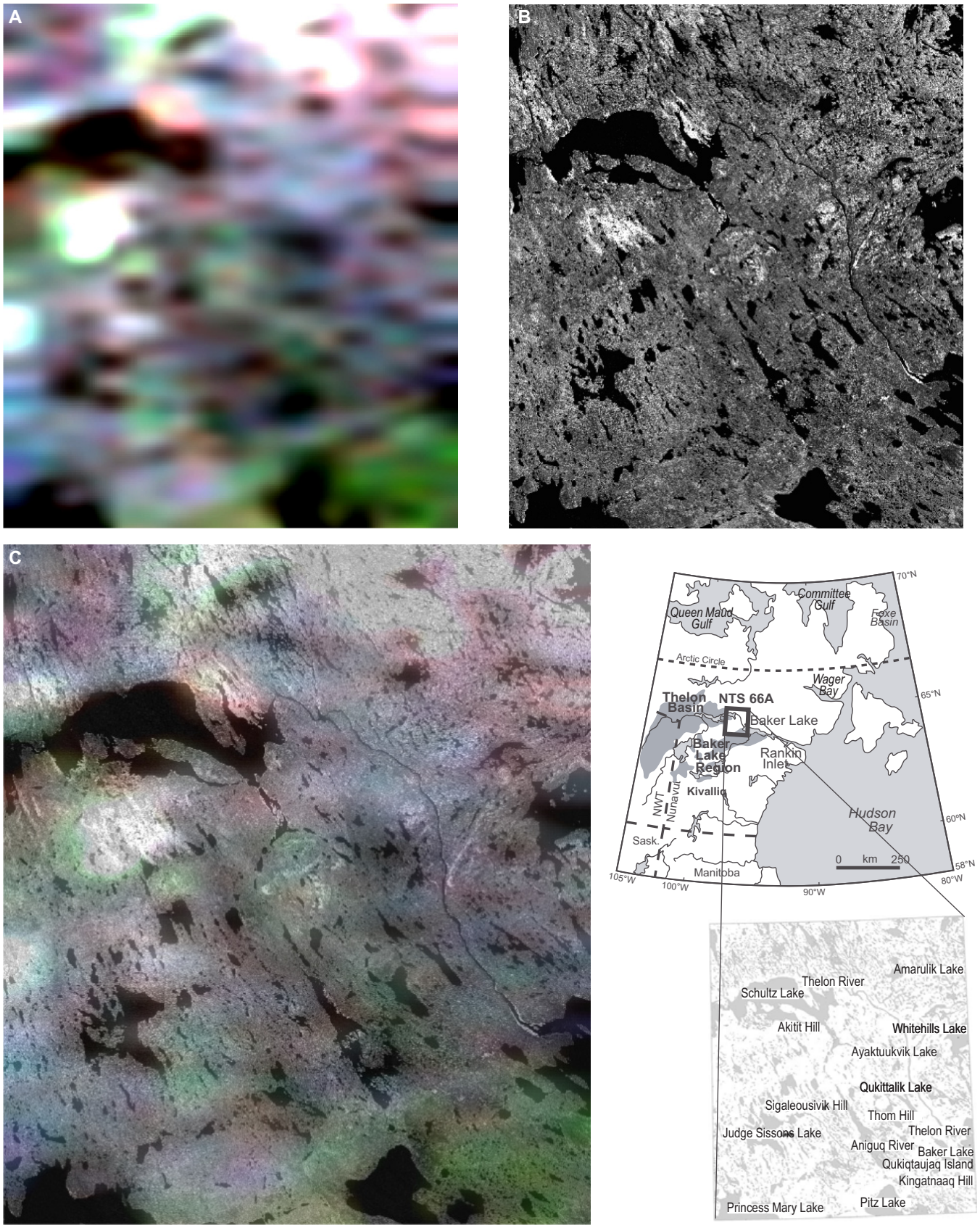

Figure 6-21. Data fusion of imagery over Shultz Lake, Nunavut (map sheet NTS 66a). **(A)** Ternary gamma-ray image (eU, %K, and eTh correspond to red, green, and blue). **(B)** RADARSAT S7a image. **(C)** Image created by fusing images A and B.

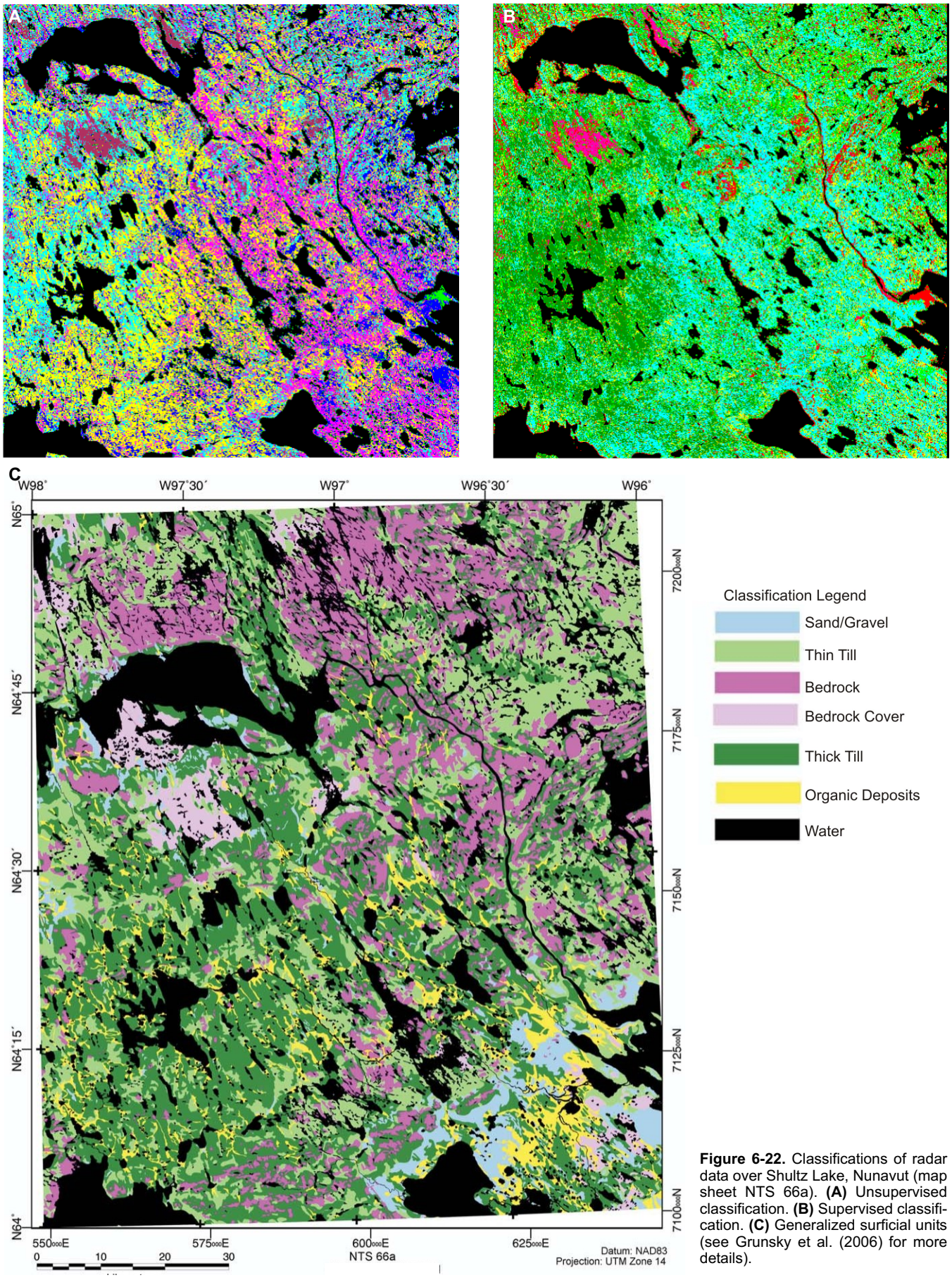

Figure 6-22. Classifications of radar data over Shultz Lake, Nunavut (map sheet NTS 66a). **(A)** Unsupervised classification. **(B)** Supervised classification. **(C)** Generalized surficial units (see Grunsky et al. (2006) for more details).

Multi-beam radar data (i.e. RADARSAT) are also amenable to multivariate processing techniques for data enhancement, analysis, and visualization. Principal component analysis (PCA) can be used to enhance and process radar imagery (Lowman et al., 1987; Grunsky, 2002; Grunsky et al., 2006). PCA processing of radar imagery, as for optical imagery, can result in enhanced images useful for both bedrock and surficial mapping (Fig. 6-18).

The Principal Component transform (PCA transform (Green et al. 1988) is an effective technique for reducing a large multi-band data set into a fewer number of components that contain the majority of information (spectral variance) of the data set. There can be as many components as there are input bands; however, each component, starting from the first, describe less and less of the overall variance of the data set. Typically only a small number of components are required to describe most of the information for the entire data set. The contribution of each component to the overall information of a multivariate data set (i.e. hyperspectral imagery) is measured by an eigenvalue (see table in Fig. 6-18). A larger eigenvalue indicates that a component contains more information from the data set. The contribution of each band to each component is measured by an eigenvector, which can be interpreted somewhat like a correlation coefficient. Eigenvectors range from –1.0 to +1.0; therefore a band with an eigenvector close to 1 indicates that the band has a large contribution to the component. Thus each component image is a linear mix of the input bands. A thorough discussion of the application of PCA applications to remotely sensed data can be found in Jensen (1996).

In this case, the input bands to the PCA transform are the following: S1 ascending, S1 descending, S7 ascending, and S7 descending. The eigenvalue table indicates that the S7a band has the strongest influence on the first component image, S1a and S7a have the strongest positive influence, whereas S7d has a strong negative weighting on the second component image. The third component image (Fig. 6-18C) is strongly weighted by S7d and S1a. Thus it can be seen that PCA is useful for combining the different images using a red-green-blue combination of the component image (as seen in Fig. 6-18D) offering a ternary image in which the different colours often represent different surficial materials.

Like any other remotely sensed image, radar data can be fused (combined) with any other raster geoscience dataset (Harris et al., 1990, 1999; Viljoen and Harris, 2007). Radar data fused with optical data produce an image in which both spectral and surface roughness properties are evident (Fig. 6-19). Imagery can be fused (combined) in many ways (see Harris et al. (1990, 1999) and Viljoen and Harris (2007)), including ternary band combinations, layer transparency functions, arithmetic transformations, colour space transformations, and specialized adaptive algorithms. A layer transparency function, offered in many graphic information systems, is the easiest to implement, whereas colour space algorithms, and especially adaptive algorithms, are more robust, which results in better preservation of the colour attributes, hue, value (intensity), and saturation. Radar data can also be fused with geophysical data (Figs. 6-20, 6-21), offering an image in which surficial features and patterns can be directly compared to magnetic signatures. Appendix 1 provides an example of how high-resolution radar data can be fused with other data for mineral exploration and mapping applications.

Multi-beam radar data can also be subjected to classification utilizing, unsupervised or supervised methodologies (Fig. 6-22).

REFERENCES

Ames, D.E., Singhroy, V., Buckle, J., Davidson, A., and Molch, K.
2006: Integrated bedrock geology-Radarsat-digital elevation data of Sudbury, Ontario; Geological Survey of Canada, Open File 4571, scale 1:75,000.

Budkewitsch, P., and D'Iorio, M.A.
1997: Contributions toward understanding C-band SAR data for lithological discrimination and structural mapping in the Canadian Arctic, *in* Proceedings of the 12th International Conference and Workshop on Applied Geologic Remote Sensing; Denver, Colorado, November 17-19, 1997, v. 1, p. 38-41.

Garrard, R.A., Nusatriyo, G., and Coffield, D.Q.
1992: The prospectivity of early Tertiary rift sequences in the Neogene fold belts of South Sulawesi, *in* Program and Extended Abstracts of the Eastern Indonesia Exploration Symposium, Petramina and Simon Petroleum Technology, Jakarta.

Graham, D.F. and Grant, D.R.
1991: A test of airborne side-looking synthetic aperature radar in central Newfoundland for geological reconnaissance; Canadian Journal of Earth Science, v. 28, p. 257-265.

Green, A.A., Berman, M., Switzer, P., and Craig, M.D.
1988: A transformation for ordering multispectral data in terms of image quality with implications for noise removal; IEEE Transactions on Geoscience and Remote Sensing, v. 26, p. 65-74.

Grunsky, E.C.
2002: The application of principal components analysis to multibeam RADARSAT-I satellite imagery: A tool for land cover and terrain mapping; Canadian Journal of Remote Sensing, v. 28, p. 758-769.

Grunsky, E., Harris, J.R., and McMartin, I.
2006: Predictive Mapping of Surfical Materials, Shultz lake Area (NTS 66A), Nunavut, Canada; Geological Survey of Canada, Open File 5153, 49 p.

Harris, J.R., Graham, D.F., Newton, R., Yatabe, S., and Miree, H.
1987: Reconnaissance Structure Mapping of the Grenville Province of Ontario and Quebec Using Remotely Sensed Data. 7th Conference on Basement Tectonics, Kingston, Ontario. p. 441-463.

Harris, J.R., Murray R., and Hirose, T.
1990: IHS Transform for the integration of radar imagery and other remotely sensed data; Photogrammetric Engineering and Remote Sensing, v. 56, p. 1631-1641.

Harris, J.R., Viljoen, D., and Rencz, A.
1999: Integration and visualization of geoscience data, *in* Remote Sensing for the Earth Sciences, (ed.) A.N. Rencz; John Wiley and Sons Inc., New York, 707 p.

Harrison, J.C. and de Freitas, T.
1998: Bedrock Geology, Bathurst Island Group (NTS 68G, 68H, 69A, 69B; small parts of 79A), District of Franklin (Nunavut), NWT; Geological Survey of Canada, Open File 3577, scale 1:125 000.

Jensen, J.R.
1996: Introductory Digital Image Processing: A Remote Sensing Perspective, 3rd Edition; Pearson; Prentice Hall, Upper Saddle River, New Jersey, 18 p.

Kenny, F., Barnett, P., and Singhroy, V.
1994: Application of airborne multispectral and radar images for Quaternary geology mapping; Canadian Journal of Remote Sensing, v. 20, p. 286-292.

Lillesand T.M. and Kiefer R.W.
1987: Remote Sensing and Image Interpretation, 2nd Edition; John Wiley and Sons Inc., New York, 736 p.

Lowman, P.
1994: Radar geology of the Canadian Shield - A 10 year review; Canadian Journal of Remote Sensing, v. 20, p. 198-209.

Lowman, P.D., Harris, J., Masuoka, P.M., Singhroy, V.H., and Slaney, V.R.
1987: Shuttle imaging radar (SIR-B) investigations of the Canadian Shield: Initial report; IEE Transactions on Geoscience and Remote Sensing, v. GE-25, p. 55-66.

Madon, Z., Trowell, N.F., Berger, B., and Ayer, J.A.
1999: Geological investigation and data integration of typical Canadian shield terrain using airborne and satellite imagery including RADARSAT Radar - Lighting River Area, Abitibi Greenstone Belt, Ontario; Canadian Journal of Remote Sensing, v. 25, p. 229-244.

McGregor, R.G., Bruton, P., Singhroy, V.H., and Brown, A.
1999: An application of remote sensing and GIS towards geological site characterization of a Canadian shield terrain; Canadian Journal of Remote Sensing, v. 29, p. 245-257.

Mungall, J.E., Ames, D.E., and Hanley, J.J.
2004: Geochemical evidence from the Sudbury structure for crustal redistribution by large bolide impacts; Nature, v. 429, p. 546-548.

Rivard, B., Corriveau, L., and Harris, L.B.
1999: Structural reconnaissance of a deep crustal orogen using RADARSAT and LANDSAT satellite imagery and airborne geophysics; Canadian Journal of Remote Sensing, v. 25, p. 258-267.

Saint-Jean R., Singhroy, V., and Rheault, M.
1999: Understanding multi-polarized airborne C-SAR images for geological mapping in Precambrian Shield terrains; Applied Geologic Remote Sensing, Proceedings of Environmental Research Institute of Michigan, 13th International Conference, Vancouver, v. 1. p. 411-418.

Singhroy, V.
1992: Radar geology, techniques and results; Episodes, v. 15, p. 15-20.
1996: Environmental and geological site characterization in vegetated areas: Image enhancement guidelines, *in* Remote Sensing and GIS: Applications and Standards, (eds.) V. Singhroy, D. Nebert, and A. Johnson; American Society for Testing and Materials, Special Technical Publication No. 1279, p. 5-17

Singhroy, V. and Barnett, P.
2003: Satellite-based standardized terrain maps: A case study, *in* Spatial Methods for Solution of Environmental and Hydrologic Problems: Science Policy and Standardization; American Society for Testing and Materials, Special Technical Publication No. 1420, p. 148-162.

Singhroy, V. and Molch, K.
2004: Geological applications of RADARSAT-2; Canadian Journal of Remote Sensing, v. 30, p. 893-902.

Singhroy, V. and Saint-Jean, R.
1999: Effects of relief on the selection of RADARSAT-1 incidence angle for geological applications; Canadian Journal of Remote Sensing, v. 25, p. 211-217.

Singhroy, V., Barnett, P., and Kenny, F.
1992: Radar imagery for Quaternary geological mapping in glaciated terrains; Canadian Journal of Remote Sensing, v. 18, p. 112.

Singhroy, V., Slaney, R., Lowman, P., Harris, J., and Moon, W.
1993: RADARSAT and radar geology in Canada; Canadian Journal of Remote Sensing, v. 14, p. 329-332.

Viljoen, D. and Harris. J.R.
2007: Saturation and Value Modulation (SVM): A new method for integrating color and grayscale imagery, *in* Digital Mapping Techniques '06, (ed.) D.R. Stoller; Workshop Proceedings, United States Geological Survey, Open File Report 2007-1285, p. 1-22.

APPENDIX 6-1. Application of High-Resolution Radar Image Fusion for Mineral Exploration and Mapping

In this Appendix, we report on the capabilities of high-resolution image-fusion techniques in support of geological mapping and mineral exploration. This investigation provides evidence that the 3 m high-resolution ultra-fine capability of RADARSAT-2, when fused with other high-resolution geophysical data, will improve current image-fusion techniques used by exploration companies and geological mapping agencies.

Harris et al. (1990), Singhroy (1992, 1996), Madon et al. (1999), McGregor et al. (1999), Rivard et al. (1999), Singhroy and Molch (2004), and others have developed interpretation techniques for RADARSAT-fused images to facilitate mineral exploration programs in Canada. In addition, several recent studies have used radar image the techniques to assist in providing information on the physical properties and distribution of surficial materials to facilitate drift prospecting in glaciated terrains (Graham and Grant, 1991; Singhroy et al., 1992, 1993; Kenny et al., 1994; Singhroy, 1996; Singhroy and Barnett, 2003). Currently, mineral exploration companies, geological agencies, and consulting firms now use these methods and interpretation guidelines routinely and as such the Canadian Space Agency has supported several contracts on RADARSAT-1 data fusion techniques to service the Canadian and international mineral and hydrocarbon exploration industry.

The Sudbury Basin and Lac Volant mineral belts are used as examples to demonstrate the capabilities of radar fusion and lineament techniques in support of mapping and exploration. The Sudbury Basin is one of Canada's richest mining areas, with world-class mineral deposits and the world's oldest, largest, and best exposed meteorite impact site (Mungall et al., 2004). This elliptical feature, known as the Sudbury Basin, is 300 km in diameter and approximately 2 billion years old. Over the past 100 years, $135 billion of nickel and copper ores have been mined from more than 90 mines distributed around the rim of the Basin. Current production is approximately $2 billion a year. Figure 6A1-1 shows some regional geological information and the distribution of mining properties of Inco Inc., one of

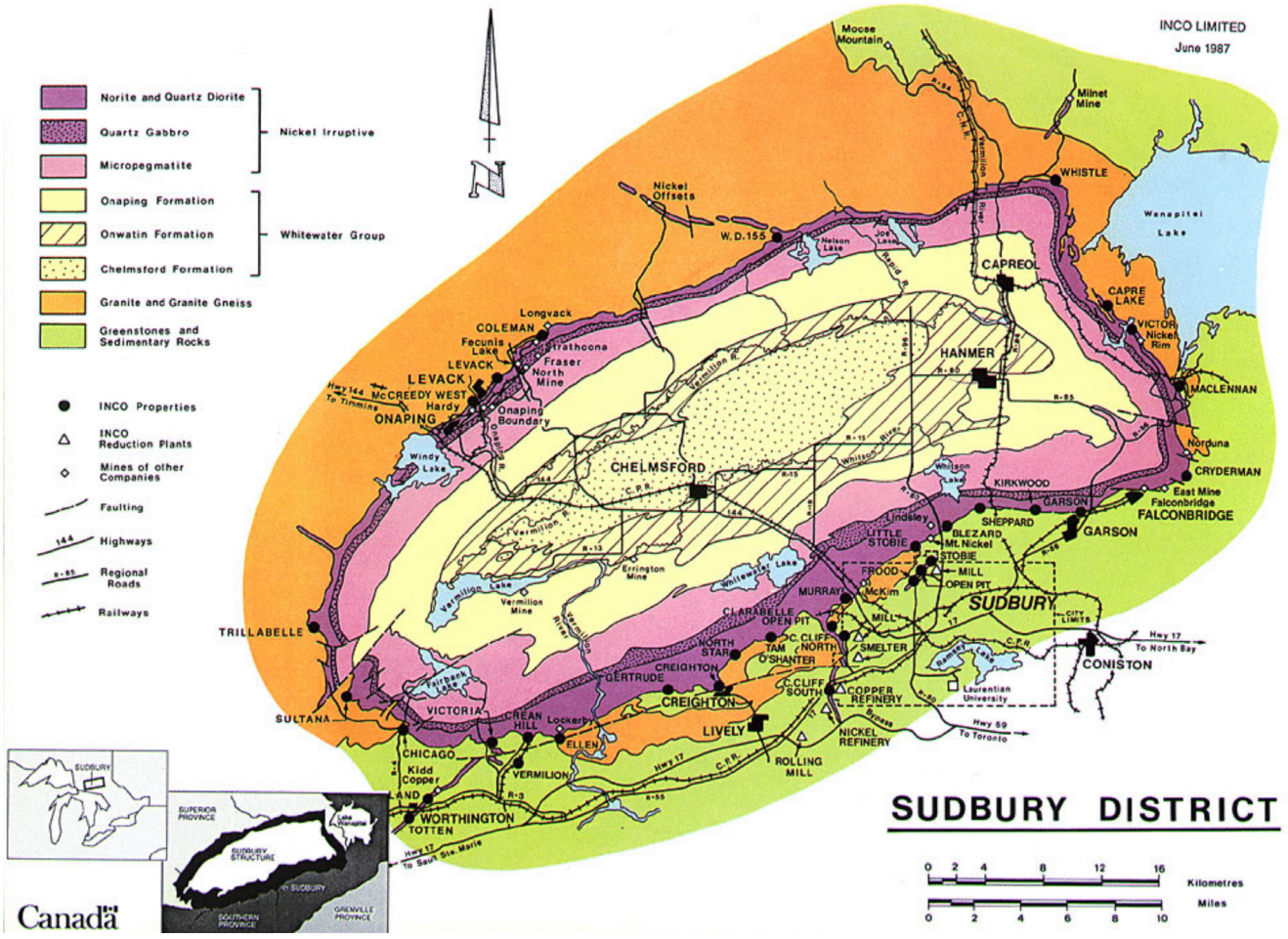

Figure 6A1-1. Geological setting of the Sudbury Basin. Mineralization predominantly occurs on the outer perimeter of the impact structure, which is where the mines (black dots) are located. Map from Ames et al. (2006).

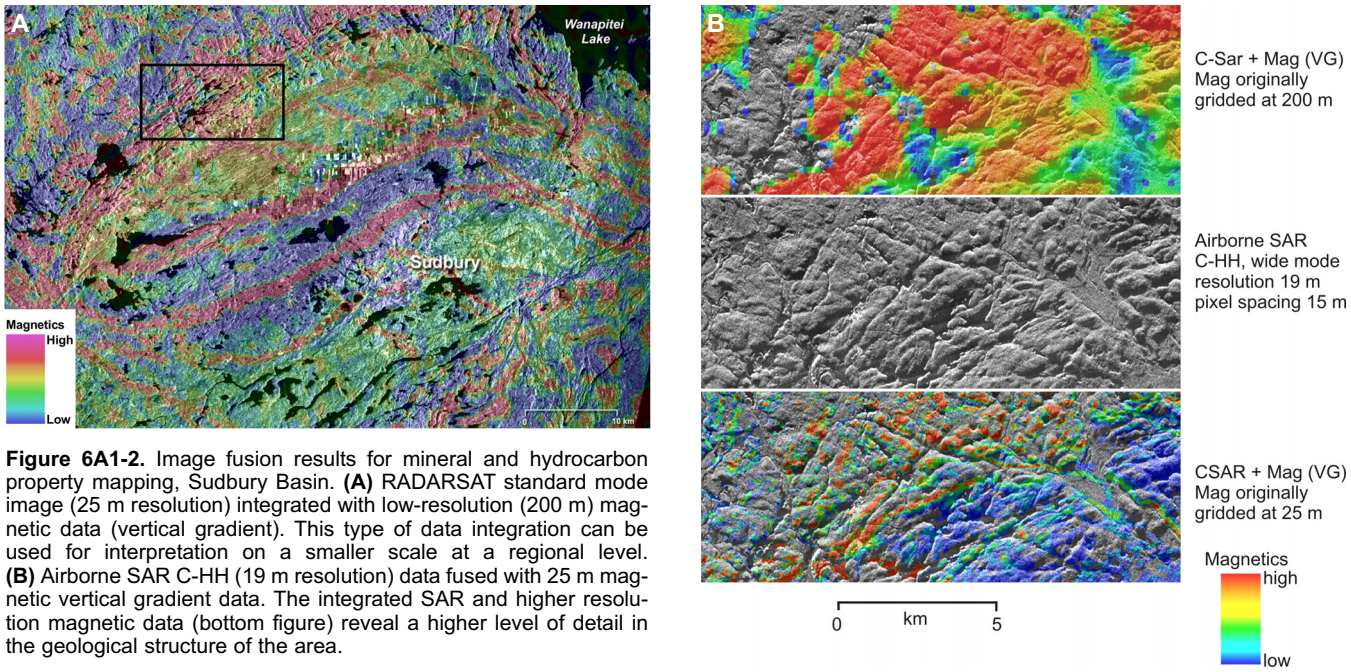

Figure 6A1-2. Image fusion results for mineral and hydrocarbon property mapping, Sudbury Basin. **(A)** RADARSAT standard mode image (25 m resolution) integrated with low-resolution (200 m) magnetic data (vertical gradient). This type of data integration can be used for interpretation on a smaller scale at a regional level. **(B)** Airborne SAR C-HH (19 m resolution) data fused with 25 m magnetic vertical gradient data. The integrated SAR and higher resolution magnetic data (bottom figure) reveal a higher level of detail in the geological structure of the area.

the largest mining companies in Canada. This simplified geological map is used to facilitate the interpretation of the fused product of the Sudbury Basin shown in Figure 6A1-2A, which consists of a Standard 1 mode RADARSAT–1 image (25 m resolution) integrated with low-resolution (200 m) magnetic data. Much remains to be learned about the structural evolution of the Sudbury Basin and the mineralized showings around it, and there are current discussions to conduct deep drilling to understand mineral emplacement and the impact structure. RADARSAT-1 images have been used to study the characteristic elliptical shape and the associated fractures around the Basin (Lowman, 1994). The standard beam mode of RADARSAT, at 20 to 27º incidence angle, provides an excellent view of the topography and structural features of the Sudbury area. Structure is expressed by differential erosion controlled by fractures, dykes, and lithology. The fused image in Figure 6A1-2A is generated using the Intensity-Hue-Saturation (IHS) integration procedure. It involves the fusion of the RADARSAT-1 SAR image to modulate the intensity, the magnetic signatures to modulate the hue, and a constant to modulate the saturation of the resulting image. The RADARSAT-1 image provides terrain information and the surface expressions of structures seen on the image, which appear as a network of linear features. The low-resolution vertical magnetic gradient image, obtained from the Geological Survey of Canada (GSC), shows geological units as expressed from their magnetic signatures. The variation in the concentration of magnetic minerals can be used to trace rock units. Therefore, the combined RADARSAT-1 and geophysical image map is useful in the geological mapping of the structures and lithology. Areas in red outline the strong magnetic signature of the Sudbury Igneous Complex (also known as the nickel eruptive). Magma-filled dykes also have highly magnetic signatures. These are seen as northeast-southwest-trending lineaments observed on both the RADARSAT-1 and geophysical images. The other colours shown on the fused image correspond to different rock types with different magnetic signatures. These types of fused images are used by geologists and mining companies to facilitate geological interpretation. The technique involves fusing RADARSAT-1 images selectively with vertical gradient magnetic, radiometric, topographic, and optical data, thus producing thematic exploration image maps at a scale of 1:100 000 for regional exploration and mapping programs. With the availability of the 3 m ultra-fine beam mode of RADARSAT-2, together with other high-resolution topographic and geophysical data sources, the image-fusion techniques shown in Figures 6A1-2 and 6A1-3 will provide an effective tool for mineral and hydrocarbon property mapping at scales of less than 1:20 000. Recently Ames et al. (2006) have used RADARSAT integrated images to update the geological mapping of the basin.

High-resolution image maps are shown in Figures 6A1-2B and 6A1-3. These are produced from CV-580 airborne high-resolution SAR data of mineral belts of the Sudbury Basin in Ontario and the Lac Volant area in Quebec. At the Lac Volant site, Saint-Jean et al. (1999) reported that some lineament orientations are enhanced by cross-polarized images. In both areas, there are current active mineral exploration programs. These areas are typical Canadian Shield terrains con-

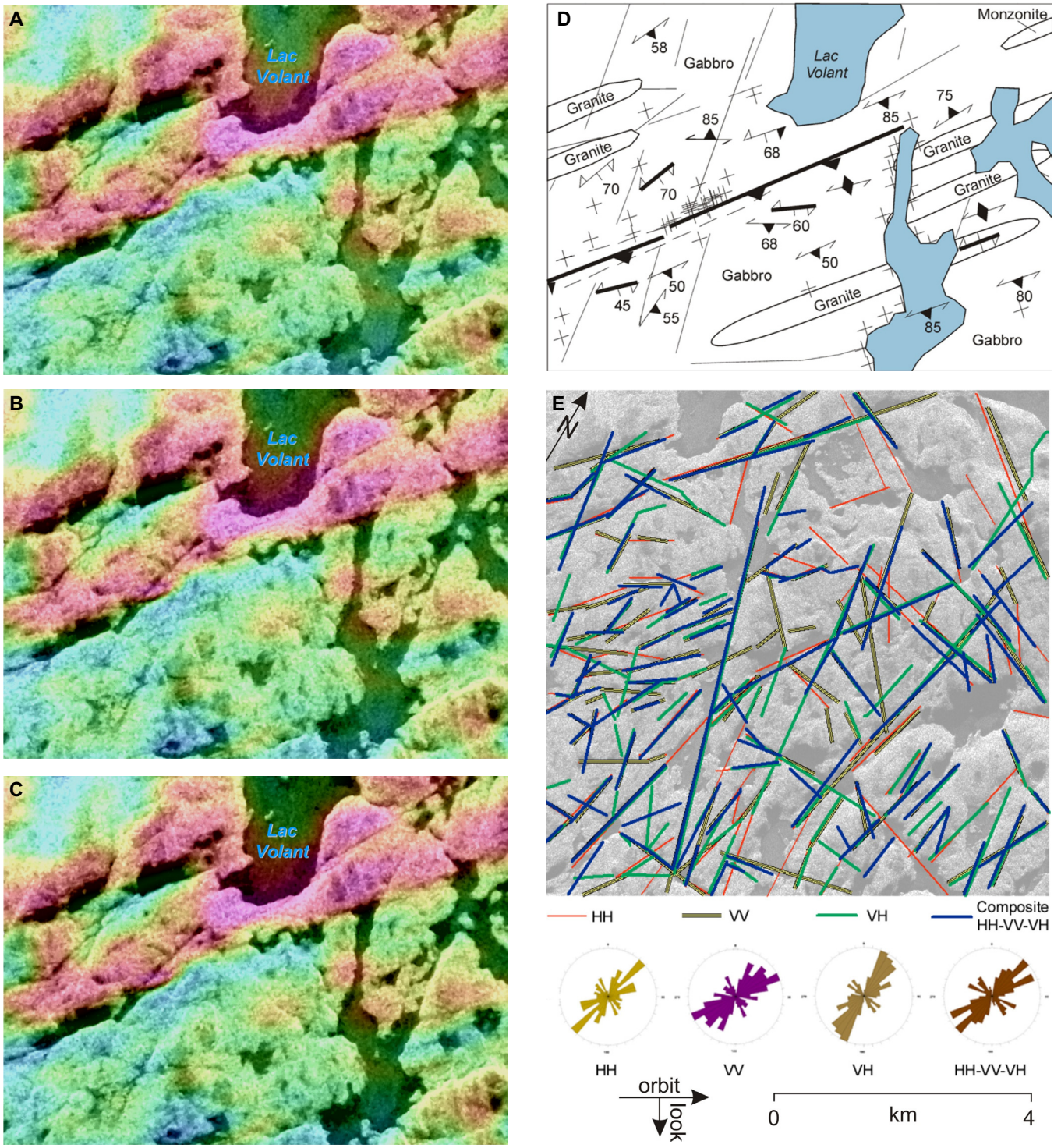

Figure 6A1-3. Fusion of polarimetric airborne CV-580 SAR and high-resolution magnetic data, Lac Volant, Quebec. **(A)** HH data fused with high-resolution magnetic data. **(B)** VV data fused with high-resolution magnetic data. **(C)** VH data fused with high-resolution magnetic data. In combination, SAR and magnetic data reveal the geological units as depicted on the geological map **(D)**. The best discrimination of the geological structure in this example was achieved with the cross-polarized (VH) SAR and magnetic vertical gradient integrated image, as shown in (C). **(E)** Rose diagrams of lineament orientations based on HH, VV, VH, and HH, VV, VH imagery together. HH= horizontal receive and transmit, VV = vertical transmit and receive, VH = vertical transmit and horizontal receive. HH and VV are referred to as like-polarized and VH is cross-polarized.

sisting of 10 to 30% Precambrian outcrops, variable drift thickness, and a dense to sparse forest cover.

The high-resolution capability of the RADARSAT-2 ultra-fine beam mode (3 m) will be very useful for geological and terrain mapping. The fusion of high-resolution SAR imagery with other high-resolution geophysical, topographic, and optical data has improved geological mapping techniques. For example, the high-res-

olution magnetic and SAR-fused image shown in Figure 6A1-2B represents a similar image map that will result from fusion with RADARSAT-2 ultra-fine beam mode data. The structural details at the outcrop level are provided by the high-resolution CV-580 airborne SAR image. High-resolution (10 m line spacing) airborne vertical gradient magnetic surveys are very expensive and are usually flown by exploration companies to provide detailed magnetic signatures of rocks for site-specific exploration programs. When the 3 m SAR image is combined with high-resolution magnetic images, the resulting large-scale (>1:20 000) fused SAR image maps will be well suited for mineral property mapping and target exploration (Fig. 6A1-2).

The Lac Volant mineralized area in Quebec provides another example of the potential of high-resolution fusion techniques for geological mapping. At this site, high-resolution vertical gradient magnetic image data has also been fused with high-resolution (5 m) airborne multi-polarization images. The results (Fig. 6A1-3) show that the fusion of several single-polarization airborne SAR images with high-resolution vertical gradient magnetic images (VH/Mag, VV/Mag, and HH/Mag) provide fusion of several single-polarization airborne SAR images with high-resolution vertical gradient magnetic images (VH/Mag, VV/Mag, and HH/Mag) provides images that are useful for structural and lithological mapping. For example, the geological map shown in Figure 6A1-3D shows the north-south and northeast-southwest structural trends that are seen on these images. In addition, the contacts between the gabbro and granite are being revised on the geological map using the high-resolution fused images. Based on information interpreted from the rose diagrams (Fig. 6A1-3E), each single- polarization image provides information on specific lineament orientation. A multi-polarization composite image of HH-VV-VH would therefore provide the most useful image for structural mapping, since it combines the orientations of all the lineaments that are enhanced by the different polarizations. This capability provided by RADARSAT 2 and ENVISAT would be an improvement on the current uses of SAR images for structural/lineament mapping.

CASE STUDY 1. Snowbird Lake, Northwest Territories

J.R. Harris[1], E. Martel[2], M. Currie[1], K. Pierce[2], M. Pilkington[1], and P. Keating[1]
1. Geological Survey of Canada, 615 Booth Street, Ottawa, Ontario K1A 0E9
2. Northwest Territories Geoscience Centre, 4601-B 52nd Avenue, Yellowknife, Northwest Territories X1A 2R3
Corresponding author's email: harris@NRCan.gc.ca

INTRODUCTION

The Snowbird Lake mapping project, an initiative of the Northwest Territories Geoscience Office (NTGO) and the Geological Survey of Canada (GSC), was one of the first geological mapping projects to adopt the Remote Predictive Mapping (RPM) strategy for producing a predictive map. This map was used in the field, not only as a mapping tool but also for the logistical planning of field work. The project was headed by Edith Martel from the NTGO and was supported by the RPM Group at the Geological Survey of Canada.

This case study represents a succinct synthesis of the work undertaken and summarizes the data and methods used to produce a predictive map. As well, some of the intermediate products (predictive maps as per the definition of remote predictive mapping (RPM), see Chapter 1) that were found to be useful for mapping and logistical planning are described. More details can be found in the following references (Martel, 2005, Martel et al., 2005b; Martel and Pierce, 2006).

OBJECTIVES

Part of the objective of this project was to produce a predictive map of bedrock units and geologic structures from available geoscience data in order to assist field mapping and logistical planning within the overall context of developing a better understanding of the geology of the Snowbird Tectonic Zone (Fig. CS1-1).

The geological terrane is primarily characterized by metamorphic and igneous rocks that are, in general, poorly exposed. Much of the area is covered by glacial sediments that blanket the bedrock. Thus, it was decided that the primary data sets would be magnetic data used in conjunction with available field data to produce a predictive map. However, LANDSAT and DEM data were also used to assist in the identification of topographically expressed structures, wetlands, and outcrop to aid logistical planning. As well, gamma ray data were inspected, especially for the identification and mapping of intrusive rocks.

The Snowbird Lake area (NTS sheet 65D) is located at the southeastern most corner of the Northwest Territories (Fig. CS1-1A), bordered to the east by Nunavut and to the south by Saskatchewan. This area is of great interest geologically, as well as economically, as it straddles the boundary between the Rae and Hearne domains of the western Churchill Province, covering most of the "Selwyn lozenge" (Fig. CS1-1B). The Selwyn lozenge, along with the Athabasca and the proposed Three Esker lozenges are thought to represent

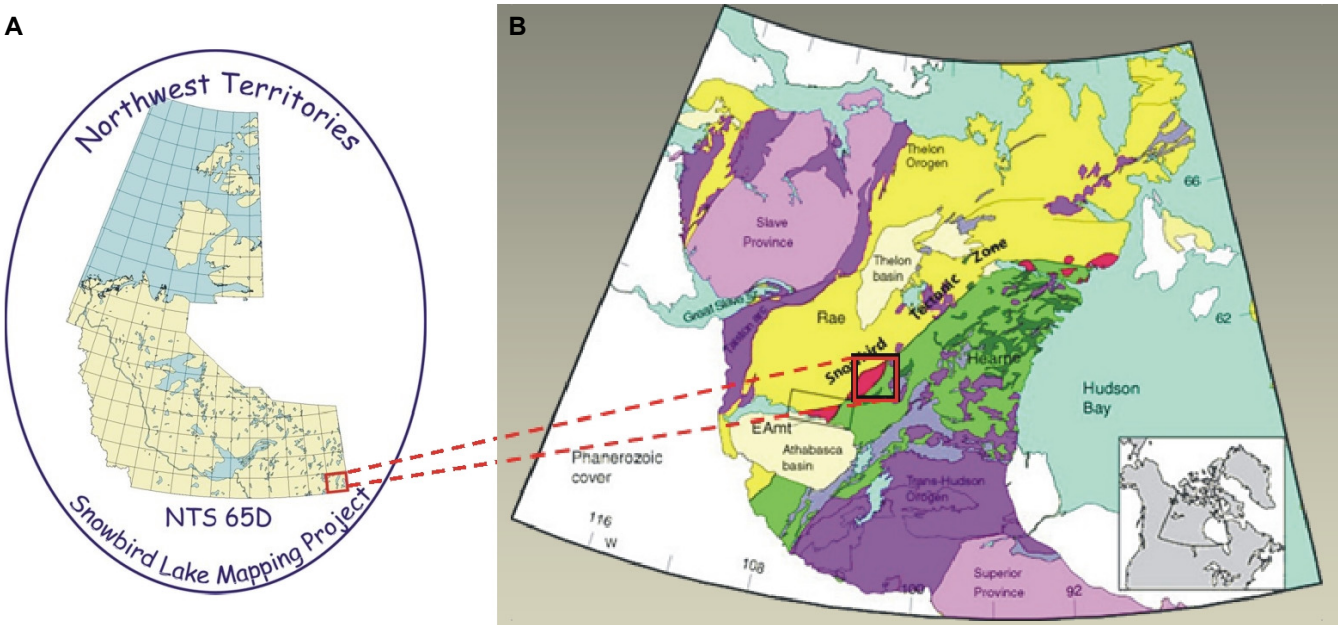

Figure CS1-1. (A) Location of NTS map sheet 65D. **(B)** Generalized geological map showing major tectonic domains and the location of the Snowbird Lake study area.

Harris, J.R., Martel, E., Currie, M., Pierce, K., Pilkington, M., and Keating, P., 2008, Snowbird Lake, Northwest Terrirotires, Case Study 1 *in* Remote Predictive Mapping: An Aid for Northern Mapping, (ed.) J.R. Harris; Geological Survey of Canada, Open File 5643, p. 161-171.

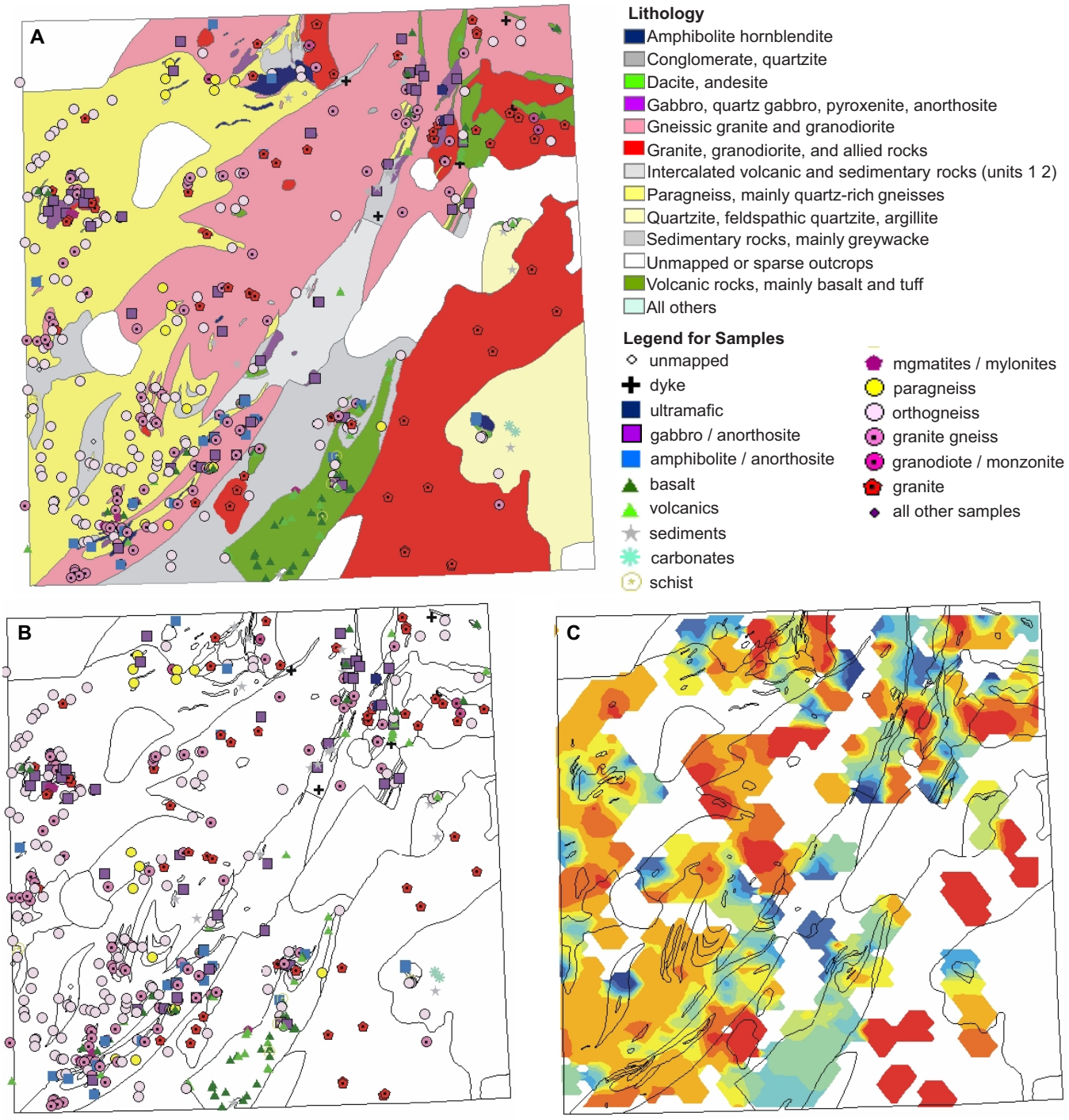

Figure CS1-2. Field and mapped geology. **(A)** Mapped geology (Taylor, 1963) with field stations overlain. Symbols represent a lithological classification based on the lithological code in the field database. **(B)** Field stations classified by lithology. **(C)** Visualization of lithological codes with each lithology generalized into felsic to mafic units using a number code ranging from 255 to 0. The data (using the code value) were then interpolated using an inverse-distance-weighted (IDW) algorithm with a fixed radius of 3 km. The warmer colours (red–orange) represent felsic intrusives and gneisses; the green and yellows, sediments; and the blue, more mafic rocks. See Figure CS1-1 for location.

a segment of the highly debated Snowbird tectonic zone. Martel (2005) provides more details on the regional geology.

DATA

Given the geological environment, it was felt that regional GSC magnetic data, in concert with available field observations, would form the base data set. However as with all RPM projects, all available geoscience data were collected over the project area (Table CS1-1) and can be found published as a digital atlas in Martel and Pierce (2006).

The data were compiled and assembled with ARCVIEW GIS for viewing and integration; interpre-

Table CS1-1. Data sources.

Data Type	Source
Magnetic data	Geological Survey of Canada
Gamma ray	Geological Survey of Canada
LANDSAT	Geogratis website
DEM	Geomatics Canada – Geobase website
Airphotos	National air photo library
Radarsat	Macdonald Detwiller and Associates (MDA)
Existing geology maps	See references
Base data - hydrology	Geomatics Canada
Sample descriptions and locations	See references
Mineral showings	See references
Assessment reports	See references

tation was done on a 'heads-up' basis direct from the computer screen.

Data Processing

The first step in producing a predictive map was to extract geological data from the existing geological maps. This data included the locations of outcrops, generalized litholgical units, gossans (mineralization zones), geological structures, and information about metamorphic grade (see Chapter 2, Table 2-2 for a list of products). This step also included the integration of existing field observations (Fig. CS1-2).

The next step was to reinterpret the geology based primarily on the enhanced magnetic data (Fig. CS1-3) in concert with gravity and gamma ray data. An example of the magnetic domains, folds, and faults interpreted from the magnetic imagery is shown in Figure CS1-4. Figure CS1-5 shows lineaments interpreted from the LANDSAT and Radarsat imagery.

In this area because of the generally thick glacial cover, the gamma ray data (not shown) were used as a secondary data source and primarily used to identify and characterize intrusive rocks.

INTEGRATION

A predictive map (Fig. CS1-6B) was visually interpreted from the geoscience data sets discussed above, with emphasis on the enhanced magnetic data (Fig. CS1-3). This can be compared directly to the historic geological map (Fig. CS1-6A) and the final map (Fig. CS1-6C), which was produced from the previously mapped geology, predictive map, and field mapping.

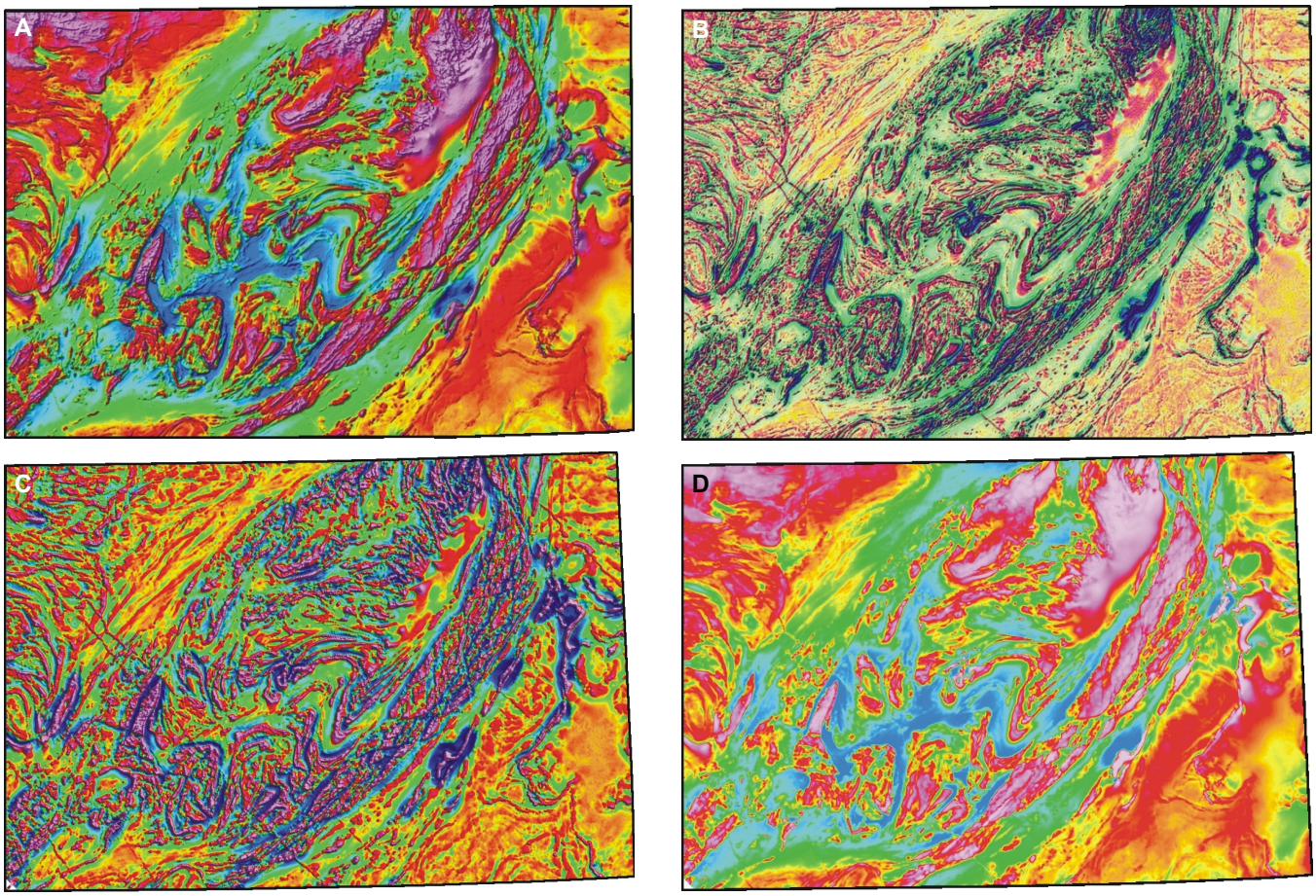

Figure CS1-3. Enhanced magnetic data plotted as **(A)** shaded and coloured total field magnetics, **(B)** coloured vertical gradient, **(C)** tilt, and **(D)** magnetic susceptibility. See Figure CS1-1 for location.

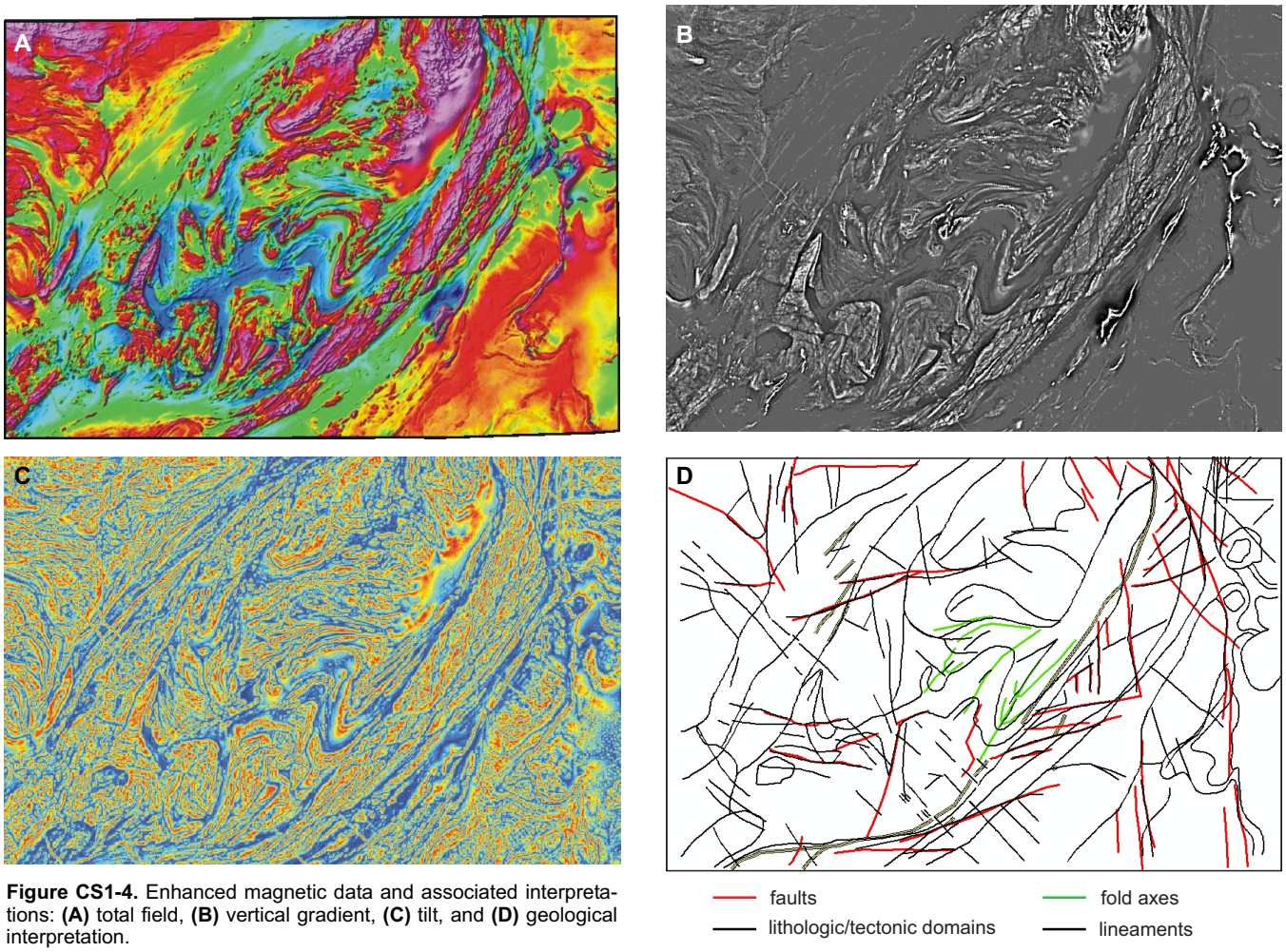

Figure CS1-4. Enhanced magnetic data and associated interpretations: **(A)** total field, **(B)** vertical gradient, **(C)** tilt, and **(D)** geological interpretation.

Results of Remote Predictive Mapping

Possible Domain Bounding Structures and Faults

Aeromagnetic trends suggest that there is a major structure between rocks previously assigned to the Rae and Hearne domains. This structure coincides with the granulite-grade Striding mylonite zone, previously interpreted as the eastern boundary of the Selwyn Lozenge and therefore part of the Snowbird Tectonic Zone. On the predictive map (Fig. CS1-6B), it appears more complicated than previously thought, with an intervening domain between the Rae and the Hearne, in which the geology shows major conflicting information. This domain (central domain) shows important northeast-trending magnetic signatures along both its margins. Based on the attitude of regional foliation, the high-pressure block inferred to the northwest likely overlies the low-pressure block to the southeast, requiring a major structural break within or along a margin of the central domain.

A number of discrete late faults are present in the map area. These faults trend both north-northwest and east-northeast, are sinistral and dextral, respectively, and show metre- to kilometre-scale brittle-ductile displacement. These faults are best outlined in the central part of the predictive map, but were not identified on the historic map.

Metamorphic and/or Structural Domains

Three domains of differing metamorphic and/or structural character are apparent from the remote predictive map (Fig. CS1-6B). They consist of a northwest domain, a central domain, and a southeast domain. The northwest domain is tentatively separated into two subdomains (north and south). The southern part of the northwest domain consists of some high-grade gneissic rocks and some lower grade metasedimentary rocks. These rocks display complex interference patterns, with an earlier fabric documented as a gneissic layering and some preserved primary bedding. These fabric/folds have an enveloping surface oriented northwest. Later fabric and folds are oriented northeast. The later folds appear to plunge both to the southwest and northeast. In the northern part, the structural trend is more complex and suggests the presence of an earlier set of fabric/folds. The central domain displays a more or less consistent subvertical northeasterly striking fabric. However, lithological and metamorphic informa-

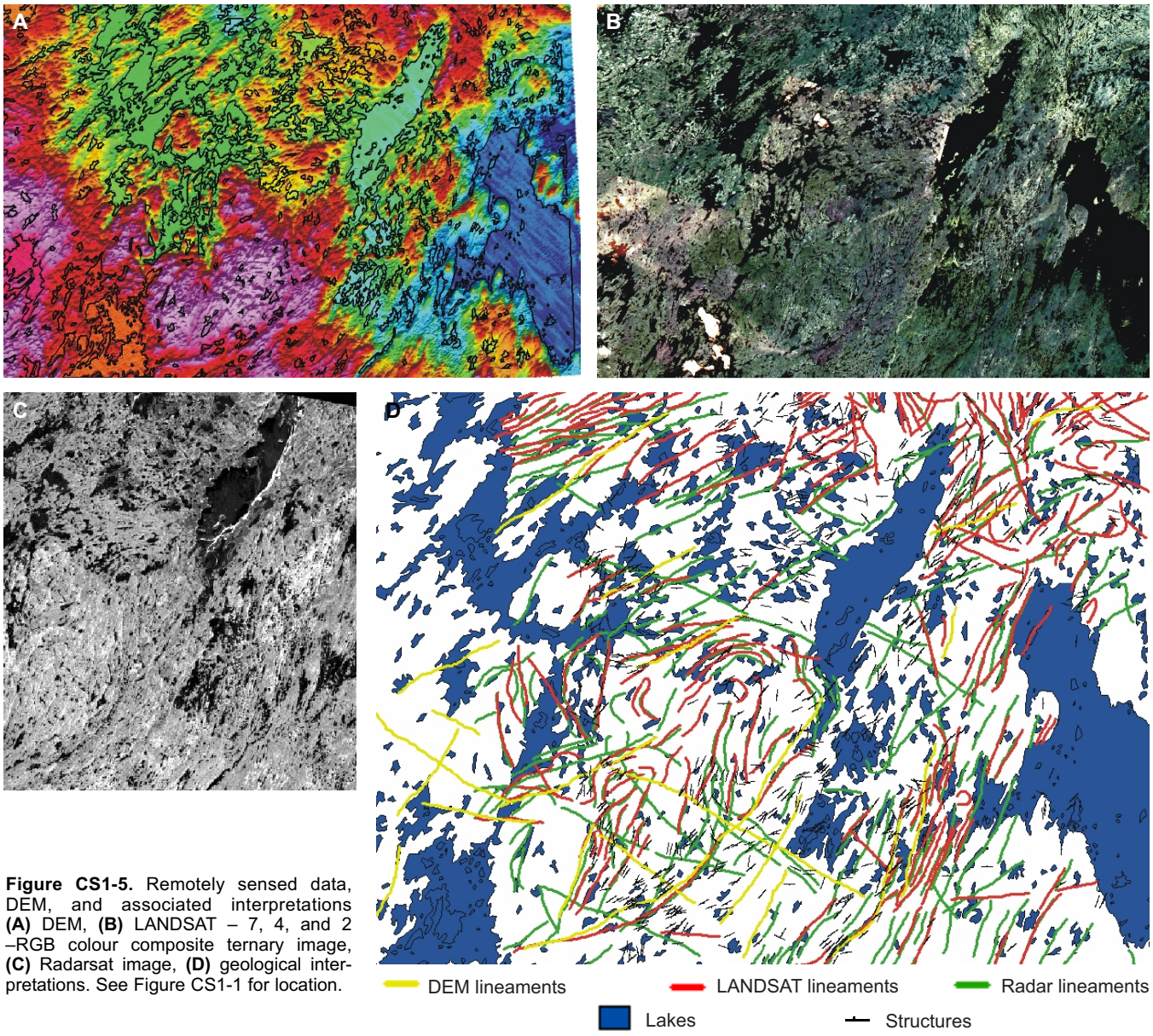

Figure CS1-5. Remotely sensed data, DEM, and associated interpretations **(A)** DEM, **(B)** LANDSAT – 7, 4, and 2 –RGB colour composite ternary image, **(C)** Radarsat image, **(D)** geological interpretations. See Figure CS1-1 for location.

tion compiled from previous maps is conflicting and indicates the presence of both gneissic rocks and low-grade mafic and sedimentary rocks.

The southeastern domain consists of greenschist-grade mafic volcanic and sedimentary rocks intruded by granite. It also includes a Proterozoic sequence containing carbonate rocks as well as mafic and felsic volcanic rocks. These rocks are described as schists and low-grade granitic rocks. The structural trend varies from southwest striking to west striking. Two generations of fabric are documented.

Results of Field Mapping

Geological and surficial mapping, complemented by geochemical and geochronological studies, were conducted on the Snowbird Lake map sheet (65D) during the summer of 2004. Based on field observations and aeromagnetic signatures, rocks of the Snowbird Lake area have been subdivided in three lithostructural domains: the Rae domain, the Hearne domain, and the newly recognized Chipman panel. The Rae domain consists mainly of granulite-grade orthogneiss, upper amphibolite- to granulite-grade metasedimentary and lesser mafic intrusive and volcanic rocks, and previously unrecognized banded iron formation (BIF). The eastern margin of the Rae domain is marked by the Striding mylonite zone, which juxtaposes the Rae domain with the Chipman panel, a highly strained, granulite-grade panel of plutonic rocks. This panel consists of Chipman tonalite (ca. >3.0 Ga) and spatially related Chipman dykes (ca. 1.9 Ga), which were previously mapped partly as mixed metavolcanic and metasedimentary rocks. The presence of high-grade orthogneiss east of the Striding mylonite zone indicates

A

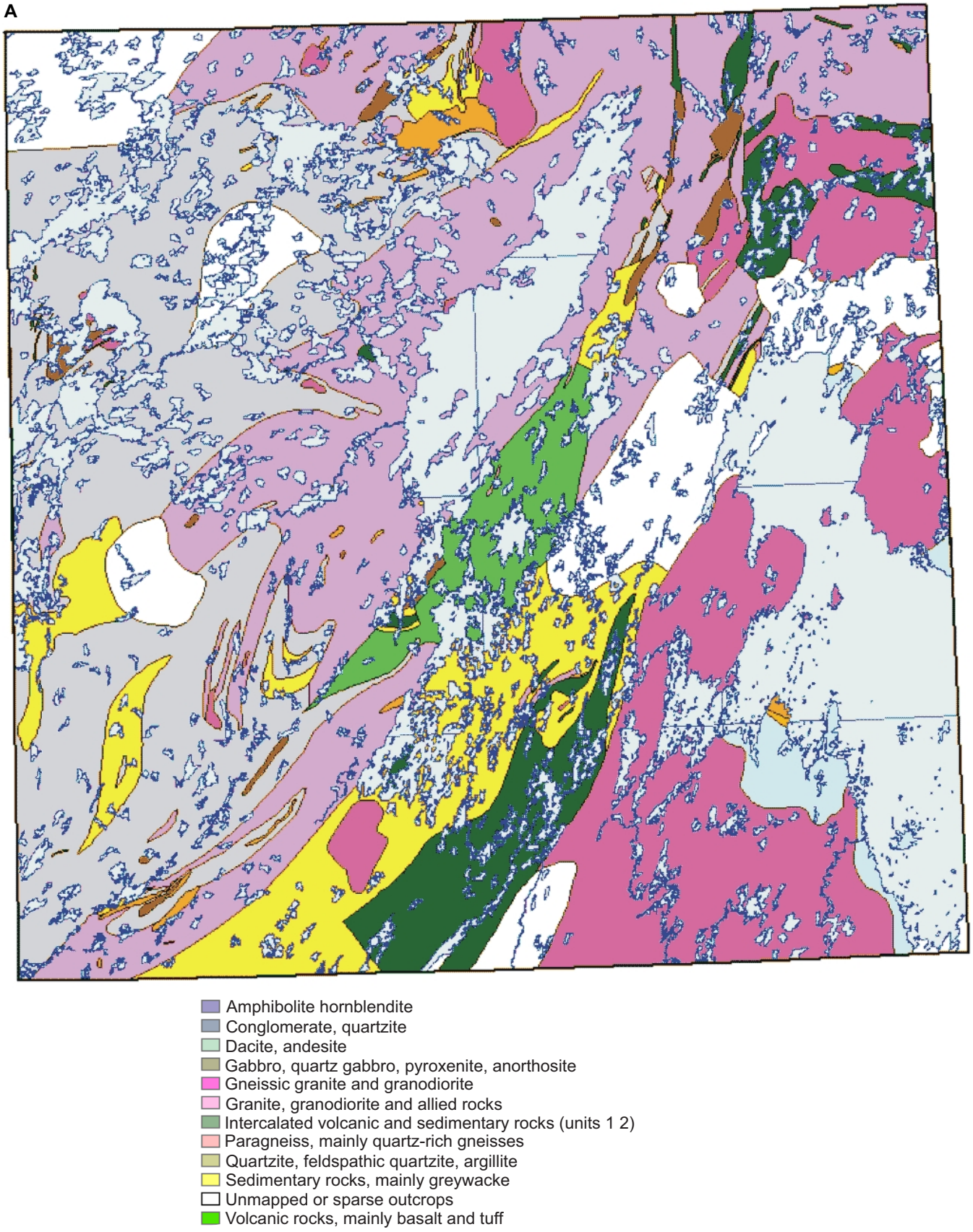

Figure CS1-6. Predicted and mapped geology. **(A)** Legacy geology map (Taylor, 1963).

B

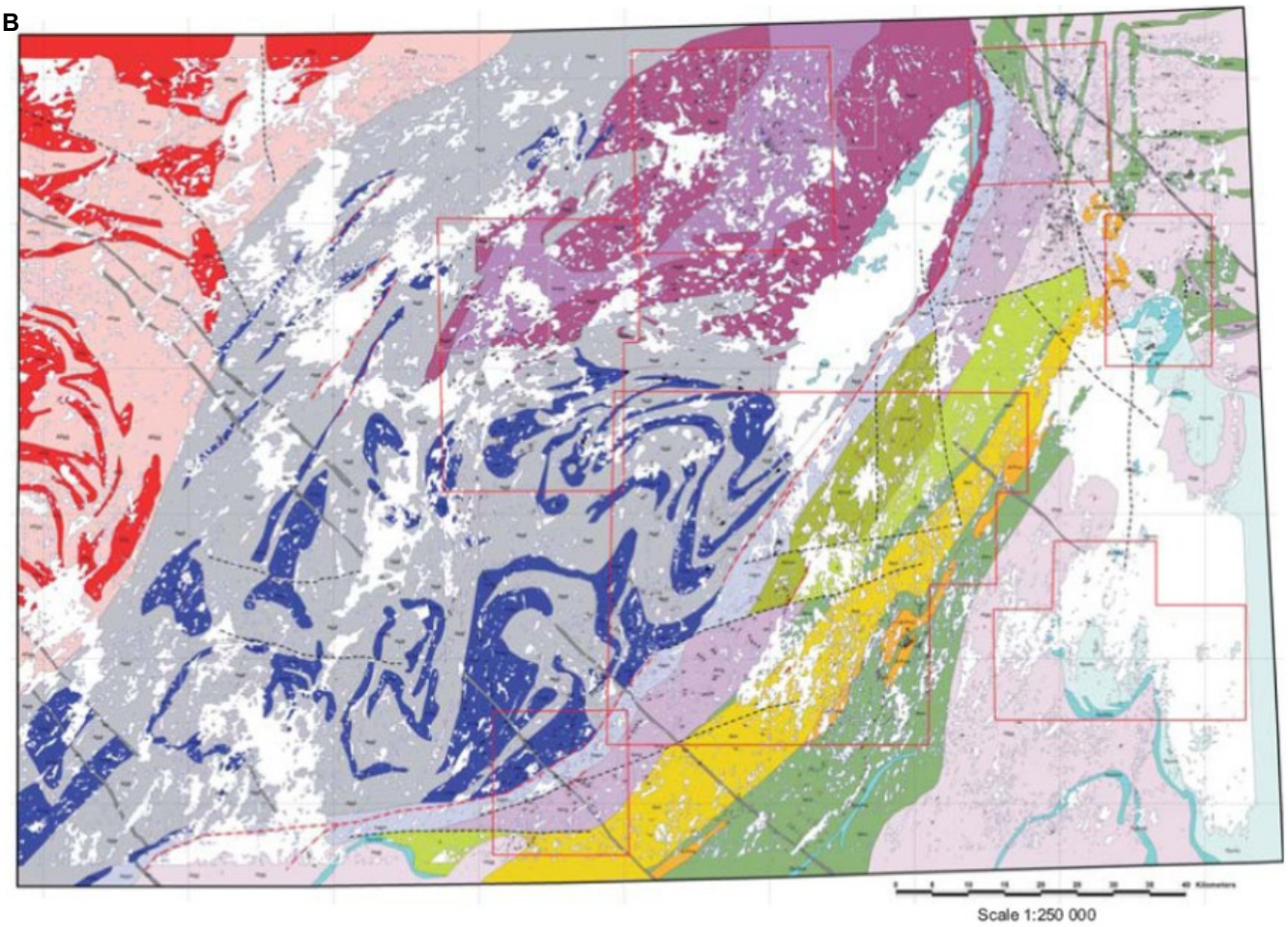

Proterozoic

- Pd — Diabase dyke of the Mackenzie Dyke Swarm
- Pcq — Conglomerate with arkose matrix, overlain by flat-lying quartzite; assigned to Christopher Island Formation (Roscoe and Miller, 1986)
- Ppmfv — Metasedimentary rocks, psammite, pelite, calc-silicate, felsic volcanic, possible amphibolite; previously assigned to Hurtwitz Group
- Ppmfvh — Pelite defines a magnetic high

- Claims/permits (archived and lapsed)
- Areas selected for geological mapping for summer 2004

- F1 fold trace
- F2 fold trace
- Brittle fault
- Mylonite zone

Interpreted from airborne magnetic survey

From Hanmer and Knopf, 1993

Archean Hearne Domain

- A/Pmp — Magnetite-rich pelites, locally preserved primary features (cross-bedding); age uncertain, could be Proterozoic (same as Ppmfvh?)
- Amg — Mafic intrusions, gabbro, diorite, amphibolite
- A — Archean, supracrustal? no geology constraints
- Amxs — Undifferentiated amphibolite facies supracrustal rocks (psammite and metavolcanic rocks)
- Aps — Metasedimentary rocks; psammite and pelitic schist
- Amv — Mafic metavolcanic flow and tuff, locally pillowed, less common felsic to intermediate volcanic rocks; locally metamorphosed to garnet-bearing amphibolite
- Atgg — Granitic to tonalitic gneisses (migmatites) with inclusions of amphibolite; includes younger (Archean) granite; may partly represent basement tocks (ca. 3.3-2.6 Ga) (Harper et al., 2001)

Snowbird Mylonite Zone (western margin)

- Aagm — Mylonite to ultramylonite; anorthositic gabbro, granitic gneisses, granulite facies

Selwyn Lozenge

- Adag — Mafic to ultramafic intrusive (?) diorite, amphibolite gabbro and amphibolite and granite gneisses
- Aggl — Granitic gneiss, possible paragneiss; defines a magnetic low
- Aggh — Undifferentiated gneisses, mainly granitic; defines a magnetic high
- Ampa — Undifferentiated amphibolite, paragneiss, granitic gneisses, volcanic rocks

Archean Rae Domain

- ARg — Poorly constrained geology, granite; magnetic high of the Rae Domain
- ARgg — Poorly constrained geology of the Rae Domain; granitic gness; magnetic low

Figure CS1-6 continued (B) Predictive geology map (Martel, 2005).

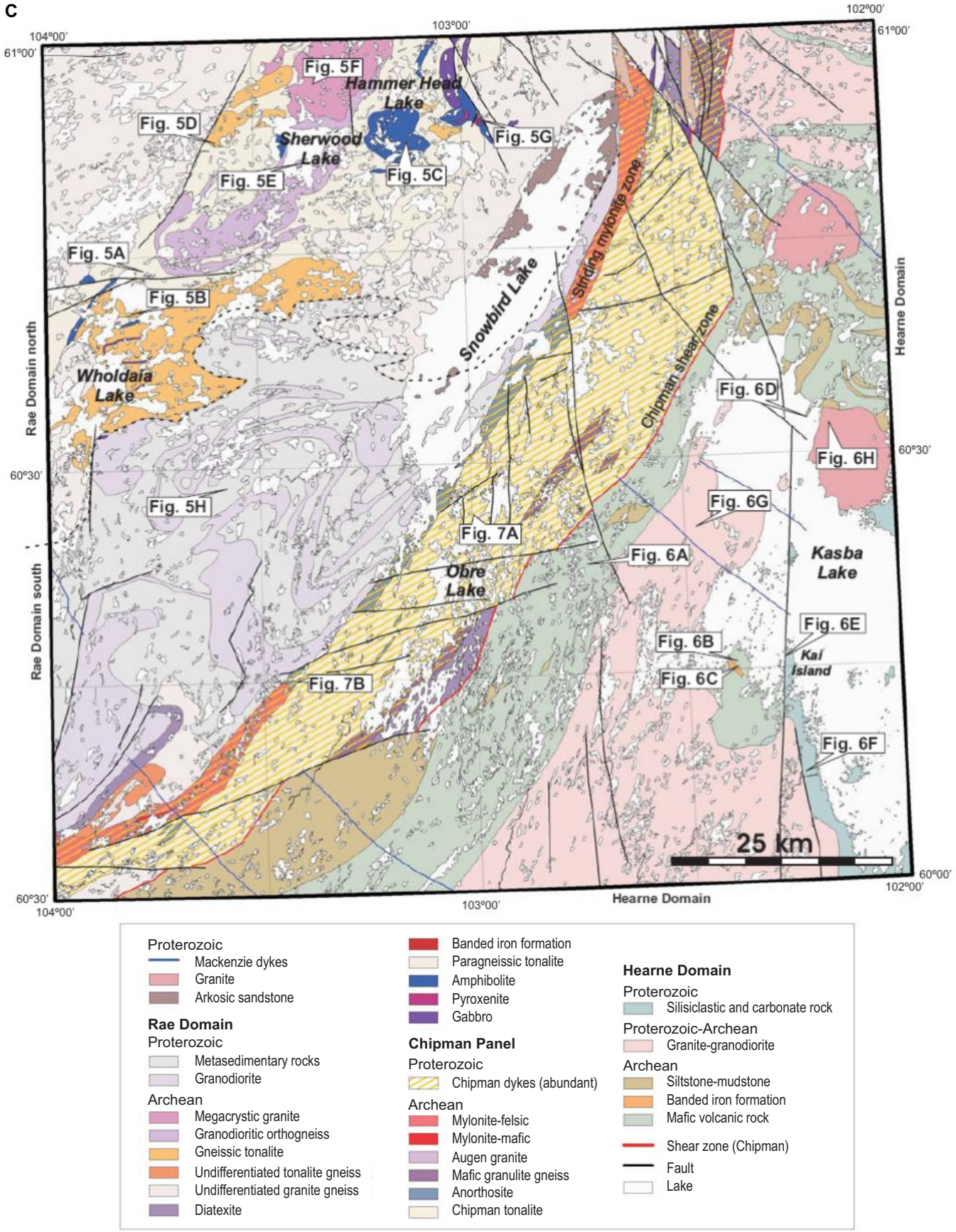

Figure CS1-6 continued. (C) Simplified geological map derived from the legacy mapping, remote predictive mapping, and field mapping (Martel and Pierce, 2006).

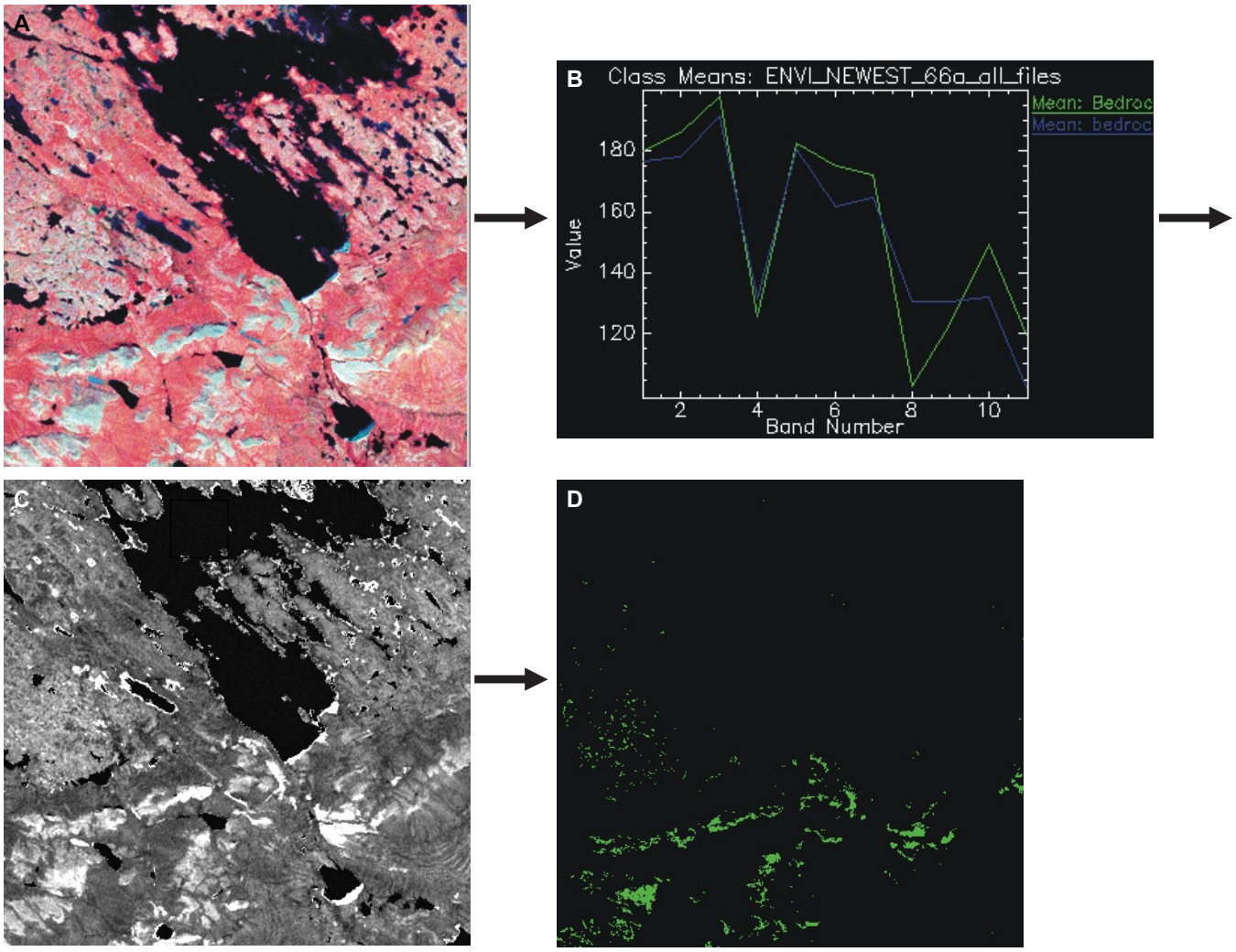

Figure CS-7. Procedure for identifying bedrock outcrop on LANDSAT data. **(A)** LANDSAT false colour composite image (bands 4, 3, and 2 correspond to red, green,and blue). **(B)** Spectral plot of LANDSAT DN values for bedrock. Note that bands 3, 5, and 7 have the highest reflectance for bedrock, whereas band 4 has the lowest. **(C)** Band 7/4 ratio image, which highlights bedrock outcrop in white. **(D)** Threshold of plot (B) was used to create a binary map of the outcrop (shown in green).

that the shear zone itself does not define the boundary between the Rae and Hearne domains as previously suggested. The eastern margin of the panel is marked by the Chipman shear zone, which juxtaposes high-grade Chipman panel rocks with generally lower grade rocks of the Hearne domain. The Hearne domain consists mainly of greenschist-grade Archean (ca. 2.73 Ga) mafic and minor felsic volcanic rocks, siltstone/volcaniclastic schists as well as Archean and Proterozoic granites, some of which are correlative with the Nueltin intrusive suite (ca. 1.75 Ga). A sequence of carbonate rocks interpreted to be correlative with the upper Hurwitz Group (ca. 1.9 Ga) overlies the Archean supracrustal rocks. Deformation and metamorphism occurred during the Archean (ca. 2.6 Ga), but major fabrics and metamorphic assemblages preserved in the map area are interpreted to be Proterozoic (ca. 1.9 Ga in the Rae domain and ca 1.8 Ga in the Hearne domain). The segment of the Snowbird tectonic zone that transects the map area encompasses two major structures (Striding mylonite zone and Chipman shear zone), as well as the Chipman panel.

FIELD LOGISTICS AND PLANNING

Outcrop mapping was facilitated by interpretation of the following data sets:

- Topographic (DEM), LANDSAT data, and airphotos were used to identify areas of wetlands – obviously traversing was not worthwhile or even possible in these areas.
- The location of existing field stations were used as a guide for new traversing.
- LANDSAT and DEM data were used to identify areas of outcrop (Fig. CS1-7).

The interpretations made on the above data allowed for the determination of main and fly camp locations,

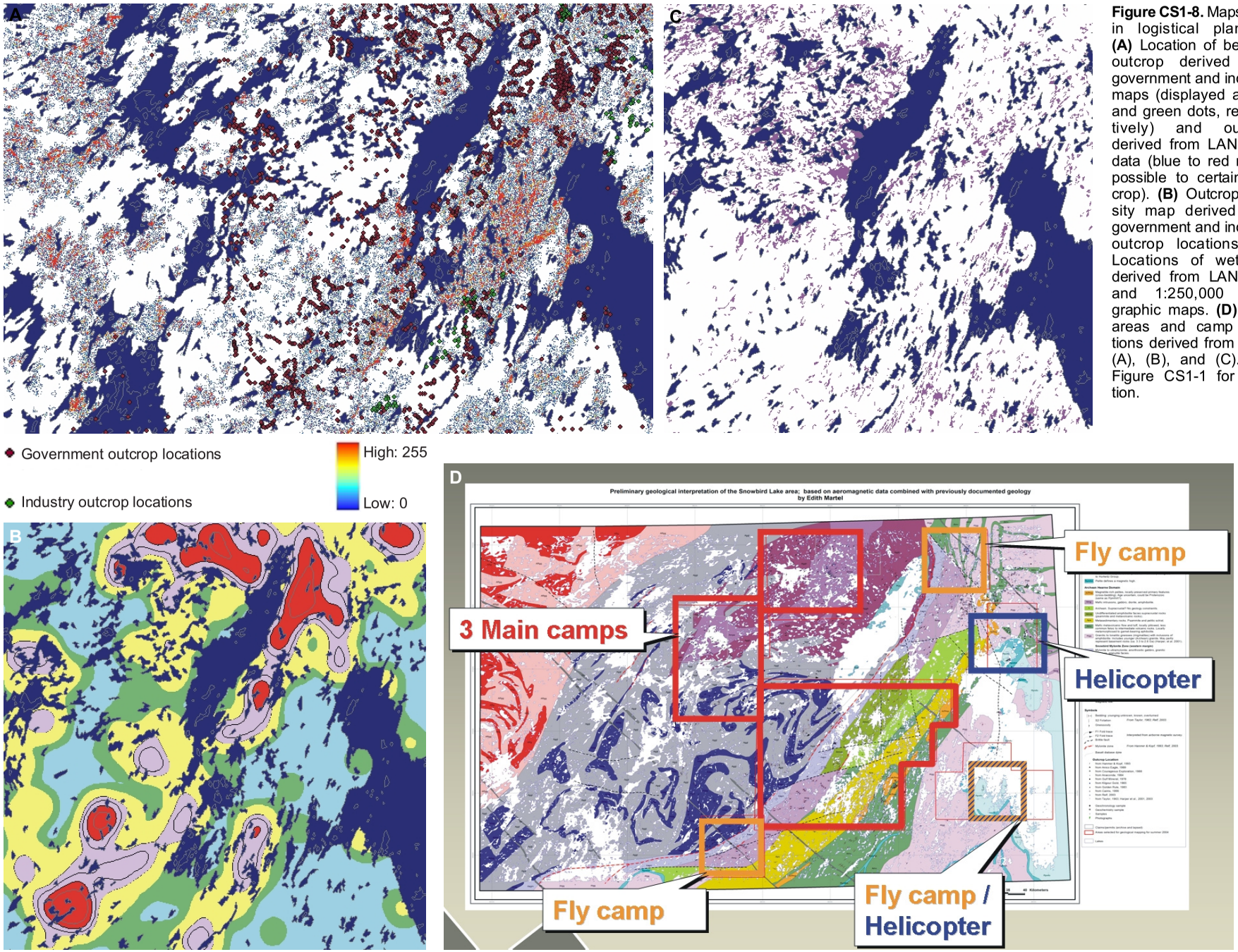

Figure CS1-8. Maps used in logistical planning. **(A)** Location of bedrock outcrop derived from government and industry maps (displayed as red and green dots, respectively) and outcrop derived from LANDSAT data (blue to red reflect possible to certain outcrop). **(B)** Outcrop density map derived from government and industry outcrop locations. **(C)** Locations of wetlands derived from LANDSAT and 1:250,000 topographic maps. **(D)** Field areas and camp locations derived from maps (A), (B), and (C). See Figure CS1-1 for location.

as well as for the planning of boat versus helicopter supported traverses (Fig. CS1-8).

EVALUATION OF THE REMOTE PREDICTIVE MAPPING PROCESS

The RPM process was largely successful, as major lithological domains, some lithological units, and major structural trends and generations were identified and mapped. Complex areas requiring more field follow-up were delineated. Also, areas of poor exposure were identified, which facilitated targeted field mapping.

In this particular area, outcrop could not be unequivocally identified in all cases and was sometimes confused with sandy deposits such as eskers. The process of outcrop identification is presently being fine-tuned to reduce confusion with other surface features. In this study, it was suggested that a forest fire distribution map would have been beneficial as burnt areas have a greater probability of bedrock exposure. For this area, the magnetic data in conjunction with the existing field observations were the most useful data for producing a predictive geological map.

REFERENCES

Hanmer, S. and Kopf, C.
1993: The Snowbird tectonic zone in District of Mackenzie, Northwest Territories, *in* Current Research, Part C; Geological Survey of Canada, Paper 93-1C, p. 41-52.

Harper, C.T., Kraus, J., Demmans, C.J., Huebert, C., Coulson, I.M., and Rainville, S.
2001: Phelps Lake Project: Geology and mineral potential of the Bonokoski Lake area (NTS 64M-11, -12, -13, and -14), *in* Summary of Investigations 2001, Volume 2; Saskatchewan Geological Survey Miscellaneous Report 2001-4.2, p. 3-18.

Martel, E.
2005: Geology of the Snowbird Lake area, western Churchill Province, NWT; Northwest Territories Open File 2005-05, 27 p.

Martel. E. and Pierce, K.
2006: An Arc View 3.x Digital Geological Atlas of the Snowbird Lake Area, NTS 65D; Northwest Territories Open File 2006-02, CD-ROM.

Martel, E., Harris, J.R., Currie, M., and Pierce, K.
2005: Snowbird Lake (NTS 65D) Remote Predictive Mapping and Geoscience Data Compilation; Northwest Territories Open File 2005-08, 1 CD-ROM.

Relf
2003:

Roscoe and Miller
1986:

Taylor, F.C.
1963: Snowbird Lake Map Area, District of Mackenzie; Geological Survey of Canada, Memoir 333, 23 p.

CASE STUDY 2. LANDSAT, Magnetic and Topographic Data for Regional Lithological Mapping, Southeast Baffin Island

J.R. Harris, E.M. Schetselaar, E. de Kemp, and M.R. St-Onge
Geological Survey of Canada, 615 Booth Street, Ottawa, Ontario K1A 0E9
Corresponding author's email: harris@NRCan.gc.ca

INTRODUCTION

This is a post-field mapping study conducted over part of southeast Baffin Island. The area was originally mapped by a Geological Survey of Canada field party led by Marc St-Onge during the late 1990s. Traditional field-mapping methods were utilized comprising equally spaced field traverses (3 km) supplemented by air photo interpretation.

OBJECTIVES

The objective of the case study was to create regional lithological maps from optical (LANDSAT), magnetic and topographic (Digital Elevation Model) data using computer-assisted processing classification techniques.

The first goal was to determine whether supracrustal (sedimentary strata and mafic sills) and crystalline basement rocks could be separated using image analysis techniques applied to airborne magnetic and LANDSAT remotely sensed data.

The second goal was to determine whether individual lithologies comprising the two main tectonic groups could be identified using the same image analysis techniques applied to the LANDSAT, magnetic and topographic data.

The study area is in southeastern Baffin Island on the Meta Incognita Peninsula (Fig. CS2-1). The bedrock lithology and structure has been mapped by St-Onge et al. (1998, 1999a,b) and the surficial cover by Hodgson (1997, 2003a,b). The area is generally well exposed, consisting of approximately 80% outcrop or weathered outcrop with low-lying shrubs, arctic grasses, moss and lichen, which is restricted mostly to river valleys and adjacent to lakes and coastlines.

Topography ranges from near sea level in the south to 800 m in the central study region. The general north-south fabric of the topography reflects foliation and/or bedding patterns in the supracrustal rocks and gneissosities in the basement orthogneisses.

Paleoproterozoic metamorphic rocks in the study area display a range of lithologies from granulite-facies mafic and quartzofeldspathic gneisses, granitoids, and mid- to upper-amphibolite supracrustal assemblages of Paleoproterozoic age (1934-1820 Ma; St-Onge et al., 2007) (Fig. CS2-2A). Regional tectonostratigraphic subdivisions in the study area include two major domains. A footwall orthogneiss complex referred to as structural Level-2 and a hanging-wall supracrustal assemblage of psammites, pelites, and quartzites with minor marbles and peridotite, which constitutes structural Level 3. The supracrustal suite in this area is an outlier of the Markham Bay assemblage. This cover unit is also variably intruded by monzogranites from

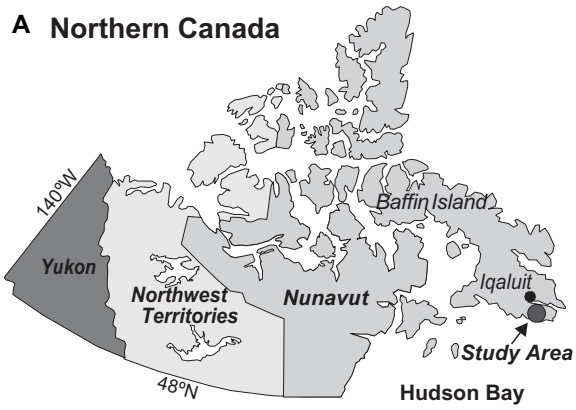

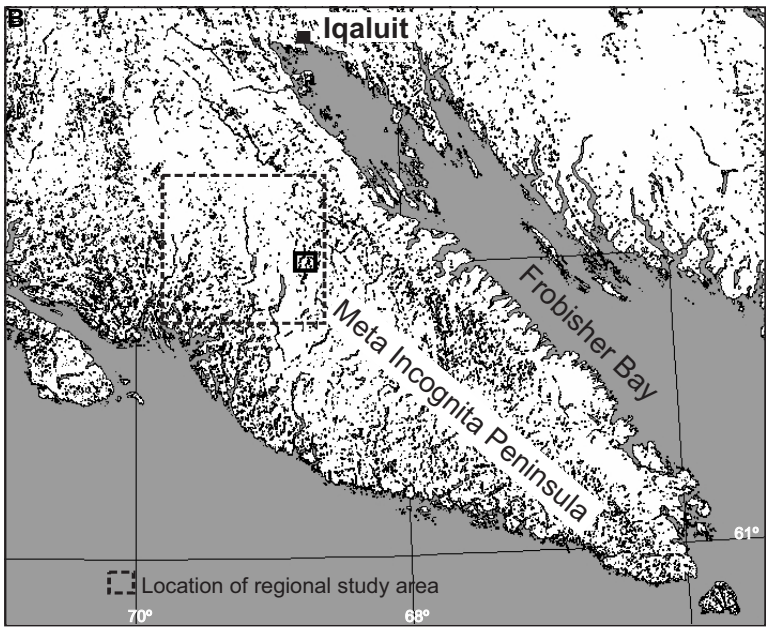

Figure CS2-1. Location of the study area, southeast Baffin Island, Nunavut.

Harris, J.R., Schetselaar, E.M., de Kemp, E., and St-Onge, M.R., 2008, Magnetic and topographic data for regional lithological mapping, southeast Baffin Island, Nunavut, Case Study 2 *in* Remote Predictive Mapping: An Aid for Northern Mapping, (ed.) J.R. Harris; Geological Survey of Canada, Open File 5643, p. 173-182.

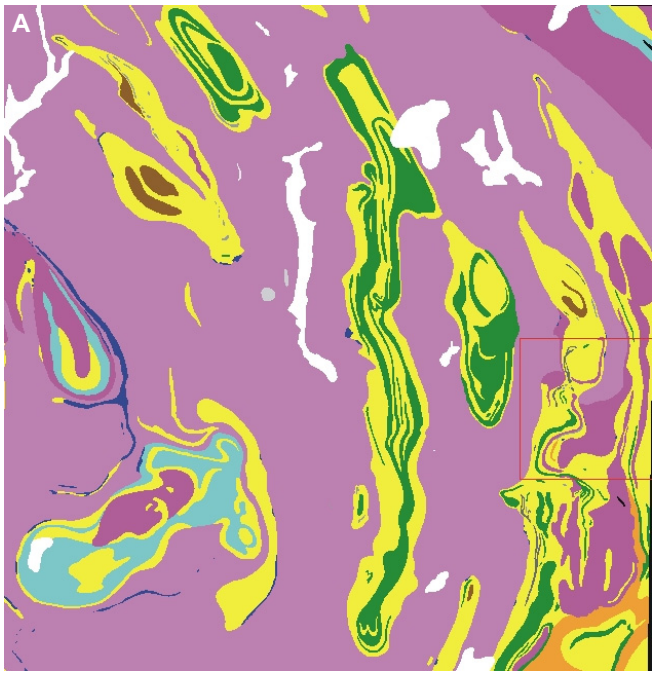

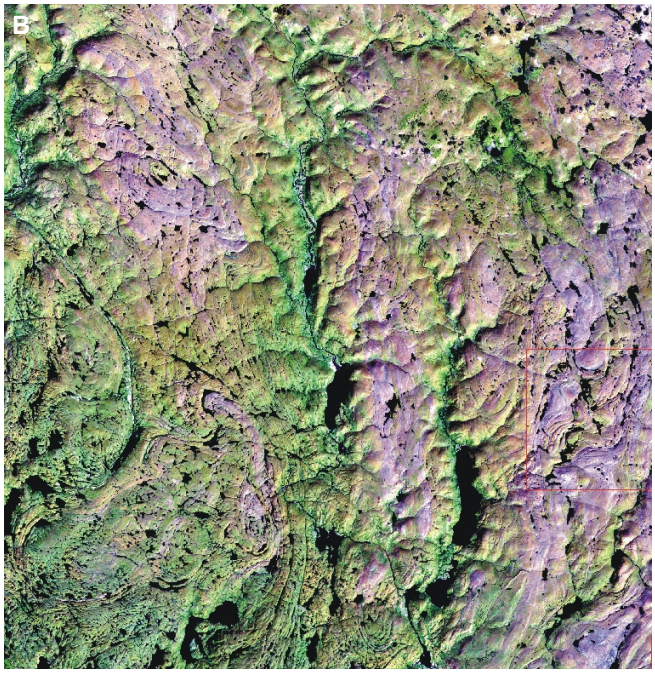

Quaternary cover

Paleoproterozoic Narsajuaq Arc
- PNmb - monzogranite

Cumberland Batholith
- PCMo- orthopyroxene

Lake Harbour Group
- PLHd - metaleucodiorite
- PLHp- metasediments
- PLHc- marble
- PLHw- white biotite-garnet monzogranite

Ramsey River Orthogneiss
- PRm- gneiss

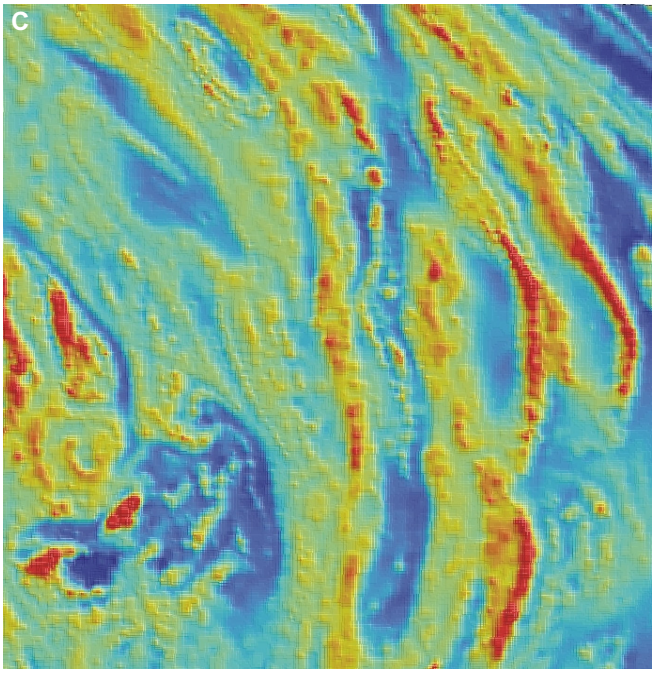

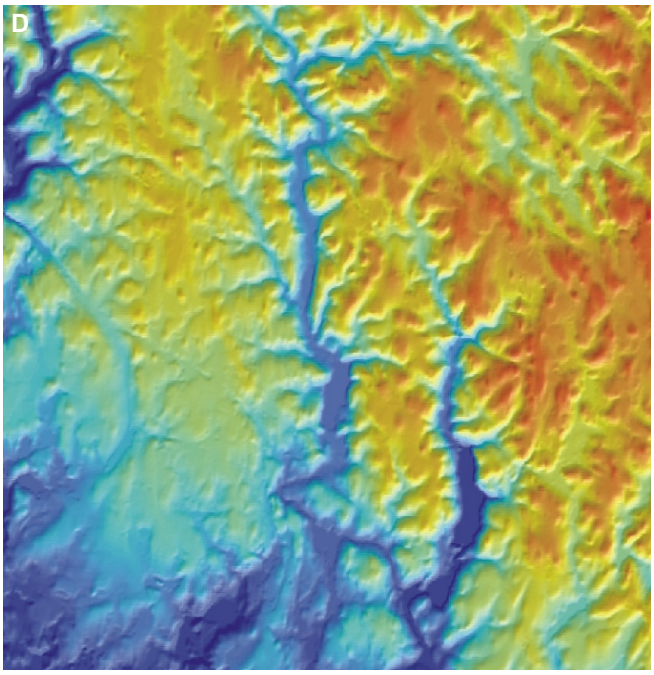

Figure CS2-2. (A) Simplified regional geological map (from St-Onge et al., 1999a,b) of the study area. **(B)** LANDSAT colour composite ternary image – bands 7, 4, 2 – RGB. **(C)** Total field magnetic images. **(D)** Digital Elevation Model (DEM) - Canadian Digital Elevation Data (CDED).

the Cumberland batholith suite. The boundary between these two regional classes is interpreted to be a regional-scale décollement or thrust that has juxtaposed the supracrustal Level-3 rocks against Level 2 orthogneisses and tonalites (St-Onge et. al., 1998, 1999a,b). For this study, the Level 2 package is referred to as 'basement' and the Level-3 rocks as 'cover' (Fig. CS-2A).

The study offers a reasonable environment for a remote study given the high percentage of outcrop and low residual soil and till cover. The approach taken in this study was to employ a supervised processing method (see Chapter 2, this volume) to produce a lithological map. This process can be used in other northern terranes with similar exposures providing that a preexisting geological map (or existing field observations) is available; even though the map used may be out-of-date and in need of upgrading.

A top-down stratified approach to classification was undertaken (Schetselaar and de Kemp, 2000) in which the major tectonic divisions were first predicted (basement versus supracrustal rocks) followed by a more detailed classification of individual lithologies. Following the methodology outlined in Chapter 2, the prediction maps were validated by comparisons to the known training areas used to produce the classifications, field observations, and the regional geological map. Both optical (LANDSAT) and magnetic data were used to produce the predictive maps.

DATA

Regional magnetic data (Fig. CS2-2C), which is available from the Geological Survey of Canada (see Chapter 2, this volume), LANDSAT data (Fig. CS2-2B), and topographical data (Canadian Digital Elevation Data, CDED) (Fig. CS2-2D), which are available through the Geological Survey of Canada, Earth Science Sector Geobase website (http://www.geobase.ca/), were used in the analysis. Both magnetic and LANDSAT data were deemed appropriate for this use due to the distinct magnetic and spectral signatures of some of the rock units within the study area.

Data Processing and Integration

Visual Assessment

One can immediately see that the LANDSAT spectral response (Fig. CS2-2B) is somewhat similar to the simplified regional geological map (Fig. CS2-2A) in that the purple, magenta, and brownish areas correspond to the supracrustal rocks and the green areas (largely representing vegetation) correlate with the basement rocks (compare Fig. CS-2A and CS2-2B). One should always make a cursory visual examination of the data before any computer classification is attempted in order to determine whether any further computer classification is even warranted. (The human brain is still a better classifier with respect to colours and patterns than the computer!)

In this case, the correlation between the magnetic data and the geological map is moderate (Fig. CS2-2A versus CS2-2C), especially with respect to the supracrustal rocks that define a series of north-south striking tight folds. The supracrustal rocks tend to have low magnetic signatures, with certain lithologies marked by a very strong response due to the presence of magnetite.

The correlation between the geological map (Fig. CS2-2A) and the Digital Elevation Model (DEM) (Fig. CS2-2D) is weak at best, indicating that for these rocks, topographic characteristics are not particularly strong factors in distinguishing between the different lithologies. Spectral and magnetic responses offer much better parameters for classifying these rocks in this particular geologic terrane.

Initial assessment of the LANDSAT and magnetic data indicated that classification of these rocks using a supervised approach is likely to be moderately successful.

Computer-Assisted Approach: Supervised Classification

Part 1. Basement versus Cover

This next section draws upon the work of Schetselaar and de Kemp (2000), who conducted classification experiments to determine whether basement rocks can be successfully predicted and separated from supracrustal rocks (cover) (Fig. CS2-2A) at a mapping scale of 1:100,000 using a combination of LANDSAT and magnetic imagery.

Supervised classification requires a priori information about the features (in this case, rock units) to be classified. As discussed in Chapter 2 of this volume, there are a number of different methods of obtaining this a priori information (referred to as training data). Typically training data are collected using random sampling of existing geological maps (or air photos). In this study, sample points along the original geological traverse lines were used. Adhering to the assumption that training sites along the traverse lines results in a higher confidence with respect to classification and that a sufficient sampling of all the lithologies along the traverse lines has been accomplished, training sites along each traverse line (Fig. CS2-3A) were selected to provide a priori information on each major unit (cover versus basement) for classification experiments. Note that off-traverse sites may lead to less certain results in the classification procedures, depending on how the geologist filled-in these areas on the final map.

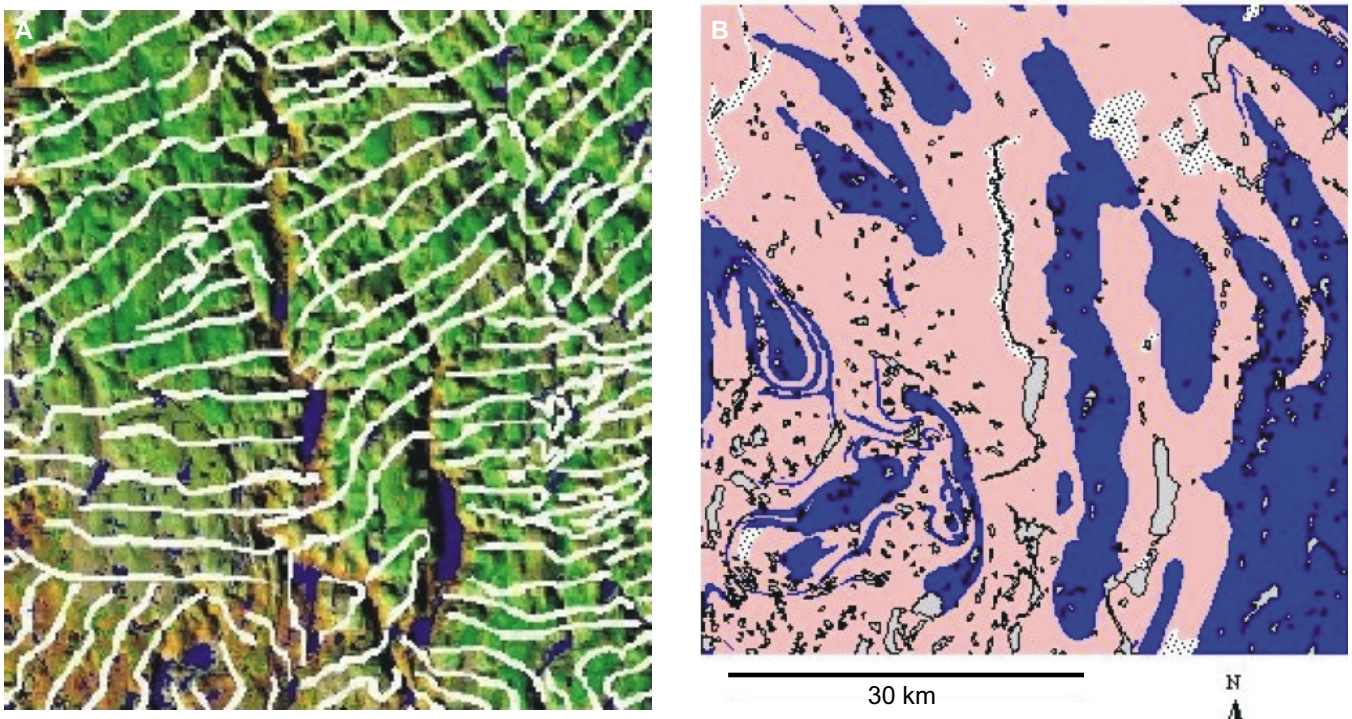

Figure CS2-3 (A) Locations of training sites along the geological (or original) field traverse lines (shown in white) overlain on a LANDSAT image. **(B)** Generalized geological map with the blue areas representing supracrustal units and pink, the basement. See Figure CS2-1 for location.

A data mask was constructed to exclude areas of water, quaternary cover, and vegetation (see Chapter 2, this volume). The vegetation component of the mask was developed using a GVI (Green Vegetation Index) (B4–B3) / (B4+B3). All values greater than zero, i.e., high GVI, were included in the mask. The total field magnetic data were processed to generate an apparent susceptibility map. This procedure essentially converts the total field measurements to a map representation of magnetization (susceptibility), provided that the magnetic anomalies arise from vertical prisms with the same depth to their tops and the same depth extent (Milligan and Gunn, 1997). Although these conditions were violated in the area of study, the reduction to the pole and downward continuation filters involved in generating such a representation more likely yield patterns that match with surface geological patterns in comparison to the total magnetic field representation (see Chapter 3, this volume, for more information on the processing of magnetic data).

Three classification experiments to predict level 2-3 areas (Fig. CS2-4A) were conducted: (1) employing the LANDSAT Thematic Mapper (TM) bands, (2) employing the magnetic susceptibility channel, and (3) a classification on the magnetic and TM channels combined. All the image channels were smoothed with their average filtered derivatives to exploit the spatial autocorrelation between pixels (Switzer, 1980). This method is applicable to the purpose of this study because the units to be classified occur on a larger scale than a single pixel. Experiments with different classification methods revealed that the classification was not sensitive to a particular algorithm. The best results, however, were obtained with the Maximum Likelihood Classifier, in which prior probabilities were set in proportion to the distribution of training samples over the two classes. No unclassified pixels were allowed to map the patterns with the greatest structural continuity possible.

Results

Part 1. Supracrustal Units versus Basement

The classification based on the TM channels (Fig. CS2-4B) shows a disproportionate performance in the prediction of basement and cover (86% versus 51%; Table CS2-1). This is largely the result of internal lithological variations in the cover that are misclassified as basement. These misclassified pixels are clearly reflected in the structural patterns that show up in the classified patterns within the cover (Fig. CS2-4B).

The classification of the magnetic data (Fig. CS2-4C) shows a greater continuity of units in comparison to the TM classification and the geological map, possibly suggesting rapid transitions from one unit to another in the near subsurface. The accuracy of classification is slightly higher (Table CS2-1) than the LANDSAT.

The TM classification fails to identify the mushroom interference patterns on the southwest quadrant of the area, only showing thin slivers of cover (Fig.

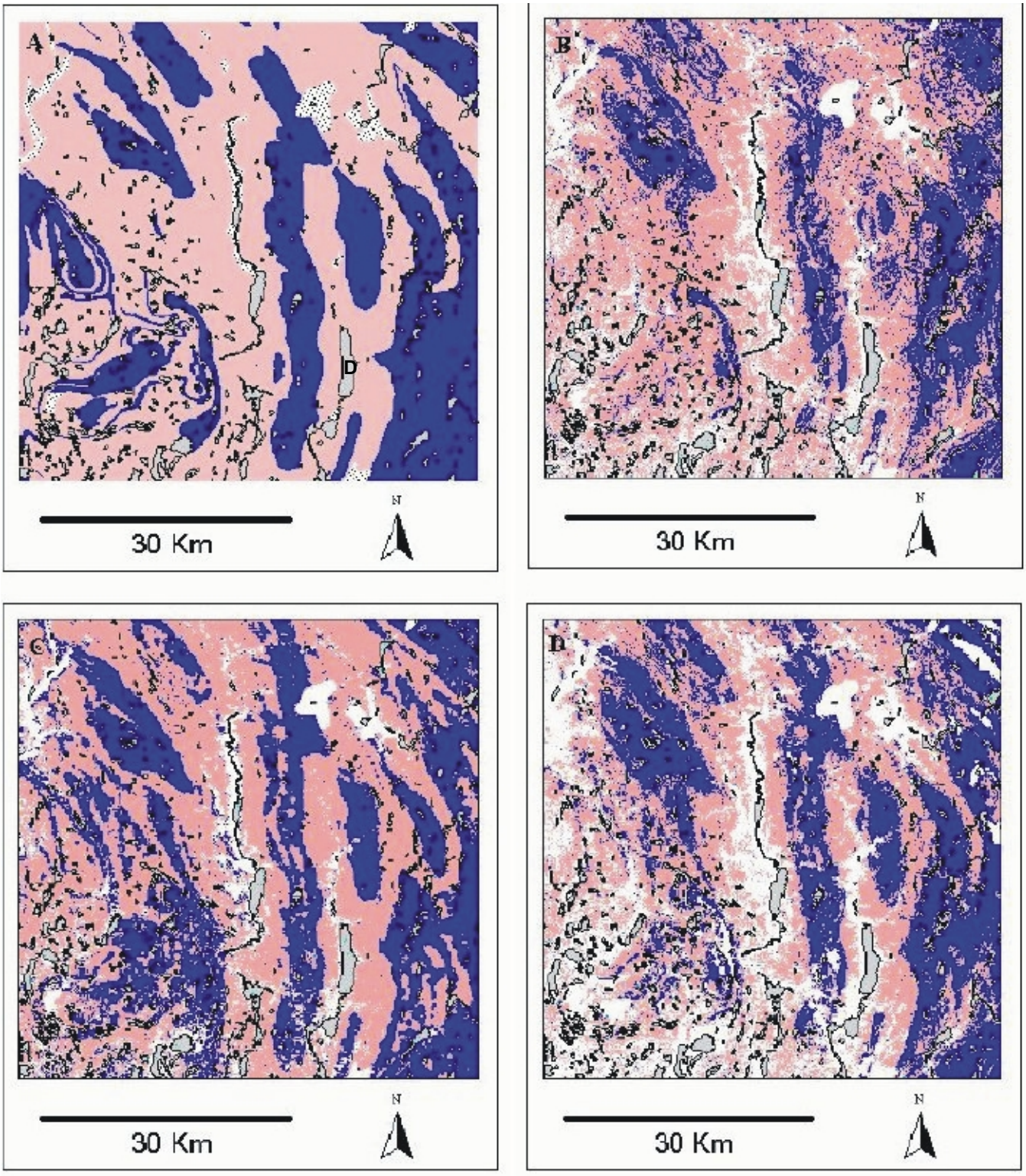

Figure CS2-4. Classifications of LANDSAT and magnetic data. **(A)** Two-fold division of the mapped geology. Note: blue = Level 3 – supracrustal units, pink = Level 2 – basement. **(B)** Classification of Level 2 and 3 units based on LANDSAT data only. **(C)** Classification based on magnetic data only. **(D)** Classification based on LANDSAT and magnetic data.

CS2-4B). This could be a result of a widening of internal class spectral signatures. This would result in the spectral overlap of basement and cover rocks, which could cause either class to be misrepresented. A geological facies change in the supracrustal suite or more paragneiss components in the basement rocks could account for this discrepancy.

An interesting observation that can be made from the results is that the classifications made on the basis

Table CS2-1. Classification results for Incognita Peninsula, southeast Baffin Island, Nunavut.

	Basement	Cover	Overall Accuracy
LANDSAT TM (14 channels)			
Basement	86.20%	49.00%	71.30%
Cover	13.80%	51.00%	
Magnetic susceptibility (2 channels)			
Basement	75.50%	27.40%	74.30%
Cover	24.50%	72.60%	
Magnetic susceptibility and LANDSAT (16 channels)			
Basement	79.00%	27.80%	76.20%
Cover	21.00%	72.20%	

Note: Results of maximum likelihood supervised classification applied to various band (channel) combinations. A combined quaternary, vegetation, and water mask was used to exclude these areas from the classification. Total accuracy was calculated by summing all correctly classified pixels and dividing by the total unmasked pixels.

of the magnetic data and on the TM data (Fig. CS2-4D) yielded similar coincidence percentages with the geological map, whereas their combined use only slightly improved the coincidence percentage (Table CS2-1). It essentially demonstrates that both data sets complement one another to only a limited extent. This result would favour a classification approach where both data sets are used independently. Discrepancies with the geological map can then be tested against classification from independent remote sensing methods, reinforcing the significance of conflicting patterns. If, for example, both suggest a conflict with the geological map in an area between traverse lines, such an area would warrant attention in follow-up field studies. An additional advantage of this approach is that the magnetic data can be used to predict the basement-cover relationships underneath overburden.

Part 2. Individual Lithologies

This section takes the above classification down one level with respect to the stratified approach and looks at the possibility of classifying individual lithologies. The data used for classification remains the same; however, the training and classification strategy differs somewhat from Part 1 in that training areas comprising a limited number of pixels (Table CS2-2) were selected based on inspection of the existing geological map (Fig. CS2-2B) in concert with the LANDSAT and magnetic data. Examination of the LANDSAT data was extremely important in the selection of training areas as only areas of bedrock outcrop or weathered outcrop (which can be seen clearly on the LANDSAT data, Fig. CS2-2B) were candidates for training areas. Thus the training data in this approach represented discrete areas as opposed to discrete sample points along traverse lines. The maximum likelihood algorithm was again used for classification; however, the prior probabilities of each lithological unit were held equal unlike the classification undertaken in Part 1 where they were adjusted based on the number of training points for each major tectonic unit (cover vs. basement).

Again, visual assessment of the LANDSAT and magnetic imagery indicates that spectral and magnetic separation of some of the lithological units was possible. This was further investigated quantitatively by using a transformed divergence (TD) statistic (Richards and Jia, 2006), which measures the degree of separation of the training data in N-dimensional space (where N represents the number of bands used in the classification). A TD value is calculated for every pair combination of lithological units and the average TD value can then be plotted (Fig. CS2-5). Values greater than approximately 1.9 indicate good separation between lithological units, values between 1.0 and 1.99 indicated moderate separation, and values less than 1.0 indicate poor separation (Richards and Jia, 2006). Thus it can bee seen that when considering only the LANDSAT spectral data, most units have moderate separation except for the white biotite-garnet-bearing monzogranites of the Lake Harbour Group and the marbles (PLHw, PLHc). However, when the magnetic data is combined with the TM data, thus using both spectral (reflectance response) and magnetic (susceptibility) characteristics, the individual lithologies are much more separable, with TD values varying around 1.99. This is at odds with respect to separating supracrustal from basement rocks as classification accuracy was not appreciably higher when using both LANDSAT and magnetic data, compared to when the individual data

Table CS2-2. Lithologies that were classified (see Fig CS2-2A) along with the number of pixels used for the training data set.

Lithology[1]	# of training pixels	Colour[1]
Paleoproterozoic Narsajuaq Arc		
PnMb – monzogranites	219	light magenta
Cumberland Batholith		
PCMo – orthopyroxene - biotite monzogranite	204	magenta
PCMg – biotite-garnet monzogranites	147	
Lake Harbour Group		
PLHw – white biotite-garnet monzogranites	39	brown
PLHd – metaleucodiorite, metatonalite	158	green
PLHc – marble	92	dark blue
PLHp – metasediments	206	yellow
Ramsey Orthogneiss		
PRm – monzogranites-tonalitic gneiss	137	cyan

1. For explaination of lithology codes and colours, see Figure CS2-2A.

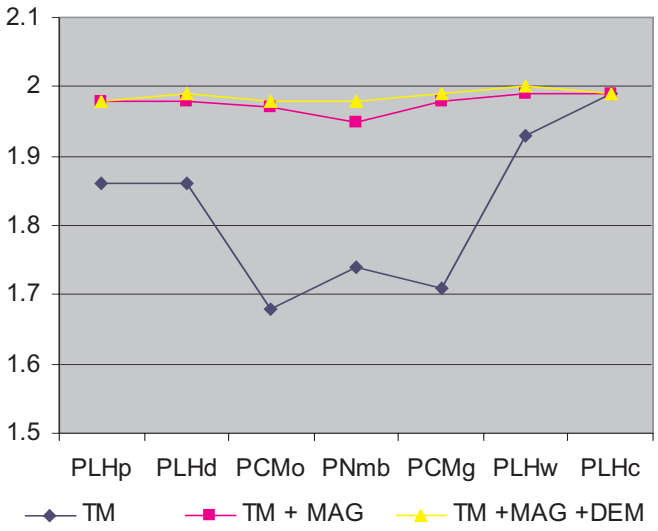

Figure CS2-5. Plot of transformed divergence values for each map unit.

sets were used. Addition of the topographic information via the DEM adds very little in terms of separation of lithological units in this area, supporting the visual assessment of topographic patterns in relation to lithology as seen on Figure CS2-2A. The marbles (PLHc) are not separable on the magnetic data but offer a distinct and unique spectral signature from the other lithologies.

Again, before proceeding with classifications, data masks were created to exclude areas of water, snow, and ice as well as vegetation from the analysis. The classification maps (or prediction maps) (Fig. CS2-6B,D) show some similarities and differences to the existing geological map (Fig. CS2-6A), although the maps are noisy in appearance. The maps can be cleaned somewhat by using a neighbourhood spatial filtering operation that cleans up some of the spurious pixels and presents a more homogeneous appearance (Fig. SC2-6C,E) and also improves classification accuracies. Figure SC2-7 shows some enlargements of the classifications compared to the mapped lithological units.

The LANDSAT alone results in an overall accuracy of almost 80% (Table CS2-3), when compared to the training data. Addition of the magnetic and DEM data increases the accuracy to 87 and 94%, respectively. As would be expected, the accuracies are much lower when comparing the predictions to the geological map. Again, addition of the magnetic data in particular, significantly improves the accuracy, increasing from 21 to 38%. Post-classification filtering of the prediction maps (to clean up heterogeneous areas) (Fig. CS2-6C,E) provides substantially better accuracies when compared to the training areas and geological map (see numbers in brackets in Table CS2-3.

GENERAL CONCLUSIONS AND RECOMMENDATIONS FOR REMOTE PREDICTIVE MAPPING

Part 1

Combined magnetic data from standard regional airborne surveys and LANDSAT TM multispectral satellite sensors can be used to give reasonable predictions of major bedrock classes. In this area, a 76% accuracy rate (compared to the training areas) was obtained for supracrustal verses orthogneiss terrain classification.

The LANDSAT data shows a spectral contrast that is related to compositional variations between lithologies within the two structural levels, which can be used to predict the basement and cover relationships. Misclassification of basement and cover from the LANDSAT data is likely due to spectral contrast, both within the cover stratigraphic sequence, as well as lateral variations within individual units.

The apparent magnetic susceptibility map provides a representation of surface and near-subsurface geological patterns. Discrepant patterns with the geological map over several flight line intervals may be interpreted as areas where the basement-cover relationships occur at shallow depths. However, this hypothesis requires further testing; such areas are potentially tar-

Table CS2-3. Classification accuracies based on comparison to original training areas used for the classification and geological map.

Classification			Accuracy (%) (number in brackets refers to filtered classifications)
LANDSAT Thematic Mapper Data	versus	Training Areas	79.9 (88.3)
LANDSAT Thematic Mapper Data	versus	Geological Map	21.1 (30.0)
LANDSAT Thematic Mapper + Magnetic Data	versus	Training Areas	87.4 (92.4)
LANDSAT Thematic Mapper + Magnetic Data	versus	Geological Map	38.1 (47.0)
LANDSAT Thematic Mapper + Magnetic + Digital Elevation Model Data	versus	Training Areas	94.3 (97.0)
LANDSAT Thematic Mapper + Magnetic + Digital Elevation Model Data	versus	Geological Map	40 (47.8)

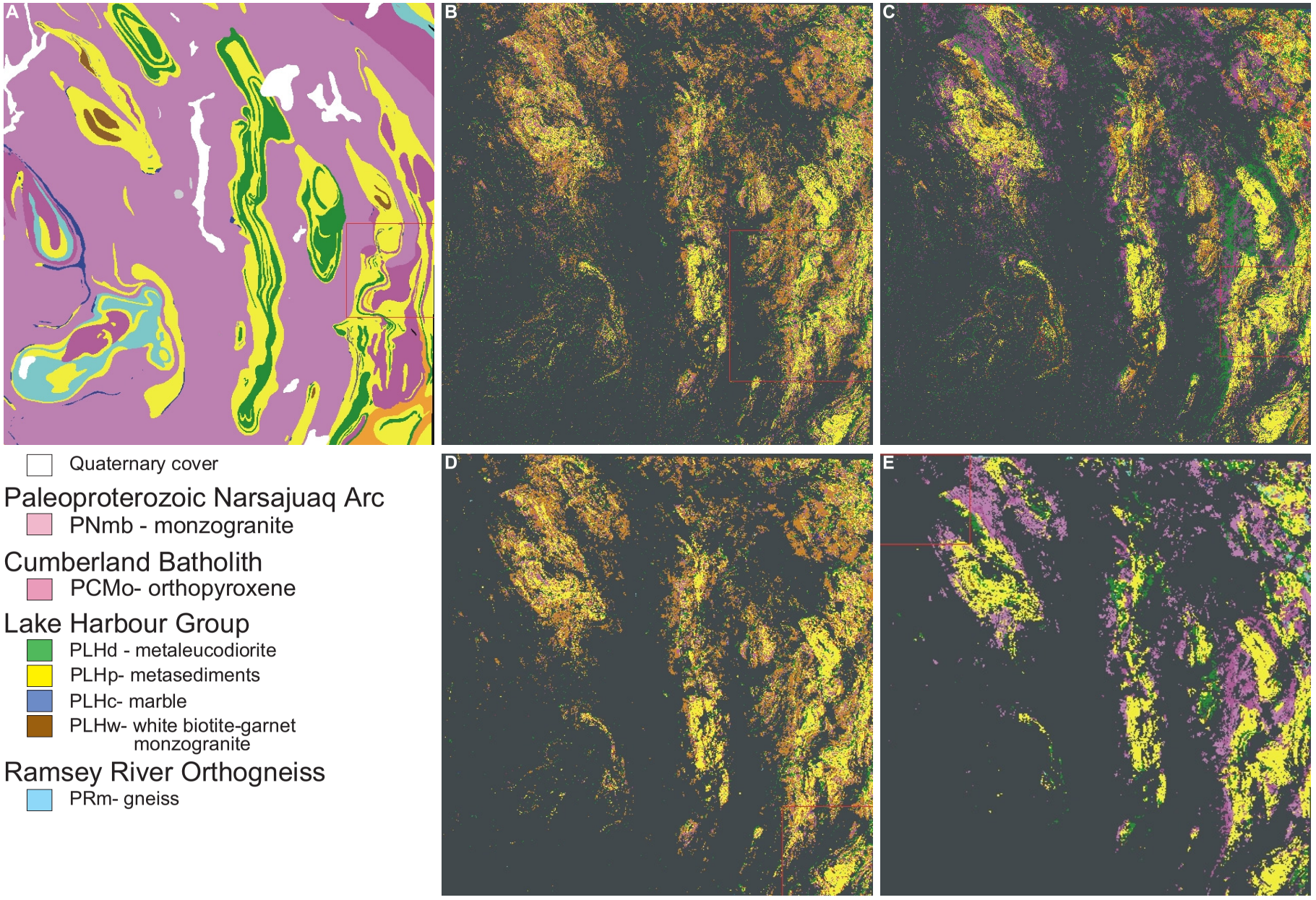

Figure CS2-6. (A) Simplified geological map of the study area (from St-Onge et al., 1999a,b). **(B)** Lithological classification based on LANDSAT data. **(C)** Filtered classification based on LANDSAT data. **(D)** Classification based on LANDSAT and magnetic data. **(E)** Filtered classification based on LANDSAT and magnetic data.

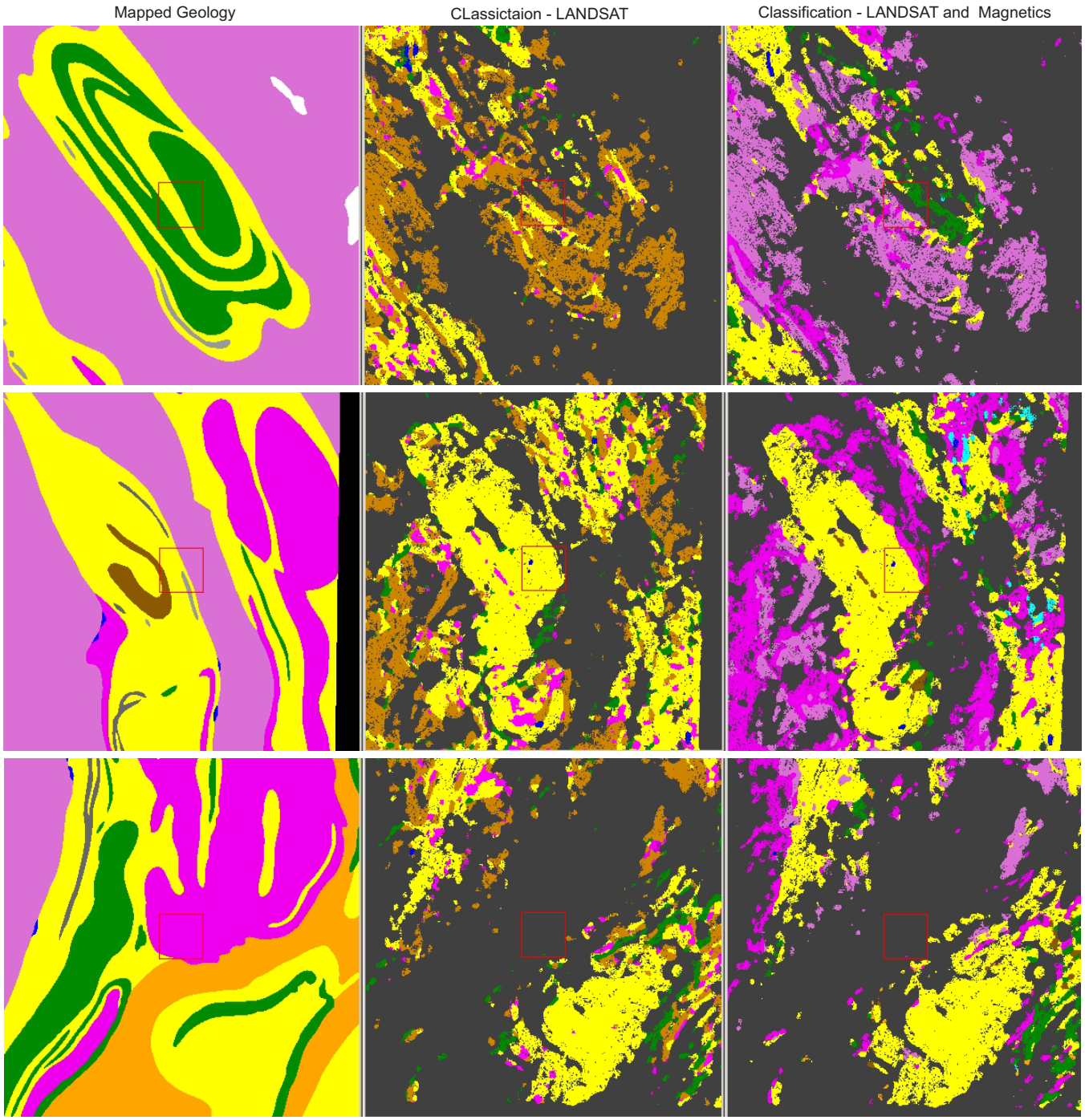

Figure CS2-7. Comparison of the simplitifed mapped geology (from St-Onge et al., 1999a,b) with lithological classifications obtained from LANDSAT and magnetic data. Small sections of the mapped geology (see Fig. CS2-2A) are compared to classifications based on LANDSAT (1st set) and combined LANDSAT and magnetic data (2nd set). See Figure CS2-6 for the geological legend.

gets for magnetic inversion. In combination with structural observations from the surface, the magnetic susceptibility map may prove useful to extend the mapping of the basement-cover relationships in the subsurface.

Classification on the basis of seven LANDSAT bands and a single magnetic susceptibility channel yielded similar performance. This result supports classification approaches for the region where the data sets are separately classified. Areas where discrepancies with geological map patterns appear in both classifications provides interesting target areas for map refinement.

Pre-field, concurrent, and post-field classification studies of this nature could be helpful during the planning stages of major field investigations, both as an aid in targeting domains for detailed analysis and in extending well mapped areas beyond the training set.

Further studies are required to determine the minimal ground truth training set that will be able to give useful predications. Further study is also required to determine which additional discriminatory data layers, such as from advanced sensor technologies (i.e. hyperspectral), will be able to enhance the predictive capacity of this method in the Arctic regions.

Part 2

Reasonably good classification accuracies were obtained (when compared to the training sites) when using either the LANDSAT or magnetic data. However in this case involving the discimination of individual lithological units, the best results were achieved when both data sets were used.

Post-classification filtering is recommended to refine classification (prediction) maps, as this tends to homogenize the various classified lithological units as well as substantially improving the accuracy of the classifications.

Given a suitable geological and surficial environment, classification of regional and moderate-resolution LANDSAT and magnetic data can provide useful predictive maps for field mapping, which are valuable for updating historical geological maps and for focusing targeted field work. Not only are the areas of concurrence between the predictive map and existing geological map important, but also areas where the predictive map differs from the mapped geology may point to areas that warrant more detailed field investigation.

REFERENCES

Hodgson, D.A.
1997: Last glacial ice flows over western Meta Incognita Peninsula, southern Baffin Island, Northwest Territories (Nunavut), *in* Current Research 1997-C; Geological Survey of Canada, p.179-184.

2003a: Surficial Geology, Hidden Bay, Baffin Island, Nunavut; Geological Survey of Canada, A-Series Map 2043A, scale 1:100 000.

2003b: Surficial Geology, McKellar Bay, Baffin Island, Nunavut; Geological Survey of Canada, A-Series Map 2044A, scale 1:100 000.

Milligan, P.R. and Gunn, P.J.
1997: Enhancement and presentation of airborne geophysical data; AGSO Journal of Australian Geology & Geophysics, v. 17, p. 63-76.

Richards, J.A. and Jia, X.
2006: Remote Sensing Digital Image Analysis: An Introduction; Springer, 4th edition, 439 p.

Schetselaar, E. and de Kemp, E.
2000: Image classification from LANDSAT TM, airborne magnetics and DEM data for mapping Paleoproterozoic bedrock units, Baffin Island, Nunavut, Canada, *in* IPRS 2000 Congress: Geoinformation for All; 16-23 July 2000, Amsterdam, Netherlands, p. 1325-1332.

St-Onge, M.R., Scott, D.J., Wodicka, N., and Luca, S.B.
1999a: Geology, Hidden Bay, Nunavut; Geological Survey of Canada, A-Series Map 1980A, scale 1:100 000.

1999b: Geology, McKellar Bay, Nunavut; Geological Survey of Canada, A-Series Map 1981A, scale 1:100 000.

St-Onge, M.R., Wodicka, N., and Ijewliw, O.
2007: polymetamorphic evolution of the Trans-Hudson Orogen, Baffin Island, Canada: Integration of petrological, structural and geochronological data; Journal of Petrology, v. 45, p. 271-302.

Switzer, P.
1980: Extensions of linear discriminant analysis for statistical classification of remotely sensed satellite imagery; Mathematical Geology, v. 12, p. 367-376.

Wodicka, N. and Scott, D.J.
1997: A preliminary report on the U-Pb geochronology of the Meta Incognita Peninsula, southern Baffin Island, Northwest Territories (Nunavut), *in* Current Research 1997-C; Geological Survey of Canada, p. 167-168.

CASE STUDY 3. The Advantages of High-Resolution Spectral and Spatial Hyperspectral Data for Lithological Mapping: An Example from Southeast Baffin Island

J.R. Harris and M. St-Onge
Geological Survey of Canada, 615 Booth Street, Ottawa, Ontario K1A 0E9
Corresponding author's email: Jeff.Harris@NRCan.gc.ca

INTRODUCTION

The trend in remote sensing technology over the past 10 years has been towards the design of sensors that are characterized by both higher spectral and spatial resolution. As opposed to simple discrimination, hyperspectral remote sensing offers a great advantage to geologists as the increase in spectral resolution affords the geologist the opportunity to uniquely identify certain minerals and rocks. Additionally, sensors characterized by high spatial resolution (i.e. QuickBird, Ikonos) now rival aerial photography in terms of spatial detail.

OBJECTIVES

The objectives of this case study are to show the advantages of higher resolution remote sensors, specifically airborne hyperspectral data sensors, for geological mapping. The material reported in this study is largely derived from Harris et al. (2005, 2006a,b).

The study area is in southeastern Baffin Island, approximately 80 km south of Iqaluit (Fig. 1). This area has been chosen as it represents a typical Arctic geological and biophysical environment, has relatively good bedrock exposure and little vegetation cover (lichens excluded), has a variety of lithologies ranging from gneissic/granitoid basement rocks to rift-related volcanic and sedimentary rocks, and has recently been mapped at a 1:100,000 scale by the Geological Survey of Canada (St-Onge et al., 1998a,b).

The surveyed area covers a 70 x 70 km section of the Meta Incognita Peninsula, which is approximately 80 km south of Iqaluit (Fig. CS3-1). Figure CS3-2 shows the regional geology of the study area, which was mapped by St-Onge et al. (1998a,b) using traverses spaced approximately 3 km apart. The study area, shown on the small box on Figure CS3-2, consists of Paleoproterozoic metasedimentary rocks, monzogranite, metatonalite, and rare ultramafic rocks. Polyphase deformation and metamorphism during the Trans-Hudson Orogeny affected the Paleoproterozoic rocks, resulting in complex fold interference geometry (St-Onge et al., 1998a,b).

The surficial environment includes rolling topography (approximately 350-600 m) with appreciable areas of exposed and weathered bedrock. Lichen is prevalent and covers up to 80% of exposed surfaces, depending on rock type. Lichen and stunted vegetation (e.g. grasses, moss, shrub willows) grows selectively on specific lithologies, including metagabbro, metadiorite, and amphibolite.

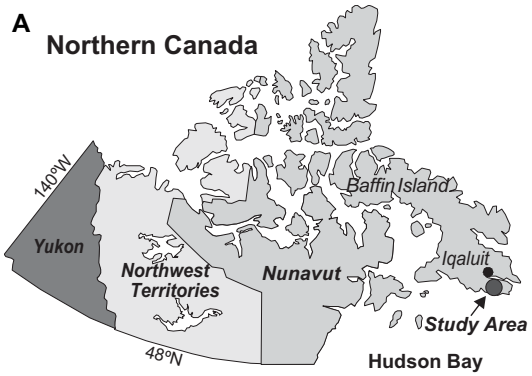

Figure CS3-1. Location of the hyperspectral study area on southeast Baffin Island, Nunavut.

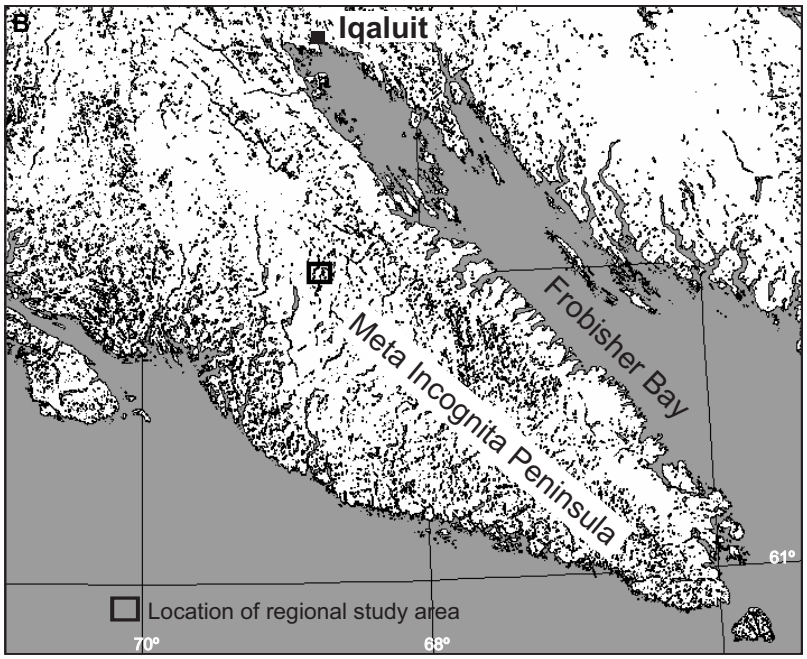

Harris, J.R. and St-Onge, M., 2008, The advantages of high-resolution spectral and spatial hyperspectral data for lithological mapping: An example from southeast Baffin Island, Case Study *3 in* Remote Predictive Mapping: An Aid for Northern Mapping, (ed.) J. R. Harris; Geological Survey of Canada, Open File 5643, p. 183-189.

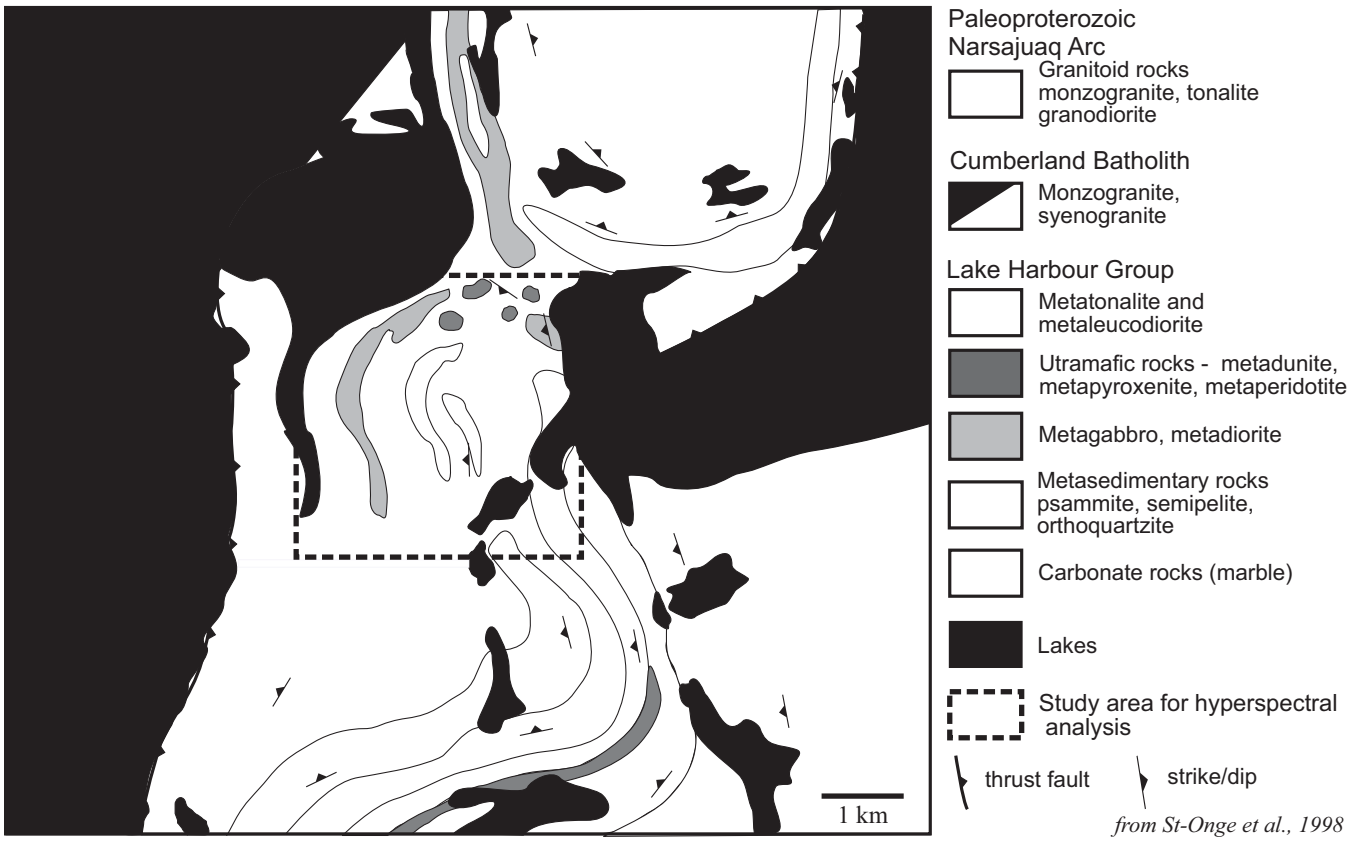

Figure CS3-2. Mapped geology of the study region (St-Onge et al., 1998a,b).

The study area offers a suitable environment for a remote sensing study of this nature given its generally good bedrock exposure along with a lack of vegetation and appreciable till cover.

The approach taken here is to first provide a general visual comparison between lower resolution data sets (LANDSAT, RADARSAT) and higher resolution (both spectral and spatial) hyperspectral data, comparing the ability to identify and delineate lithology, and then to provide a summary of approaches utilizing various image analysis techniques for the production of a lithological map from high-resolution hyperspectral data.

DATA

LANDSAT thematic mapping (TM) data acquired during the summer of 2000 (Fig. CS3-3A) were used in conjunction with airborne hyperspectral data (Fig. CS3-3C). Both these sensors acquire data in the optical and infrared portion of the electromagnetic (EM) spectrum. Two RADARSAT scenes (Fig. CS3-3D,E) were also used in the analysis, as well as digital elevation model (DEM) data (Fig. CS3-3F).

Noranda Ltd. collected hyperspectral data along several flight lines using the airborne PROBE sensor in mid July 2000. Swath width for each line was approximately 7 km and was 50 km in length. Spatial resolution, which is partially defined by the flight altitude, was approximately 5 metres for this data set. The data consisted of 128 bands with a bandwidth of 15 nanometres, ranging from 0.4 to 2.5 μm.

Products and Processing

Visual Assessment

The advantage of higher spatial resolution data for discriminating and identifying various geological features (i.e. rock type, structure) can be clearly seen on Figure CS3-3 when comparing the various image types. The radar data (Fig. CS3-3D,E) have a typical salt-and-pepper appearance, from which topographic patterns reflecting differences in lithologies and structures can be seen. However, very little lithological differentiation can be seen. The LANDSAT imagery (Fig. CS3-3A) offers a little more lithogical differentiation. Even a simple three-band ternary image of the hyperspectral data (Fig. CS3-3C) offers a "better picture" of lithological variation within the study area (metasediments are purple and basement rocks are green), partly due to the 5 m spatial resolution versus 30 m for LANDSAT and 22 m for the RADARSAT data. There does not appear to be any significant correlation between the geology (Fig. CS3-3B) and the DEM data (Fig. CS3-3E); however, again this is in part due to the low resolution of the DEM (1:250,000 Canadian Digital Elevation data).

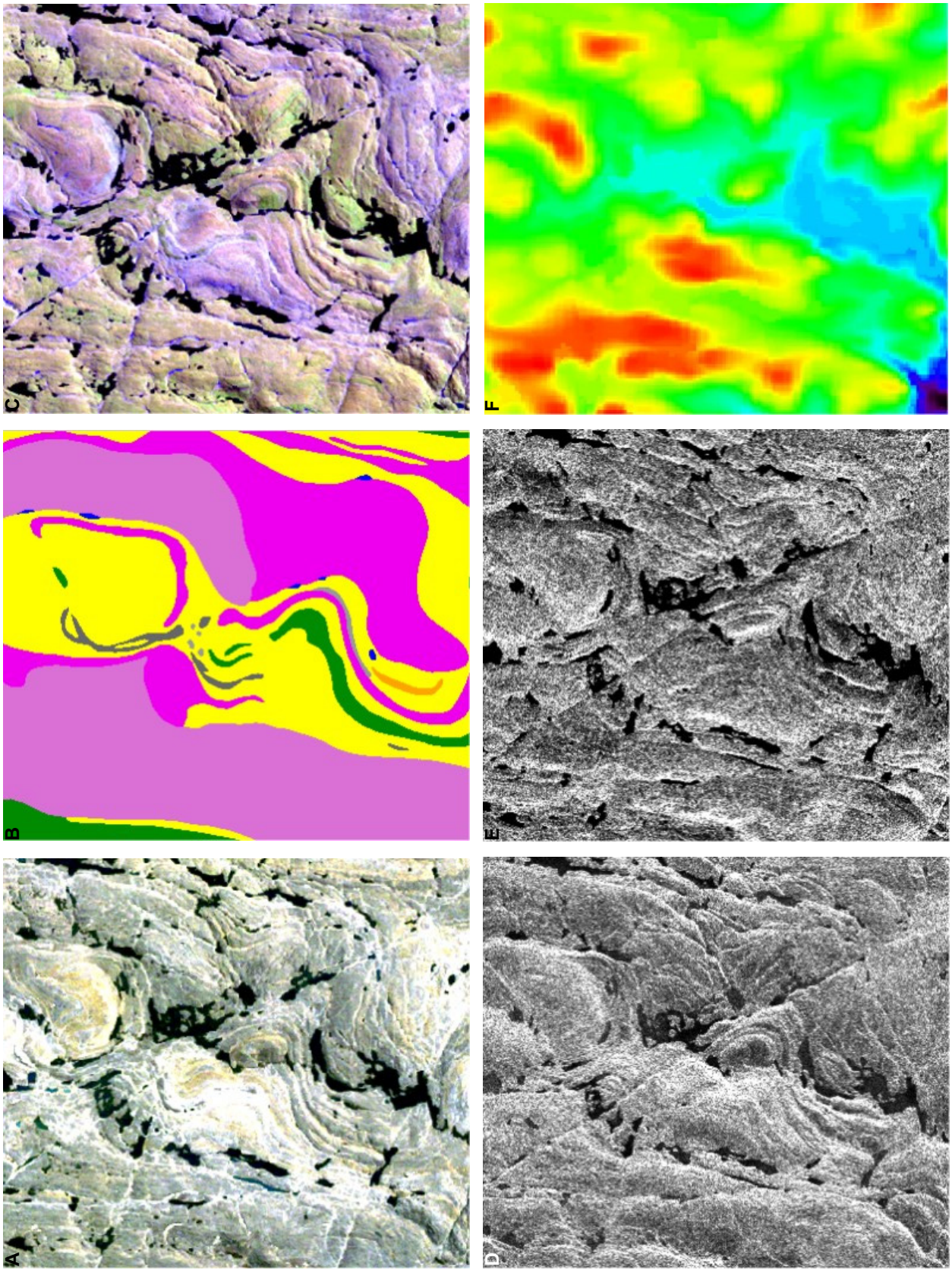

Figure CS3-3. Data used for this study (see Fig. CS3-2 for area of each image). **(A)** LANDSAT bands 7, 4, 2 (red, green blue, respectively) colour composite ternary image. **(B)** Regional geology (St-Onge et al., 1998a,b). Yellow – metasediments; green – tonalite; purple – monzogranite; dark grey – metagabbro. **(C)** Hyperspectral colour composite ternary image. **(D)** and **(E)** RADARSAT images acquired from different passes and incidence angles. **(F)** Canadian digital elevation data (CDED) - digital elevation model (DEM) topographic data.

Computer-Assisted Approach – Supervised Classification

Figure CS3-4, taken form Harris et al. (2006b), shows a suggested approach for processing a hyperspectral data set to produce a spectral map that, in this case, can be directly related to variations in lithology. This involves four steps:

- transforming the data to into fewer numbers of variables (in this case from 128 to 10) using a minimum noise fraction (MNF) transform,
- displaying three of these newly created channels as a ternary image that shows the variation in lithologies clearly,
- selecting training areas representative of each lithology from this image (supported by field work),
- and creating a spectral map through classification (matched filtering).

It also noted in Figure CS3-4 that the MNF ternary image supplies a base for visually interpreting lithology. Other methods can also be employed that range from purely automatic to computer assisted (see Chapter 2, this volume). The output from these two processing streams is shown in Figures CS3-5 and CS3-6. The MNF ternary map provides an image in which different lithological units are characterized by distinct colours. The colours on the classified image

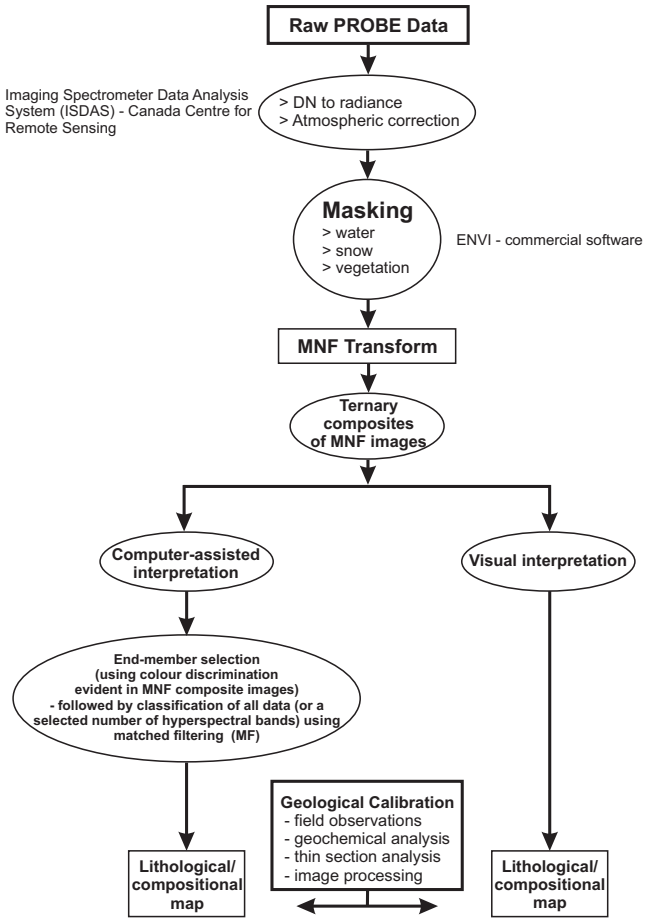

Figure CS3-4. Processing flow chart for hyperspectral data processing (after Harris et al., 2006a).

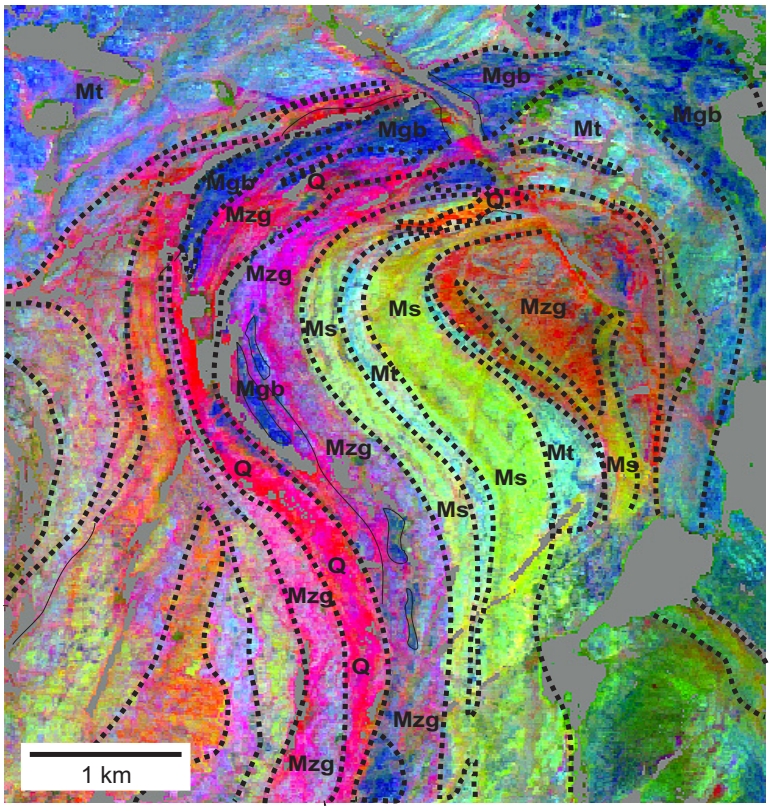

Ms - metasediment (primarily psammite, and minor semipelite); compositional unit

Q - quartzite; compositional unit

Mgb - metagabbro, metadiorite, amphibolite; lithological unit

Mzg - monzogranite; compositional unit

Mt - metatonalite; lithological unit

- - - - - interpreted lithological and compositional contacts

Figure CS3-5. Minimum noise fraction (MNF) transformed hyperspectral image in which variations in hue reflect different rock units (from Harris et al., 2006a)

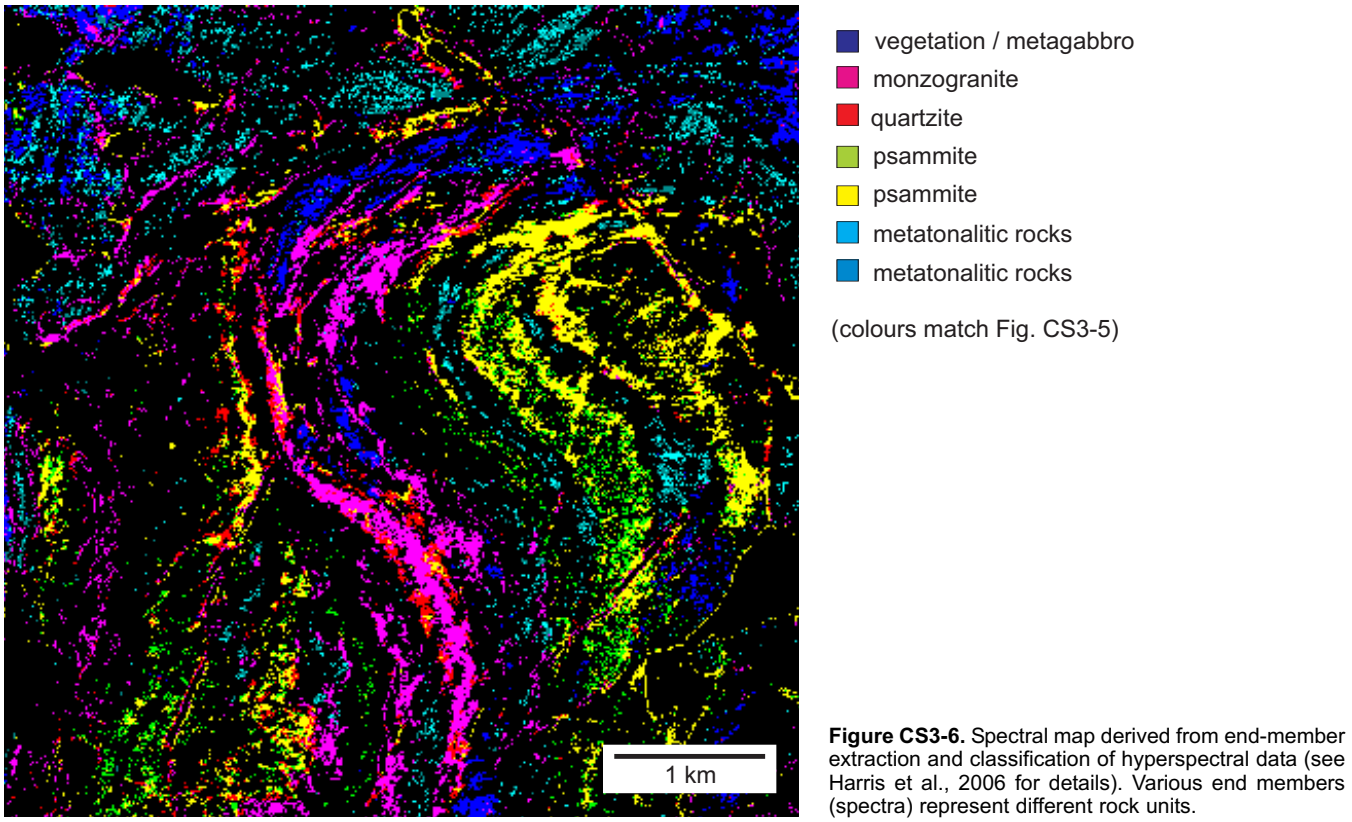

Figure CS3-6. Spectral map derived from end-member extraction and classification of hyperspectral data (see Harris et al., 2006 for details). Various end members (spectra) represent different rock units.

(Fig. CS3-6) represent areas that closely match the training spectra for each lithological unit (Fig.CS3-7; refer to Harris et al. (2005) for discussion of spectra).

Comparison of LANDSAT and Hyperspectral Data

Various classification results of the LANDSAT and hyperspectral data are presented in Figure CS3-8. One can clearly see that the classifications (see figure caption CS3-8 for details) based on the hyperspectral data more closely resemble the existing geology map. In fact, a number of sub-units, especially within the metasedimentary package (psammites, quartzites, and pelites), are evident. This demonstrates the advantage of sensors characterized by higher spectral and spatial resolutions for geological mapping.

The hyperspectral data provides more spectra detail than the LANDSAT and RADARSAT data, allowing for better discrimination, and in some cases unique identification of certain minerals (calcite, dolomite) or groups of minerals and their associated weathering products. Both LANDSAT and hyperspectral data can identify carbonates and calc-silicates based on their unique spectral characteristics in the short-wave infrared (SWIR) portion of the electromagnetic spectrum. However, hyperspectral data can uniquely identify calcite from dolomite based on subtle differences in spectra, again in the SWIR portion (P. Budkewitsch, oral comm., 2007). In addition, the generally higher

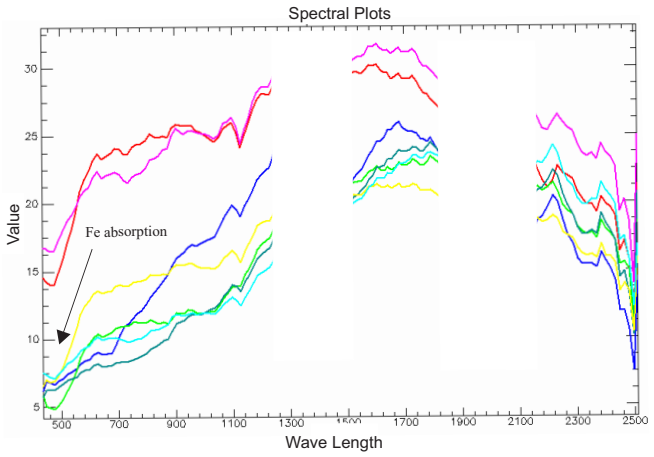

Spectral plots of end members derived from minimum noise function ternary image

- Vegetation (metagabbro) - blue on Fig. CS3-5
- Psammite 1 - green on Fig.CS3- 5
- Psammite 2 - yellow on Fig. CS3-5
- Metatonalite - dark cyan on Fig. CS3-5
- Metatonalite - light cyan on Fig. CS3-5
- Quartzite - red on Fig. CS3-5
- Monzogranite - - purple on Fig. CS3-5

Figure CS3-7. Spectra for each rock unit shown in Figures CS3-5 and CS3-6.

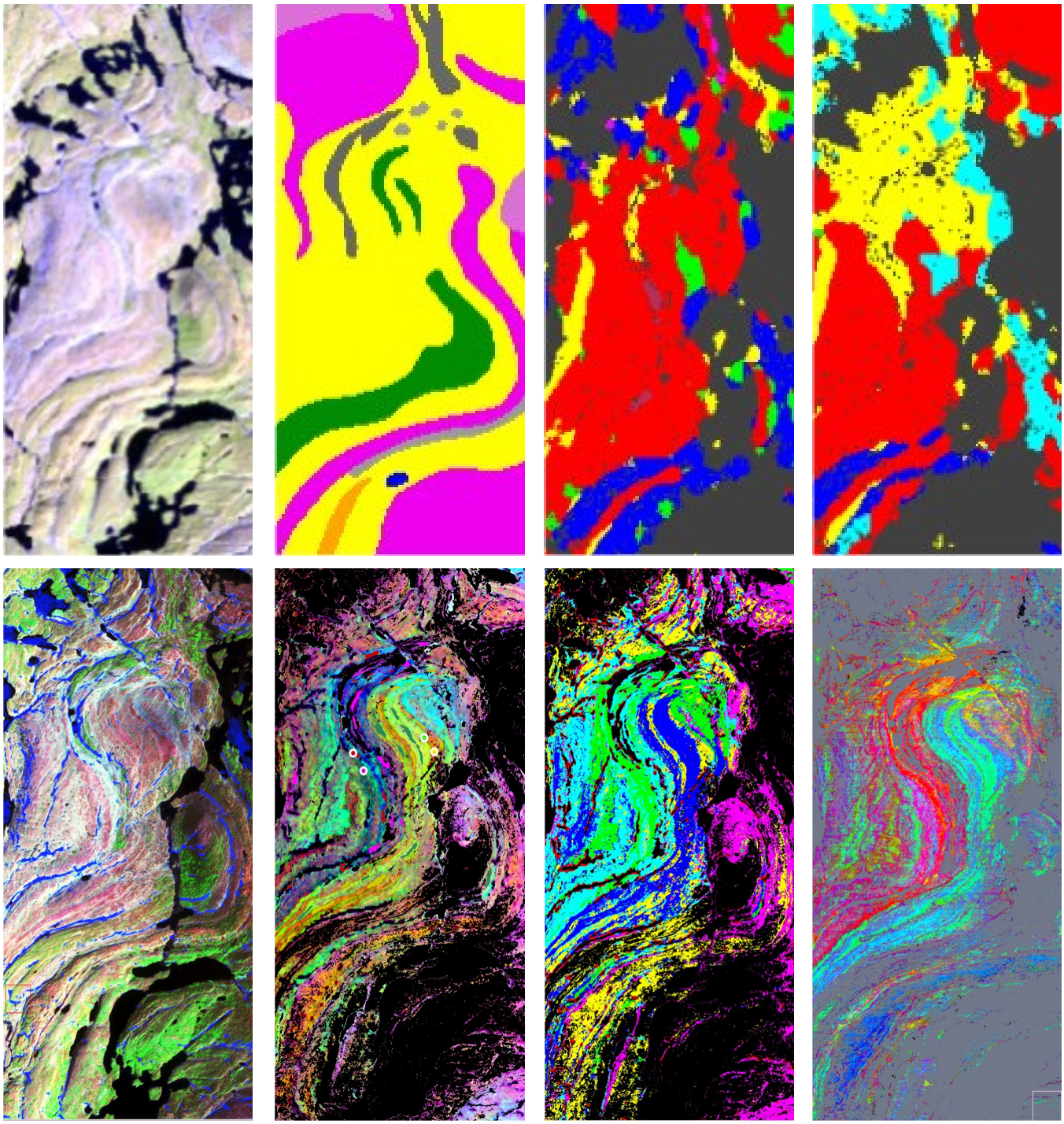

Figure CS3-8. Various predictive (classified) maps derived from LANDSAT and airborne hyperspectral data. **(A)** LANDSAT bands 7, 4, and 2 (red, green, blue, respectively) colour composite ternary image. **(B)** Mapped geology (St-Onge et al., 1998a,b). See figure caption for Figure CS3-3B for a description of the colours. **(C)** Unsupervised classification of LANDSAT data. **(D)** Supervised classification of LANDSAT data. **(E)** Hyperspectral colour composite image. **(F)** Minimum noise fraction (MNF) transformed hyperspectral image. **(G)** Unsupervised classification of MNF-transformed hyperspectral data. **(H)** Supervised classification of hyperspectral data using end-member spectra and matched filtering (see Harris et al., 2006a,b for more details). See Figure CS3-2 for map locations.

spatial resolution of hyperspectral data allows for the identification and mapping of various structural features not seen as easily, if at all, on lower resolution data such as LANDSAT.

SUMMARY

Hyperspectral data requires more rigorous preprocessing and correction than lower resolution optical sensors. Atmospheric correction, for example, is paramount to reliable, quantitative analysis of spectra.

However, atmospheric correction of hyperspectral data collected in northern environments is often difficult due to low sun angles. Furthermore, at present there is no satellite system that routinely collects data similar to LANDSAT. Thus most hyperspectral mapping applications are restricted to a very limited number of areas where airborne data have been collected. Although hyperspectral data can be used to advantage for geological mapping as demonstrated by a limited number of case studies within Canada (Budkewitsch et al., 2000; Harris et al., 2005, 2006a,b), the routine use of such data will have to wait until a spaceborne system is developed. Currently the Canadian Space Agency (CSA) is contemplating the development of a hyperspectral sensor (HERO) but even if the program goes ahead, data will not be available in the foreseeable future. Given this scenario, the application of hyperspectral data to geological mapping is likely to remain on an ad hoc basis as it is not anticipated that it would be economically feasible to fly an airborne survey for every new mapping campaign.

REFERENCES

Budkewitsch, P., Staenz, K., Neville, R.A., Rencz, A.N., and Sangster, D.
2000: Spectral signatures of carbonate rocks surrounding the Nanisivik MVT Zn-Pb mine and implications of hyperspectral imaging for exploration in Arctic environments, *in* New Ideas for a New Millennium; Ore Deposit Workshop, Technical Volume, East Kootenay Chamber of Miners, Cranbrook, British Columbia, May 5-6, 2000, p. 1-11.

Harris, J.R., Rogge, D., Hitchcock, R., Ijewliw, O., and Wright, D.
2005: Mapping lithology in Canada's Arctic: Application of hyperspectral data using the minimum noise fraction (MNF) transform and matched filtering; Canadian Journal of Earth Science, v. 42, p. 2173-2193.

Harris, J.R., Ponomarev, P., Shang, J., and Rogge, D.
2006a: Noise reduction and best band selection techniques for improving classification results using hyperspectral data: Application to lithological mapping in Canada's Arctic; Canadian Journal of Remote Sensing, v. 32, p. 341-342

Harris, J.R., Ponomarev, P., Shang, J., Budkewitsch, P., and Rogge, D.
2006b: A comparison of automatic and supervised methods for extracting lithological end members from hyperspectral data: Application to lithological mapping in southern Baffin Island, Nunavut, *in* Current Research 2006-C4; Geological Survey of Canada, 19 p.

St-Onge, M.R., Scott, D.J., and Wodicka, N.
1998a: Geology, Hidden Bay, District of Franklin, Northwest Territories; Geological Survey of Canada, Open File 3536, scale 1:100 000.

1998b: Geology, McKellar Bay, District of Franklin, Northwest Territories; Geological Survey of Canada, Open File 3537, scale 1:100 000.

CASE STUDY 4. The Application of Remotely Sensed Data for Structural Mapping, Southwest Baffin Island

J.R. Harris[1], M. Sanborn-Barrie[1], M. St-Onge[1], M. Pilkington[1], T. Lynds[1], and R. McGregor[2]
1. Geological Survey of Canada, 615 Booth Street, Ottawa, Ontario K1A 0E9
2. Canada Centre for Remote Sensing, 588 Booth Street, Ottawa, Ontario K1A 0Y7
Corresponding author's email:Jeff.Harris@NRCan.gc.ca

INTRODUCTION

This study is a contribution to the Southwest Baffin Island Integrated Geosciences (SWBIG) project, undertaken by the Geological Survey of Canada in partnership with the Canada-Nunavut Geoscience Office, and the Qikitani Inuit Association. The goal of the project was to update the geoscience knowledge of the southwestern Baffin Island region of eastern Nunavut (Fig. CS4-1). As part of the project, Remote Predictive Mapping (RPM) techniques were employed to assist with geological interpretation of southwestern Baffin Island in order to expand the tools that may be used to identify tectonic features and distinctive structural domains, to target field mapping areas, and to contribute to existing geological map compilations (St-Onge et al., 2007a,b). For this study, remotely sensed data and regional aeromagnetic data were utilized. Interpretation was undertaken using a 'heads-up' digitization process of various enhanced images.

DATA

LANDSAT data, downloaded from the Canadian government's Geogratis website (http://geogratis.cgdi.gc.ca), was used by the Canada Centre for Remote Sensing (CCRS) to produce an orthorectified mosaic of Baffin Island, part of which is shown in Figure CS4-2 (Budkewitsch and McGregor, 2007). An enhanced LANDSAT mosaic, generated by RESMap Ltd., a commercial company specializing in deriving enhanced LANDSAT mosaics of Canada's North, was also used.

A mosaic of Advanced Synthetic Aperture Radar (ASAR) data was produced by CCRS from a series of swaths and a horizontal-vertical (HV) polarized mosaic and was used for interpretation.

Advanced Spaceborne Thermal Emission and Reflection Radiometer (ASTER) data and QUICKBIRD data were also acquired over a small area within the project area (see Fig. CS4-1) to examine the impact of very high-resolution data for structural mapping.

A high-resolution aeromagnetic survey flown over the eastern half of the map area in early 2006 (Figs. CS4-2, CS4-3), provided information on the regional magnetic properties of exposed and subsurface bedrock, as well as superimposed tectonic structures.

Published geological maps for the study area (Blackadar, 1967a,b; Taylor, 1986), as well as new field data collected during the 2006 SWBIG field season (St-Onge et al., 2007a,b) validated the RPM interpretations.

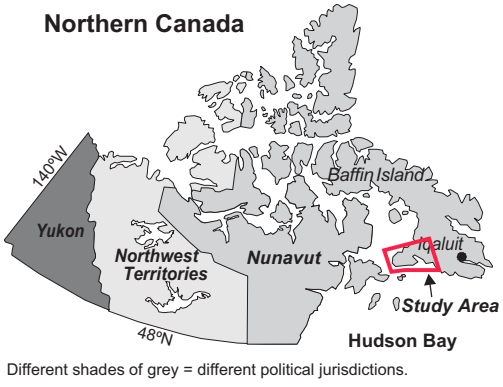

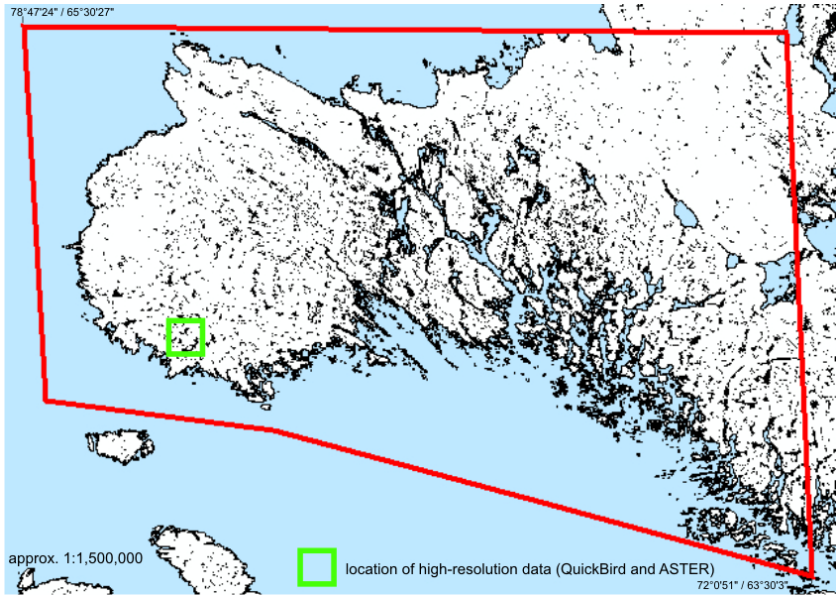

Figure CS4-1. Location of the study area.

Harris, J.R., Sanborn-Barrie, M., St-Onge, M., Pilkington, M., Lynds, T., and McGregor, R., 2008, The application of remotely sensed data for structural mapping: Southwest Baffin Island, Case Study 4 *in* Remote Predictive Mapping: An Aid for Northern Mapping, (ed.) J. R. Harris; Geological Survey of Canada, Open File 5643, p. 191-202.

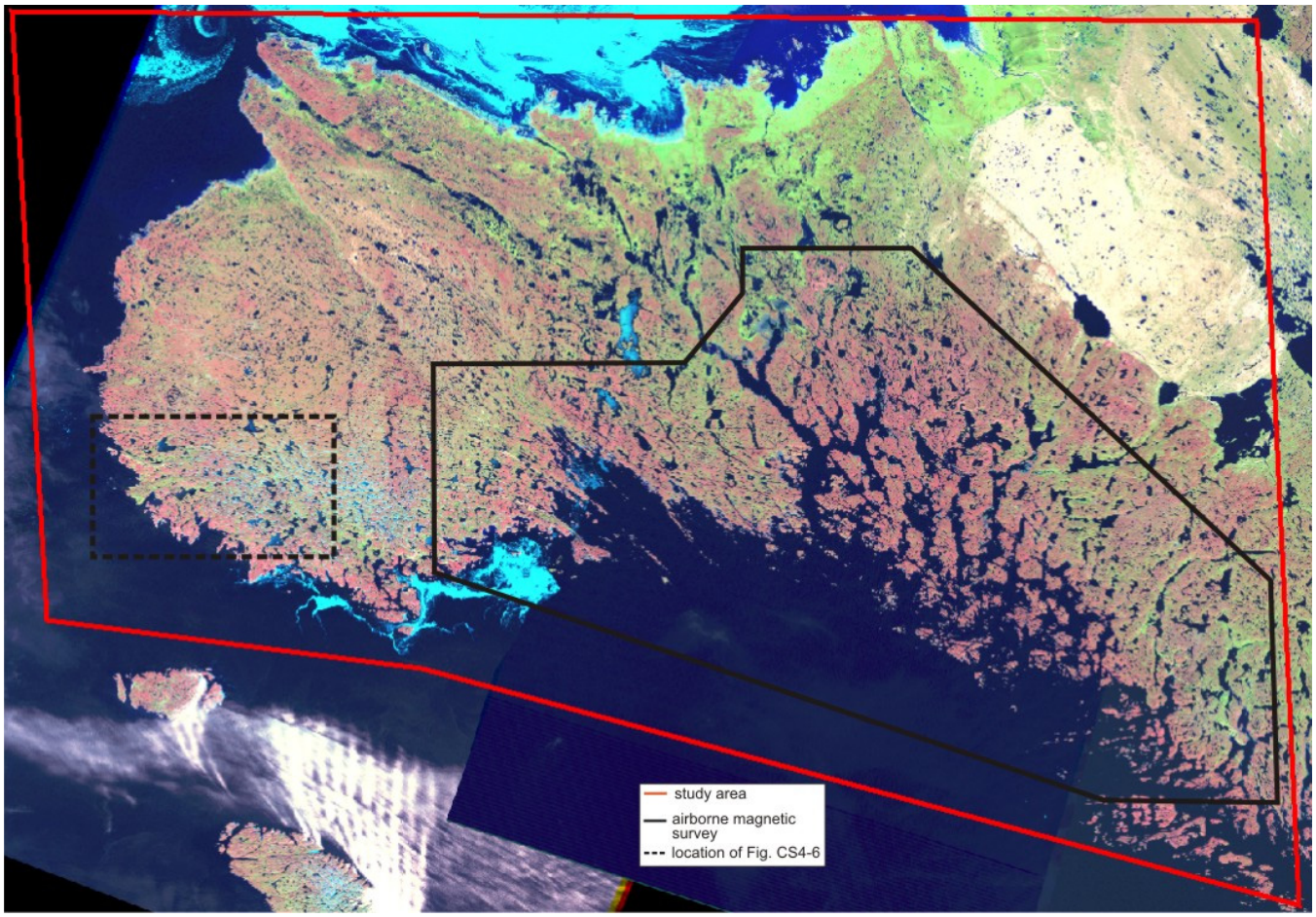

Figure CS4-2. LANDSAT false colour composite ternary image of southwestern Baffin Island with red, green, and blue corresponding to bands 7, 4, and 2 (from Budkewitsch and McGregor, 2007).

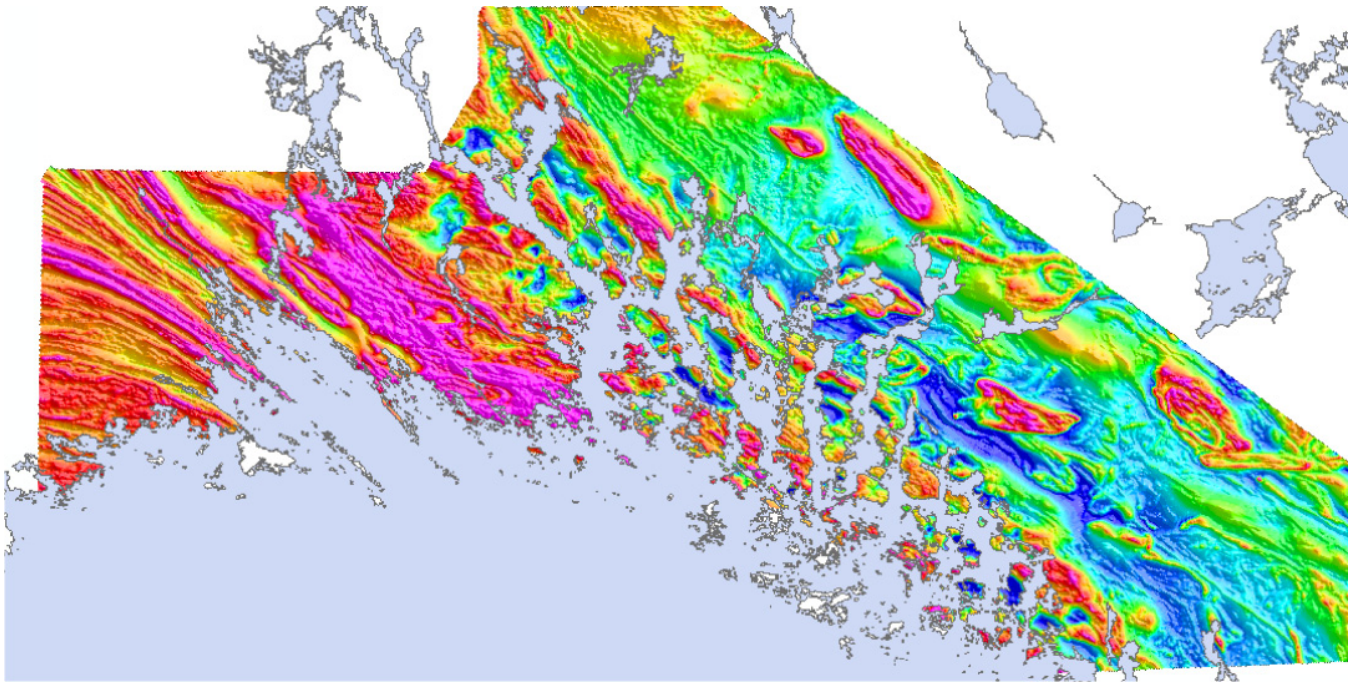

Figure CS4-3. Airborne magnetic image (shaded total field) from Dumont et al. (2006).

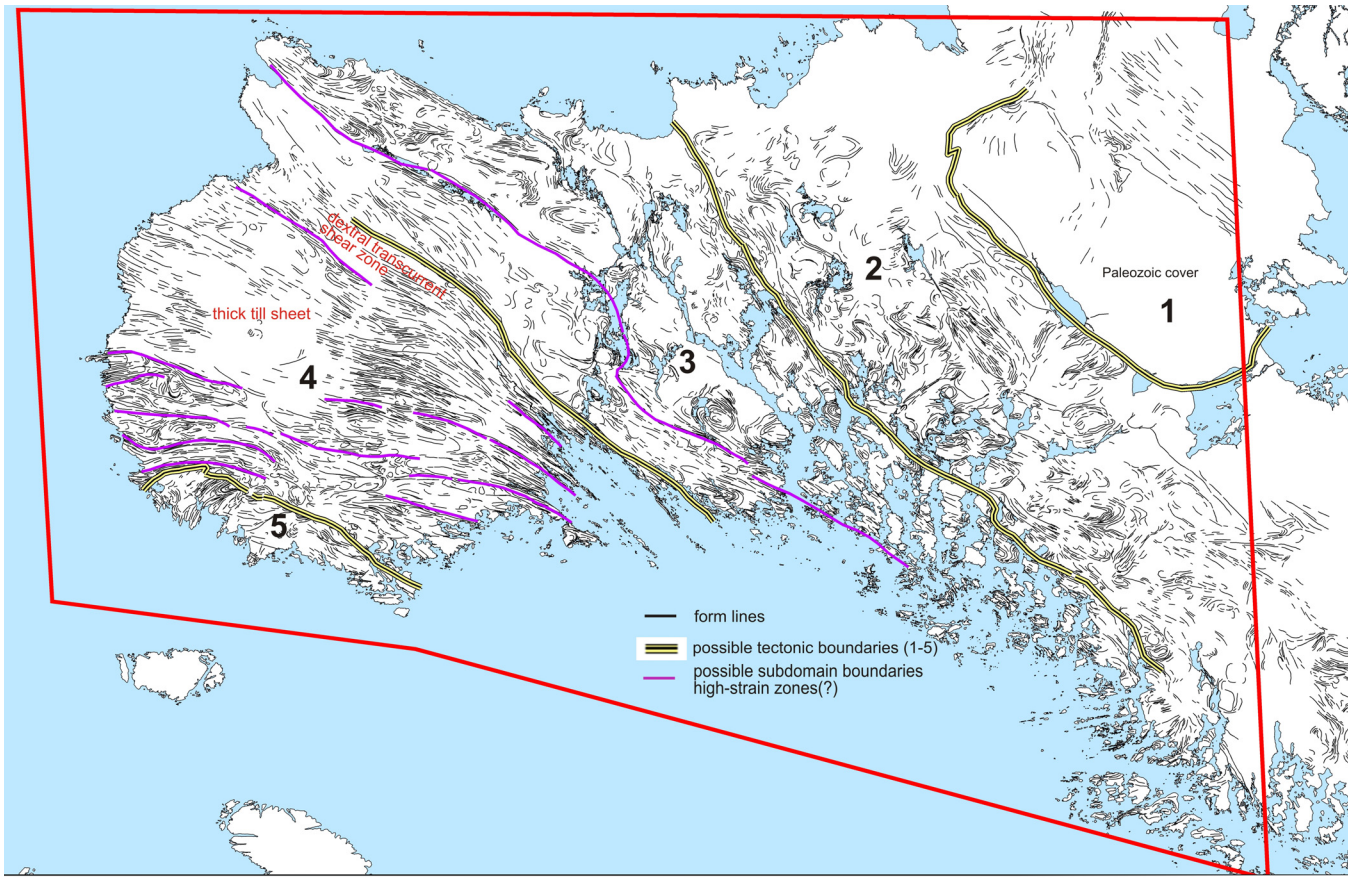

Figure CS4-4. Structural interpretation of the LANDSAT data with five subdivisions. Zone 1 is characterized by an absence of trend information and corresponds to flat-lying Paleozoic (Ordovician) carbonate rocks devoid of mappable structures. Zone 2 comprises the magnetically low supracrustal rocks of the Lake Harbour Group, which are intruded by magnetite-bearing plutonic rocks and subsequently folded. Zone 3 represents a corridor of uniformly high magnetic intensity with variable form patterns comprising straight zones and smaller folds. Zone 4 is characterized by straight northwest-trending form lines reflecting tectonic modification by a major dextral transcurrent shear zone (Sanborn-Barrie et al., 2007). Zone 5 correlates with supracrustal rocks of the Lona Bay and Schooner Harbour sequences (Sanborn-Barrie et al., 2007) and is characterized by a number of northeast-plunging folds. See the text for a more thorough discussion.

DATA PROCESSING

Simple enhancements, such as contrast stretching and edge sharpening (see Chapters 2 and 5 of this volume), were applied to the LANDSAT, ASAR, ASTER, and QUICKBIRD data to create enhanced images suitable for on-screen structural interpretations. A digital elevation model (DEM) obtained from Geomatics Canada (http://ess.nrcan.gc.ca/geocan/index_e.php) was also fused with the LANDSAT data, creating an image in which both topographic and spectral patterns were enhanced (see Chapter 2 of this volume). Several enhancements, such as vertical and horizontal derivatives, tilt, and analytical signal (see Chapter 3 of this volume), were applied to the magnetic data, again to create images suitable for on-screen interpretation.

On-screen GIS interpretation allowed imagery of various types to be superimposed, compared, and combined with field data, facilitating a detailed and exhaustive interpretation in which all available data were consulted. Many independent interpretations can be easily undertaken using GIS software. Furthermore each interpretation is made in a georeferenced framework, forming part of the GIS database without laborious digitizing, scanning, or reprojection. This, in turn, minimizes potential errors that may be introduced through such data/image manipulations.

In order to contribute to the structural interpretation of the southwest Baffin Island area, ductile structures, such as form lines and high strain zones, as well as brittle features, such as faults and lineaments, were interpreted from the enhanced imagery. The interpretations were validated by comparing the remotely predicted trends and structures to new and existing field data.

RESULTS

Regional Study

Ductile

Ductile features interpreted from LANDSAT and aeromagnetic data are compiled in predictive maps of ductile form lines and fold patterns in Figures CS4-4 and CS4-5, respectively. Two areas with relatively few interpreted structures emerge on Figure CS4-4. In the

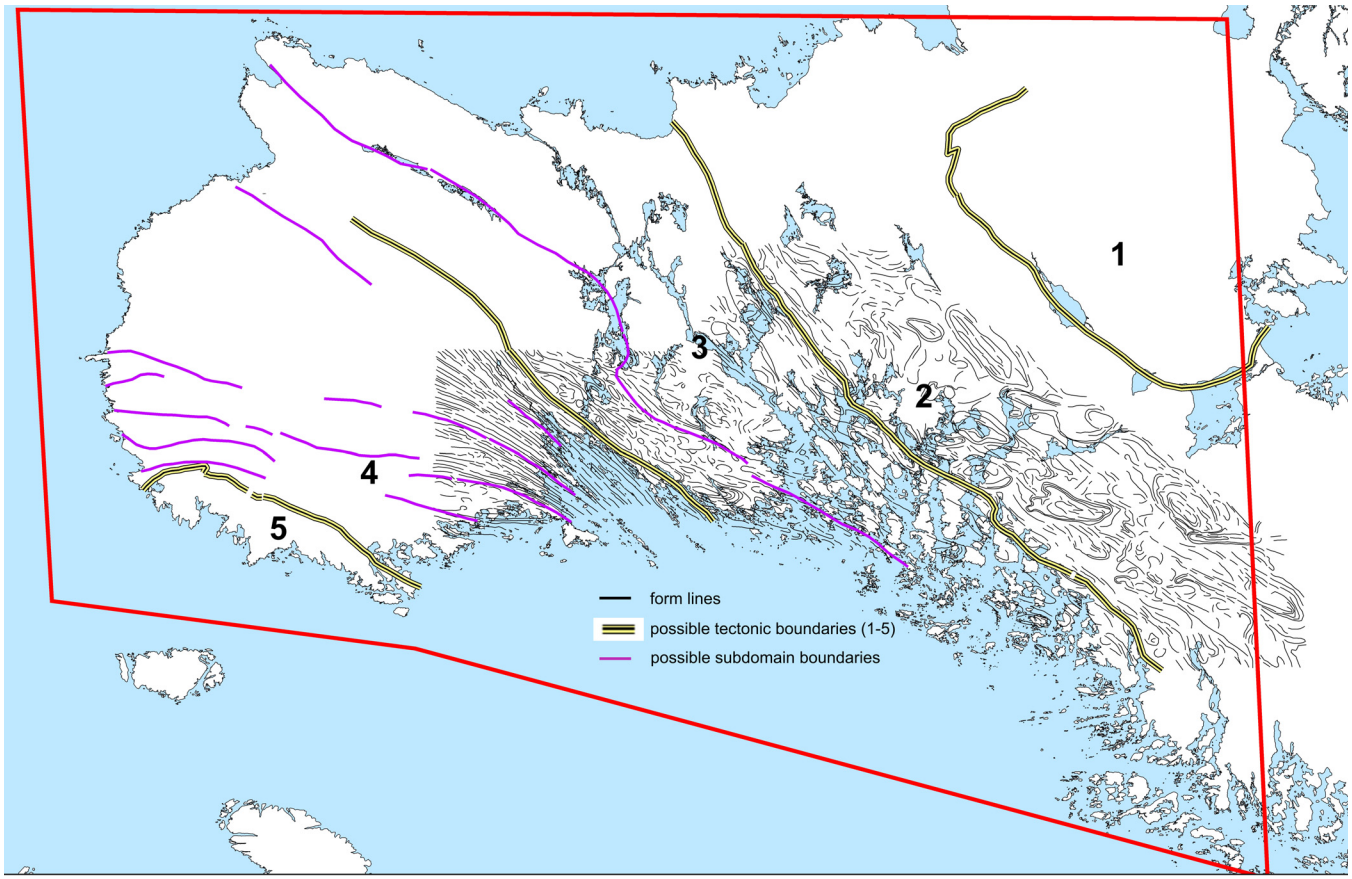

Figure CS4-5. Structural interpretation of the magnetic data.

western part of the map area, a thick layer of glacially deposited till obscures underlying bedrock structures; whereas in the northeastern part of the map area flat-lying Paleozoic sedimentary rocks offer little structural information (see Fig. CS4-4).

The form lines interpreted from LANDSAT and magnetic data represent tectonic trend lines derived from a variety of structures, including bedding and foliation trends of various generations (D_1 to D_3). In some cases, the trend lines highlight fold interference patterns that are clearly evident in the magnetic data and expressed as circular to ovoid structures delineated by magnetically variable units. Close inspection of the LANDSAT data reveals that many of these folds can also be traced on the basis of drainage and topographic patterns (i.e. distribution of bedrock ridges). In fact, correlation between form lines interpreted on the LANDSAT and magnetic data is extremely high, indicating that, in this area, both data sets offer similar information and can act as a proxy for one another. That the remotely predicted ductile structures can be corroborated with structural measurements made in the field (see below) highlights the value of LANDSAT and/or aeromagnetic data sets in regional geological interpretation.

The trend lines interpreted from LANDSAT and regional aeromagnetic data allow the southwest Baffin Island map area to be divided into five major zones (Figs. CS4-4, CS4-5).

Zone 1 is characterized by an absence of trend information, given that it corresponds to flat-lying Paleozoic (Ordovician) carbonate rocks devoid of mappable structures. The carbonates have a distinctive, highly reflective spectral signature, which is illustrated on the LANDSAT data (Fig. CS4-2), and are therefore easily 'remotely mapped'. However, further subdivision of the Ordovician strata into the five established stratigraphic formations for this area (St-Onge et al., 2007a) requires on-the-ground mapping and examination of the fossil faunal assemblages.

Zone 2 is characterized by generally low magnetic intensity punctuated by high-intensity domal structures, the latter reflected in both the magnetic and satellite data. Zone 2 comprises the magnetically low supracrustal rocks of the Lake Harbour Group, which are intruded by magnetite-bearing plutonic rocks and subsequently folded. The structures are a result of F_2-F_3 fold interference that exposes the magnetically contrasting lithologies in a dome-and-basin type of regional fold-interference pattern (St-Onge et al., 2007a).

Zone 3 represents a corridor of uniformly high magnetic intensity with variable form patterns comprising

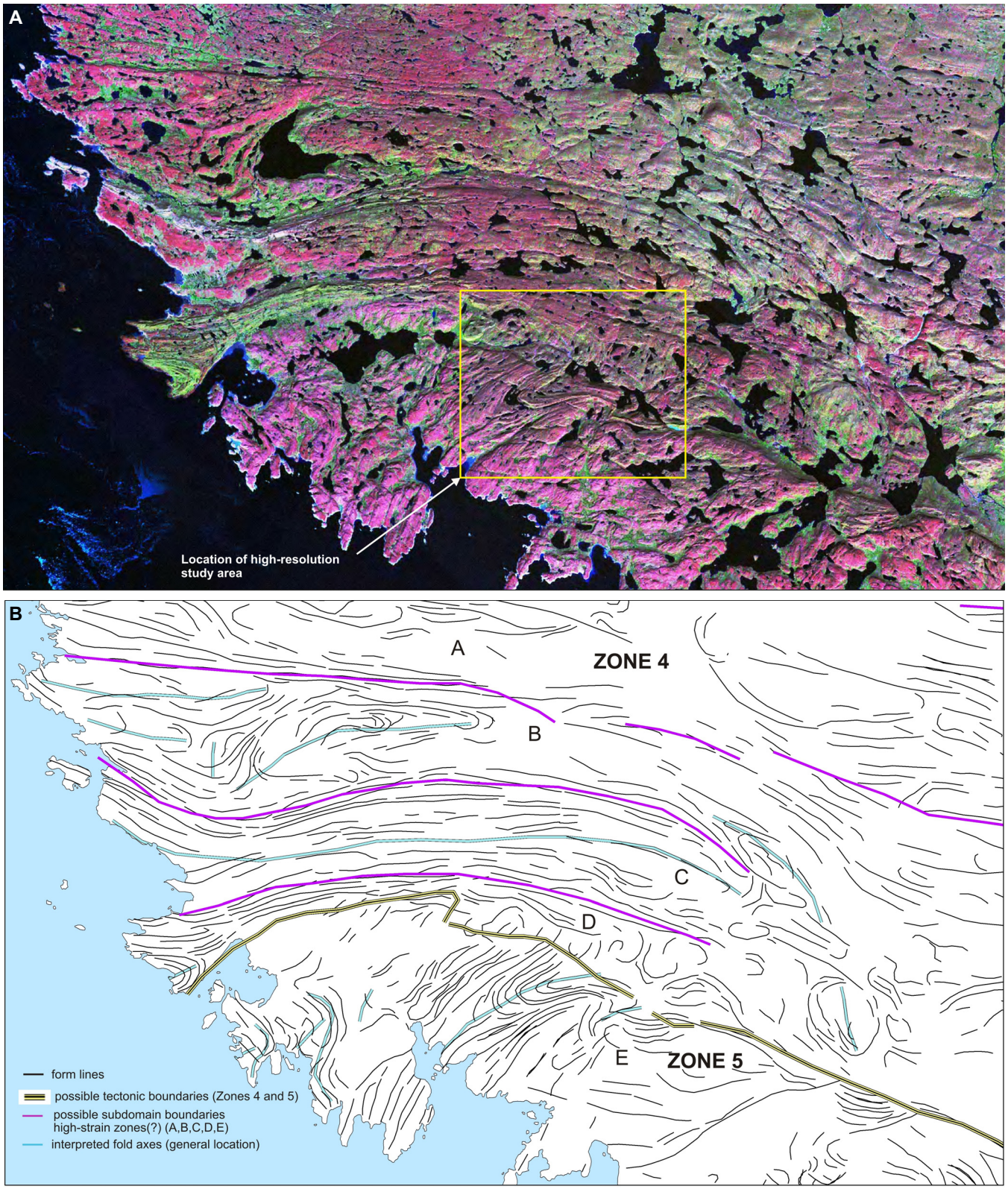

Figure CS4-6. LANDSAT and associated interpretations of a subarea (see Fig. CS4-2 for the location of the subarea). **(A)** LANDSAT image with red, green, and blue corresponding to bands 5, 4, and 2. **(B)** Structural interpretation of the LANDSAT image.

straight zones and smaller folds. This zone corresponds to a major F_3 antiformal culmination that exposes structurally lower magnetite-bearing charnokite and biotite-bearing monzogranite (Sanborn-Barrie et al., 2007).

Zone 4 is characterized by straight northwest-trending form lines reflecting tectonic modification by a major dextral transcurrent shear zone (Sanborn-Barrie et al., 2007). Much of this zone is not covered by the

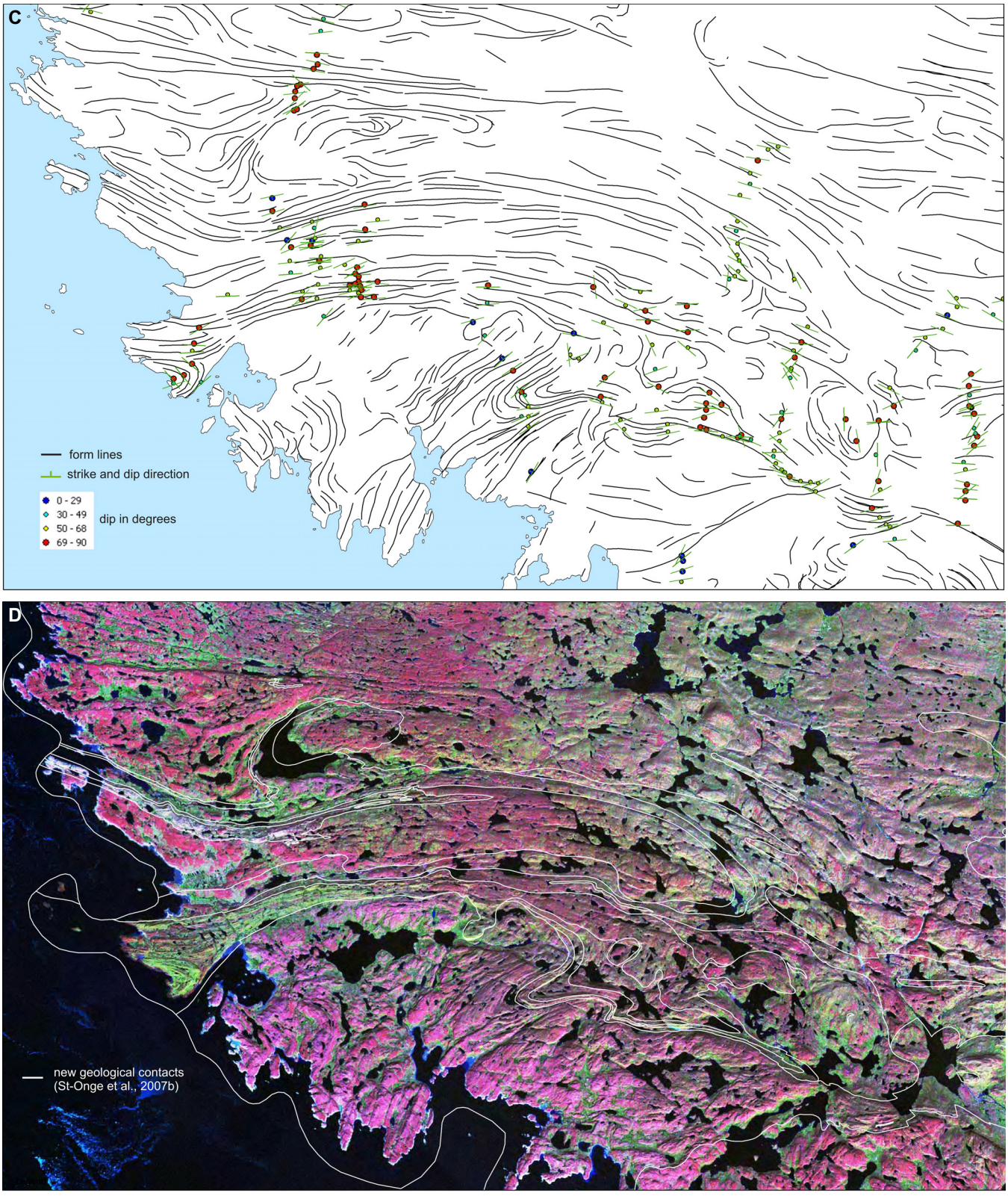

Figure CS4-6 continued. (C) Selected strike and dip measurements from the Southwest Baffin Island Integrated Geosciences Project field work in 2006. **(D)** LANDSAT and geological map-unit polygons from St-Onge et al. (2007b).

magnetic data, however, the LANDSAT data permits extrapolation of straight northwest-trending form lines northwestward across the Foxe Peninsula (see Fig. CS4-4; St-Onge et al., 2007b). A number of divisions, perhaps representing high strain zones, are interpreted based on their generally straight pattern, which appear to separate more curvilinear areas. One strain zone (see Fig. CS4-4) has been confirmed in the field (Sanborn-

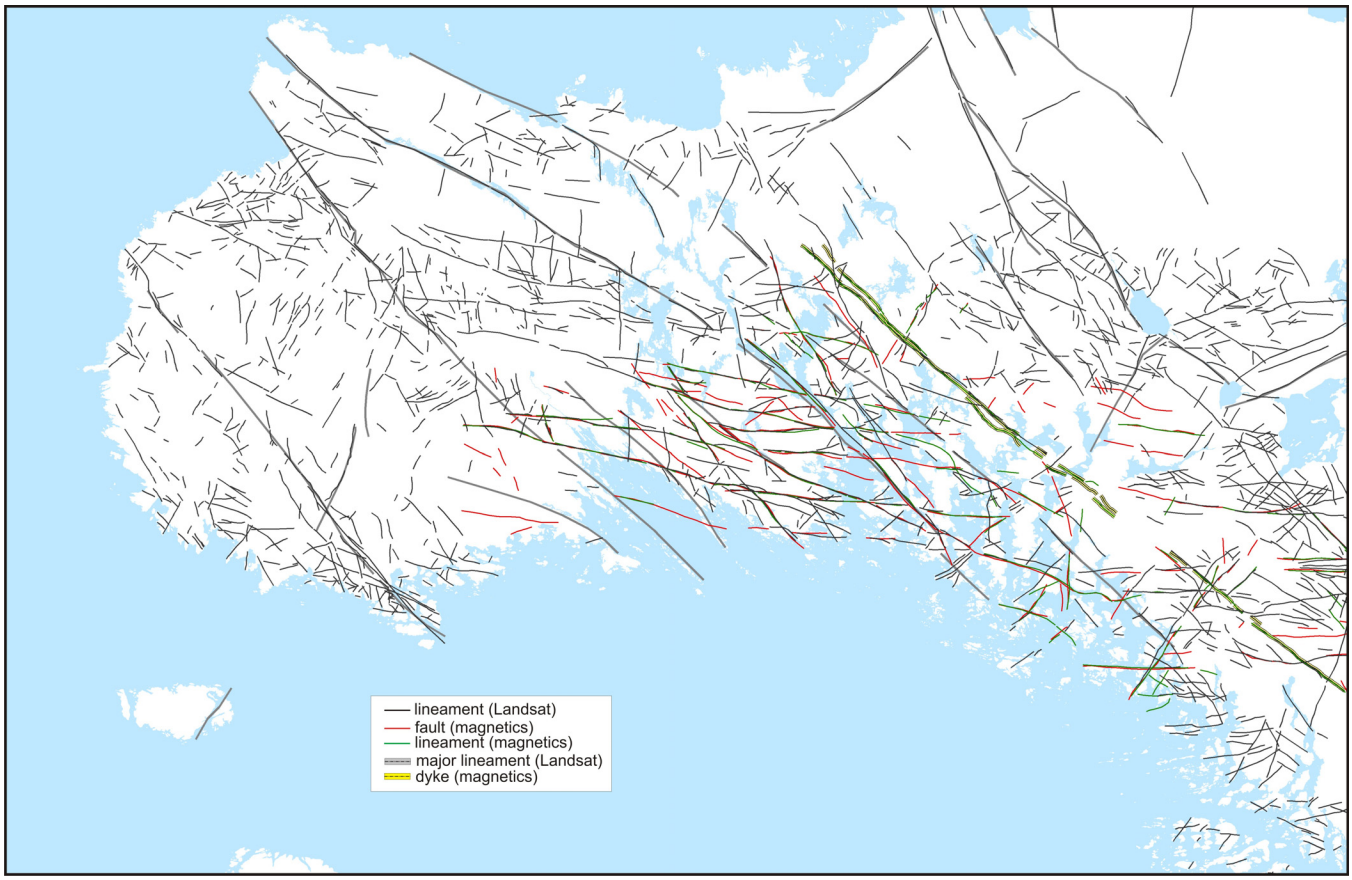

Figure CS4-7. Interpretation of brittle structures from LANDSAT data.

Barrie et al., 2007) and represents a dextral transcurrent shear zone (Andrew Gordon Bay shear zone). As previously mentioned, structural patterns in the central part of the zone (Foxe Peninsula) are obscured by a large circular till sheet.

Zone 5 correlates with supracrustal rocks of the Lona Bay and Schooner Harbour sequences (Sanborn-Barrie et al., 2007) and is characterized by a number of northeast-plunging folds.

Within Zones 4 and 5, the LANDSAT data (Fig. CS4-6A) and associated interpretations (Fig. CS4-6B,C) highlight a series of west-trending subdomains (labeled A to E on Fig. CS4-6B) separated by linear to curvilinear (high strain (shear?)) bounding corridors. Some of the subdomains are characterized by an internally broadly folded geometry (subdomains B and E), whereas others (subdomains A, C, and D) are mainly characterized by straight form lines. Correlation between strike of foliation measured in the field and the interpreted form lines is generally good (Fig. CS4-6C).

Subdomain A (Fig. CS4-6B), internally comprising a number of possible broad plunging folds, is bound to the south by a straight lineament that appears to define a sharp escarpment extending eastwards for approximately 50 km before it bends towards the southeast. The lithology, which can not be unequivocally determined on the LANDSAT image, correlates with monzogranitic rocks. These are presumed to comprise part of the Proterozoic rocks of the Cumberland Batholith on the existing geology map (Fig. CS4-6D; St-Onge et al., 2007b).

To the south, subdomain B (Fig. CS4-6B) is bound to the north by the lineament discussed above and to the south by a curvilinear zone of straight form lines, in part containing a marble unit that is very distinct on the LANDSAT data (linear white zone). Internally this package comprises a number of broad folds and an elliptical intrusive body. Fold axes have been interpreted (Fig. CS4-6B) and appear to define F_2 folds (Sanborn-Barrie et al., 2007).

Subdomain C exposes an east-plunging fold (Fig. CS4-6B). This zone appears to be internally homogeneous but is bounded by thicker units representing sedimentary rocks. The northern boundary defines a fairly thick curvilinear marble unit mentioned previously.

The western portion of subdomain D is characterized by an intense green hue on the LANDSAT image (Fig. CS4-6A) and corresponds to verdant meadow and moss vegetation growing on green- and black-weathering, mafic to ultramafic volcanic rocks of the Schooner Harbour sequence (Sanborn-Barrie et al., 2007). The extreme western portion of this zone defines a south-

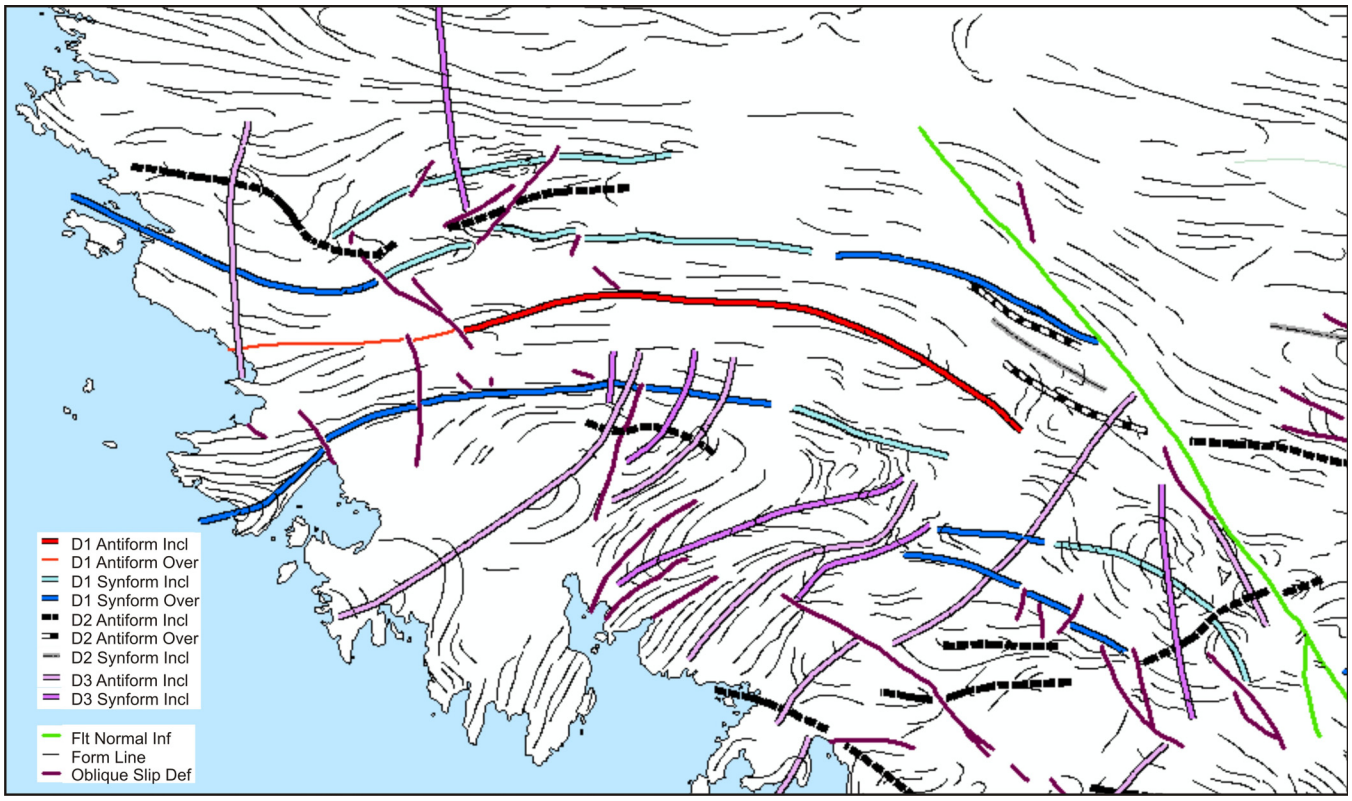

Figure CS4-8. Mapped structures in the area (from St-Onge et al., 2007b).

westward-plunging, F_1 synform clearly displayed on the LANDSAT image (Fig. CS4-6A). Dips in this zone are relatively steep (Fig. CS4-6C). Eastward the generally straight pattern of form lines becomes more curvilinear, defining several folds and circular intrusive bodies.

Subdomain E (Fig. CS4-6B) corresponds to a highly folded zone in which fold axes trend generally north-east-southwest (F_3). This zone comprises mainly F_2 folded quartzite and feldspathic arenite of the Lona Bay sequence (Sanborn-Barrie et al., 2007).

Brittle

Interpreted lineaments, faults, dykes, and major breaks are shown on Figure CS4-7. Faults have been interpreted where displacements are evident in the magnetic anomalies and where ductile structures evident in the satellite imagery are displaced or truncated. The lineaments represent possible faults and fractures that appear to form a dominant west-northwest set and a minor north-northeast set. The major breaks represent northwest-striking, Paleozoic normal faults that are pervasive throughout southern Baffin Island.

Structural Synthesis

Figure CS4-8 shows the final structural compilation of the area shown in Figure CS4-6 after field mapping. The similarity to the RPM interpretation (Fig. CS4-6B) is evident, especially the form lines that define various fold patterns. However, field work has enabled a more detailed evaluation of deformational events and the recognition of different generations of folds, as well as the unequivocal identification of antiformal and synformal structures.

High-Resolution Study

Figure CS4-9 shows a series of images and associated interpretations over a small area in the southern Fox Peninsula (see Fig. CS4-6A for location). These images are displayed at a scale of approximately 1:65,000 and demonstrate the advantages of higher spatial resolution imagery for geological interpretation. The LANDSAT colour composite image (Fig. CS4-9a), enlarged to 1:65,000 scale, is somewhat blocky in appearance with groups of pixels being seen. However, the plunging synform is clearly visible and form lines (Fig. CS4-9B) can be delineated, outlining the local structural setting. LANDSAT has a spatial resolution (pixel size) of 30 m and at scales less than 1:100,000 can be difficult to interpret' although in this case the well defined fold structure remains recognizable. The ASTER image (Fig. CS4-9C), with a resolution of 15 m, provides a clearer rendition of this local fold structure. The series of QUICKBIRD images (Fig. CS4-9D,E,F) at a 0.625 m resolution for the panchromatic data (Fig. CS4-9D), 2.5 m resolution for the MSS data (Fig. CS4-9E), and a fused image of the black and white and MSS data (Fig. CS4-9F) provide exceptional detail (see Fig. CS4-

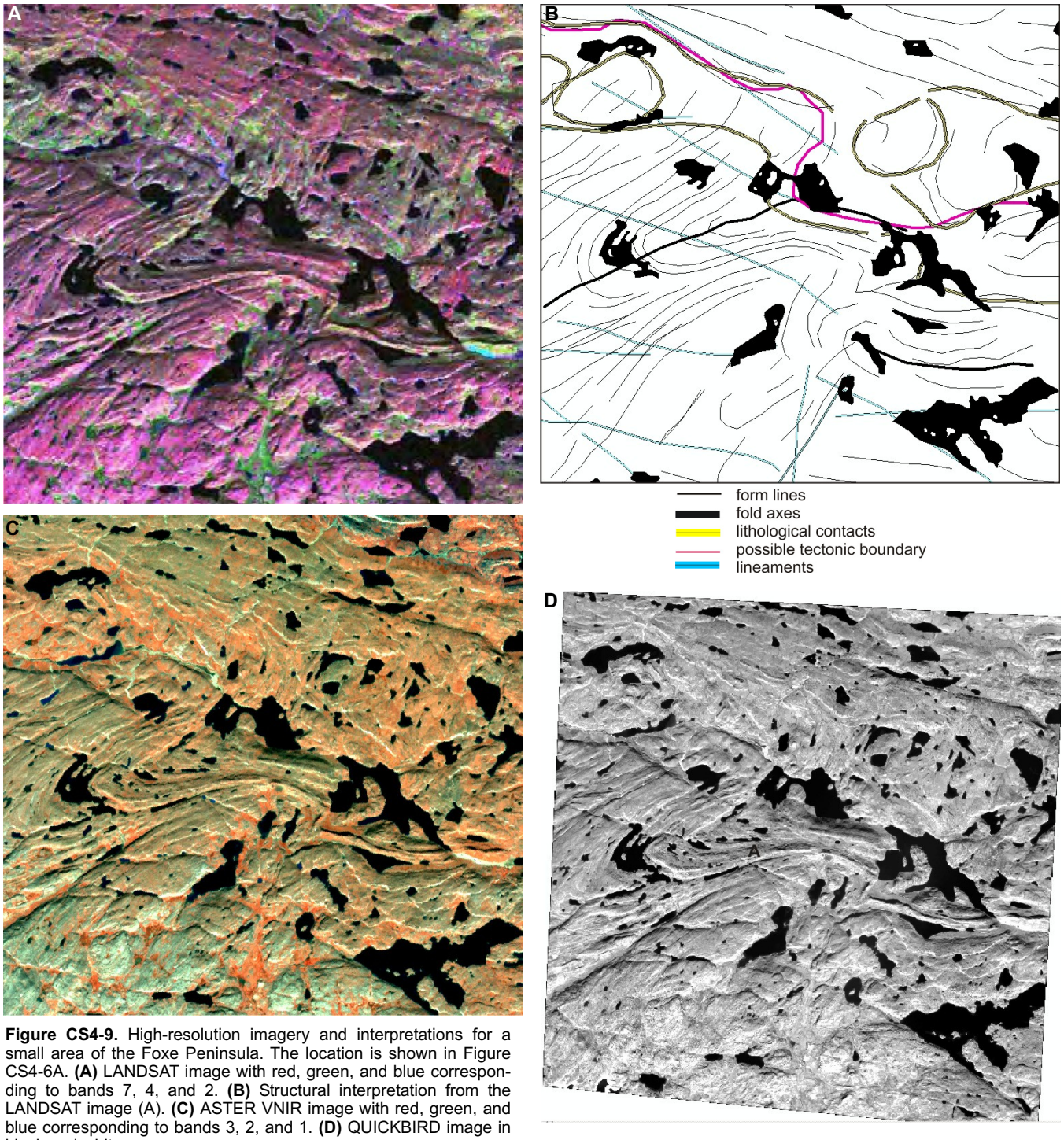

Figure CS4-9. High-resolution imagery and interpretations for a small area of the Foxe Peninsula. The location is shown in Figure CS4-6A. **(A)** LANDSAT image with red, green, and blue corresponding to bands 7, 4, and 2. **(B)** Structural interpretation from the LANDSAT image (A). **(C)** ASTER VNIR image with red, green, and blue corresponding to bands 3, 2, and 1. **(D)** QUICKBIRD image in black and white.

9G for interpretation) that exceeds that of the 1:60,000 scale airphoto (Fig. CS4-9H), albeit at a much greater cost (e.g. $3000 versus $13.99). A DEM of the area (Fig. CS4-9I), which is based on 1:50,000 and 1:250,000 CDED data, provides regional geomorphologic information in which the plunging synform is mappable due to its strong topographic expression. In the higher resolution data, a general indication of northward dip of the southern limb of the synform can be ascertained by strong reflection from the scarp slopes facing the sun azimuth and less reflection along the dip slopes (see Area "A" on Fig. CS4-9D,E). Finally, Figure CS4-9J shows the mapped geology for the same area as the previous images, following field observations, measurements, and compilation work in 2006, within the context of the SWBIG project (St-Onge et al., 2007). The geological structures on the predictive maps (Fig. CS4-9B.G) compare favourably

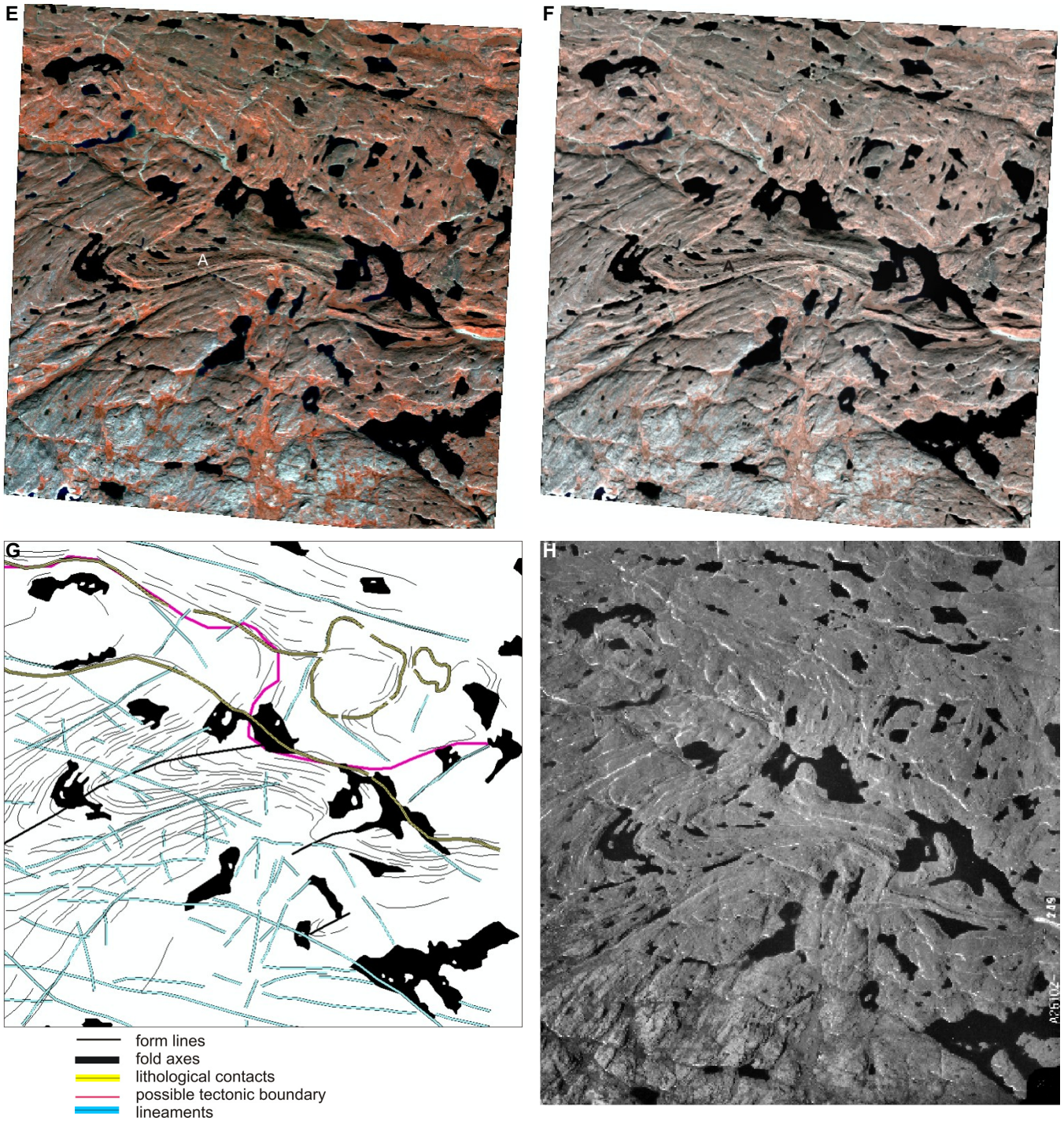

Figure CS4-9 continued. (E) QUICKBIRD MSS image with infrared, green and blue. **(F)** Fusion of the QUICKBIRD black and white image (D) and the QUICKBIRD MSS image (E). **(G)** A structural interpretation of the QUICKBIRD images. **(H)** Airphoto of the area.

with the final geology map (Fig. CS4-9J) when comparing form lines and fold axes. However, once again, field work is required to fine tune the predictions and unequivocally identify various geological structures and folds. In this area there is a paucity of lithological information provided by the LANDSAT, ASTER, and QUICKBIRD imagery (compare Fig. CS4-6A,C,D,E and F with Fig. CS4-9J).

SUMMARY AND DISCUSSION

Remotely sensed data, such as satellite and radar imagery, provided useful information from southwestern Baffin Island on various geological structures, which assisted in focusing regional field-mapping studies and provided information valuable to both regional and local geological compilations. Although high-resolution aeromagnetic data should form an integral part of any mapping campaign, the data might not be avail-

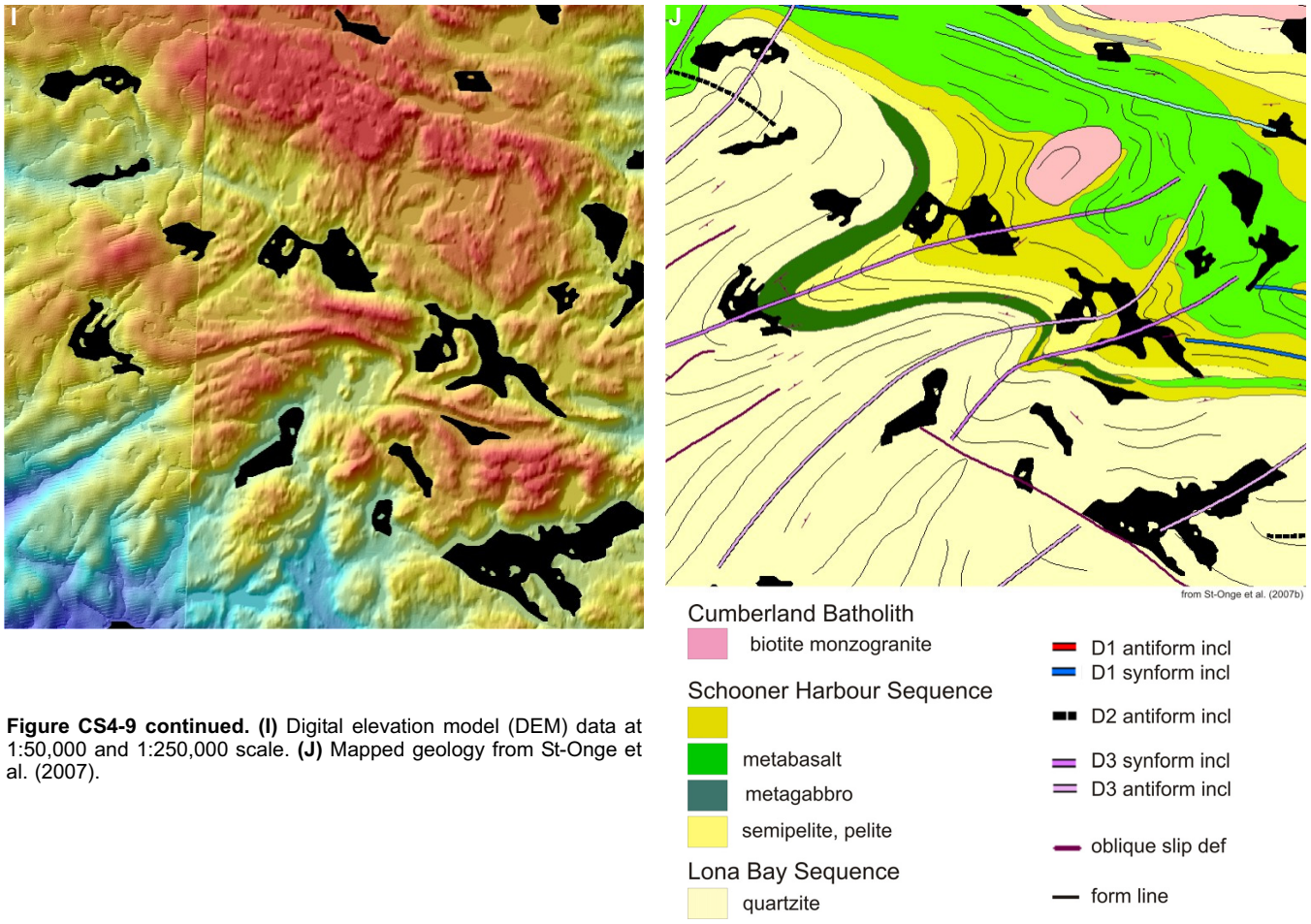

Figure CS4-9 continued. (I) Digital elevation model (DEM) data at 1:50,000 and 1:250,000 scale. **(J)** Mapped geology from St-Onge et al. (2007).

able for an area and can be expensive to fly. As seen in this study, LANDSAT can provide some information from which form lines, lineaments, and faults can be interpreted. Accordingly, LANDSAT data may serve as an important data source in areas where other remotely sensed data (such as magnetic data) are not available. Certainly one advantage of LANDSAT imagery is that it is free to obtain (see Chapter 5 of this volume).

The value of higher resolution, remotely sensed data has been demonstrated in this short study. QUICKBIRD and IKONOS data can offer a wealth of structural information that rivals, and in some cases surpasses, information obtained from aerial photographs. These high-resolution sensors offer better spectral resolution than air photographs at comparable spatial resolutions. Furthermore, because the data are digitally acquired and can be purchased fully georeferenced from the vendor, they can be input directly into a GIS without having to laboriously scan, mosaic, and georeference the data, as is required for digital aerial photograph coverage. The QUICKBIRD and IKONOS data can also be used to assist field mapping by directly uploading the data to hand-held field devices (e.g. ArcPad). The main drawback to high-resolution spectral data is the very high cost, typically $25 to $40 per km^2, in comparison to 13¢ per km^2 for aerial photograph coverage. However, sensors like SPOT 5 can offer high-resolution panchromatic data (approximately 5 m) that is more affordable. Presently within the SWBIG project, Spot 5 is being evaluated for future mapping and logistical purposes.

REFERENCES

Blackadar, R.G.
1967a: Geology, Foxe Peninsula, District of Franklin; Geological Survey of Canada, Preliminary Map 16-1966, scale 1:506 880.
1967b: Geology, Mingo Lake – Macdonald Island, Baffin Island, District of Franklin; Geological Survey of Canada, Map 1185A, scale 1:253 440.

Budkewitsch, P. and McGregor, R.G.
2007: Landsat, southern Baffin Island, Nunavut, *in* Digital Geoscience Atlas of Baffin Island (South of 70ºN and East of 80ºW), Nunavut, (eds.) M.R. St-Onge, A. Ford, and I. Henderson; Geological Survey of Canada, Open File 5116.

Dumont, R., Potvin, J., and Sanders Geophysics
2006: Residual Total Magnetic Field, Aeromagnetic Survey Baffin Island 2005, 36 B/12, Nunavut; Geological Survey of Canada, Open File 5206, 1 sheet.

Sanborn-Barrie, M., St-Onge, M.R., Young, M.D., and James, D.T.
2007: Bedrock geology of southwest Baffin Island: Expanding the tectonostratigraphic framework with relevance for base-metal, carving stone and gemstone potential, in Current Research; Geological Survey of Canada, in press.

St-Onge, M.R., Sanborn-Barrie, M., and Young, M.

2007a: Geology, Mingo Lake, Baffin Island, Nunavut; Geological Survey of Canada, Open File Map 5433, scale 1:250 000.

2007b: Geology, Foxe Peninsula, Baffin Island, Nunavut; Geological Survey of Canada, Open File Map 5434, scale 1:250 000.

Taylor, F.C.

1986: Geology, Cape Dorchester – Cape Dorset, District of Franklin, Northwest Territories; Geological Survey of Canada, Map 1607A, scale 1:250 000.

CASE STUDY 5. Application of Gamma-Ray Spectrometer Data for Lithological Mapping in a Cordilleran Environment, Sekwi Region, Northwest Territories

J. R. Harris, K. Ford, B. Charbonneau, and J. Buckle
Geological Survey of Canada, 615 Booth Street, Ottawa, Ontario K1A 0E9
Corresponding author's email:Jeff.Harris@NRCan.gc.ca

INTRODUCTION

The SEKWI Mountain (NTS 105P) mapping project initiated by the Northwest Territories Geoscience Office, NTGO, is intended as a three-year multidisciplinary study. This project is a collaboration of the NTGO, the Geological Survey of Canada (GSC), universities, and industry.

This project aims to provide a better understanding of the structure, stratigraphy, geochronology, geochemistry and tectonic history of a segment of the MacKenzie Mountains as well as the metallogenic and hydrocarbon potential.

The area is prospective for a variety of deposit types, including stratiform Pb-Zn-Cu, stratabound Zn-Pb±Cu-Ag-Ba polymetallic veins, tungsten, gold, and gem beryl (emerald) in skarns, and Li and REE in pegmatites. A number of showings and deposits were previously recognized in the region, some of which have reached the advanced exploration stage and are currently being re-investigated (Howards Pass, Mactung, Cantung, Lened) (e.g. Atkinson and Baker, 1983; Jefferson and Spirito, 2003).

The geophysical study area lies almost entirely within the Northwest Territories, with only a small segment in the southwest in Yukon (Fig. CS5-1). The transect covers Neoproterozoic to late Devonian sedimentary rocks, which are intruded by Cretaceous plutons in the southwest, and includes a number of mineral deposit types (Fig. CS5-2).

OBJECTIVES

The aim of this case study is to demonstrate the value of gamma-ray spectrometry data in conjunction with magnetic and LANDSAT data for mapping lithology in a mountainous environment.

DATA

The NTGO recently funded two combined gamma-ray spectrometry and residual magnetic total field surveys in the Sekwi Mountain area. The adjoining surveys were flown in 2005 over a northeast-trending transect about 17 km wide, roughly following the Canol trail for 125 km from the MacMillan Pass in the southwest to near the Keele River in the northeast (Figs. CS5-1, CS5-2). Figure CS5-3 presents the equivalent uranium (eU), equivalent thorium (eTh), potassium (K), ternary, eTh/K, eU/eTh, and residual magnetic total field maps for the Sekwi and Canol surveys along with a multivariable stacked profile for flight line 4074 from the Sekwi survey. The term 'equivalent' (or 'e') is used for reporting concentrations of uranium and thorium determined by gamma-ray spectrometry.

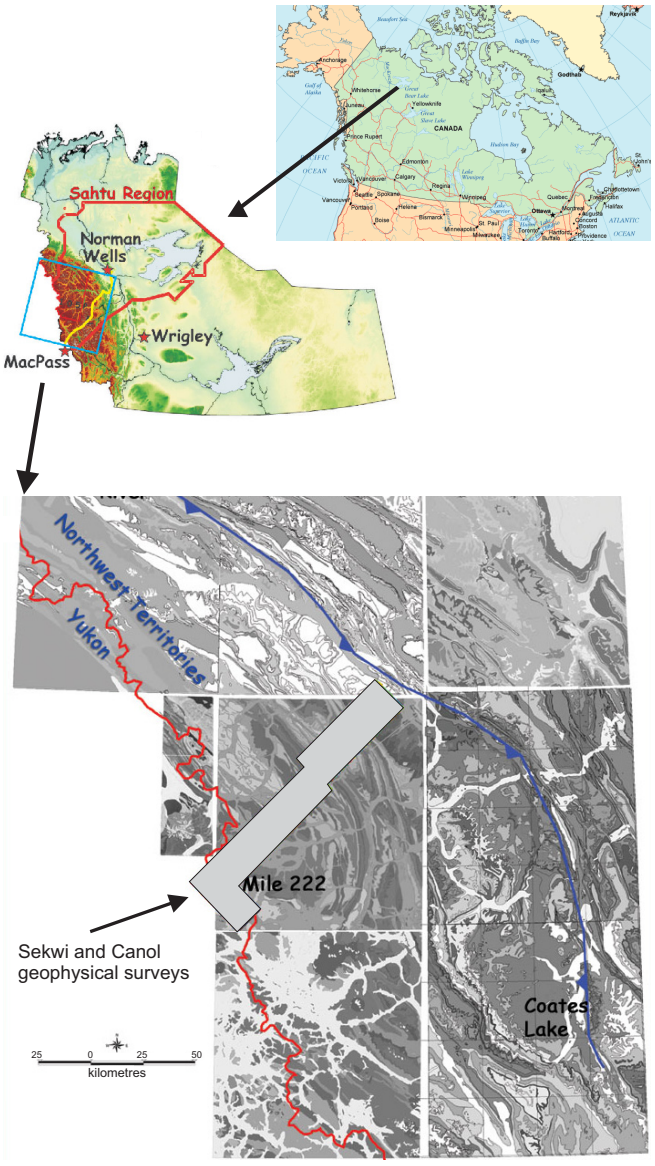

Figure CS5-1. Location of the Sekwi and Canol gamma-ray spectrometry and magnetic surveys.

Harris, J.R., Ford, K., Charbonneau, B., and Buckle, J., 2008, Application of gamma-ray spectrometer data for lithological mapping in a Cordilleran environment, Sekwi Region, Northwest Territories, Case Study *5 in* Remote Predictive Mapping: An Aid for Northern Mapping, (ed.) J. R. Harris; Geological Survey of Canada, Open File 5643, p. 203-223.

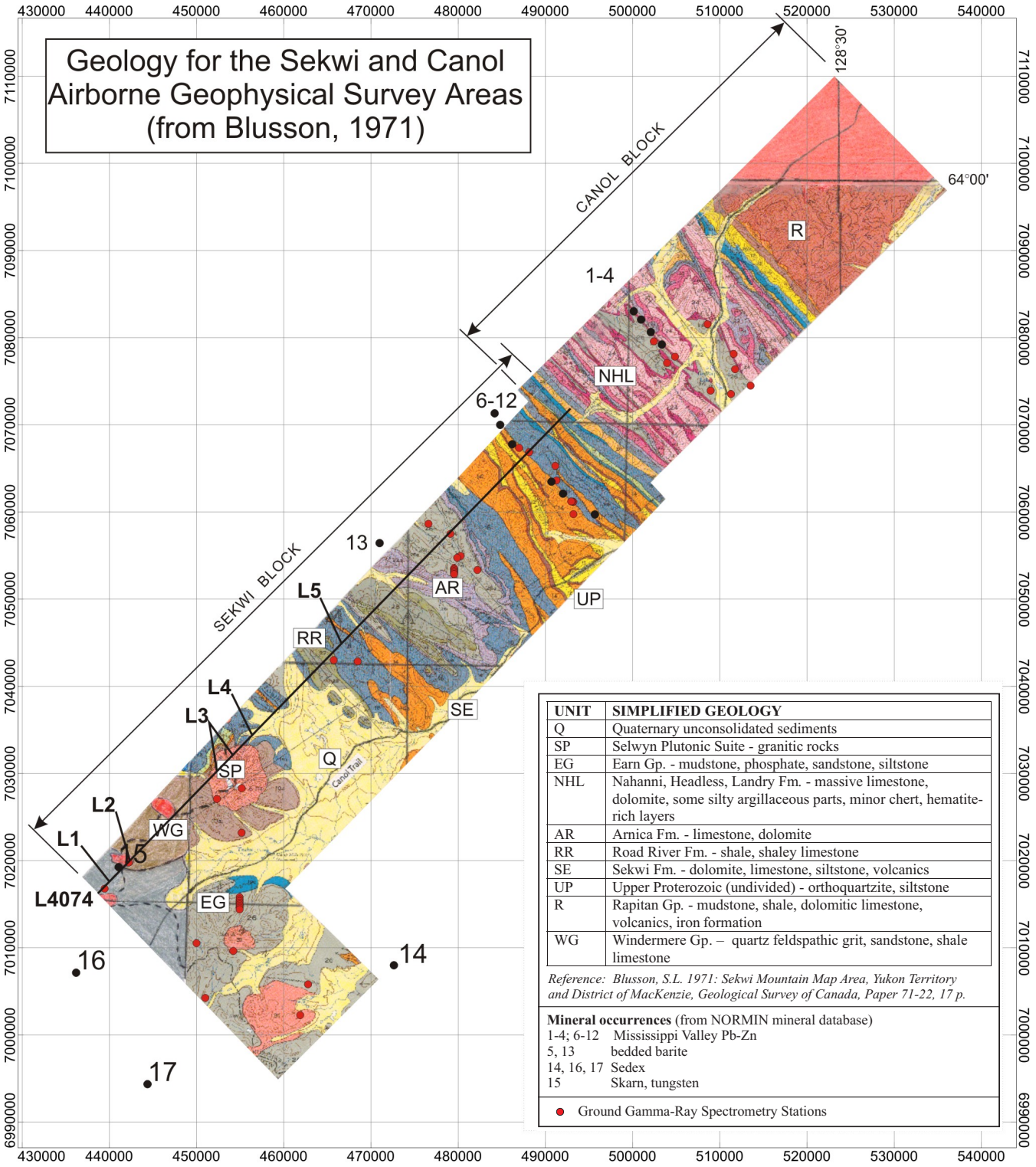

Figure CS5-2. Geology of the study area (after Blusson, 1971) showing the Sekwi and Canol airborne geophysical survey areas. Mineral occurrences are from the NORMIN mineral database.

One of the major concerns when interpreting the survey results is the rugged topography in this area. The survey area has a maximum variation of more than 1000 m. The fact that the survey was flown with a drape surface reduces the effect of the rugged terrain. A visual analysis of the data revealed that there is no persistent correlation of the radiometric patterns with topography. The survey has yielded reliable regional patterns when compared with the mapped geology, and terrain corrections should only be a concern in specific locations. A report by Charbonneau (2007) provides more detail on the gamma-ray data and the acquisition parameters.

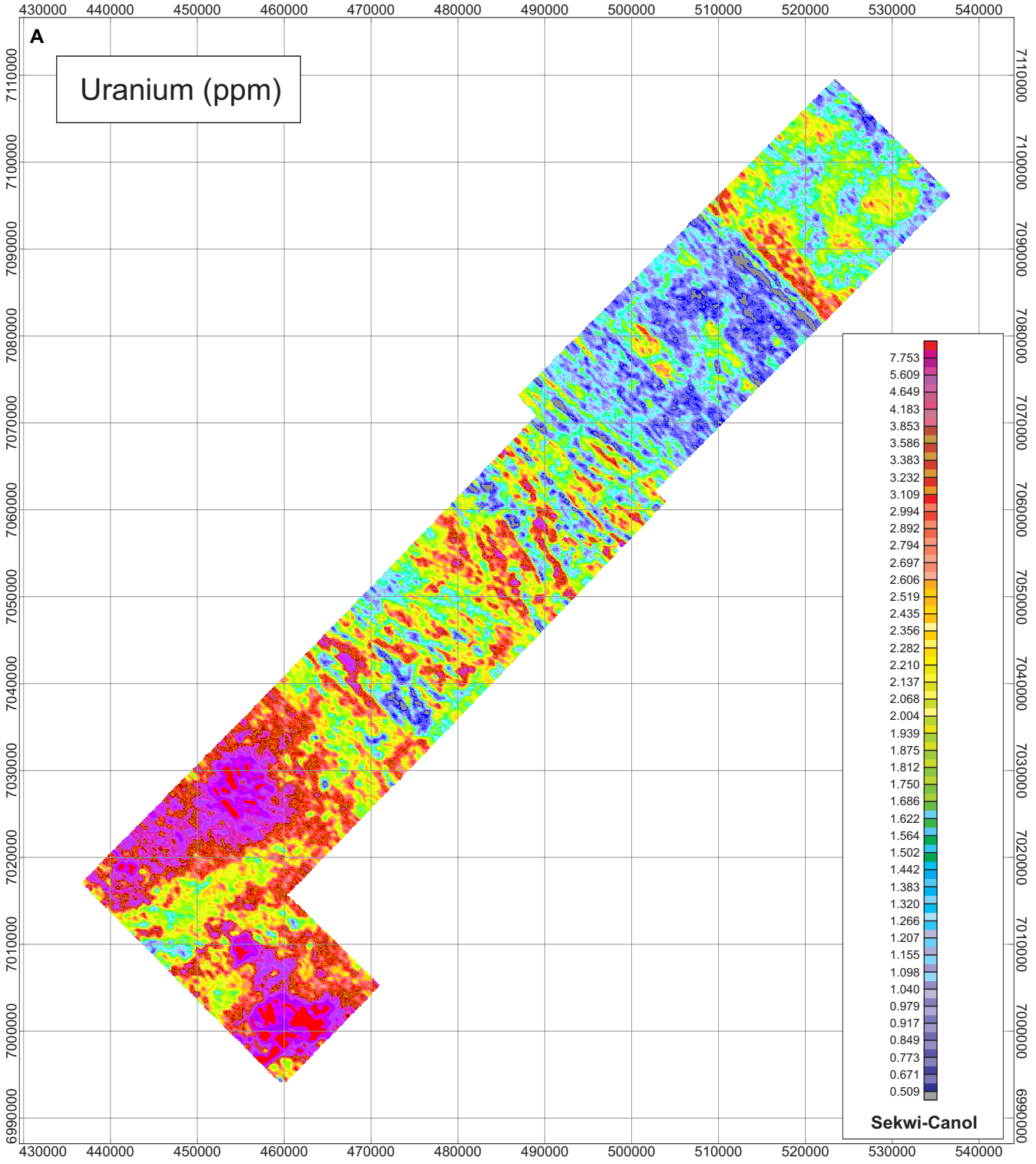

Figure CS5-3. Images of the gamma-ray spectrometry and residual magnetic total field data for the Sekwi and Canol airborne geophysical surveys. **(A)** Equivalent uranium (eU, ppm).

LANDSAT images were also used in this study; these were downloaded from the *Geogratis* website (www.geogratis.cgdi.gc.ca) and mosaiced using image processing software (ENVI™ and PCI™)(Fig. CS5-4).

Ground gamma-ray spectrometry (GGRS) measurements were collected in selected areas during the 2006 summer field season using an Exploranium GR320 gamma-ray spectrometer. These data were used to help validate interpretations made from the airborne gamma-ray data (AGRS) and assist in characterizing the radioelement signatures of the various lithologies.

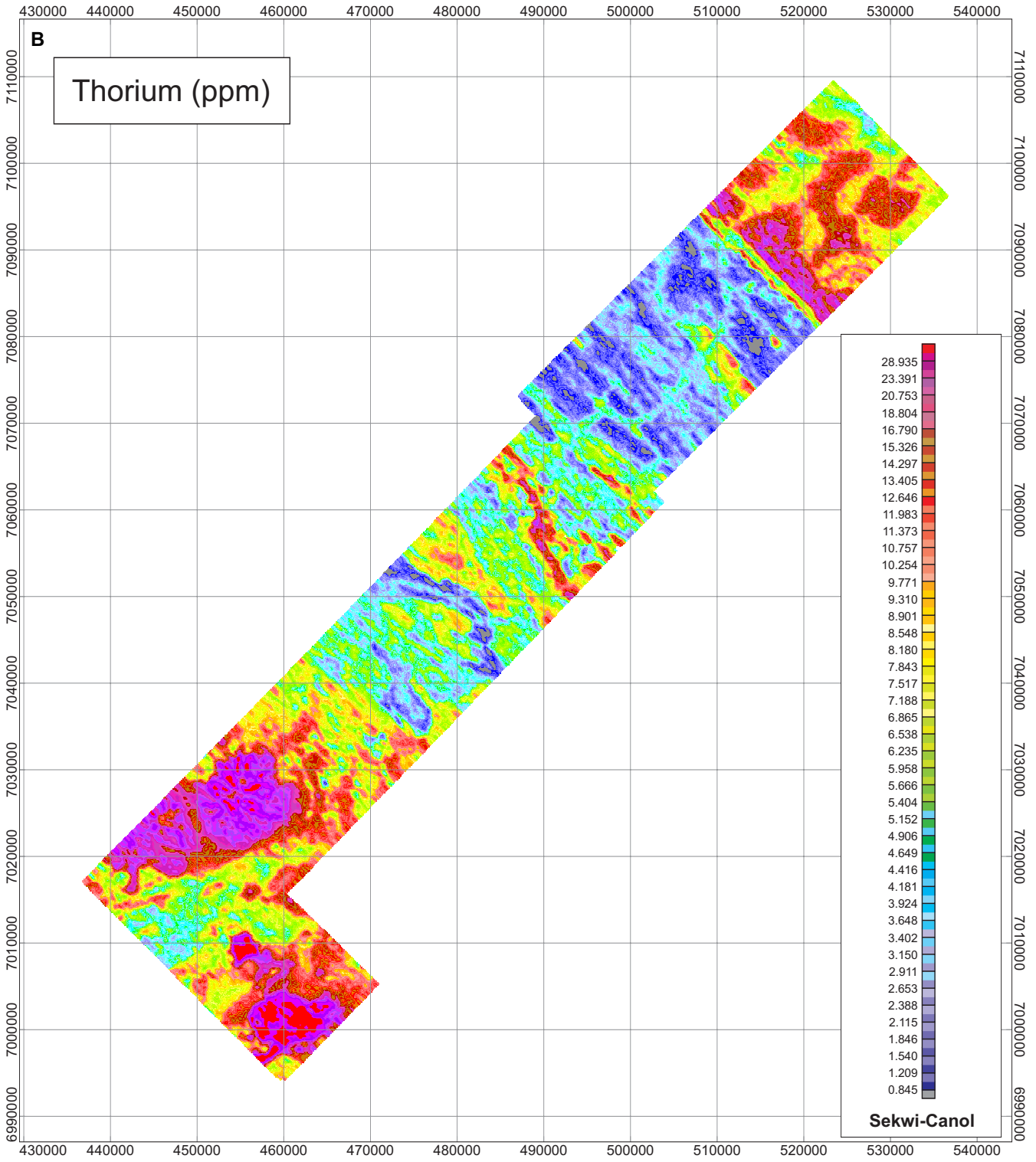

Figure CS5-3 continued. (B) Equivalent thorium (eTh, ppm).

DATA PROCESSING AND INTEGRATION

Both visual analysis and interpretation of the various data as well as computer-assisted techniques were employed to produce predictive maps. Supervised and unsupervised classification processes were used (see Chapter 4 of this volume). This involved identifying representative training areas of each generalized lithological unit, gathering statistics (radioelement signatures from the gamma-ray spectrometry data, spectral reflectance from the LANDSAT data, and residual magnetic total field) from each data type and then employing a maximum likelihood algorithm to produce a classified (predictive) map of lithological units. The predictive maps were validated using a cross-tabulation pro-

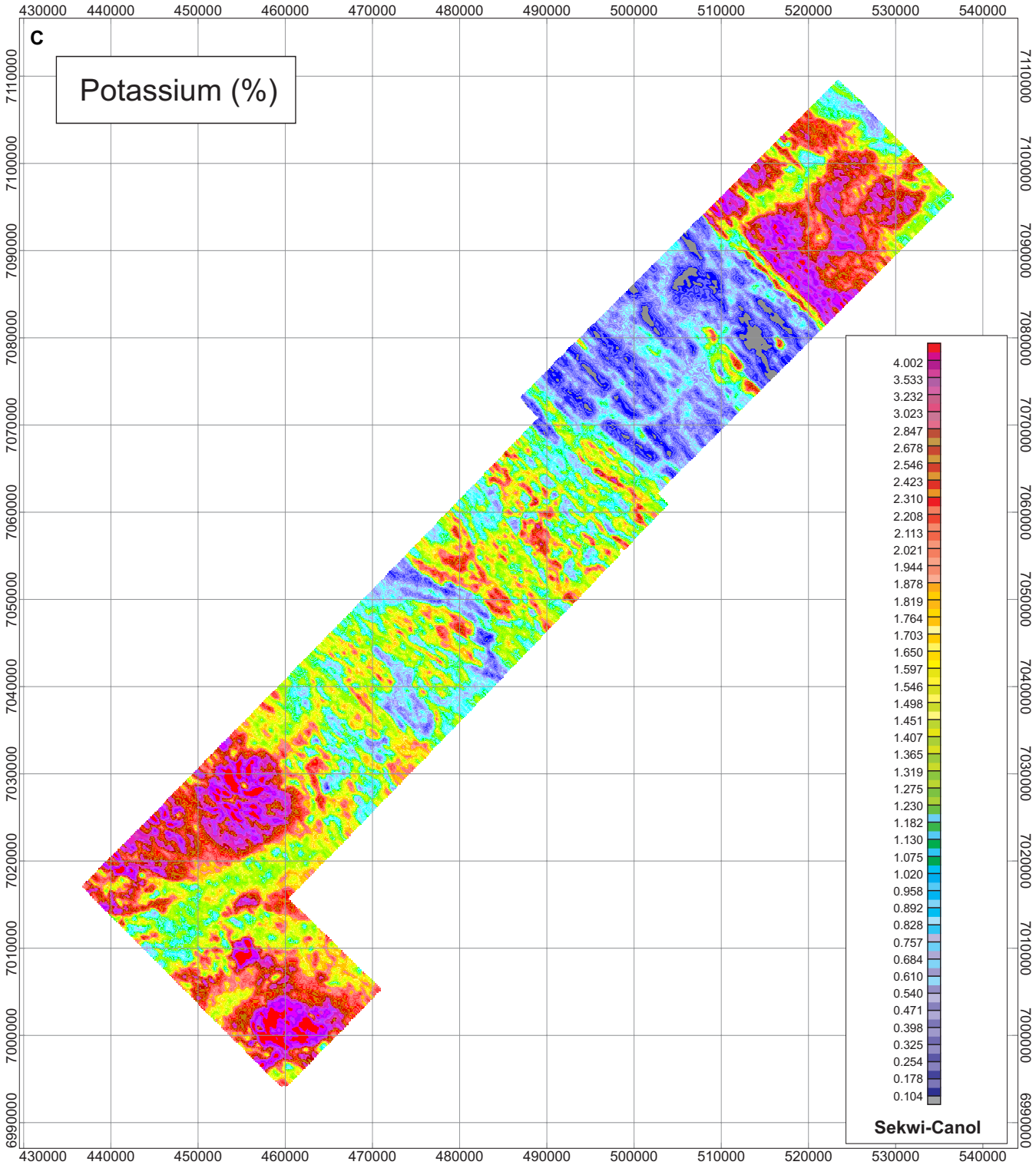

Figure CS5-3 continued. (C) Potassium (K, %).

cedure in which the classified map was compared to the original training areas as well as the mapped geology.

RESULTS

Analysis of Ground Measurements

Ground gamma-ray spectrometry (GGRS) measurements clearly indicate that granites and sedimentary rocks have distinctly different signatures (Fig. CS5-5). As would be expected, the granites are characterized by appreciably higher K, eU, and eTh concentrations than the sedimentary rocks. Scatterplots of the GGRS data that show different groupings related to different lithologies, are clearly evident (Fig. CS5-6). The high concentration of eU in some of the black shale units is

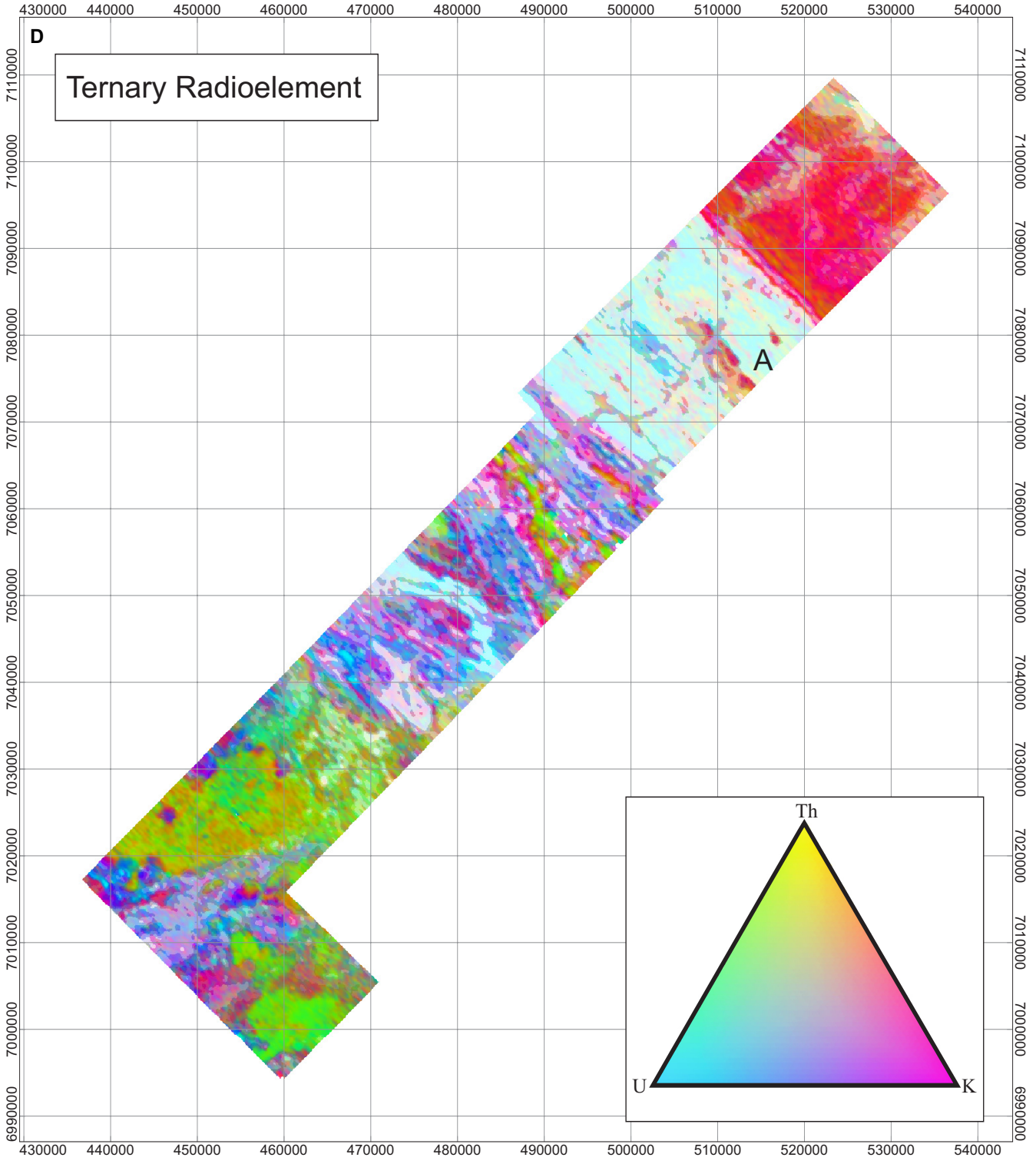

Figure CS5-3 continued. (D) Ternary radioelement image.

also evident (Fig. CS5-6A). These contrast markedly from other black shale units characterized by higher potassium concentrations. Sandstone and conglomerate units have low K and eU concentrations. Measurements on four of the Cretaceous plutons (Fig. CS5-2) show the highest radioelement concentrations, with the exception of eU, in some of the black shale units (Fig. CS5-6B). The small pluton located in close proximity to the MacTung deposit (Fig. CS5-2) is characterized by high eU/eTh ratio values compared with other intrusive rocks. This results in an abnormally high eU/eTh ratio value. Elsewhere (Ford and O'Reilly, 1985) similar radioelement signatures have

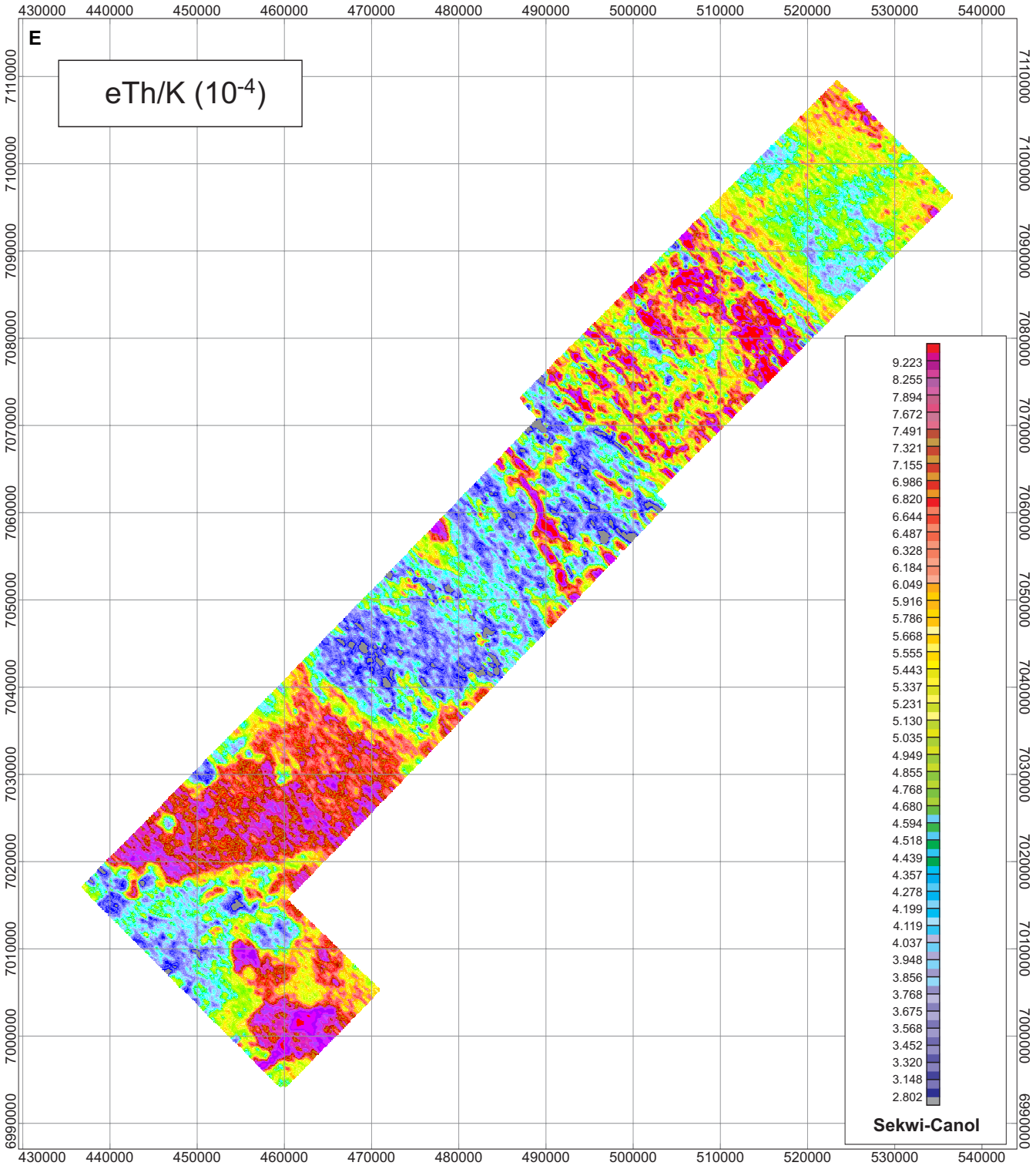

Figure CS5-3 continued. (E) eTh/K ratio.

exploration significance for granite-related mineralization (see Chapter 4 of this volume).

Automatic clustering (using a k-means algorithm) of the sample data can be invoked to look for natural groupings in the data (Fig. CS5-7). Six distinct clusters can be found in the radioelement data, with higher concentrations (shown in red) representing granitoid rocks. The geographic location of each sample that was classified can be plotted based on the cluster number and lithological attribute from the field database (Fig. CS5-5D). This matches well with the mapped geology and in some cases provides divisions within mapped units (compare Figs CS5-5D and CS5-2).

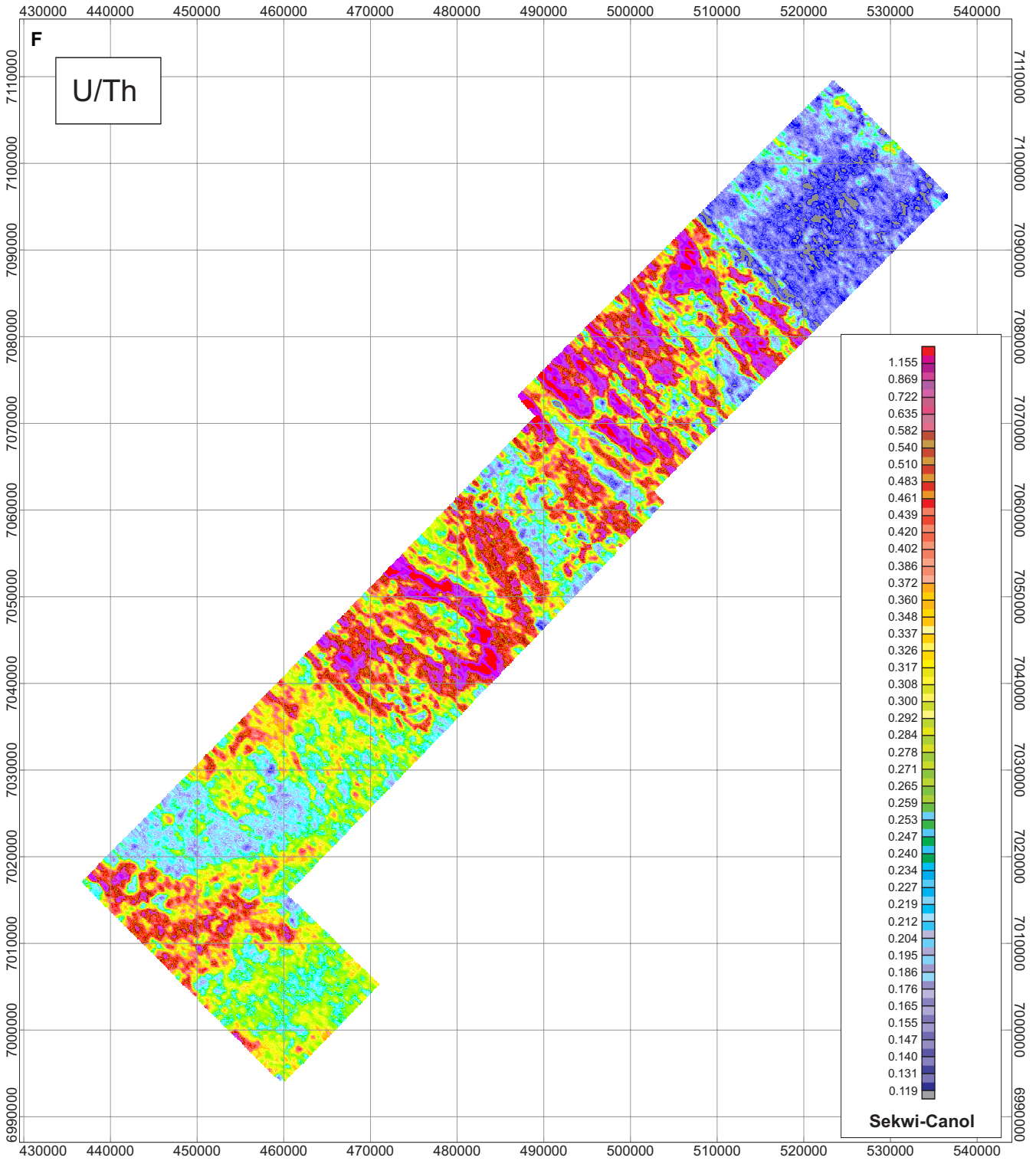

Figure CS5-3 continued. (F) eU/eTh ratio.

Airborne versus Ground Measurements

The radioelement signatures derived from GGRS measurements show a moderate to strong correlation with the AGRS signatures sampled at the same geographic locations as the GGRS measurement sites (Fig. CS5-8A,B,C). Strong correlations exist between eTh (0.96) and moderately strong correlations between K (0.79) and eU (0.73) for the GGRS and AGRS measurements. Based on the lithology recorded in the field at each GGRS location, the AGRS data also shows significant variations (Fig. CS5-8D,E,F), although sample size is very small for some lithologies and thus the results are not statistically robust.

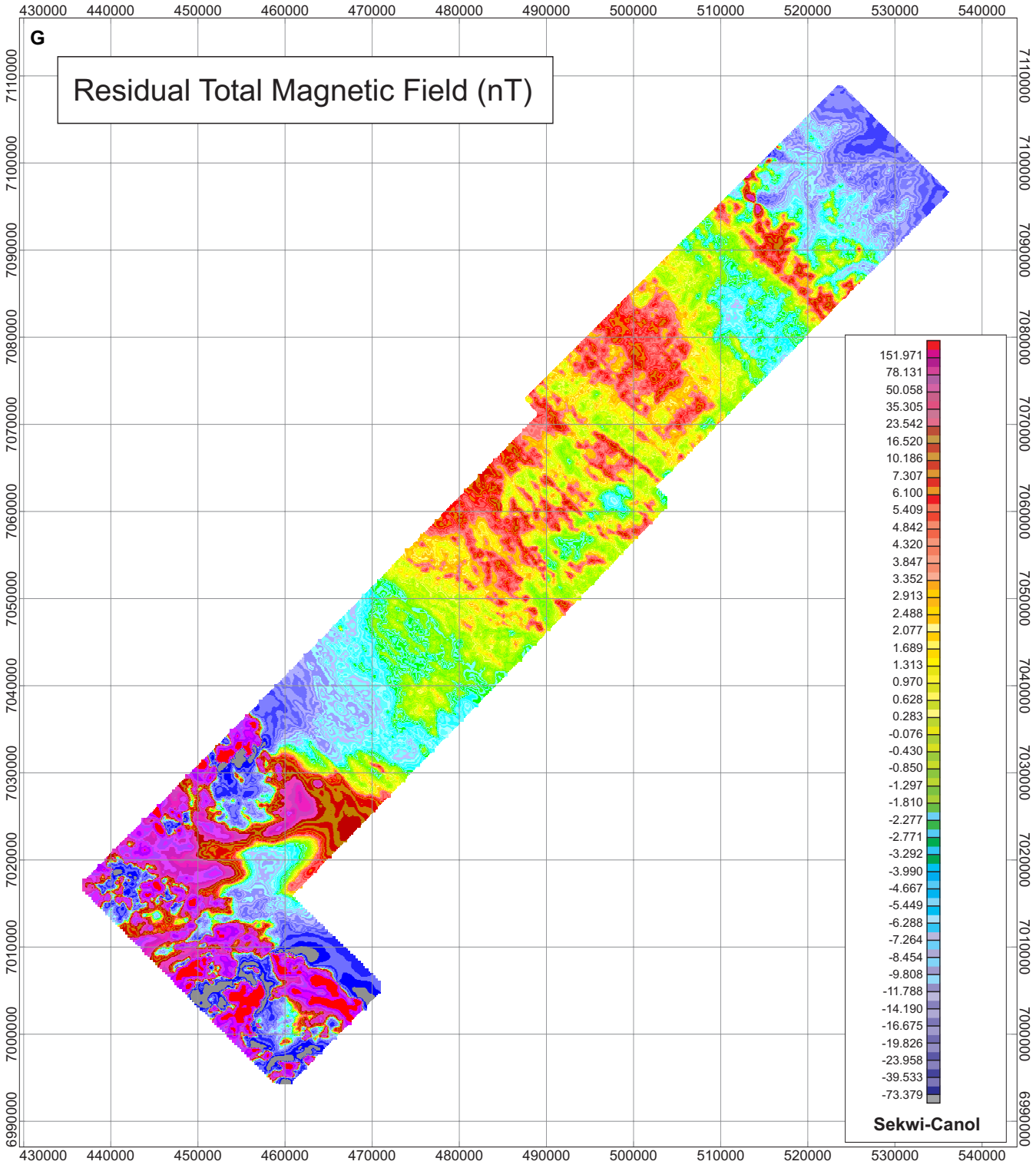

Figure CS5-3 continued. (G) Residual magnetic total field.

Analysis of Airborne Gamma-Ray Data

Visual

There is a general perception that because of higher radioactive element concentrations and contrasts that AGRS surveys are more suited to mapping granitic and gneissic dominated terrains, those large 'sea of pink' areas on regional-scale geological compilations. However, recent results from the McKenzie Mountains illustrate that AGRS surveys are equally suitable in sedimentary-dominated terrains. The Sekwi Mountain survey (Fig. CS5-3A-F) covers Neoproterozoic to late Devonian sedimentary rocks that are intruded by

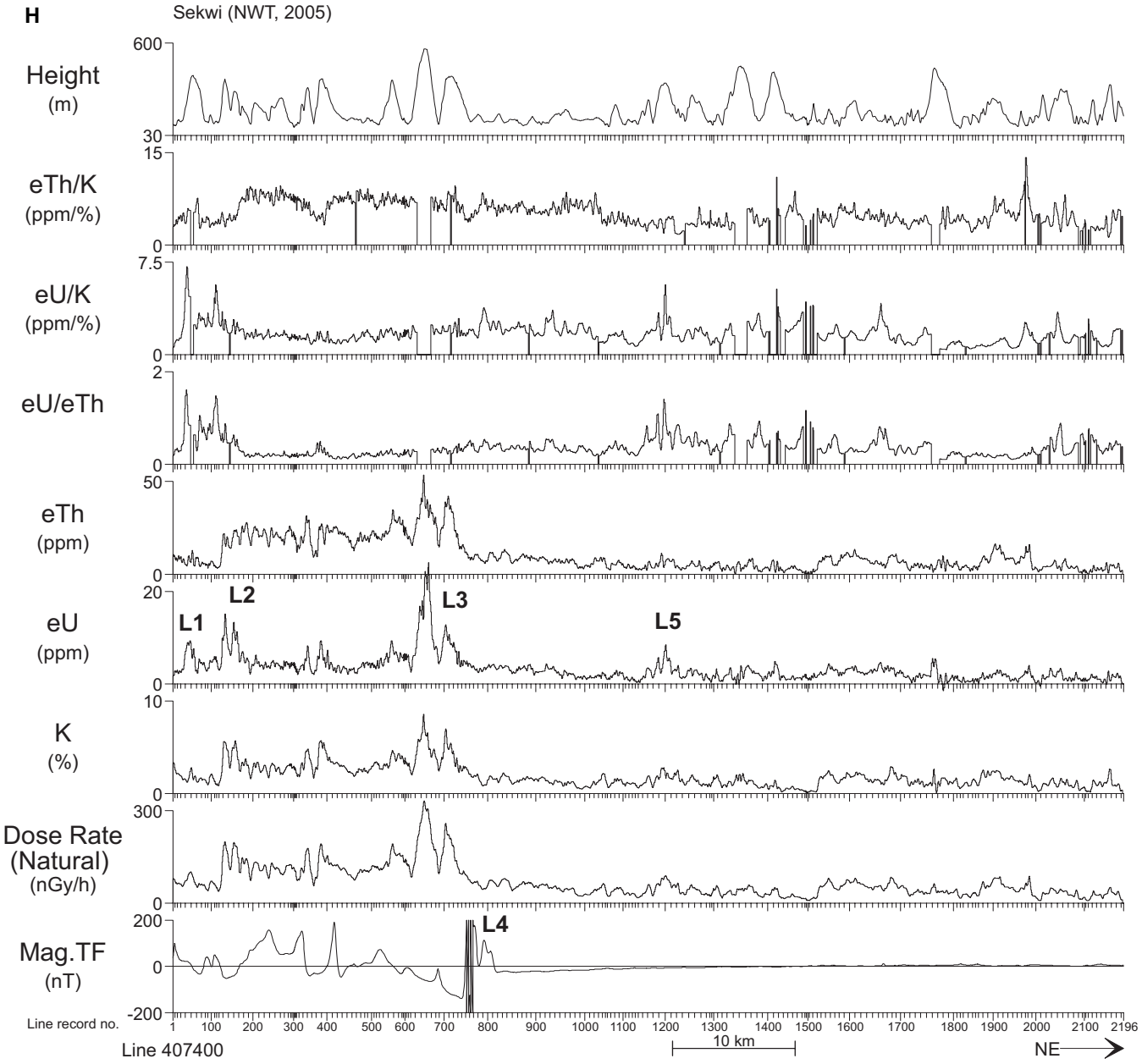

Figure CS5-3 continued. (H) Multivariable stacked profile for flight line 4074 from the Sekwi airborne geophysical survey (Carson et al., 2006) (see Fig.CS5-2 for location). A number of anomalous features include: L1 - high eU and eU/eTh ratios associated with black shales south of the Mactung W deposit; L2 - a high eU and eU/eTh ratio and low magnetic signature associated with the small Cretaceous pluton located just north of the Mactung W deposit; L3 - the high K, eU, and eTh, and low magnetic signature of the larger Cretaceous pluton; L4 - a prominent magnetic anomaly in slates adjacent to the pluton; and L5 - a high eU and eU/eTh anomaly adjacent to a low eTh/K ratio anomaly in the Road River Formation.

Cretaceous plutons in the southwestern part of the survey area. The geology of the survey area is shown in Figure CS5-2 (Blusson, 1971). The main geological elements of the survey area, from northeast to southwest, are 1) an area of flat-lying to gently dipping Proterozoic clastic units of the Rapitan Group, 2) a folded and faulted belt of predominantly Paleozoic carbonate rocks, and 3) a belt of mostly Paleozoic shale units. Towards the southwest, small Cretaceous plutons intrude Upper Proterozoic to Mississippian shales and slates.

A close visual inspection of the AGRS patterns (Fig. CS5-3A-F) shows a strong correlation with mapped geology. The range of natural air absorbed dose rate or total radioactivity levels are as would be expected for the lithologies within the survey area. Limestones and dolostones (NHL, Fig. CS5-2) have very low NADR (air-absorbed dose rate (nG y/h) or total radiation), K, eU, and eTh levels, whereas shales and siltstones (EG and RR, Fig. CS5-2) have substantially higher levels. These shale- and siltstone-dominated units also exhibit a wide range of K, eU, and eTh levels. These variable shale sig-

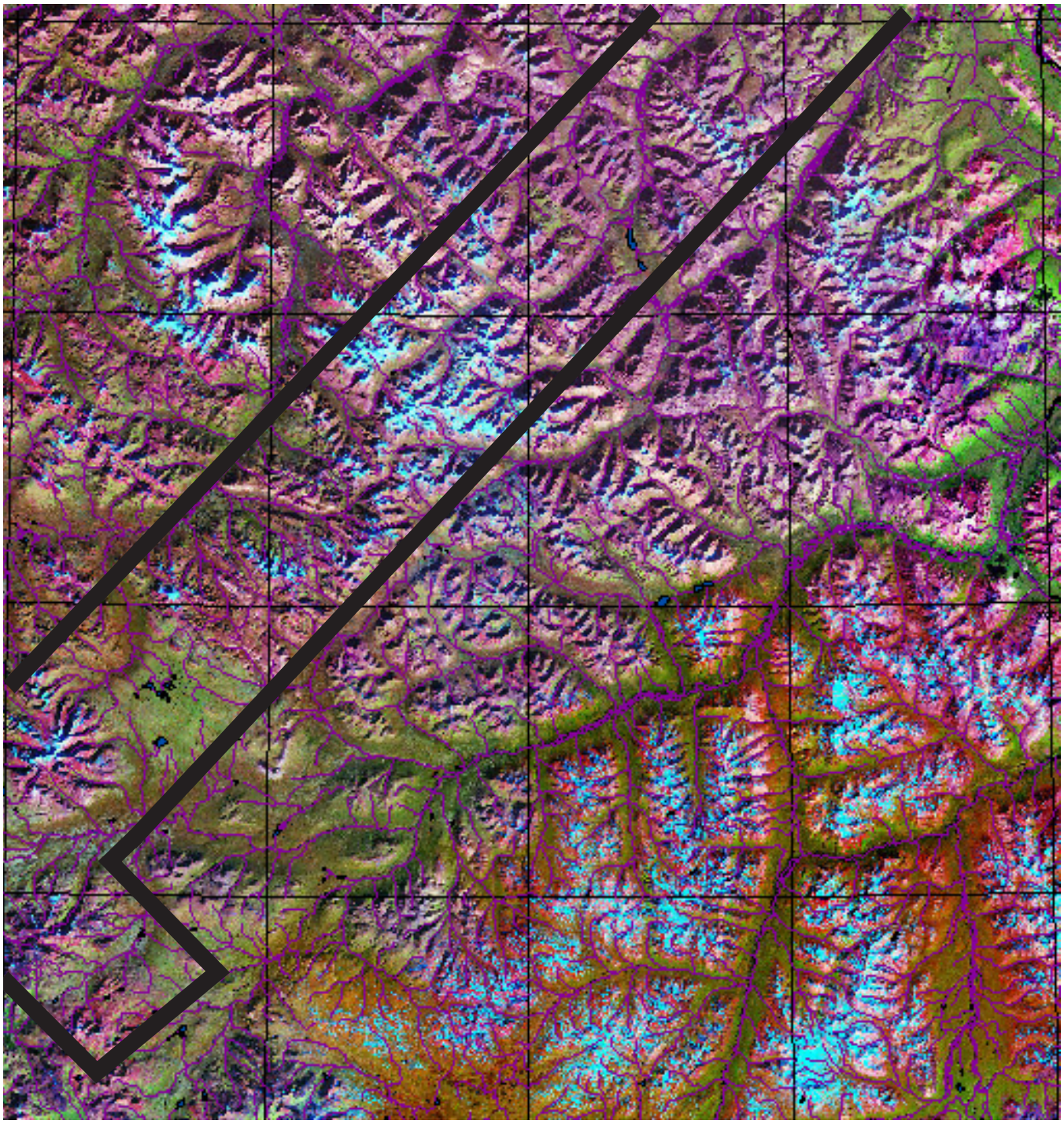

Figure CS5-4. LANDSAT data (bands 5,4,3 – red, green, blue, respectively). The location of the airborne geophysical survey is shown as a black rectangle (see Fig. CS5-1 for scale).

natures are best illustrated on the ternary radioelement map (Fig. CS5-3D in the northeast half of the Sekwi block and the central part of the Canol block, around Godlin Lakes (Area A on Fig. CS5-3D)). In contrast to the very low NADR, K, eU, and eTh levels exhibited by the carbonate units, substantial portions of the Rapitan Group (R, Fig. CS5-2), the Windermere Group (WG), an undivided Upper Proterozoic unit (UP), and Cretaceous plutons of the Selwyn plutonic suite (SP) exhibit the highest levels of NADR, K, eU and eTh.

Cretaceous intrusive rocks of the Selwyn plutonic suite occupy six bodies in the southwestern part of the survey area (Fig. CS5-2). The three larger plutons are characterized by high NADR, K, eU, and eTh signatures. Equivalent thorium levels for the three smaller plutons are much lower, resulting in elevated eU/eTh

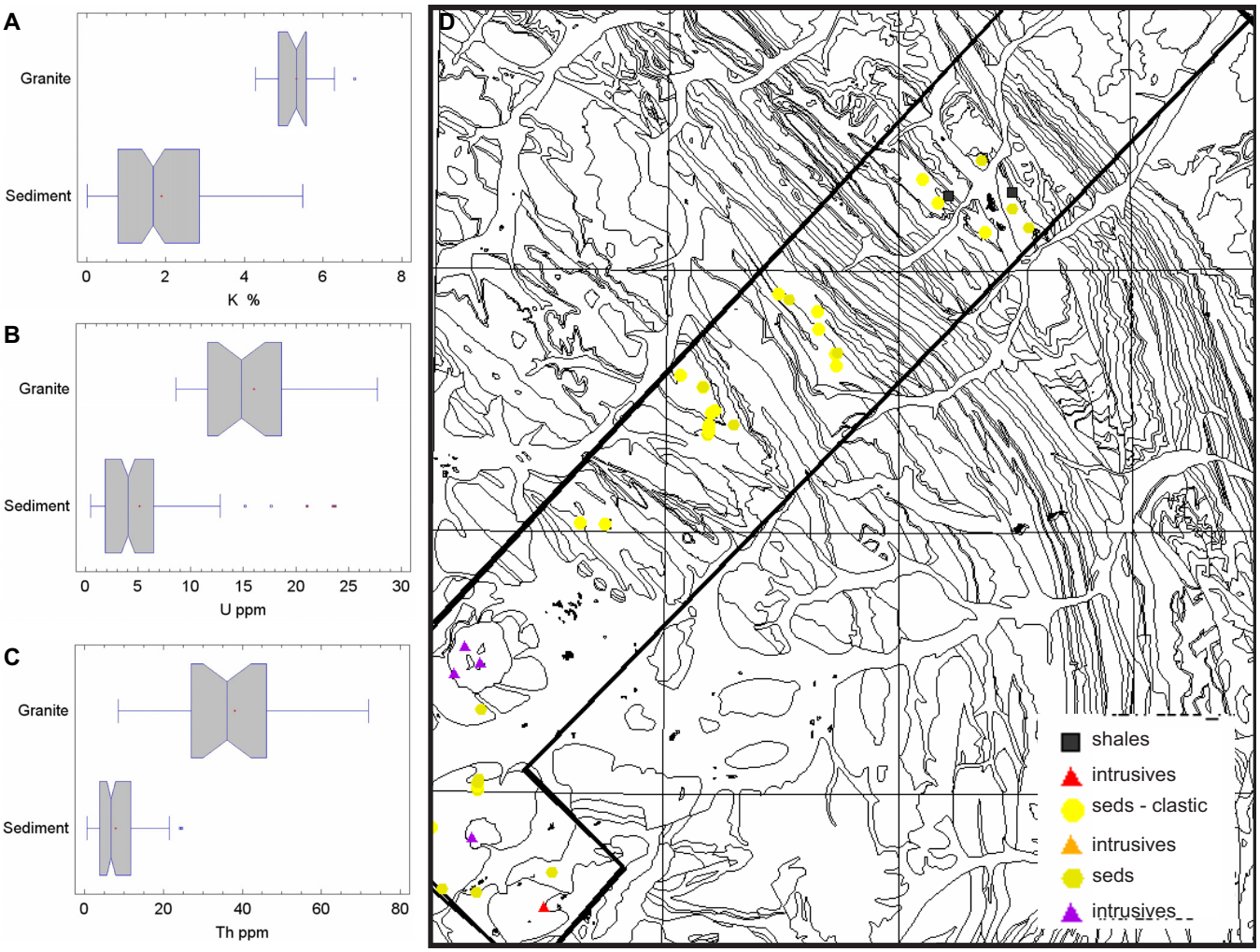

Figure CS5-5. Analysis of ground gamma-ray spectrometry (GGRS) measurements. **(A)** Box and whisker plot (K) for granites and sediments. **(B)** Box and whisker plot (eU) for granites and sediments. **(C)** Box and whisker plot (eTh) for granites and sediments. **(D)** Plot of sample locations, classified by lithology. Based on the radioelement signature (sediments versus clastic sediments and shale), the classification of the field data divisions within mapped units are apparent.

ratio values. Figure CS5-3H shows the multivariable stacked profile for flight line 4074 located on Figure CS5-2. A number of anomalous features are indicated; these include 1) high eU and eU/eTh ratio associated with black shales south of the Mactung W deposit, 2) high eU and eU/eTh ratio and low magnetic signature associated with the small Cretaceous pluton located just north of the Mactung W deposit, 3) the high K, eU, and eTh and low magnetic signature of the larger Cretaceous pluton, 4) a prominent magnetic anomaly in slates adjacent to the pluton, and 5) a high eU and eU/eTh ratio adjacent to a low eTh/K ratio in the Road River Formation. Elsewhere high eU/eTh ratio anomalies have been associated with W skarn mineralization, especially if associated plutonic rocks have low magnetic characteristics (Yeates et al., 1982). Low eTh/K ratios have been described as an excellent indicator of potassium enrichment associated with alteration related to mineralization (Shives et al., 1995, 1997, 2000). Charbonneau (2007) notes that high eU and eU/eTh ratios with adjacent low eTh/K ratios, similar to those shown in Figure CS5-3E, would be likely associated with Sedex-style Pb-Zn mineralization similar to Howards Pass.

Computer-Assisted (Supervised) Classification

Two different strategies were employed in the selection of training sites with which to base supervised classification (see Fig. 2 in Chapter 2 for description of supervised classification). The first approach involved generalizing the geology map (Fig. CS5-2) into major units (see Fig CS5-9A). Training sites for each generalized unit were then selected (Fig. CS5-9B) based on analysis of the AGRS signature in various gamma-ray images (see Fig. CS5-3). Thus, the lithological code for the training sites is based on the geological map. The second approach involved creating training areas based on the GGRS measurement sites (Fig. CS5-5B) and expanding each training area based on the signature from the gamma-ray data. In this approach, the litho-

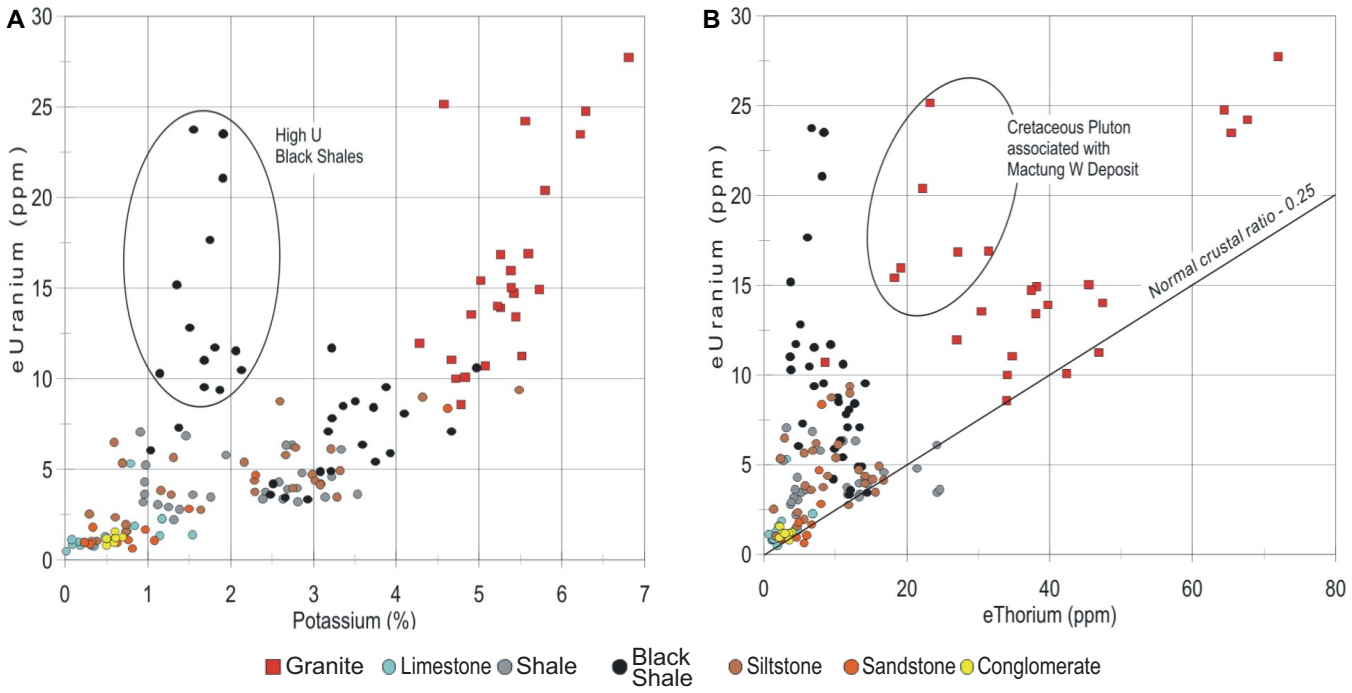

Figure CS5-6. Scatterplots showing statistical distribution of ground gamma-ray spectrometry measurements colour-coded by lithology. **(A)** eU versus potassium. Note the distribution of black shales (high eU) and granitoid rocks, which are high in both K and eU. Limestone, siltstone, and shale have a much lower response. **(B)** eU versus eTh. Note the high eU/eTh ratio for the pluton associated with MacTung deposit and also the high ratio values for some of the black shale.

logical code is based on what was noted in the field. Once the statistics (i.e. gamma-ray signature) for the training areas were calculated the next step was to assess the statistical separation of each to determine whether classification would even be an option. If the classes (i.e. various lithologies) are not separable, then classification would be pointless. Many methods are available to assess statistical separability, such as simple visual methods such as box and whisker plots (Fig. CS5-8), basic statistical tests (i.e. t-tests for means), or measures that consider the distance between classes in N-dimensional scatterplots (i.e. transformed divergence (TD)). Figure CS5-10 shows a transformed divergence plot for each training class derived using approach 1 (discussed above) for the LANDSAT, gamma-ray and magnetic data. A similar plot was con-

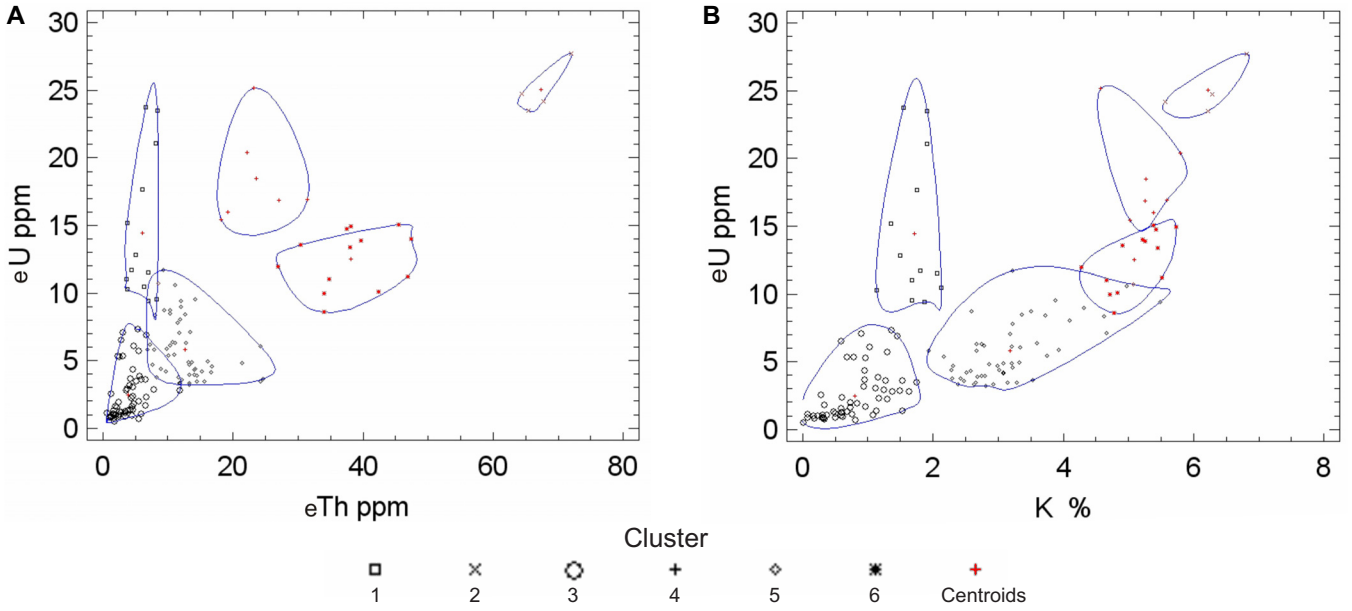

Figure CS5-7. Results of automatic clustering of ground gamma-ray spectrometry measurements with respect to radioelement response. **(A)** eU versus eTh. **(B)** eU versus K. Six naturally occurring clusters can be found in the data. Granite samples are shown in red and sedimentary samples are shown in black.

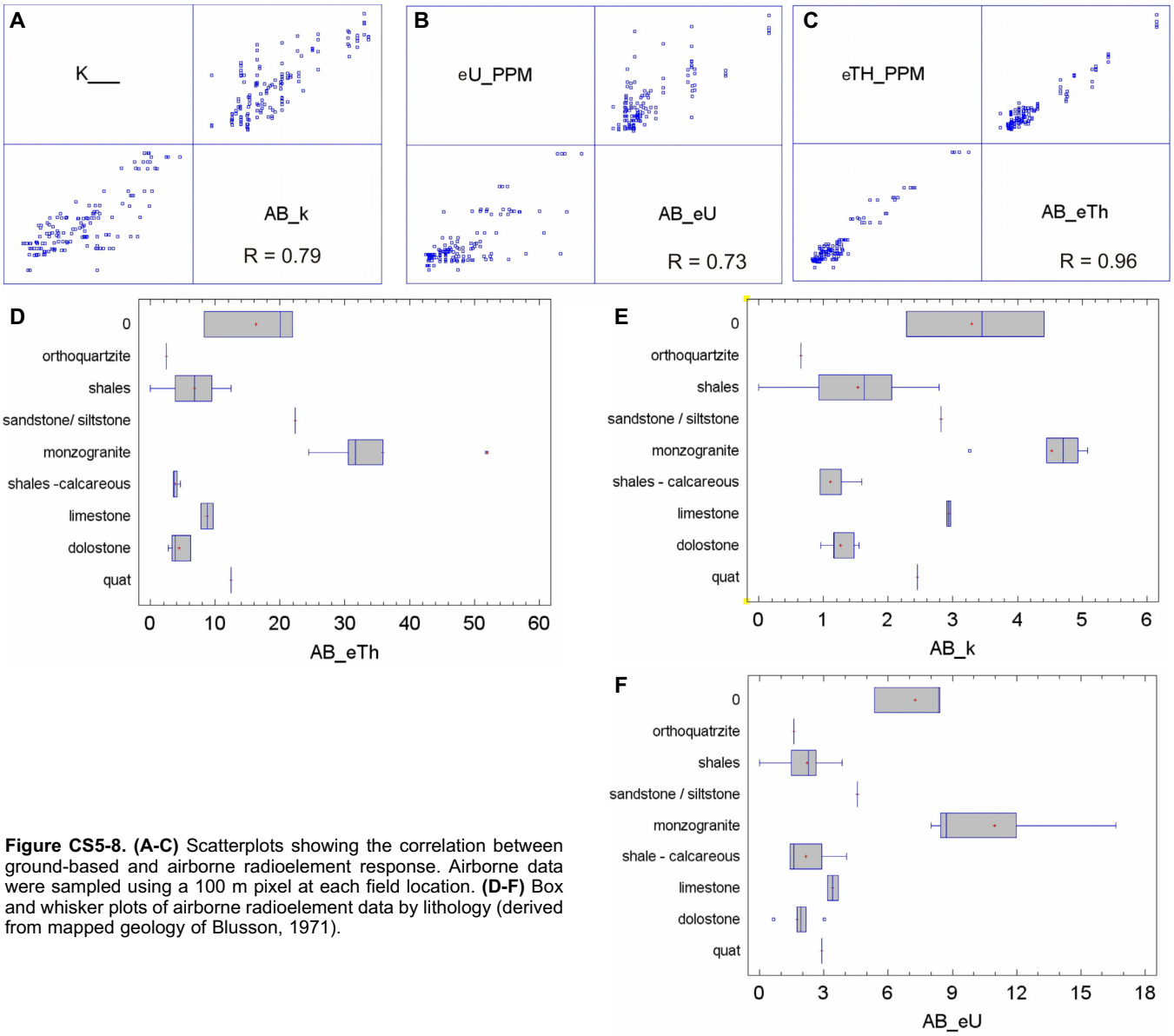

Figure CS5-8. (A-C) Scatterplots showing the correlation between ground-based and airborne radioelement response. Airborne data were sampled using a 100 m pixel at each field location. **(D-F)** Box and whisker plots of airborne radioelement data by lithology (derived from mapped geology of Blusson, 1971).

structed based on approach 2 (not shown). Values of approximately 1.9 or greater indicate good statistical separation between classes (in this case mapped lithology), whereas values between 1 and 1.9 indicate moderate separation, and values less than 1 indicate very poor separation (Richards and Xia, 2006).The TD plot clearly indicates that for most major lithological units, the gamma-ray data based on AGRS signatures offer better separation than does the LANDSAT data based on spectral response. This will not be the case in all geological terranes; however, in this fairly young terrane characterized primarily by well exposed sedimentary rocks and granitic intrusions, the gamma-ray response is superior to spectral response for separating lithology. The gamma-ray data offer better separation than the LANDSAT data for all units, with the exception of dolomites. Addition of the radioelement ratio data provides even better separation of all units, especially the limestones. Addition of the magnetic data does not provide better separation than that provided by the gamma-ray data (measured (K, eU, and eTh) and derived (ratios)). The TD results were very similar, based on approach 2 for defining training areas.

The statistical separation, offered particularly by the gamma-ray data, indicates that reasonable results can be expected from supervised classification. Figure CS5-11A is a classification of just the LANDSAT data based on the training areas derived from approach 1. Areas of vegetation, clouds, and cloud shadows were masked and not considered in the classification exercise. Figure CS5-11B shows the results of applying a maximum likelihood algorithm to just the measured AGRS data (K, eU, and eTh), Figure CS5-11C to the measured and derived (ratios) gamma-ray data, and Figure CS5-11D to all data including the residual magnetic total field data. Figure CS5-12A shows the same

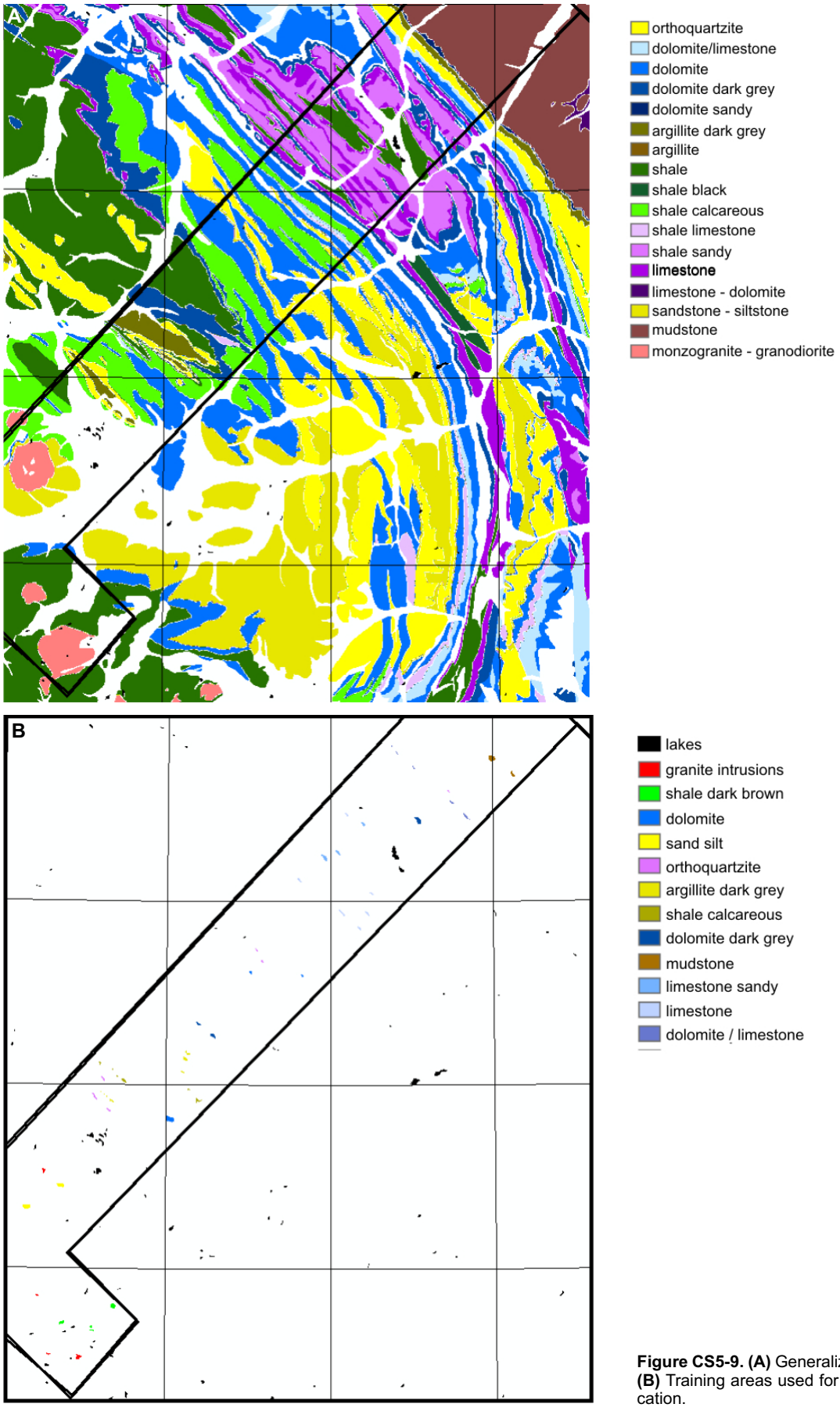

Figure CS5-9. (A) Generalized geology (Blusson, 1971). **(B)** Training areas used for maximum likelihood classification.

Table CS5-1. Classification accuracies. The numbers in brackets in Table CS5-1 represent the accuracies using approach 2 (field locations, see Fig. CS5-5D), whereas the other number represents the accuracy using approach 1 (map based, see Fig. CS5-9B).

Data	Accuracy	Kappa coeffients
LANDSAT – all bands except thermal (just over outcrop)	67% (72%)	0.63 (0.67)
Gamma ray – eU, eTh, %K	83% (87.4)	0.8 (0.85)
Gamma ray – eU, eTh, %K, ratios	89% (89%)	0.88 (0.88)
All gamma ray and total field	93% (87.8%)	0.92 (0.86)
Gamma ray, magnetic, LANDSAT	97% (92%)	0.97 (0.91)

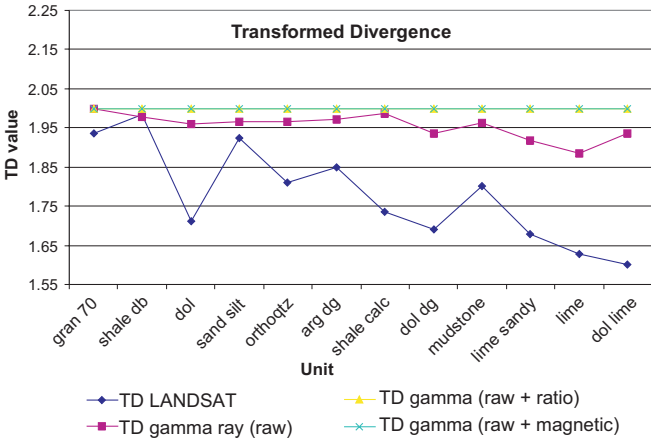

Figure CS5-10. Transformed divergence (TD) plot (Richards and Xia, 2006) for various lithologies based on the generalized map shown in Figure CS5-2.

Table CS5-2. Confusion matrices, which are commonly used to evaluate the accuracy of a classification of remotely sensed data. Table CS5-2A shows pixel numbers whereas Table CS5-2B shows percentages. The ground truth pixels (training areas) are listed horizontally and the classification results of the training pixels are listed vertically. Often the accuracy is measured by comparing the classification to the training areas used to produce the classification, but more commonly a set of check training areas are used for comparison purposes. The classification can also be compared directly to a pre-existing map. The training areas can be from field observations (stations) of a given class type or from analysis of the remotely sensed imagery in concert with ancillary information (air photos, maps, etc.).

Table CS5-2A

Class	G	Sh	D	Sd	Oqtz	Arg dg	Sh clc	D dg	Md	L s	L	D l	Total
G	**944**	0	0	0	14	0	0	0	0	0	0	0	958
Sh	16	**1059**	0	0	0	1	0	0	0	0	0	0	1076
D	0	0	**1026**	0	56	23	40	0	0	19	0	18	1182
Sd	52	0	0	**1314**	28	0	0	0	0	0	0	0	1394
Oqtz	0	0	14	0	**371**	11	0	0	0	0	26	22	444
Arg dg	0	0	29	0	187	**725**	29	0	0	0	0	0	970
Sh calc	0	0	86	0	230	31	**765**	19	0	0	0	3	1134
D dg	0	0	0	0	0	0	0	**1168**	0	0	21	0	1189
Md	0	0	0	0	0	0	0	0	**1117**	0	0	14	1131
L s	0	0	32	0	0	0	0	0	0	**1109**	83	0	1224
L	0	0	0	0	0	0	0	52	0	26	**901**	0	979
D l	0	0	78	0	54	0	0	0	45	0	0	**587**	764
Total	1012	1059	1265	1314	940	791	834	1239	1162	1154	1031	644	12445

Table CS5-2B

Class	G	Sh	D	Sd	Oqtz	Arg dg	Sh clc	D dg	Md	L s	L	D l	Total
G	**93.2**	0	0	0	1.4	0	0	0	0	0	0	0	7.7
Sh	1.5	**100**	0	0	0	0.1	0	0	0	0	0	0	8.6
D	0	0	**81.1**	0	5.9	2.9	4.8	0	0	1.6	0	2.8	9.5
Sd	5.1	0	0	**100**	2.9	0	0	0	0	0	0	0	11.2
Oqtz	0	0	1.1	0	**39.4**	1.3	0	0	0	0	2.5	3.4	3.5
Arg dg	0	0	2.2	0	19.8	**91.6**	3.4	0	0	0	0	0	7.7
Sh calc	0	0	6.8	0	24.4	3.9	**91.7**	1.5	0	0	0	0.4	9.1
D dg	0	0	0	0	0	0	0	**94.2**	0	0	2	0	9.5
Md	0	0	0	0	0	0	0	0	**96.1**	0	0	2.1	9
L s	0	0	2.5	0	0	0	0	0	0	**96.1**	8	0	9.8
L	0	0	0	0	0	0	0	4.2	0	2.2	**87.3**	0	7.8
D l	0	0	6.1	0	5.7	0	0	0	3.8	0	0	**91.1**	6.1
Total	100	100	100	100	100	100	100	100	100	100	100	100	100

Overall Accuracy = (11086/12445) – 89.08%; Kappa Coefficient = 0.8806

Table CS5-2C

Class	Commission (%)	Omission (%)	Commission (pixels)	Omission (pixels)
G	1.46	6.72	14/958	68/1012
Sh	1.58	0	17/1076	0/1059
D	13.2	18.89	156/1182	239/1265
Sd	5.74	0	80/1394	0/1314
Oqtz	16.44	60.53	73/444	569/940
Arg dg	25.26	8.34	245/970	66/791
Sh calc	32.54	8.27	369/1134	69/834
D dg	1.77	5.73	21/1189	71/1239
Md	1.24	3.87	14/1131	45/1162
L s	9.4	3.9	115/1224	45/1154
L	7.97	12.61	78/979	130/1031
D l	23.17	8.85	177/764	57/644

Table CS5-2D

Class	Product Accuracy (%)	User Accuracy (%)	Product Accuracy (pixels)	User Accuracy (pixels)
G	93.28	98.54	944/1012	944/958
Sh	100	98.42	1059/1059	1059/1076
D	81.11	86.8	1026/1265	1026/1182
Sd	100	94.26	1314/1314	1314/1394
Oqtz	39.47	83.56	371/940	371/444
Arg dg	91.66	74.74	725/791	725/970
Sh calc	91.73	67.46	765/834	765/1134
D dg	94.27	98.23	1168/1239	1168/1189
Md	96.13	98.76	1117/1162	1117/1131
L s	96.1	90.6	1109/1154	1109/1224
L	87.39	92.03	901/1031	901/979
D l	91.15	76.83	587/644	587/764

The overall accuracy of the classification is simply derived from summing the diagonal of the matrix in (A) and dividing by the total number of pixels:

(944 + 1059 + 1026 + 1314 + 371 + 725 + 765 + 1168 + 1117 + 1109 + 901 + 587) / 12445 = 89.08%

The kappa coefficient (k) provides a measure of overall agreement between the training areas and classification. Statistically k is a measure of the difference between the actual agreement between training data and the classification, and the chance agreement between the training data and a randomly classified map as defined below:

$$k = \frac{\Pr(a) - \Pr(e)}{1 - \Pr(e)}$$

where

$\Pr(a)$ is the observed agreement

$\Pr(e)$ is the chance agreement

This is calculated from the confusion matrix using

$$k = \frac{N\sum_{i=1}^{r} x_{ii} - \sum_{i=1}^{r} (x_{i+} * x_{+i})}{N^2 - \sum_{i=1}^{r} (x_{i+} * x_{+i})}$$

where

r = number of rows in confusion matrix

N = total number of observations included in the matrix

x_{ii} = the number of observations in row i and column j (on the major diagonal)

x_{i+} = total of observations in row i (shown as marginal total to right of the matrix)

(after Lillesand and Kieffer, 2000)

To illustrate this calculation using Table CS5-2A:

$\sum_{i=1}^{r} x_{ii}$ = (944 + 1059 + 1026 + 1314 + 371 + 725 + 765 + 1168 + 1117 + 1109 + 901 + 587) = 11086

$\sum_{i=1}^{r} (X_{i+} * X_{+i})$ = (958 * 944) + (1076 * 1059) + (1182 * 1265) + (1349 * 1314) + (444 * 940) + (970 * 791) + (1134 * 834) + (1189 * 1239) + (1131 * 1162) + (1224 * 1154) + (979 * 1031) + (764 *664) = 13267566

$$k = \frac{12445(11086) - 13267566}{(12445)^2 - 13267566} = 0.88$$

This coefficient is always less than or equal to 1 with a value of 1 implying a perfect agreement, and values less than 1 implying a less than perfect agreement. One possible interpretation of the kappa coefficient is as follows:

- Poor agreement = <0.20
- Fair agreement = 0.20 to 0.40
- Moderate agreement = 0.40 to 0.60
- Good agreement = 0.60 to 0.80
- Very good agreement = 0.80 to 1.00

Thus the matrix in Table CS5-2A, which is obtained from a classification of gamma-ray (measured and derived (ratio)) data for lithology compared to check training areas, results in an overall level of agreement (accuracy) of 89% and a kappa coefficient of 0.88 indicating that the gamma-ray data can be used successfully to classify lithology.

Errors of omission (Table CS5-2C) represent pixels that belong to the ground truth class but have been incorrectly classi-

fied into another class (i.e. the pixel is sandstone but has been incorrectly classified as shale). Thus the pixel has been left out of the proper class when it should have been included on the classified map. In the matrix shown in Table CS5-2C, the errors of omission (and commission – see below) are listed for each lithology. The calculation is column based. Using granite (G) as an example, 944 pixels or 93.2% of the training pixels were correctly classified, however, 16 pixels were actually classified as shales (Sh) and 52 as sandstones (sd). Thus the error of omission for granite is (16 + 52) / 1012 (total pixels), which is 6.72%.

Errors of commission (Table CS5-2C) represent pixels that belong to another class (lithology) but are labeled as belonging to the class of interest. Thus these pixels have been included in a class when they do not belong to the class. TableCS5- 2C also shows the errors of commission for each lithology, the calculation of which are row based. For example, the granite has 958 training pixels where 944 have been correctly classified and 14 have been incorrectly classified as orthoquartzite (Oqtz). Thus the error of commission for granite is (14 / 958), which equals 1.46%.

High errors of omission and commission for a given class indicate poor classification.

The 'producer's accuracy' (Table CS5-2D) is a reference-based accuracy that is determined by looking at the predictions produced for a class and calculating the percentage of correct predictions. For example, if the geologist knows that a particular area is limestone (determined from the training area), what is the probability that on the classified map this area will be classified as limestone. In other words, the 'producers' accuracy' is a measure of how well the geologist did when producing the classified map. It is calculated for each row in the matrix, hereby the proportion of correctly classified pixels (the number of pixels in the cell on the diagonal to the total number of pixels in that column expressed as a percentage). Thus for granite, the number of correctly classified pixels / column total is (944 / 1012), which is 93.2%. The producer's accuracy will be different for each rock group, as some lithologies are more distinct based on their gamma-ray signatures than others.

The 'users' accuracy' is a map-based accuracy that is computed by looking at the training data for a class and determining the percentage of correct predictions for those pixels. For example, if the geologist selects any pixel on the classified map as limestone, what is the probability that the geologist would find limestone at that pixel location in the field?

If one examines the calcareous shales (Sh calc) unit in Table CS5-2D, the producer accuracy is high (91.1%), but the users accuracy is much lower (76.8%). This means that even though 91% of the 'Sh calc' areas have been correctly identified as Sh calc, only 67% of the areas identified as Sh calc in the classification are truly of that category. Thus, the producer of this classification can claim that 91.1% of the time an area of Sh calc was identified as such, a user of the map would find that only 67% of the time will an area visited on the ground that the classification says is Sh calc actually be Sh calc. The most reliable classifications will have both a high producer and users' accuracy. For the example above, all the units, with exception of Oqtz, have reasonable classification accuracies.

type of map as Figure CS5-11D except that the training areas were derived using approach 2. Figure CS5-12B shows a classified map based on the LANDSAT, all the gamma-ray data, and the magnetic data using approach 1 to define the training areas.

The classification based on the LANDSAT data (Fig. CS5-11A) is visually the least similar to the geology map (Fig. CS5-2). The blank areas (unclassified) represent vegetation, clouds, and/or cloud shadow. The remaining classifications (Fig. CS5-11B-D, CS5-12) are similar in overall appearance. The four major divisions discussed in the section on visual analysis can be seen clearly.

Validation

Visual comparison to the generalized geology indicates many similarities. Confusion matrices were produced comparing the classifications to the original training areas (Fig. CS5-5D, Table CS5-1) as well as the generalized map (Fig. CS5-9A, Table CS5-2). The numbers in brackets in Table CS5-1 represent the accuracies using approach 2 (field locations, see Fig. CS5-5D), whereas the other number represents the accuracy using approach 1 (map based, see Fig. CS5-9B).

When compared to the actual generalized geological map (Fig. CS5-9A), the accuracies are generally much lower (20-50%). This is typical when comparing classifications based on remotely sensed data to existing geological maps, as the remotely sensed data offer a more detailed 'look'[1] at the surface. The higher spectral and spatial resolution offered by remote sensing provide imagery (in this case imagery of radioelement response) that is often difficult to match with units on a geological map, which represent a synthesis and generalization of a variety of geological criteria (information) obtained from field mapping. In many cases, the remotely sensed imagery provide information on the variation of various properties (spectral roughness, AGRS and GGRS signatures, magnetic susceptibility) within a mapped unit that is very useful for subdividing individual lithological units or packages.

The accuracies of the classified maps increase when more data are added to the classification process (Table CS5-1). Analysis of LANDSAT data by itself results in the lowest accuracy, whereas when all the data are used, much higher accuracies are achieved (>90%). Analysis of the gamma-ray data by itself results in accuracies in excess of 80%. Addition of the magnetic data improves accuracies by approximately 4% and the addition of LANDSAT data results in improvements of approximately 5%. Overall, both methods used for training area identification offer similar accuracies, indicating both can be used successfully for classification purposes.

Based on analysis of confusion matrices, an example of which is shown in Table CS5-2 (see description on Table CS5-2 for definition of a confusion matrix and

1. 'look' refers to the response characteristics of each remote sensor (i.e. radioelement emission for gamma-ray data, spectral reflectance for optical data, and backscatter for radar data) as well as the spatial resolution of each sensing device.

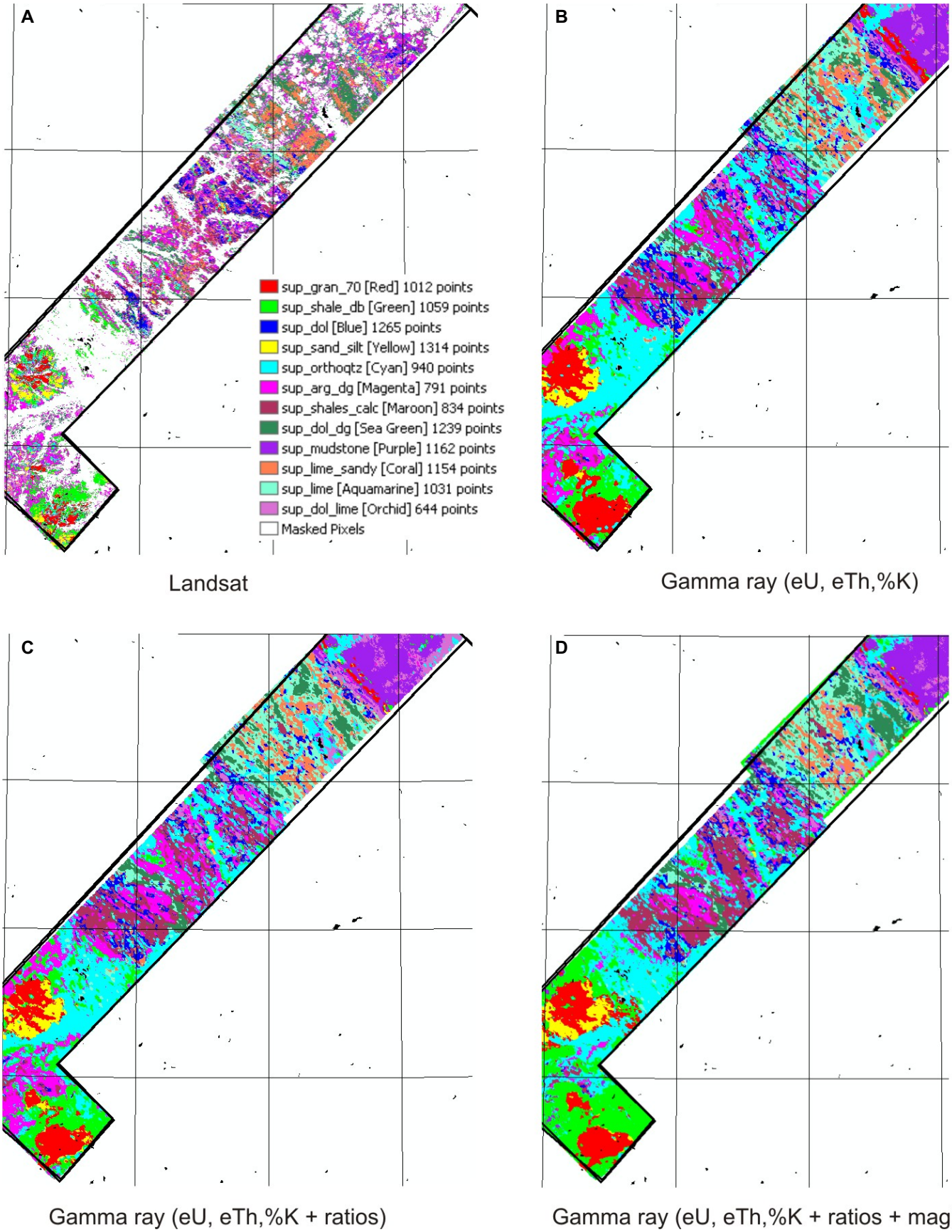

Figure CS5-11. Predictive (classification) maps using on supervised classification **(A)** based on LANDSAT data, **(B)** based on gamma-ray spectrometry data (U, K, Th), **(C)** based on gamma-ray spectrometry data (U, K ,Th, and ratios), and **(D)** based on all gamma-ray and magnetic data.

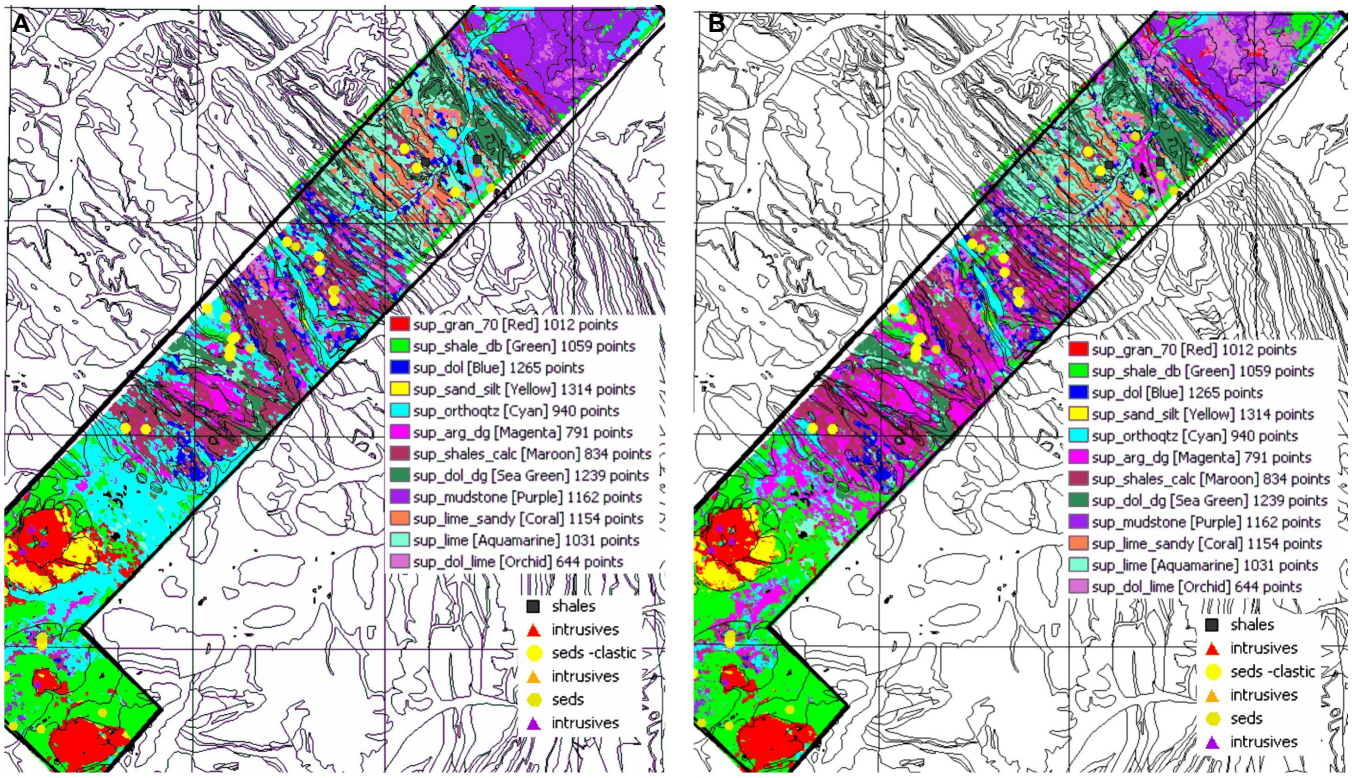

Figure CS5-12. (A) Supervised classification using all gamma-ray data and using approach number 2 (see text) to define the representative training areas (based on field locations) for each rock type. **(B)** Supervised classification based on LANDSAT, all gamma-ray, and magnetic (total field) data using approach number 1 (see text) to define the training areas (based on the geology map) for each rock type.

associated parameters), LANDSAT, which is based on spectral response, poorly classified orthoquartzites, dark grey argillites, and dolomites, with accuracies of 45%, 41%, and 51%, respectively. Dark brown shales and sandstone/siltstone are the most accurately classified (91% and 79%, respectively). The gamma-ray data offers better discrimination of all units with sandstone, siltstone, dark grey dolomite, dark brown shale, and limestone classification having accuracies in excess of 90%. Note that the dark grey dolomite was classified with a much higher accuracy based on its radioelement signature than spectral reflectance. However, orthoquartzite was better discriminated, but only marginally, based on its radioelement signature. In general, errors of commission and omission (see description for Table CS5-2) were much lower for the classifications based on the gamma-ray data. Addition of the radioelement ratio data, along with measured K, eU, and eTh, improved accuracies of most units by approximately 5% compared to accuracies based on just the measured data alone (Table CS5-2). The biggest improvement in accuracies when using the ratio data were for calcareous shales (63-91%), limestone (65-87%), and dolomitic limestone (60-90%).

DISCUSSION AND IMPLICATIONS FOR REMOTE PREDICTIVE MAPPING

This study has indicated that airborne data, given the right geological conditions and rock types, can play a significant role in the remote mapping of different lithologies. In this study, a wide range of units, including granite, shale, sandstone, and carbonate, could be identified based on characteristic radioelement signatures. In some cases, a number of distinct subdivisions within some units (i.e. black shales, various granitoid phases) could be clearly mapped. A very high correlation between GGRS measurements of K, eU, and eTh (used to characterize the signatures of the major lithologies) and the airborne data was found. This indicates that despite some surficial and vegetation cover, the airborne data were responsive to the bedrock.

Supervised classification using two training-area strategies, one based on field locations and the other on definition form the generalized geology map, was found to be successful for producing a predictive (classified) map of lithological units. The classified maps derived from the gamma-ray data were more accurate, when compared to check training areas, than the map produced from LANDSAT data. The ‘best’ map was produced from using all the gamma-ray data, together with the residual magnetic total field data, and the LANDSAT data, supporting the notion that a variety of geoscience data, each responsive to different characteristics of rocks (spectral reflectance, radioelement concentrations and magnetic susceptibility), provide the most accurate results.

Multisensor geophysical surveys, which include both magnetic and gamma-ray data, are highly recommended for mapping programs in Canada's North.

REFERENCES

Atkinson, D. and Baker, D. J.
1983: Recent developments in the geologic understanding of Mactung, *in* Mineral Deposits of Northern Cordillera, (ed.) J.A. Morin; Canadian Institute and Metallurgy, Special Volume 37, p. 234-244.

Blusson, S.L.
1971: Sekwi Mountain map area, Yukon Territory and District of MacKenzie (NTS 105P); Geological Survey of Canada, Paper 71-71, 17 p.

Charbonneau, B.W.
2007: Evaluation of Radiometric and Magnetic Airborne Survey Data, Sekwi Transect, NWT; unpubl. report, 12 p.

Ford, K.L. and O'Reilly, G.A.
1985: Airborne gamma ray spectrometric surveys as an indicator of granophile element specialization and associated mineral deposits in the granitic rocks of the Meguma zone of Nova Scotia, Canada, *in* Proceedings of the High Heat Production (HHP) Granites, Hydrothermal Circulation and Ore Genesis; Institute of Mining Metallurgy, St. Austell, Cornwall, England, p. 113-133.

Jefferson, C.W. and Spirito, W.A.
2003: Mineral Resource Assessment of the Tlogotsho Plateau, Nahanni Karst, Ragged Ranges and Adjacent Areas under Consideration for Expansion of the Nahanni National Park Reserve, NWT; Geological Survey of Canada, Open File 1686.

Lillesand T.M. and Kieffer, R.W.
2000: Remote Sensing and Image Interpretation, 4th edition; John Wiley and Sons, Inc. New York, 724 p.

Northwest Territories Geoscience Office
2005: Aeromagnetic and Gamma Ray Spectrometric Survey, Canol Block, Sekwi Mountain area, Northwest Territories, parts of 105P and 106A; Open File 2006-15, 10 maps and digital data.

Richards, J.A. and Jia, X.
2006: Remote Sensing Digital Image Analysis: An Introduction, 4th edition; Springer-Verlag, Berlin, Germany, 439 p.

CASE STUDY 6. Surficial Mapping of Northern Baffin Island Using LANDSAT and Topographic Data

O. Brown[1], J.R. Harris[2], and D. Utting[1]
1. Nunavut Geoscience Centre, P.O. Box 2319, 626 Tumiit Plaza, Suite 202, Iqaluit, Nunavut X0A 0H0
2. Geological Survey of Canada, 615 Booth Street, Ottawa, Ontario K1A 0E9
Corresponding author's email: Jeff.Harris@nrcan.gc.ca

INTRODUCTION

The geoscience knowledge base for Nunavut is generally inadequate to meet the current demands of the mineral exploration industry. Improving the knowledge base requires the collection of large amounts of high-quality geoscience data. Capturing geoscience data using traditional ground-based activities is resource intensive and regional-scale mapping projects can take years to complete. A map of surficial units generated by integrating and interpreting various types of remotely sensed data in concert with ground-based field observations and produced in advance of field work, has significant potential for increasing the effectiveness and efficiency of regional-scale geoscience studies.

OBJECTIVES

The approach taken in this case study is to utilize a computer-assisted methodology to generate a map of surficial units from LANDSAT and digital elevation model (DEM) data. This process involves the collection of representative training samples of each surficial unit (e.g. bedrock, glaciolacustrine, fluvial, till) to be classified (predicted), which are derived from analysis of air photographs in concert with field observations. Representative signatures for each of the training areas are then derived from LANDSAT and topographic (DEM) data and used to produce a predictive map employing a maximum-likelihood classification algorithm.

The study area, which is shown in Figure CS6-1, is located on northeastern Baffin Island in NTS 37E (Conn Lake sheet) and lies mainly within the Baffin Uplands, north of the Barnes Ice Cap (Bostock, 1970). The area is underlain by rocks of the Rae Domain, in the western Churchill Province, an Archean granite-greenstone terrane, which includes north- to northeast-striking rocks of the Mary River Group (Jackson, 2000). Mapping of the surficial geology at 1:500 000 scale was completed for a portion of the study area by Hodgson and Haselton (1974). The study area contains relatively little vegetation cover. Grasses are restricted mainly to river valleys and lichen covers some areas. Lichen-free areas are associated with the expansion of perennial snowfields during the Little Ice Age (LIA) (Wolken et. al., 2005).

Geomorphologic features in the study areas include steep-sided fjords, high plateaus, rolling hills, valleys, moraines, flutings, deltas, and meltwater channels and eskers (Little et al., 2004). The study area is dominated by glacial drift; however, bedrock, and glaciolacustrine and fluvial material also occur sporadically throughout.

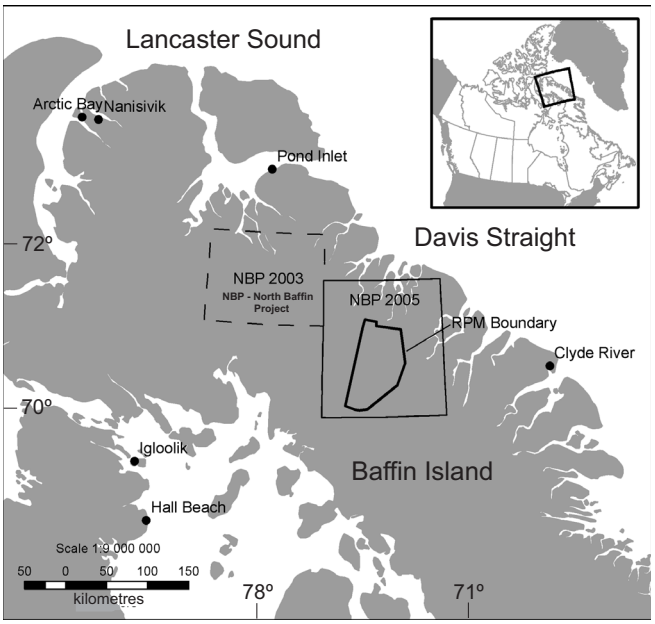

Figure CS6-1. Study area location, northern Baffin Island, Nunavut.

DATA

Orthorectified LANDSAT data (Fig. CS6-2), obtained from the Geogratis website (www.geogratis.cgdi.gc.ca) and a digital terrain model (DEM) (Fig. CS6-3) obtained through Geomatics Canada from the Geobase website (www.geobase.ca), were used in this study.

Data Processing and Integration

Visual Assessment

Cursory examination of the LANDSAT data (Fig CS6-2) indicates that LANDSAT does show sufficient spectral variability that may relate to various surficial deposits to warrant further computer analysis. Surficial units that are lichen-free, which often occur at higher elevations, appear very bright compared to surrounding areas on the LANDSAT imagery of the study area (Fig. CS6-2). Fluvial materials also appear bright on the imagery but do not occur at high elevation. Prior to incorporating the DEM data into the classification, lichen-free areas were confused with fluvial material.

Brown, O., Harris, J.R., and Utting, D., 2008, Surficial mapping of northern Baffin Island using LANDSAT and topographic data, Case Study 6 *in* Remote Predictive Mapping: An Aid for Northern Mapping, (ed.) J. R. Harris; Geological Survey of Canada, Open File 5643, p. 225-232.

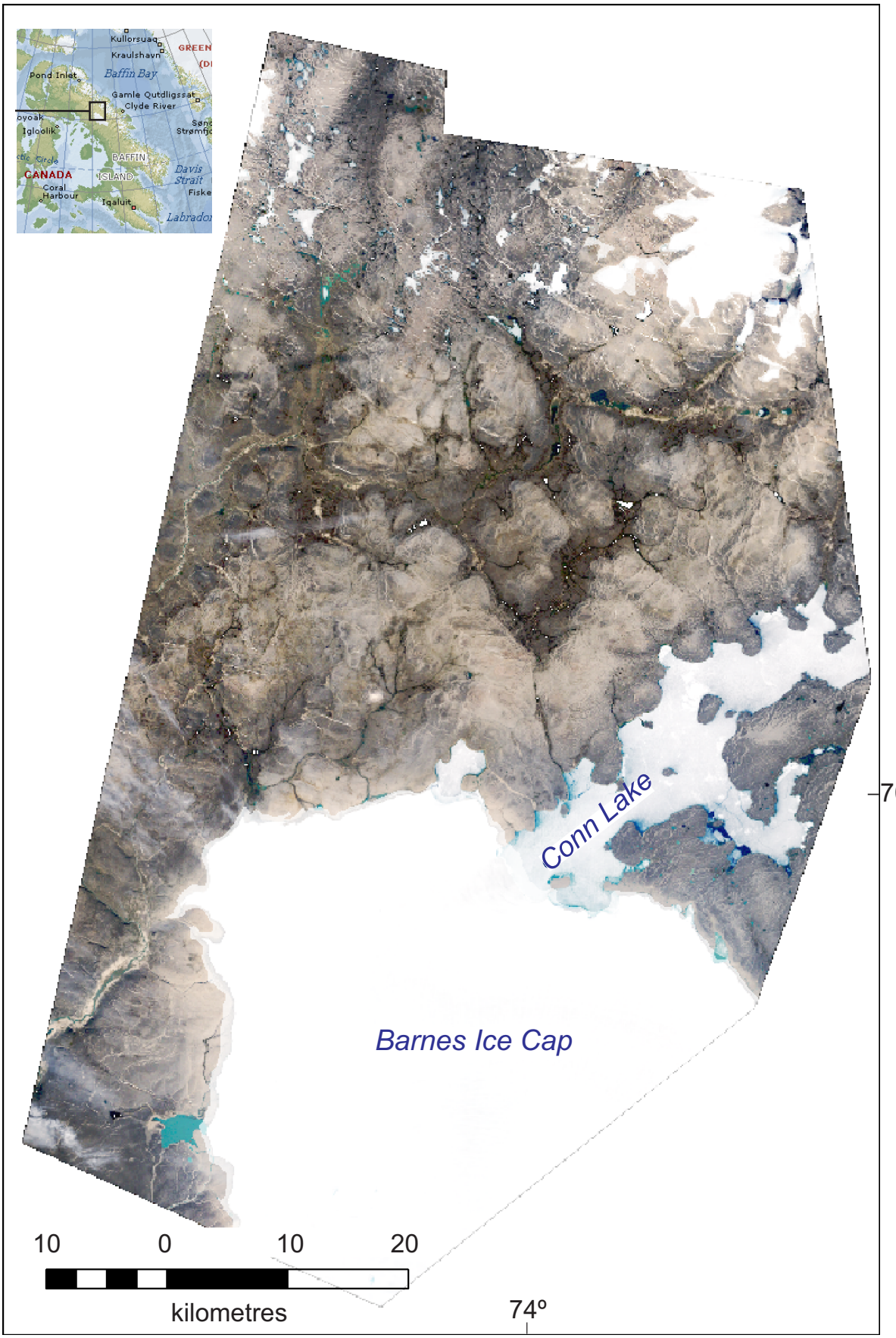

Figure CS6- 2. LANDSAT image of the sturdy area (red, green, blue = bands 3, 2, 1).

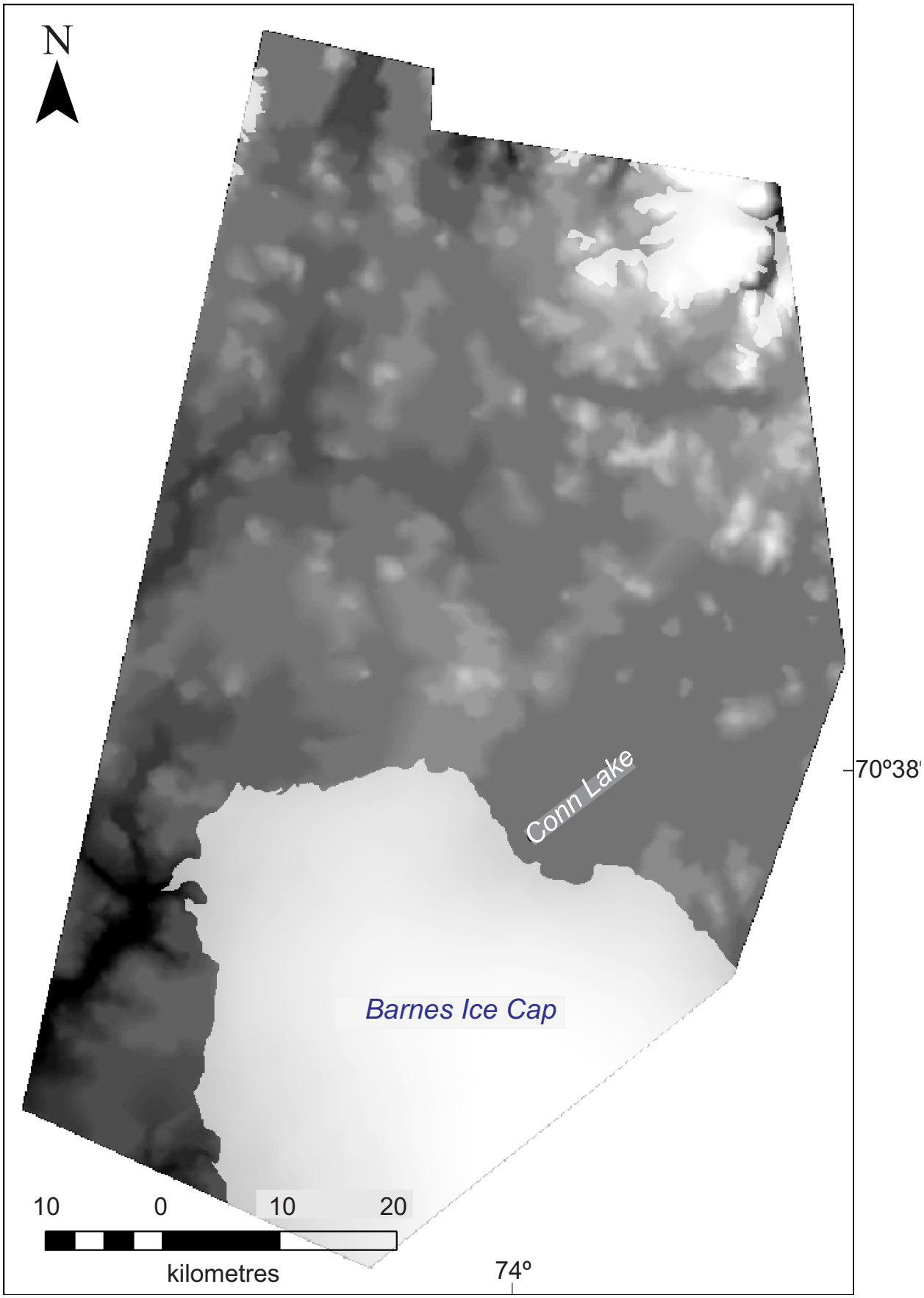

Figure CS6-3. Digital Elevation Model (DEM) 1:250,000 scale Canadian Digital Eleveation Data (CDED) for the sturdy area.

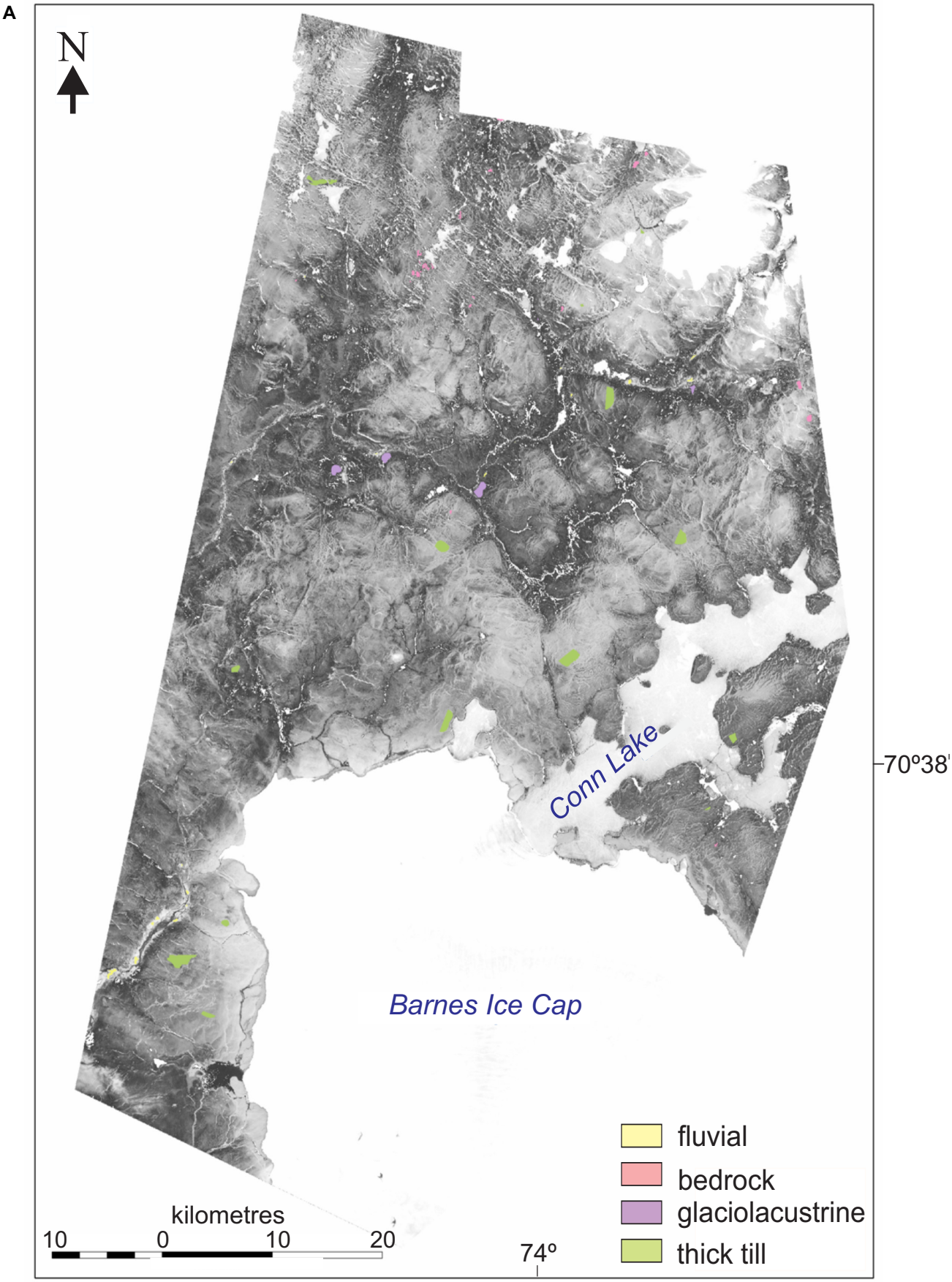

Figure CS6-4. (A) Training areas used for classification.

B

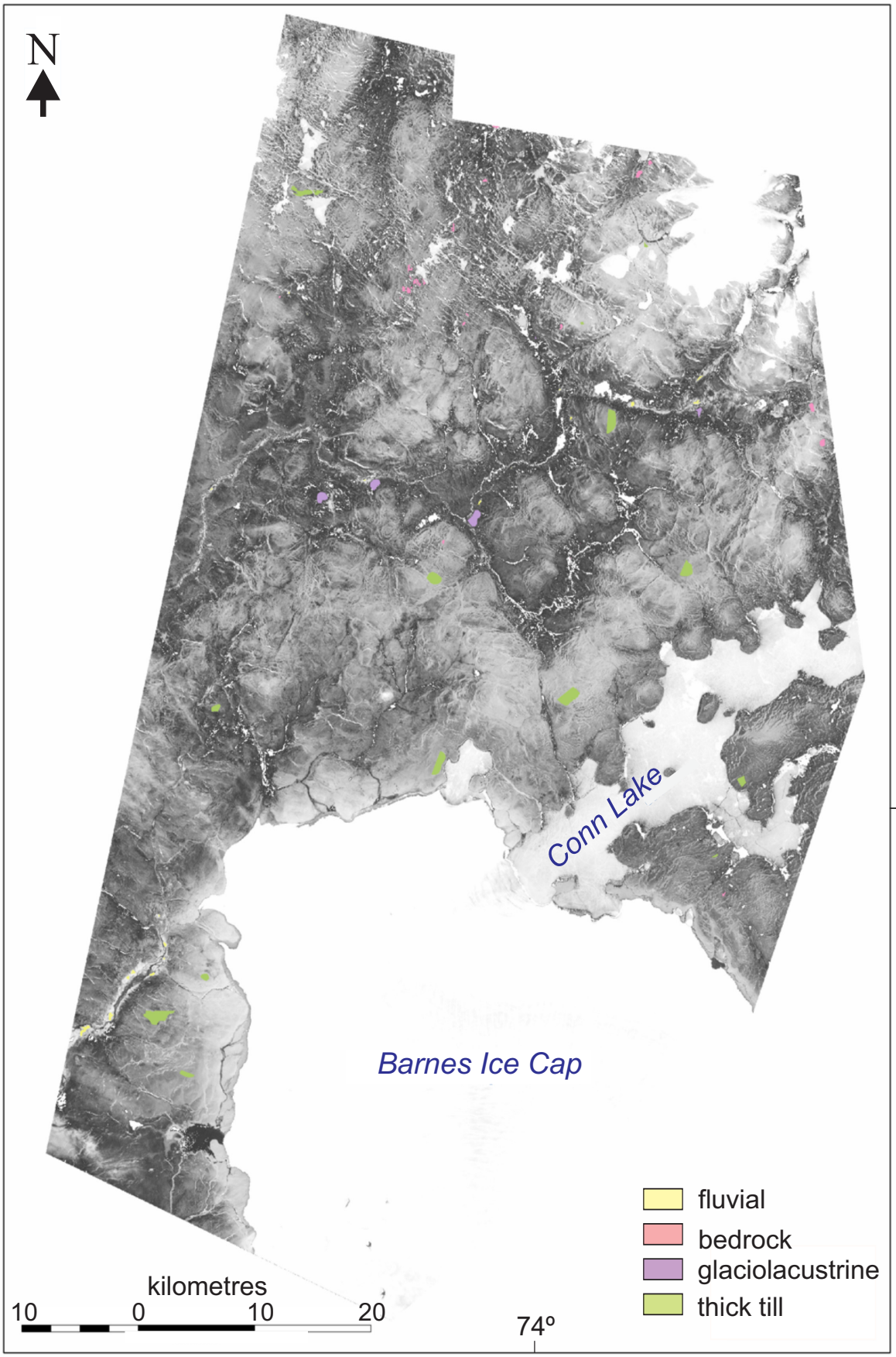

Figure CS6-4 continued. (B) Training areas used for validation.

Computer-Assisted Approach – Supervised Classification

Figure CS6-4 shows the distribution of the training areas for each surficial unit, which were derived from the analysis of airphotos and LANDSAT imagery and supported by field observations. Two sets of training areas were selected (Fig. CS6-4A,B) to evaluate the variability in classifications as a result of different training area sets (see Grunsky et al., 2006 and Brown et al., 2007 for more details on this validation process).

Training classes must be statistically separable to produce robust and meaningful classification results (Jensen, 1995; Lillesand et al., 2004). Measures of separability in N-dimensional space (in this case six LANDSAT bands and a DEM, resulting in seven dimensions), such as transformed divergence (TD), are used to determine the separability of signatures prior to classification. If the various training classes are found not to be sufficiently separable on a statistical basis in this step, then classification of the data is pointless. However, in this case separability between the four surficial units to be predicted (bedrock, glaciolacustrine, till, and fluvial) was deemed sufficient (Table CS6-1 and Fig. CS6-5) to warrant progression to the next step, that of classification.

The resulting prediction (classification) maps for both training data sets are shown in Figure CS6-6.

Table CS6-1. Transformed divergence values for four training classes using LANDSAT TM and DEM data.

Name	Fluvial	Bedrock	Glaciolac
Bedrock	2		
Glaciolac	2	2	
Till	1.995	1.082	2

When this predicted map is compared to the original training areas used for the classification, an overall accuracy of 85% was achieved. However, when compared to check sites for each surficial unit established in the field, only 50% accuracy was achieved. Inclusion of the DEM data with the LANDSAT data resulted in an improvement in overall accuracy of only 1%.

DISCUSSION AND IMPLICATIONS FOR REMOTE PREDICTIVE MAPPING

The importance of selecting representative training areas is highlighted in this study as 5 to 10% variability in the accuracy of the classified maps resulted when using different training groups. However, even with the apparent prudent selection of training areas, difficulties can still arise when trying to define training areas for surficial classes from either ground-based observations or high-resolution air photographs and then applying these to imagery such as LANDSAT, which is characterized by only moderate spatial resolutions (i.e. 30 m). What LANDSAT 'sees' from a spectral point of view

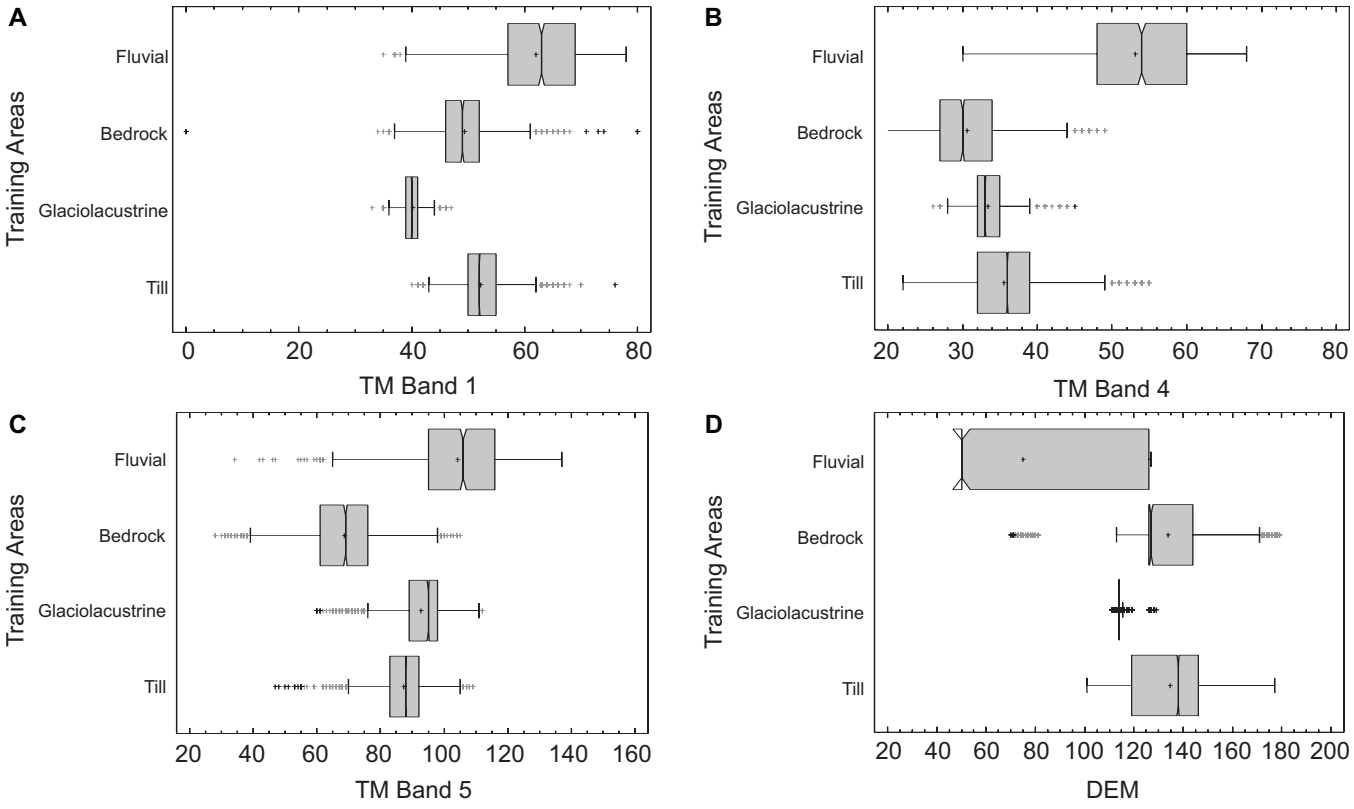

Figure CS6-5. Box and whisker plots for training areas. **(A)** LANDSAT TM band 1. **(B)** LANDSAT TM band 4. **(C)** LANDSAT TM band 5. **(D)** Digital elevation model (DEM) data.

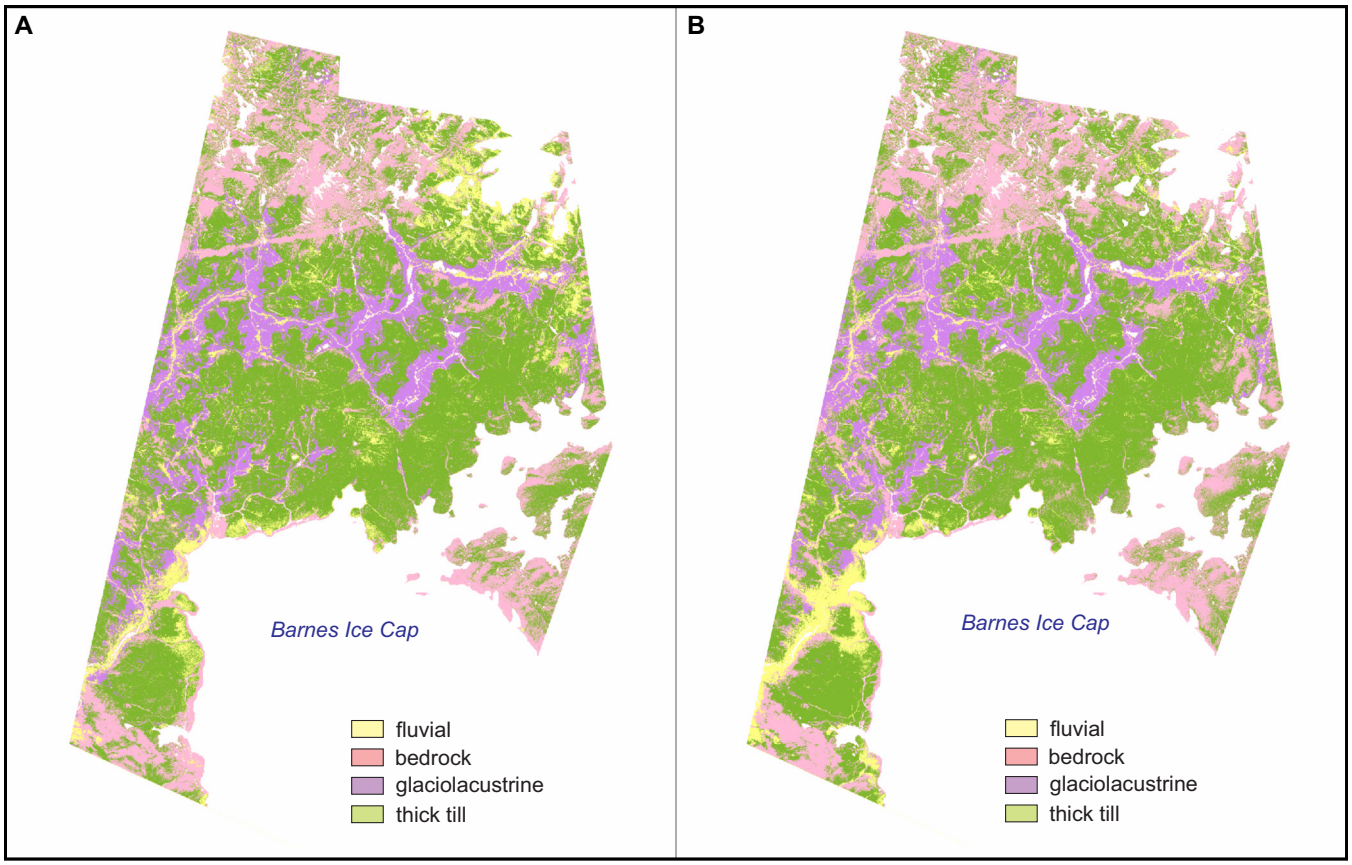

Figure CS6-6. LANDSAT classifications. **(A)** Maximum-likelihood classification based on training areas. **(B)** Maximum-likelihood classification based on check training areas.

can be quite different from what is seen on the ground or on high-resolution imagery. High-resolution imagery tends to capture more surface textural and con-textual spatial variations seen by an observer on the ground, as well as what is captured on aerial photographs. Lower resolution imagery tends to average out these textural variations. This study has based classification on just the spectral properties of LANDSAT data; future studies will incorporate textural measures in attempt to capture more of the detailed information seen on the ground or in higher resolution remotely sensed data.

Accuracy results when compared to the training areas were generally good (approximately 80-90%). However, when compared to the field observations on surficial materials, the accuracy of the maps was much lower (approximately 50%). This does not meet the stated goal of predicting till with 80% accuracy. This is not an unexpected result given the discrepancy between scale (resolution) of training area definition and the data used for classification. This is in part due to what the observer 'sees' on the ground, the data they use to define the training areas, and the data to which the classification is applied. Areas of thin till and bedrock can even be difficult to separate in the field, given the transitional and heterogeneous nature of the two material types. Given the lower resolution of the LANDSAT data, this problem is compounded when attempting to undertake classification using only a spectral signature. Furthermore, LANDSAT is not able to capture smaller areas of outcrop, given its 30 m resolution limitation. However, from a mapping perspective, being 50% correct may be better than going out in the field with no information at all!

Post-classification filtering is recommended, as classification accuracies improved when comparing the filtered maps to the training areas. Incorporation of topographic information (DEM) is also recommended, as the statistical separation between training areas improved when the DEM was incorporated with the LANDSAT data in the classification process. Furthermore classification accuracies also improved slightly.

REFERENCES

Bostock, H.S.
1970: Physiographic regions of Canada; Geologic Survey of Canada, Map 1254, scale 1:500 000.

Brown, O., Harris, J.R., Utting, D., and Little, E.C.
2007: Remote predictive mapping of surficial materials on northern Baffin Island: Developing and testing techniques using LANDSAT TM and digital elevation data, *in* Current Research 2007-B1; Geological Survey of Canada, 12 p.

Grunsky, E., Harris, J.R., and McMartin, I.
2006: Predictive Mapping of Surficial Material, Schultz Lake (NTS66a); Geological Survey of Canada, Open File 5153, 49 p.

Hodgson, D.A. and Haselton. G.M.
1974: Reconnaissance Glacial Geology, Northeastern Baffin Island; Geological Survey of Canada, Paper 74-20, 10 p.

Jackson, G.D.
2000: Geology of the Clyde-Cockburn Land Map Area, North-Central Baffin Island, Nunavut; Geological Survey of Canada, Memoir 440, 303 p.

Jensen, J.R.
1995: Introductory Digital Image Processing: A Remote Sensing Perspective, 2rd edition; Prentice Hall, 316 p.

Lillesand, T.M., Kieffer, R.W., and Chipman, J.W.
2004: Remote Sensing and Image Interpretation, 5th edition; John Wiley and Sons, 736 p.

Little, E.C., Holme, P.J., Hilchey, A.C., and Young, M.D.
2004: Glacial geology, ice movement chronology, and drift prospecting in the vicinity of Icebound Lakes, northern Baffin Island, Nunavut, *in* Current Research 2004-D1; Geological Survey of Canada; 16 p.

Richards, J.A. and Jia, X.
2006: Remote Sensing Digital Image Analysis: An Introduction; 4th edition, Springer-Verlag; New York., 439 p.

Wolken, G.J., England, J.H., and Dyke, A.S.
2005: Re-evaluating the Relevance of Vegetation Trimlines in the Canadian Arctic as an Indicator of Little Ice Age Paleoenvironments; Arctic, v. 58, p. 341-353.

CASE STUDY 7. Classification of Remotely Sensed Imagery for Surficial Geological Mapping in Canada's North

J.R. Harris, E. Grunsky, and I. McMartin
Geological Survey of Canada, 615 Booth Street, Ottawa, Ontario K1A 0E9
Corresponding author's email: Jeff.Harris@NRCan.gc.ca

INTRODUCTION

Mapping in the North is an expensive proposition due to remoteness, lack of infrastructure, logistical problems, and the generally short mapping season. Remotely sensed data offers a useful source of information to the mapping geologist for not only updating existing geological maps but as a first-order source of geological information in areas that have not been well mapped. Needless to say, areas that have not been mapped in detail comprise many areas of Canada's North.

The Geological Survey of Canada (GSC) has undertaken a project to map large sections of Canada's North through an initiative entitled "Resource Identification Through Remote Predictive Mapping" (RPM), which is part of the Earth Sciences Sector (ESS) Northern Resources Development Program. The RPM project is a pan-North initiative that utilizes remotely sensed and geophysical data to focus field efforts in the North, extend mapping coverage, and maximize economic impact. Using a range of remotely sensed data, the RPM project contributions will include the production of digital maps that are quantitative, predictive, reliable, and cover significant areas.

The RPM method differs from current methods for mapping the North, which traditionally relied on a homogeneous grid of traverses spaced 1 to 5 km apart over the area of interest, regardless of the complexity of geology and supplemented with the interpretation of air photos. The advantage of RPM maps is that they can show both geologically homogeneous and heterogeneous areas, allowing more field emphasis to be placed on the complex areas. In addition, the signatures that have been extracted from various geoscience data sets over an area that has been verified (mapped), can be used to help predict areas of similar geology where mapping is not possible.

OBJECTIVES

This paper focuses on the use of remotely sensed data (RADARSAT, LANDSAT) in conjunction with a digital elevation model (DEM) data for producing predictive (classifications) maps of surficial units in the Shultz Lake area (NTS 66A), Nunavut and is based on work by Grunsky (2002) and Grunsky et al. (2006). A computer-assisted approach is employed, which involves identifying representative areas on airphotos (supported by field work) of various surficial units, collecting signatures of these 'training areas' from the remotely sensed imagery, and then identifying similar areas on the imagery using a maximum likelihood classification algorithm. The methodology for producing predictive maps of surficial units presented in this paper can be used in other northern environments.

In the summer of 2004, the GSC conducted Quaternary field mapping in the Schultz Lake map area (NTS 66A) in central Nunavut (McMartin and Dredge, 2005; McMartin et al., 2005) This field mapping, in conjunction with RPM techniques, will help in understanding ice-flow directions, till provenance, and assist in the identification of surficial units, all of which will enhance mineral exploration, particularly drift prospecting for gold and diamonds.

The Schultz Lake map area (Fig. CS7-1) includes the community of Baker Lake, located about 300 km inland from the west side of Hudson Bay. Relief is subdued, with elevations ranging from 3 m at Baker Lake to 283 m above sea level along a bedrock ridge west of Pitz

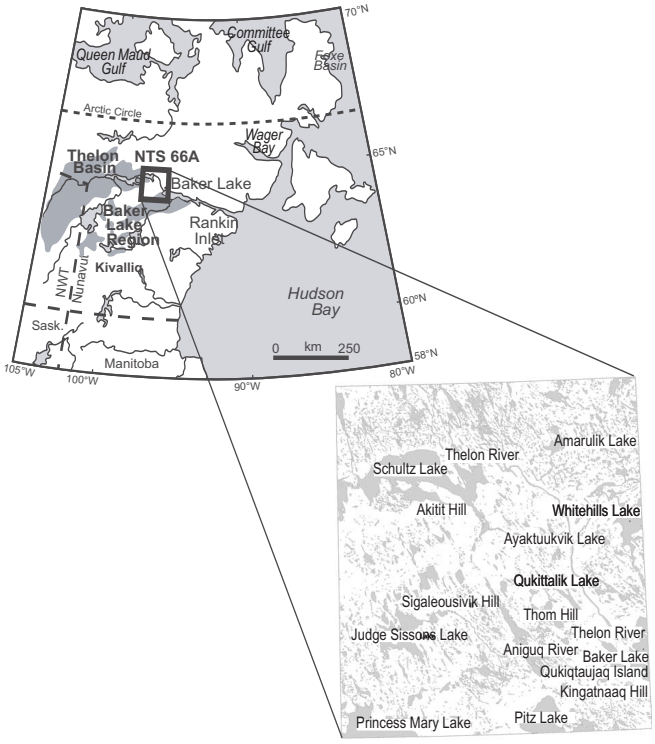

Figure CS7-1. Location map of NTS 66A, Schultz Lake, Nunavut, Northwest Territories.

Harris, J.R., Grunsky, E., and McMartin, I., 2008, Classification of remotely sensed imagery for surficial geological mapping in Canada's north, Case Study *7 in* Remote Predictive Mapping: An Aid for Northern Mapping, (ed.) J. R. Harris; Geological Survey of Canada, Open File 5643, p. 233-244.

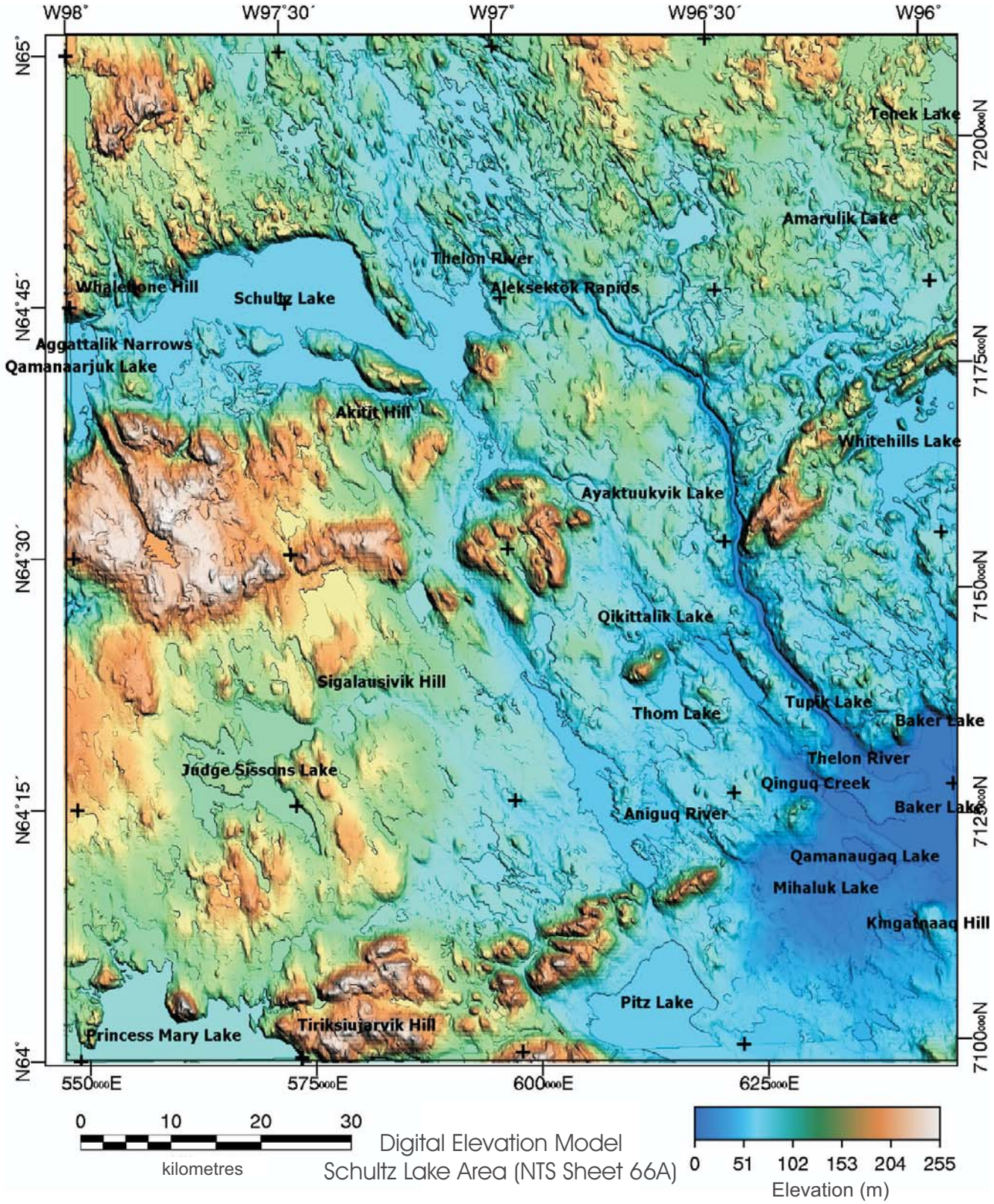

Figure CS7-2. Shaded digital elevation model of the Schultz Lake area.

Lake (Fig. CS7-2). The area lies within the Archean Rae Domain of the Western Churchill Province and is underlain by Archean granitoid and gneissic rocks, and metamorphosed Archean and Proterozoic sedimentary and volcanic rocks (Fig. CS7-3) (Hadlari et al., 2004). The area is also covered by thick sequences of distinctive red volcanic and sedimentary rocks of the Proterozoic Dubawnt Supergroup. Drift is relatively

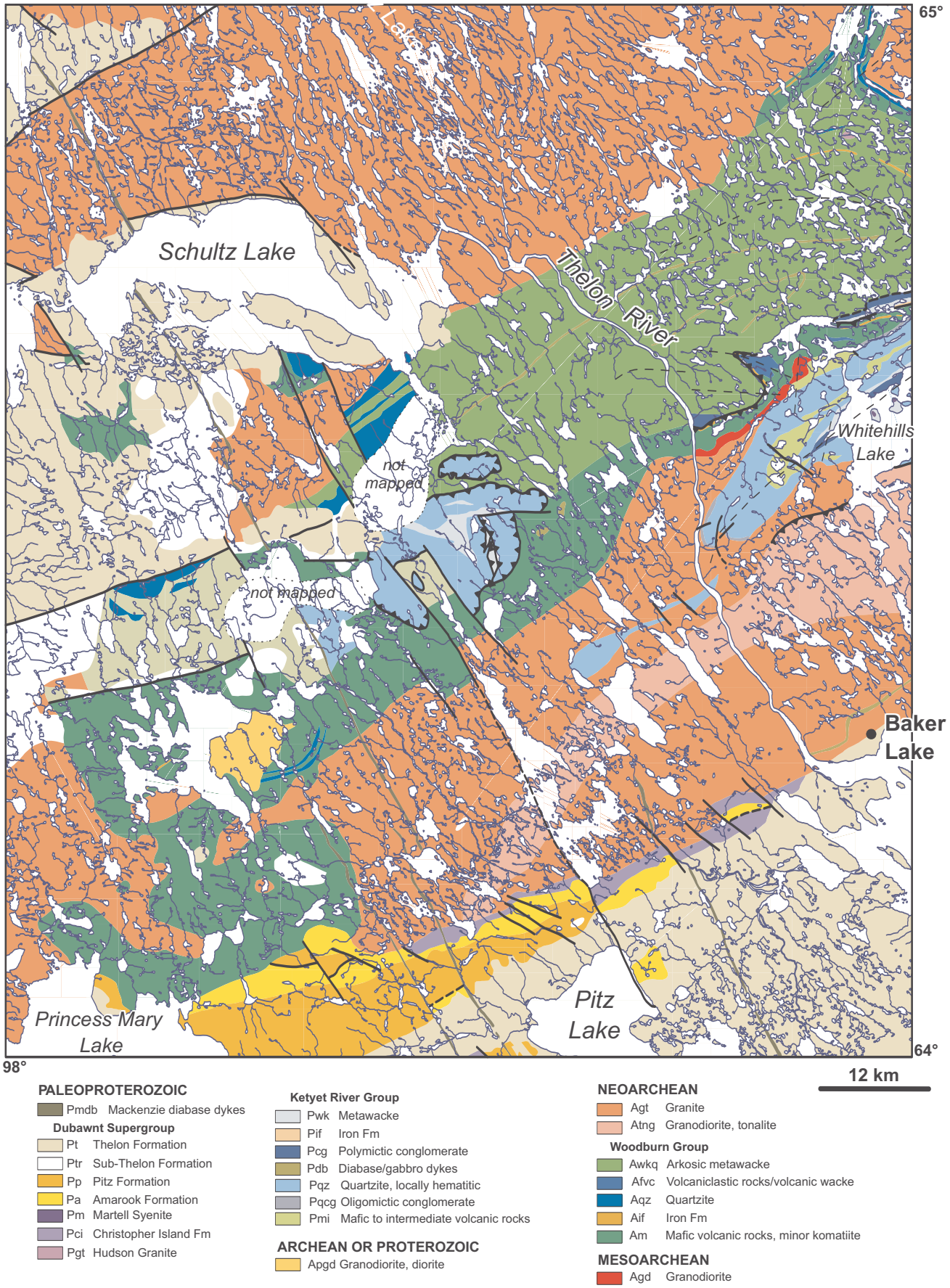

Figure CS7-3. Bedrock geology of the Schultz Lake area (after Hadlari et al., 2004).

thick (>5 m) and more continuous south of the Thelon River, forming rolling till plains, locally streamlined. In contrast, thin till (<2 m) and exposed bedrock are predominant north of the river. Marine (and/or glaciolacustrine) sediments occur in poorly drained, low-lying terrain, or form flights of raised strandlines on the sides of till and broad bedrock hills. This map area is essentially devoid of glaciofluvial sediments although there are restricted areas north and south of Schultz Lake that show evidence for pro-glacial and sub-glacial meltwater erosion (i.e. boulder fields).

The generalized surficial geology of the area is shown in Figure CS7-4 (after Aylsworth et al., 1990). These surficial materials are not unique and there is considerable overlap between their spectral and surface roughness characteristics. For example, substantial areas of bedrock are overlain by a blanket of thin till. When viewing satellite imagery at a spatial resolution of 30 m, it is often difficult to determine the amount of thin till that overlies the bedrock. In addition, sand and gravel, a component of till, can have the same textural and spectral properties as the sand and gravel that is associated with the near-shore marine environment. In fact, in many cases, the latter is likely reworked till below the former upper marine limit. Nonetheless, these general categories of surficial types can assist in characterizing the surficial geology of the area and assist in identifying specific surficial materials.

DATA

Two types of satellite imagery were assessed for their potential to identify surficial materials in the study area: multibeam RADARSAT-1 (Fig. CS7-5) and LANDSAT TM7 (Fig. CS7-6). A digital elevation model (Fig. CS7-2), obtained from the Canadian Digital Elevation Data (CDED) of the National Topographic Database, was also used to test whether elevation differences play a role in mapping the various surficial units.

LANDSAT TM7 imagery was used for the identification of surficial materials that can be mapped based on reflective properties in the optical and near infrared wavelengths of the electromagnetic spectrum (band 1: 0.45-0.52 μm, band 2: 0.52-0.60 μm, band 3: 0.63-0.69 μm, band 4: 0.76-0.90 μm, band 5: 1.55-1.75 μm, and band 7: 2.08-2.35 μm). The use of multibeam radar imagery was employed to discriminate surficial features that have distinctive backscatter responses. The RADARSAT-1 satellite imagery uses C-band (5.6 cm) horizontally transmitted and received (HH) energy to create an image of the Earth's surface. The side-viewing geometry and long-wavelength energy used for sensing makes radar very sensitive to variations in surface topography, roughness, and moisture (see Chapter 6 of this volume).

DATA PROCESSING AND INTEGRATION

In the Schultz Lake area, the surficial geological map was visually generalized into six surficial types (Fig. CS7-4), using the same material types determined from the remotely sensed data: 1) sand and gravel, 2) organics, 3) till veneer, 4) thick till, 5) bedrock, and 6) boulder cover. Training areas representative of each of the generalized surficial units were chosen on the basis of airphoto analysis along with field checking and analysis of the satellite imagery. Figure CS7-7 shows the combined training areas that were used for the initial overall classification. A supervised classification using the maximum likelihood method (Richards and Jia, 1999) was carried out on various combinations of the remotely sensed data using the statistics for each band derived from each training area. Classification using all training areas listed above (no water or clouds) (Fig. CS7-7) was conducted on the LANDSAT and RADARSAT data independently and in combination with each other, and also with the DEM. Prior probabilities in the classification were assumed to be equal.

The success of any supervised classification depends on the nature (accuracy) of the training data used. If the statistics for the training areas are not separable, classification accuracy will be low and the results will be unpredictable and possibly misleading. One way to test the discriminating power of the training sets is through the calculation of the transformed divergence statistic (TD), discussed in Richards and Jia (1999). Transformed divergence is a mathematical technique for determining how well classes are separated in N-dimensional space. Transformed-divergence values greater than 1.9 indicate good statistical separation between classes, values between 1.0 and 1.9 indicate moderate separation, and values less than 1.0 indicate poor separation.

Another method to evaluate the statistical variation of the training areas and thus uncertainty of the resulting classified maps is through cross-validation. Three sets of randomly selected training areas were chosen from the complete set of training areas (Fig. CS7-7) using the signatures from the RADARSAT, LANDSAT, and DEM data. Each training area set was used to produce a separate classification of surficial units. Each classification was then cross-checked for accuracy with the other training area sets (validation sets) that were not used to derive the specific classification. This allows for estimation in the uncertainty of the classification procedure.

Results

Statistical Separation of Training Areas

Statistical separation between training areas for both radar and optical imagery is only moderate at best,

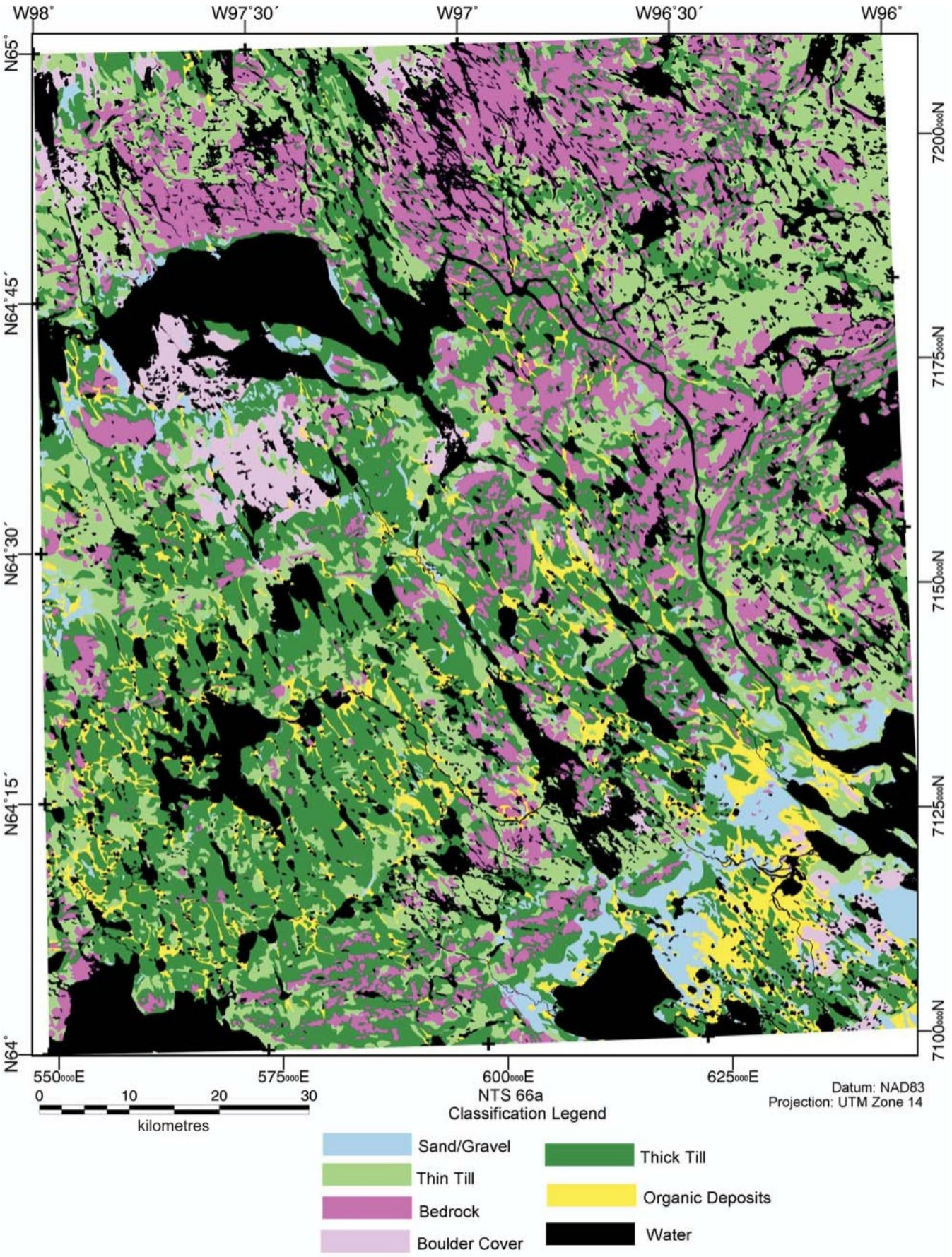

Figure CS7-4. Generalized surficial geology of the Schultz Lake area (modified from Aylsworth et al., 1990).

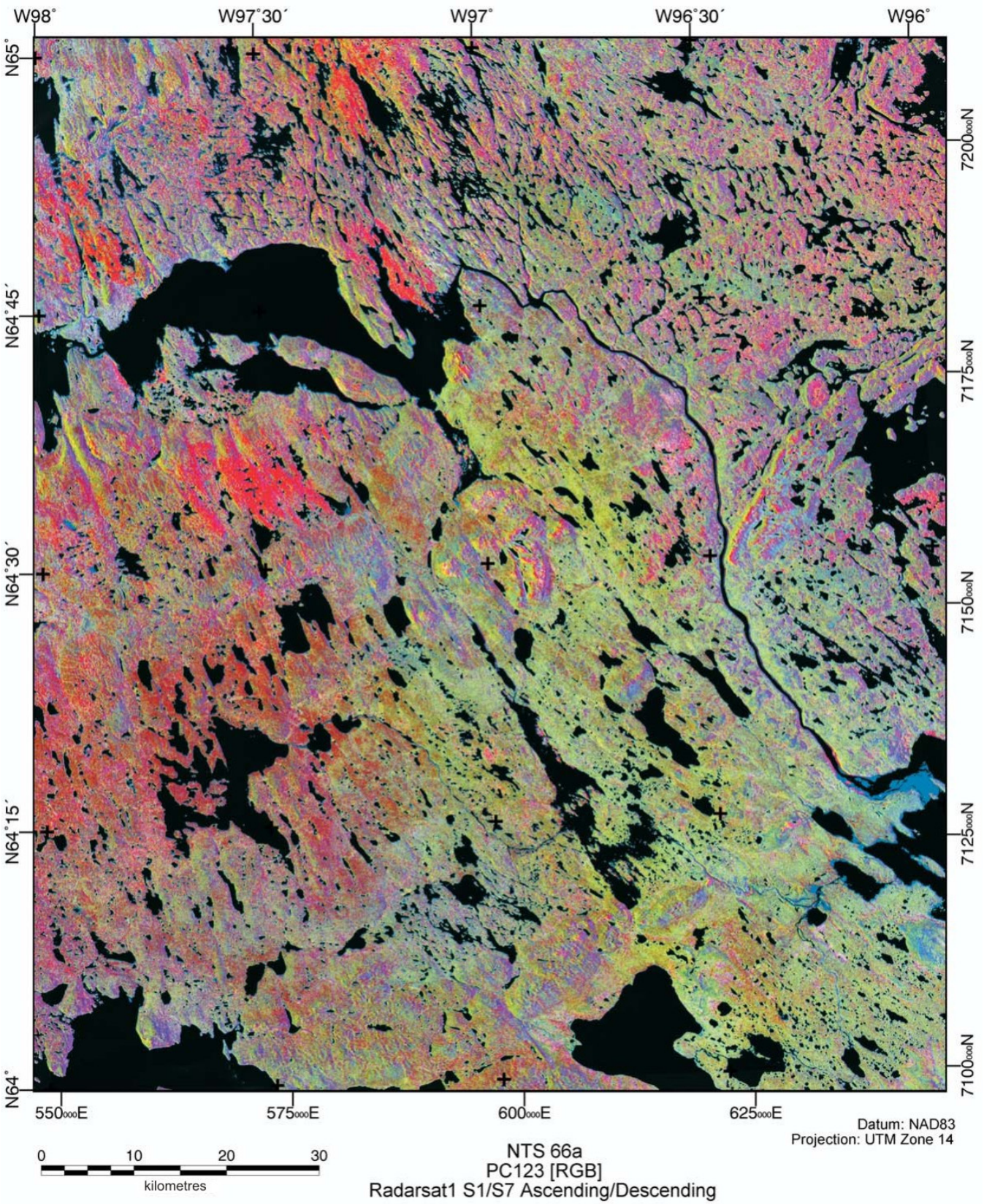

Figure CS7-5. First three principal components derived from S1/S7 ascending/descending RADARSAT-1 imagery shown as a ternary colour composite image (principal component 1 – red, principal component 2 – green, principal component 3 – blue).

although overall, the LANDSAT data offers slightly better separation of surficial units based on Transformed Divergence (TD) analysis of the training areas (Fig. CS7-8). This is especially true for organics,

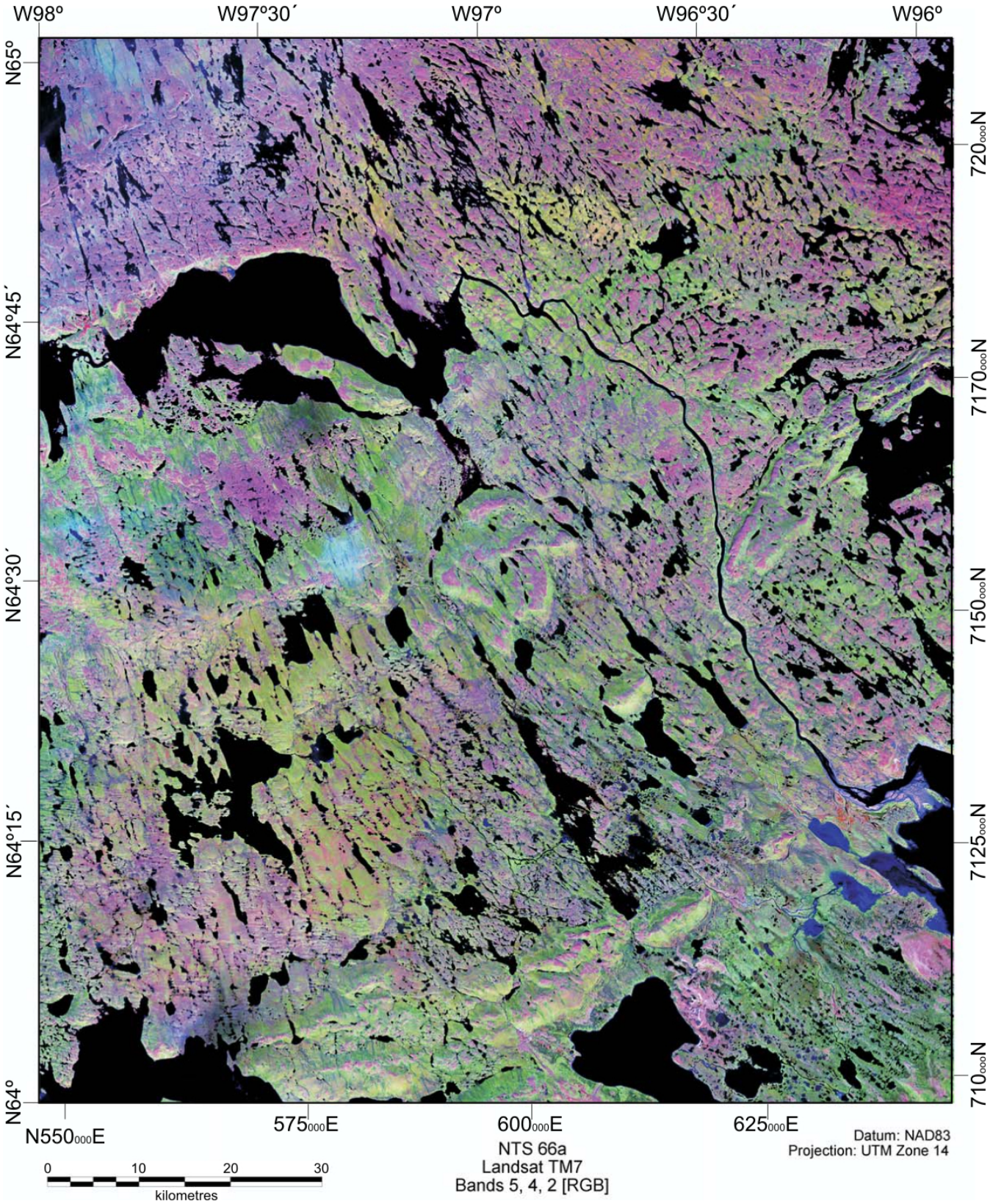

Figure CS7-6. LANDSAT TM7 false colour image of bands 5, 4, 2 (red, green, blue).

thin and thick till, and sand and gravel (Fig. CS7-8G).

However, there is very little difference in separation between the radar and LANDSAT TM data for bedrock and boulders. The best separation exists for boulders for both LANDSAT and radar data, organics for LANDSAT data, and thick till for LANDSAT data, all which have TD values in excess of 1.4 (Fig. CS7-8G), indicating moderate separation at best. Boulders also

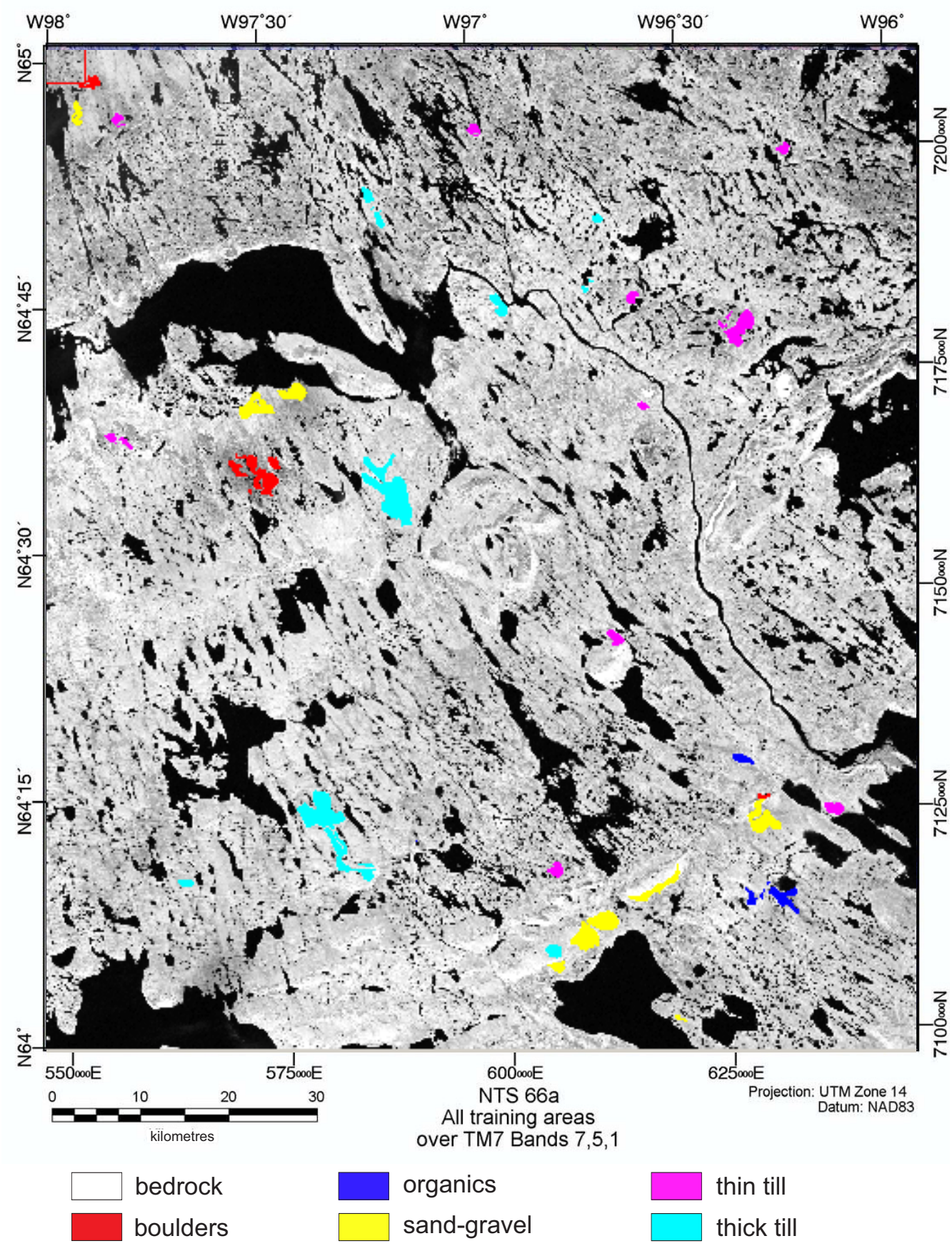

Figure CS7-10. Plot of classification accuracy based on a comparison of maps produced from LANDSAT, RADARSAT, and digital elevation model data versus training areas for each surficial unit (R – RADARSAT, L – LANDSAT, D – DEM).

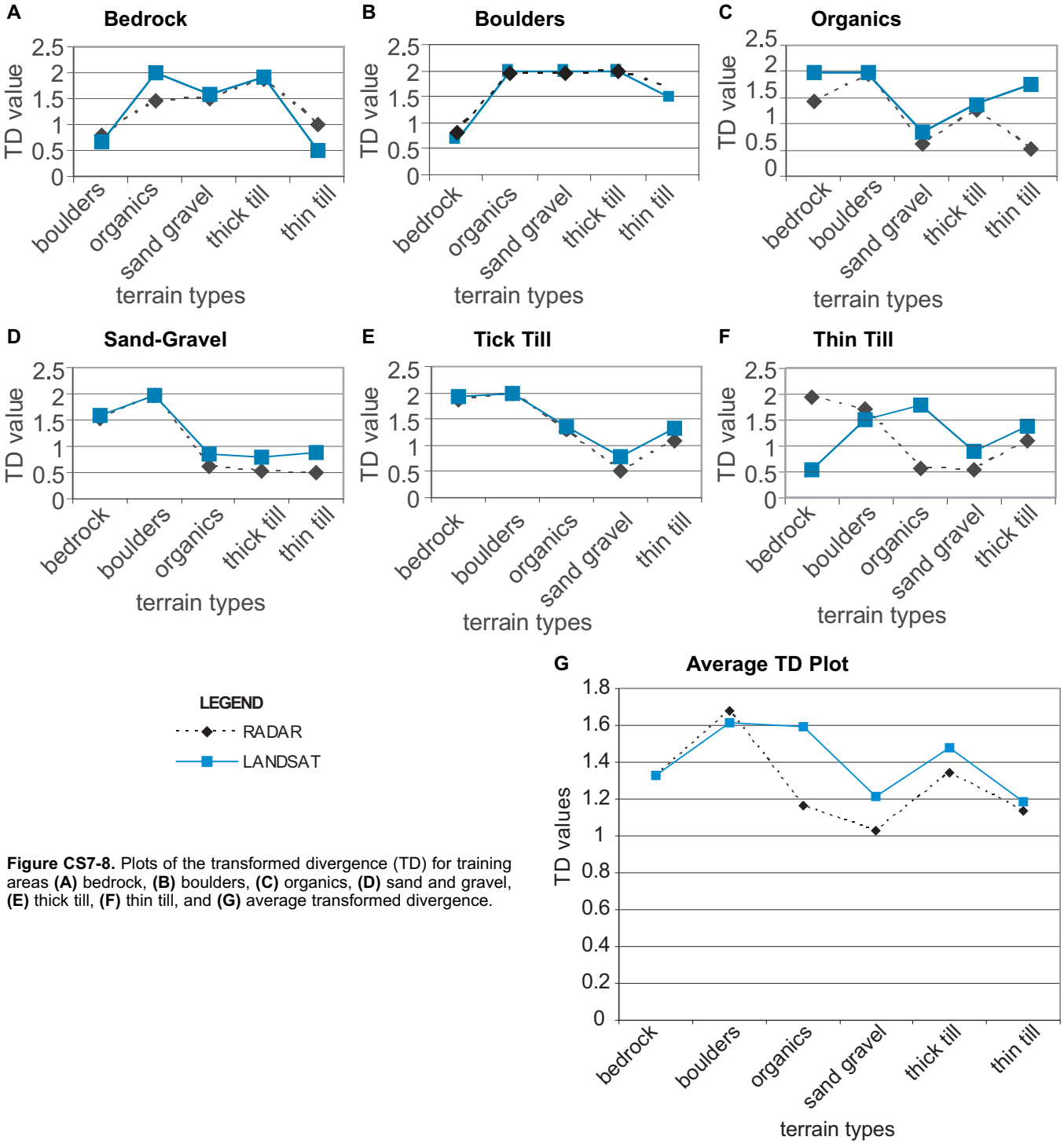

Figure CS7-8. Plots of the transformed divergence (TD) for training areas **(A)** bedrock, **(B)** boulders, **(C)** organics, **(D)** sand and gravel, **(E)** thick till, **(F)** thin till, and **(G)** average transformed divergence.

have moderate separation on both LANDSAT and radar (approximate TD values of 1.3) images. LANDSAT data offers slightly better discrimination for all units, except for boulders, which is nearly identical to radar data (Fig. CS7-8A-E), and generally much better separation of thin till units, except where bedrock and boulders are present (Fig. CS7-8F). Sand and gravel deposits are poorly separated from organic deposits, and thick and thin till on both the radar and LANDSAT (Fig. CS7-8D) images, as are areas of thin till from bedrock (LANDSAT images only), organics and sand and gravel (Radar images only) (Fig. CS7-8F). In summary, any values below 1 on the TD plots (Fig. CS7-8) indicate poor separation between surficial material types.

Classification Results

Figure CS7-9 presents the classifications based on LANDSAT (Fig. CS7-9A), radar (Fig. CS7-9B), LANDSAT and radar data (Fig. CS7-9C), and LAND-

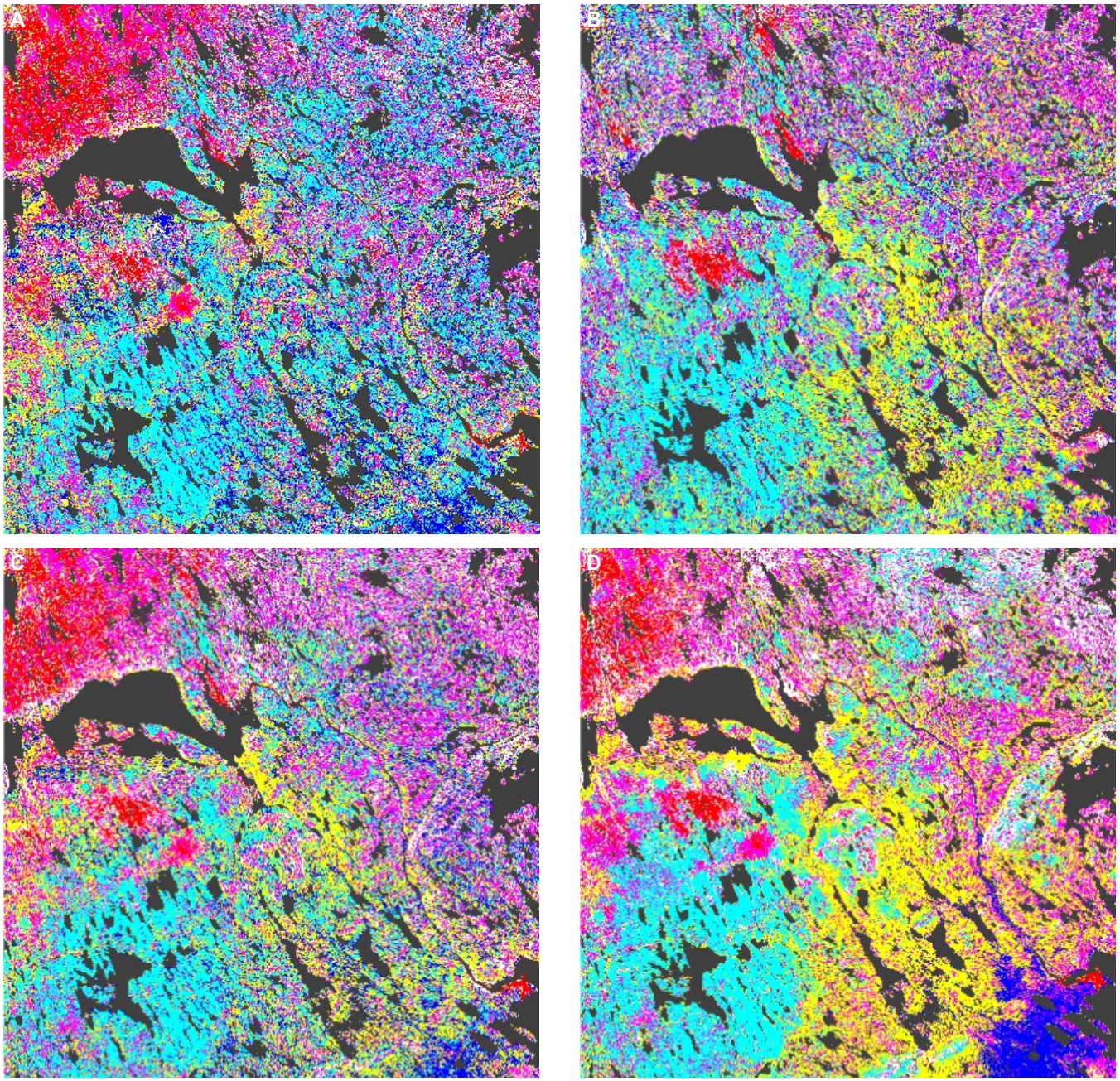

Figure CS7-9. Maximum likelihood classifications **(A)** LANDSAT, **(B)** RADARSAT, **(C)** LANDSAT and RADARSAT, and **(D)** LANDSAT, RADARSAT and digital elevation model data.

SAT, radar, and DEM data (Fig. CS7-9D). The maps are similar in appearance; however, a more quantitative measure, based on cross-tabulation of map categories, can be employed to assess their similarity. A summary of this analysis is presented in Table CS7-1.

Thick till shows the greatest agreement (46%) between the radar and LANDSAT maps, whereas the lowest is for organics (13%) and boulders (16%). The greatest similarity between the classified maps is between the radar/LANDSAT and radar/LANDSAT/DEM maps indicating that the DEM data contributes the least to the separation of surficial materials.

When the original training areas used for classifications are compared, the radar and LANDSAT data have similar accuracies (Table CS7-2), indicating that neither spectral nor roughness characteristics are sufficient to separate surficial materials. However, when both sensors are used for classification, a much higher accuracy (70%) is achieved and when elevation data (DEM) is included, the accuracy rises to almost 80%.

The surficial units that are poorly classified on LANDSAT include bedrock, sand-gravel, and thin till, whereas boulders, organics, and thick till are accurately classified using the training areas. Thick till and boulders are also reasonably accurately classified on the

Table CS7-1. Summary of the comparison (cross-tabulation) between classification maps shown in Figure CS7-9. The first number in each cell indicates per cent agreement and second number indicates kappa coefficient.

	RADARSAT	LANDSAT	RADARSAT + LANDSAT	RADARSAT + LANDSAT + DEM
RADARSAT		31.0 / .13	53 / .4	50 / .36
LANDSAT			62 / .52	51 / .39
RADARSAT + LANDSAT				72 / .64
RADARSAT + LANDSAT + DEM				

radar data, although organics are poorly classified. For both radar and LANDSAT data, confusion exists between boulders and bedrock. This might be expected based on spectral response (LANDSAT), as both of these categories would have similar spectra. There is less confusion between boulders and bedrock units on the radar data, as boulder fields would present a rougher surface to the radar than would bedrock areas. Organic areas are more accurately classified using spectral response (absorption due to wet soils) (i.e. LANDSAT), than by differences in surface roughness or secondary moisture (dielectric) responses. Thin till is not accurately classified on either the radar or LANDSAT maps; even when used together, at best they only classify thin till with slightly over 50% accuracy. This indicates that areas of thin till are heterogeneous from both a spectral and roughness perspective. Furthermore, the addition of elevation data to the LANDSAT data did not improve the classification accuracy, reflecting diversity in elevation underlying areas of thick till. Elevation data did, however, marginally improve the classification of outcrop, as these areas tend to occur in areas of higher elevation.

Cross-Validation of Training Areas

The three classifications using the three different sets of training areas are denoted as CV1, CV2, and CV3 in Table CS7-3. Of the three cross-validation classification procedures, CV2 appears to be the most accurate, with an accuracy of 86% when compared to the training areas used to perform the classification, followed by CV3 at 83%, and CV1 at 81%. The kappa coefficients are 0.81, 0.77, and 0.75 for CV2, 3, and 1, respectively. However, when each classification is compared to the check training areas (not used for producing the classified map), the accuracies are generally much lower (off-diagonal elements).

The average accuracy when comparing the classifications to the check areas is on the order of 70%. The average range in accuracy (lowest to highest accuracy for each row in Table CS7-3) is approximately 17%, thus representing the uncertainty in classification as a function of the variability in the signatures for the training areas. This suggests that the definition of training areas is critical in the classification process. The best accuracies are achieved with a subset of training areas (CV1 in Table CS7-3).

Table CS7-2. Summary of accuracies and kappa coefficients for maps shown in Figure CS7-9. The maps are compared to the original training areas used for the classification.

	% accuracy	kappa coefficients
RADARSAT	57.5	0.44
LANDSAT	51.1	0.44
RADARSAT+LANDSAT	70.3	0.61
RADARSAT+LANDSAT+DEM	79	0.71

These surficial materials show considerable overlap because of the gradational nature of their boundaries. A given pixel can have the potential to belong to several classes, but it is assigned to the class with the shortest Mahalanobis distance[1] in the maximum likelihood classification procedure. The use of the transformed divergence plots highlights where training areas overlap and caution should be applied when interpreting some of the classes.

DISCUSSION AND IMPLICATIONS FOR REMOTE PREDICTIVE MAPPING

The use of remotely sensed imagery for predictive mapping of surficial materials is enhanced by the integration of both RADARSAT and LANDSAT satellite imagery. It is important to note that a combination of surface roughness and spectral properties can better distinguish one type of surficial material from another than when one property is used alone. However, both radar and LANDSAT imagery show different measures of confusion. In this study, the radar imagery could not readily distinguish bedrock from thin till, whereas the optical imagery could not distinguish bedrock from boulder fields. In the former case, the roughness of bedrock is similar to the roughness of thin till, whereas in the latter case, the spectral properties of bedrock are very similar to those of boulder fields. The classifica-

Table CS7-3. Summary of the classification accuracy and kappa coefficients (in brackets) for cross-validation study.

	CV1	CV2	CV3
CV1	**81.4 (0.75)**	77.5 (0.63)	87.1 (0.79)
CV2	67.2 (0.56)	**86.3 (0.81)**	69.6 (0.6)
CV3	65.7 (0.55)	68.1 (0.51)	**83.6 (0.77)**

1. The Mahalanobis Distance (MD) is similar to the Euclidian distance between points in multi- (or N-) dimensional space, except that the MD takes into account the covariance among the variables in calculating distances. Thus the problems of scale and correlation inherent in Euclidian distance are no longer an issue (Richards, 1999).

tion of organic deposits using radar is confused with sand and gravel as well as thick till, all of which have similar surface roughness. LANDSAT is much better at classifying organic deposits based on the unique spectral response, which is a function of vegetation and high moisture content.

Both radar and LANDSAT imagery can successfully classify thick till because of its unique surface roughness and spectral properties (due to vegetation), which are quite distinct from the other materials. Classification by radar or by optical imagery often confuses thin till with bedrock and exposed thick till because of its variable surface roughness and spectral properties, which are similar in all three surficial types (thick till, thin till, bedrock), and most likely because it is very discontinuous in nature, and gradually merges with bedrock and thick till over a broad transition zone.

The combination of radar and optical imagery results in a more effective classification with less confusion and errors. Bedrock, boulder fields, organic deposits, and thick till have lower measures of confusion, and errors of omission and commission are decreased when the two image types are combined for classification. The distinction between sand and/or gravel and thin till was slightly improved relative to the separate use of radar and optical imagery.

The addition of the digital elevation model resulted in a higher classification rate. It appears, from the high classification scores for bedrock, boulders, thin till, and thick till, that the effect of elevation has some control over the location of specific materials. The textural and spectral properties of the materials are related to elevation in the following way. The areas of highest elevation are typically exposures of bedrock, which are unique in their spectral and textural properties. Materials between the upper limit of marine reworking and the exposure of bedrock display textures and spectral responses from organic, thick, and thin till materials. Materials below the upper limit of marine reworking have a similar spectral response to the materials above the marine limit, but a very distinctive texture that is the result of marine reworking.

Image classification in the Schultz Lake area (NTS 66A) has shown that RADARSAT-1 and LANDSAT TM7 imagery have the potential to classify certain surficial materials. Combining radar and optical imagery allows both roughness and spectral properties to be used for the classification of surficial materials, which results in classification accuracies that are higher than when each data type is used alone. Classification with RADARSAT-1 S1/S7 ascending/descending imagery, LANDSAT TM7 Bands 1, 2, 3, 4, 5, and 7, and a digital elevation model of the area results in different looking classification maps (Fig. CS7-9) and varying classification accuracies (Table CS7-2). The choice of training areas plays an important role in the supervised classification process. As shown in Table CS7-3, the variability in the training area polygon selection produces differences in classification accuracy. The pseudo cross-validation-like approach utilized in this study tests the validity of the training areas chosen for classification and allows for the assessment of the efficacy (uncertainty) of the classification based on the selected training areas (~5% in this study). The classification procedure presented in this study represents a method of mapping large areas where the surface roughness and spectral properties are distinctive. This approach facilitates the creation of maps where surficial materials can be predicted with a certain level of probability (uncertainty). These maps can be used to focus fieldwork or as first-order surficial material maps in areas where follow-up fieldwork is not possible.

Supervised classification of radar and LANDSAT data can provide the geologist with maps that can assist in field mapping activities, providing a unique 'first look' at the range of variability in the terrain and surficial cover throughout a study area.

REFERENCES

Aylsworth, J.M., Cunningham, C.M., and Shilts, W.W.
1990: Surficial Geology, Schultz Lake, District of Keewatin, Northwest Territories; Geological Survey of Canada, Preliminary Map 43-1989, scale 1:25,000.

Grunsky, E.C.
2002: The application of principal components analysis to multibeam RADARSAT-I satellite imagery: A tool for land cover and terrain mapping; Canadian Journal of Remote Sensing, v. 28, p. 758-769.

Grunsky, E.C., Harris, J.R., and McMartin, I.
2006: Predictive mapping of surficial materials, Schultz Lake area (NTS 66A), Nunavut, Canada, Geological Survey of Canada, Open File 5153, 1 DVD.

Hadlari, T., Rainbird, R.H., and Perhsson, S.J.
2004: Geology, Schultz Lake, Nunavut; Geological Survey of Canada, Open File 1839, scale 1:250,000.

McMartin, I. and Dredge, L.A.
2005: History of ice flow in the Schultz Lake (NTS 66A) and Wager Bay (NTS 56G) areas, Kivalliq Region, Nunavut; Geological Survey of Canada, Current Research 2005-B-2, 10 p.

McMartin, I., Dredge, L.A., and Robertson, L.
2005: Ice Flow Maps and Datasets: Schultz Lake (NTS 66A) and Wager Bay (NTS 56G) areas, Kivalliq Region, Nunavut; Geological Survey of Canada, Open File 4926, 1 CD-ROM.

Richards, J.A.
1999: Remote Sensing Digital Image Analysis; Springer-Verlag, Berlin, 240 p.

Richards, J.A. and Jia, X.
1999: Remote Sensing Digital Image Analysis, An Introduction; Springer-Verlag, New York. 3rd Edition, 363 p.

StatGraphics Software
2000: StatGraphics Plus 5.0; Manugistics Inc., Rockville, Maryland, USA.

CASE STUDY 8. Geological Mapping Derived from Topography

W.A. Morris, H. Ugalde, H. Slavinski, and K. Markham
Applied Geophysics Group, School of Geography and Earth Sciences, McMaster University, Hamilton, Ontario L8S 4K1
Corresponding author's email: morriswa@mcmaster.ca

ABSTRACT

A geological boundary is outlined by topography when the two lithologies meeting at the contact have contrasting physico-chemical characteristics. The topographic response of the contact is related to the differential response of the various rock types to local weathering activities. Local climatic conditions may either accentuate or retard the erosion of rock types.

Derivation of topographic information comes from three types of surveys: distance ranging, stereogrammetry, and interferometry. For each of the three types of surveys, there are variations in the methods with which data are acquired. One of the most critical issues concerns the acquisition format. If isolated elevation points are acquired, then computation of a representative Digital Elevation Model (DEM) necessitates a gridding algorithm and care must be exercised to understand the impact of the gridding. In contrast, when a swath of elevation points is acquired, the quality of the DEM is defined by the pixel resolution of the acquisition instrument.

Examples of the use of topographic mapping of geology are given for a) flat-lying strata (Cypress Hills, Alberta); b) regional-scale folded strata (Whitefish Falls, Ontario), and c) highly deformed gneiss terrain (Grenville Province, Key Harbour, Ontario).

INTRODUCTION

Complete outcrop exposure is rare in geologically extensive areas of the Earth's crust. During field mapping, the geologist records information about individual outcrops and then attempts to make a connection between the isolated observations.

The final geological map represents each geologist's individual interpretation of the connections between the isolated observations based on a set of geological principles that include factors such as lateral changes in bed thickness, the geometry of intrusions, and structural fold patterns.

To the field geologist, a geological contact, by definition, represents a laterally continuous boundary between two lithological units that have distinctive optical and mineralogical characteristics. These same two lithological units may also have quite different physical properties. This physical contrast is often reflected by a noticeable change in local topography. A prime example might be the simple juxtaposition of shale and limestone. In this situation, as seen in the Niagara Escarpment, the limestone produces resistive horizons having steep slopes, while the more easily eroded shale is associated with more gentle slopes. It is often common field practice for a geologist to follow a break in slope when searching for the possible continuation of a given lithological contact.

There are numerous factors controlling the topographic response of the Earth's surface. The chemical composition of the rock is described by Gilchrist's reaction series. Similar to Bowen's reaction series for crystallization, this series states that more mafic and felsic rocks are more susceptible to chemical degradation in the oxygenating environment of the Earth's surface. The grain size of crystals and the cementation within a rock also help to modulate the surface reaction rate. If individual crystals are bound together by cement, as occurs in most sediment, then both the chemistry of the cement and the composition of the regional fluids will be an important constraint on topography. The physical response of a rock is also controlled by its level of deformation. The presence of joints, faulting, or folding can increase the incursion of regional fluids and thereby increase erosion.

Overriding the physical and chemical attributes of the rocks is the nature of the weathering process. Detailed aspects of a topographic surface are highly dependent upon the local climatic conditions. Variations between areas of high rainfall and desert, cold and hot, humid and dry have a direct influence on the resulting geomorphology. The duration of exposure of a topographic surface is recorded in the amplitude of differences associated with lithological elements.

In summary, local topography is closely associated with lithological contrasts. However, it must be cautioned that in many cases the topography associated with bedrock geology can be masked by topography associated with the deposition of surficial materials. For example, there is an extensive literature on the use of topography for mapping glacial deposits.

This case study examines methods by which new high-resolution elevation data can be created. These techniques are methods used for interpolating Digital Elevation Models (DEMs) from contours, spot elevations, and hydrography and present a compilation of possible sources for topographic data. Finally, we pres-

Morris, W.A., Ugalde, H., Slavinski, H., and Markham, K., 2008, Geological mapping derived from topography, Case Study 8 *in* Remote Predictive Mapping: An Aid for Northern Mapping, (ed.) J. R. Harris; Geological Survey of Canada, Open File 5643, p. 245-259.

Table CS8-1. Sources of digital elevation data.

Resolution	DEM Source	Pixel Spacing	Horizontal Accuracy	Vertical Accuracy
LOW	GTOPO30	1 km		±30 m
	SRTM–C - Band	90 m	±20 m	16 m
	SRTM–X - Band	30 m	±20 m	16 m
MEDIUM	**STEREO**			
	SPOT	10 m	±15–20 m	5–15 m
	IRS	6 m	±20–25 m	10–30 m
	ASTER	15 m		15–25 m
	IKONOS	1m	±10 m	2–4 m
	RADARSAT Fine	6.25 m		10–25 m
	RADARSAT Std	25 m		10–35 m
	INTERFEROMETRY			
	ERS (Tandem)	23 m	±30 m	10–15 m
	Airborne			
HIGH	INTERFEROMETRY	1.25 m	±2 m	±0.5 m
	LIDAR	0.2–2.5 m	±0.3–2.5 m	±0.1–2 m
	PHOTOGRAMMETRY	0.1–0.2 m	±0.3–2.5 m	±0.07–0.1 m

ent three examples where topographic information has been used to derive geological mapping.

NEW DATA ACQUISITION

There are a number of possible procedures that one can use to generate topographic data sets. The spatial and elevation resolution of each of the methods is directly related to the individual data acquisition process (Table 1). Often this resolution sensitivity is reflected in the relative cost of the individual methods.

Distance Ranging

Distance ranging, the most direct form of elevation measurement, involves measuring the distance between the ground surface and some known observation point. The elevation of the surface is then defined in terms of the reference system for the observation platform. There are number of variants of this basic concept.

Geodetic Total Station

The topographic surface is defined using conventional surveying techniques. The observer records distances and angles between consecutive observation points. Changes in elevation are computed relative to the initial reference point. The starting point maybe a floating local reference point, in which case the resulting elevation file describes only the relative changes in topography within the survey area. Alternatively, the survey may be tied into a number of reference bench-marks, in which case the resulting topography is defined in the absolute terms of the reference base (datum and projection) that was used for the bench marks. The quality of the derived topographic information can be tested by looping back to previous survey points. Acquisition of each data point requires operator input, and the operator has to systematically move around the study area. Hence the density of observation points is controlled by the time commitment required to collect the data. While providing very high-resolution elevation information (at a scale of less than 1 cm), this technique is of limited applicability for regional-scale geological mapping.

Differential Global Positioning System

Global satellite positioning (GPS) has now become ubiquitous in all aspects of regional surveying. In this configuration, the elevation of an observation point is defined by reference to the time signal derived from a minimum of four (or more) satellites. The location of each observation point is defined by the intersection of the time signals from each of the satellites. Since time is equivalent to distance, the position of the observation point is defined in terms of the reference system used by the GPS satellites. Critical to this application is that the satellites have extremely stable orbits and that the time signal they emit be accurate. In differential GPS, two sensors (a base and a rover) are ideally recording time signals from identical satellites. Variations in the observed position of the base station are used to correct the position calculated for the rover. This may be achieved in real time by a radio linkage or satellite connection between the base and the rover, or during post-survey processing when data from the rover and base are merged in a single computer. In all cases, a GPS-derived definition of the elevation position of a point on the surface is more poorly controlled than its location. All of the satellites used in the computation are located above the observation point. In a worst case scenario, the only satellites that are visible to the observer may lie in one quadrant of the sky. The intersection point between common arcs from the satellites is therefore poorly constrained in elevation. In order to make use of Differential Global Positioning Systems (DGPSs) for ground-based surveying, it is necessary to use high-end GPS technology. Arial coverage is limited by mobility of the ground-based sensor (a person walking or the sensor mounted on a mobile platform). A more limiting factor is the requirement for a direct line-of-sight of the satellite. Depending on the location, this can be compromised by high-rise buildings, mountains, or dense vegetation. Practically this technology is limited to providing mapping at a centimetre-scale resolution of local areas. See Fix and Burt (1995) and Twigg (1998) for a further discussion of GPS-based topographic mapping.

Radar Altimetry

The position of an aircraft in flight is recorded by reference to a DGPS reference system, and the orientation of the sensor platform is defined by an inertial navigation package. The distance between the aircraft and a point on the ground is defined by a radar altimeter. The

elevation of the surface point can then be computed by combining the distance between surface and the height of the aircraft. A basic limitation of this method is the sensitivity associated with the radar signal, which normally would have a centimetre-scale wavelength. A second limitation is imposed by the pattern of the survey specifications. The elevation is recorded only at points over which the aircraft passes. When acquired as part of an aeromagnetic survey, this results in a series of observations along flight lines and orthogonal tie lines. The spacing of observation points along a flight line, the distance between adjacent flight lines, and the number and spacing of the tie lines are all predefined in the original survey specifications. The dimensions of the radar footprint on the Earth's surface, and therefore the elevation information integrated at one observation point, is dependent upon the separation between the aircraft and the surface. The lower an aircraft is flown, the smaller the radar footprint and the less positional error is associated with the estimated position of the observation point (Brenner et al., 1983). The presence of the cross-over points between the tie lines and the flight lines allows for an assessment of possible errors in the estimated topography. This technique has the ability to provide regional-scale elevation information with metre-scale resolution. Richardson (2000) has presented a discussion of the possible errors that one might expect with this type of approach.

Light Detection And Ranging (LiDAR)

The limited elevation resolution provided by radar altimetry can be overcome by reducing the wavelength of the output signal and by acquiring a swath of data points. LiDAR technology uses a high-frequency laser, typically of near infrared wavelength. Laser-emission rates can be varied from a few pulses per second to thousands of pulses per second. Typical raw laser point spacing on the ground, ranges from 2 to 4 m. LiDAR data acquisition is centred on vertical, with symmetrical scans of varying magnitude. Scan angles are often restricted within plus or minus 20 degrees of vertical. The advantage of near-vertical viewing is that there is limited positional distortion in the location of an observation point. The size of a surface point illuminated by LiDAR is dependent upon the elevation of the aircraft, but typically is between 10 and 100 cm. The resulting data set of a LiDAR survey is an irregular or semi-regular grid of x, y, z coordinates. There is no integration of information between adjacent observation points. In areas of rapid topographic change, such as a cliff face or mine pit wall, LiDAR will provide a detailed rendition of the sharp topographic edges. Typical elevation resolution provided by LiDAR-based systems is a vertical accuracy of ±0.25 m and a horizontal accuracy of ±0.50 m.

The LiDAR signal reflects back to the detector from all objects located in the beam path. Where trees are present, it is possible to have multiple returns from the canopy and then eventually from the bare earth surface. Editing of the data file can differentiate between areas dominated by vegetation, thereby giving a Digital Terrain Model (DTM). In such situations, the bare earth, or Digital Elevation Model (DEM), would be interpolated from the information collected between patches of vegetation. For a more detailed discussion of the use LiDAR see Baltsavias (1999), Flood (1999), Wehr and Lohr (1999), and Toth et al. (2001).

Stereogrammetry

Our binocular vision gives us the ability to estimate the distance from an observed object. Fundamental to this capability is the parallax created by having two views of the same object produced by two sensors having a known spatial separation. Estimation of the relative elevation of a point is derived from a computation of the similarity between regions in a stereo pair of images. The displacement of the location of an object between adjacent images is a direct estimate of elevation. Therefore any remote sensing package that is capable of acquiring multiple images of the same point from different view angles can be used for stereogrammetry. Possible sensors include: aerial photography, optical satellite imagery (SPOT, IRS, ASTER, IKONOS, or ALOS) and radar (RADARSAT). Since the calculation of elevation is dependent on the comparison of pixels, the capability of this approach to produce high-resolution topographic data is dependent upon the pixel (spatial) resolution of the original imagery. Elevation resolution ranges from submetre capability with high-quality aerial photography to 10 m resolution with SPOT imagery. The quality of the DEM that can be produced by stereogrammetry depends on four factors:

1) Matching accuracy. In addition to simple pixel resolution, this also includes careful assessment of similarity between adjacent scenes. It also requires distinctive features within the scene to have sharp edges. If most of scene contains gradational changes between objects, there is a consequential degradation in the ability to accurately obtain an optimum pixel match.

2) Parallax angle. If views are taken from very similar orientations, then there will be limited parallax produced. Increased angular separation will result in increased elevation resolution.

3) Geometric model accuracy. To convert the observed relative height differentials to absolute orientation, it is necessary to have accurate information regarding the position of the sensor pack-

age at the time of data acquisition. Further, when using ground control points for calibration, there needs to be an adequate range and distribution of known elevation points.

4) Terrain or slope effects. Viewing an object from an off-nadir viewpoint produces foreshortening or, in the worst-case scenario, layover of the image. The severity of this problem depends on the relationship between the depression angle of the sensor and the slope of the topographic surface.

A number of companies offer software packages capable of calculating a DEM from stereo-image pairs; these include PCI Ortho Engine, Atlantis Stereo DEM, and ENVI topographic module. Like most other techniques based on satellite or airborne imagery, this method has the advantage of providing broad spatial coverage. But for defining the bare earth DEM, this is limited to only those areas not covered by dense vegetation. It is only possible to obtain the high-resolution sensitivity promised by aerial photography in regions with little ground cover and where there aren't many discrete, distinctive features within the image. See Ackermann (1978), Day and Muller (1988), Lemmens (1988), Sasowsky et al. (1992), Welch et al. (1998), and Toutin (2002) for a further discussion of stereogrammetry.

Radar Interferometry

Interferometry-based elevation estimates are also derived from two radar images over the same surface. However for interferometry, one uses data acquired from similar view directions: the baseline or distance between the two images is relatively small. In Interferometric Synthetic Aperture Radar (IfSAR or InSAR), two antennas are housed in the same aircraft. For the Shuttle Radar Topography Mission (SRTM), the second antenna was mounted on a retractable boom (Farr and Kobrick, 2000). Satellite applications of interferometry (InSAR) use either two passes of the same satellite (Radarsat), or one pass of two similar satellites (ERS-1 and ERS-2). In all cases, the sensor package acquires side-looking (off-nadir) imagery. The operating principle behind interferometry involves a comparison of the travel time between the same points on the two images. If the position and orientation of the sensor package is accurately known then the target height is easily calculated from simple trigonometric principles. Specific to interferometry is use of the phase of the output signal. The path difference, and hence indirectly height, is computed from the phase difference between the wave fronts received sequentially at the two antennas. Because the phase difference can only have a value between 0 and 2, there is a repeating cyclicity across the image, commonly termed an interferogram. Elevation information is extracted after the application of a 'phase unwrapping' technique (Goldstein et al., 1988). Simultaneous to the generation of the interferogram, most packages also generate a coherence diagram that compares the amplitude of radar response from the two images. Poor reflectors, such as water surfaces, commonly produce poor coherence images, which in turn correspond to poorly defined topographic information. Spatial and elevation resolution is dependent on the beam mode, incidence angle, and wavelength of the radar beam. Spot imagery with a pixel spacing of 10 m is capable of producing 10 m elevation resolution, while ERS satellite (Tandem pairs) with a pixel resolution of 23 m is capable of producing 15 m elevation resolution. Essential to proper rendering of interferometry-derived topography is the availability of ground calibration bench marks. Seymour and Cumming (2004) have suggested that by using previously acquired low-resolution DEM data (from stereogrammetry or distance ranging), it is possible to achieve a marked improvement in the accuracy of the final topographic image. An advantage of the longer radar wavelengths used by InSAR is that the signal can penetrate cloud and haze. InSAR produces a regular grid of elevation points With the calculated elevation at each observation point representing the summation of all responses from the footprint of the output beam. The image is therefore a smoothed representation of the overall topographic surface. References outlining procedures used in interferometry include Goldstein et al. (1988) and Gray and Farris-Manning (1993). Massonnet and Feigl (1998) provide both a background to interferometry and a broad range of geological applications of the technique for detecting regional-scale changes in topography. Norheim et al. (2002) report a comparison between LiDAR and InSAR DEMs using a dense network of ground control points. As might be expected, the two methods exhibited greater difference with increasing slope. Perhaps more surprising is the difference between north- and south-facing slopes, where the sense of the difference between the two techniques is reversed. Compared to the ground control points, InSAR exhibited a greater mean error than LiDAR, and a significantly larger standard deviation.

TOOLS FOR INTERPOLATING DIGITAL ELEVATION MODELS

The data-acquisition procedures outlined above are capable of generating topographic information with three data structures: regular grids, isolated and/or clusters of data points, and contours. Conversion from one data format to another format generally involves some form of interpolation. There are an infinite number of interpolation procedures to produce regular square grids from distributed observation points. Each

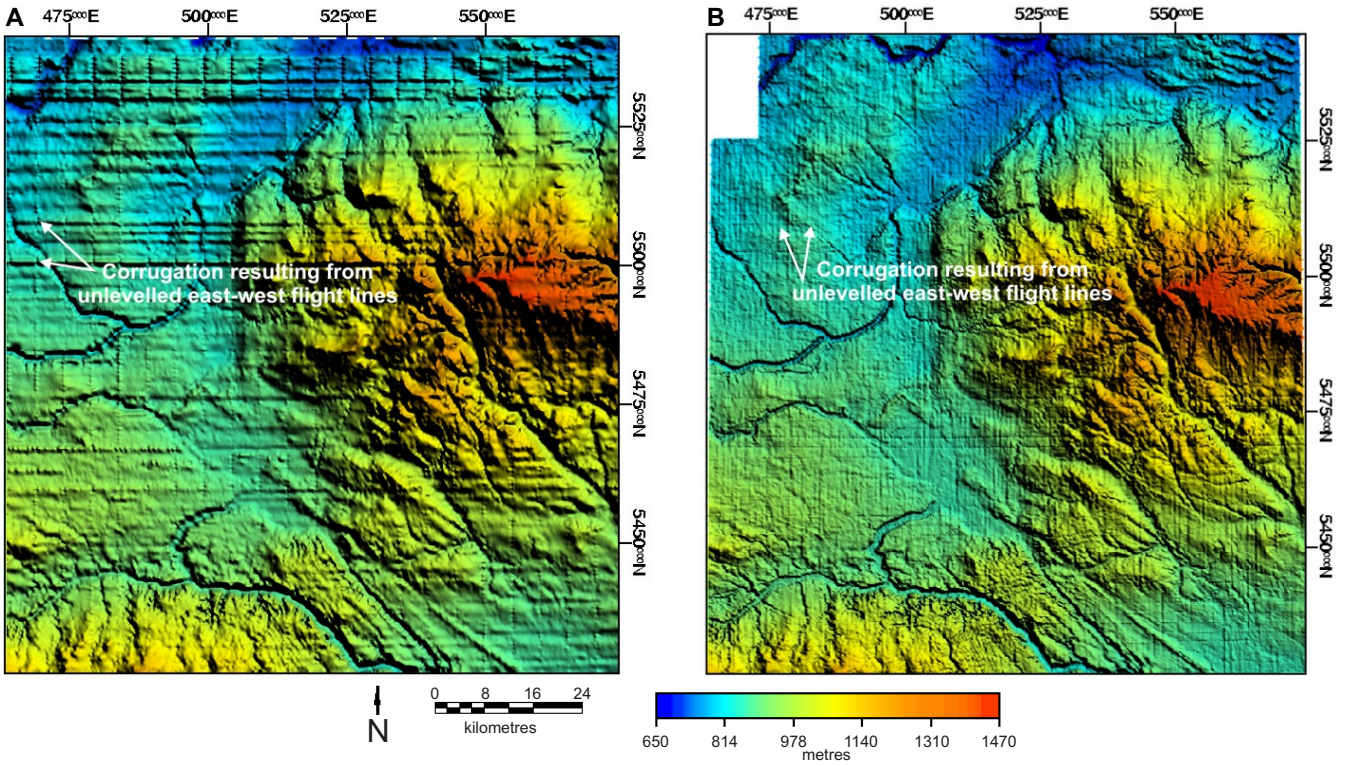

Figure CS8-1. Raw topographic image derived from radar altimeter information acquired during aeromagnetic surveys of the Cypress Hills area, southern Alberta. **(A)** Survey CYP-92 was flown using east-west flight lines and north-south tie lines. Note the coarse east-west lineaments and more widely spaced north-south lines, which indicates problems with line-to-line leveling of the data. Along the northern portion of the image, one block is consistently high. **(B)** Survey CYP-97 was flown using north-south flight lines and east-west tie lines. The spacing of both the flight lines and tie lines is much smaller than was used for survey CYP-92. The amplitude of the corrugations is much less, indicating a significant improvement in GPS technology.

approach applies some form of bias to the resulting image. General data-contouring packages such as SURFER provide at least six different weighting schemes for calculating the elevation of at specific pixel point. In order of increasing complexity, these procedures include simple distance-based weighting schemes, minimum curvature surface fitting, and geostatistical kriging-based approaches. There are a large number of software packages that can be used to generate square-grid DEMs. Included in this list are packages such as Surfer, Oasis Montaj, ESRI Arc-Info, and GlobalMapper. Most of the common remote sensing packages, such as ENVI, ER Mapper, and PCI Geomatica, also include contour-generating routines. When not focussed on generating a uniformly spaced sample grid, triangulated irregular networks (TINs) have been used to produce a faceted image of the spatial variations of topography.

All standard gridding procedures have a number of inherent problems fully representing the nature of topographic change. First, through the selection of a grid cell size, the operator is limiting the spatial resolution of the topographic image. Second, generalized gridding packages fail to accommodate some of the more important details of topographic surfaces, such as the existence of an abrupt discontinuity that might represent a cliff or an eroded escarpment (e.g. the Niagara Escarpment). Third, a river channel forms a distinct niche in the form of the topography. Failure to incorporate information derived from stream pathways will generate a smoother topographic surface than is truly present. Some software packages, MicroDEM and specifically ANUDEM (the earlier version of which is called by the TOPOGRID command in Arc-Info), include routines for incorporating stream line information.

The presence of errors in DEMs has been extensively reviewed by Wilson and Gallant (2000, p. 15). As noted by Wilson and Gallant (op. cit.) any errors in either the original data or created through the process of gridding are accentuated once one calculates topographic attributes based on second-order derivatives. For hydrological flow pathway analysis, the creation of a localized depression in the topographic surface could have serious ramifications. For geological mapping, this may be inconsequential. There is clearly a need to associate the nature of the gridding and analysis process with the required spatial and elevation resolution of the final image. When looking at regional-scale topographic data, it is inappropriate to be attaching any significance to small elevation changes.

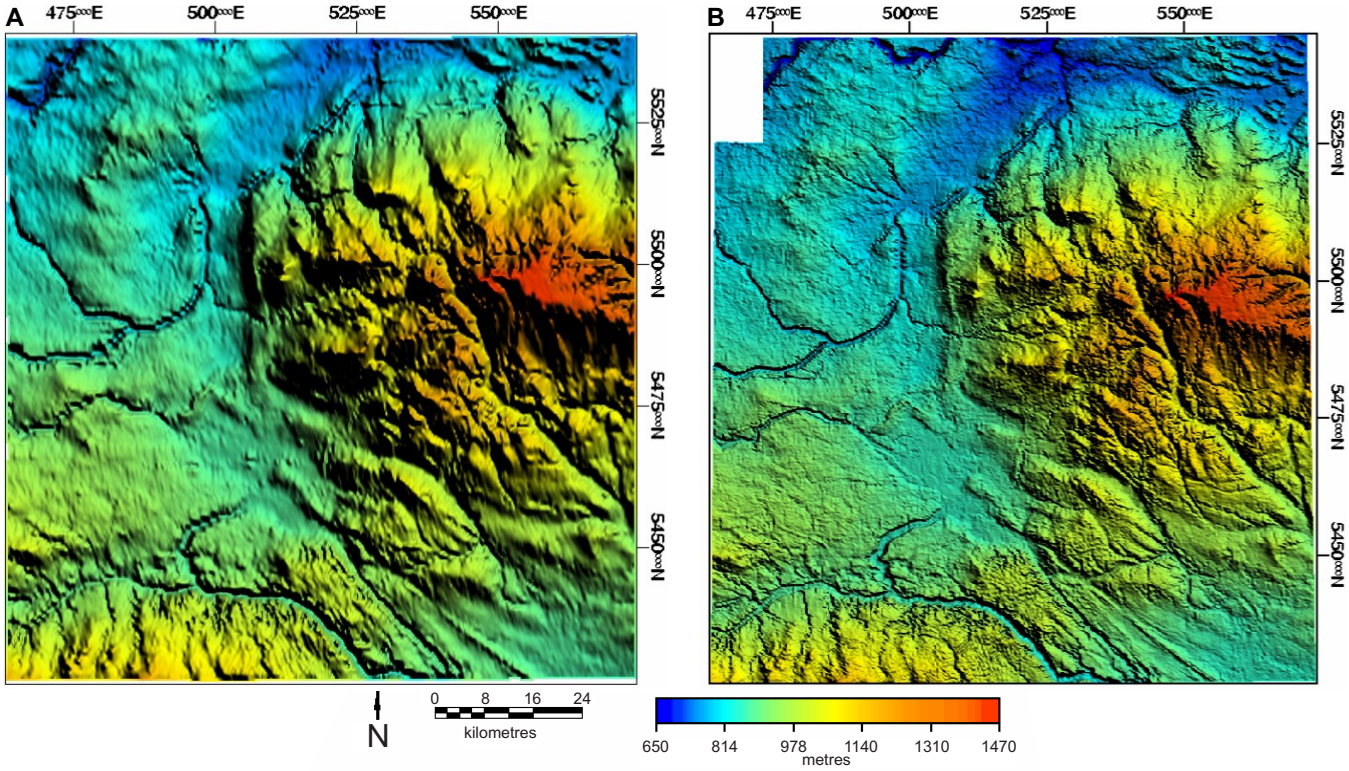

Figure CS8-2. Digital Elevation Models (DEMs) produced from topographic data using the Geosoft minimum curvature algorithm. **(A)** Topographic data supplied by Canadian Digital Elevation Database. Note the flat surfaces in areas of low topographic change. **(B)** Topographic data derived from the combination of aeromagnetic surveys CYP-92 and CYP-97. Radar altimetry data from the two surveys have been leveled to a common reference base that is tied to benchmarks and microlevelled to remove discrepancies between flight and tie lines.

EXAMPLES OF TOPOGRAPHY-DERIVED GEOLOGICAL MAPPING

Flat-Lying Strata

The Cypress Hills' area of southern Alberta is formed by a near flat-lying sequence of Cretaceous sediments consisting of sandstone with intervening carbonate and shale (Westgate, 1968). Edges between individual strata define sharp changes in the topographic slope, which are readily apparent in LANDSAT imagery. Crosscutting the region is a number of major northwest-trending faults. Two aeromagnetic surveys have been flown over this area. During both of these surveys both radar altimeter and barometer data were recorded, in addition to the standard total field magnetic data. The first survey, flown in 1992, had flight specifications of 800 m spaced east-west flight lines, 5000 m spaced tie lines, and a ground-clearance height of 150 m (Fig. CS8-1A). The second survey, flown in 1997, had flight specifications of 400 m spaced north-south flight lines, 2400 m spaced east-west tie lines, and a mean flight height of 120 m (Fig. CS8-1B). Both data sets covered a similar area but none of the individual flight lines completely overlapped. As a consequence of the orthogonal survey pattern, there are, however, a large number of cross-over points between flight paths within an individual survey and between the two surveys. Since the surveys covered the same area, there should be no difference between the calculated elevations at the cross-over points. Using the elevation differences observed at these cross-over points, we applied a levelling approach to bring the data from each of the surveys to a common base. Two types of errors were observed: 1) 'static' errors that produce constant differences throughout the survey, and 2) 'dynamic' errors that produce time, and therefore location-dependent shifts through the data. Static errors can be explained by factors such as differential location of radar altimeter and GPS in the aircraft between surveys. The dynamic errors reflect variations associated with aircraft movement and attitude, and errors associated with either the GPS and/or radar altimeter. It is noted that the 1992 survey shows higher variance than the 1997 survey, reflecting a marked improvement in GPS sensor technology. The resulting combined data set was gridded using a minimum curvature algorithm with a grid cell spacing of 50 m (Fig. CS8-2B). A final calibration of the data was achieved by comparison of the generated grid with 250 ground control points. The root mean square error between the ground control points and the equivalent points on the calculated DEM grid was 5.2 m.

The resulting DEM grid contains more detail than that provided by the equivalent grid derived from the

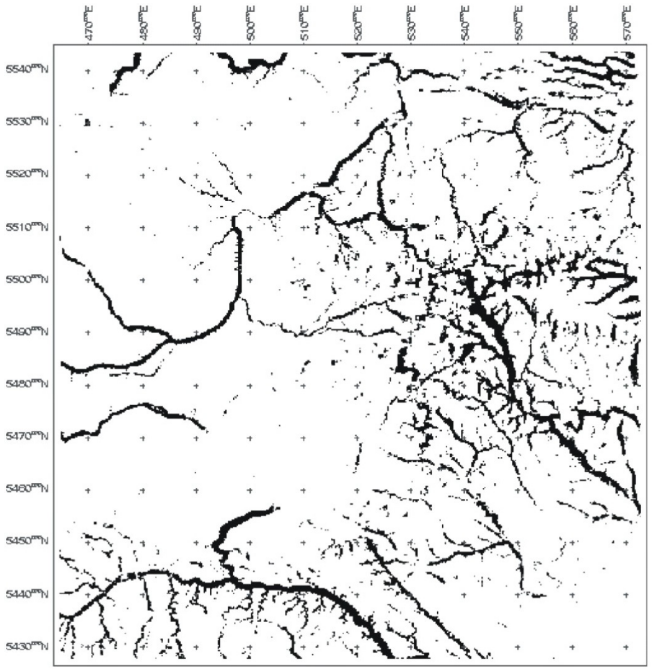

Figure CS8-3. Map of topographic incisions, which are regions where the topographic surface is locally below the regional surface. The image was created by gridding topographic data with a coarse and a fine grid cell size and then subtracting the data from the coarse grid from the data from the fine grid. Possible fault lines are identified in grey.

Canadian Digital Elevation Data Base (Fig. CS8-2A). This is not surprising since the aeromagnetic-survey-derived grid has a higher sampling density and a significantly improved elevation resolution. To extract geological information from this topographic image, we made a number of simple assumptions. Firstly, the issue of locating faults was addressed. It is generally recognized that the presence of a fault will be accentuated by erosional processes. The increased fracturing associated with the fault increases the weathering rate. Therefore in seeking a fault, we areas of increased localized erosion should be identified. This was achieved by using a differential gridding scheme. The DEM was gridded using two different grid-cell sizes. Using the minimum curvature approach, coarser grid-cell size will average out local features and produce a smooth surface while the smaller grid-cell size will show the small-scale features. Subtracting the coarse (regional) grid from the fine (local) grid accentuates local topographic deviations. By highlighting only the negative deviations, the presence of enhanced erosional features is accentuated. The resulting image contains a natural dendritic drainage pattern overlain be a series of northwest-southeast-oriented fault-induced linear drainage patterns (Fig. CS8-3). More mathematically rigorous approaches to lineament detection have been proposed (Wang and Howarth, 1990; Jordan and Schott, 2005) but a simplified approach has been used for the purposes of this demonstration.

Secondly, the issue of locating geological contacts was addressed. As noted earlier, in this area lithological contacts are primarily associated with changes in resistance to erosion, i.e., sandstone adjacent to shale. This type of contact is defined by a sharp inflection in topography. Hence a simplistic approach to finding a lithological contact would be to isolate localized inflec-

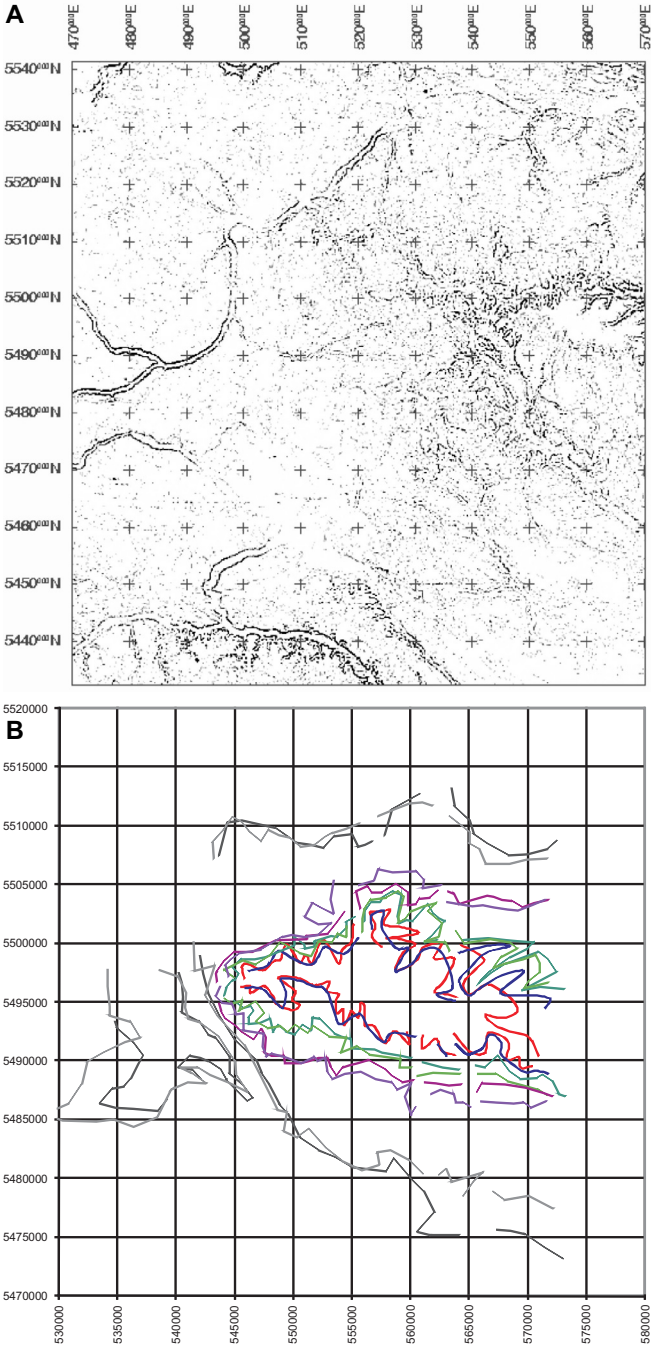

Figure CS8-4. (A) Inferred geological contacts were derived from inflexions in the topographic slope. The inflexion points were derived by gridding the topographic slope with a coarse and a fine grid cell size and then subtracting the data from the coarse grid from the data from the fine grid. The edges of the incised river channels are strongly outlined. **(B)** Comparison of geological contacts, which were derived from topography, with the lithological contacts, which were mapped in the field by Westgate (1988).

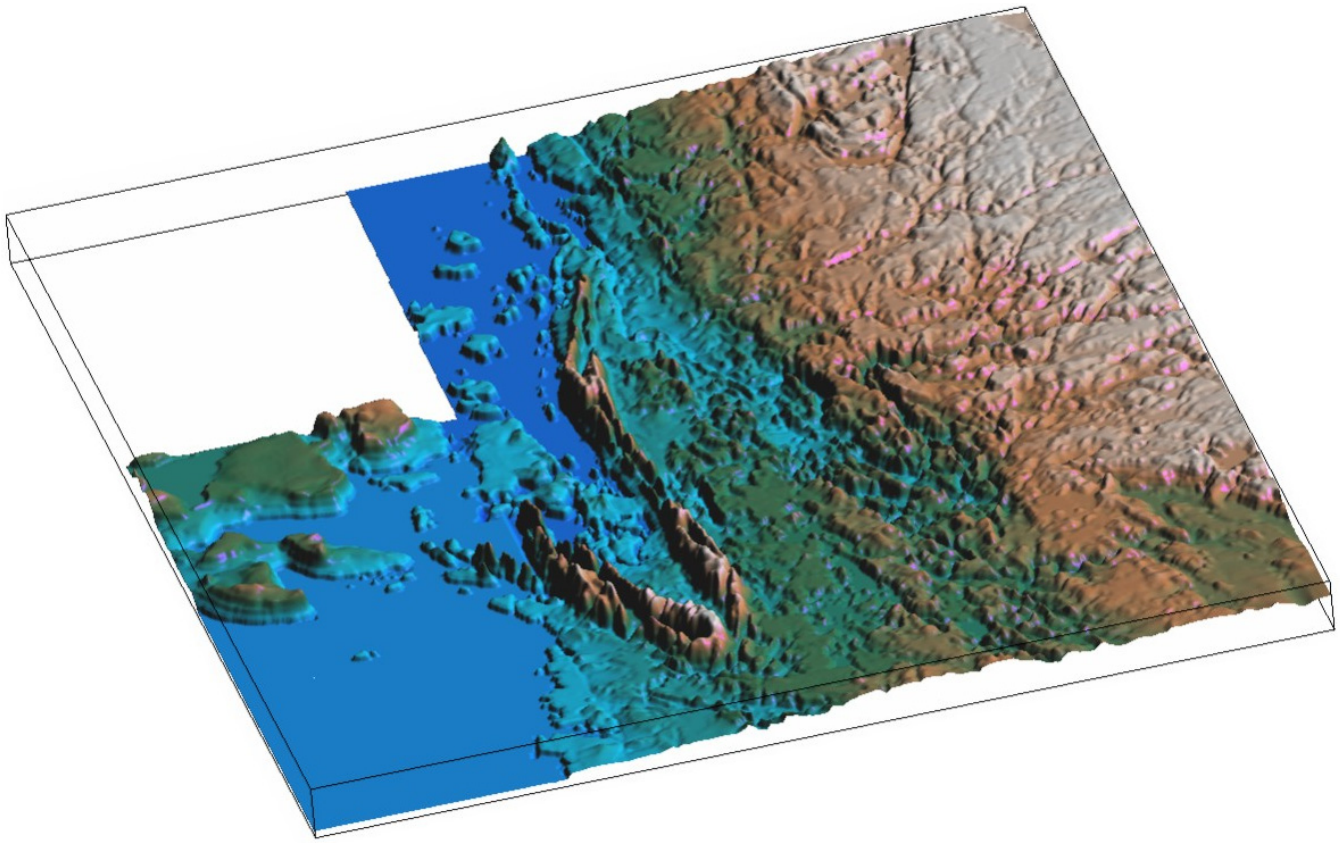

Figure CS8-5. Three-dimensional representation of the topographic surface along the north shore of Lake Huron. Data used in the compilation were derived from 50,000 topographic map sheets. The DEM surface was created using the Geosoft minimum curvature algorithm. The Lorrain Quartzite forms a pair of prominent ridges that correspond to a regional-scale fold structure.

tion points. This was achieved by comparing the local topographic slope gridded at coarse and fine grid-cell sizes (Fig. CS8-4A). Again subtracting the two grids accentuates inflection points having a smaller radius of curvature than apparent in the coarse-scale grid (Fig. CS8-4A). Much of the low land in the study area is masked by thick glacial sediment. In these areas, this process provides no information on the nature of the bedrock. However, in the upland area of the Cypress Hills, which is dominated by bedrock outcrops, the resulting technique provides a very close approximation to the geological contacts (Fig. CS8-4B) as mapped by Westgate (1968). Overlying fault patterns on these contacts serves to further emphasize the close similarity between the geology derived from this analysis of topographic variations and that reported by Westgate (1968) from a number of field mapping seasons. It must be stated however, that while this technique has located contacts and faults, it provides no information regarding the actual lithologies present.

Folded Strata

On the north shore of Lake Huron is a thick sequence of sedimentary rocks, the Huronian Supergroup, that was deposited in a shallow marine environment between 2100 and 2500 Ma. Each subgroup within the Supergroup contains a repeated sequence of sedimentary units, commonly with coarse-grained sandstone at the base and conglomerate at the top. Separating the groups are unconformities or disconformities. Following deposition, the sediments have been undergone three distinct periods of deformation. The earliest orogenic event in this region deformed the sediments into a series of broad folds with east-west-trending axes. Incremental deformation during the period from 2100 to 1250 Ma lead to fault reactivation and localized shear zone development. During the Wisconsinian glaciations, the north shore of Lake Huron was extensively glaciated, resulting in physical denudation of the Huronian sediments. High-frequency topographic forms (e.g. P-forms, roche mountonnées) produced by the glacial erosion are abundant on an outcrop scale, but are not visible on the larger scale topographic maps. Differential rates of erosion, due to compositional differences between individual stratigraphic units, have resulted in the topography that we see today. Units that are more resistant to erosion, such as the coarse-grained quartz-rich Lorrain Quartzite, now form topographic highs. Less competent units, such as the Gowganda argillite, have been eroded down into topographic lows.

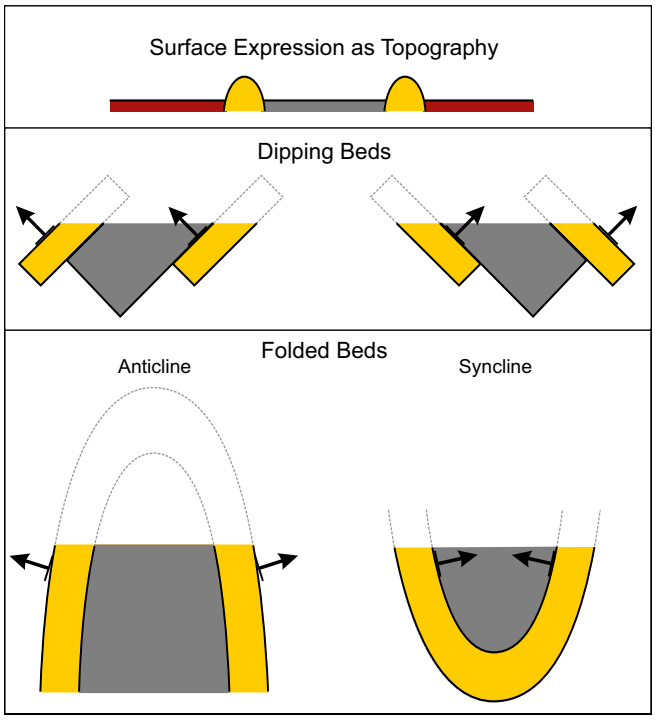

Figure CS8-6. On the basis of the topographic data alone, it is not possible to discriminate between four different geological models: beds dipping to the north, beds dipping to the south, an anticline, or a syncline. The difference between each of these models is defined by the facing directions.

Topographic data for this region was derived from the Ontario topographic data base. For these regions, the original topographic data was calculated from stereo-photogrammatic analyses of multiple aerial photographs. Calibration of the aerial photography-derived topography to an absolute reference frame was achieved through the application of ground control points. The data used in the generation of the topographic surface were point information, which have an elevation resolution of 10 m and spacing between observation points of 100 m. This data set was gridded using a Geosoft minimum-curvature gridding algorithm to generate an estimate of the regional topographic surface.

The resulting topographic image shows a broad curve dominated by the highly resistant Lorrain Quartzite, which appears to conform to that of a fold plunging to the east (Fig. CS8-5). Looking in detail, the broad curve appears to comprise two parallel tracks that converge towards the fold nose. Using topographic data alone, there are many possible geometrical interpretations that could explain this fold-like pattern. In the absence of any evidence concerning facing direction or bedding dip within the sedimentary units, it is not possible to determine if the broad-scale fold feature represents a syncline or an anticline. Further, the relationship between the two parallel ridges can be explained by either two parallel layers separated by a thin, more erosive horizon or a tight fold structure (Fig. CS8-6). As the original topography was derived from high-resolution aerial photography, more information would be needed to resolve the fold structure.

In a similar situation, Banerjee and Mitra (2004) used the aerial photography to identify the location of bedding-plane surfaces within their topographic image. Then by determining the elevation of three points on that bedding-plane surface, they were able to obtain a local estimate of the dip and dip direction of the sedimentary layers. Following the method proposed by Banerjee and Mitra (2004), a georeferenced aerial photo mosaic was compiled over the area covered by

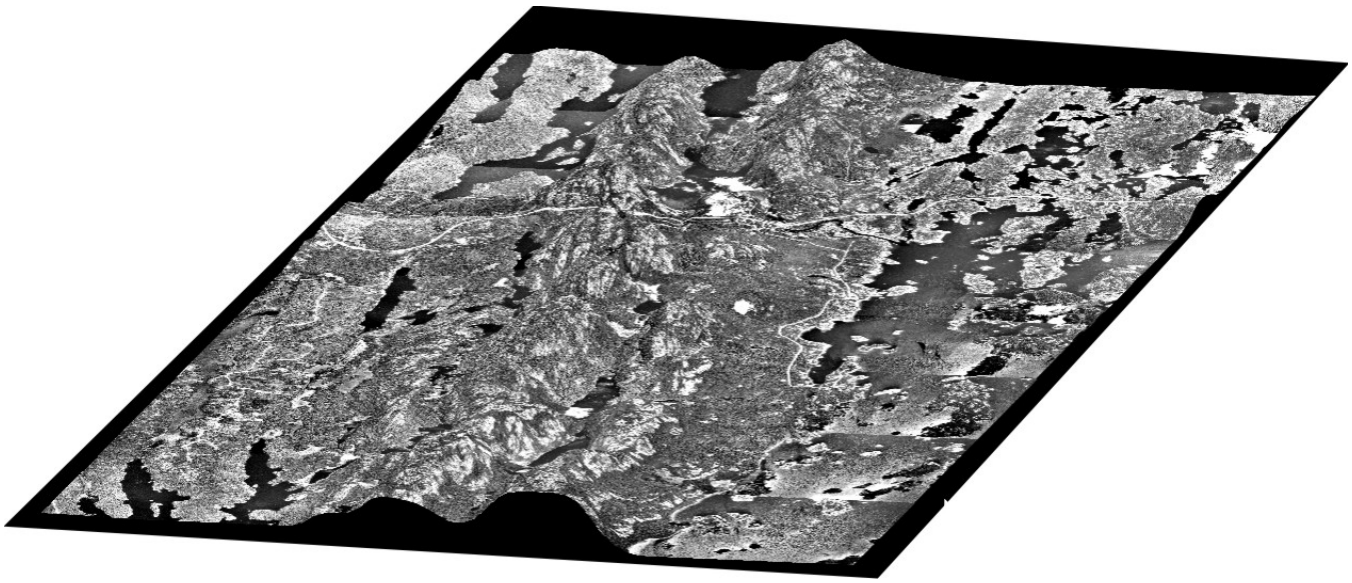

Figure CS8-7. The north shore of Lake Huron as viewed from the west. In order to investigate the evidence for facing direction, an airphoto mosaic was constructed. Each air photograph was initially georeferenced to an IKONOS image that used the same datum and projection as the topographic data DEM. Individual photos in the mosaic were balanced, leveled, and stitched. Discrepancies remain over water bodies. The final mosaic was orthorectified to the topographic surface.

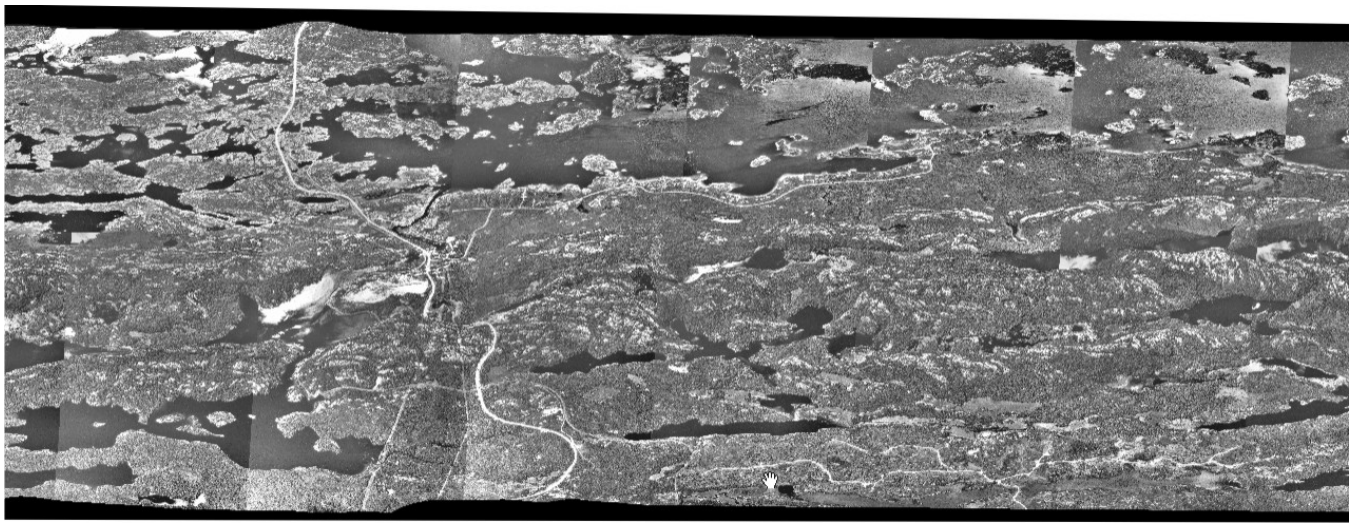

Figure CS8-8. The north shore of Lake Huron as viewed from the north, looking down dip of the northern ridge of the Lorrain Quartzite. The calculated DEM has insufficient resolution to be able to locate individual bedding-plane surfaces. Details of crosscutting bedding-plane structures show that for this ridge the facing direction is to the south.

the topography. Each aerial photograph was georeferenced to an IKONOS image that was supplied in a georeferenced format. As a final step the resulting aerial photo-mosaic was orthorectified onto the topographic surface to produce a three-dimensional rendition of the surface of the Lorraine Quartzite (Fig. CS8-7).

Unfortunately the topographic data used in this exercise had insufficient spatial and elevation resolution to identify any bedding plane surfaces. Further, the intense glaciation experienced by this area has also lead to rounding off of individual outcrops. In the absence of direct bedding-plane measurements, one must use other approaches to determining facing direction. All sedimentary rock units contain sedimentary structures related to the original mode of deposition. Many of these features are found on the scale of a single outcrop and hence beyond the resolution of the photographic imagery. Some features, such as erosional channels, large-scale cross-bedding, and unconformable surfaces, occur on a scale that will be visible in photographic imagery. In this instance, draping the aerial photography over the calculated DEM reveals the presence of a number of erosional channel surfaces and large-scale bedforms (Figs. CS8-8, CS8-9). From this imagery, it can be shown that the parallel tracks associated with the northern limb of the broad-scale fold actually represent a shallow tight synclinal structure (Fig. CS8-10). From this it follows that the broad fold must be an open plunging anticline and the southern parallel tracks represent another tight shallow syn-

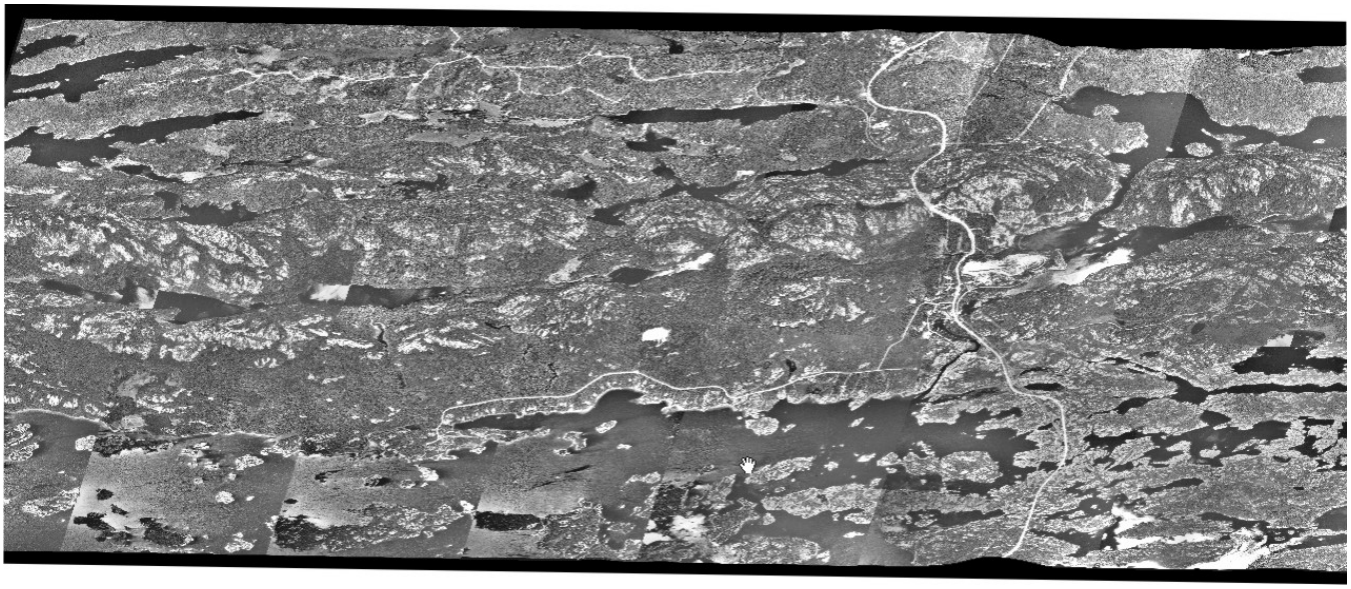

Figure CS8-9. The view of the north shore of Lake Huron taken from the south, looking down dip of the southern ridge of the Lorrain Quartzite. The calculated DEM has insufficient resolution to be able to locate individual bedding-plane surfaces. Details of cross-cutting bedding-plane structures show that for this ridge the facing direction is to the north.

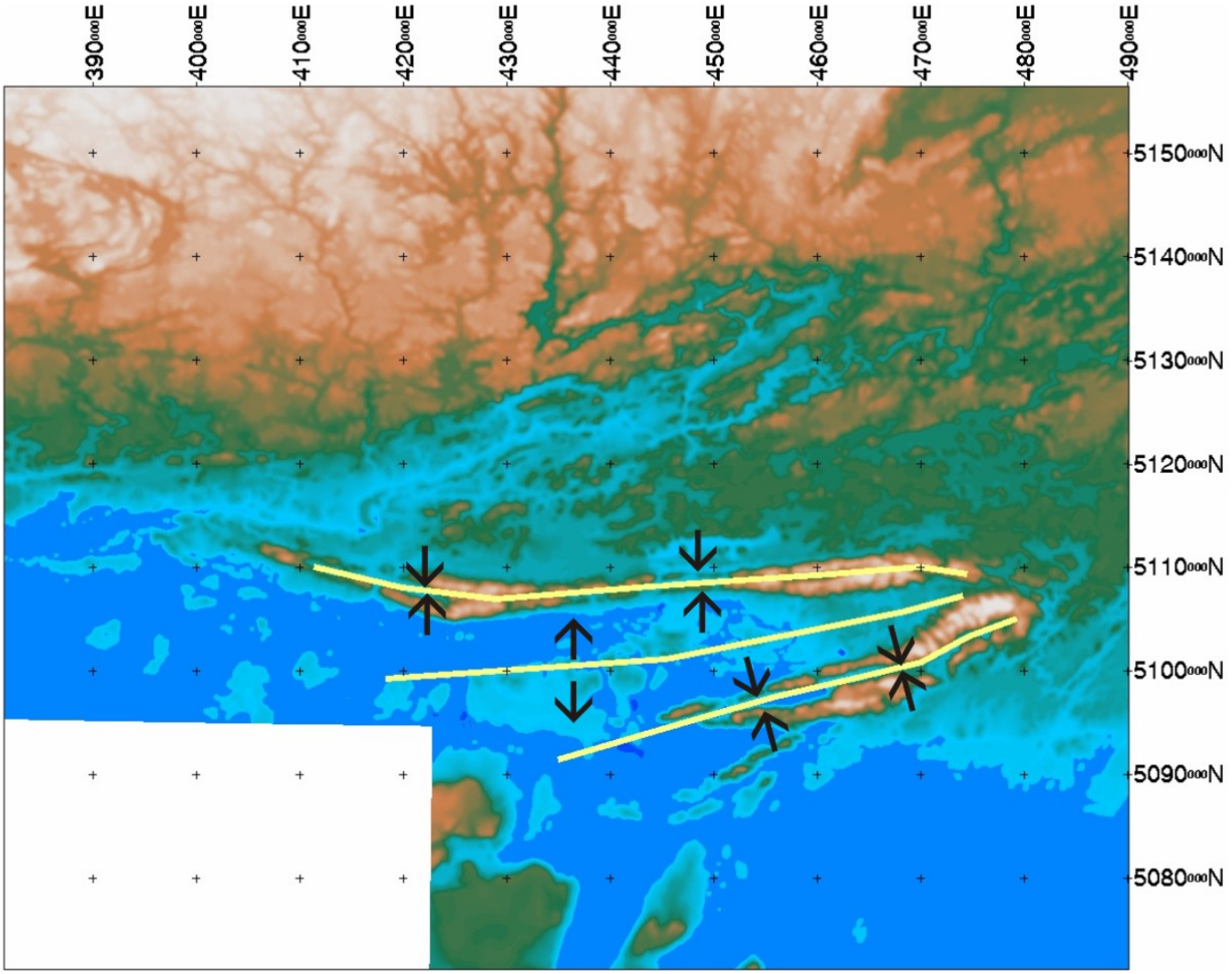

Figure CS8-10. Combining evidence from the airphoto mosaic with the topographic data indicates that the northerly pair of ridges must represent a tight syncline. It then follows that the region between the two pairs of ridges must be an open plunging anticline. The southern pair of ridges is another syncline. Geologically the northern syncline and anticline have been mapped as the LaCloche syncline and the McGregor Bay anticline, respectively.

cline. Field geological mapping has recorded these features as the La Cloche Syncline and the McGregor Bay Anticline (Card, 1978).

Highly Folded Strata

Critical to the application of topographic mapping in highly deformed terrain is the geometry of the fold structure. If all of the folds have subhorizontal fold axes then it is possible that this situation could have little or no influence on the resulting topographic record. If, however, the fold axes are subvertical then it is quite possible that the geometry of the fold morphology will be fully described in the topography.

The Grenville Province in Ontario comprises a complex series of highly deformed lithotectonic domains (Rivers, 1997; Ketchum and Davidson, 2000). All of the rocks in the Grenville Province have been subjected to high-grade metamorphism; as noted by Davidson (1986), this could be described as a ‘sea of gneisses’. Commonly the boundaries between lithotectonic domains can be recognized by the presence of locally intense deformation zones in many instances these zones of high deformation correspond to thrust margins. The northern limit of the Grenville Province is marked by the Grenville Boundary Fault. The next most southerly boundary is the Allochthonous Boundary Thrust (ABT). Dickin (2000), on the basis of neodymium isotope ages, has proposed the existence of region called Barillia between the ABT and the Grenville Front. Within this region, rocks were emplaced in the crust around 1700 Ma. Rocks north of the boundary are of Archean age. Hence the northern margin of Barillia represents a boundary between two regions having different tectonic histories. Such a contrast should have an equivalent tectonic signature. Thomas et al. (1987), originally looking at gravity data,

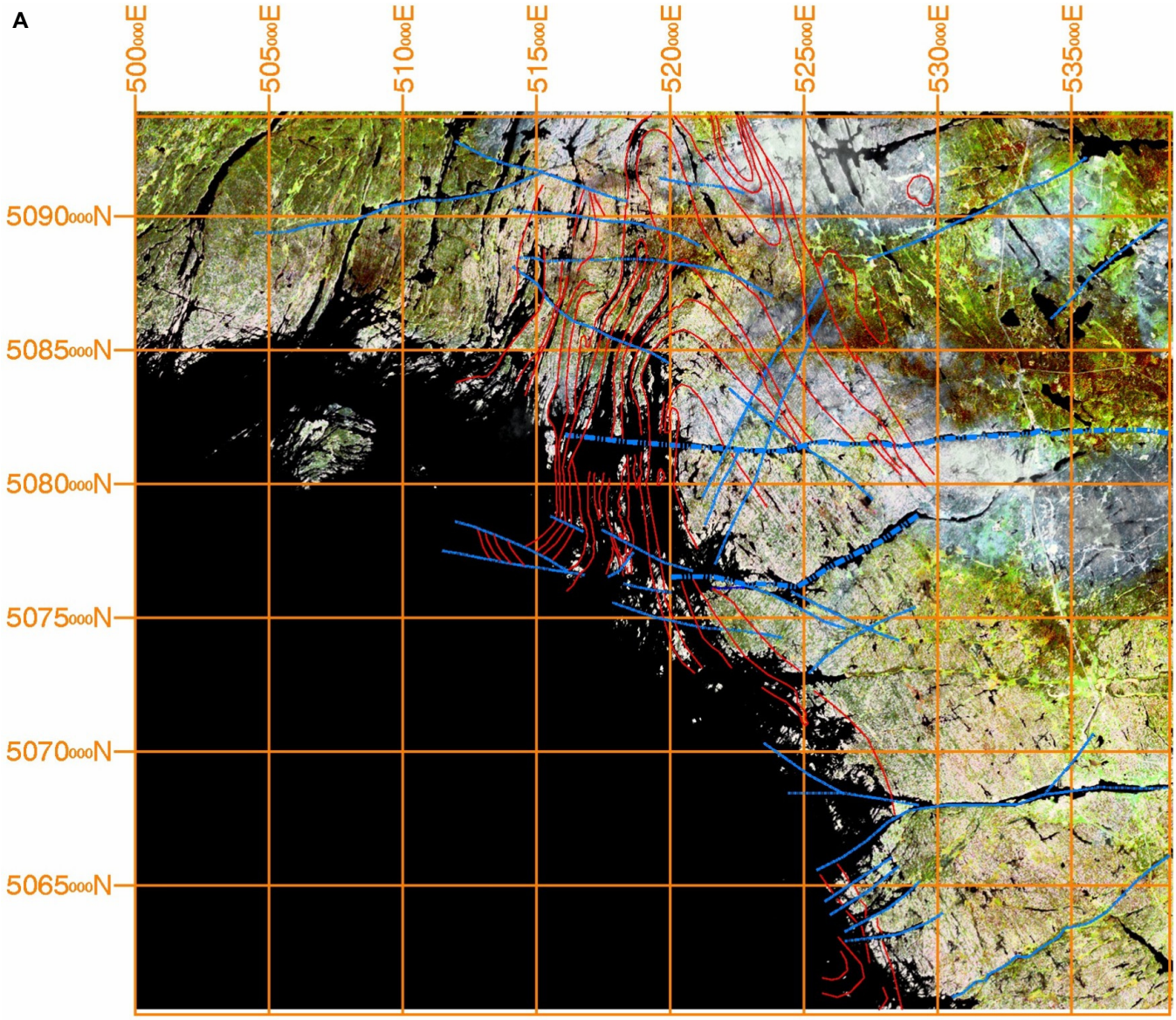

Figure CS8-11. (A) LANDSAT Bands 3, 2, 1 (red, green, blue) image of the northern margin of Georgian Bay. The spacing of the data points in the air photograph, which are based on CDED imagery, are too widely spaced to provide any resolution. The topographic detail, as imaged by LANDSAT imagery, provides details of the complex fold structure within the Grenville tectonic province. Small valleys, which are accentuated by the increased weathering, create regions of increased vegetation that then become apparent in a visible spectrum image. The locus of the Allochthonous Boundary Thrust is defined by a sharp discontinuity in the fold structure.

showed that it is possible to define terrain boundaries on the basis of regional-scale fabric contrasts.

Unfortunately, topographic data available for this area have insufficient resolution to outline the locus of the boundary. However, simple analysis of the textures present in a standard LANDSAT 7 ETM image with 30 m resolution provides direct evidence of the boundary. This area on the north shore of Lake Huron has very limited vegetation coverage with rock outcrop of approximately 60%. Within Barillia, the fold axes are near vertical, while in the Archean terrain to the north the fold axes appear to be more horizontal (Fig. CS8-11A). Including aeromagnetic data with the LANDSAT imagery enhances the contrast between individual lithologies (Fig. CS8-11B). This arises because individual geological units are characterized by varying amounts of magnetic minerals. In situations where high-resolution hyperspectral imagery is available, it is also possible to accentuate lithological boundaries on the basis of spectral "mineralogy" (see Chapter 5, this volume).

SUMMARY

Even broad-scale topographic data contains elements of the underlying structure. Higher resolution spatial and elevation data, correctly linked by a reference datum and map projection, offer many possibilities for geological mapping. Fault displacements and their frequency of occurrence can be defined in situations where sufficient outcrop and topographic variation are

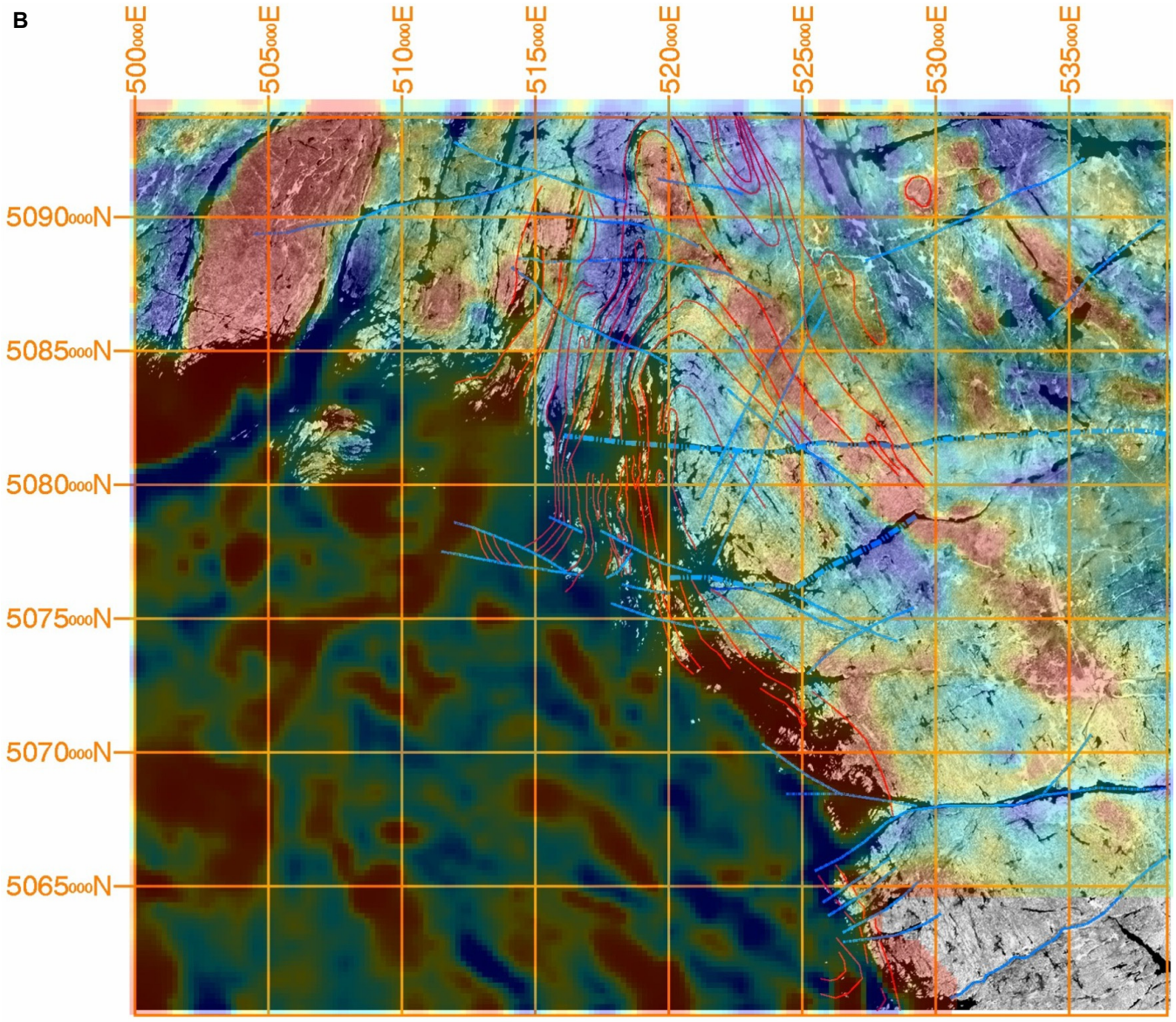

Figure CS8-11 continued. B) Overlay of the regional aeromagnetic data on the LANDSAT Bands 3, 2, 1 (red, green, blue) image. Magnetic data accentuates the contrast between the lithological rock units. The geometry of the fold structures is outlined by the differences in magnetic mineral contents of adjacent rock units.

available. The ultra high spatial resolution provided by LiDAR surveys has the potential to offer new insights into textural attributes of topography that could potentially have applications in defining alteration zones, deformation zones, and fault morphology. The availability of topographic data will lead to improved interpretation of multi- and hyperspectral imagery. For example, it will be feasible to examine possible linkages between slope and/or aspect and observed spectral response.

The examples included in this discussion provide a brief insight into possible applications of topographic analysis for geological mapping. Depending on the nature of the region being studied and the resolution of the topographic data available, this technology is capable of locating the approximate location of geological contacts. In addition, it can be used to derive estimates of displacements on fault surfaces and provide constraints on fold morphology. The techniques outlined in this study are purposely simplistic in order to demonstrate how far one can proceed with some basic concepts. More complex analyses are possible and are expected to provide even more constraints on the construction of three-dimensional geological models.

REFERENCES

Ackermann, F.
1978: Experimental investigation into the accuracy of contouring from DTMs; Photogrammetric Engineering and Remote Sensing, v. 40, p. 299-302.

Baltsavias, E.P.
1999: Airborne laser scanning: Existing systems and firms and other resources; Remote Sensing of the Environment, v. 54, p. 164-198.

Bannerjee, S. and Mitra, S.
2004: Remote surface mapping using orthophotos and geological maps draped over digital elevation models: Application to the Sheep Mountain anticline, Wyoming; American Association of Petroleum Geologists, v. 88, p. 1227-1237.

Brenner, A.C., Bindschadler, R.A., Thomas, R.H., and Zwally, H.J.
1983: Slope-induced errors in radar altimetry over continental ice sheets; Journal of Geophysical Research, v. 88, p. 1617-1623.

Card, K.D.
1978: Geology of the Sudbury – Manitoulin area, Districts of Sudbury and Manitoulin, Ontario; Ontario Geological Survey, Report 166.

Davidson, A.
1986: New interpretations in the southwestern Grenville Province, *in* The Grenville Province, (ed.) J.M. Moore, A. Davidson, and A.J. Baer; Geological Association of Canada, Special Paper 31, p. 61-74.

Day, T. and Muller, J.-P.
1988: Quality assessment of digital elevation models produced by automatic stereo matchers from SPOT image pairs; International Archives of Photogrammetry and Remote Sensing, v. 27, p. 148-159.

Dickin, A.P.
2000: Crustal formation in the Grenville Province: Nd-isotope evidence; Canadian Journal of Earth Sciences, v. 37, p. 165-181.

Farr, T.G. and Kobrick, M.
2000: Shuttle radar topography mission produces a wealth of data; EOS Transactions of the American Geophysical Union, v. 81, p. 583-585.

Fix, R.E. and Burt, T.P.
1995: Global positioning system: An effective way to map a small area of catchment; Earth Surface Processes and Landforms, v. 20, p. 817-827.

Flood, M.
1999: Commercial development of airborne laser altimetry: A review of the commercial instrument market and its projected growth, *in* Mapping Surface Structure and Topography by Airborne and Spaceborne Lasers, (eds.) B.M. Csatho; International Archives of Photogrammetry and Remote Sensing Vol. XXXII-3/W14, Proceedings of Workshop, La Jolla, CA, November 9-11, 1999, p.13-20.

Goldstein, R.M., Zebker, H.A., and Werner, C.L.
1988: Satellite radar interferometry: Two-dimensional phase unwrapping; Radio Science, v. 23, p. 713-720.

Gray, L.A. and Farris-Manning, P.J.
1993: Repeat–pass Interferometry with airborne synthetic aperture radar; Institute of Electrical and Electronics Engineers Transactions on Geoscience and Remote Sensing, v. 31, p. 180-191.

Ketchum, J.W.F. and Davidson, A.
2000: Crustal architecture and tectonic assembly of the Central Gneiss Belt, southwestern Grenville Province, Canada: A new interpretation; Canadian Journal of Earth Sciences, v. 37, p. 217-234.

Jordan, G. and Schott, B.
2005: Application of wavelet analysis to the study of spatial pattern morphotectonic lineaments in digital terrain models. A case study; Remote Sensing of the Environment, v. 94, p. 31-38

Lemmens, M.J.P.M.
1988: A survey on stereo matching techniques; International Archives of Photogrammetry and Remote Sensing, v. 27, p. V11-V23.

Massonnet, D. and Feigl, K.L.
1998: Radar interferometry and its application to changes in the Earth's surface; Reviews of Geophysics, v. 36, p. 441-500.

Norheim, R.A., Queija, V.R., and Haugerud, R.A.
2002: Comparison of LIDAR and INSAR DEMs with dense ground control, in Proceedings of Environmental Systems Research Institute 2002 User Conference, http://gis.esri.com/library/userconf/proc02/pap0442/p0442.htm, accessed November 2003.

Richardson, L.M.
2000: Errors in Digital Elevation Models Derived from Airborne Geophysical Data; Australian Geological Survey, Organisation Record 2000/37, 22 p.

Rivers, T.
1997: Lithotectonic elements of the Grenville Province: Review and tectonic implications; Precambrian Research v. 86, p. 117-154.

Sasowsky, K.C., Petersen, G.W., and Evans, B.M.
1992: Accuracy of SPOT digital elevation model and derivatives: Utility for Alaska's North Slope; Photogrammetric Engineering and Remote Sensing, v. 58, p. 815-824.

Seymour, M. and Cumming, I.
2004: Updating DEMs using Radarsat-1 data; Canadian Journal of Remote Sensing, v. 30, p. 927-942.

Thomas, M.D., Sharpton, V.L., and Grieve, R.A.F.
1987: Gravity patterns and Precambrian structure in the North American Central Plains; Geology, v.1 5, p. 489-492.

Toth, C.K., Berning, S., Leonard, J., and Grejner-Brzezinska, D.A.
2001: Integration of LiDAR data with simultaneously acquired digital imagery, *in* Proceedings of ASPRS 2001, Gateway to the New Millennium; American Society for Photogrammetry and Remote Sensing 2001, St Louis, Missouri.

Toutin, T.
2002: Three-dimensional topographic mapping with ASTER stereo data in rugged topography; Institute of Electrical and Electronics Engineers, Transactions on Geoscience and Remote Sensing, v. 40, p. 2241-2247.

Twigg, D.R.
1998: The global positioning system and its use for terrain mapping and monitoring, *in* Landform Monitoring, Modelling and Analysis, (ed.) S.N. Lane, K.S. Richards, and J.H. Chandler; Wiley, New York, p.37-62.

Westgate, J.A.
1968: Surficial geology of the Foremost-Cypress Hills Area, Alberta; Research Council of Alberta, Bulletin 22.

Wang, J. and Howarth, P.J.
1990: Use of Hough transform in automated lineament detection; Institute of Electrical and Electronics Engineers, Transactions on Geoscience and Remote Sensing, v. 28, p. 561-566.

Wehr, A. and Lohr, U.
1999: Airborne laser scanning – an introduction and overview; Journal of the International Society of Photogrammetry and Remote Sensing, v. 54, p. 68-82.

Welch, R., Jordan, T., Lang, H., and Murakami, H.
1998: ASTER as a source for topographic data in the late 1990s; Institute of Electrical and Electronics Engineers, Transactions on Geoscience and Remote Sensing, v. 36, p. 1282-1289.

Westgate, J. A.
1968: Surficial Geology of the Foremost-Cypress Hills Area, Alberta; Research Council of Alberta, Bulletin 22, 122 p.

Wilson, J.P. and Gallant, J.C.
2000: Terrain Analysis: Principles and Applications; Wiley, New York, 512 p.

WEBSITES FOR TOPOGRAPHIC DATA

http://www.geo.ed.ac.uk/geoinfo/dem.send

http://data.geocomm.com/catalog/

http://www.terrainmap.org/

http://edcsns17.cr.usgs.gov/EarthExplorer/

http://maps.nrcan.gc.ca/index_e.php

CASE STUDY 9. A Remote Predictive Mapping Case Study of the Boothia Mainland Area, Nunavut, Canada

Ernst M. Schetselaar[1] and James J. Ryan[2]
1. Geological Survey of Canada, 601 Booth Street, Ottawa, Ontario K1A 0E8
2. Geological Survey of Canada, 625 Robson Street, Vancouver, British Columbia V6B 5J3
Corresponding author's email:Ernst.Schetselaar@NRCan.gc.ca

ABSTRACT

Remote predictive mapping was applied to regional-scale bedrock mapping in support of the Boothia Integrated Geoscience Project. An integrated interpretation of high-resolution airborne magnetic, Landsat TM, and legacy geological field data resulted in a provisional geological map that was used to guide regional bedrock mapping. After the newly acquired field data were incorporated into the geoscience database, the RPM was upgraded to 1:250 000 scale geological maps in a second iteration of image interpretation and map compilation. This case study outlines the applied RPM methodology and discusses the resulting interpretations from new insights obtained by field mapping.

INTRODUCTION

The time- and cost-efficient revision of geological maps is one of the most essential activities in modernizing the geoscience information infrastructure that supports natural resource exploration. The process of geological map revision is increasingly being fulfilled by a data integration approach known as Remote Predictive Mapping or RPM. RPM aims at increasing the efficiency of geological mapping by the implementation of remotely sensing and geographic information system (GIS) technologies. RPM can be as basic as the provision of enhanced image products to a geological field party and as complex as the on-site application of quantitative methods for feature extraction such as statistical pattern recognition and geophysical inversion. In general, RPM aims at the prediction of geologically significant patterns from remotely sensed data in support of fieldwork planning and map compilation.

This paper presents the results of a RPM study in which, in advance of field mapping, a provisional geological map was provided by the integrated interpretation of remotely sensed, airborne geophysical, and legacy geological field data. The resulting remote predictive map outlines tentative geological units and structural patterns in the survey area that honour legacy geological field data acquired during a helicopter reconnaissance survey in 1960. The RPM, in addition, includes the outlines of new, potentially geologically significant features, in hitherto unvisited areas. This approach provides the field geologist with targets to test while in the field, rather than rely on serendipity during the course of traditional systematic traversing. After new field data were acquired the RPM was upgraded to publishable geological maps in a second iteration of integrated interpretation.

In this paper, the RPM methodology is described in a sequence of processing and interpretation steps and examples are provided on how various geological features were extracted through integrated visual interpretation of Landsat ETM (enhanced thematic mapper), airborne magnetic, and geological field data. In addition, the 1st RPM iteration is validated with the newly acquired field data and conclusions are drawn on the merits of RPM for the Boothia Integrated Geoscience Project.

THE BOOTHIA INTEGRATED GEOSCIENCE PROJECT

The Boothia Integrated Geoscience Project is a multi-year geoscience mapping collaboration in the Boothia mainland area, Kitikmeot Region, Nunavut, being carried out by the Geological Survey of Canada and the Canada-Nunavut Geoscience Office. Bedrock mapping in 2005 covered parts of NTS map sheets Pelly Bay (57A), Rae Strait (57B), Spence Bay (57C) and Harrison Island (57D), at 1:250 000 scale (Ryan et al., 2008a,b). ,The Boothia project represents the most recent and northerly, of a series of mapping projects initiated in the summer of 2000 in this part of the Canadian Shield, that attempts to unravel the extent, tectonic setting, and mineral potential of supracrustal belts of the north-central Rae Domain of the western Churchill Province (see also Sandeman et al., 2001a,b, 2005; Sanborn-Barrie et al., 2002, 2003; Skulski et al., 2002, 2003a,b,c). The Boothia project was launched in 2004 with acquisition of a new aeromagnetic survey consisting of 101,000 line kilometres flown at a spacing of 400 m and 150 m elevation (Coyle et al., 2005). This is the first aeromagnetic data that are publicly available north of 68 degrees in this part of Nunavut and is available for download on the GSC's Geoscience Data Repository (http://gdr.nrcan.gc.ca/index_e.php).

GENERAL GEOLOGY

The Boothia mainland area is located in the north-central Rae Domain of the western Churchill Province

Schetselaar, E.M. and Ryan, J.J., 2008, A remote predictive mapping case study of the Boothia mainland area, Nunavut Canada, Case Study 9 *in* Remote Predictive Mapping: An Aid for Northern Mapping, (ed.) J. R. Harris; Geological Survey of Canada, Open File 5643, p. 261-281.

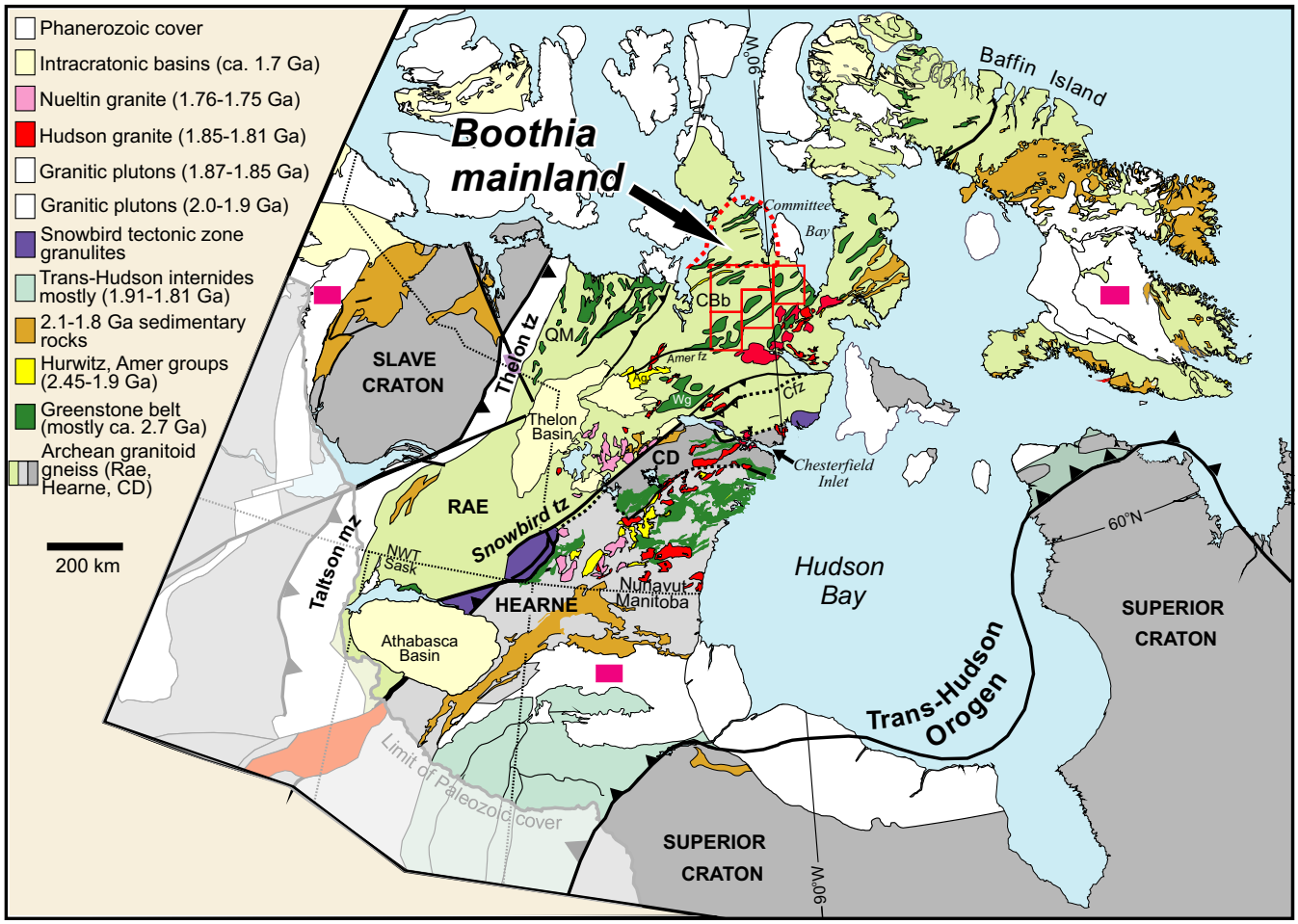

Figure CS9-1. Regional tectonic map of the Churchill Province (modified from Berman et al., 2005). The red dotted polygon outlines the Boothia mainland area. Red squares outline prior mapping projects of the Committee Bay greenstone belt (Skulski et al., 2003 and references therein; Sandeman et al., 2005). (Ag = Amer Group; Amer lz = Amer Lake shear zone; CBb = Committee Bay belt; CD = Central Hearne domain; Cfz = Chesterfield fault zone; QM = Queen Maud block; Taltson mz = Taltson magmatic zone; Thelton tz = Thelon tectonic zone; Wg = Woodburn Lake Group.

(wCP) in the Canadian Shield (Fig. CS9-1). The wCP constitutes a composite (or collage) of polymetamorphic and multiply deformed Archean terrains, characterized by Paleoproterozoic successor sedimentation, magmatism, and tectonothermal reworking (Hoffman, 1988) flanked by Paleoproterozoic orogenic belts (Fig. CS9-1). Bedrock geology of the Boothia mainland area (Ryan et al., 2008a) is fairly typical of the north-central Rae Domain. It comprises a high-grade gneissic terrain dominated by Neoarchean metaplutonic rocks (Hinchey et al., in prep), lesser Archean and Paleoproterozoic supracrustal sequences (Hinchey et al., 2007) and migmatitic gneiss (Ryan et al., 2008b).

REMOTE PREDICTIVE MAPPING METHODOLOGY

The remote predictive geological mapping of the Boothia mainland area was based on an iterative digital compilation approach. During the first iteration in 2005, a provisional geological map was compiled in advance of field mapping through the integrated interpretation of archived laboratory and legacy field data, a regional geological map compilation of the Churchill Province (Patterson and LeCheminant, 1985) and remotely sensed data, including a high-resolution aeromagnetic survey and Landsat 7 ETM scenes. In the subsequent iteration in 2006, newly acquired field and laboratory data were incorporated such that the first provisional geological map compilation could be upgraded towards publishable 1:250 000 scale geological maps in a continuous work flow. There were three fundamental differences of this work flow from the more traditional approach to geological mapping:

1. A provisional geological map compilation was prepared before the fieldwork commenced (1st RPM iteration).
2. The predictive map was used to strategically guide new fieldwork rather than using traditional systematically spaced traverses.
3. The remotely sensed data and 1st RPM iteration were used for compilation of publishable geologi-

Table CS9-1. Specifications of geoscience data sets used in the compilation of a remote predictive geological map of the Boothia mainland area prior to the 2005 fieldwork.

Dataset	Spatial resolution	Source georeference	Source
Landsat 7 ETM	Six 30 m multispectral bands, one 15 m panchromatic band	NAD83	Geogratis website http://geogratis.cgdi.gc.ca
Aeromagnetic data, residual total field (RTF) magnetic, 1st & 2nd vertical derivative and magnetic tilt grids	400 m line spacing, 80 m grid resolution	NAD83	Coyle et al. (2005); Geoscience data repository http://gdr.nrcan.gc.ca/aeromag/index_e.php
Regional geological map		NAD27, Lambert conformal	Heywood (1961)
Legacy geological field data (rock samples linked to topographic maps with field stations and notes)		NAD27 UTM (zones 15 & 16)	Heywood (1961), Tunney's Pasture (hard copy archive)

cal maps in the 2nd RPM iteration. This allowed for the interpretation and prediction of geological units and structures between field sites that were visited in 2005.

Hence, RPM was implemented as a spatial reconnaissance mapping tool predicting geological units and structures of the survey area before and after geological fieldwork. It contributed to focussing fieldwork traverses or helicopter visits because predictions yielded hitherto unknown spatial patterns that warranted follow-up field visits. The following sections provide a step-by-step description of the RPM methodology applied to geological mapping of the Boothia mainland area.

Compilation of Existing Data Sources in a Geographical Information System Environment

The data sets that were used for remote predictive mapping of the Boothia mainland area are listed in Table CS9-1. Datum and projection transformations were applied (from Lambert conformal NAD27 and UTM NAD27) before the data sets were georeferenced on UTM Zone 15, NAD83. In addition to the data sets acquired over the project area, medium-resolution aeromagnetic data (800 m line spacing) Landsat 7 ETM scenes and geological maps from the Darby Lake-Arrowsmith River area (Sandeman et al., 2005) and the Committee Bay area (Skulski et al., 2003c and references therein) to the south of the Boothia mainland area were incorporated in regional geological interpretation. This provided insight and preliminary guidelines to what extent bedrock units and structures could be identified on remotely sensed data acquired over the Boothia mainland.

Analysis of Legacy Geological Field Data

About 125 georeferenced rock samples that were collected in helicopter surveys in the 1960s by Heywood and co-workers (Heywood, 1961) were available at the Geological Survey of Canada's sample archives at Tunney's Pasture, Ottawa. The rock samples were examined and classified on the basis of modern rock-classification concepts. Emphasis in the rock classification was given on the igneous and sedimentary protoliths (e.g. porphyritic monzogranite) in favour of merely metamorphic terms (orthogneiss) in order to permit differentiation of regionally deformed and metamorphosed plutonic rocks, which dominate the bedrock geology of the area. Petrographic thin sections, available for some of the archived samples, were studied to establish metamorphic mineral assemblages and grade. In addition to these macroscopic and microscopic studies, five magnetic susceptibility measurements were taken of each rock sample to guide geological interpretation of the aeromagnetic dataImage Processing and Enhancement

Landsat 7 ETM scenes were enhanced in colour composites, wherein the dynamic ranges of bands 7, 3, and 1 were linearly stretched and assigned to, respectively, the red, green, and blue channels of the computer display (Fig. CS9-2A). In order to exploit the 15 metre resolution of the panchromatic band, the 30 metre resolution multispectral bands were pansharpened using the additive image fusion technique (Chavez et al., 1991).

The combination of Landsat ETM bands 7, 3, and 1 is favourable for geological applications, since the inclusion of band 7 in the mid-infra red region of the electromagnetic spectrum enables detection of absorption features induced by carbonate and hydroxyl-bearing mineral groups, as well as iron oxides, by variations in the slope of the electromagnetic spectrum between band 1 (reflected visible blue) and band 3 (reflected visible red) (Drury, 2001).

For the rocks exposed in Boothia mainland, this suggests potential spectral discrimination of carbonate rocks (limestone, marble), muscovite-bearing rocks, and iron-rich metasediments including iron formation.

In addition to the colour composite image, outcrop prediction (Fig. CS9-3) and bedrock-enhanced images were generated by defining thresholds in the pixel values of band 7 to mask water, Quaternary overburden, and snow; thresholds in the pixel values of the green vegetation index image (Lillesand and Kiefer, 2000)

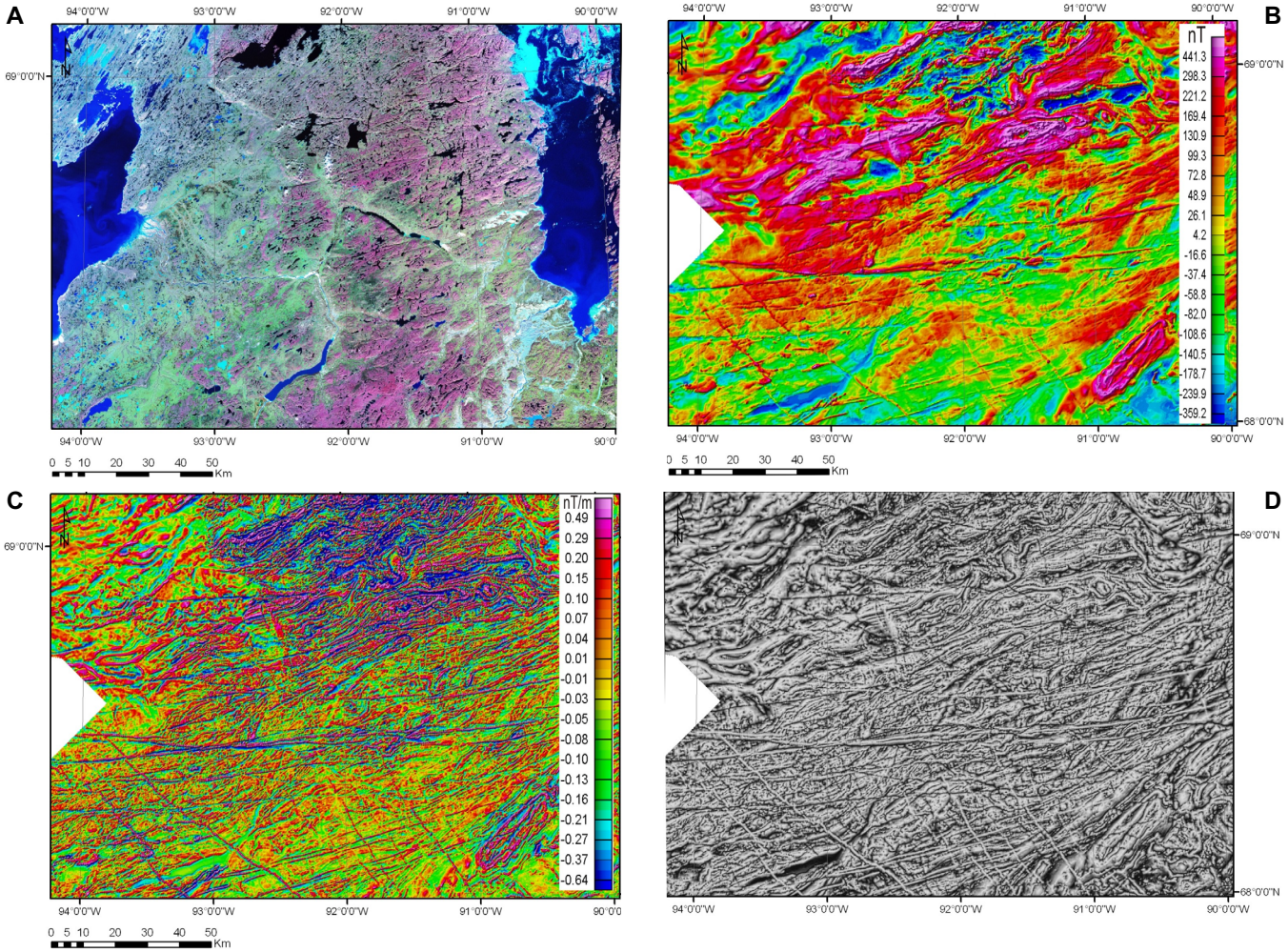

Figure CS9-2. Geoscience data sets and derivatives used in geological image interpretation for remote predictive mapping of the Boothia mainland. **(A)** Landsat ETM colour-enhanced composite image. Red = ETM band 7, green = ETM band 3, and blue = ETM band1. **(B)** Colour-shaded relief image of residual total field magnetic intensity. **(C)** Colour image of the 1st vertical magnetic derivative. **(D)** Greyscale image of the magnetic tilt data. Note that the 1st vertical magnetic derivative and tilt data are particularly useful in delineating geological structures and dyke swarms.

masked green vegetation. The removal of vegetation-water-sediment-snow pixels not only served as an outcrop prediction tool, but also enhanced spectral contrast between rock units and structures in the Landsat ETM scenes by effectively enlarging the dynamic range of the outcrop pixels in red-green-blue (RGB) colour space. Note, for example, in the upper quadrant of Figure CS9-3B the contrast between the light grey tone of Ordovician limestone cover and pink hues of the Archean basement when compared to the original Landsat 731 colour composite image shown in Figure CS9-3A. A bedrock-enhanced colour composite image was generated by applying the 1-99% histogram cut-offs from the outcrop prediction image to the original Landsat scene. This effectively mapped all pixels of ground-cover classes other than bedrock to the extremes of the red, green, and blue dynamic ranges in the RGB colour space of the display without masking them from the scene.

Residual total field (RTF) magnetic data and their first and second vertical derivatives were presented as relief-shaded colour grids. The colour coding employed histogram equalization to map the dynamic range of the grid values into 40 classes. The light source used for relief shading was positioned at declination and inclination angles of 315º and 45º, respectively (Fig. CS9-2B,C,D).

Geological Image Interpretation

Once the enhanced image data and the legacy field data were co-registered to the NAD83 datum and UTM (Zone 15N) map projection, spatial relationships between magnetic anomaly patterns, Landsat ETM colour composite images, and the rock sample descriptions were analyzed in a GIS environment. Geological units and structures were outlined using the diagnostic elements of visual image interpretation, which include tone, texture, shape, shadow, size, patterns, or their associations (see Chapter 2 of this volume for more

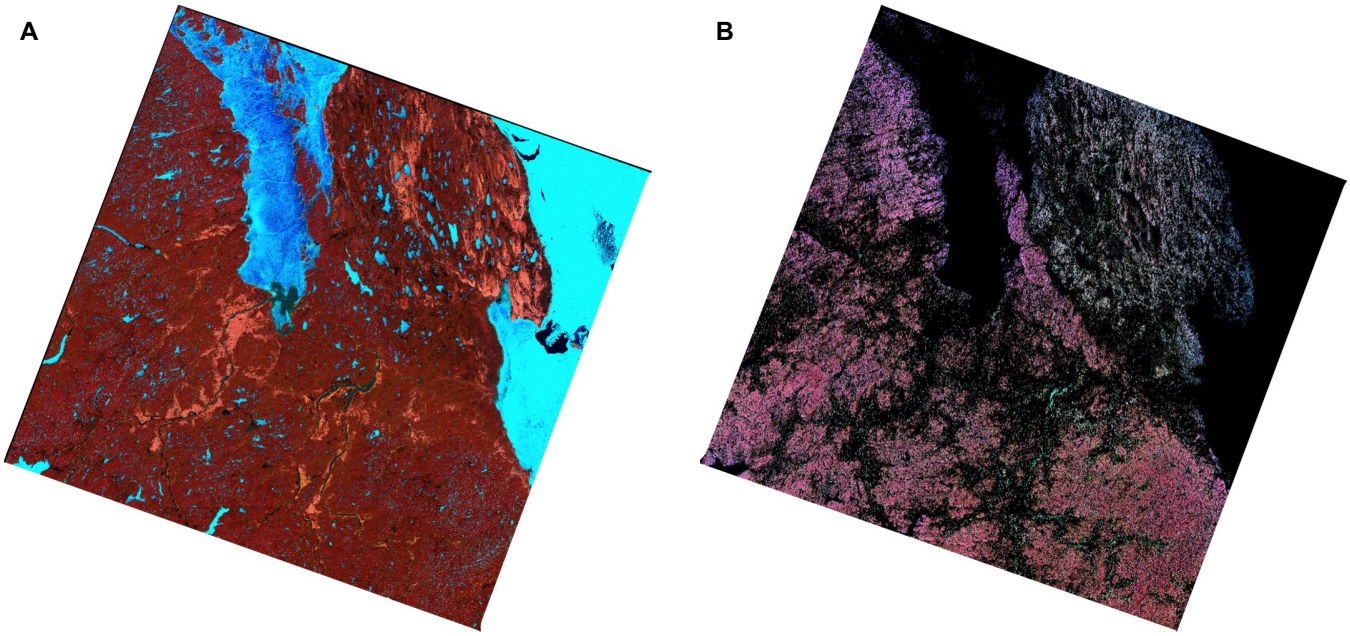

Figure CS9-3. Landsat 7 ETM scenes acquired over the northeast Boothia mainland (each scene covers an area of 180 x 180 km). **(A)** Colour composite image of the original ETM bands 7, 3, and 1. **(B)** Colour composite image of bands 7, 3, and 1 of predicted outcrop areas with masked water, snow, vegetation, and Quaternary sand pixels merging with the black background. Note how the outcrop prediction enhanced the spectral contrast between the Ordovician limestone (light grey, right-hand side) and the Archean basement (pink) as well as the structure (top left quadrant) within the Archean basement.

details on visual image interpretation). Both the rock sample descriptions and map compilation of Heywood (1961) were used to tentatively assign the image-interpreted units to one or a combination of geological units with consistent image diagnostics. Bedrock units, however, may have similar remotely sensed signatures; hence the interpretation may yield units that group multiple rock types. Narrow prominent magnetic anomalies, for example, were attributed to iron formation as well as mafic metavolcanic rocks. Both lithologies occur within supracrustal belts and are indistinguishable, as a result of their association with similarly shaped magnetic anomalies and overlapping magnetic susceptibility ranges.

Traverse Planning

The combined analysis of the outcrop prediction and remote predictive geology maps guided where geological contacts and structures could be ground-truthed during fieldwork. Provisional routes for traversing were outlined directly on the computer screen based on perceived terrain accessibility (interpreted mainly from the 15 m resolution panchromatic band 8 of Landsat), outcrop density, and optimal crossings of image-interpreted unit boundaries.

Map Compilation

The geological map resulting from the 1st iteration of RPM is shown in Figure CS9-4. The RPM is represented on a 1:250 000 scale topographic base with a legend of image-interpreted bedrock units and structures. Bedrock units include those that were inferred from integrated interpretation of the Landsat, magnetic, and the legacy geological database. The structural information on the compilation includes foliation trajectory patterns with outlines of regional folds, fault zones, and dyke swarms. The locations of rock samples examined at the GSC archives at Tunney's Pasture, Ottawa were plotted, as well as their newly assigned rock names (not shown in Fig. CS9-4).

The geology map compilation completed after the 2005 field season (Ryan et al., 2008a) is considered another step in the iterative RPM procedure (i.e. RPM 2nd iteration). This map is shown in Figure CS9-5. It is currently being published as a GSC Open File map (Ryan et al. 2008a) and the geology is described in more detail in Ryan et al. (2008b). Much of the methodology employed in the second iteration was the same as that followed in the first, except there were 1) field observations at 1730 new field stations, 2) an experienced context of the physical makeup of the geological units, 3) an understanding of the nature of their contacts (i.e., sharp or diffuse) and a better understanding of the scale and character of structural geometries. While much confidence can be given to the geological observations and nature of unit contacts along the path of the foot traverses, particularly in the vicinity of the field stations, that confidence erodes away from the stations and traverse paths. This is particularly true for helicopter landings, which generally do not have the cumulatively developed geological context typical of a foot traverse. Hence, the compilation of contacts away

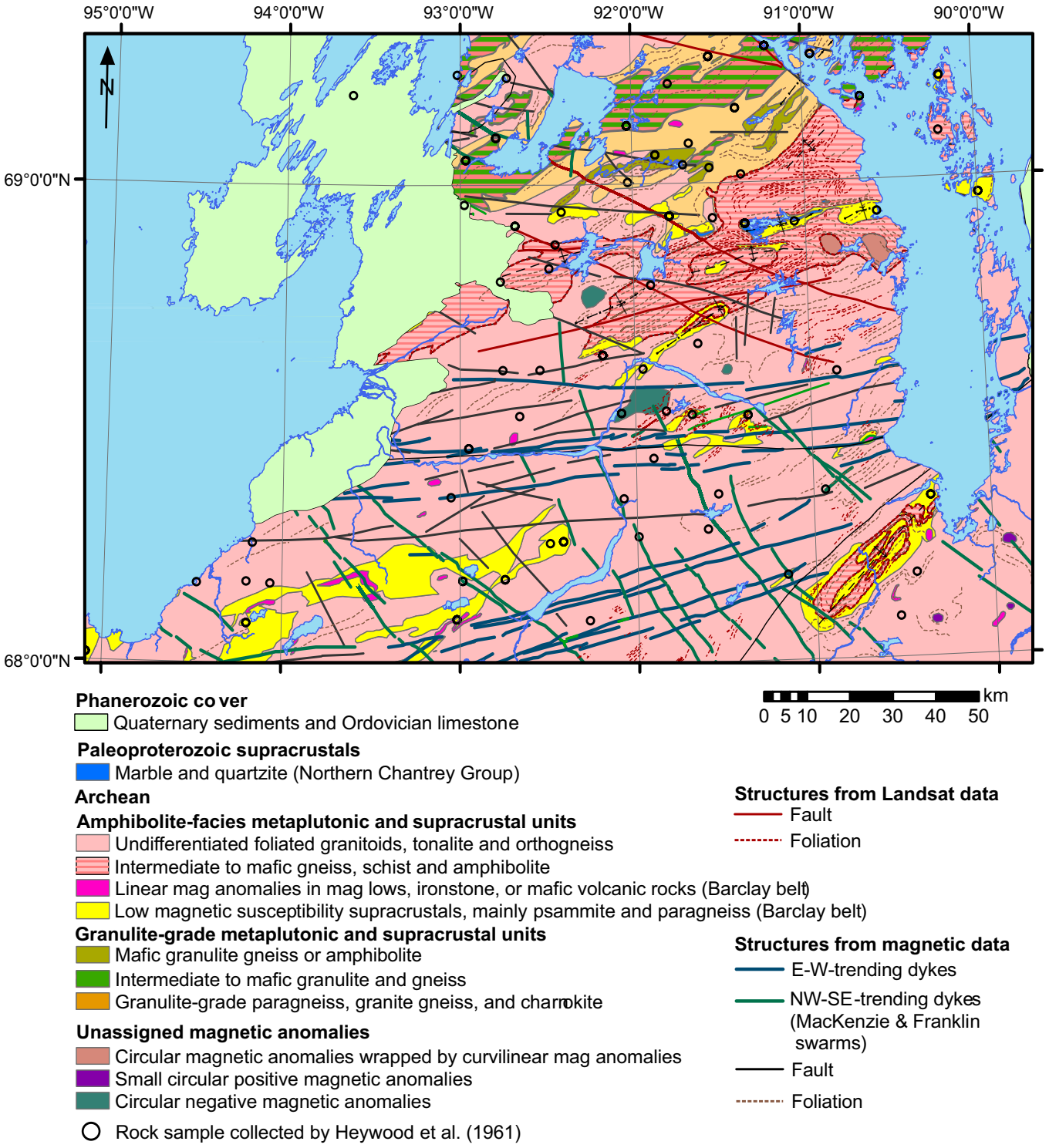

Figure CS9-4. Remote predictive map of the Boothia mainland (1st RPM iteration) based on geological interpretation of Landsat ETM, magnetic, and legacy field data.

from observation stations and between traverses continued to be a prediction.

The 1st RPM iteration provided a spatial reference, along with the aeromagnetic and Landsat data, for map analysis and unit compilation from the 2005 field data. The first step in the 2nd RPM iteration was to synthesize the units observed in the field into a common logical legend that would be the foundation for the map. At the 1730 field stations, rock-type observations were placed into the context of lithological units. Reading through digital field notes for this many stations is a time consuming and difficult task and the process was sped up by simplifying and symbolizing the observed geological rock types.

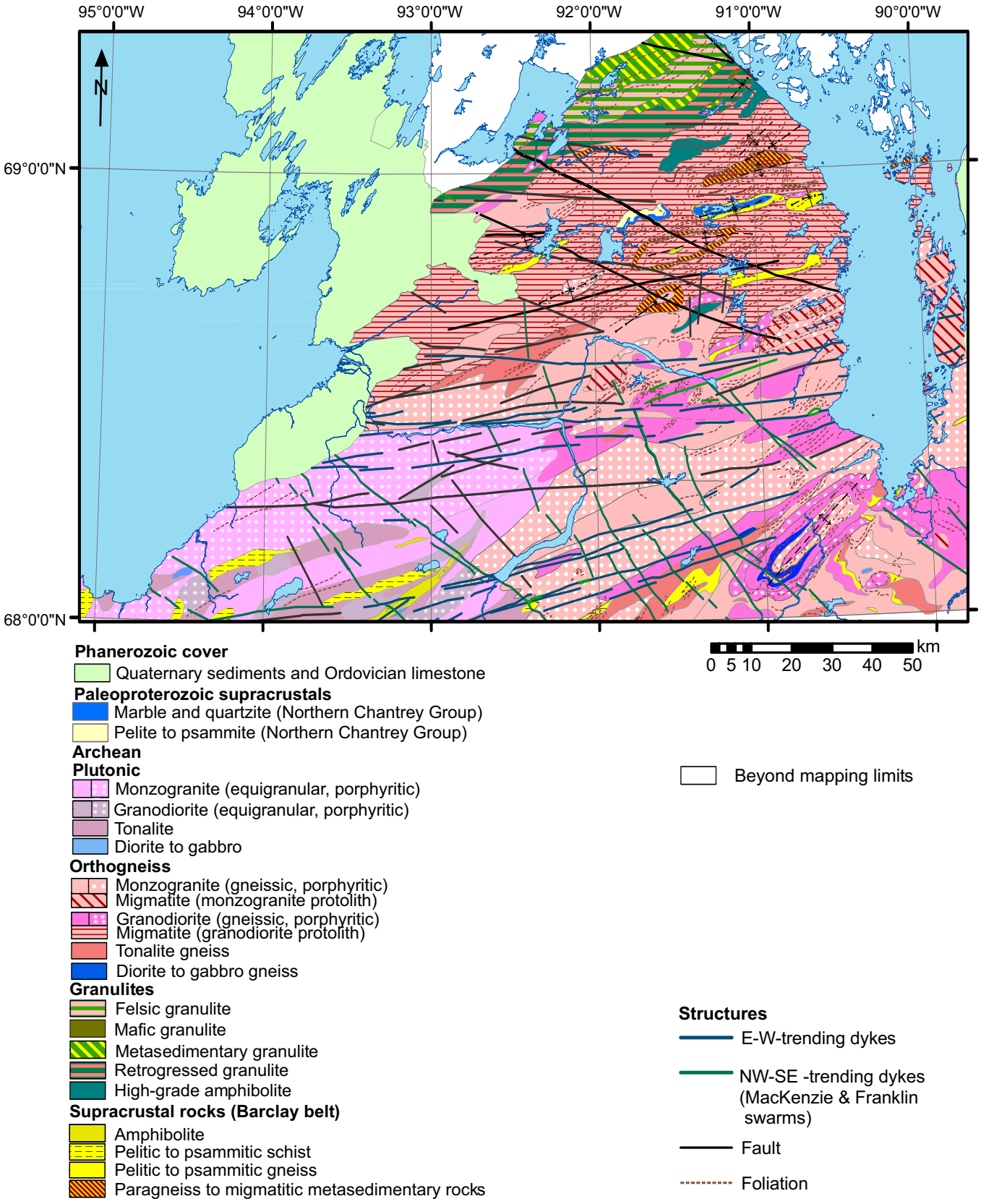

Figure CS9-5. Geological map of the Boothia mainland compiled after the 2005 fieldwork (2nd RPM iteration).

As twelve different geologists made observations during the 2005 field season, all with highly varied schooling and experience backgrounds (a complicating factor in most regional mapping projects), and rock-

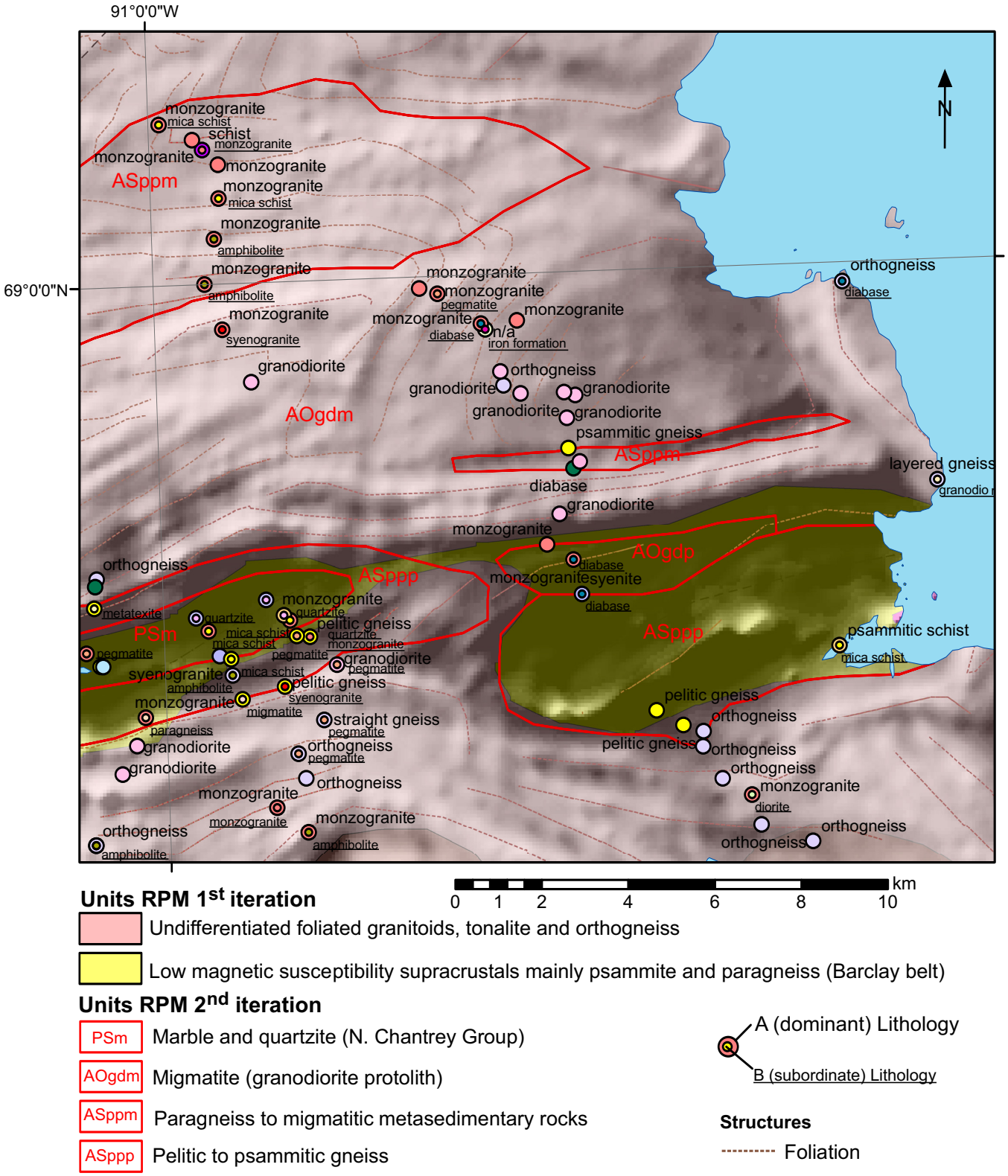

Figure CS9-6. GIS overlays used for map compilation (2nd RPM iteration) by integrating the 1st RPM iteration, the RTF magnetic-intensity grid, and rock-type observations from the 2005 field database. See text for a more detailed discussion.

type determination in gneissic terrain is highly subjective, there was inevitable inconsistency in the rock-type records. In addition, considering the highly layered gneissic terrain, four rock-type observations were commonly recorded per station (rock type a, b, c, d). For the map compiler, it is difficult to visually process and digest this much information. Since the map was intended to be compiled at a scale of 1:125 000, but

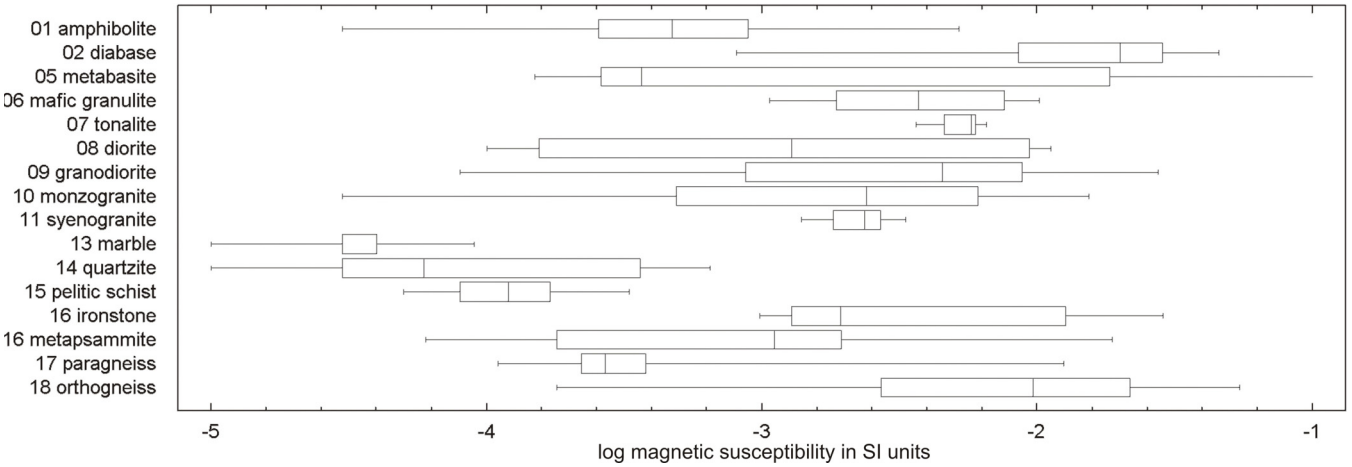

Figure CS9-7. Magnetic susceptibility measurements of archived rock samples collected in the Boothia mainland region by Heywood and co-workers in the early 1960s and used in support of the interpretation of high-resolution magnetic data acquired in 2005.

displayed at a scale of 1:250 000, the minor rock types at any outcrop could not be shown on the map and locally the rock unit had to be simplified to what made up the majority of the outcrop or region. Therefore, only the two most prominent rock types (a and b) per outcrop were symbolized for synthesizing the units. Geological domain boundaries were then drawn around regions with similar rock-type associations and image 'signatures' in defining map units. Figure CS9-6 illustrates the compilation strategy for a small portion of the map area. In this example, rock types (a and b) are rendered against the 1st RPM iteration in transparency with a grey-scale image of the shaded-relief RTF magnetic grid in the background. Units compiled during the 2nd iteration of RPM using the 2005 field data are shown in red outlines. Note that the field data still provide limited and ambiguous constraints for defining contacts and map units. Also note how the significance of a linear magnetic anomaly has been re-evaluated in defining the elongated 'ASppm' unit from a single paragneiss outcrop observation.

In order to reconcile geological contacts with recently completed mapping immediately to the south in the Darby Lake-Arrowsmith River areas (Sandeman et al., 2005), particular attention was paid to map observations there in order to avoid map boundary conflicts. Observations were quite consistent between projects and no major conflicts were noted. In some areas with particularly poor bedrock exposure, the 1st iteration RPM exercise predicted rock types of particular economic interest (e. g. supracrustal rocks) and these were given particular emphasis for ground truthing during the 2005 fieldwork. In some regions of poor to no bedrock exposure, however, the prediction could not be properly tested. In the 2nd RPM iteration, these regions were still interpreted to be underlain my metasedimentary units that warrant closer inspection for follow-up.

GEOLOGICAL IMAGE INTERPRETATION RESULTS BEFORE THE 2005 FIELDWORK (1st RPM ITERATION)

The preliminary analysis of medium-resolution magnetic data and 1:250000 scale geological maps (Sandeman et al., 2005; Skulski et al., 2003c) of the Committee Bay region reveals that the general structural trend, greenstone belt lithologies, diabase dykes, and faults in this region can be easily identified on colour-relief shaded grids of the 1970s vintage, medium-resolution magnetic data acquired at a flight line spacing of 800 metres (http://gdr.nrcan.gc.ca/aeromag/index_e.php). The greenstone belts generally correspond to broad featureless magnetic lows with internal linear positive anomalies associated with iron-rich psammite, amphibolite, ultramafic rocks (komatiite), and iron formation. A similar association between magnetic lows and supracrustal belts is apparent on the new, high-resolution magnetic data in the Boothia mainland area (Fig. CS9-2B). Some of the supracrustal belts that were outlined on the basis of the supracrustal units on the regional compilation of the Churchill Province (Patterson and LeCheminant, 1985), however, appeared to be associated with elongated domains with curvilinear magnetic highs outlining doubly plunging folds. After fieldwork, it appeared that these domains were, in fact, not associated with supracrustal rocks, but rather to folded metaplutonic units with contrasting magnetic susceptibilities. Another limitation revealed by the preliminary analysis was that no diagnostic magnetic anomaly patterns or Landsat spectral signatures allowed differentiating metaplutonic units in the Committee Bay region. The same limitation was encountered in the interpretation of the high-resolution magnetic data acquired over the Boothia mainland.

Box whisker plots of magnetic susceptibility measurements taken from rock samples collected by

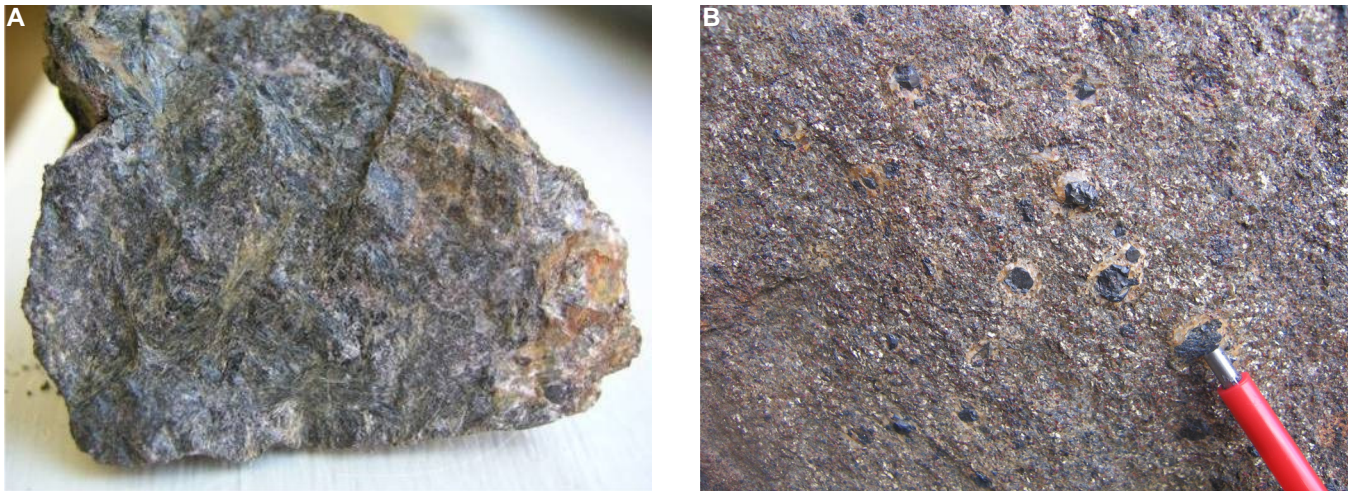

Figure CS9-8. Laboratory and outcrop observations of iron-bearing minerals that are important for interpreting magnetic data in the RPM project of the Boothia mainland. **(A)** Rock sample of grunerite-bearing iron formation, metamorphosed at amphibolite facies, with low magnetic susceptibility. The longest dimension of the sample is approximately 12 cm. **(B)** Magnetite porphyroblasts with resorption halos in metamorphosed monzogranite (this rock tends to have high magnetic susceptibility).

Heywood and co-workers are shown in Figure CS9-7. Five measurements were taken for each rock sample. Typically, the measurements of the rock samples show large overlapping ranges in magnetic susceptibility that do not unequivocally reflect rock classes differentiated on the basis of classical petrological rock classification, in which accessory minerals (particularly magnetite) are ignored (Clarke, 1997). Some broad trends, however, can be observed that provide guidelines for RPM when used in combination with the shape, patterns, and spatial context of the magnetic anomalies.

The magnetic susceptibilities of Archean and Paleoproterozoic supracrustal rocks, with the exception of iron-rich psammite and iron formation, generally range from 0.00001 to 0.001 SI, whereas the magnetic susceptibilities of metaplutonic granitoid rocks (e.g. tonalite, granodiorite, monzogranite, and syenogranite), as well as mafic granulites, range from 0.0001 to 0.1 SI. This first-order magnetic susceptibility contrast is consistent with the magnetic response of the Committee Bay greenstone belt where the regionally extensive magnetic low associated with supracrustal rocks contrasts with the high magnetic background measured over areas that are dominated by metaplutonic rocks. The preservation of low magnetic susceptibilities in psammite and paragneiss, as opposed to high magnetic susceptibilities of metaplutonic rocks, can be explained by their lower oxygen fugacities such that iron tends to remain chemically bound to sulphides or silicates (as opposed to the relative high oxidation states in metagranitoid domains favourable to new growth of magnetite).

Exceptions to this general trend are prominent linear magnetic anomalies associated with iron formation or amphibolite. The magnetic susceptibility measurements of two samples, however, suggest that even iron formation occurrences are not all associated with prominent positive magnetic anomalies. One grunerite- and garnet-bearing iron formation sample metamorphosed at amphibolite facies (Fig. CS9-8A) showed conspicuously low magnetic susceptibilities with an average value of 0.0013 SI, whereas samples of iron formation metamorphosed in the greenschist facies exhibited significantly higher magnetic susceptibilities with an average value of 0.0157 SI. This suggests that magnetic susceptibility was lowered by alteration of Fe-oxides (hematite and/or magnetite) into Fe-silicates (grunerite) during prograde metamorphism. Granodiorite, tonalite, monzogranite, and orthogneiss samples, on the other hand, commonly contain magnetite porphyroblasts and have relatively high magnetic susceptibilities, ranging from 0.001 to 0.08 SI. Metre-wide layers hosting 0.5 to 1 cm magnetite porphyroblasts observed in outcrop (Fig. CS9-8B) suggest that the high magnetic susceptibility values of these rock units are at least partly due to new growth of magnetite during high-grade metamorphism.

A first-order subdivision of the colour-shaded relief image of the RTF magnetic grid yields two regional domains with consistent internal low wave number anomaly patterns and background values (Fig. CS9-9). Domain 1, located in the northern part of the study area, exhibits regional-scale alternating linear magnetic lows and highs corresponding respectively to felsic and mafic granulites. This domain can be clearly distinguished from Domain II to the south, which has a more homogeneous, relatively high magnetic background with elongated irregular magnetic lows that are associated with supracrustal belts. Short-wavelength curvilinear magnetic anomalies in both domains outline F_4 fold patterns, as evident from the high correlation between the trends of curvilinear and linear magnetic

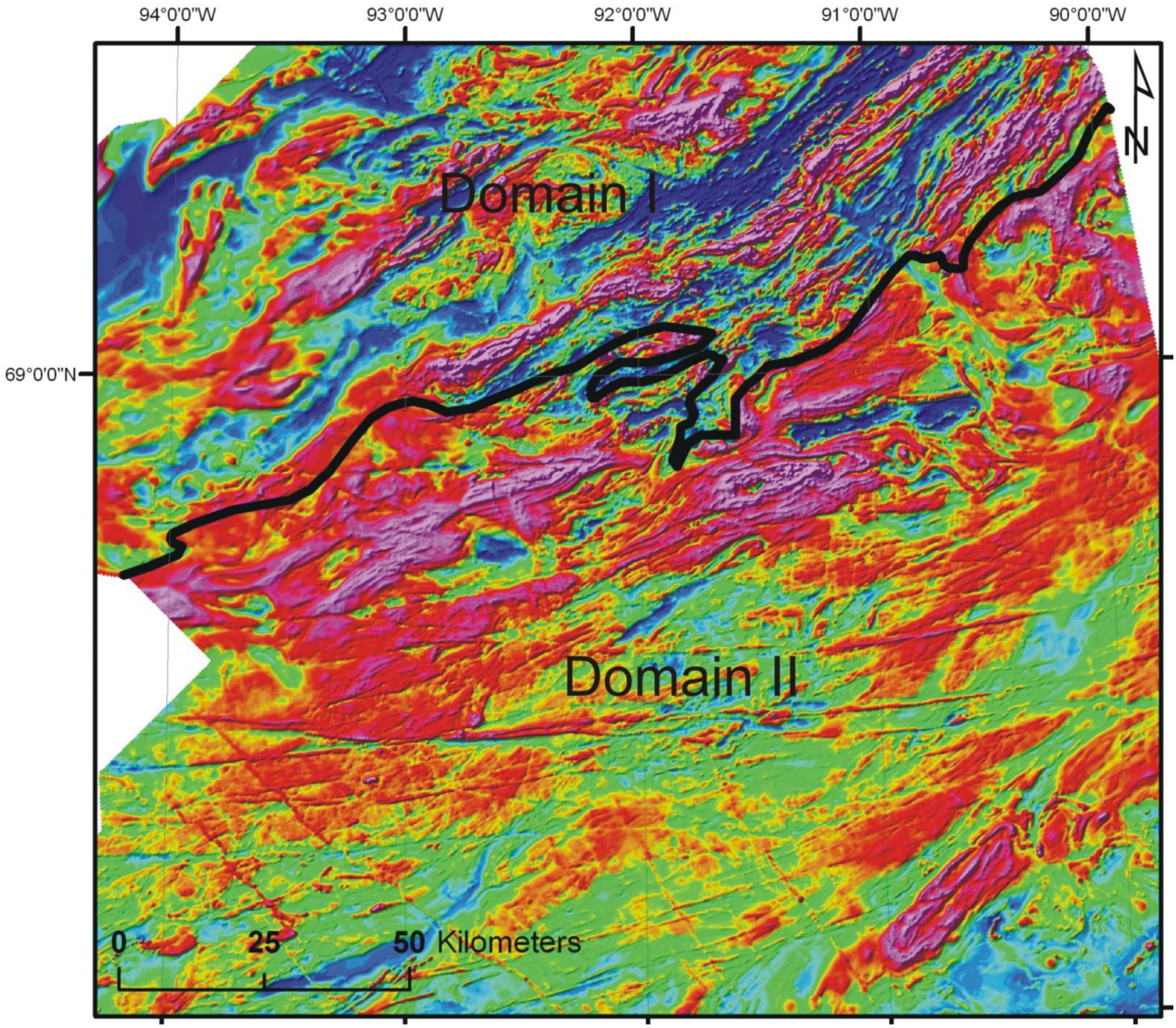

Figure CS9-9. Colour-shaded relief image of the RTF magnetic grid of the RPM survey area with an interpretation of first-order magnetic domains superimposed. Domain I is characterized by an alternation of magnetic highs and lows corresponding to mafic and felsic/metasedimentary granulite belts, respectively. Domain II is characterized by elongated irregular magnetic lows corresponding to supracrustal belts in a relatively high magnetic background corresponding to migmatized plutonic units metamorphosed (locally retrogressively) at amphibolite facies.

anomalies, the trends of Landsat curvilinears, and the strike orientation of field-established S_1 fabric elements (Fig. CS9-10).

East to west- and east-northeast to west-southwest-trending, predominantly featureless magnetic lows and highs within Domain II were interpreted as Archean supracrustal rocks of the Barclay belt. This interpretation was based on the legacy rock sample locations that were assigned to supracrustal rock types, the overall low magnetic susceptibility of supracrustal rocks samples (Fig. CS9-7), and the match between some magnetic lows and supracrustal units of the regional 1: 250 000 scale map compilation of Heywood (1961). Local prominent positive linear anomalies within these magnetic lows were outlined as an internal magnetic unit that, due to the overlapping ranges in their relatively high magnetic susceptibility, were interpreted to either correspond to basic metavolcanic rocks or iron formation (Fig. CS9-11).

Marble and quartzite outcrops of Paleoproterozoic metasediments of the northern Chantrey Group stand out as spectrally contrasting units on Landsat ETM data. These rocks have a light cyan colour on the bedrock-enhanced Landsat ETM bands 7, 3, and 1 colour composite image that strongly contrasts with the pink background colours associated with Archean

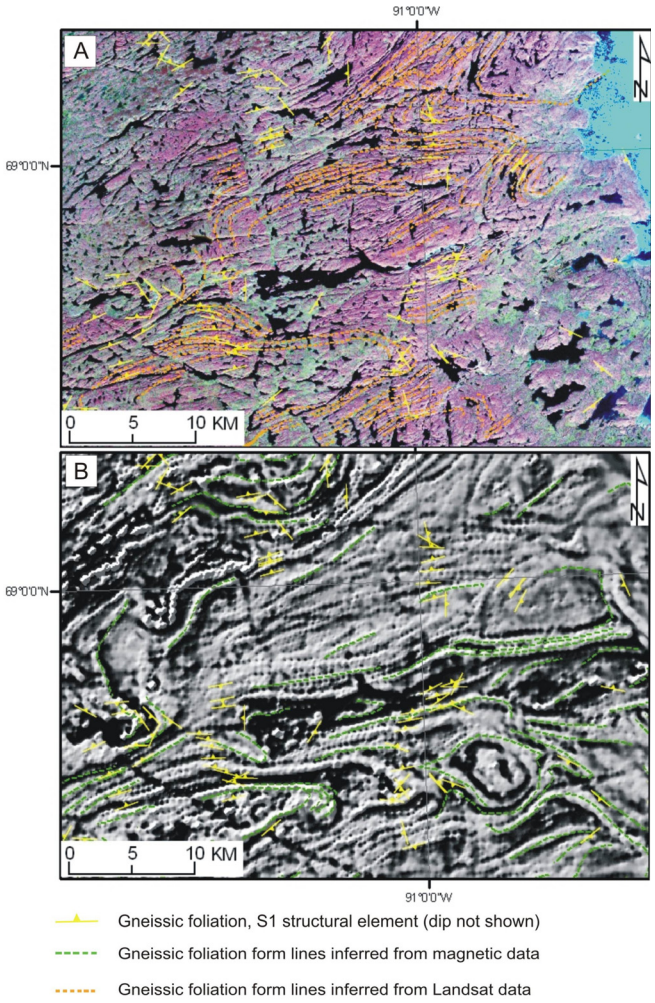

Figure CS9-10. RPM interpretations of gneissic foliation elements. **(A)** Structural interpretation of gneissic foliation from Landsat ETM and gneissic foliation elements. **(B)** Structural interpretation from first vertical derivative magnetic data and gneissic foliation. In both interpretations, the outlines of gneissic foliation trajectories define regional F_4 folds.

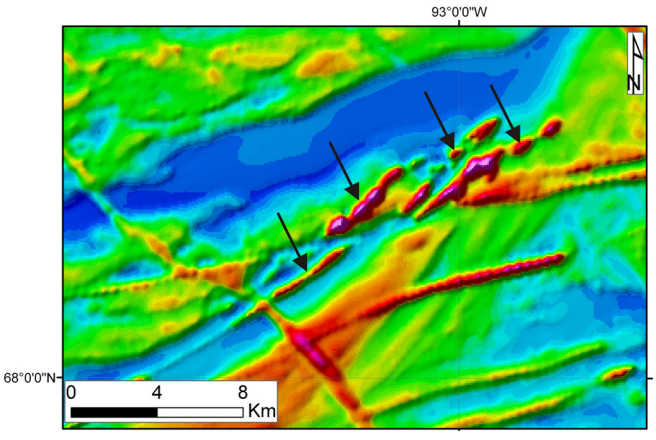

Figure CS9-11. Linear magnetic anomalies on a RTF magnetic grid associated with the Barclay supracrustal belt (featureless magnetic low in blue colour). The prominent linear anomalies (arrows) correspond to iron formation and linear mafic metavolcanic units.

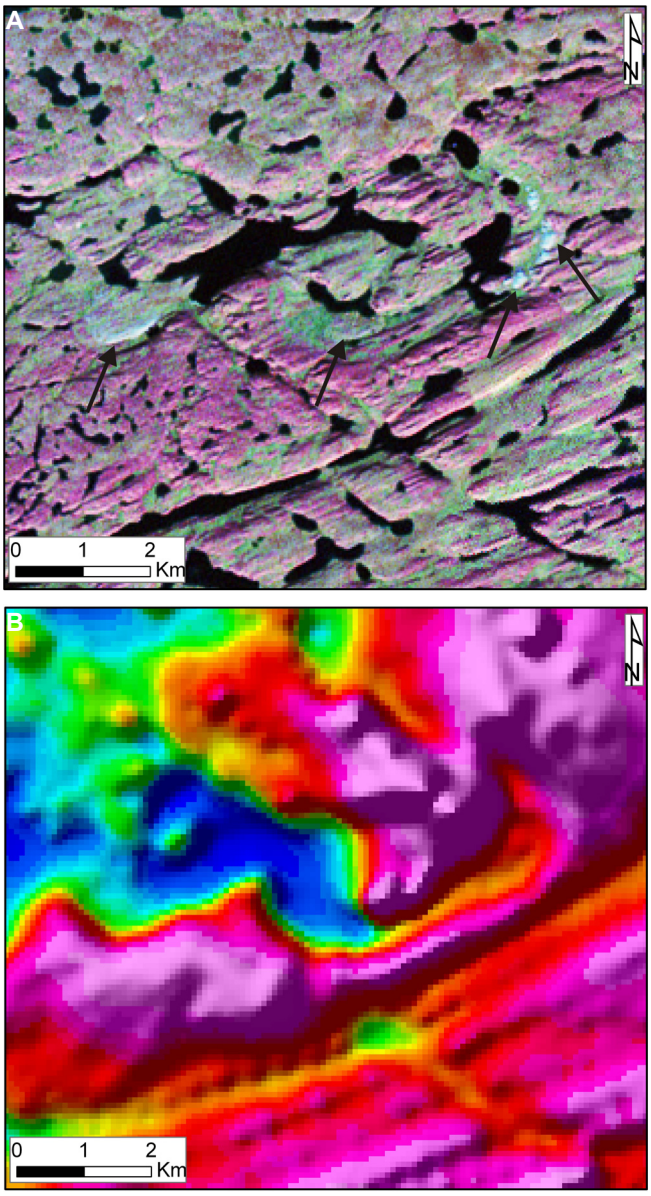

Figure CS9-12. Remote predictive mapping of Chantrey Group units. **(A)** Marble and quartzite of the Chantrey Group corresponding to light cyan tones (arrows) in a pink background of Archean metagranitoids on the bedrock-enhanced Landsat ETM bands 731 colour composite image. **(B)** Curvilinear magnetic low on a colour-shaded relief image of the RTF magnetic grid outlines the same Chantrey Group supracrustals as shown on the Landsat subscene of (A).

metaplutonic units (Fig. CS9-12A). The unique spectral signature of these metasedimentary rocks is due to the carbonate absorption feature in the wavelength range of ETM band 7 and the high albedo (i.e. the spectral reflectance integrated over the full spectral width of the band triplet) of the marble and quartzite outcrops. The metasediments of the Chantrey Group can also be identified on the RTF magnetic grid as a curvilinear magnetic low (Fig. CS9-12B). The Landsat ETM colour composite image, however, provides better diagnostics, since the magnetic anomaly can not be unequivocally differentiated from the magnetic lows associated with occurrences of the Barclay belt.

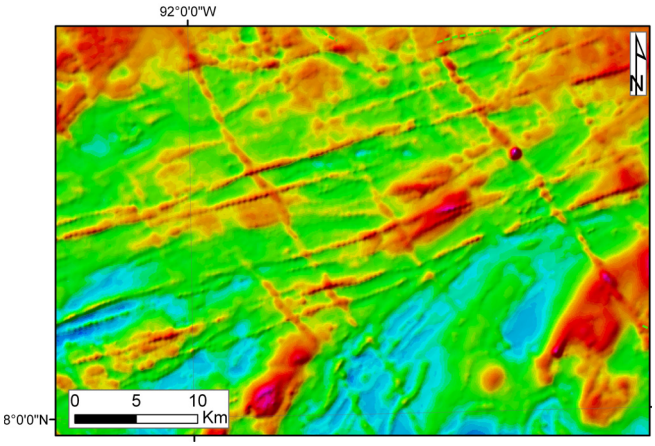

Figure CS9-13. Colour-shaded relief image of the RTF magnetic grid showing the northwest-southeast Mackenzie and unknown west-southwest to east-northeast trending dyke swarms.

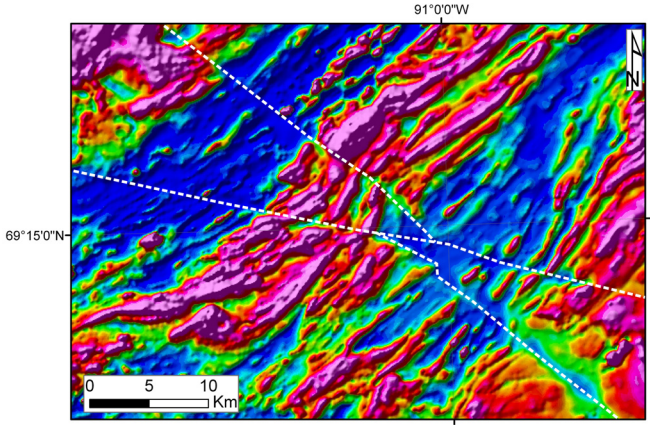

Figure CS9-14. Northwest-southeast and north-south intersecting magnetic lineaments on colour-shaded relief image of the RTF magnetic grid. The opposite sense in apparent offsets and their acute angle of approximately 60 degrees suggest the presence of a conjugate set of brittle shears.

A set of positive linear magnetic anomalies trending NW-SE and E-W to ENE-WSW correspond to the McKenzie and a hitherto unknown dyke swarms (now termed the Pelly Bay dyke swarm; Ryan et al., 2008b), respectively (Fig. CS9-13). Some of these anomalies appear negatively magnetized along their strike. Locally, evidence for surface exposures of these dykes were established using aerial photographs. Faults and brittle shear zones, trending in N-S, NW-SE, E-W, and ENE-WSW directions, mostly parallel to the dyke swarms, are easily recognized on both the magnetic and Landsat TM data. In places, intersection of NW-SE- and N-S-trending faults with consistent opposing apparent offsets suggest the presence of conjugate fault pairs (Fig. CS9-14).

The Phanerozoic cover, consisting of Ordovician limestone and Quaternary till, can be differentiated from the Precambrian basement on both the Landsat and magnetic data. The marine and glacial sedimentary units are recognized on the Landsat 731 colour composite images by their light tone and smooth image texture (Fig. CS8-15A). Linear patterns within the Ordovician limestone correspond to bedding traces. On the 1st, but particularly on the 2nd vertical derivative of the magnetic field, the sedimentary cover shows a lack of the highest spatial frequencies in comparison to the magnetic anomaly spectrum underlain by Precambrian basement (Fig. CS9-15B). The nonmagnetic nature of these sediments has a 'smoothing' effect that is similar to applying an upward continuation to the magnetic data, since the overburden effectively increases the distance between the magnetic sources and the magnetometer.

A number of small circular negative and positive magnetic anomalies were outlined that could not be assigned to any of the known geological features in the area (Fig. CS9-4). Although many of the circular magnetic anomaly patterns in exposed areas were concordant with the local orientation of structures observed in the outcrops, they did not appear to be associated with particular intrusions (or other distinct bedrock units). The majority of the smaller circular features, however, occurred in unexposed areas (mainly muskeg, ponds, and glacial till) so that their identity could not be verified in the field.

GEOLOGICAL FIELDWORK AND MAPPING RESULTS AFTER THE 2005 FIELDWORK (2nd RPM ITERATION)

Field mapping confirmed the results of the 1st RPM iteration in that the Boothia mainland area is dominated by voluminous granitoids. Metamorphic grade increases to the northeast across the study area from middle amphibolite facies in the southwest to granulite facies defining a broad zone in the northeast part of the region (Fig. CS9-5). The boundary between amphibolite- and granulite-facies metamorphism approximately coincides with the boundary between the two major domains outlined in the interpretation of the RTF magnetic grid (Fig. CS9-9). Apart from the granulite-facies domain in the north, there is local preservation of granulite-facies assemblages in the central and southern portions of the study area, suggesting that granulite-facies rocks may have been more widespread than their present distribution. The metaplutonic rocks are generally characterized by biotite ± hornblende ± magnetite monzogranite, as well as volumetrically minor intrusions ranging from diorite to syenogranite. In the granulites to the northeast, the metaplutonic rocks are orthopyroxene-bearing. Although in the 1st RPM iteration granitoid units could not be differentiated, field mapping revealed that porphyritic (augen) varieties of the monzogranite to granodiorite plutonic rocks occur as mappable intrusions throughout the area. Variation in the state of strain is broadly coincident with varia-

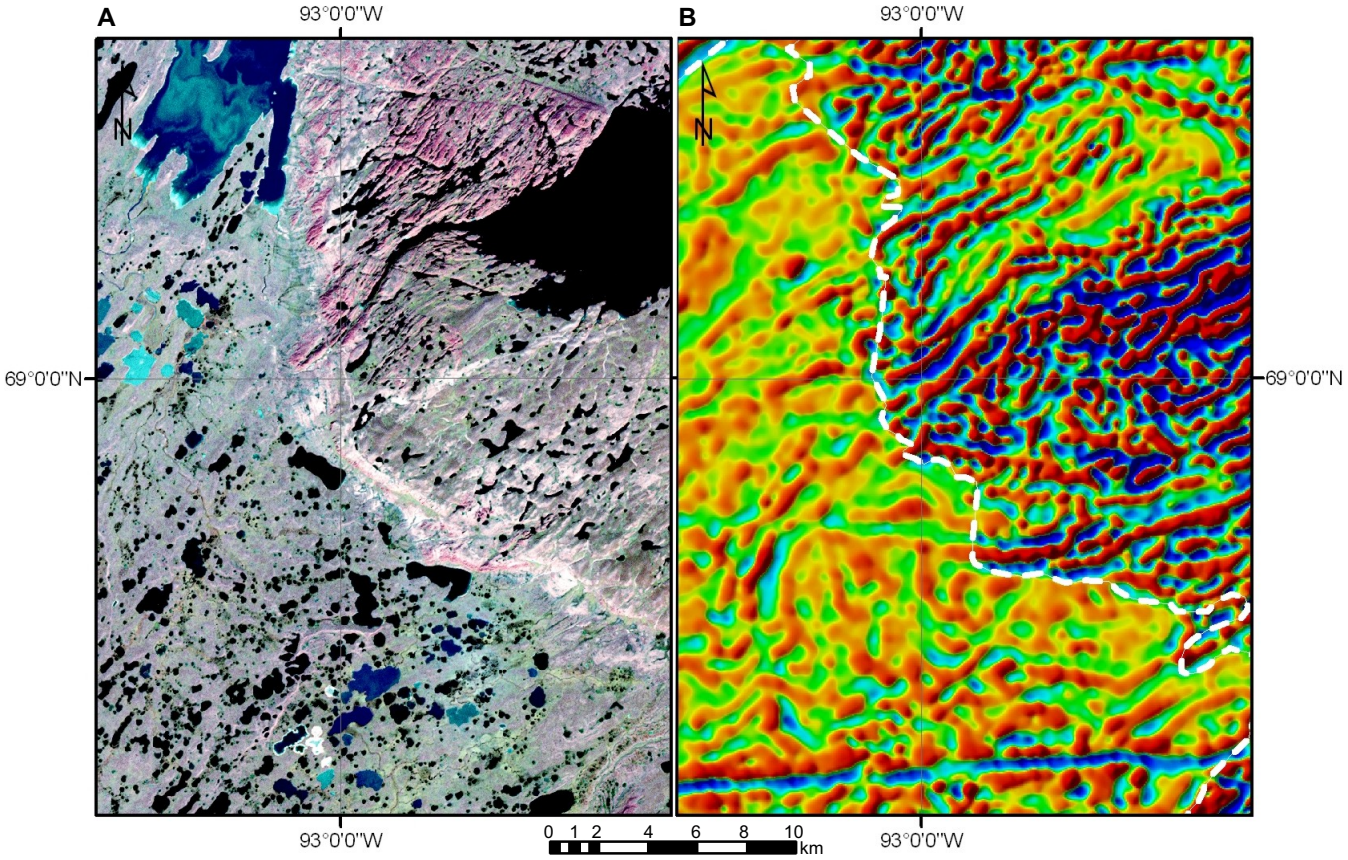

Figure CS9-15. Contact between Archean basement and Quaternary sedimentary cover inferred from a Landsat ETM colour composite image **(A)** and a second vertical derivative image **(B)**. The contact stands out on the Landsat colour composite by contrasting spectral reflectance and image texture (grey-green smooth-textured areas correspond to Quaternary cover, whereas pink linearly patterned areas correspond to Archean basement). The contact (white dashed line) stands out on the 2nd vertical derivative of the magnetic field by contrasting wavelengths of the magnetic anomaly patterns (linear anomaly patterns with high spatial frequency correspond to Archean basement while patterns with lower wave number magnetic anomaly patterns correspond to Archean basement underneath Quaternary cover. Note the east-west-trending, negatively magnetized dyke in the area of sedimentary cover.

tion in metamorphic grade; the metaplutonic suite varies from massive to weakly deformed in the southwest to highly strained and strongly gneissic in the eastern and northern parts of the study area. This trend is consistent with an increase in prominent curvilinear and linear magnetic anomaly patterns towards the northeast (Fig. CS9-9). Preliminary zircon ages indicate that the intrusive rocks are part of a 2.61 to 2.59 Ga pan-Rae magmatic event (Hinchey et al., in prep).

Barclay Belt

Field mapping confirmed that the majority of featureless magnetic lows were underlain by Archean supracrustal rocks, termed the Barclay belt (Frisch, 2000 and references therein). They form narrow, northeast-striking, dismembered belts consisting of volcanic and sedimentary rocks that outcrop discontinuously from the southeast shore of Chantrey Inlet into the Boothia mainland area (Fig. CS9-1). The belts consist mainly of psammite, semi-pelite, metabasalt, local ultramafic horizons, and sulphide-bearing (lean) iron formation, metamorphosed at lower to upper amphibolite facies. U-Pb geochronology studies of a psammitic schist from the belt gave a maximum depositional age of 2764 ±23 Ma based on the youngest detrital zircon (Hinchey et al., 2007). The lithological characteristics of the Barclay belt and the detrital zircon signature suggest that the sequence is correlative with the lower stratigraphic levels of other Archean volcano-sedimentary sequences in the Rae Domain, such as the Prince Albert Group (Hinchey et al., 2007). The metaplutonic rocks and derived gneissic rocks that dominate the region (Fig. CS9-1) are interpreted to have intruded this package of supracrustal rocks. In the southwestern portion of the map area, the supracrustal rocks preserve upper greenschist-facies to lower amphibolite-facies metamorphic conditions.

Northern Chantrey Group

The second supracrustal sequence in the Boothia mainland area is dominated by marble, pelitic schist with minor psammitic schist, and quartzite layers (Fig. CS9-5). This succession is preserved as two complex infolds in the central map area and unconformably overlies the foliated monzogranite intrusions that dominate the region (Fig. CS9-5). Both were recognized as

supracrustal belts from their magnetic signatures on the magnetic data. Only the most westerly in-fold, however, was identified on spectral contrast on the Landsat ETM colour composite image, which permitted its differentiation from the Archean supracrustal inliers of the Barclay belt. The sedimentary package was metamorphosed to at least upper-amphibolite facies conditions synchronous with folding (F_4) and the pelitic units contain garnet-sillimanite-cordierite-bearing leucosome. The correlation of this unit with the Chantrey Group, exposed some 120 km to the south-southwest, is based on lithological affinities and the absence of intrusive relationships with Neoarchean intrusive bodies. U-Pb geochronology studies of two samples of psammitic schist from different stratigraphic levels within the dominantly marble-quartzite sequence of the northern Chantrey Group gave a maximum depositional age of 2454 ±13 Ma based on the youngest detrital zircon age (Hinchey et al., 2007). The detrital zircon signature and lithological characteristics support the correlation of this package with the Paleoproterozoic sedimentary sequences that occur throughout the Rae Domain, including the Chantrey Group as well as the Amer, Ketyet River, and Piling groups (Hinchey et al., 2007).

Migmatite

The central portion of the map area is underlain by a region of migmatite derived from both metasedimentary and metaplutonic protoliths, indicating that these rocks were subjected to high-temperature metamorphism. The migmatite domain broadly coincides on the RPM to an undifferentiated unit of intermediate to mafic gneiss, schist, and amphibolite, recognized on relatively high magnetic background values on the RTF magnetic grid. The migmatitic nature of this unit was not recognized in the 1st RPM iteration (i.e. before field mapping) because the limited dimensions of the hand samples did not show the spatial context of mafic and felsic components of migmatized rocks. Determining the age of this migmatization event(s) is complicated, because regional metamorphism in this area appears to be polyphase. Also complicating the issue is confident determination of the migmatite protolith; while metasedimentary protoliths are easier to determine where index minerals like aluminum silicates and garnets are present, melted plutonic rocks tend to yield fewer hints of protolith.

Crosscutting Diabase Dykes

Paleoproterozoic and Archean rocks and the structures they carry, are cut by three sets of undeformed diabase dykes, which are conspicuous on the colour-shaded relief images of the high-resolution magnetic data. The oldest, northwest-trending dykes are provisionally assigned to the Mackenzie and Franklin swarm. The east and east-northeast-trending sets, which were not previously recognized and have no known correlatives (Nadeau et al., 2005), have recently been named the Pelly Bay swarm (Ryan et al., 2008b). Because the east-trending sets are cut by the northwest-trending dyke swarm that are provisionally associated with the Mackenzie swarm dated at 1267 Ma (LeCheminant and Heaman, 1989), all regional deformation and metamorphism is considered to be older than 1267 Ma.

Structural Geology

The state of strain varies regionally, from mainly massive rocks in the southwestern part of the study area to strongly gneissic, migmatitic, and highly strained rocks in the east and northern part of the study area (Ryan et al., 2008b; Berman et al., in press). Metamorphic grade varies from lower amphibolite-facies andalusite-staurolite-bearing rocks in the southwestern volcanic belt to granulite facies in the north and northeast. The granulite-facies rocks are characterized by an assemblage of orthopyroxene-clinopyroxene-garnet in metaplutonic rocks and orthopyroxene-biotite-garnet-silica-corundum-k-feldspar in metasedimentary rocks.

Except for in the very well exposed north-central part of the area, the combination of fracture and weathering patterns, as well as glacial cover, make it difficult to decipher the structural grain across the area from air photographs and satellite imagery. However, a highly variable structural fabric across the area is extremely well exhibited by the first vertical derivative magnetic field (Coyle et al., 2005), which is consistent with structural measurements recorded at field stations. Through the high-amplitude linear magnetic anomalies caused by dyke swarms, a strong northeast-trending structural grain is evident, which is typical of the north-central Churchill Province (Fig. CS9-1). Analysis of the structural field data shows that the northeast-trending fabric is dominantly northwest-dipping and apparently southeast-verging.

At any location in the study area there is generally one main foliation (S_1), which varies in character from schistosity in metasedimentary rocks, to shape fabric and strong mineral alignment in metaplutonic rocks, to strong gneissosity at higher grade and higher strain equivalents. The gneissosity tends to be accentuated by injected igneous veinlets. Throughout the survey area, the strike of linear and curvilinear magnetic anomaly patterns shows a strong correlation to the strike from structural compass measurements of this fabric (Fig. CS9-10). Although evidence for a pre-S_1 fabric was seen very locally in some migmatitic rocks, this fabric is not systematic or prevalent. S_1 foliation occurs only in Archean rocks and is prevalent in metaplutonic rocks across the entire area. Preliminary geochronology

results indicate that S_1 foliation developed at ca. 2.60 Ga (Berman et al., in press; Hinchey et al., in prep) demonstrates that the main foliation at any one locality is not always S_1, but sometimes an overprint on S_1. This has important implications for interpreting the mineral fabric relations. Field relationships indicate that the main migmatization event (M1) through the central part of the area was synchronous with S_1 foliation development. Berman et al. (in press) determined that in the granulite belt, S_1 foliation and M1 migmatization occurred at granulite facies at 2.60 Ga. This age is consistent with findings in the southeast part of the study area, where a pegmatite that crosscuts S_1 foliation is dated at 2.58 Ga (Hinchey et al., in prep). Local metre-scale, isoclinal F_2 folds of S_1 foliation are difficult to link to map-scale folds and we assume that these folds formed late in the same, progressive deformational event (D1) as the S_1 foliation.

Berman et al. (in press) distinguished a second metamorphic event (M_2) in the Boothia mainland by in situ dating of monazite rim overgrowths and matrix monazite at between ca. 2.5 Ga and ca. 2.35 Ga, probably reflecting the Arrowsmith Orogeny recorded in the Committee Bay region (Carson et al., 2004; Berman et al., 2005). In the Boothia mainland area, no deformational fabric has yet been linked to this metamorphism. It is possible that F_2 folds could actually be associated with M_2.

The next fabric element (S_3) in the area is the first foliation recorded in the folded metasedimentary panels of Paleoproterozoic northern Chantrey Group. This foliation was not recognized in the Archean basement rocks, which suggests that it only developed in the Chantrey Group. The north-dipping structural geometry of the Chantrey Group indicates that it dips under the Archean basement, possibly indicating that the Archean rocks are thrust over the Chantrey Group. It is possible that the development of the localized S_3 fabric was associated with this thrusting event.

A regionally pervasive set of northeast- to east-northeast-trending folds (F_4) controls the structural geometry and map pattern across the area and deforms Archean and Paleoproterozoic rocks. These folds are well outlined in the aeromagnetic data. It is difficult to determine the vergence of the F_4 folds, but they generally appear to verge south. There is generally no axial planar S_4 foliation developed in the metaplutonic rocks, however, a weak crenulation cleavage is seen locally in the northern Chantrey Group and the Barclay belt. The F_4 folding is tentatively linked to a ca. 1.83 to 1.80 Ga phase of metamorphism (M_3) identified in monazite in the central and southern portions of the area by Berman et al. (in press). It is possible that the S_3 foliation and the F_4 folding are part of the same progressive deformation event. F_4 folds in Boothia mainland area correlate with D_2 deformation in the Committee Bay area (Carson et al., 2004; Berman et al., 2005).

A more weakly developed set of northwest- to north-trending F_5 open folds and warps cause F_4 folds to doubly plunge, creating domains of dome-and-basins in the tectonostratigraphy that were detected during the RPM exercise. F_5 folds are interpreted to be Paleoproterozoic since they involve the northern Chantrey Group and F_4 folds. A locally developed north-northwest-trending crenulation cleavage in the northern Chantrey Group (Kraft, 2006) is attributed to an axial planar fabric associated with F_5 folds. This crenulation cleavage probably correlates with F3 folds in the Committee Bay region (Carson et al., 2004; Berman et al., 2005). A ca. 1.79 Ga metamorphic event (M4) has been recorded in the area (Berman et al., in press; Hinchey et al., in prep), which is most likely associated with F_5 folding.

REMOTE PREDICTVE MAPPING ACCURACY ASSESSMENT

A quantitative assessment of the remote predictive map obtained in the 1st RPM iteration was made by tallying the agreements and disagreements between its units and the units of the geological map (RPM 2nd iteration) at 1680 field stations visited during 2005 (note that only a point-to-point comparison at the field stations leads to an unbiased analysis, since the outlines of the geological map units away from the field stations are themselves dependent on both RPM iterations). The legends of both maps, however, are not comparable because the relationships between field diagnostics and imaged physical properties of the bedrock units are inherently incongruent. Consequently, the legends of both maps had to be generalized into 4 classes in order to make a one-to-one comparison possible. The four units of this generalized legend include (i) granulites, (ii) intermediate to basic meta-igneous units, (iii) metagranitoids, and (iv) supracrustal rocks. The two generalized maps with an overlay of the field stations are shown in Figure CS9-16. The statistics of the quantitative assessment are presented in the confusion matrix shown in Table CS9-2. The diagonal elements of the confusion matrix represent the number of field stations at which the 1st RPM iteration and geological maps are in agreement, whereas the off-diagonal elements represent the number of field stations at which the 1st RPM iteration and geological maps are in conflict. The sum of the diagonal elements divided by the total number of field stations yields the overall accuracy of the prediction (82.3%), whereas the row and column sums provide the so called class accuracies and class reliabilities, respectively.

Among the four classes there is an extreme variability in the prediction rates. Note for example that none of

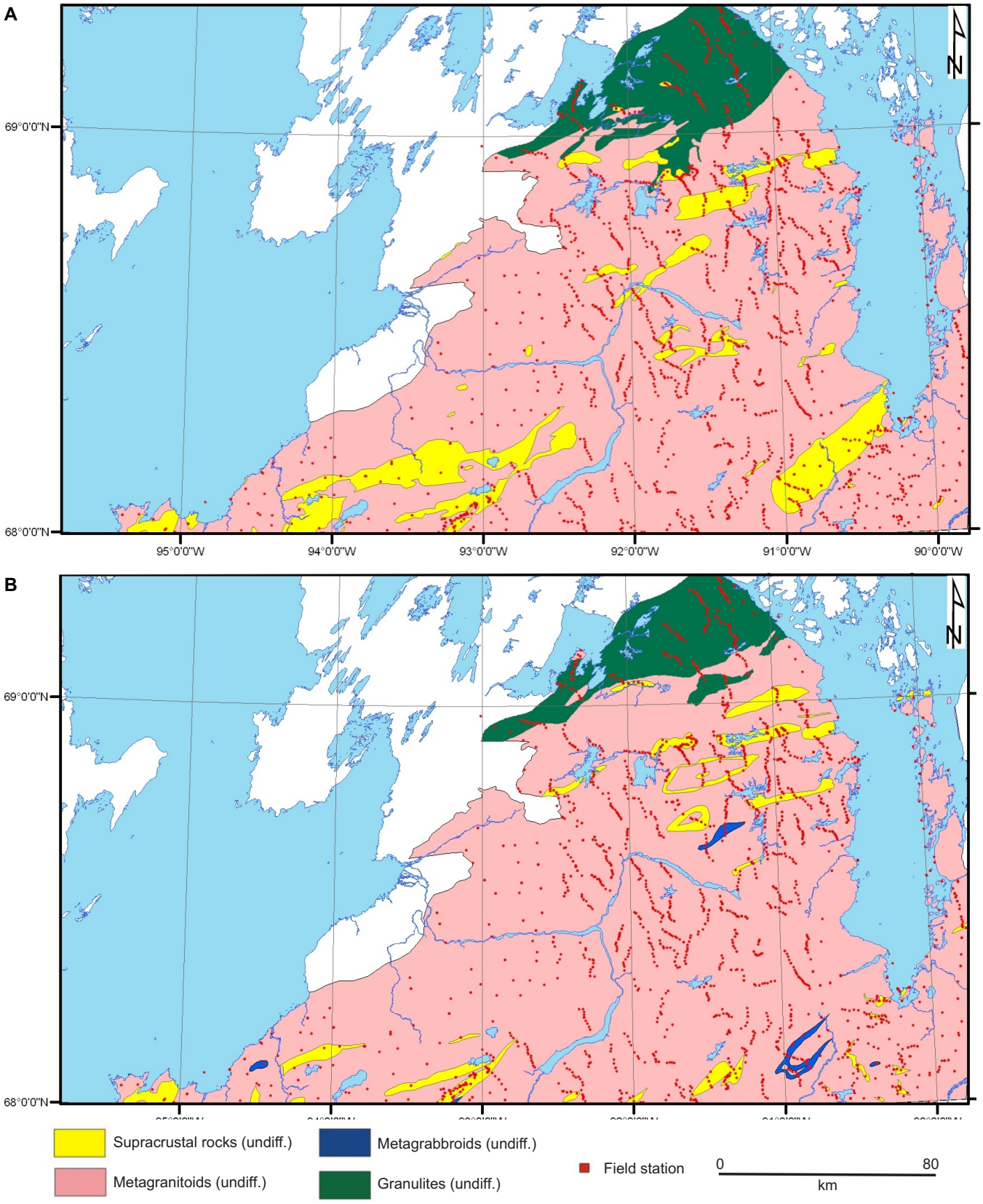

Figure CS9-16. Generalized legend-harmonized geological maps of the Boothia mainland area from the 1st iteration of RPM **(A)** and from the newly published geological maps **(B)** (2nd iteration RPM from the stations of the 2005 field season; Ryan et al., 2008a,b).

Table CS9-2. Confusion matrix showing the matching (diagonal elements) and non-matching (off-diagonal elements) percentages between the generalized RPM and 1: 250 000 scale geological maps at 2005 field stations.

		Generalized units (geological map) at 2005 field stations, Ryan et al. (2007)				
		Metagabbroid	Metagranitoid	Granulite	Supracrustal	Accuracy
Generalized units (Remote Predictive Map) at 2005 field stations	Metagabbroids	0	7	9	1	0
	Metagranitoids	0	1216	17	132	0.89
	Granulites	0	7	106	5	0.9
	Supracrustals	0	112	7	61	0.34
	Reliability	0	0.91	0.76	0.31	
					Average accuracy:	53.20%
					Average reliability:	65.80%
					Overall accuracy:	**82.30%**

the metagabbro occurrences established as a result of field mapping were predicted. This is probably due to their rare occurrence in the legacy rock samples in addition to a lack of diagnostic features that would allow their unique identification in Landsat and magnetic data. On the other hand, generalized unit classes that dominate the area, such as the granulites and metagranitoids, matched the new geological map compilation for approximately 90%. Clearly the metagranitoid and granulite units stand out as regionally distinct magnetic domains with characteristic linear and curvilinear internal anomaly patterns that can be easily differentiated from the featureless magnetic lows associated with the supracrustal belts (Fig. CS9-9). For the supracrustal belts, approximately one out of three (34%) of the field stations matched with the 1st RPM iteration, whereas 2 out of 3 were erroneously classified as metagranitoids. In general, the 1st RPM iteration showed an exaggerated aerial extent of supracrustal units. This either suggests that the near subsurface aerial extent of supracrustal inliers may actually be larger than their exposed surface area or, alternatively, that metagranitoid units with relatively low magnetic susceptibility are misinterpreted as supracrustal rock units. In addition, a magnetic anomaly pattern erroneously interpreted as a supracrustal belt occurs in a F_4 doubly plunging antiformal structure east of the 91º meridian (Fig. CS9-16).

This structure was inferred from the magnetic data on the ground of an elongated positive magnetic subdomain with curvilinear magnetic anomalies. Field mapping, however, revealed that this pattern corresponded to the folded contacts between panels of metadiorite and metamonzogranite (Fig. CS9-16). On the other hand, there are supracrustal belts that were identified in field mapping that were not differentiated by RPM. The omission of these supracrustal rafts in the RPM occur within 20 kilometres south from the 69º parallel (Fig. CS9-13), which may be explained by migmatization events that essentially acted to homogenize igneous and sedimentary protoliths.

CONCLUSIONS

Remote predictive mapping in this study was undertaken through the compilation of a provisional 1:250 000 scale geological map involving integrated interpretation of Landsat and high-resolution magnetic data. The integration of legacy geological field data was particularly useful in constraining the geological interpretation of rock units in a complex terrain dominated by metamorphosed granitoids with limited and/or ambiguous spectral and magnetic susceptibility contrasts between the various mappable units. The new growth of magnetite during prograde metamorphism in the higher amphibolite and granulite facies has obliterated magnetic susceptibility contrasts between protoliths and hence render distinction of bedrock units difficult, particularly in metaplutonic assemblages and migmatized supracrustal units. On the other hand the new growth of magnetite in metaplutonic units that constitute approximately 90% of the bedrock geology has allowed tracing of the regional ductile geological structures, in addition to dyke swarms and faults, over large strike lengths, providing an unprecedented tool for continuous structural mapping in regions of little to no field control. Although RPM obviously could not replace field mapping, it guided mapping and filled in the blanks between sparsely distributed field stations during various stages of map compilation. The following summarizes the most important findings.

The voluminous metagranitoid domains inferred through RPM showed a high correlation to the dominance of metagranitoid units encountered at the field stations visited in 2005 (90% correspondence), which suggested in advance of the field season that the aerial percentage of supracrustal sequences would be low. Subdivision of the metagranitoid domains into the bedrock units that were established during subsequent field mapping, including megacrystic monzogranite, monzogranite, granodiorite and a variety of migmatite units, was not feasible.

The granulite belt was outlined with 90% agreement to the field stations where granulites were encountered. The RPM mapping has essentially shifted the belt north

with respect to its general outline in the regional Churchill compilation map (Patterson and LeCheminant, 1985). The belt outlined through RPM also shows a more sutured folded boundary, in better agreement with the involvement of this interface with lower grade domains as a result of regional Paleoproterozoic folding and thrusting.

There is a relatively low (31%) agreement between the predictions of supracrustal sequences and those encountered at field stations. Some rock types in migmatite in the field, however, were contentious due to difficulty among various geologists in determining protolith of some of the migmatitic rocks. The predicted map pattern of supracrustal rocks through the RPM exercise, however, was more complete than would have come out of fieldwork alone. This is because the supracrustals in the Boothia mainland area are conspicuously poorly exposed and are generally expressed as shallow topographic lows covered by lakes and muskeg. In fact, these conditions made it difficult to examine these feature in detail in the field, due to the danger of walking through deep ice-water laden regions. Much of the supracrustal belts were spot-checked by helicopter stops, limiting our understanding of their context and geological contacts.

Marble and quartzite outcrops of the Paleoproterozoic northern Chantrey Group were identified on their spectral reflectance and high albedo on Landsat ETM colour composite images. Reinterpretation of the Landsat colour composite image has identified additional outcrops of marble and quartzite that were confirmed by follow-up fieldwork in 2007.

In advance of fieldwork, the RPM predicted the likelihood that not all narrow highly magnetic anomalies within magnetic lows would necessarily be iron formations. This held true. Many of these anomalies were simply layers of rocks rich in magnetite porphyroblasts (e.g. amphibolite, pyroxenites, and granite) complicating the interpretation of unit boundaries.

The gneissic foliation patterns inferred through RPM allowed establishing the regional structural pattern in the map area, something that would not have been possible through fieldwork alone. In the northern part of the area, the structural grain could be fairly well identified and outlined by the interpretation of the Landsat imagery. The foliation trends inferred from the Landsat imagery was highly consistent with the curvilinear magnetic anomaly patterns and gneissic foliation strike measurements. In the south however, there was poor topographic expression of the structural grain and therefore, it had to be deciphered almost exclusively from the magnetic data. In all cases, there was excellent correlation between predicted form surface and field structural measurements. Several major folds and faults were predicted, providing good targets for field mapping aimed at solving the structural evolution and searching for fault-related mineralization.

The RPM exercise for predicting field traverses in advance of arriving in the field had mixed success. In well exposed regions, with easier walking, the testing of targets was straightforward and highly valuable. In many regions, however, because the Landsat imagery was generally used at a resolution of 15 m for predicting the traverses, ground conditions dictated that many of these traverses could not be completed at the desired locations because they were cut off by small rivers, swampy muskeg, or small cliffs.

Dyke swarms are evident on the high-resolution magnetic data, particularly on the 1st and 2nd vertical derivatives and tilt magnetic grids. A new dyke swarm (Pelly Bay swarm) was discovered by interpretation of the high-resolution aeromagnetic data. Precious few segments of dyke occurrences were seen in either Landsat or aerial photographs because they do not seem to have much erosive contrast in the Boothia mainland area. They locally form sharp gullies where dykes fractured and were plucked out during glaciation, but these valleys look similar to ice-gouged fractures. Without the aid of the magnetic data and RPM interpretation, occurrences in the field were dependant on serendipity. Fieldwork alone would not have allowed mapping of these feature to much extent, which is why they were generally not observed by Heywood's reconnaissance mapping (Heywood, 1961).

The geological map resulting from the 2nd iteration of RPM was compiled by reinterpreting units and structures, adding the newly acquired field data to the legacy data set in the GIS environment. The approximate twelve-fold increase in size of the geological control data set in this second iteration obviously provided an unprecedented improvement to the geoscience knowledge base. Even at this more advanced stage, however, the integrated interpretation of image and field data is still useful from a geometrical map-quality perspective. Hence, image interpretation still contributed to improving the geometry of units and structures between field control, considering the wide spacing between field traverses typical for 1:250 000 scale bedrock mapping projects in remote regions, such as the Canadian Arctic.

ACKNOWLEDGEMENTS

The 2005 Boothia project field season was funded by the Geological Survey of Canada's Northern Resources Development Program, the Canada-Nunavut Geoscience Office, and the Polar Continental Shelf Project. Special thanks to fellow bedrock mappers Leo Nadeau, Donald James, Alana Hinchey, Hamish

Sandeman, Jamie Kraft, Jenrene Martel James Rae, Andrew Smye, Roxanne Takpanie-Brière, Nesha Trenholm, Kate Rubingh, and Crystal LaFlamme. Hamish Sandeman assisted greatly in the rock archives, and in the field, comparing the geology with that of the Darby Lakes - Arrowsmith River area to the south. Big thanks to Mike Young for setting up the project's Geodatabase, and for assisting in map development. Tracy Lynds helped initially set up the project GIS database and information management, and Steve Williams is thanked for GIS expertise in the field camp, and for developing and setting up our hand-held computer platform that allowed use to access remote sensing images and validate RPM results during field mapping. We thank Maurice Coyle and other members of the GSC's Regional Geophysics Section for expediting and making available the Boothia aeromagnetic survey for our use. We thank Warner Miles and Jeff Harris for a thorough review of the manuscript.

REFERENCES

Berman, R.G., Sanborn-Barrie, M., Stern, R.A., and Carson, C.J.
2005: Tectonometamorphism at ca. 2.35 and 1.85 Ga in the Rae Domain, western Churchill Province, Nunavut, Canada; insights from structural, metamorphic and in situ geochronological analysis of the southwestern Committee Bay Belt; The Canadian Mineralogist, v. 43, p. 409-442.

Berman, R.G., Ryan, J.J., Davis, W.J., and Nadeau, L.
in press: Preliminary results of linked in-situ SHRIMP dating and thermobarometry of the Boothia mainland area, north-central Rae Province, Nunavut, in Current Research 2008-2; Geological Survey of Canada.

Carson, C.J., Berman, R.G., Stern, R.A., Sanborn-Barrie, M., Skulski, T., and Sandeman, H.A.I.
2004: Paleoproterozoic tectono-metamorphic evolution of the Committee Bay region, western Churchill Province, Canada: Evidence from in-situ monazite SHRIMP geochronology; Canadian Journal of Earth Sciences, v. 41, p. 1049-1076.

Chavez, P.S., Sides, S.C., and Anderson, J.A..
1991: Comparison of three different methods to merge multiresolution and multispectral data: Landsat TM and SPOT Panchromatic; Photogrammetric Engineering and Remote Sensing, v. 57, p. 295-303.

Clarke, D.A.
1997: Magnetic petrophysics and magnetic petrology: Aids to geological interpretation of magnetic surveys; AGSO Journal of Australian Geology and Geophysics, v. 17, p. 83-104.

Coyle, M., Dumont, R., Kiss, F., and Potvin, J.
2005: High-resolution maps of the shaded residual total magnetic field and shaded magnetic first vertical derivative with Keating correlation coefficients, Boothia Peninsula area, Nunavut (NTS 57A/SW, 57 A/NW, 57 B/SW, 57 B/SE, 57 B/NW, 57 B/NE, 57 C/SW, 57 C/SE, 57 C/NE, 57 D/SW, 57 D/NW); 22 colour maps, scale 1:100 000, April 2005. http://gdr.nrcan.gc.ca/aeromag/surveys/316_boothia_peninsula_e.php

Drury, S.A.
2001: Image Interpretation in Geology, 3rd edition; Blackwell Science, 304 p.

Frisch, T.
2000: Precambrian Geology of Ian Calder Lake, Cape Barclay and Part of Darby Lake Map Areas, South-Central Nunavut; Geological Survey of Canada, Bulletin 542, 51 p.

Heywood, W.W.
1961. Geological Notes, northern District of Keewatin; Geological Survey of Canada, Paper 61-18, 9 p.

Hinchey, A.M., Ryan, J.J., Davis, W.J., Nadeau, L., and James, D.T.
2007: Detrital zircon geochronology of the Archean volcano-sedimentary sequence of the Barclay belt and the Paleoproterozoic marble-quartzite sequence of the northern Chantrey Group, Boothia mainland area, Kitikmeot Region, Nunavut, *in* Current Research 2007-C1; Geological Survey of Canada, 19 p.

Hinchey, A.M., Davis, W.J., Ryan, J.J., and Nadeau, L.
2008: Neoarchean high-potassium granites of the Boothia mainland area, Rae domain, Churchill Province: Geochronological and isotopic constraints; Canadian Journal of Earth Sciences, in prep.

Hoffman, P.F.
1988: United plates of America, the birth of a craton; early Proterozoic assembly and growth of Laurentia; Annual Review of Earth and Planetary Sciences, v. 16, p. 543-603.

Kraft, J.
2006: Petrology, geochronology and tectonometamorphism of the Paleoproterozoic Northern Chantrey Group, northern Rae Domain, Churchill Province, Nunavut; B.Sc. thesis, University of Alberta, Edmonton, Alberta, 66 p.

LeCheminant, A.N. and Heaman, L.M.
1989: Mackenzie igneous events, Canada; middle Proterozoic hotspot magmatism associated with ocean opening; Earth and Planetary Science Letters, v. 96, p. 38-48.

Lillesand T.M. and Kiefer, R.W.
2000: Remote Sensing and Image Interpretation, 4th edition; John Wiley and Sons Inc., New York, 724 p.

Nadeau, L., Schetselaar, E.M., Ryan, J.J., and James, D.T.
2005: Fracture patterns of the Boothia mainland, Nunavut: An analysis of dykes, faults, fractures and lineaments; 33rd Annual Yellowknife Geoscience Forum, November 16-18, 2005, Program and Abstracts of Talks and Posters.

Patterson, J.G. and LeCheminant, A.N.
1985: A preliminary geological compilation map of the northeastern Barren Grounds, parts of the Districts of Keewatin and Franklin; Geological Survey of Canada, Open File 1138, 16 p.

Ryan, J.J., Nadeau, L., Hinchey, A.M., James, D.T., Young, M.D., Williams, S.P., and Schetselaar, E.M.
2008a: Geology, southern Boothia mainland area, Pelly Bay-Rae Strait-Harrison Island map area, Nunavut; Geological Survey of Canada, Open File, scale 1:250 000, in prep.

Ryan, J.J., Nadeau, L., Hinchey, A.M., James, D.T., Sandeman, H.A., and Schetselaar, E.M.
2008b: Bedrock geology of the southern Boothia mainland area (Pelly Bay-Rae Strait-Spence Bay map areas), Kitikmeot region, Nunavut, in Current Research 2008; Geological Survey of Canada, in prep.

Sanborn-Barrie, M., Skulski, T., Sandeman, H., Berman, R., Johnstone, S., MacHattie T., and Hyde, D.
2002: Structural and metamorphic geology of the Walker Lake Arrowsmith River area, Committee Bay Belt, Nunavut, *in* Current Research 2002-C12; Geological Survey of Canada, 13 p.

Sanborn-Barrie, M., Sandeman, H., Skulski, T., Brown, J., Young, M., MacHattie, T., Deyell, C., Carson, C., Panagapko, D., and Byrne, D.
2003: Structural geology of the northeastern Committee Bay belt, Ellice Hills area, central Nunavut, in Current Research 2003-C23,; Geological Survey of Canada, 13 p.

Sandeman, H.A., Brown, J., Studnicki-Gizbert, C., MacHattie, T., Hyde, D., Johnstone, S., Greiner, E., and Plaza, D.
2001a: Bedrock mapping in the Committee Bay Belt, Laughland Lake area central mainland, Nunavut, *in* Current Research 2001-C12; Geological Survey of Canada, 20 p.

Sandeman, H.A., Studnicki-Gizbert, C., Brown, J., and Johnstone, S.
2001b: Regional structural and metamorphic geology of the Committee Bay Belt, Laughland Lake area, central mainland, Nunavut, *in* Current Research 2001-C13; Geological Survey of Canada, 11 p.

Sandeman, H.A., Schultz, M. and Rubingh, K.
2005: Results of bedrock mapping of the Darby Lake - Arrowsmith River north map areas, central Rae Domain, Nunavut, *in* Current Research 2005-C2; Geological Survey of Canada, 11 p.

Skulski, T., Sandeman, H., Sanborn-Barrie, M., MacHattie, T., Hyde, D., Johnstone, S., Panagapko, D., and Byrne, D.
2002: Contrasting crustal domains in the Committee Bay belt, Walker Lake-Arrowsmith River area, central Nunavut, *in* Current Research 2002-C11; Geological Survey of Canada, 11 p.

Skulski, T., Sandeman, H., MacHattie, T., Sanborn-Barrie, Rayner, N., and Byrne, D.
2003a: Tectonic setting of the 2.73-2.70 Ga Prince Albert group, Rae domain, Nunavut; Geological Association of Canada–Mineralogical Association of Canada–Society of Economic Geologists Joint Annual Meeting, Vancouver, British Columbia, Abstracts Volume 28, p. 158.

Skulski, T., Sandeman, H., Sanborn-Barrie, M., MacHattie, T., Young, M., Carson, C., Berman, R., Brown, J., Rayner, N., Panagapko, D., Byrne, D., and Deyell, C.
2003b: Bedrock geology of the Ellice Hills area and new constraints on the regional geology of the Committee Bay area, Nunavut, *in* Current Research 2003-C22; Geological Survey of Canada, 11 p.

Skulski, T., Sanborn-Barrie, M., Sandeman, H.
2003c: Geology, Walker Lake and Arrowsmith River Area, Nunavut; Geological Survey of Canada, Open File 3777, 2 sheets, scale 1:100,000.

CASE STUDY 10. Lithological Mapping Using ASTER, Belcher Islands, Nunavut

L.M. Wickert[1], P. Budketwitsch[2], and W.A. Morris[1]
1. MAGGIC - McMaster Applied Geophysics and Geological Imaging Centre, School of Geography and Earth Sciences, McMaster University, 1280 Main Street West, Hamilton, ON L8S 4K1
2. Canada Centre for Remote Sensing (CCRS), Natural Resources Canada, 588 Booth Street, Ottawa, ON K1A 0Y7
Corresponding author's email:wickerlm@mcmaster.ca

INTRODUCTION

There is a significant lack of regional-scale or more detailed geological mapping of Canada's Arctic, yet it is this information that forms the primary basis for decisions regarding future resource exploration in the North. While traditional field mapping campaigns produce excellent geological maps, the spatial coverage is limited by the large distances and short field seasons, which are typical of Canada's North. Typically, the funds available to address the gap between the need and availability of geological information are very limited. Consequently, newer, more technologically based solutions are being investigated and implemented. The Remote Predictive Mapping (RPM) project was developed to specifically address this gap, and to help build the link between information provided by geological field mapping and that offered by Earth observation (EO) and associated technologies (Desnoyers and Harris, 2003). This project was initiated by the first author as a topic for doctoral research at McMaster University, during a period of research participation with the Geological Survey of Canada (GSC). The research was undertaken as a contributing study to the Remote Identification Through Predictive Mapping Project, part of Natural Resources Canada's Northern Resource Development Program.

Rock-forming minerals exhibit spectral absorption features predominately in the 0.4 to 2.5 μm range, the visible to near-infrared (VNIR) through to the short-wave infrared (SWIR) regions of the electromagnetic spectrum. Some minerals also exhibit spectral features in the thermal infrared (TIR). Composite characteristic spectral absorption features of different lithologies can often be used to remotely map the geology of an area with a great degree of success. This technology has been demonstrated using both hyperspectral and multispectral imagery for various locations around the world (Abrams et al., 1977; Kruse et al., 2002; Rowan et al., 2004). For regional or larger scale geological mapping, hyperspectral imagery, which provides data for hundreds of bands, can sometimes be cost-prohibitive for both acquisition and subsequent processing. Hence a multispectral spaceborne sensor that provides data for the spectral absorption bands of the prime minerals can provide a cost-effective alternative. Specifically, the Advanced Spaceborne Thermal Emission and Reflection Radiometer (ASTER) multispectral sensor has been used successfully for geological mapping in many parts of the world. Several good examples include lithological applications in California (Rowan and Mars, 2003; Mars and Rowan, 2006), Australia (Rowan et al., 2005) and in Asia (Watts et al, 2005). The aim of this study within RPM project is to provide information on specific capabilities of ASTER data as a geological mapping tool for the Canadian Arctic.

A distinguishing feature of the ASTER sensor is that the spectral bands of the ASTER short wave infrared (SWIR) sensor were designed to measure reflected solar radiation in six bands (1.65, 2.17, 2.21, 2.26, 2.34, and 2.40 μm), from the near infrared (NIR) to the short-wave infrared. This capability of the ASTER sensor increases the spectral-resolution capability of available multispectral sensors significantly, as the only previously available multispectral sensor, LANDSAT-7, only has two bands (5 and 7), centred at 1.65 and 2.22 μm, respectively. Furthermore, ASTER bands are narrower, increasing the spectral resolution from that provided by LANDSAT (Fig. 10-1). This increases the ability of ASTER to differentiate between lithologies, and increases its usefulness for geological mapping significantly. Work carried out by Rowan and Mars (2003) has illustrated that ASTER is capable of differentiating various minerals, although it is generally been shown to be most successful in mapping mineral groups (Rowan and Mars, 2003; Rowan et al., 2003).

STUDY OBJECTIVES

The Canadian Arctic is a somewhat inaccessible and relatively poorly mapped region of Canada. The Belcher Islands lies north of the tree-line and represents an environment suitable for this investigation because it is a relatively accessible area in the Arctic, and has good bedrock exposure due to glacial scouring and relatively little vegetation. The geology of the area comprises a variety of metavolcanic and metasedimentary rock types including erosion-resistant metavolcanic units that produce a measureable topographic relief. Deformation has produced regional-scale structures that are readily apparent in remotely sensed imagery; hence, the study area provides an excellent geological site for validating the spatial and spectral resolving capability of the ASTER sensor for geologi-

Wickert, L.M., Budketwitsch, P., and Morris, W.A., 2008, Lithological mapping using ASTER, Belcher Islands, Nunavut, Case Study 10 *in* Remote Predictive Mapping: An Aid for Northern Mapping, (ed.) J. R. Harris; Geological Survey of Canada, Open File 5643, p. 283-

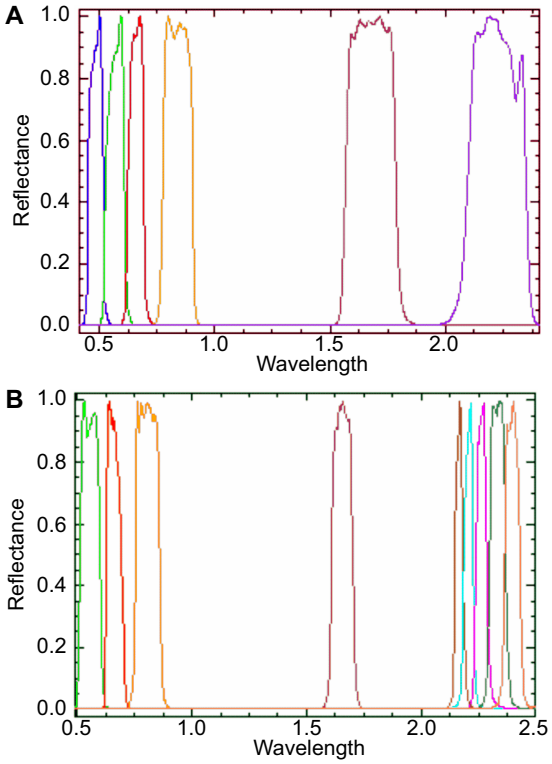

Figure 10-1. A comparison of LANDSAT-7 ETM+ and ASTER spectral response functions, illustrating band position and width, over the visible to short wave infrared (0.4-2.5 µm) range of the electromagnetic spectrum.

cal applications. Prior to this study, lithological mapping had never been demonstrated or reported for a site in Arctic Canada using ASTER data. Important study objectives are to validate if the spectral resolution of the sensor is sufficient to (spectrally) distinguish the different lithological units. Another is to assess whether the spatial resolution of the sensor is sufficient for identifying the various lithologies at the scale of published maps. Specifically, it is the aim of this study is to investigate whether ASTER can resolve and identify lithological contacts, discriminate patterns of sequential lithologies and crosscutting relationships, which in turn can provide information on relative age relationships of geological units, and to determine whether meaningful and accurate geological maps can be produced from ASTER data. A last objective was to identify if any satellite-specific data-processing requirements and techniques are required for the successful use of ASTER imagery for geological mapping. Initial results from this research were published as Wickert and Budkewitsch (2004).

GEOLOGY

The Belcher Group is a series of geological units that are well exposed as low-lying islands in the southeastern part of Hudson Bay, Nunavut (Fig. 10-2). They constitute one of the southernmost segments of the Circum Ungava Fold Belt, marked by two stages of Proterozoic volcanism (Legault et al., 1994). Broadly defined as metamorphosed intermixed volcanic and sediment units, these rocks were deformed during the middle Proterozoic, resulting in the formation of successive north-northeast-trending folds that occur as anticlines and synclines, doubly plunging to the north or south. Later glaciation and deformation of the area led to the relatively low relief and exposure of most of the units in the sequence (Jackson, 1960; Legault et al., 1994).

The first detailed mapping of the Belcher Islands was undertaken at a scale of 1 inch to 2 miles (~1:127,000) by Jackson (1960), during which a total of 16 different units were identified. More detailed mapping and an evaluation of the sedimentary history of the Belcher Group was carried out by Ricketts (1979) and Ricketts and Donaldson (1981). All major formation boundaries in the succession are either conformable or disconformable; no angular unconformities were noted (Ricketts and Donaldson, 1981). A reassessment and reclassification of the lithologies into 14 formations, an undivided unit, and glacial drift (see Fig. 10-3) was carried out more recently by Jackson (G.D. Jackson, pers. comm., 2004).

The thick (7-9 km), laterally continuous sequence of intermixed lithologies of the Belcher Group formed as

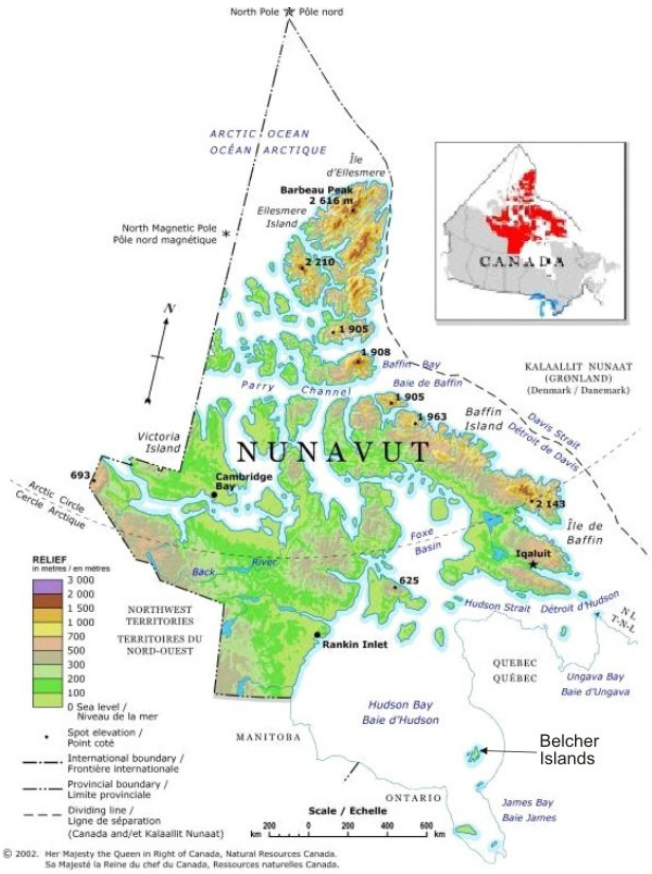

Figure 10-2. Location of the study area, Belcher Islands, Hudson Bay, Nunavut, Canada.

a series of cyclic shallow to deep marine clastic and carbonate units, interrupted by two episodes of mafic (tholeiitic) basalt intrusion (Fig. 10-4) (Legault et al., 1994). Ricketts and Donaldson (1981) and later Ricketts et al. (1982) interpreted the genesis of the Belcher Group as a series of three episodes of sedimentation separated by two phases of tectonic deformation that preceded the main Hudsonian Orogeny event. A fourth episode of deformation, defined by intrusion of a few gabbro dykes (Haig and later intrusive units), has been related to a tectonic event during the Grenvillian Orogeny (Ricketts and Donaldson, 1981). All units are sporadically covered by patches of Quaternary glacial drift (Jackson, 1960).

Clastic metasediments occur as coarsening-up repetitive sequences, with interspersed carbonate-rich horizons. The clastic sequences range in grain size from mudstone up to conglomerate and occasionally breccia. Carbonate horizons are predominately dolomitic and many have been marked by occurrences of stomatolites (Ricketts and Donaldson, 1981). Locally there are some exposures of sedimentary iron- formation in the Kipalu Formation, which have been reported as hematite and magnetite-rich. Other Fe-rich units, such as red argillite, may be present in both sedimentary and volcanic sequences.

The emplacement of the thick laterally continuous basalts of the Belcher Group has been linked in origin to other volcanic units on the margin of the Trans-Hudson Orogen. Although both the Eskimo and Flaherty formations are volcaniclastic, they are compositionally and texturally different, and also vary in minor and trace element (REE) compositions (Legault et al., 1994). The Eskimo Formation is composed mainly of aphanitic to fine-grained basalt, with some coarser grained gabbro, chert, quartz arenite, and red and green argillite with local clastic and carbonate sequences. The basalt consists mainly of massive lava flows, with a pillowed-unit in the centre. The tops of the massive flows are often brecciated and oxidized, indicative of subaerial eruption. Interbedding of Eskimo volcanic rocks with the thinly bedded clastic units may include at times as much as 50% carbonate matrix. A transgressive clastic and carbonate sequence with stromatolitic dolostone and algal mounds directly overlies the Eskimo Formation (Ricketts and Donaldson, 1981). This sequence, along with the thinly bedded nature of the volcanic rocks, is indicative of subaerial exposure.

The younger Flaherty Formation comprises thick dark green-gray aphanitic basalt, and mainly fine-grained clastic sequences (Jackson, 1960). The basalt is predominately pillowed flows, with an increasing tendency for more massive flows towards the east. Interbedded turbidite, and pyroclastic and clastic debris flows are common in the Flaherty Formation. Two prominent coarse debris flows occur near the base. The first two units are composed mainly of chloritized pumice and volcanic fragments, as well as plagioclase and pyroxene phenocrysts. The matrix is predominately calcareous with fine volcanic fragments. The high preponderance of carbonate sediments in the Flaherty Formation, along with the pillowed lavas, is considered indicative of a subaqueous depositional environment (Ricketts and Donaldson, 1981).

DATA

Imaging data used for this study were collected by the Advanced Spaceborne Thermal Emission and Reflection Radiometer (ASTER) sensor (Abrams, 2000). Mounted on the TERRA satellite, this multispectral sensor was designed for Earth observation, with a particular focus on geological and environmental applications. The sensor is consists of three optical subsystems with four telescopes: one telescope with 3 bands in the visible to near infrared (VNIR) (bands 1 to 3), a second VNIR back-looking telescope with a single panchromatic band (3B), a third with 6 bands in the short wave infrared (SWIR) (bands 5 to 9), and a fourth telescope with 5 bands in the thermal infrared (TIR) (bands 10 to 14), for a total of 15 different channels or bands. The spatial resolution varies with the optical subsystem, and is 15 m in the VNIR, 30 m in the SWIR, and 90 m in the TIR. Each ASTER scene is approximately 60 by 60 km. The combination of a down-looking (nadir) and a back-looking VNIR band provides the instrument stereoscopic capability, and hence the ability to generate Digital Elevation Models (DEM) from the data (Fujisada, 1995). TERRA tracks about 30 minutes behind LANDSAT-7 ETM+, and is pointable to allow for an ASTER scene coverage anywhere within the much wider LANDSAT-7 ETM+ swath, which is about 185 km. Abundant background information on the ASTER sensor and the TERRA mission is available from the National Aeronautics and Space Administration (NASA) Jet Propulsion Laboratory (JPL) ASTER website (http://asterweb.jpl.nasa.gov); the ASTER Science Project website (www.science.aster.ersdac.or.jp), and the Earth Remote Sensing Data Analysis Center (ERSDAC) Ground Data System (GDS) website (www.gds.aster.ersdac.or.jp).

ASTER data was collected for this project from the Land Processes Distributed Active Archive Centre (LP DAAC) Earth Observing System (EOS) Data Gateway operated by NASA / United States Geological Survey (USGS). The original objective of this study was to collect multiple scenes of ASTER data covering the entire Belcher Islands, however, a data acquisition request in 2004 did not yield a set of sufficiently snow-free and cloud-free data, and existing scenes of this quality within the archive were limited. Hence, only

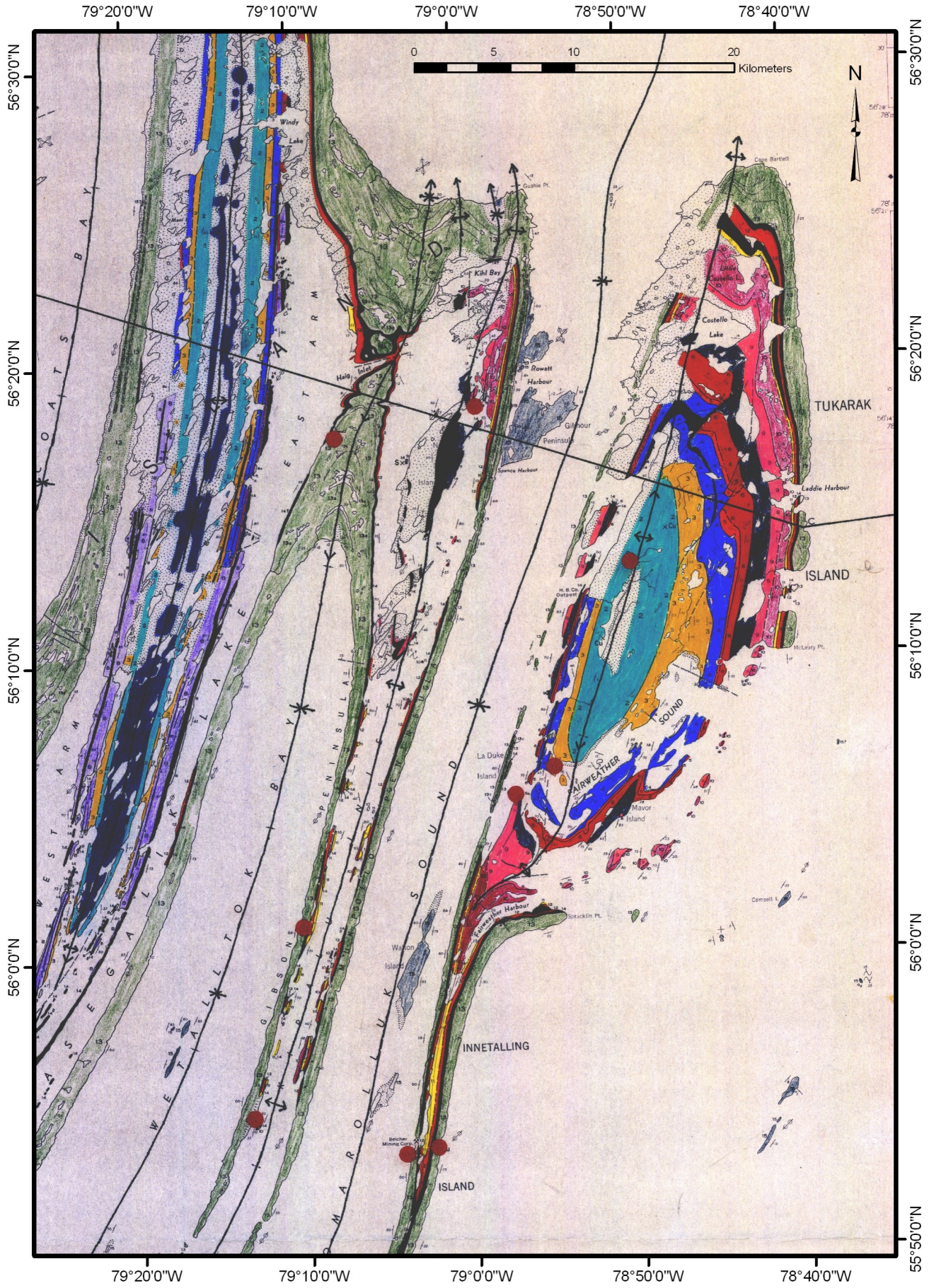
79°20'0"W
79°10'0"W
79°0'0"W
78°50'0"W
78°40'0"W
56°30'0"N
56°20'0"N
56°10'0"N
56°0'0"N
55°50'0"N
0
5
10
20
Kilometers
N
Windy Lake
Kihl Bay
Haig Inlet
Rowatt Harbour
Gilmour Peninsula
Spence Harbour
Cape Bartlett
Costello Lake
TUKARAK
Laddie Harbour
ISLAND
McLeary Pt.
FAIRWEATHER SOUND
La Duke Island
Mavor Island
Fairweather Harbour
Spracklin Pt.
Camsell I.
Walton Island
INNETALLING
ISLAND
Belcher Mining Corp.
WEST ARM
EAST ARM
WETALLTOK BAY
GIBSON PENINSULA
MAROLLUK SOUND

one scene of ASTER data, primarily over Tukarak Island, was obtained (Fig. 10-2). Data collected consisted of a Level 1B processed scene, imaged on 29 September, 2001. Only the VNIR and SWIR data from the ASTER L1B scene were used in this study.

Additional geospatial data were compiled to assist in the evaluation of the ASTER data. National Topographic Database (NTDB) shapefiles of digital topographic vectors from Natural Resource Canada (Centre for Topographic Information (CTI), Sherbrooke; now available from www.geobase.ca), were used to validate coastlines and to help with various masking procedures (see below). Topographic data from the Shuttle Radar Topography Mission (SRTM) were also used to assist with lithological mapping. In the SRTM mission, the Space Shuttle Endeavour collected 3 arc second (~90 metre) digital elevation data worldwide between 60 degrees latitude north and 56 degrees latitude south in February of 2000. Processed C-band SRTM data were downloaded for this study from the JPL SRTM website (http://www2.jpl.nasa.gov/srtm/cbanddataproducts.html) but is now available through the EOS Data Gateway or the USGS National Map Seamless Server (http://seamless.usgs.gov/products/srtm3arc.php).

Data Correction and/or Preprocessing

ASTER level 1A (L1A) data are unprocessed raw image data with appended radiometric and geometric correction coefficients. The data are most suited for DEM generation, and not for spectral mapping. ASTER L1B data are unprocessed raw radiance at sensor data that has been radiometrically calibrated and geometrically coregistered, and corrected for parallax effects (SWIR). This data set is suitable for spectral applications.

All satellite data, including ASTER, have sensor- or platform-related errors associated with the acquisition process. Many of these corrections are applied prior to the delivery of the data, using the level 1A to level 1B (L1B) processing (PGE) algorithm. These errors are generally known and corrected before the satellite data are distributed to users. Nonetheless, it is important for users to verify some of the predelivery processing applied to the data before making a data selection. For example, it is important to ensure that an acceptable PGE version has been applied to L1A to L1B processing. This is important to ensure that all available and known radiometric and geometric corrections to the distributed data have been applied. PGE version 04.00R07 or later is suggested, based on successive improvements to the PGE processing algorithm. The data collected for this study had PGE version 04.00R10 applied. ERSDAC and the NASA LP DAAC have now moved to on-demand L1A to L1B processing delivery, which means that the latest PGE processing algorithm is automatically applied to the delivered L1B data.

ASTER, being a research sensor, still contains some errors in the distributed ASTER L1B data that should be corrected prior to use for spectral interpretation and mapping. Corrections to the received ASTER L1B data set that should be applied prior to spectral mapping applications include conversion of the data from Digital Number (DN) to radiance, correction for band-to-band crosstalk (discussed in more detail below), and finally conversion of the data from radiance to reflectance. Correction of the data for a scratch on the SWIR interference filter may also be considered for certain applications or data sets, but was not implemented in this study as the impact of this error is small. Additional information on corrections for the scratch on the SWIR filter can be found in Iwasaki and Oyama (2005).

Although the specifications indicate that ASTER L1B data are in radiance, it is actually delivered in units of digital number (DN), and must be converted to

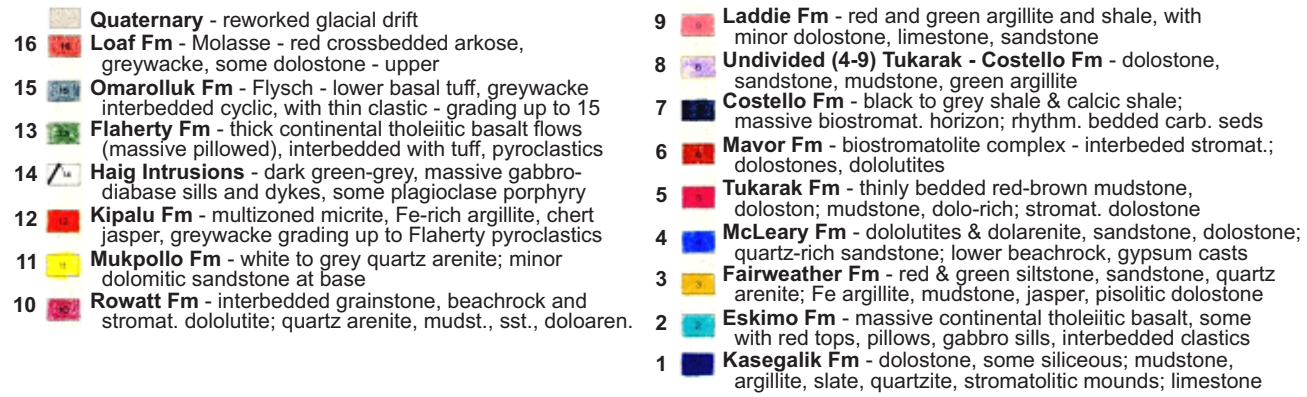

Figure 10-3. Geological map of the study area in the Belcher Islands, primarily Tukarak Island (after Jackson, 1960; Ricketts, 1979). Lithology in the legend was reinterpreted by G.D. Jackson (pers. comm., 2004).

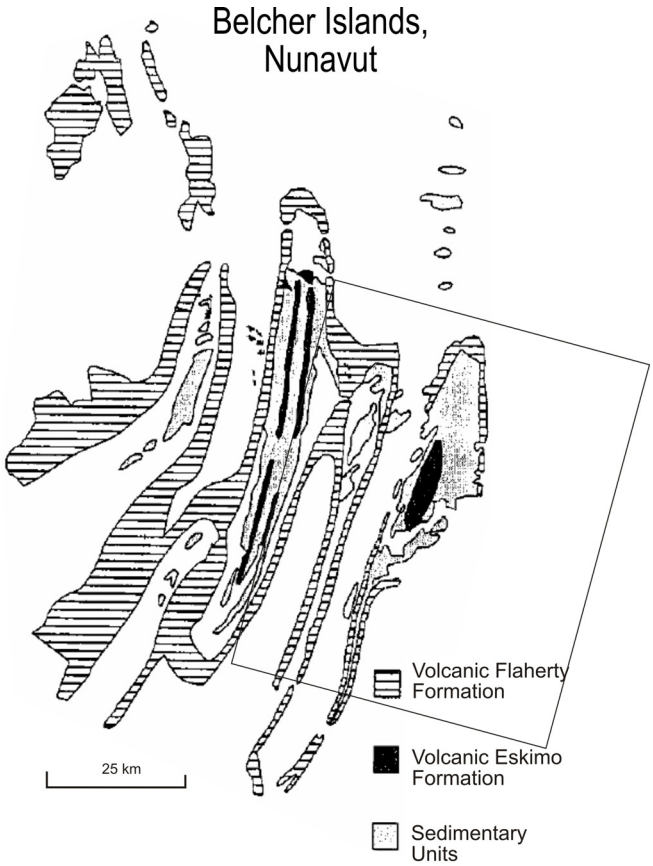

Figure 10-4. Generalized geological map of the Flaherty and Eskimo formations metavolcanic and metasedimentary units in the Belcher Islands (modified from Legault et al., 1994). The box shows the approximate location of the ASTER scene used for this study within the Belcher Islands grouping.

radiance ($W/m^2/sr/\mu m$) via the application of unit conversion coefficients. This is an important step that some researchers often miss with first use of the data. To address this problem, newer versions of many remote sensing processing software packages (i.e. ENVI v.4.2 and later) now automatically apply the unit conversion coefficients when opening ASTER L1B data, ensuring the data is in radiance units when opened. It is important to be aware of the data format at all stages of the processing flow, as well as what transformations are being applied to the data automatically by various software routines. Information on the unit conversion coefficients is available in the ASTER metadata

Crosstalk is a phenomenon that occurs due to leaking of stray light from one band to another within the detectors, which results in higher than expected radiance values for that band (Iwasaki and Tonooka, 2005). Much of the dispersed stray light originates from Band 4, with the biggest impact on the adjacent detectors for Bands 5 and 9 (Hewson, 2002). There are a number of methods for correction of crosstalk, including a dark point correction (Cudahy, 1999). Crosstalk correction for this scene was carried out using the Earth Remote Sensing Data Analysis Centre (ERSDAC) software, Crosstalk3 (Earth Remote Sensing Data Analysis Centre, 2003).

A final correction is conversion of the data from at-sensor radiance to at-surface reflectance, which involves accounting for water vapour and other spectral absorption features originating from the atmosphere. There are a number of methodologies for accomplishing this, including Flat Field Correction (FFC), Internal Average Relative Reflectance (IARR), and empirical line correction (ELC) or the use of a MODTRAN (MODerate resolution atmospheric TRANsmission) based atmospheric correction algorithm implemented in software routines such as FLAASH (Fast Line-of-Sight Atmospheric Analysis of Spectral Hypercubes) or ACORN (Atmospheric CoRrection Now). The first three methods are typically faster and most often used for a single scene correction, and will produce a correction to at-surface relative reflectance based on estimates of atmospheric conditions from in-scene information.

In this case study, a conversion from at-sensor radiance to at-surface relative reflectance was carried out using the IARR method, in which images are normalized to a scene average spectrum. As the majority of the landmass in this scene is surrounded by water, a water mask was first generated for the ASTER L1B data using a combination of coastline, SRTM and ASTER spectral data. The ASTER L1B data were then masked to isolate the land pixels over the study area during the IARR conversion to at-surface reflectance.

Corrections were also carried out on the SRTM data prior to use. A total of six 1 degree by 1 degree SRTM data tiles with a 3 arc-second grid for the Belcher Islands were downloaded from the JPL website. The data tiles were mosaiced to provide complete coverage over the islands, then corrected for no-data holes and errors. After data correction, the SRTM data set was smoothed and interpolated to provide a continuous relief surface for the Belcher Islands, and for visualization purposes, was cropped to the area of the ASTER L1B scene.

Spectral Data Processing and Results

ASTER L1B data, corrected to apparent reflectance, were processed further for geological mapping applications. The first step in such mapping is to ensure that the contributions from any non-geological sources are minimized. For this data set, this required the construction of image masks for vegetation and clouds. The data set had already been masked for water, as previously mentioned. The ASTER L1B scene used in this study was generally cloud-free with a low density of vegetation cover comprising mainly grasses and lichen (G.D. Jackson, pers. comm., 2004). Vegetation within the study area was found not to be a barrier for geolog-

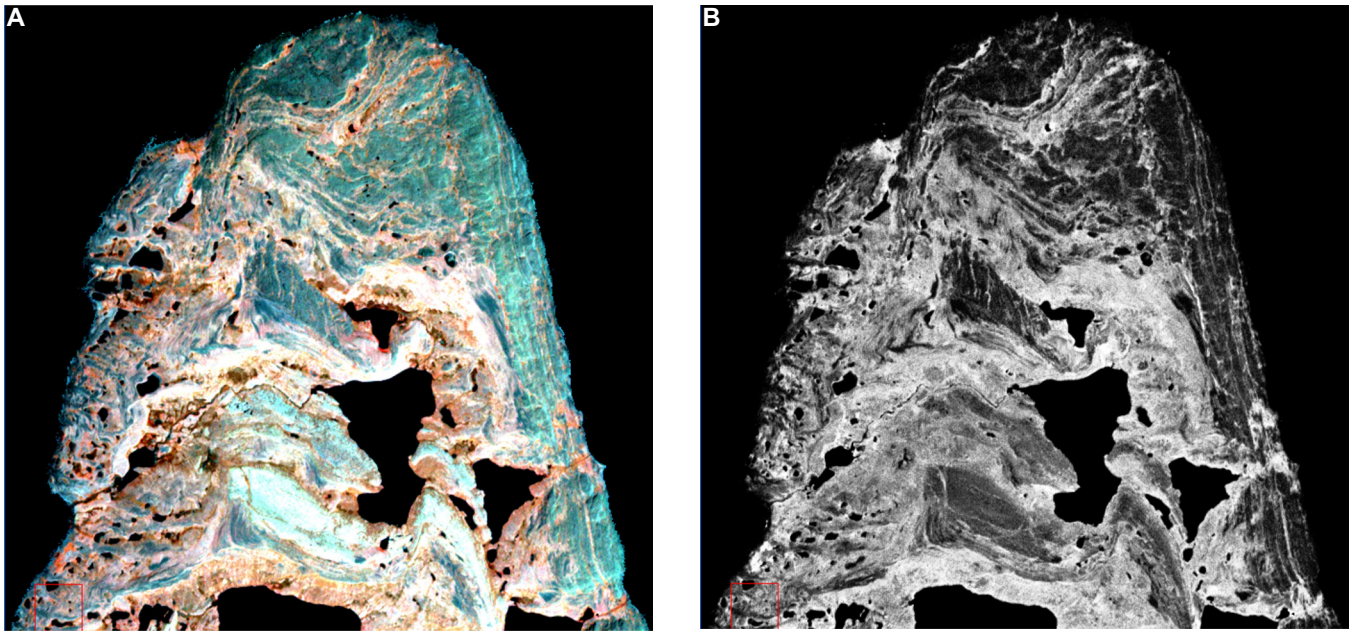

Figure 10-5. ASTER image data of the northeast portion of the Belcher Island within the study area. **(A)** ASTER visible near infrared (VNIR) image with the vegetation highlighted in various colours of red (bands 3, 2, 1 mapped to red, green, blue), equivalent to LANDSAT-7 ETM+ bands 4, 3, and 2. Areas of more or healthier vegetation will appear as a deeper red colour. **(B)** ASTER Normalized Difference Vegetation Index (NVDI) (band 3 – band 2)/ (band 3 + band 2) calculated from Figure 10-5A. Areas of more vegetation will be whiter in colour. ASTER Path Image; Image date: September 29, 2001.

ical mapping; hence it was left in the scene for further lithological discrimination and mapping. A number of different image processing techniques (many of which are presented in Chapter 5 of this volume) were applied to evaluate the use of ASTER data for geological mapping in this study and are described below. Lastly, ASTER data was orthorectified using the ASTER satellite ephemeris data which is inherent to the L1B dataset, along with the SRTM DEM data. The total elevation difference across the study area was low, less than 100 metres.

Band Imaging Procedures

The first image processing techniques applied included separate evaluations of VNIR and SWIR using RGB (red-green-blue) ternary (colour composite) images, band ratio calculations, and a decorrelation stretch. An equivalent evaluation of the combined VNIR and SWIR data was also undertaken by resampling the SWIR bands to a spatial resolution equivalent to the VNIR data (15 m). Band ratioing of different wavelengths provides imagery that can potentially highlight differences between various lithologies as well as associated vegetation. This is because minerals associated with different lithologies have unique spectral characteristics associated with particular portions of the VNIR or SWIR data. These differences in spectral reflectance characteristics can be demonstrated by displaying different wavelengths (bands) through separate primary colours (RGB) used in additive computer (Figs. 10-5A, 10-6A). The RGB image map in Figure 10-5A highlights the presence of vegetation in red, largely due to the strong spectral response of the vegetation in NIR Band 3. Band ratios work similarly, isolating and highlighting bands at particular wavelengths in the EM spectrum that may be associated with concentrations of clay, iron, or silicate minerals. Band ratios are determined through calculation of a ratio of one band's response over another on a pixel-by-pixel basis, then mapping each ratio to RGB for display. Band ratio methods are useful because effects such as differences in illumination angle, view angle, and topography tend to be minimized in the division process. NVDI (Normalized Difference Vegetation Index) is a common ratio that is often calculated to highlight the presence of vegetation in multispectral imagery. NVDI is calculated by subtracting the spectral radiance for NIR Band 3 (B3) from the predominately red part of the EM spectrum from Band 2 (B2), and then dividing this by the sum of the spectral response of the same two bands. Displaying this ratio as a greyscale image (Fig. 10-5B) results in areas with more vegetation showing up as whiter tones. Other specific band ratios can be used to highlight lithology, as illustrated in Figure 10-6A where the volcanic units are highlighted as green and a greenish yellow, the diabase dykes in white, and the bulk of the sediments in blue. A decorrelation stretch of an RGB image can also be very effective in discriminating lithology. The decorrelation technique enhances the colour differences in an image by removing interband spectral correlation between the bands. A decorrelation stretch on a SWIR

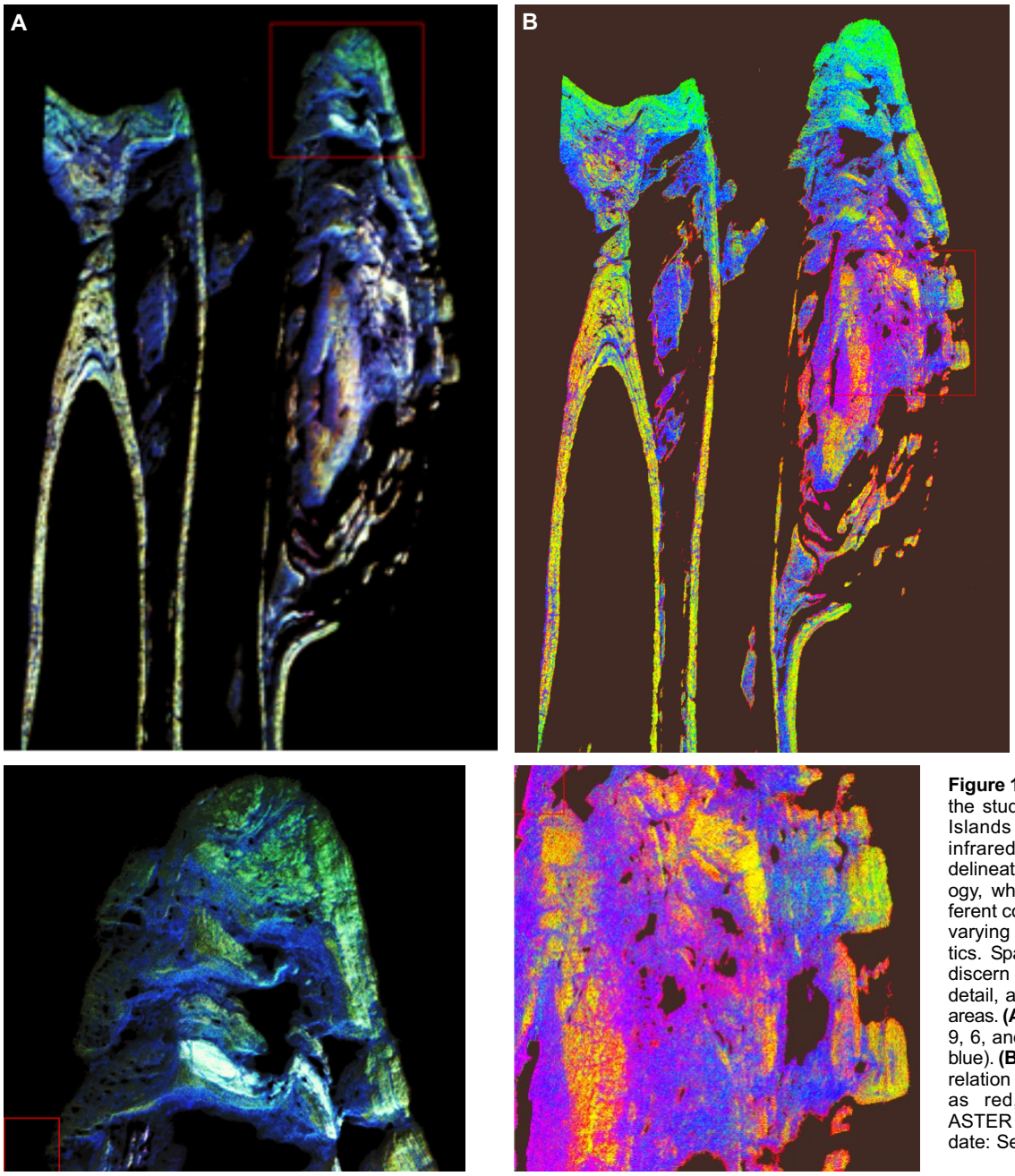

Figure 10-6. ASTER images of the study area in the Belcher Islands using short-wave infrared (SWIR) bands to delineate variability in lithology, which are shown as different colours because of their varying spectral characteristics. Spatially it is possible to discern significant lithological detail, as is shown in zoomed areas. **(A)** ASTER SWIR (bands 9, 6, and 4 as red, green, and blue). **(B)** ASTER SWIR decorrelation stretch (bands 9, 6, 4 as red, green, and blue). ASTER Path Image; Image date: September 29, 2001.

RGB ternary image is illustrated in Figure 10-6B, which highlights broad lithological differences in the volcaniclastic and sedimentary units.

Relative Band Depth Procedures

A second series of techniques utilized for lithological mapping in this study included producing Relative Band Depth (RBD) images (Crowley et al., 1989). This technique involves computation of the magnitude of the signal absorption at a specific wavelength. The background signal level is estimated from the signal observed in adjacent image spectral bands. Central to this approach is the premise that absorption at certain specific wavelengths is directly related to a restricted range of lithological types. If, for example, a particular lithology was identified to have a spectral minimum in SWIR Band 6, then the RBD for band 6 would be calculated by summing the spectral response for each of the shoulders on each side of the spectral minimum (adjacent bands 5 and 7), and then dividing the result by the spectral response for the absorption minima (band 6). One such RBD image Band 7, helps to discriminate between the volcanic and the sedimentary units, as well as highlight contacts and compositional variability between the different units of each group, depending on the colour map applied. Compositional variability for the different lithologies using this digital filtering technique is illustrated in Figure 10-7.

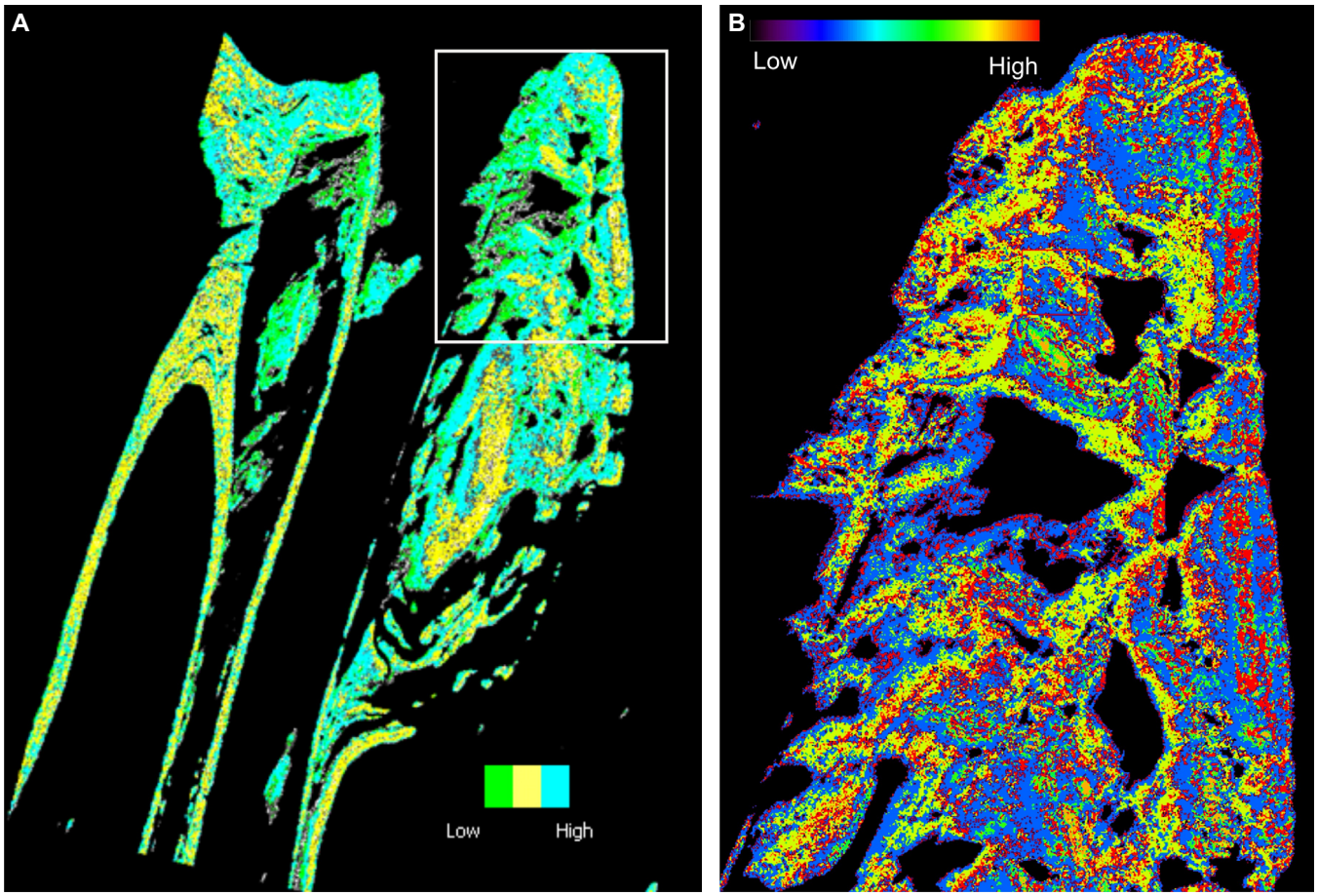

Figure 10-7. ASTER SWIR image over the study area. Lithological discrimination using the Relative Band Depth (RBD) technique with different colour maps applied. Maps illustrates the match of the low or high values to the particular calculated ratio; the values can be linked to the probability of a match to mineral groups associated with certain lithologies and the spectral absorption features within that band. **(A)** ASTER SWIR B7 RBD (calculated using (band 6 + band 8) / band 7). **(B)** ASTER SWIR band 7 RBD (calculated using RBD (band 6 + band 8) / band 7)) over the northern part of Tukarak Island. (Image date: Sept. 29, 2001).

Band Correlation Procedures

The last series of spectral mapping techniques utilized in this study were spectral techniques for correlation and classification for both the VNIR and SWIR data sets. Spectral band correlation techniques that were applied were Principal Component Analysis (PCA) and Minimum Noise Fraction (MNF) transformations, which are particularly effective in highlighting differences in spectral response by minimizing noise. The MNF transformation, in particular, proved very useful for highlighting lithological variation in the study area. Figure 10-8 illustrates an image map of MNF bands 1, 2, and 3 mapped to RGB, which discriminates the volcanic from sedimentary units very well. It is possible to see compositional differences between the two volcanic units, as well as between different members of the sedimentary units. Discrimination is in fact detailed enough to map the position of structural features such as small-scale folding, lineaments, and fault displacements (see boxed area on Fig. 10-8). The reason that the MNF transform works so well is probably related to the primary MNF computational step that derives the local spectral coherence of adjacent pixels. In an ideal geological setting, spatially adjacent pixels that cover the same lithological unit should be spectrally similar. Wavelengths (spectral bands) exhibiting similar spectral response are accentuated relative to those bands that have only noise. Like the PCA transform, the MNF analysis is a linear transform of the data using orthogonal axis to highlight bands with the most uncorrelated spectral information (based on co-variance), but it has the additional 'noise whitening' step which sorts the data based on noise.

It is known that certain minerals can be differentiated using optical remote sensing data. The spectral features of OH-bearing minerals in particular are especially useful in the 0.4-2.5 μm region of the EM spectrum (Clark et al., 1990). In general, it is the oxidized weathering surfaces, many of which contain clay and iron, that provide the distinctive signatures of the lithologies that can be used for spectral differentiation (see Harris et al., 2005). This was the rationale behind the inclusion of band 7 in the later LANDSAT satellites (LANDSAT 5 and 7). Many clay minerals contain Al-

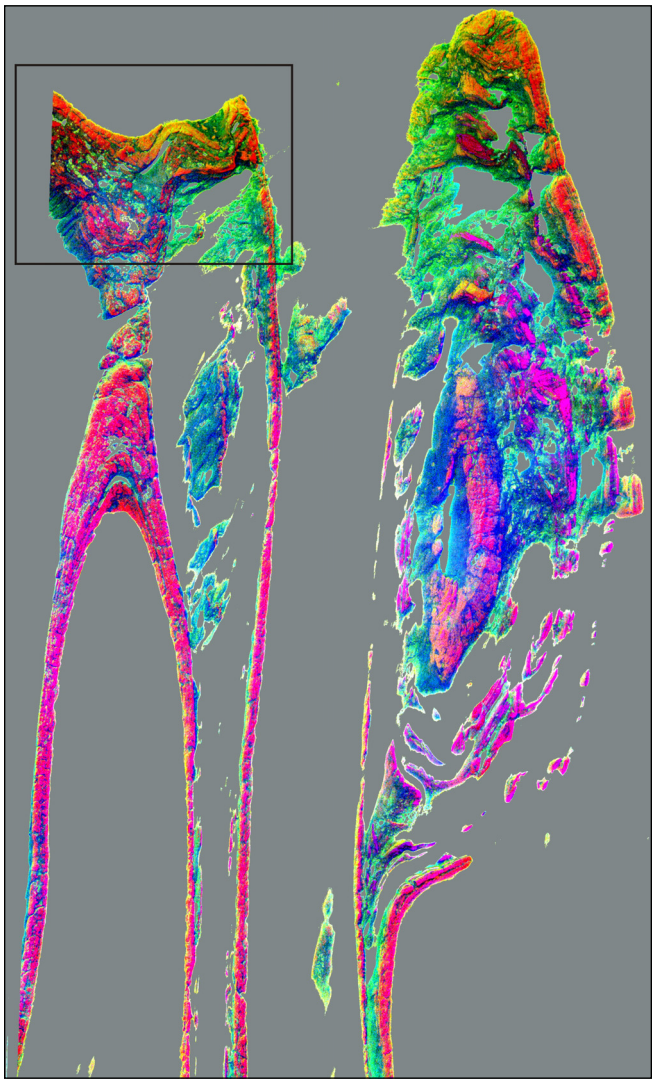

Figure 10-8. ASTER lithological discrimination utilizing the SWIR minimum noise fraction (MNF) technique, Belcher Island (MNF bands 1, 2, and 3 mapped to red, green, and blue). Metavolcanic rocks (Eskimo Formation, Flaherty Formation, and Haig Intrusions) and some carbonate-rich metasediments appear as pink and red; Quaternary and other metasediments appear as green to blue. The box shows the position of the enlarged area in Figure 10-10B.

OH, Fe, Mg-OH, H-O-H, and CO_3 bonds as part of their crystalline structure and each of these bonds are associated with distinctive absorption features that are observed in the SWIR. Similarly, the combined spectral characteristics of the combination of minerals that characterize a particular lithology can be utilized to spectrally differentiate this lithology from the surrounding rocks. An empirical evaluation by the author has shown that while the unweathered fresh surfaces of many rocks may not be spectrally distinct, their surface alteration products are particularly distinct and extremely useful for spectral mapping purposes.

Spectral Matching

By examining existing geological maps it is possible to isolate small areas that are expected to correspond to a

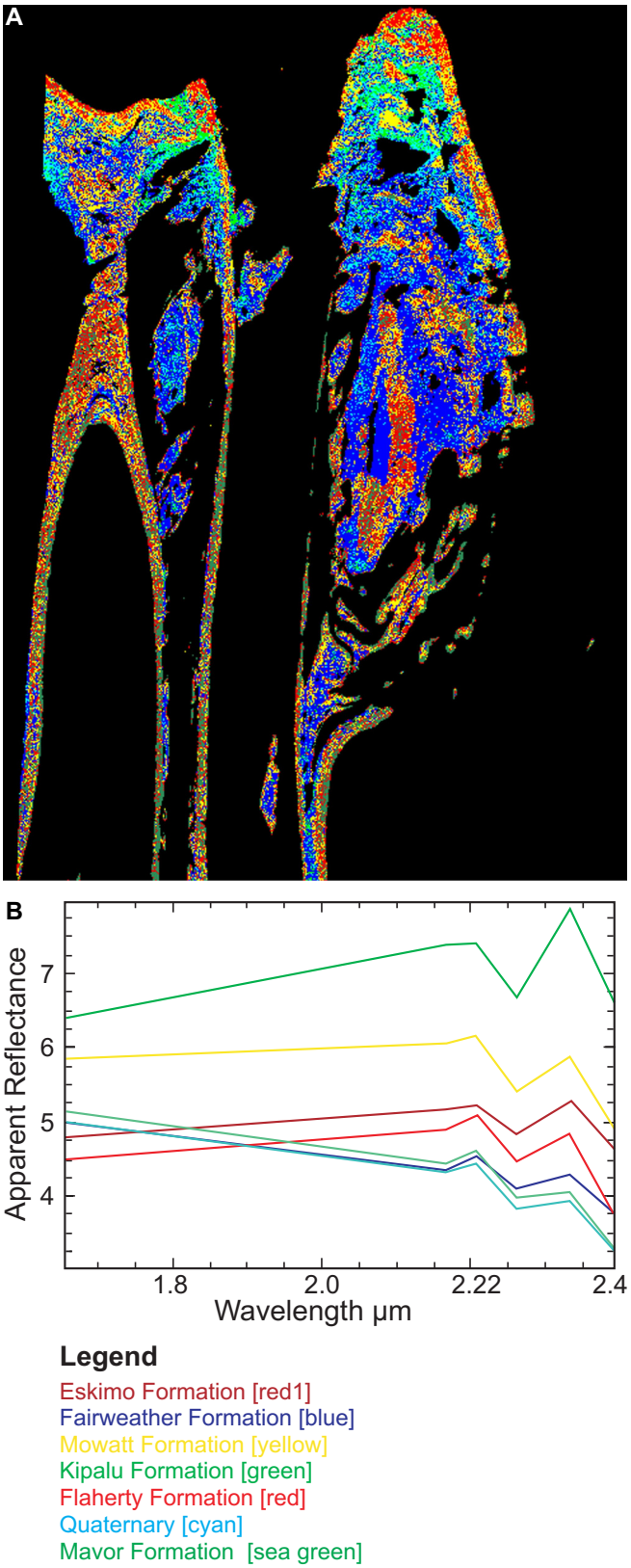

Figure 10-9. Spectral matching results for seven Belcher Island lithologies using the Spectral Angle Mapper (SAM) technique. **(A)** Spectral unmixing results mapped according to the end-member legend. **(B)** Mean end-member spectral signatures for six ASTER SWIR bands (by wavelength). Geological map and legend are shown in Figure 10-3.

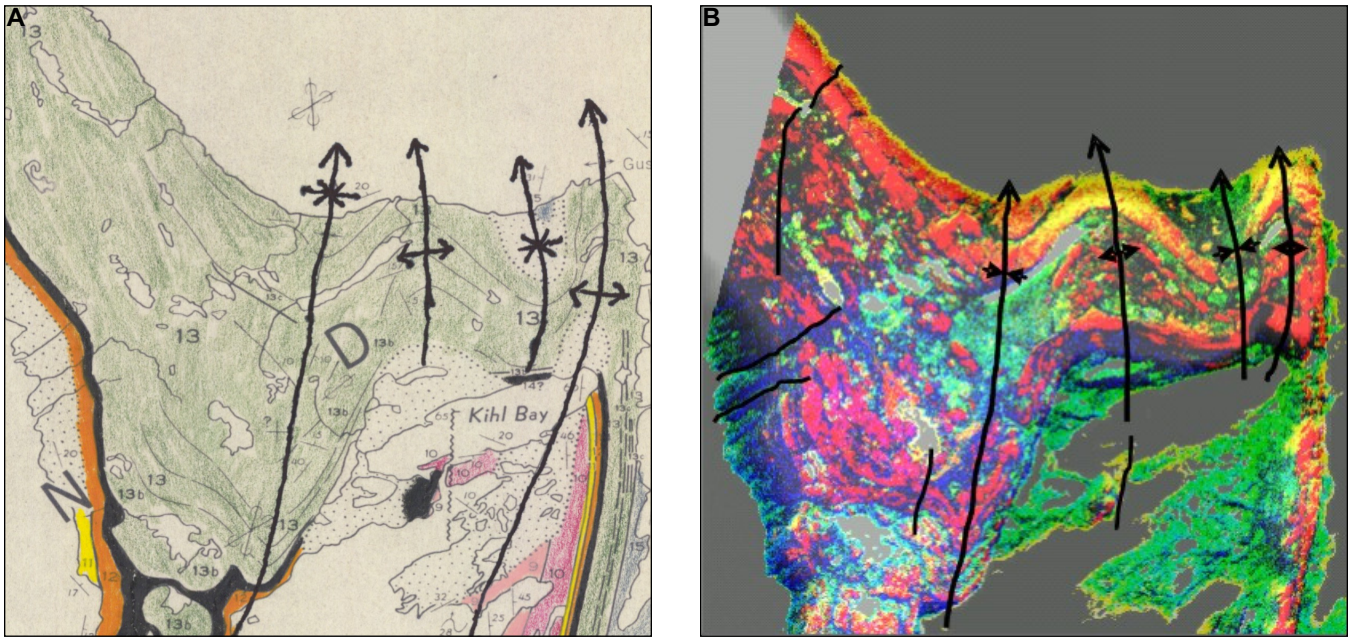

Figure 10-10. Structural interpretation from ASTER lithological mapping. **(A)** Structural interpretation shown on the published geological map from the northern part of Figure 10-3A. **(B)** The image is a structural interpretation of the boxed area in the northern part of Figure 10-8. Other picture edits as indicated above.

single lithological entity. If the image of this same area is associated with a spectrally coherent signal, then one can use the information from the test data set to search for all similar occurrences of the same spectral signature (i.e. supervised classification, see Chapters 2, 4, 5, and 6 of this volume). In this study, information on the location of a specific suite of lithologies was chosen from prior spectral mapping information, as well as the existing geological maps, to aid in spectral matching (classification) procedures. A small region of interest (i.e. training site) was identified for a spectrally representative location for a suite of selected lithologies, and a mean spectral signature (end member) was collected from each training area (Fig. 10-9B). These signatures were then used to create image subsets of the composite VNIR + SWIR data set. Discrimination of spectral similarity between observed pixels and the reference spectral signatures was achieved using the Spectral Angle Mapper (SAM) classification algorithm. The SAM algorithm determines the spectral similarity between two spectra by calculating the angle between the image spectra and the reference spectra; each spectra is treated as a vector in a space with dimensionality equal to the number of bands. SAM compares the angle between the end member spectrum vector and each pixel vector in n-D space. Smaller angles represent closer matches to the reference spectrum. In applying the SAM technique, one must identify some threshold value that discriminates an acceptable level of spectral signature match. The degree of match is then illustrated in a 2-D image map, referenced to the end member spectra for each lithology, as indicated in Figure 10-9A.

Mapping Scale

Although the spatial resolution for ASTER VNIR/SWIR imagery is only 15/30 m, experience has indicated that for areas with a high percentage of rock exposure the imagery can be used for more detailed mapping than regional scale. Most regional-scale mapping in Canada is done at a scale of 1:250.000, with detailed mapping at 1:50,000 or sometimes smaller, depending on the project. An assessment of the level of detail provided by the ASTER imagery was undertaken for this study area relative to the existing 1:127,000 and 1:50,000 scale mapping by Jackson (1960) and Ricketts, (1979), respectively (Fig. 10-10). There is significantly more detail about the location of particular units, their orientation, and relative spatial association with surrounding units from the ASTER data. Furthermore, this added level of detail aids significantly in the interpretation of local structural details, such as faults and their relative movements, crosscutting relationships, as well as the likely position of fold axes in the study area. In fact, such an interpretation can be enhanced considerably through the direct use of topographic information in conjunction with spectral mapping results. This is because changes in lithology are often manifested in changes in surface topography. Figure 10-11 illustrates how the use of the two data sets together can aid significantly in the identification of lithology by utilizing topography together with spectral composition to identify structural details such as faults, folds, and compositional trends.

Although such an interpretation does not replace the advantages of on-site field mapping, the information

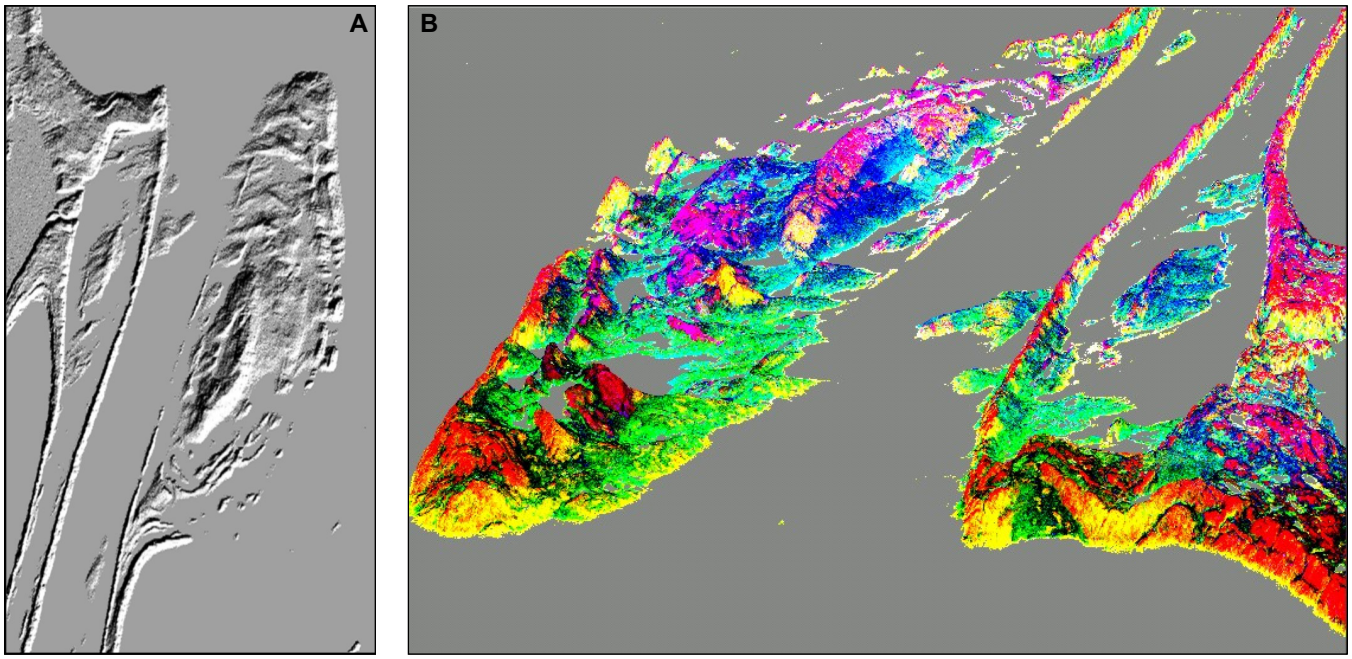

Figure 10-11. Utilization of Shuttle Radar Topography Mission (SRTM) data with spectral results to visualize geological characteristics. **(A)** SRTM data over Tukarak Island in the Belcher Islands, Nunavut case study area, illustrating the topography. **(B)** Draping of the Minimum Noise Fraction (MNF) spectral analysis results over topography, Tukarak Island. The image indicates how volcanic units (predominately purple and red) are more resistant to erosion and hence show up as topographic highs on the surface. Sedimentary units are more susceptible to erosion and are topographically lower (green, cyan, blue, etc.).

generated for every 30 m pixel from such imagery assists significantly in forming an overall geological interpretation of an area, from which portions can be selected for specific field validation. This helps to provide continuous information for map production and, in areas of greater complexity, helps to highlight areas that should be the focus of detailed field mapping campaigns.

CONCLUSIONS AND RECOMMENDATIONS

This study has shown that the VNIR and SWIR data from the ASTER satellite can be used effectively to differentiate and map geological rock types in Canada's North. Satellite-sourced data from the VNIR subsystem of the ASTER sensor is particularly effective in providing a high-resolution (15 m pixel) overview of an area, in which barriers to mapping can be identified, including snow, cloud, cloud shadows, and vegetation. VNIR data is also very effective in differentiating vegetative cover. Data from the SWIR subsystem of ASTER is particularly useful for differentiating mineralogical differences due to a combination of enhanced spectral resolution with 6 bands, with a moderate spatial resolution (30 m pixel). Spectral characteristics of the weathered or oxidized surficial rocks in an area results in a typical mineral mixture that is characteristic of the mineralogical mixture of the lithology. These mixtures become a signature or fingerprint that distinguishes them from each other. When data are collected during snow-free and cloudless conditions, lithological mapping is maximized, as spectral characteristics in the VNIR and SWIR data sets can be used in combination for differentiating between the lithologies. Patterns in differentiated lithology at the surface can also provide information on the structure, timing, and relationships between the different units, which is a by-product of any mapping campaign.

Various techniques can be employed to differentiate and map lithologies, and the best choice for an area is essentially a function of the lithological variability in an area. In this study, differentiation of rock types (i.e. metavolcanic versus metasediment) was relatively easy and could be achieved using simple band mapping, and band math and ratio techniques. More advanced techniques, such as RBD images, or the use of noise reduction algorithms (i.e. PCA or MNF techniques), provided additional differentiation, including the capability of being able to map interformational compositional variability. Lastly, spectral unmixing and classification-based mapping techniques allowed for specific lithological mapping, based on the collection of in-scene end members for selected lithologies. This was illustrated by the ability to differentiate between metavolcanic units, as well as metasediment units (carbonate, clastic, or red beds) in the study area.

The use of ASTER optical satellite data is recommended as a technically productive and cost-effective solution for regional mapping studies in Canada's North. Although ASTER will not provide the level of lithological and mineralogical differentiation that is

achievable when using hyperspectral sensors, it can be said to provide approximately a 70 % solution (depending on the rock type), at a fraction of the cost. It also has the added bonus of highlighting mineral alteration zones due to its sensitivity to mineral oxidation and weathering and, although it can't map individual minerals, it very effectively highlights mineral groups. Hence, if there is a deposit is suspected in an area, it will likely show up as an anomaly, highlighting a need for future investigation. With its additional spectral bands in the SWIR, ASTER provides much more information and mineral mapping capability than the LANDSAT-7 sensor (ETM+), with almost the same data and processing cost (~$2-5/km^2) (Taranik, 2002). ASTER is therefore recommended as an initial geological tool for use in all mapping projects in northern Canada.

ACKNOWLEDGEMENTS

Support for this research was forthcoming from an NSERC IPS with Falconbridge Ltd. (now Xtrata), an NSERC IPS supplement from the Geological Survey of Canada, as well as support from McMaster University (MAGGIC) and CRESTech. Part of this work has been supported by the Canadian Space Agency Government-Related Initiatives Program.

REFERENCES

Abrams, M.
2000: The Advanced Spaceborne Thermal Emission and Reflection Radiometer (ASTER); data products for the high spatial resolution imager on NASA's TERRA platform; International Journal of Remote Sensing, v. 21, p. 847-859.

Abrams, M.J., Ashley, R.P., Rowan, L.C., Goetz, A.F.H., and Kahle, A.B.
1977: Mapping of hydrothermal alteration in Cuprite Mining District, Nevada, using aircraft scanner images for the spectral region 0.46 to 2.34 μm; Geology, v. 5, p. 713-718.

Alley, R.E.
1996: Algorithm Theoretical Basis Document for Decorrelation Stretch, Version 2.2, AST-06; Jet Propulsion Laboratory, 18 p.

Clark, R.N., King, T.V.V., Klejwa, M., and Swayze, G.A.
1990: High spectral resolution reflectance spectroscopy of minerals; Journal Geophysical Research, v. 95, p. 12653-12680.

Crowley, J.K., Brockely, D.W., and Rowan, L.C.
1989: Airborne imaging spectrometer data for the Ruby Mountains, Montana: Mineral discrimination using relative absorption band-depth images; Remote Sensing of Environment, v. 29, p. 121-134.

Cudahy, T.
1999: Mapping the Earth with ASTER; Commonwealth Scientific and Industrial Research Orgnisation Workshop, Geological Remote Sensing Group (GRSP) Annual Meeting, London, December 7-10.

Desnoyers, D.W. and Harris, J.R.
2003: Remote Predictive Mapping – A new tool for geoscience mapping; 31st Yellowknife Geoscience Forum, 19-21 November, Abstract.

Earth Remote Sensing Data Analysis Center
2003: Crosstalk Correction Software Users Guide". Earth Remote Sensing Data Analysis Centre (ERSDAC) website: (http://www.gds.aster.ersdac.or.jp/gds_www2002/service_e/u.tools_e/ cross/ GUIDEED.PDF) , 21 p. (27 November, 2007).

Farr, T. G. Rosen, P.A., Caro, E., Crippen, R., Duren, R., Hensley, S., Kobrick, M., Paller, M., Rodriguez, E., Roth, L., Seal, D., Shaffer, S., Shimada, J., Umland, J., Werner, M., Oskin, M., Burbank, D., and Alsdorf, D.
2007: The Shuttle radar topography mission; Reviews of Geophysics, v. 45, RG2004, 33 p., doi:10.1029/2005RG000183.

Fujisada, H.
1995: Design and performance of ASTER instrument, *in* Advanced and Next-generation Satellites, (eds.) H. Fujisada and M.N. Sweeting; International Society Optical Engineering, v. 2583, p. 16-25.

Harris, J.R., Rogge, D., Hitchcock, R., Ijewliw, O., and Wright, D.
2005: Mapping lithology in Canada's Arctic: Application of hyperspectral data using the Minimum Noise Fraction (MNF) transform and matched filtering; Canadian Journal of Earth Science, v. 42, p. 2173-2193.

Hewson, R.
2002: 22nd ASTER Science Meeting Minutes; Advanced Sspaceborne Thermal Emission and Reflection Radiometer (ASTER) Science Team, May 20-23, Tokyo, Japan, http://www.cossa.csiro.au/reports/hewson/22aster.htm.

Iwasaki, A. and Oyama, E.
2005: Correction of stray light and filter scratch blurring for ASTER imagery; Institute of Electrical and Electronics Engineers (IEEE) Transactions on Geoscience and Remote Sensing, v.43, p. 2763-2768.

Iwasaki, A. and Tonooka, H.
2005: Validation of a crosstalk correction algorithm for ASTER/SWIR; Institute of Electrical and Electronics Engineers (IEEE) Transactions on Geoscience and Remote Sensing, v.43, p. 2747-2751.

Jackson, G.D.
1960: Belcher Islands, Northwest Territories 33M, 34D, E; Geological Survey of Canada, Paper 60-20, 13 p.

Kruse, F.A., Boardman, J.W., Huntington, J.F., Mason, P., and Quigley, M.A.
2002: Evaluation and Validation of EO-1 Hyperion for Geologic Mapping; Institute of Electrical and Electronics Engineers (IEEE) International Geoscience and Remote Sensing Symposium (IGARSS), 24-28 June, Toronto, 3 p.

Legault, F., Francis, D., Hynes, A., and Budkewitsch, P.
1994: Proterozoic continental volcanism in the Belcher Islands: Implication for the evolution of the Circum Ungava Fold Belt; Canadian Journal of Earth Science, v. 31, p. 1536-1549.

Mars, J.C. and Rowan, L.C.
2006: Regional mapping of phyllic-and argillic-altered rocks in the Zagros Magmatic Arc, Iran, using Advanced Spaceborne Thermal Emission and Reflection Radiometer (ASTER) data and logical operator algorithms; Geosphere, May, p. 161-186.

Ricketts, B.D.
1979: Sedimentology and Stratigraphy of Eastern and Central Belcher Islands, Northwest Territories; Ph.D. Thesis, Carleton University, Ottawa, Ontario, 314 p.

Ricketts, B.D. and Donaldson, J.A.
1981: Sedimentary history of the Belcher Group of Hudson Bay, *in* Proterozoic Basins of Canada. (ed.) F.H.A Campbell; Geological Survey of Canada, Paper 81-10, p. 235-254.

Ricketts, B.D., Ware, M.J., and Donaldson, A.
1982: Volcaniclastic rocks and volcaniclastic facies in the Middle Precambrian (Aphebian) Belcher Group, Northwest Territories, Canada; Canadian Journal of Earth Science, v.19, p. 1275-1294.

Rowan, L.C. and Mars, J.C.
2003: Lithologic mapping in the Mountain Pass, California, area using Advanced Spaceborne Thermal Emission and Reflection Radiometer (ASTER) data; Remote Sensing of Environment, v.84, p. 350-366.

Rowan, L.C., Hook, S.J., Abrams, M.J., and Mars, J.C.
2003: Mapping hydrothermally altered rocks at Cuprite, Nevada, using the Advanced Spaceborne Thermal Emission and Reflection Radiometer (ASTER), a new satellite-imaging system; Economic Geology; v. 98, p. 1019-1027.

Rowan, L.C., Simpson, C.J. and Mars, J.C.
2004: Hyperspectral analysis of the ultramafic complex and adjacent lithologies at Mordor, NT, Australia; Remote Sensing of Environment, v. 91, p. 419-431.

Rowan, L.C., Mars, J.C., and Simpson, S.J.
2005: Lithologic mapping of the Mordor, Northern Territory, Australia Ultramafic Complex by using the Advanced Spaceborne Thermal Emission and Reflection Radiometer (ASTER); Remote Sensing of the Environment, v. 99, p. 105-126.

Taranik, D.
2002: ASTER Unveiled; Geological Remote Sensing Group Annual Meeting, December 2002, London, U.K., Opening Address.

Watts, D.R., Harris, B.W., and the NASA 2002 GLENN SOARS Working Group
2005: Mapping granite and gneiss in domes along the North Himalayan Antiform with ASTER SWIR band ratios; Bulletin of the Geological Society of America, v. 117, p. 879-886.

Wickert, L.M. and Budkewitsch, P.
2004: ASTER – A Geological Mapping Tool for Canada's North. Case Study: The Belcher Islands, Hudson Bay, Nunavut, Canada; Proceedings of the Institute of Electrical and Electronics Engineers (IEEE) International Geoscience and Remote Sensing Symposium (IGARSS), 20-24 September, Anchorage, Alaska, v. 2, p. 1300-1303.